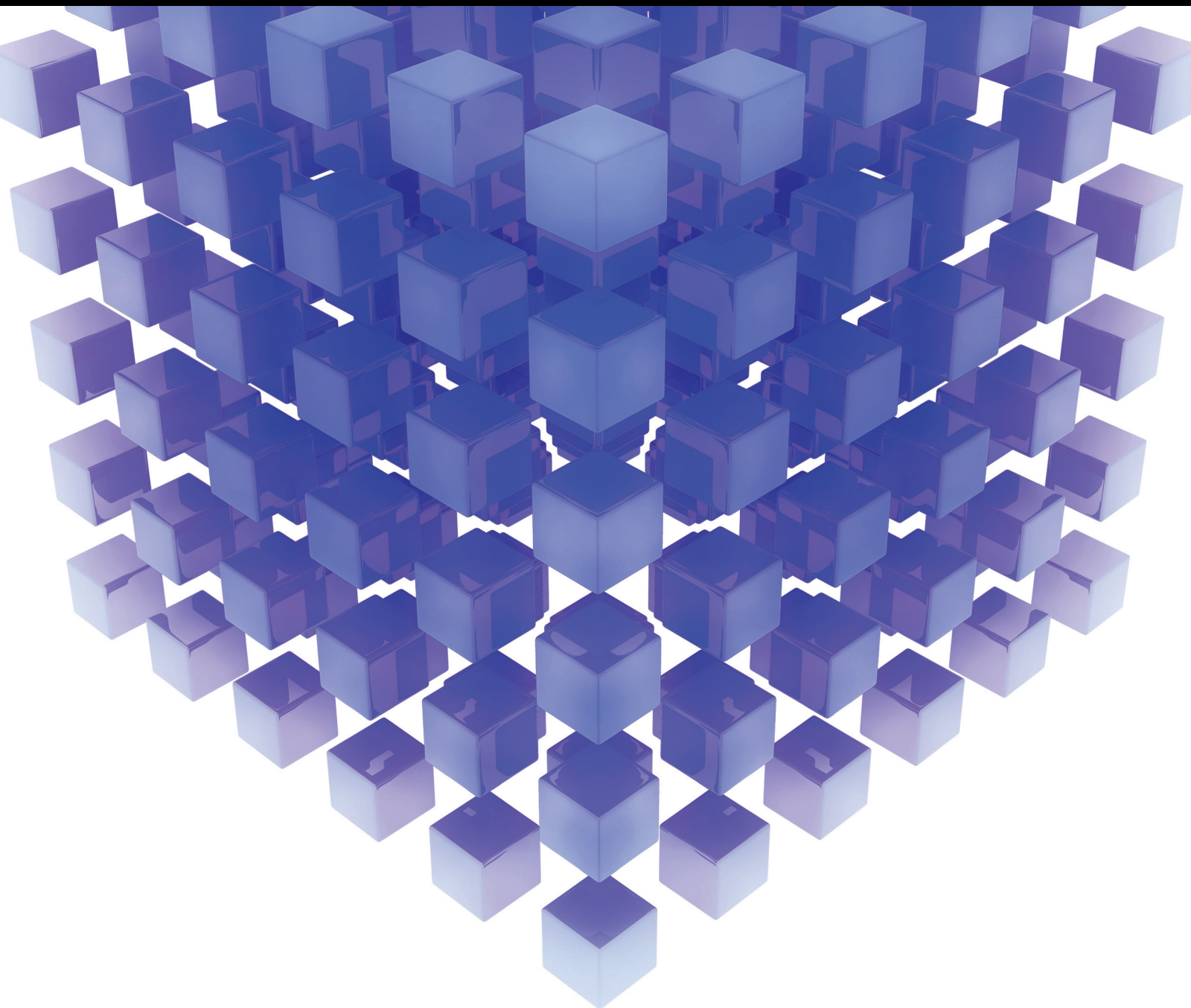


Mathematical Problems in Engineering

Advances in Numerical Techniques for Modelling Water Flows

Special Issue Editor in Chief: Jian G. Zhou

Guest Editors: Alistair Borthwick, Haifei Liu, and Ling Qian





Advances in Numerical Techniques for Modelling Water Flows

Mathematical Problems in Engineering

Advances in Numerical Techniques for Modelling Water Flows

Special Issue Editor in Chief: Jian G. Zhou

Guest Editors: Alistair Borthwick, Haifei Liu, and Ling Qian



Copyright © 2018 Hindawi. All rights reserved.

This is a special issue published in “Mathematical Problems in Engineering.” All articles are open access articles distributed under the Creative Commons Attribution License, which permits unrestricted use, distribution, and reproduction in any medium, provided the original work is properly cited.

Editorial Board

- Mohamed Abd El Aziz, Egypt
AITOUCHE Abdelouhab, France
Leonardo Acho, Spain
José Ángel Acosta, Spain
Paolo Adesso, Italy
Claudia Adduce, Italy
Ramesh Agarwal, USA
Francesco Aggogeri, Italy
Juan C. Agüero, Australia
R Aguilar-López, Mexico
Tarek Ahmed-Ali, France
Elias Aifantis, USA
Muhammad N. Akram, Norway
Guido Ala, Italy
Andrea Alaimo, Italy
Reza Alam, USA
Salvatore Alfonzetti, Italy
Mohammad D. Aliyu, Canada
Juan A. Almendral, Spain
José Domingo Álvarez, Spain
Cláudio Alves, Portugal
J. P. Amezcua-Sanchez, Mexico
Lionel Amodeo, France
Sebastian Anita, Romania
Renata Archetti, Italy
Felice Arena, Italy
Sabri Arik, Turkey
Francesco Aristodemo, Italy
Fausto Arpino, Italy
Alessandro Arsie, USA
Edoardo Artioli, Italy
Fumihiko Ashida, Japan
Farhad Aslani, Australia
Mohsen Asle Zaeem, USA
Romain Aubry, USA
Matteo Aureli, USA
Richard I. Avery, USA
Viktor Avrutin, Germany
Francesco Aymerich, Italy
Michele Bacciocchi, Italy
Seungik Baek, USA
Adil Bagirov, Australia
Khaled Bahlali, France
Laurent Bako, France
Pedro Balaguer, Spain
Stefan Balint, Romania
Ines Tejado Balsera, Spain
Alfonso Banos, Spain
Jerzy Baranowski, Poland
Roberto Baratti, Italy
Andrzej Bartoszewicz, Poland
Chiara Bedon, Italy
Azeddine Beghdadi, France
Denis Benasciutti, Italy
Ivano Benedetti, Italy
Rosa M. Benito, Spain
Elena Benvenuti, Italy
Giovanni Berselli, Italy
Michele Betti, Italy
Jean-Charles Beugnot, France
Pietro Bia, Italy
Carlo Bianca, France
Simone Bianco, Italy
Vincenzo Bianco, Italy
Vittorio Bianco, Italy
Gennaro N. Bifulco, Italy
David Bigaud, France
Antonio Bilotta, Italy
Paul Bogdan, USA
Rodolfo Bontempo, Italy
Alberto Borboni, Italy
Paolo Boscariol, Italy
Daniela Boso, Italy
Guillermo Botella-Juan, Spain
Fabio Bovenga, Italy
Francesco Braghin, Italy
Ricardo Branco, Portugal
Maurizio Brocchini, Italy
Julien Bruchon, France
Matteo Bruggi, Italy
Michele Brun, Italy
Vasilis Burganos, Greece
Tito Busani, USA
Raquel Caballero-Águila, Spain
Filippo Cacace, Italy
Pierfrancesco Cacciola, UK
Salvatore Caddemi, Italy
Roberto Caldelli, Italy
Alberto Campagnolo, Italy
Eric Campos-Canton, Mexico
Marko Canadija, Croatia
Salvatore Cannella, Italy
Francesco Cannizzaro, Italy
Javier Cara, Spain
Ana Carpio, Spain
Caterina Casavola, Italy
Sara Casciati, Italy
Federica Caselli, Italy
Fernando Castanos, Mexico
Carmen Castillo, Spain
Inmaculada T. Castro, Spain
Nicola Caterino, Italy
Alberto Cavallo, Italy
Gabriele Cazzulani, Italy
Luis Cea, Spain
Miguel Cerrolaza, Venezuela
M. Chadli, France
Gregory Chagnon, France
Ludovic Chamoin, France
Ching-Ter Chang, Taiwan
Qing Chang, USA
Michael J. Chappell, UK
Kacem Chehdi, France
Peter N. Cheimets, USA
Xinkai Chen, Japan
Luca Chiapponi, Italy
Francisco Chicano, Spain
Nicholas Chileshe, Australia
Adrian Chmielewski, Poland
Ioannis T. Christou, Greece
Hung-Yuan Chung, Taiwan
Simone Cinquemani, Italy
Roberto G. Citarella, Italy
Joaquim Ciurana, Spain
John D. Clayton, USA
Francesco Clementi, Italy
Piero Colajanni, Italy
Giuseppina Colicchio, Italy
Enrico Conte, Italy
Francesco Conte, Italy
Alessandro Contento, USA
Mario Cools, Belgium

José A. Correia, Portugal
 Jean-Pierre Corriou, France
 J.-C. Cortés, Spain
 Carlo Cosentino, Italy
 Paolo Crippa, Italy
 Andrea Crivellini, Italy
 Frederico R. B. Cruz, Brazil
 Erik Cuevas, Mexico
 Maria C. Cunha, Portugal
 Peter Dabnichki, Australia
 Luca D'Acierno, Italy
 Weizhong Dai, USA
 Andrea Dall'Asta, Italy
 Purushothaman Damodaran, USA
 Farhang Daneshmand, Canada
 Giuseppe D'Aniello, Italy
 Sergey N. Dashkovskiy, Germany
 Fabio De Angelis, Italy
 Samuele De Bartolo, Italy
 Pietro De Lellis, Italy
 Luciano R. O. de Lima, Brazil
 Alessandro De Luca, Italy
 Stefano de Miranda, Italy
 Filippo de Monte, Italy
 Maria do Rosário de Pinho, Portugal
 Michael Defoort, France
 Alessandro Della Corte, Italy
 Xavier Delorme, France
 Laurent Dewasme, Belgium
 Angelo Di Egidio, Italy
 Roberta Di Pace, Italy
 Ramón I. Diego, Spain
 Yannis Dimakopoulos, Greece
 Zhengtao Ding, UK
 M. Djemai, France
 Alexandre B. Dolgui, France
 Georgios Dounias, Greece
 Florent Duchaine, France
 George S. Dulikravich, USA
 Bogdan Dumitrescu, Romania
 Horst Ecker, Austria
 Saeed E. Eftekhar Azam, Italy
 Ahmed El Hajjaji, France
 Antonio Elipe, Spain
 Fouad Erchiqui, Canada
 Anders Eriksson, Sweden
 R. Emre Erkmen, Australia
 Gilberto Espinosa-Paredes, Italy
 Andrea L. Facci, Italy
 Giacomo Falcucci, Italy
 Giovanni Falsone, Italy
 Hua Fan, China
 Nicholas Fantuzzi, Italy
 Yann Favennec, France
 Fiorenzo A. Fazzolari, UK
 Giuseppe Fedele, Italy
 Roberto Fedele, Italy
 Arturo J. Fernández, Spain
 Jesus M. Fernandez Oro, Spain
 Massimiliano Ferrara, Italy
 Francesco Ferrise, Italy
 Eric Feulvarch, France
 Barak Fishbain, Israel
 S. Douwe Flapper, Netherlands
 Thierry Floquet, France
 Eric Florentin, France
 Alessandro Formisano, Italy
 Francesco Franco, Italy
 Elisa Francomano, Italy
 Tomonari Furukawa, USA
 Juan C. G. Prada, Spain
 Mohamed Gadala, Canada
 Matteo Gaeta, Italy
 Mauro Gaggero, Italy
 Zoran Gajic, USA
 Erez Gal, Israel
 Jaime Gallardo-Alvarado, Mexico
 Ugo Galvanetto, Italy
 Akemi Gálvez, Spain
 Rita Gamberini, Italy
 Maria L. Gandarias, Spain
 Arman Ganji, Canada
 Zhiwei Gao, UK
 Zhong-Ke Gao, China
 Giovanni Garcea, Italy
 Luis Rodolfo Garcia Carrillo, USA
 Jose M. Garcia-Aznar, Spain
 Akhil Garg, China
 Alessandro Gasparetto, Italy
 Oleg V. Gendelman, Israel
 Stylianos Georgantzinis, Greece
 Fotios Georgiades, UK
 Mergen H. Ghayesh, Australia
 Georgios I. Giannopoulos, Greece
 Agathoklis Giaralis, UK
 Pablo Gil, Spain
 Anna M. Gil-Lafuente, Spain
 Ivan Giorgio, Italy
 Gaetano Giunta, Luxembourg
 Alessio Gizzi, Italy
 Jefferson L.M.A. Gomes, UK
 Emilio Gómez-Déniz, Spain
 Antonio M. Gonçalves de Lima, Brazil
 David González, Spain
 Chris Goodrich, USA
 Rama S. R. Gorla, USA
 Nicolas Gourdain, France
 Kannan Govindan, Denmark
 Antoine Grall, France
 George A. Gravvanis, Greece
 Fabrizio Greco, Italy
 Simonetta Grilli, Italy
 Jason Gu, Canada
 Federico Guarracino, Italy
 José L. Guzmán, Spain
 Quang Phuc Ha, Australia
 Petr Hájek, Czech Republic
 Zhen-Lai Han, China
 Thomas Hanne, Switzerland
 Mohammad A. Hariri-Ardebili, USA
 Xiao-Qiao He, China
 Sebastian Heidenreich, Germany
 Luca Heltai, Italy
 Alfredo G. Hernández-Díaz, Spain
 M.I. Herreros, Spain
 Eckhard Hitzer, Japan
 Paul Honeine, France
 Jaromir Horacek, Czech Republic
 Muneo Hori, Japan
 András Horváth, Italy
 S. Hassan Hosseinnia, Netherlands
 Mengqi Hu, USA
 Gordon Huang, Canada
 Sajid Hussain, Canada
 Asier Ibeas, Spain
 Orest V. Iftime, Netherlands
 Przemyslaw Ignaciuk, Poland
 Giacomo Innocenti, Italy
 Emilio Insfran Pelozo, Spain
 Alessio Ishizaka, UK
 Nazrul Islam, USA

Benoit Jung, France
 Benjamin Ivorra, Spain
 Payman Jalali, Finland
 Mahdi Jalili, Australia
 Łukasz Jankowski, Poland
 Samuel N. Jator, USA
 Juan C. Jauregui-Correa, Mexico
 Reza Jazar, Australia
 Khalide Jbilou, France
 Piotr Jędrzejowicz, Poland
 Isabel S. Jesus, Portugal
 Linni Jian, China
 Bin Jiang, China
 Zhongping Jiang, USA
 Emilio Jiménez Macías, Spain
 Ningde Jin, China
 Xiaoliang Jin, USA
 Liang Jing, Canada
 Dylan F. Jones, UK
 Palle E. Jorgensen, USA
 Vyacheslav Kalashnikov, Mexico
 Tamas Kalmár-Nagy, Hungary
 Tamas Kalmár-Nagy, Hungary
 Tomasz Kapitaniak, Poland
 Julius Kaplunov, UK
 Haranath Kar, India
 Konstantinos Karamanos, Belgium
 Krzysztof Kecik, Poland
 Jean-Pierre Kenne, Canada
 Chaudry M. Khalique, South Africa
 Do Wan Kim, Republic of Korea
 Nam-Il Kim, Republic of Korea
 Jan Koci, Czech Republic
 Ioannis Kostavelis, Greece
 Sotiris B. Kotsiantis, Greece
 Manfred Krafczyk, Germany
 Frederic Kratz, France
 Petr Krysl, USA
 Krzysztof S. Kulpa, Poland
 Shailesh I. Kundalwal, Canada
 Jurgen Kurths, Germany
 Kyandoghere Kyamakya, Austria
 Davide La Torre, Italy
 Risto Lahdelma, Finland
 Hak-Keung Lam, UK
 Giovanni Lancioni, Italy
 Jimmy Lauber, France
 Antonino Laudani, Italy
 Hervé Laurent, France
 Aimé Lay-Ekuakille, Italy
 Nicolas J. Leconte, France
 Dimitri Lefebvre, France
 Eric Lefevre, France
 Marek Lefik, Poland
 Yaguo Lei, China
 Kauko Leiviskä, Finland
 Thibault Lemaire, France
 Roman Lewandowski, Poland
 Chen-Feng Li, China
 Jian Li, China
 Zhiyun Lin, China
 Peide Liu, China
 Peter Liu, Taiwan
 Wanquan Liu, Australia
 Bonifacio Llamazares, Spain
 Alessandro Lo Schiavo, Italy
 Jean Jacques Loiseau, France
 Francesco Lolli, Italy
 Paolo Lonetti, Italy
 Sandro Longo, Italy
 Sebastian López, Spain
 Pablo Lopez-Crespo, Spain
 Luis M. López-Ochoa, Spain
 Ezequiel López-Rubio, Spain
 Vassilios C. Loukopoulos, Greece
 Jose A. Lozano-Galant, Spain
 Helen Lu, Australia
 Gabriel Luque, Spain
 Valentin Lychagin, Norway
 Antonio Madeo, Italy
 José María Maestre, Spain
 Alessandro Magnani, Italy
 Fazal M. Mahomed, South Africa
 Noureddine Manamanni, France
 Paolo Manfredi, Italy
 Didier Maquin, France
 Giuseppe Carlo Marano, Italy
 Damijan Markovic, France
 Francesco Marotti de Sciarra, Italy
 Rui Cunha Marques, Portugal
 Luis Martínez, Spain
 Rodrigo Martínez-Bejar, Spain
 Guiomar Martín-Herrán, Spain
 Denizar Cruz Martins, Brazil
 Benoit Marx, France
 Elio Masciari, Italy
 Franck Massa, France
 Paolo Massioni, France
 Alessandro Mauro, Italy
 Fabio Mazza, Italy
 Laura Mazzola, Italy
 Driss Mehdi, France
 Roderick Melnik, Canada
 Pasquale Memmolo, Italy
 Xiangyu Meng, USA
 Jose Merodio, Spain
 Alessio Merola, Italy
 Mahmoud Mesbah, Iran
 Luciano Mescia, Italy
 Laurent Mevel, France
 Mariusz Michta, Poland
 Leandro F. F. MIGUEL, Brazil
 Aki Mikkola, Finland
 Giovanni Minafò, Italy
 Hiroyuki Mino, Japan
 Pablo Mira, Spain
 Dimitrios Mitsotakis, New Zealand
 Vito Mocella, Italy
 Sara Montagna, Italy
 Roberto Montanini, Italy
 Francisco J. Montáns, Spain
 Luiz H. A. Monteiro, Brazil
 Gisele Mophou, France
 Rafael Morales, Spain
 Marco Morandini, Italy
 Javier Moreno-Valenzuela, Mexico
 Simone Morganti, Italy
 Caroline Mota, Brazil
 Aziz Moukrim, France
 Dimitris Mourtzis, Greece
 Emiliano Mucchi, Italy
 Josefa Mula, Spain
 Jose J. Muñoz, Spain
 Giuseppe Muscolino, Italy
 Marco Mussetta, Italy
 Hakim Naceur, France
 Alessandro Naddeo, Italy
 Hassane Naji, France
 Mariko Nakano-Miyatake, Mexico
 Keivan Navaie, UK
 AMA Neves, Portugal

Luís C. Neves, Portugal
Dong Ngoduy, New Zealand
Nhon Nguyen-Thanh, Singapore
Tatsushi Nishi, Japan
Xesús Nogueira, Spain
Ben T. Nohara, Japan
Mohammed Nouari, France
Mustapha Nourelfath, Canada
Włodzimierz Ogryczak, Poland
Roger Ohayon, France
Krzysztof Okarma, Poland
Mitsuhiro Okayasu, Japan
Enrique Onieva, Spain
Calogero Orlando, Italy
Alejandro Ortega-Moñux, Spain
Sergio Ortobelli, Italy
Naohisa Otsuka, Japan
Erika Ottaviano, Italy
Pawel Packo, Poland
Arturo Pagano, Italy
Alkis S. Paipetis, Greece
Roberto Palma, Spain
Alessandro Palmeri, UK
Pasquale Palumbo, Italy
Jürgen Pannek, Germany
Elena Panteley, France
Achille Paolone, Italy
George A. Papakostas, Greece
Xosé M. Pardo, Spain
Vicente Parra-Vega, Mexico
Manuel Pastor, Spain
Petr Páta, Czech Republic
Pubudu N. Pathirana, Australia
Surajit K. Paul, India
Sitek Paweł, Poland
Luis Payá, Spain
Alexander Paz, USA
Igor Pažanin, Croatia
Libor Pekař, Czech Republic
Francesco Pellicano, Italy
Marcello Pellicciari, Italy
Haipeng Peng, China
Mingshu Peng, China
Zhengbiao Peng, Australia
Zhi-ke Peng, China
Marzio Pennisi, Italy
Maria Patrizia Pera, Italy

Matjaz Perc, Slovenia
A. M. Bastos Pereira, Portugal
Ricardo Perera, Spain
Francesco Pesavento, Italy
Ivo Petras, Slovakia
Francesco Petrini, Italy
Lukasz Pieczonka, Poland
Dario Piga, Switzerland
Paulo M. Pimenta, Brazil
Antonina Pirrotta, Italy
Marco Pizzarelli, Italy
Vicent Pla, Spain
Javier Plaza, Spain
Dragan Poljak, Croatia
Jorge Pomares, Spain
Sébastien Poncet, Canada
Volodymyr Ponomaryov, Mexico
Jean-Christophe Ponsart, France
Mauro Pontani, Italy
Cornelio Posadas-Castillo, Mexico
Francesc Pozo, Spain
Christopher Pretty, New Zealand
Luca Pugi, Italy
Krzysztof Puzynski, Poland
Giuseppe Quaranta, Italy
Vitomir Racic, Italy
Jose Ragot, France
Carlo Rainieri, Italy
K. Ramamani Rajagopal, USA
Ali Ramazani, USA
Higinio Ramos, Spain
Alain Rassineux, France
S.S. Ravindran, USA
Alessandro Reali, Italy
Jose A. Reinoso, Spain
Oscar Reinoso, Spain
Fabrizio Renno, Italy
Nidhal Rezz, France
Ricardo Rianza, Spain
Francesco Riganti-Fulginei, Italy
Gerasimos Rigatos, Greece
Francesco Ripamonti, Italy
Jorge Rivera, Mexico
Eugenio Roanes-Lozano, Spain
Bruno G. M. Robert, France
Ana Maria A. C. Rocha, Portugal
José Rodellar, Spain

Luigi Rodino, Italy
Rosana Rodríguez López, Spain
Ignacio Rojas, Spain
Alessandra Romolo, Italy
Debasish Roy, India
Gianluigi Rozza, Italy
Rubén Ruiz, Spain
Antonio Ruiz-Cortes, Spain
Ivan D. Rukhlenko, Australia
Mazen Saad, France
Kishin Sadarangani, Spain
Andrés Sáez, Spain
Mehrdad Saif, Canada
Salvatore Salamone, USA
Vicente Salas, Spain
Jose V. Salcedo, Spain
Nunzio Salerno, Italy
Miguel A. Salido, Spain
Roque J. Salterén, Spain
Alessandro Salvini, Italy
Sylwester Samborski, Poland
Ramon Sancibrian, Spain
Giuseppe Sanfilippo, Italy
Miguel A. F. Sanjuan, Spain
Vittorio Sansalone, France
José A. Sanz-Herrera, Spain
Nickolas S. Sapidis, Greece
Evangelos J. Sapountzakis, Greece
Luis Saucedo-Mora, Spain
Marcelo A. Savi, Brazil
Andrey V. Savkin, Australia
Roberta Sburlati, Italy
Thomas Schuster, Germany
Oliver Schütze, Mexico
Lotfi Senhadji, France
Junwon Seo, USA
Joan Serra-Sagrissa, Spain
Gerardo Severino, Italy
Ruben Sevilla, UK
Stefano Sfarra, Italy
Mohamed Shaat, Egypt
Mostafa S. Shadloo, France
Leonid Shaikhet, Israel
Hassan M. Shanechi, USA
Bo Shen, Germany
Suzanne M. Shontz, USA
Babak Shotorban, USA

Zhan Shu, UK
Nuno Simões, Portugal
Christos H. Skiadas, Greece
Konstantina Skouri, Greece
Neale R. Smith, Mexico
Bogdan Smolka, Poland
Delfim Soares Jr., Brazil
Alba Sofi, Italy
Giovanni Solari, Italy
Francesco Soldovieri, Italy
Raffaele Solimene, Italy
Jussi Sopanen, Finland
Marco Spadini, Italy
Bernardo Spagnolo, Italy
Paolo Spagnolo, Italy
Ruben Specogna, Italy
Vasilios Spitas, Greece
Sri Sridharan, USA
Ivanka Stamova, USA
Rafał Stanisławski, Poland
Florin Stoican, Romania
Salvatore Strano, Italy
Yakov Strelniker, Israel
Guang-Yong Sun, China
Sergey A. Suslov, Australia
Thomas Svensson, Sweden
Andrzej Swierniak, Poland
Andras Szekrenyes, Hungary
Kumar K. Tamma, USA
Yang Tang, Germany
Hafez Tari, USA
Alessandro Tasora, Italy
Sergio Teggi, Italy
Ana C. Teodoro, Portugal
Tai Thai, Australia
Alexander Timokha, Norway
Gisella Tomasini, Italy
Francesco Tornabene, Italy
Antonio Tornambe, Italy
Javier Martinez Torres, Spain

Mariano Torrisi, Italy
George Tsiatas, Greece
Antonios Tsourdos, UK
Federica Tubino, Italy
Nerio Tullini, Italy
Andrea Tundis, Italy
Emilio Turco, Italy
Vladimir Turetsky, Israel
Mustafa Tutar, Spain
Ilhan Tuzcu, USA
Efstratios Tzirtzilakis, Greece
Filippo Ubertini, Italy
Francesco Ubertini, Italy
Hassan Ugail, UK
Giuseppe Vairo, Italy
Eusebio Valero, Spain
Pandian Vasant, Malaysia
Marcello Vasta, Italy
Carlos-Renato Vázquez, Mexico
M. E. Vázquez-Méndez, Spain
Josep Vehi, Spain
Martin Velasco Villa, Mexico
K. C. Veluvolu, Republic of Korea
Fons J. Verbeek, Netherlands
Franck J. Vernerey, USA
Georgios Veronis, USA
Vincenzo Vespri, Italy
Venkatesh Vijayaraghavan, Australia
Anna Vila, Spain
Rafael J. Villanueva, Spain
Francisco R. Villatoro, Spain
Uchechukwu E. Vincent, UK
Francesca Vipiana, Italy
Stanislav Vitek, Czech Republic
Thuc P. Vo, UK
Jan Vorel, Czech Republic
Michael Vynnycky, Sweden
Hao Wang, USA
Liliang Wang, UK
Shuming Wang, China

Yongqi Wang, Germany
Roman Wan-Wendner, Austria
Jarosław Waś, Poland
P.H. Wen, UK
Waldemar T. Wójcik, Poland
Changzhi Wu, Australia
Desheng D. Wu, Sweden
Hong-Yu Wu, USA
Yuqiang Wu, China
Michalis Xenos, Greece
Guangming Xie, China
Xue-Jun Xie, China
Gen Q. Xu, China
Hang Xu, China
Joseph J. Yame, France
Xinggang Yan, UK
Mijia Yang, USA
Yongheng Yang, Denmark
Luis J. Yebra, Spain
Peng-Yeng Yin, Taiwan
Qin Yuming, China
Elena Zaitseva, Slovakia
Arkadiusz Żak, Poland
Daniel Zaldivar, Mexico
Francesco Zammori, Italy
Vittorio Zampoli, Italy
Rafal Zdunek, Poland
Ibrahim Zeid, USA
Huaguang Zhang, China
Kai Zhang, China
Qingling Zhang, China
Xian-Ming Zhang, Australia
Xuping Zhang, Denmark
Zhao Zhang, China
Yifan Zhao, UK
Jian G. Zhou, UK
Quanxin Zhu, China
Mustapha Zidi, France
Gaetano Zizzo, Italy

Contents

Advances in Numerical Techniques for Modelling Water Flows

Jian G. Zhou , Alistair Borthwick , Haifei Liu , and Ling Qian 
Editorial (2 pages), Article ID 8175674, Volume 2018 (2018)

Numerical Modeling of Wave-Current Flow around Cylinders Using an Enhanced Equilibrium Bhatnagar-Gross-Krook Scheme

Liming Xing , Haifei Liu , Yu Ding, and Wei Huang
Research Article (9 pages), Article ID 8516879, Volume 2018 (2018)

Study on Force Schemes in Pseudopotential Lattice Boltzmann Model for Two-Phase Flows

Yong Peng , Bo Wang , and Yunfei Mao
Research Article (9 pages), Article ID 6496379, Volume 2018 (2018)

Numerical Simulation of an Offset Jet in Bounded Pool with Deflection Wall

Xin Li, Yurong Wang, and Jianmin Zhang
Research Article (11 pages), Article ID 5943143, Volume 2017 (2018)

(2 + 1)-Dimensional Coupled Model for Envelope Rossby Solitary Waves and Its Solutions as well as Chirp Effect

Xin Chen, Hongwei Yang, Min Guo, and Baoshu Yin
Research Article (12 pages), Article ID 1378740, Volume 2017 (2018)

Development of Embedded Element Technique for Permeability Analysis of Cracked Porous Media

Peng Qian and Qianjun Xu
Research Article (12 pages), Article ID 6713452, Volume 2017 (2018)

Flood Risk Zoning by Using 2D Hydrodynamic Modeling: A Case Study in Jinan City

Tao Cheng, Zongxue Xu, Siyang Hong, and Sulin Song
Research Article (8 pages), Article ID 5659197, Volume 2017 (2018)

A One-Dimensional Hydrodynamic and Water Quality Model for a Water Transfer Project with Multihydraulic Structures

Yujun Yi, Caihong Tang, Zhifeng Yang, Shanghong Zhang, and Cheng Zhang
Research Article (11 pages), Article ID 2656191, Volume 2017 (2018)

Comparison of Three Different Parallel Computation Methods for a Two-Dimensional Dam-Break Model

Shanghong Zhang, Wenda Li, Zhu Jing, Yujun Yi, and Yong Zhao
Research Article (12 pages), Article ID 1970628, Volume 2017 (2018)

Two-Dimensional Simulation of Flows in an Open Channel with Groin-Like Structures by iRIC Nays2DH

Md. Shahjahan Ali, Md. Milon Hasan, and Masuma Haque
Research Article (10 pages), Article ID 1275498, Volume 2017 (2018)

Comparison of Different Turbulence Models for Numerical Simulation of Pressure Distribution in V-Shaped Stepped Spillway

Zhaoliang Bai and Jianmin Zhang

Research Article (9 pages), Article ID 3537026, Volume 2017 (2018)

A New Mathematical Method for Solving Cuttings Transport Problem of Horizontal Wells: Ant Colony Algorithm

Liu Yongwang, Liu Yu-ming, Qiu Heng-bin, and Bai Yan-feng

Research Article (8 pages), Article ID 7898647, Volume 2017 (2018)

Multispeed Lattice Boltzmann Model with Space-Filling Lattice for Transcritical Shallow Water Flows

Y. Peng, J. P. Meng, and J. M. Zhang

Research Article (5 pages), Article ID 8917360, Volume 2017 (2018)

Numerical Study for Near-Bed Variables in Velocity-Skewed Oscillatory Sheet Flow Transport

Xin Chen, Zichao Zhang, Yong Li, and Xiaoyan Shi

Research Article (10 pages), Article ID 2614943, Volume 2017 (2018)

Lattice Boltzmann Method of a Flooding Accident at Gopeng, Perak, Malaysia

Siti Habibah Shafai, Diana Bazila Shahruzzaman, Goh Juin Xien, and Mohamed Latheef

Research Article (10 pages), Article ID 3478158, Volume 2017 (2018)

Comprehensive Numerical Investigations of Unsteady Internal Flows and Cavitation Characteristics in Double-Suction Centrifugal Pump

Xuelin Tang, Mingde Zou, Fujun Wang, Xiaoqin Li, and Xiaoyan Shi

Research Article (13 pages), Article ID 5013826, Volume 2017 (2018)

Shallow-Water-Equation Model for Simulation of Earthquake-Induced Water Waves

Hongzhou Ai, Lingkan Yao, Haixin Zhao, and Yiliang Zhou

Research Article (11 pages), Article ID 3252498, Volume 2017 (2018)

Numerical Investigation of the FSI Characteristics in a Tubular Pump

Shuo Wang, Liaojun Zhang, and Guojiang Yin

Research Article (9 pages), Article ID 7897614, Volume 2017 (2018)

Editorial

Advances in Numerical Techniques for Modelling Water Flows

Jian G. Zhou ¹, Alistair Borthwick ², Haifei Liu ³, and Ling Qian ¹

¹*School of Computing, Mathematics and Digital Technology, Manchester Metropolitan University, Manchester, UK*

²*School of Engineering, University of Edinburgh, Edinburgh, UK*

³*School of Environment, Beijing Normal University, Beijing, China*

Correspondence should be addressed to Jian G. Zhou; j.zhou@mmu.ac.uk

Received 29 January 2018; Accepted 29 January 2018; Published 15 May 2018

Copyright © 2018 Jian G. Zhou et al. This is an open access article distributed under the Creative Commons Attribution License, which permits unrestricted use, distribution, and reproduction in any medium, provided the original work is properly cited.

This special issue aims to present recent advances in approaches to modelling water flows and their applications in engineering. Water occupies about 71% of the earth's surface area and is essential for the survival of human beings, but natural disasters pose substantial societal, environmental, and economic hazards. Important and extremely challenging research topics arise from the need to understand water flows and develop mitigation measures against potential adverse impacts, such as urban flooding and coastal storm surge inundation.

Advances in modern computer technology have made it possible for computational models to be intensively applied to the study of water flow problems in science and engineering. In this special issue, X. Li et al. describe the numerical simulation of an offset jet in bounded pool. P. Qian and Q. Xu present an embedded element technique for the permeability analysis of cracked porous media. Y. Yi et al. describe a one-dimensional model that is applied to a water transfer project with multihydraulic structures. X. Tang et al. examine the cavitation characteristics of a double-suction centrifugal pump. H. Ai et al. simulate earthquake-induced water waves using a numerical solver based on the shallow water equations.

As computational methods progress, numerical models of free surface flow are becoming increasingly effective as routine analysis tools to improve infrastructure resilience and identify countermeasures against natural disasters related to water flows. T. Cheng et al. apply a coupled hydrological and hydrodynamic model to study flood risks in the main urban area of Jinan, China. Z. Bai and J. Zhang study the effect of different turbulence models on numerical simulations for

understanding of pressure distribution in V-shaped stepped spillways. X. Chen et al. numerically study the behaviour of near-bed variables in velocity-skewed oscillatory sheet flow. S. Wang et al. undertake a numerical investigation into the characteristics of fluid-structure interaction for turbulent flow through a turbine. M. S. Ali et al. carry out numerical simulation of two-dimensional flows in an open channel with groin-like structures.

Meanwhile, new and increasingly accurate, robust numerical methods are being developed to solve the governing equations for water flows. Herein, Y. Peng et al., H. Liu et al., and S. H. Shafiai et al. use the lattice Boltzmann method to investigate two-phase flows, wave-current interaction, and flood inundation. S. Zhang et al. compare three different parallel computation methods and apply the methods to the simulation of a two-dimensional dam-break with a case study for the Pangtoupao flood storage in Songhua River basin, China. Y. Liu et al. describe a new numerical method for solving the problem of cuttings transport in drilling horizontal wells. Y. Peng et al. show that a multispeed lattice Boltzmann model with space-filling lattice is able to simulate transcritical shallow water flows with Froude number larger than one. X. Chen et al. propose a coupled model for Rossby solitary waves using a multiple-scales perturbation method and derive its analytical solution.

The aforementioned examples reflect the development and application of numerical techniques for water flows and demonstrate the sheer variety of engineering problems that are tractable through modern numerical models. Although there is much still to be done to simulate accurately

complicated environmental water flows involving multiple scales in space and time, the editors hope that this special issue meets its primary aim of reporting on recent progress towards better modelling techniques by which to study complicated free surface flow problems, leading to a better understanding of water flows in the natural environment.

Jian G. Zhou
Alistair Borthwick
Haifei Liu
Ling Qian

Research Article

Numerical Modeling of Wave-Current Flow around Cylinders Using an Enhanced Equilibrium Bhatnagar-Gross-Krook Scheme

Liming Xing ¹, Haifei Liu ^{1,2}, Yu Ding,¹ and Wei Huang³

¹The Key Laboratory of Water and Sediment Sciences of Ministry of Education, School of Environment, Beijing Normal University, Beijing 100875, China

²State Key Laboratory of Hydraulics and Mountain River Protection, College of Water Resource and Hydropower, Sichuan University, Chengdu 610065, China

³State Key Laboratory of Simulation and Regulation of Water Cycle in River Basin, China Institute of Water Resources and Hydropower Research, Beijing 100038, China

Correspondence should be addressed to Haifei Liu; haifei.liu@bnu.edu.cn

Received 28 June 2017; Revised 11 January 2018; Accepted 23 January 2018; Published 15 February 2018

Academic Editor: Salvatore Alfonzetti

Copyright © 2018 Liming Xing et al. This is an open access article distributed under the Creative Commons Attribution License, which permits unrestricted use, distribution, and reproduction in any medium, provided the original work is properly cited.

Flow around cylinders is a classic issue of fluid mechanics and it has great significance in engineering fields. In this study, a two-dimensional hydrodynamic lattice Boltzmann numerical model is proposed, coupling wave radiation stress, bed shear stress, and wind shear stress, which is able to simulate wave propagation of flow around cylinders. It is based on shallow water equations and a weight factor is applied for the force term. An enhanced equilibrium Bhatnagar-Gross-Krook (BGK) scheme is developed to treat the wave radiation stress term in collision step. This model is tested and verified by two cases: the first case is the flow around a single circular cylinder, where the flow is driven by current, wave, or both wave and current, respectively, and the second case is the solitary waves moving around cylinders. The results illustrate the correctness of this model, which could be used to analyze the detailed flow pattern around a cylinder.

1. Introduction

The phenomena of flow around cylinders, which represent blunt bodies, widely exist in aviation, mechanical, and environmental engineering. In recent years, an increasing number of problems about complex flow around cylinders have been raised with the development of coastal engineering projects. Therefore, this topic attracts much attention among researchers.

Flow around cylinders is a classic and complicated problem. The cross section is contracted, the velocity increases, and the pressure decreases along the path when the flow encounters cylinders. The separation of the boundary layer is formed around cylinders due to the viscous force, which is called the flow around cylinders. Additionally, cylinders are non-streamline objects, which influence the characteristics of

flow around cylinders by many factors, such as the Reynolds number, the surface roughness, the turbulence intensity, and the cylinder size. All these lead to the complexity of flow around cylinders. The wave is one of the most common movement forms in water, and it is worth studying wave motion in shipping, coastal, and ocean engineering. Therefore, the research of wave propagation around cylinders is complicated, but significant.

With the development of the fluid mechanics theory and the continuous updating of computer equipment, computational fluid dynamics has been greatly developed and numerical simulation became an important tool in research. Saiki and Biringen [1] introduced a virtual boundary technique to simulate uniform flows around cylinders, and the oscillations caused by this method can be attenuated by high-order finite differences. Based on this, Lima E Silva et

al. [2] proposed the physical virtual model in which this immersed boundary was represented with a finite number of Lagrangian points, distributed over the solid-fluid interface. Ofengeim and Drikakis [3] presented numerical research on the interaction of plane blast waves and a cylinder, revealing that the blast-wave duration significantly influenced the unsteady flow around the cylinder. Breuer [4] computed the turbulent flow around a cylinder ($Re = 3900$) via large eddy simulation. Meneghini et al. [5] used a fractional step method to simulate laminar flows between two cylinders. Hu et al. [6] built a fully nonlinear potential model based on a finite element method to investigate the wave motion around a moving cylinder, and it provided certain important features that were absent in the linear theory. Wu and Shu [7] proposed a local domain-free discretization method that is able to simulate flow around an oscillating cylinder easier due to its advantage of handling the boundary. Claus and Phillips [8] used spectral/hp element methods to study the flow around a confined cylinder. The nonconforming spectral element method and adaptive meshes method were tested by Hsu et al. [9], demonstrating its feasibility on curve surfaces of cylinder.

The lattice Boltzmann method (LBM) is a promising numerical simulation method of recent decades. Compared to traditional methods, LBM has many advantages: the algorithm is simple; it can deal with complicated boundary conditions; and it is suitable for parallel processing. These superiorities lead to wide usage of LBM in many research fields. Ginzburg and D'Humieres [10] introduced a new kind of boundary conditions, improving the accuracy close to the quasianalytical reference solution. Jiménez-Hornero et al. [11] used LBM to simulate the turbulent flow structure in an open channel with the influence of vegetation. Liu et al. [12] established a two-dimensional multiblock lattice Boltzmann model for solute transport in shallow water flows. Based on the Chapman-Enskog process, Liu and Zhou [13] proposed a lattice Boltzmann model to simulate the wetting-drying front in shallow flows.

At the same time, many scholars have investigated the flow around cylinders based on the LBM. However, most studies are related to the heat transfer around cylinders. Yan and Zu [14] presented a numerical strategy to handle curved and moving boundaries for simulating viscous fluid around a rotating isothermal cylinder with heat transfer. Rabienataj Darzi et al. [15] used the LBM to analyze mixed convection flow and heat transfer between two hot cylinders. However, up to now, there is no LBM model for wave-current flow around cylinders.

In this study, considering wave-current interaction, a two-dimensional hydrodynamic numerical model is developed based on the LBM. The model couples three types of stresses, including wave radiation stress, wind shear stress, and bed shear stress. Meanwhile, an enhanced local equilibrium function is developed to treat the wave radiation stress. It is used to simulate the propagation of waves in the flow around cylinders, and then two classic examples are used for validation, which can provide characteristics of flow around cylinders.

2. Methodology

2.1. Governing Equations. The two-dimensional shallow water equations including the continuity equation and momentum equation can be written in a tensor form as

$$\begin{aligned} \frac{\partial h}{\partial t} + \frac{\partial(hu_j)}{\partial x_j} &= 0, \\ \frac{\partial(hu_i)}{\partial t} + \frac{\partial(hu_i u_j)}{\partial x_j} &= -g \frac{\partial}{\partial x_i} \left(\frac{h^2}{2} \right) + \nu \frac{\partial^2(hu_i)}{\partial x_j \partial x_j} \\ &\quad - g \bar{h} \frac{\partial Z_b}{\partial x_j} + \frac{\partial S_{ij}}{\partial x_j} + F_i, \end{aligned} \quad (1)$$

where the subscripts i and j represent the space direction indices and the Einstein summation convention is used; x_j represents the Cartesian coordinate, taking x , y , and z in turn; u_j represents the velocity component which takes u and v corresponding to that in x and y and directions, respectively. h represents the water depth; t represents the time; ν represents the kinematic viscosity; Z_b represents the bed height of the datum plane and F_i represents the force term and defined as

$$F_i = \frac{\tau_{wi}}{\rho} - \frac{\tau_{bi}}{\rho}, \quad (2)$$

where τ_{wi} represents the wind shear stress and τ_{bi} represents the bed shear stress.

Wave Radiation Stress (S_{ij}). Longuet-Higgins and Stewart [16] defined the difference between the time-average momentum value and the static water pressure on the water column per unit area, known as the wave radiation stress.

In (3), the wave radiation stresses S_{xx} , S_{xy} , S_{yx} , and S_{yy} are determined via local wave parameters. The wave radiation stress along the direction of wave propagation is $S_x = E(2C_g/C - 1/2)$, and the lateral one is $S_y = E(C_g/C - 1/2)$, where $E = (1/8)\rho g H_w^2$, C is wave velocity, C_g represents the group velocity, and H_w represents the wave height. The conversion is conducted in the Cartesian coordinate system [17]:

$$\begin{aligned} S_{xx} &= S_x \cos^2 \theta - S_y \sin^2 \theta, \\ S_{yy} &= S_x \sin^2 \theta - S_y \cos^2 \theta, \\ S_{xy} &= S_{yx} = S_x \sin 2\theta \cos \theta - S_y \cos \theta \sin \theta, \end{aligned} \quad (3)$$

where θ represents the angle between the wave direction and the x -axis.

Bed Shear Stress (τ_{bi}). Bed shear stress (τ_{bi}) is generated by the wave-current interaction in the i direction, calculated as follows [18]:

$$\begin{aligned} \tau_{bi} &= \rho C_b u_i \sqrt{u_j u_j} + \frac{\pi \rho}{8} f_w \sqrt{u_{wj} u_{wj}} u_{wj} \\ &\quad + \frac{F_B \rho}{\pi} \sqrt{2} (C_b f_w)^{1/2} \sqrt{u_{wj} u_{wj}} u_{wj}, \end{aligned} \quad (4)$$

in which C_b represents the bed friction coefficient, which may be either constant or calculated from $C_b = g/C_z^2$, where C_z represents the Chezy coefficient given based on the Manning coefficient n_b ,

$$C_z = \frac{h^{1/6}}{n_b}; \quad (5)$$

u_{wi} represents the wave bottom frictional velocity; F_B represents the wave-current influence factor, which is equal to 0.917 for the waves and currents are in the same direction, -0.1983 for perpendicular relation and 0.359 for other angles [19]; and f_w represents the wave friction factor, which is from 0.006 to 0.001 in practice [20].

Wind Shear Stress (τ_{wi}). Wind shear stress (τ_{wi}) is usually expressed as

$$\tau_{wi} = \rho_a C_w u_{wi} \sqrt{u_{wj} w_{wj}}, \quad (6)$$

where ρ_a is the density of air; C_w is the resistance coefficient; and u_{wi} is the component of the wind velocity in i direction.

2.2. Lattice Boltzmann Method. On account of the lattice Boltzmann method with a D2Q9 lattice, an enhanced equilibrium BGK Scheme is developed in this paper. The wave radiation stress S_{ij} is treated in local equilibrium function at collision step.

The discrete evolution process in the LBM with the enhanced force term [12, 21] can be written as

$$\begin{aligned} & f_\alpha(X + e_\alpha \Delta t, t + \Delta t) - f_\alpha(X, t) \\ &= -\frac{1}{\tau} (f_\alpha - f_\alpha^{\text{eq}}) - 3\Delta t \omega_\alpha e_{\alpha j} \frac{gh}{e^2} \frac{\partial Z_b}{\partial x_j} + \Delta t F_\alpha, \end{aligned} \quad (7)$$

where the external force term can be written as

$$F_\alpha = 3\omega_\alpha \frac{1}{e^2} e_{\alpha i} \left(\frac{\tau_{wi}}{\rho} - \frac{\tau_{bi}}{\rho} \right), \quad (8)$$

where ω_α represents the weight factor: $\omega_\alpha = 4/9$ for $\alpha = 0$; $\omega_\alpha = 1/9$ for $\alpha = 1, 3, 5, 7$; $\omega_\alpha = 1/36$ for $\alpha = 2, 4, 6, 8$. f_α represents the distribution function of particles; f_α^{eq} represents the local equilibrium distribution function; Δt represents the time step; τ represents the single relaxation time; and e_α represents the velocity vector of a particle in the α link.

For the D2Q9 lattice shown in Figure 1, each particle moves one lattice at its direction. The velocity of each particle is defined by

$$e_\alpha = \begin{cases} (0, 0) & \alpha = 0, \\ e \left[\cos \frac{(\alpha-1)\pi}{4}, \sin \frac{(\alpha-1)\pi}{4} \right] & \alpha = 1, 3, 5, 7, \\ \sqrt{2}e \left[\cos \frac{(\alpha-1)\pi}{4}, \sin \frac{(\alpha-1)\pi}{4} \right] & \alpha = 2, 4, 6, 8, \end{cases} \quad (9)$$

where $e = \Delta x / \Delta t$ and Δx is the lattice size.

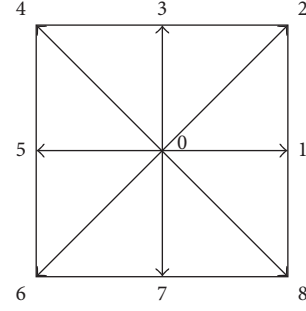


FIGURE 1: D2Q9 lattice.

An equilibrium distribution function f_α^{eq} can be expressed as

$$f_\alpha^{\text{eq}} = A_\alpha + B_\alpha e_{\alpha i} u_i + C_\alpha e_{\alpha i} e_{\alpha j} u_i u_j + D_\alpha u_i u_i. \quad (10)$$

Therefore, the equilibrium distribution function can be written as

$$f_\alpha^{\text{eq}} = \begin{cases} A_0 + D_0 u_i u_i & \alpha = 0, \\ \bar{A} + \bar{B} e_{\alpha i} u_i + \bar{C} e_{\alpha i} e_{\alpha j} u_i u_j + \bar{D} u_i u_i & \alpha = 1, 3, 5, 7, \\ \tilde{A} + \tilde{B} e_{\alpha i} u_i + \tilde{C} e_{\alpha i} e_{\alpha j} u_i u_j + \tilde{D} u_i u_i & \alpha = 2, 4, 6, 8, \end{cases} \quad (11)$$

where there must be

$$\begin{aligned} A_1 &= A_3 = A_5 = A_7 = \bar{A}, \\ A_2 &= A_4 = A_6 = A_8 = \tilde{A} \end{aligned} \quad (12)$$

due to symmetry.

Moreover, the local equilibrium distribution function must satisfy the following three conditions:

$$\begin{aligned} \sum_\alpha f_\alpha^{\text{eq}}(X, t) &= h(X, t), \\ \sum_\alpha e_{\alpha i} f_\alpha^{\text{eq}}(X, t) &= h(X, t) u_i(X, t), \\ \sum_\alpha e_{\alpha i} e_{\alpha j} f_\alpha^{\text{eq}}(X, t) &= \frac{1}{2} g h^2(X, t) \delta_{ij} - S_{ij} \\ &\quad + h(X, t) u_i(X, t) u_j(X, t). \end{aligned} \quad (13)$$

Hence, the relations among A_0 , \bar{A} , and \tilde{A} are

$$\begin{aligned} A_0 + 4\bar{A} + 4\tilde{A} &= h, \\ 2e^2\bar{A} + 4e^2\tilde{A} &= \frac{1}{2} g h^2 - S_{ij}, \\ \bar{A} &= 4\tilde{A}. \end{aligned} \quad (14)$$

We can obtain

$$\bar{B} = \frac{h}{3e^2},$$

$$\bar{C} = \frac{h}{4e^2},$$

$$\bar{D} = -\frac{h}{6e^2},$$

$$\tilde{B} = \frac{h}{12e^2},$$

$$\tilde{C} = \frac{h}{8e^2},$$

$$\tilde{D} = -\frac{h}{24e^2}.$$

(15)

Therefore, the enhanced equilibrium distribution function f_α^{eq} is

$$f_\alpha^{\text{eq}} = \begin{cases} h - \frac{5gh^2}{6e^2} + \frac{5S_{ij}}{3e^2} - \frac{2h}{3e^2}u_i u_i, & \alpha = 0, \\ \frac{gh^2}{6e^2} - \frac{S_{ij}}{3e^2} + \frac{h}{3e^2}e_{\alpha i}u_i + \frac{h}{2e^4}e_{\alpha i}e_{\alpha j}u_i u_j - \frac{h}{6e^2}u_i u_i, & \alpha = 1, 3, 5, 7, \\ \frac{gh^2}{24e^2} - \frac{S_{ij}}{12e^2} + \frac{h}{12e^2}e_{\alpha i}u_i + \frac{h}{8e^4}e_{\alpha i}e_{\alpha j}u_i u_j - \frac{h}{24e^2}u_i u_i, & \alpha = 2, 4, 6, 8. \end{cases} \quad (16)$$

2.3. *Recovery of Wave-Current Coupling Equations.* The recover deductions are following the Chapman-Enskog procedure.

Based on (7), assuming Δt is small, taking Taylor expansion in time and space around point (X, t) leads to

$$\begin{aligned} f_\alpha(X + e_\alpha \Delta t, t + \Delta t) &= f_\alpha(X, t) + \Delta t \left(\frac{\partial}{\partial t} + e_{\alpha j} \frac{\partial}{\partial x_j} \right) f_\alpha(X, t) \\ &+ \frac{1}{2} \Delta t^2 \left(\frac{\partial}{\partial t} + e_{\alpha j} \frac{\partial}{\partial x_j} \right)^2 f_\alpha(X, t) + o(\Delta t^2). \end{aligned} \quad (17)$$

From Chapman-Enskog expansion, we have

$$f_\alpha = f_\alpha^{(0)} + \Delta t f_\alpha^{(1)} + \Delta t^2 f_\alpha^{(2)} + o(\Delta t^2). \quad (18)$$

Substitution of (17) and (18) into (7), one can obtain

$$\begin{aligned} \Delta t \left(\frac{\partial}{\partial t} + e_{\alpha j} \frac{\partial}{\partial x_j} \right) (f_\alpha^{(0)} + \Delta t f_\alpha^{(1)} + \Delta t^2 f_\alpha^{(2)}) &+ \frac{1}{2} \Delta t^2 \left(\frac{\partial}{\partial t} + e_{\alpha j} \frac{\partial}{\partial x_j} \right)^2 (f_\alpha^{(0)} + \Delta t f_\alpha^{(1)} + \Delta t^2 f_\alpha^{(2)}) \\ &= -\frac{1}{\tau} (\Delta t f_\alpha^{(1)} + \Delta t^2 f_\alpha^{(2)}) - 3\Delta t \omega_\alpha e_{\alpha j} \frac{g\bar{h}}{e^2} \frac{\partial Z_b}{\partial x_j} \\ &+ \Delta t F_\alpha. \end{aligned} \quad (19)$$

To order Δt , it is

$$\left(\frac{\partial}{\partial t} + e_{\alpha j} \frac{\partial}{\partial x_j} \right) f_\alpha^{(0)} = -\frac{1}{\tau} f_\alpha^{(1)} - 3\omega_\alpha e_{\alpha j} \frac{g\bar{h}}{e^2} \frac{\partial Z_b}{\partial x_j} + F_\alpha. \quad (20)$$

To order Δt^2 , it is

$$\begin{aligned} \left(\frac{\partial}{\partial t} + e_{\alpha j} \frac{\partial}{\partial x_j} \right) f_\alpha^{(1)} + \frac{1}{2} \left(\frac{\partial}{\partial t} + e_{\alpha j} \frac{\partial}{\partial x_j} \right)^2 f_\alpha^{(0)} \\ = -\frac{1}{\tau} f_\alpha^{(2)}. \end{aligned} \quad (21)$$

Substitution of (20) into (21), we have

$$\begin{aligned} \left(1 - \frac{1}{2\tau} \right) \left(\frac{\partial}{\partial t} + e_{\alpha j} \frac{\partial}{\partial x_j} \right) f_\alpha^{(1)} \\ = -\frac{1}{2} \left(\frac{\partial}{\partial t} + e_{\alpha j} \frac{\partial}{\partial x_j} \right) \left(-3\omega_\alpha e_{\alpha j} \frac{g\bar{h}}{e^2} \frac{\partial Z_b}{\partial x_j} + F_\alpha \right) \\ - \frac{1}{\tau} f_\alpha^{(2)}. \end{aligned} \quad (22)$$

Taking $\sum [(20) + \Delta t \times (22)]$ about α provides

$$\begin{aligned} \frac{\partial}{\partial t} \left(\sum_\alpha f_\alpha^{(0)} \right) + \frac{\partial}{\partial x_j} \left(\sum_\alpha e_{\alpha j} f_\alpha^{(0)} \right) \\ = -\varepsilon \frac{1}{12e^2} \frac{\partial}{\partial x_j} \left(\sum_\alpha e_{\alpha j} e_{\alpha k} F_k \right). \end{aligned} \quad (23)$$

Taking $\sum e_{\alpha i} [(20) + \Delta t \times (22)]$ about α provides

$$\begin{aligned} \frac{\partial}{\partial t} \left(\sum_\alpha e_{\alpha j} f_\alpha^{(0)} \right) + \frac{\partial}{\partial x_j} \left(\sum_\alpha e_{\alpha j} e_{\alpha k} f_\alpha^{(0)} \right) \\ + \Delta t \left(1 - \frac{1}{2\tau} \right) \frac{\partial}{\partial x_j} \left(\sum_\alpha e_{\alpha j} e_{\alpha k} f_\alpha^{(1)} \right) \\ = \left(-g\bar{h} \frac{\partial Z_b}{\partial x_j} + F_i \right) \delta_{ij}. \end{aligned} \quad (24)$$

TABLE 1: The flow variables and wave parameters.

Test	u_0 (m/s)	v_0 (m/s)	Wave period (s)	Wave amplitude (m)
1	1	0	-	-
2	0	0	0.5	0.1
3	1	0	0.5	0.1

According to the law of conservation of mass, we know

$$\sum_{\alpha} f_{\alpha}(X, t) = \sum_{\alpha} f_{\alpha}^{\text{eq}}(X, t). \quad (25)$$

If the center-scheme for the force term is applied, evaluation of the other terms in the above equations using (13) and (25) simplifies (23) and (24) and obtains

$$\begin{aligned} \frac{\partial h}{\partial t} + \frac{\partial(hu_j)}{\partial x_j} &= 0 \\ \frac{\partial(hu_i)}{\partial t} + \frac{\partial(hu_i hu_j)}{\partial x_j} &= -g \frac{\partial}{\partial x_i} \left(\frac{h^2}{2} \right) - \frac{\partial}{\partial x_j} \Lambda_{ij} - g \bar{h} \frac{\partial Z_b}{\partial x_j} + \frac{\partial S_{ij}}{\partial x_j} + F_i, \end{aligned} \quad (26)$$

with

$$\begin{aligned} \Lambda_{ij} &= \frac{\Delta t}{2\tau} (2\tau - 1) \sum_{\alpha} e_{\alpha i} e_{\alpha j} f_{\alpha}^{(1)} \\ &\approx -\nu \left[\frac{\partial(hu_i)}{\partial x_i} + \frac{\partial(hu_j)}{\partial x_i} \right]. \end{aligned} \quad (27)$$

Substitution of (27) into (26) leads to the following equations which were referred to as wave-current coupling equations (1).

3. Numerical Tests

3.1. Wave-Current Flow around a Circular Cylinder. This model is built based on the verified LBM hydrodynamic model [22]. The layout diagram of the channel is shown in Figure 2. The length is 7 m, and the width is 2 m. The bottom is flat and a solid cylinder with a 0.12 m radius is located at 2 m, 1 m. The initial water depth is 1 m and the flows go from the left to the right. The computational domain is divided by 140×40 computational grids. The time step is 0.01 s.

This case includes three different tests, which are driven by currents, by waves, and by both wave and current, respectively. The flow variables and wave parameters of three types situations are shown in Table 1 (u_0 is initial horizontal velocity and v_0 is initial vertical velocity).

Test 1 (driven by the current). It can be seen that the water depth and flow velocity obviously varied due to the presence of the middle column (see Figure 3).

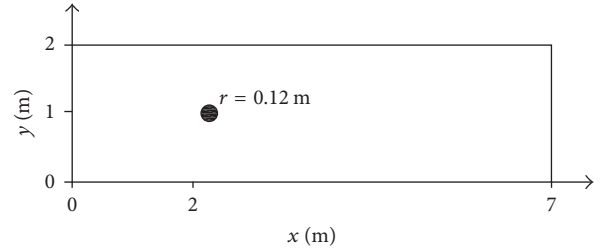


FIGURE 2: The layout sketch of the channel.

When the flow encounters the cylinder, it passes around and a weak area emerges just behind the cylinder, where the circulation and a drop of water surface can be found.

Test 2 (driven by the wave). The initial water is still and a wave maker is set at the inlet, where the incident waves are parallel generated in the x -axis. The water depth is intuitively depicted in Figure 4, where one can find regular wave propagation although there is a deformation caused by the cylinder.

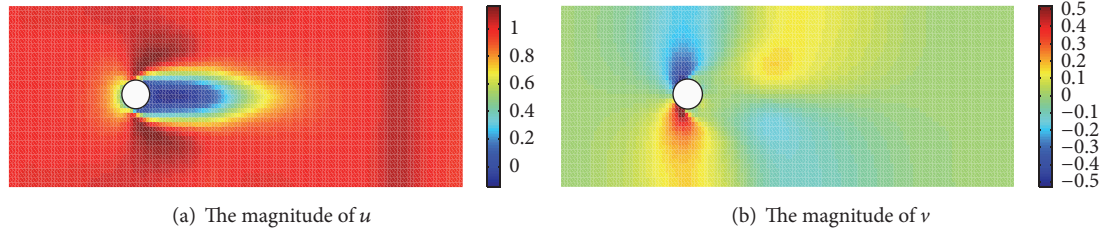
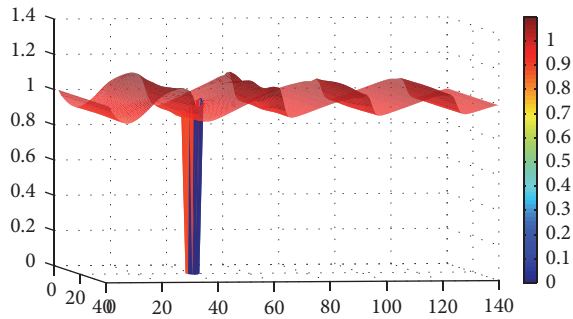
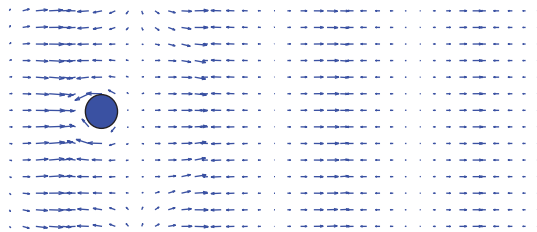
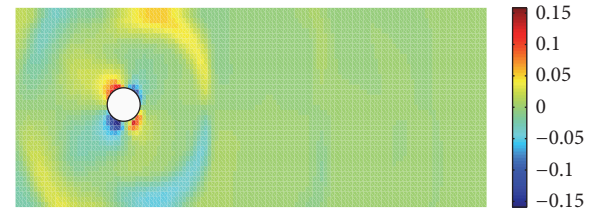
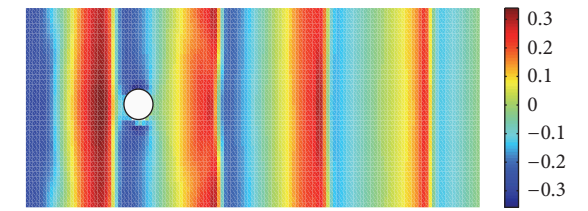
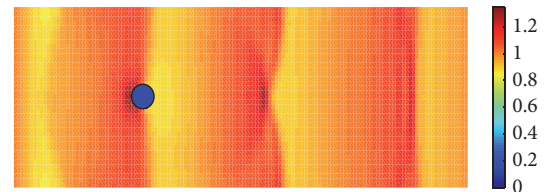
In terms of the longitudinal velocity u , it is not always positive, as the flow is only driven by the wave (see Figures 4 and 5). This phenomenon is further described in Figure 6.

Test 3 (driven by both wave and current). Under the interaction effects of waves and currents, the wave run-up is pushed higher than before (see Figures 7 and 8), and the deformation process is more apparent (see Figure 9).

To illustrate the effects of currents and waves, the comparisons of the velocity u and the water depth h are plotted in Figures 10 and 11, respectively. It can be found that the wave-current interaction is not a simple superposition of waves and currents, and furthermore, wave-current interaction effects are greater than summation of these two effects separately.

3.2. Solitary Waves around Cylinders. This case is a classic cylinder model that has been simulated by many researchers before [23, 24]. In this section, a solitary wave around a cylinder is simulated first. The whole water channel is 60 m long and 30 m wide, and there is a circular cylinder with $R = 1.5875$ m in the center of the channel. The initial solitary wave with amplitude of 0.4 m is incident from left. Lattice size is 0.4 m, and the time step is 0.01 s.

Figure 12 shows the plots of three-dimensional perspective view of water surface at $t = 8.7$ s and 16 s. The solitary wave climbs up and a sequence of significant disperse waves after initial wave encountering the cylinder can be observed. At $t = 16$ s, the solitary wave is about to propagate out of the area. At the same time, disperse waves are fully developed

FIGURE 3: x, y direction of the velocity ($t = 3$ s).FIGURE 4: Three-dimensional water depth diagram ($t = 3$ s).FIGURE 5: Velocity vector diagram ($t = 3$ s).FIGURE 6: The magnitude of u and v ($t = 3$ s).FIGURE 7: The magnitude of water surface ($t = 3$ s).

to cover almost all the channel behind the frontal wave. The results are consistent with previous research [23].

Furthermore, a solitary wave around four cylinders is simulated. The simulation is conducted in an area of constant water depth (1 m), being 60 m long and 40 m wide. The distance between the centers of any two adjacent cylinders is 7.17 m, and the radius of four cylinders is the same with 2 m (see Figure 13). The whole domain is divided by 150×100 computational grids. The time step is 0.01 s.

Figure 14 is the three-dimensional water depth of the wave around four cylinders at different times. The climbing up of water on the first cylinder can be observed at $t = 7$ s. At $t = 9$ s, the solitary wave encounters two middle cylinders and then runs up the front sides. Furthermore, a circular back disperse wave begins to turn up and propagates along the channel. The height of the middle part of the solitary wave decreases significantly due to obstruction of the frontal cylinder. The solitary wave encounters the rear cylinder at $t = 10.5$ s. The results show that the back disperse waves induced by the frontal cylinder form a circular wave pattern propagating towards the left open boundary. At the same time, the circular disperse waves, emerging from the two

middle cylinders, are also expanded. Due to the complicated interactions between waves and cylinders, the diffracted wave patterns become fully irregular in the domain at $t = 16$ s. The results of the proposed model agree well with the work conducted by Zhong and Wang [23].

4. Conclusion

This paper proposes a two-dimensional hydrodynamic model to investigate the wave-current interaction around cylinders. The lattice Boltzmann method was used to discretize the mathematical model in numerical simulation. A BKG scheme with an enhanced equilibrium is used to treat the wave radiation stress. The numerical results of both cases are in good agreement with practicalities and previous studies, demonstrating that this new model is able to produce reliable results for studying cylinders problems.

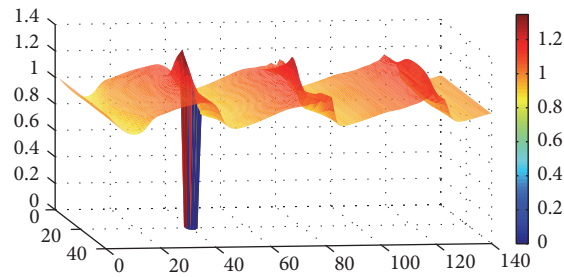
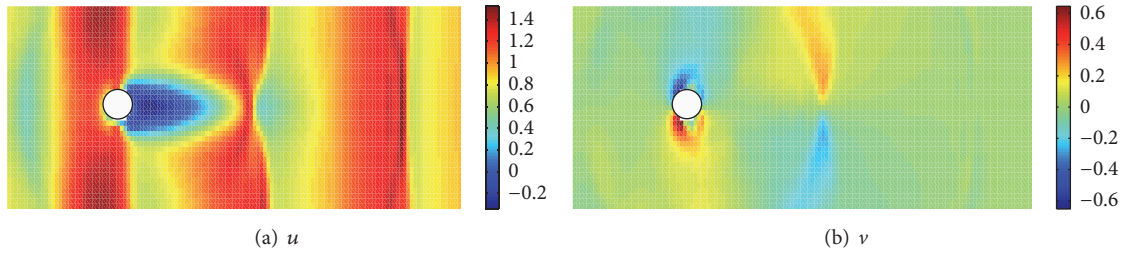


FIGURE 8: Three-dimensional water depth diagram ($t = 3$ s).



(a) u

(b) v

FIGURE 9: The magnitude of u and v ($t = 3$ s).

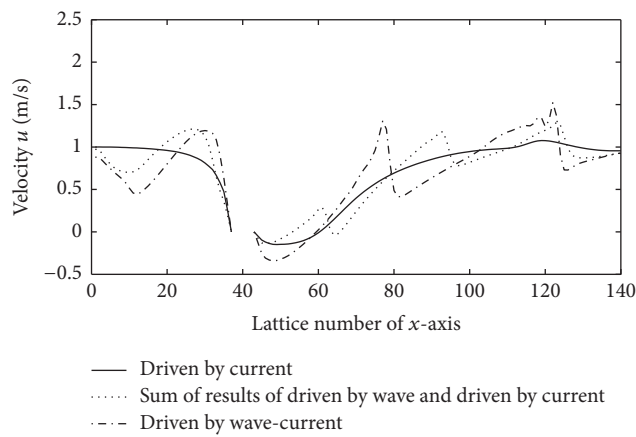


FIGURE 10: Comparison of u ($y = 20$, $t = 3$ s).

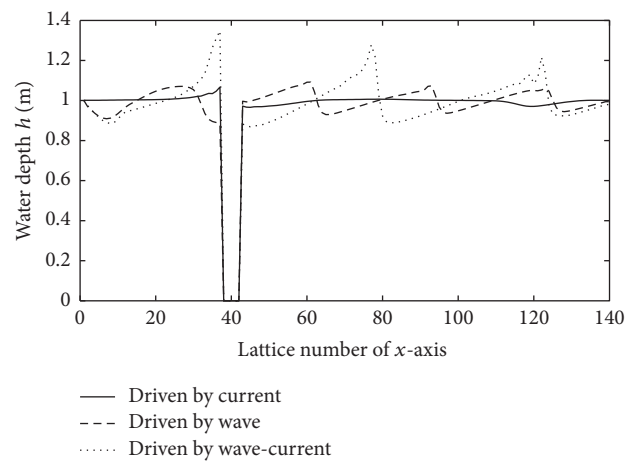


FIGURE 11: Comparison of h ($y = 20$, $t = 3$ s).

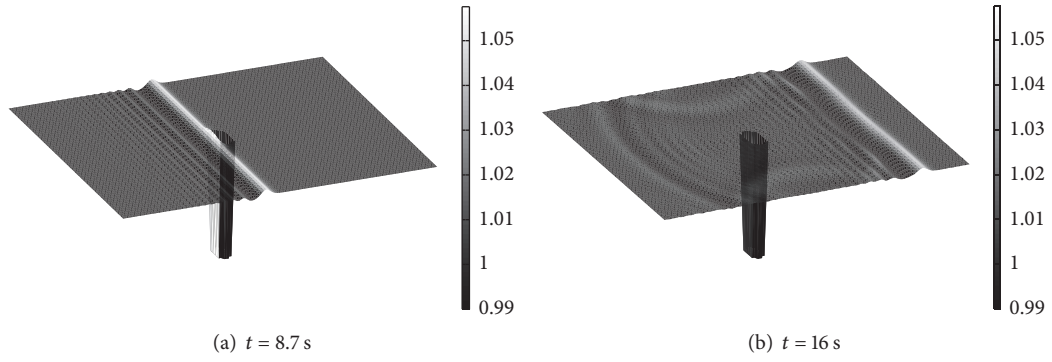


FIGURE 12: The plots of three-dimensional perspective view of water surface.

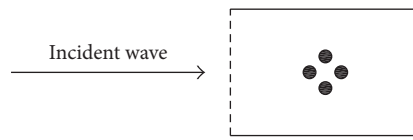


FIGURE 13: The layout of the channel.

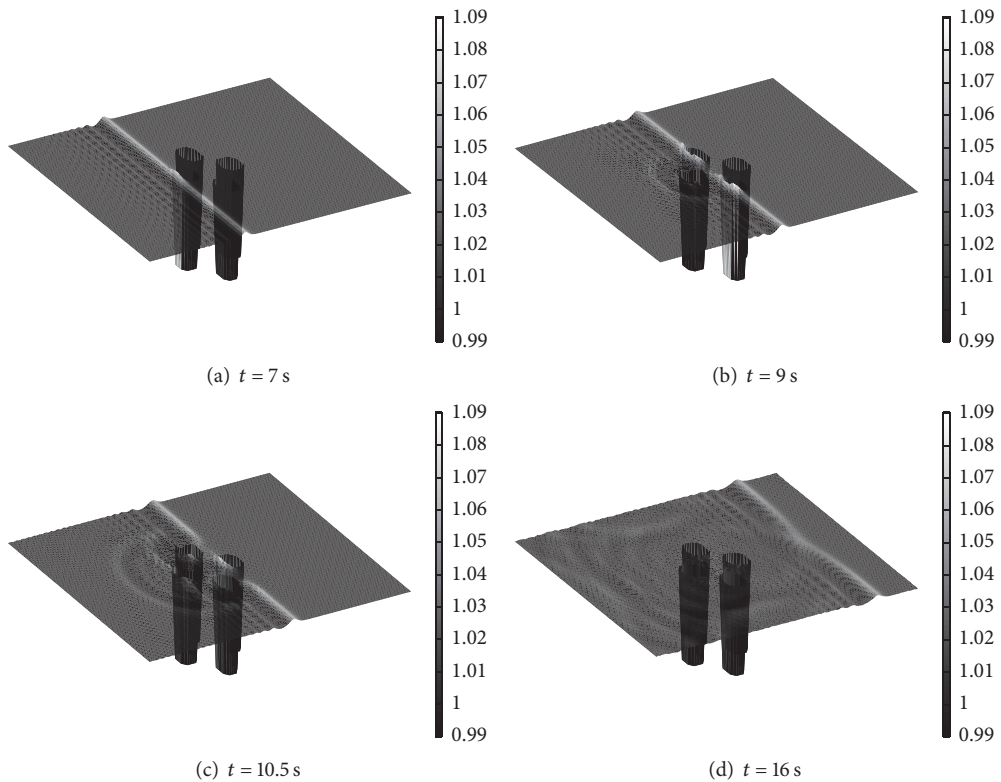


FIGURE 14: The plots of three-dimensional perspective view of water surface.

Conflicts of Interest

The authors declare that there are no conflicts of interest regarding the publication of this paper.

Acknowledgments

This study was supported by the National Natural Science Foundation of China (51379001) and the Open Fund of

State Key Laboratory of Hydraulics and Mountain River Engineering (SKHL1518).

References

- [1] E. M. Saiki and S. Biringen, "Numerical simulation of a cylinder in uniform flow: Application of a virtual boundary method," *Journal of Computational Physics*, vol. 123, no. 2, pp. 450–465, 1996.
- [2] A. L. F. Lima E Silva, A. Silveira-Neto, and J. J. R. Damasceno, "Numerical simulation of two-dimensional flows over a circular cylinder using the immersed boundary method," *Journal of Computational Physics*, vol. 189, no. 2, pp. 351–370, 2003.
- [3] D. K. Ofengeim and D. Drikakis, "Simulation of blast wave propagation over a cylinder," *Shock Waves*, vol. 7, no. 5, pp. 305–317, 1997.
- [4] M. Breuer, "Large eddy simulation of the subcritical flow past a circular cylinder: Numerical and modeling aspects," *International Journal for Numerical Methods in Fluids*, vol. 28, no. 9, pp. 1281–1302, 1998.
- [5] J. R. Meneghini, F. Saltara, C. L. R. Siqueira, and J. A. Ferrari Jr., "Numerical simulation of flow interference between two circular cylinders in tandem and side-by-side arrangements," *Journal of Fluids and Structures*, vol. 15, no. 2, pp. 327–350, 2001.
- [6] P. Hu, G. X. Wu, and Q. W. Ma, "Numerical simulation of nonlinear wave radiation by a moving vertical cylinder," *Ocean Engineering*, vol. 29, no. 14, pp. 1733–1750, 2002.
- [7] Y. L. Wu and C. Shu, "Application of local DFD method to simulate unsteady flows around an oscillating circular cylinder," *International Journal for Numerical Methods in Fluids*, vol. 58, no. 11, pp. 1223–1236, 2008.
- [8] S. Claus and T. N. Phillips, "Viscoelastic flow around a confined cylinder using spectral/hp element methods," *Journal of Non-Newtonian Fluid Mechanics*, vol. 200, pp. 131–146, 2013.
- [9] L.-C. Hsu, J.-Z. Ye, and C.-H. Hsu, "Simulation of Flow Past a Cylinder with Adaptive Spectral Element Method," *Journal of Mechanics*, vol. 33, no. 2, pp. 235–247, 2017.
- [10] I. Ginzburg and D. D'Humieres, "Multireflection boundary conditions for lattice Boltzmann models," *Physical Review E: Statistical, Nonlinear, and Soft Matter Physics*, vol. 68, no. 6, Article ID 066614, 2003.
- [11] F. J. Jiménez-Hornero, J. V. Giráldez, A. M. Laguna, S. J. Bennett, and C. V. Alonso, "Modelling the effects of emergent vegetation on an open-channel flow using a lattice model," *International Journal for Numerical Methods in Fluids*, vol. 55, no. 7, pp. 655–672, 2007.
- [12] H. Liu, J. G. Zhou, M. Li, and Y. Zhao, "Multi-block lattice Boltzmann simulations of solute transport in shallow water flows," *Advances in Water Resources*, vol. 58, pp. 24–40, 2013.
- [13] H. Liu and J. G. Zhou, "Lattice Boltzmann approach to simulating a wetting-drying front in shallow flows," *Journal of Fluid Mechanics*, vol. 743, pp. 32–59, 2014.
- [14] Y. Y. Yan and Y. Q. Zu, "Numerical simulation of heat transfer and fluid flow past a rotating isothermal cylinder - A LBM approach," *International Journal of Heat and Mass Transfer*, vol. 51, no. 9-10, pp. 2519–2536, 2008.
- [15] A. Rabienataj Darzi, A. H. Eisapour, A. Abazarian, F. Hosseinejad, and H. H. Afrouzi, "Mixed Convection Heat Transfer Analysis in an Enclosure with Two Hot Cylinders: A Lattice Boltzmann Approach," *Heat Transfer - Asian Research*, vol. 46, no. 3, pp. 218–236, 2017.
- [16] M. S. Longuet-Higgins and R. W. Stewart, "Radiation stresses in water waves; a physical discussion, with applications," *Deep-Sea Research and Oceanographic Abstracts*, vol. 11, no. 4, pp. 529–562, 1964.
- [17] B.-C. LIANG, H.-J. LI, and D.-Y. LEE, "Bottom Shear Stress Under Wave-Current Interaction," *Journal of Hydrodynamics*, vol. 20, no. 1, pp. 88–95, 2008.
- [18] F. Yang, Y. Li, L. Yang, and W. Du, "Modeling study of thermal discharge under current influence of wave and current," *Pearl River*, vol. 6, pp. 60–63, 2007.
- [19] Y. Lu, L. Zuo, H. Wang, and H. Li, "Two-dimensional mathematical model for sediment transport by waves and tidal currents," *Journal of Sediment Research*, vol. 6, pp. 1–12.
- [20] J. P. Le Roux, "Wave friction factor as related to the shields parameter for steady currents," *Sedimentary Geology*, vol. 155, no. 1-2, pp. 37–43, 2003.
- [21] J. G. Zhou and H. Liu, "Determination of bed elevation in the enhanced lattice Boltzmann method for the shallow-water equations," *Physical Review E: Statistical, Nonlinear, and Soft Matter Physics*, vol. 88, no. 2, Article ID 023302, 2013.
- [22] J. G. Zhou, *Lattice Boltzmann Methods for Shallow Water Flows*, Springer, Heidelberg, Germany, 2004.
- [23] Z. Zhong and K. H. Wang, "Modeling fully nonlinear shallow-water waves and their interactions with cylindrical structures," *Computers & Fluids*, vol. 38, no. 5, pp. 1018–1025, 2009.
- [24] S. Woo and L. Liu, "Finite element model for modified Boussinesq equations i: model development," *Journal of Waterway Port Coastal and Ocean Engineering*, vol. 130, pp. 1–16.

Research Article

Study on Force Schemes in Pseudopotential Lattice Boltzmann Model for Two-Phase Flows

Yong Peng , Bo Wang , and Yunfei Mao

State Key Laboratory of Hydraulics and Mountain River Engineering, Sichuan University, Chengdu, Sichuan 610065, China

Correspondence should be addressed to Bo Wang; wangbo@scu.edu.cn

Received 7 July 2017; Revised 11 October 2017; Accepted 22 November 2017; Published 9 January 2018

Academic Editor: Manfred Krafczyk

Copyright © 2018 Yong Peng et al. This is an open access article distributed under the Creative Commons Attribution License, which permits unrestricted use, distribution, and reproduction in any medium, provided the original work is properly cited.

Multiphase flows are very important in industrial application. In present study, the force schemes in the pseudopotential LBM for two-phase flows have been compared in detail and the force schemes include Shan-Chen, EDM, MED, and Guo's schemes. Numerical simulations confirm that all four schemes are consistent with the Laplace law. For Shan-Chen scheme, the smaller τ is, the smaller the surface tension is. However, for other schemes, τ has no effect on surface tension. When $0.6 < \tau \leq 1$, the achieved density ratio will reduce as τ reduces. During this range of τ , the maximum density ratio of EDM scheme will be greater than that of other schemes. For a constant T , the curves of the maximum spurious currents (u') has a minimum value which is corresponding to τ' except for EDM schemes. In the region of $\tau' < \tau \leq 1$, u' will reduce as τ decreases. On the other hand, in the area of $\tau \leq \tau'$, u' will increase as τ decreases. However, for EDM scheme, u' will increase as τ increases.

1. Introduction

Multiphase flows are very important in industrial application [1]. Recently, the lattice Boltzmann method (LBM) has been applied widely for studying the two-phase flows and demonstrated its advantages [2–4]. The LBM for two-phase flows can be divided into the following four kinds: pseudopotential model [5, 6], free energy model [7], kinetic theory based model [8], and color model [9, 10], in which the pseudopotential LBM is very popular because of its simplicity.

In pseudopotential LBM, the interactions between fluids are simulated by an artificial interparticle potential. So, the force scheme is very important to simulate two-phase flows accurately. There are four main kinds of force schemes in the pseudopotential LBM: the first is Shan and Chen's force scheme [5, 6], the second is the Exact Difference Method (EDM) scheme [11–13], the third is Method of Explicit Derivative (MED) scheme [8], and the last is Guo's scheme which considered the discrete lattice effects [14]. Shan [15] showed that the spurious current present in LBM is due to the insufficient isotropy of operator and proposed a method to improve it. Shan [16] proposed a general approach of

calculating the pressure tensor for nonideal gas LBM. Yu and Fan [17] combined adaptive mesh refinement method and lattice Boltzmann method to improve the two-phase flow simulation. It should be noted that the EDM scheme is Galilean invariant and the results obtained by EDM scheme do not depend on relaxation time [11, 18]. Kupershtokh et al. [13] compared three kinds of approximation of the gradient of special potential ("local," "mean-value," and "general") and showed that the "general" approximation was most precise and stable. Moreover, the maximal density ratio was larger than 10^7 for the van der Waals Equation of State and up to 10^9 for the Carnahan-Starling Equation of State. Recently, Huang et al. [19] and Sun et al. [20] investigated the performance of different forcing schemes in the pseudopotential LBM. Li et al. [21] carried out a theoretical analysis of the Shan-Chen and EDM schemes in the pseudopotential LBM. Hu et al. [22] carried out the comparative analysis of different force schemes in pseudopotential LBM. Zheng et al. [23] studied the different force treatments in detail in Shan-Chen two-phase LBM by theoretical analysis.

Based on above analysis, although some studies have been carried out on the force schemes in pseudopotential LBM, but the detailed comparison of different force schemes is scarce in

available literature. In present study, a detailed comparison of force schemes including Shan-Chen, EDM, MED, and Guo's schemes will be carried out.

2. Pseudopotential Lattice Boltzmann Model for Two-Phase Flows

2.1. Shan-Chen Scheme. The first pseudopotential lattice Boltzmann model for two-phase flows is proposed by Shan and Chen [5, 6] and is expressed as follows:

$$\begin{aligned} f_\alpha(\mathbf{x} + \mathbf{e}_\alpha \Delta t, t + \Delta t) &= f_\alpha(\mathbf{x}, t) \\ &\quad - \frac{1}{\tau} [f_\alpha(\mathbf{x}, t) - f_\alpha^{\text{eq}}(\rho, \mathbf{u})], \\ \mathbf{u}^{\text{eq}} &= \mathbf{u}(\mathbf{x}, t) + \tau \Delta \mathbf{u}, \\ \Delta \mathbf{u}(\mathbf{x}, t) &= \frac{\mathbf{F}(\mathbf{x}, t) \Delta t}{\rho(\mathbf{x}, t)}. \end{aligned} \quad (1)$$

The equilibrium distribution functions can be calculated by

$$f_\alpha^{\text{eq}}(\rho, \mathbf{u}) = \rho w_\alpha \left(1 + \frac{\mathbf{e}_\alpha \cdot \mathbf{u}}{\theta} + \frac{(\mathbf{e}_\alpha \cdot \mathbf{u})^2}{2\theta^2} - \frac{\mathbf{u}^2}{2\theta} \right). \quad (2)$$

The density and flow velocity can be obtained by the following:

$$\begin{aligned} \rho &= \sum_\alpha f_\alpha, \\ \mathbf{u} &= \frac{1}{\rho} \sum_\alpha \mathbf{e}_\alpha f_\alpha. \end{aligned} \quad (3)$$

The actual fluid velocity can be defined according to Ginzburg and Adler [24] as

$$\tilde{\mathbf{u}} = \mathbf{u} + \frac{\mathbf{F} \Delta t}{(2\rho)}. \quad (4)$$

2.2. EDM Scheme. The pseudopotential lattice Boltzmann model with EDM [11, 12] can read

$$\begin{aligned} f_\alpha(\mathbf{x} + \mathbf{e}_\alpha \Delta t, t + \Delta t) &= f_\alpha(\mathbf{x}, t) \\ &\quad - \frac{1}{\tau} [f_\alpha(\mathbf{x}, t) - f_\alpha^{\text{eq}}(\rho, \mathbf{u})] \\ &\quad + f_\alpha^{\text{eq}}(\rho, \mathbf{u} + \Delta \mathbf{u}) \\ &\quad - f_\alpha^{\text{eq}}(\rho, \mathbf{u}), \end{aligned} \quad (5)$$

where $\rho \mathbf{u} = \sum_\alpha \mathbf{e}_\alpha f_\alpha$, $\Delta \mathbf{u} = \mathbf{F} \Delta t / \rho$ and the equilibrium distribution function is shown as follows:

$$f_\alpha^{\text{eq}}(\rho, \mathbf{u}) = \rho w_\alpha \left(1 + \frac{\mathbf{e}_\alpha \cdot \mathbf{u}}{\theta} + \frac{(\mathbf{e}_\alpha \cdot \mathbf{u})^2}{2\theta^2} - \frac{\mathbf{u}^2}{2\theta} \right). \quad (6)$$

The real fluid velocity can be obtained from Ginzburg and Adler [24] as follows:

$$\tilde{\mathbf{u}} = \mathbf{u} + \frac{\mathbf{F} \Delta t}{2\rho}. \quad (7)$$

2.3. Guo's Scheme. The pseudopotential lattice Boltzmann model with Guo's force scheme [14] can be shown as follows:

$$\begin{aligned} f_\alpha(\mathbf{x} + \mathbf{e}_\alpha \Delta t, t + \Delta t) &= f_\alpha(\mathbf{x}, t) \\ &\quad - \frac{1}{\tau} [f_\alpha(\mathbf{x}, t) - f_\alpha^{\text{eq}}(\rho, \mathbf{u})] \\ &\quad + \left(1 - \frac{1}{2\tau} \right) F_\alpha(t) \Delta t, \end{aligned} \quad (8)$$

with $F_\alpha = w_\alpha [(\mathbf{e}_\alpha - \tilde{\mathbf{u}}) / C_s^2 + (\mathbf{e}_\alpha \tilde{\mathbf{u}} / C_s^4) \mathbf{e}_\alpha] \cdot \mathbf{F}$.

The density and flow velocity can be obtained by the following [24]:

$$\begin{aligned} \rho &= \sum_\alpha f_\alpha, \\ \tilde{\mathbf{u}} &= \frac{1}{\rho} \sum_\alpha \mathbf{e}_\alpha \left(f_\alpha + \frac{\Delta t}{2} F_\alpha \right). \end{aligned} \quad (9)$$

2.4. MED Scheme. The pseudopotential lattice Boltzmann model with MED force scheme [8] can be shown as follows:

$$\begin{aligned} \bar{f}_\alpha(\mathbf{x} + \mathbf{e}_\alpha \Delta t, t + \Delta t) &= \bar{f}_\alpha(\mathbf{x}, t) \\ &\quad - \frac{1}{\tau} [\bar{f}_\alpha(\mathbf{x}, t) - \bar{f}_\alpha^{\text{eq}}(\rho, \mathbf{u})] \\ &\quad + \Delta t \left(1 - \frac{1}{2\tau} \right) \frac{(\mathbf{e}_\alpha - \mathbf{u}) \cdot \mathbf{F}}{\rho C_s^2} f_\alpha^{\text{eq}}(\rho, \mathbf{u}), \end{aligned} \quad (10)$$

with $\bar{f}_\alpha = f_\alpha - (\Delta t / 2) (((\mathbf{e}_\alpha - \mathbf{u}) \cdot \mathbf{F}) / \rho C_s^2) f_\alpha^{\text{eq}}$.

The density and flow velocity can be obtained by

$$\begin{aligned} \rho &= \sum_\alpha \bar{f}_\alpha, \\ \rho \mathbf{u} &= \sum_\alpha \bar{f}_\alpha \mathbf{e}_\alpha + \frac{\Delta t}{2} \mathbf{F}. \end{aligned} \quad (11)$$

3. Carnahan-Starling Equation of State (C-S EOS)

In order to get relatively large density ratio, the Carnahan-Starling Equation of State (C-S EOS) is used in the present study [25]:

$$p = \rho RT \frac{1 + b\rho/4 + (b\rho/4)^2 - (b\rho/4)^3}{(1 - b\rho/4)^3} - a\rho^2, \quad (12)$$

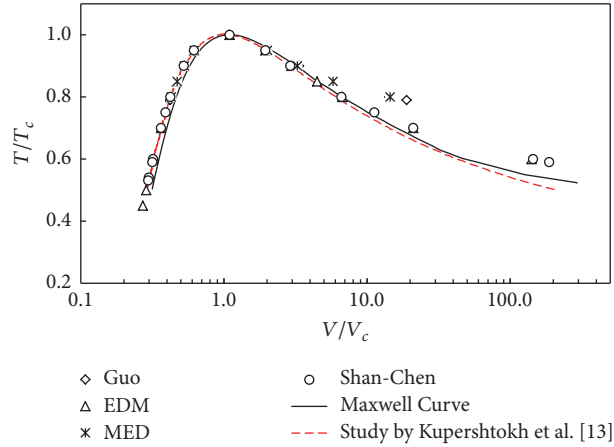


FIGURE 1: Predicted coexistence densities of two-phase separation by of Shan-Chen, EDM, MED, and Guo's schemes ($\tau = 1$).

in which $a = 0.4963R^2T_c^2/p_c$, $b = 0.18727RT_c/p_c$, and T_c and P_c can be obtained by

$$\begin{aligned} T_c &= \frac{0.3773a}{bR}, \\ P_c &= \frac{0.0706}{b^2}, \end{aligned} \quad (13)$$

where $a = 1$, $b = 4$, $R = 1$ are used in the present study.

4. Application Cases

4.1. Two-Phase Separation. In this section, two-phase separation will be used to test four schemes of Shan-Chen, EDM, MED, and Guo. The force term can be calculated by the following:

$$\mathbf{F}(x, t) = -G\psi \sum_{\alpha} w_{\alpha} \psi(x + \mathbf{e}_{\alpha} \Delta t) \mathbf{e}_{\alpha}, \quad (14)$$

where w_{α} is weights and, for D2Q9 model, $w_{\alpha} = 4/9$ ($\alpha = 1$), $w_{\alpha} = 1/9$ ($\alpha = 2, 3, 4, 5$), $w_{\alpha} = 1/36$ ($\alpha = 6, 7, 8, 9$).

In the present work, the interaction potential is defined according to the method by Chen et al. [26] as follows:

$$\psi(\rho) = \sqrt{\frac{2(p - \rho c_s^2)}{Gc_s^2}}. \quad (15)$$

In computation, $\rho_0 = 1$, 101×101 grids have been used; the periodic boundary conditions are used for all boundaries. The initial density for whole area is critical density, and a random density fluctuation of plus or minus 1% is added at the beginning for whole area. When the computation gets to equilibrium, gas and liquid phases will separate clearly. The simulated results are shown in Figure 1.

It can be known from Figure 1 that all of four schemes perform almost the same and agree well with the analytical

solution. Besides, it is clear that the present study agrees with that by Kupershtokh et al. [13].

4.2. Surface Tension. Surface tension is of great importance in the two-phase flows and its relationship with bubble radius is consistent with the Laplace law. In this section, Laplace's law will be used to verify four schemes and the effect of τ and T on the surface tension will be discussed. The simulated results are shown in Table 1 and Figures 2–4.

It can be seen from Figures 2 and 3, the pressure difference between the inside and outside the bubble is linearly related to the reciprocal of the radius. This agrees well with the Laplace's law. Figure 3 shows that τ has no effect on surface tension for the EDM, MED, and Guo's schemes.

4.3. Maximum Two-Phase Density Ratio. The study shows that the simulation will become unstable when T is low for four schemes, so T has a certain range for stable computation. To demonstrate the numerical stability of four schemes and get the minimum T with stable computation, two-phase separation case is tested by adjusting τ and the results are shown in Figure 5.

It can be seen from Figure 5 that the minimum T will become larger as τ reduces when $0.5 < \tau \leq 1$ and it means that achieved maximum ratio of two-phase densities will become smaller. For the same τ , the maximum density ratio of EDM scheme will be larger than those of other schemes for $0.6 < \tau \leq 1$.

4.4. Spurious Currents. The spurious current is one of the important criteria to evaluate pseudopotential models because it will lead to the computation instability. In order to study the effect of four force schemes on spurious current, a series of tests have been carried out. The maximum spurious currents for different T and τ have been shown in Table 2 and Figure 6. It shows that the spurious current will increase as T reduces with the same τ for all of four schemes. That is

TABLE 1: The effect of τ and T on the surface tension for $T = 0.8T_c$.

τ	$1/r$	dp
	EDM scheme	
0.75	4.14E-02	3.13E-04
	4.50E-02	3.42E-04
	4.95E-02	3.77E-04
	5.49E-02	4.19E-04
	6.16E-02	4.71E-04
	7.28E-02	5.61E-04
0.8	4.14E-02	3.14E-04
	4.50E-02	3.42E-04
	4.95E-02	3.77E-04
	5.49E-02	4.20E-04
	6.16E-02	4.72E-04
	7.28E-02	5.62E-04
0.85	4.14E-02	3.14E-04
	4.50E-02	3.43E-04
	4.95E-02	3.77E-04
	5.49E-02	4.20E-04
	6.16E-02	4.72E-04
	7.28E-02	5.62E-04
0.9	4.14E-02	3.14E-04
	4.50E-02	3.43E-04
	4.95E-02	3.78E-04
	5.49E-02	4.20E-04
	6.16E-02	4.72E-04
	7.28E-02	5.62E-04
0.95	4.14E-02	3.14E-04
	4.50E-02	3.43E-04
	4.95E-02	3.78E-04
	5.49E-02	4.20E-04
	6.16E-02	4.73E-04
	7.28E-02	5.63E-04
1	4.14E-02	3.14E-04
	4.50E-02	3.43E-04
	4.95E-02	3.78E-04
	5.49E-02	4.21E-04
	6.10E-02	4.71E-04
	7.95E-02	6.15E-04
	MED scheme	
0.8	4.19E-02	1.83E-04
	4.58E-02	1.99E-04
	5.05E-02	2.19E-04
	5.64E-02	2.43E-04
	6.38E-02	2.74E-04
	7.38E-02	3.13E-04
0.85	4.19E-02	1.83E-04
	4.58E-02	1.99E-04
	5.05E-02	2.19E-04
	5.63E-02	2.43E-04
	6.38E-02	2.73E-04
	7.38E-02	3.13E-04

TABLE 1: Continued.

τ	$1/r$	dp
0.9	4.19E-02	1.83E-04
	4.58E-02	1.99E-04
	5.05E-02	2.19E-04
	5.63E-02	2.43E-04
	6.38E-02	2.73E-04
	7.38E-02	3.13E-04
0.95	4.19E-02	1.83E-04
	4.58E-02	1.99E-04
	5.05E-02	2.19E-04
	5.63E-02	2.43E-04
	6.38E-02	2.73E-04
	7.39E-02	3.13E-04
1	4.19E-02	1.83E-04
	4.58E-02	1.99E-04
	5.05E-02	2.19E-04
	5.63E-02	2.43E-04
	6.38E-02	2.74E-04
	7.39E-02	3.14E-04
	Guo's scheme	
0.85	4.14E-02	1.97E-04
	4.50E-02	2.16E-04
	4.95E-02	2.38E-04
	5.47E-02	2.65E-04
	6.48E-02	3.17E-04
0.9	4.14E-02	1.97E-04
	4.50E-02	2.16E-04
	4.95E-02	2.38E-04
	5.47E-02	2.65E-04
	6.48E-02	3.17E-04
	7.54E-02	3.75E-04
0.95	4.14E-02	1.97E-04
	4.50E-02	2.16E-04
	4.95E-02	2.38E-04
	5.47E-02	2.65E-04
	6.48E-02	3.17E-04
	7.54E-02	3.74E-04
1	4.14E-02	1.97E-04
	4.50E-02	2.16E-04
	4.95E-02	2.38E-04
	5.47E-02	2.65E-04
	6.48E-02	3.16E-04
	7.54E-02	3.74E-04

why computation is instable when T is small. The maximum spurious current of MED scheme is slightly larger than that of other schemes.

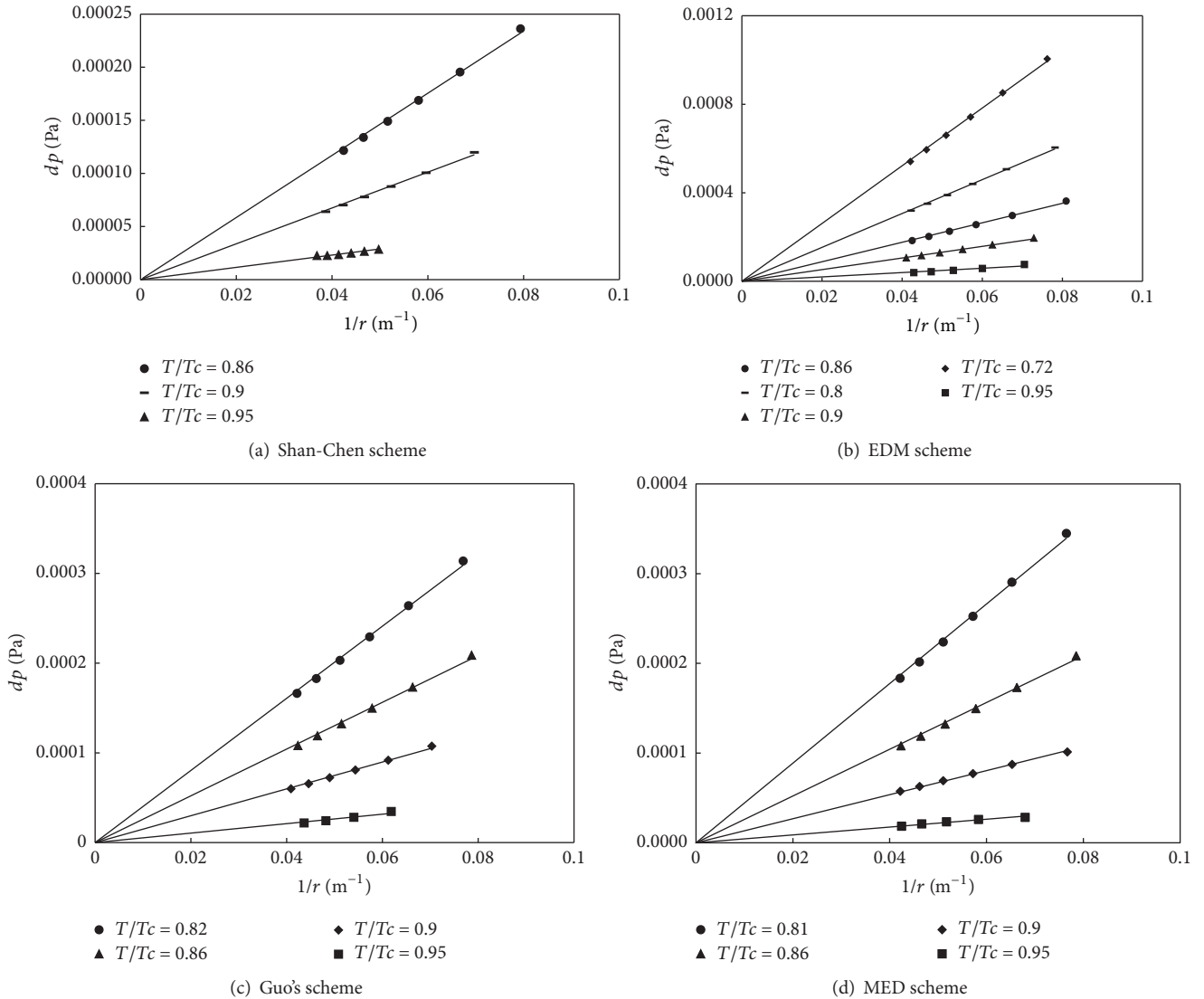


FIGURE 2: Relationship between bubble radius and pressure difference at different temperatures for $\tau = 0.7$.

Moreover, it can be seen from Figure 6 that, with a constant T , for Shan-Chen, MED, and Guo's schemes, the curves of u' have a minimum value which is corresponding to τ' . During this region of $\tau' < \tau \leq 1$, u' will reduce as τ decreases. On the other hand, in the area of $\tau \leq \tau'$, u' will increase as τ decreases. But for EDM scheme, u' will increase as τ increases. Moreover, present study is compared with that by Kupershtokh et al. [13] and both of results are similar as shown in Figure 7.

5. Conclusions

In present study, the force schemes in the pseudopotential LBM for two-phase flows have been compared in detail and the force schemes include Shan-Chen, EDM, MED, and Guo's schemes. The LBM with four schemes have been used to study the two-phase separation and surface tension. Besides,

the maximum two-phase density ratio and spurious currents also are discussed in detail. Based on the above study, the following conclusions can be drawn:

(1) Numerical simulations confirm that all four schemes are consistent with the Laplace law. For the EDM, MED, and Guo's schemes, τ has no effect on surface tension.

(2) When $0.5 < \tau \leq 1$, the achieved density ratio will reduce as τ reduces. For the same τ , the maximum density ratio of EDM scheme will be greater than that of other schemes $0.6 < \tau \leq 1$.

(3) Except for the EDM scheme, the curves of the maximum spurious currents (u') have a minimum value which is corresponding to τ' for three schemes. In the region of $\tau' < \tau \leq 1$, u' will reduce as τ decreases. On the other hand, in the area of $\tau \leq \tau'$, u' will increase as τ decreases. But for EDM scheme, u' will increase as τ increases.

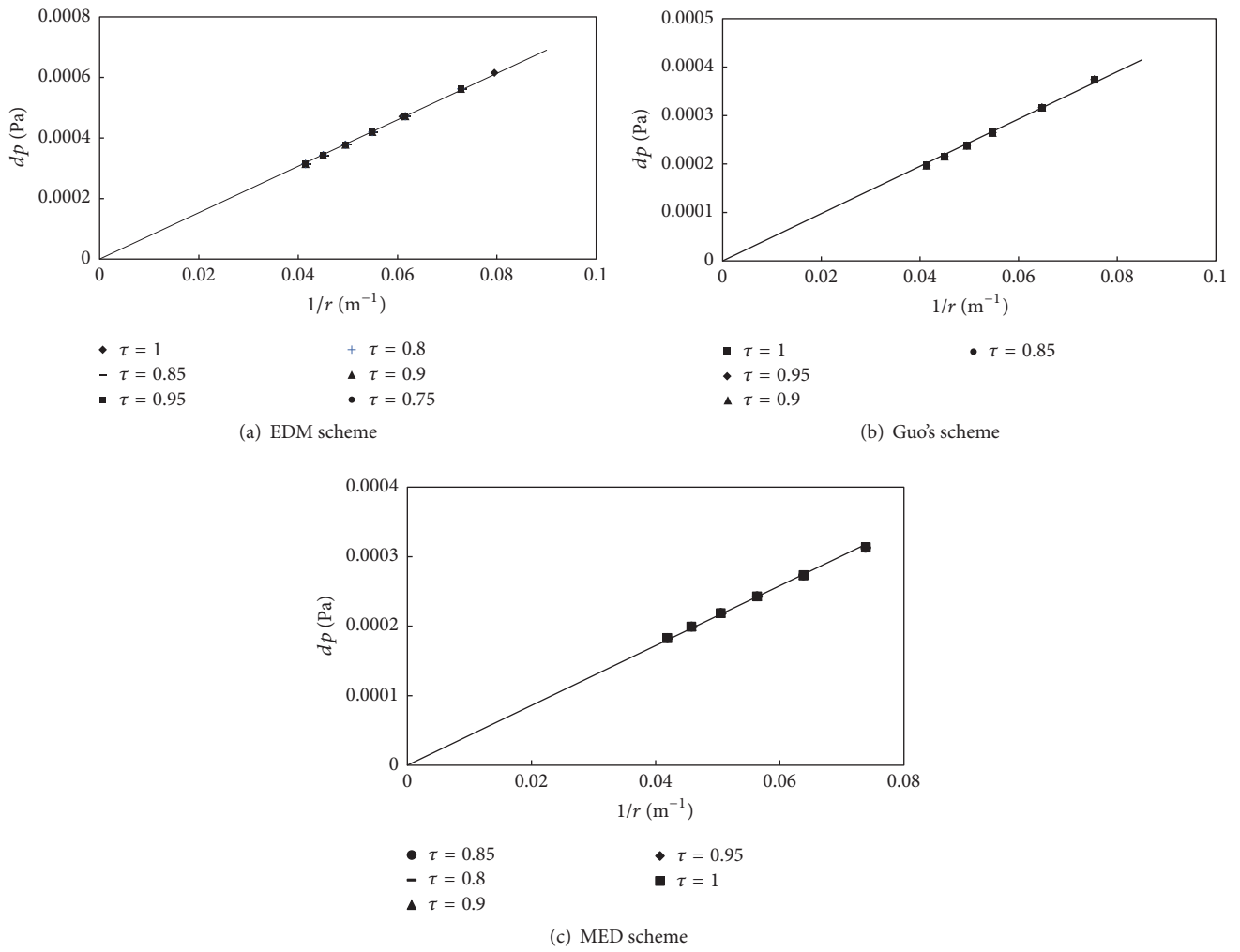


FIGURE 3: Relationship between bubble radius and pressure difference at different τ for $T = 0.8T_c$.

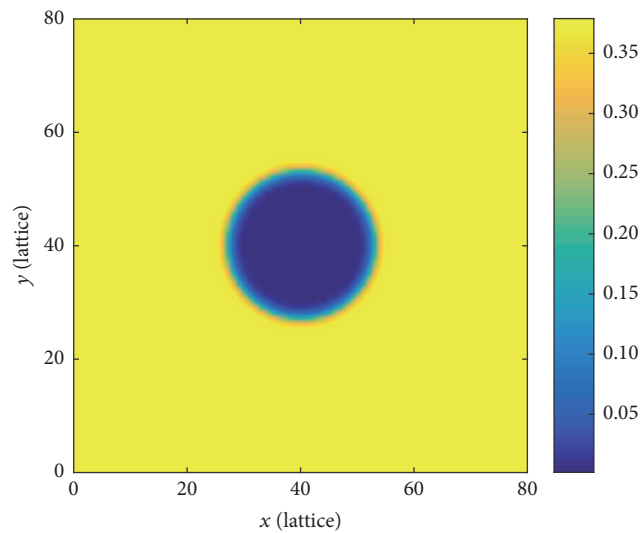


FIGURE 4: The density distribution of stable bubble with EDM force scheme.

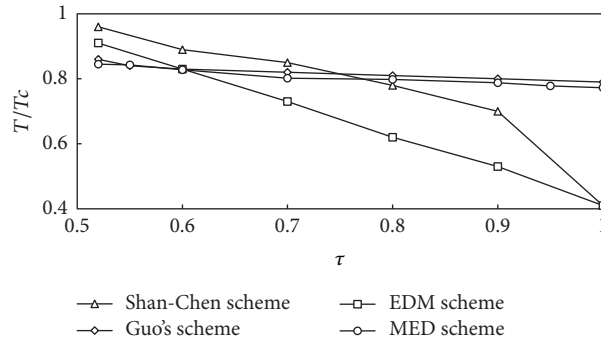


FIGURE 5: The minimum T with stable computation at different τ for Shan-Chen, EDM, MED, and Guo's schemes.

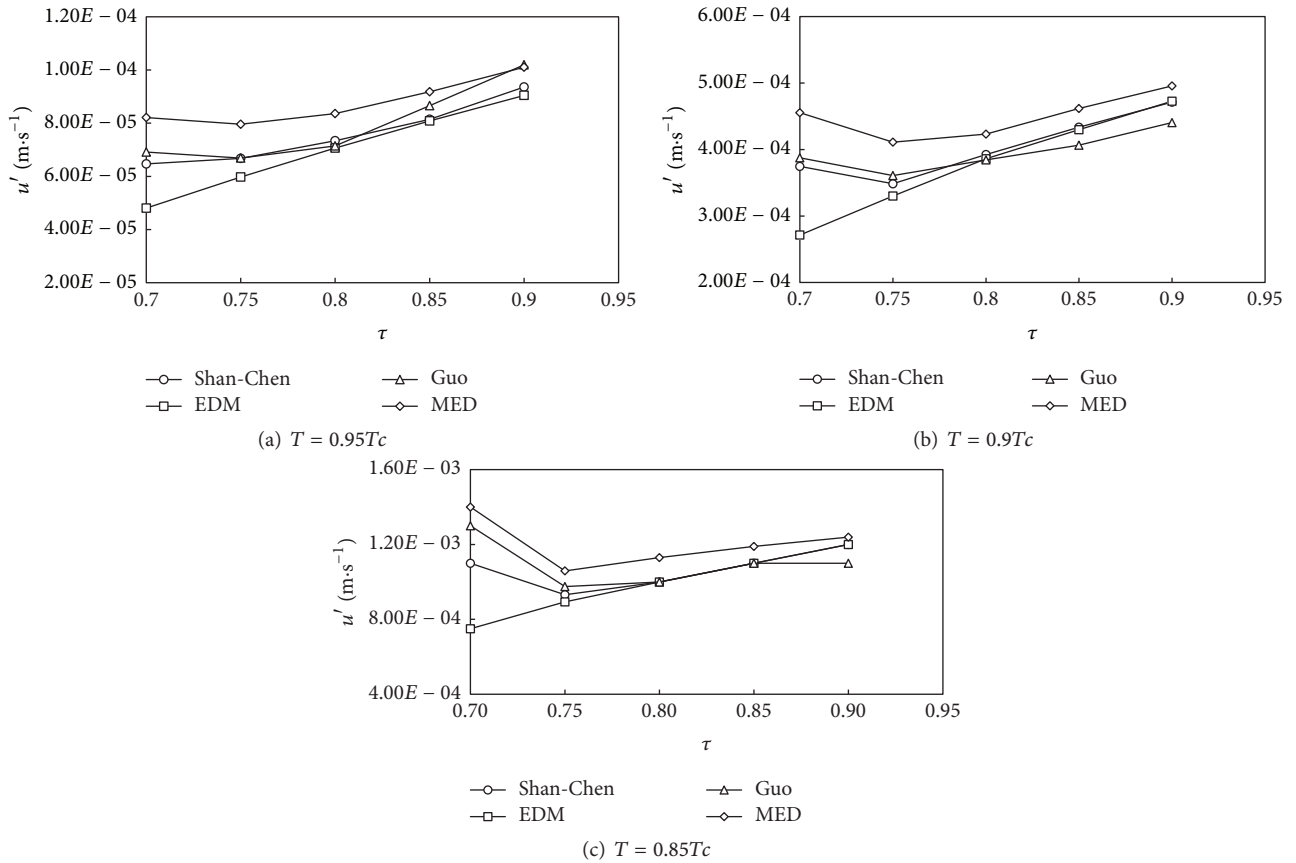


FIGURE 6: The maximum spurious currents of Shan-Chen, EDM, MED, and Guo's schemes for different τ and T .

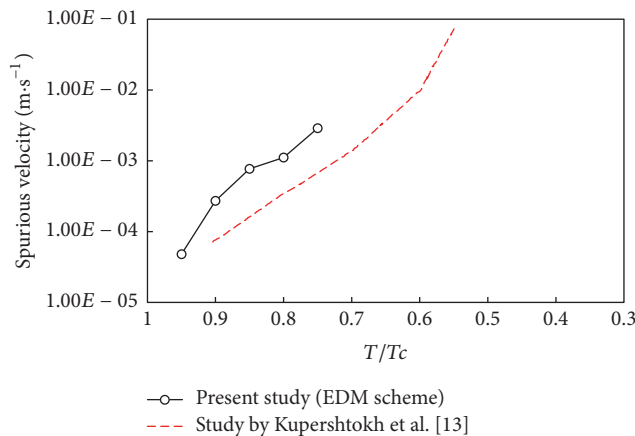


FIGURE 7: Comparison of maximum spurious currents for EDM scheme between Kupershtokh et al. [13] (τ is unknown) and present study with $\tau = 0.7$.

TABLE 2: Maximum spurious currents for Shan-Chen, EDM, Guo's, and MED schemes.

T/T_c	τ	u'			
		Shan-Chen scheme	EDM scheme	Guo's scheme	MED scheme
0.95	0.90	$9.36E-05$	$9.04E-05$	$1.02E-04$	$1.01E-04$
	0.85	$8.14E-05$	$8.09E-05$	$8.66E-05$	$9.18E-05$
	0.80	$7.34E-05$	$7.07E-05$	$7.14E-05$	$8.36E-05$
	0.75	$6.67E-05$	$5.97E-05$	$6.69E-05$	$7.96E-05$
	0.70	$6.47E-05$	$4.81E-05$	$6.92E-05$	$8.21E-05$
0.90	0.90	$4.71E-04$	$4.73E-04$	$4.41E-04$	$4.96E-04$
	0.85	$4.34E-04$	$4.30E-04$	$4.07E-04$	$4.62E-04$
	0.80	$3.93E-04$	$3.86E-04$	$3.84E-04$	$4.23E-04$
	0.75	$3.49E-04$	$3.30E-04$	$3.61E-04$	$4.11E-04$
	0.70	$3.75E-04$	$2.71E-04$	$3.88E-04$	$4.55E-04$
0.85	0.90	$1.20E-03$	$1.20E-03$	$1.10E-03$	$1.24E-03$
	0.85	$1.10E-03$	$1.10E-03$	$1.10E-03$	$1.19E-03$
	0.80	$1.00E-03$	$1.00E-03$	$1.00E-03$	$1.13E-03$
	0.75	$9.31E-04$	$8.94E-04$	$9.75E-04$	$1.06E-03$
	0.70	$1.10E-03$	$7.50E-04$	$1.30E-03$	$1.40E-03$
	0.65	$1.90E-03$	$7.72E-04$	—	$2.31E-03$

Conflicts of Interest

The authors declare that there are no conflicts of interest regarding the publication of this paper.

Acknowledgments

The first author would like to acknowledge the financial support of the National Natural Science Foundation of China (Grants nos. 51409183, 51579166, and 51611130203). Besides, this work was also supported by the National Key Technologies R&D Program of China (no. 2015BAD24B01).

References

- [1] M. Ishii and T. Hibiki, *Thermo-Fluid Dynamics of Two-Phase Flow*, Springer, New York, NY, USA, 2007.
- [2] M. C. Sukop and D. T. Thorne, *Lattice Boltzmann Modeling: An Introduction for Geoscientists and Engineers*, Springer, Heidelberg, Germany, 2006.
- [3] C. K. Aidun and J. R. Clausen, "Lattice Boltzmann method for complex flow," *Annual Review of Fluid Mechanics*, vol. 42, no. 1, pp. 439–472, 2010.
- [4] H. Safari, M. H. Rahimian, and M. Krafczyk, "Consistent simulation of droplet evaporation based on the phase-field multiphase lattice Boltzmann method," *Physical Review E*, vol. 90, no. 3, Article ID 033305, 2014.
- [5] X. Shan and H. Chen, "Lattice Boltzmann model for simulating flows with multiple phases and components," *Physical Review E*, vol. 47, no. 3, pp. 1815–1820, 1993.
- [6] X. Shan and H. Chen, "Simulation of nonideal gases and liquid-gas phase transitions by the lattice Boltzmann equation," *Physical Review E*, vol. 49, no. 4, pp. 2941–2948, 1994.
- [7] M. R. Swift, W. R. Osborn, and J. M. Yeomans, "Lattice Boltzmann simulation of non-ideal fluids," *Physical Review Letters*, vol. 75, no. 5, pp. 830–833, 1995.
- [8] X. Y. He, X. W. Shan, and G. D. Doolen, "Discrete Boltzmann equation model for nonideal gases," *Physical Review E*, vol. 57, no. 1, pp. R13–R16, 1998.
- [9] A. K. Gunstensen, D. H. Rothman, S. Zaleski, and G. Zanetti, "Lattice Boltzmann model of immiscible fluids," *Physical Review A: Atomic, Molecular and Optical Physics*, vol. 43, no. 8, pp. 4320–4327, 1991.
- [10] J. Tölke, S. Freudiger, and M. Krafczyk, "An adaptive scheme using hierarchical grids for lattice Boltzmann multi-phase flow simulations," *Computers & Fluids*, vol. 35, no. 8-9, pp. 820–830, 2006.
- [11] A. L. Kupershtokh, "New method of incorporating a body force term into the lattice Boltzmann equation," in *Proceedings of the 5th International EHD Workshop*, pp. 241–246, 2004.
- [12] A. L. Kupershtokh, "Criterion of numerical instability of liquid state in LBE simulations," *Computers and Mathematics with Applications*, vol. 59, no. 7, pp. 2236–2245, 2010.
- [13] A. L. Kupershtokh, D. A. Medvedev, and D. I. Karpov, "On equations of state in a lattice Boltzmann method," *Computers and Mathematics with Applications*, vol. 58, pp. 965–974, 2009.
- [14] Z. Guo, C. Zheng, and B. Shi, "Discrete lattice effects on the forcing term in the lattice Boltzmann method," *Physical Review E*, vol. 65, Article ID 046308, 2002.
- [15] X. Shan, "Analysis and reduction of the spurious current in a class of multiphase lattice Boltzmann models," *Physical Review E*, vol. 73, no. 2, Article ID 047701, 2006.
- [16] X. Shan, "Pressure tensor calculation in a class of nonideal gas lattice Boltzmann models," *Physical Review E*, vol. 77, no. 2, Article ID 066702, 2008.
- [17] Z. Yu and L.-S. Fan, "An interaction potential based lattice Boltzmann method with adaptive mesh refinement AMR for two-phase flow simulation," *Journal of Computational Physics*, vol. 228, no. 17, pp. 6456–6478, 2009.
- [18] P. J. Dellar, "Lattice Boltzmann formulation for linear viscoelastic fluids using an abstract second stress," *SIAM Journal on Scientific Computing*, vol. 36, no. 6, pp. A2507–A2532, 2014.

- [19] H. Huang, M. Krafczyk, and X. Lu, "Forcing term in single-phase and Shan-Chen-type multiphase lattice Boltzmann models," *Physical Review E: Statistical, Nonlinear, and Soft Matter Physics*, vol. 84, no. 4, Article ID 046710, 2011.
- [20] K. Sun, T. Wang, M. Jia, and G. Xiao, "Evaluation of force implementation in pseudopotential-based multiphase lattice Boltzmann models," *Physica A*, vol. 391, no. 15, pp. 3895–3907, 2012.
- [21] Q. Li, K. H. Luo, and X. J. Li, "Forcing scheme in pseudopotential lattice Boltzmann model for multiphase flows," *Physical Review E*, vol. 86, no. 1, Article ID 016709, 2012.
- [22] A. Hu, L. Li, and R. Uddin, "Force method in a pseudo-potential lattice Boltzmann model," *Journal of Computational Physics*, vol. 294, pp. 78–89, 2015.
- [23] L. Zheng, Q. Zhai, and S. Zheng, "Analysis of force treatment in the pseudopotential lattice Boltzmann equation method," *Physical Review E*, vol. 95, no. 4, Article ID 043301, 2017.
- [24] I. Ginzburg and P. M. Adler, "Boundary flow condition analysis for the three-dimensional lattice Boltzmann model," *Journal de Physique II*, vol. 4, no. 2, pp. 191–214, 1994.
- [25] N. F. Carnahan and K. E. Starling, "Intermolecular repulsions and the equation of state for fluids," *AIChE Journal*, vol. 18, no. 6, pp. 1184–1189, 1972.
- [26] S. Chen, X. He, and L.-S. Luo, "Computational methods for multiphase flow," in *Lattice Boltzmann Models for Multiphase Flow*, A. Prosperetti and G. Tryggvason, Eds., chapter 6, pp. 157–192, Cambridge University Press, Cambridge, UK, 2007.

Research Article

Numerical Simulation of an Offset Jet in Bounded Pool with Deflection Wall

Xin Li, Yurong Wang, and Jianmin Zhang

State Key Laboratory of Hydraulics and Mountain River Engineering, Sichuan University, Chengdu 610065, China

Correspondence should be addressed to Jianmin Zhang; zhangjianmin@scu.edu.cn

Received 7 July 2017; Accepted 8 October 2017; Published 31 October 2017

Academic Editor: Ling Qian

Copyright © 2017 Xin Li et al. This is an open access article distributed under the Creative Commons Attribution License, which permits unrestricted use, distribution, and reproduction in any medium, provided the original work is properly cited.

The k - ε turbulent model and VOF methods were used to simulate the three-dimensional turbulence jet. Numerical simulations were carried out for three different kinds of jets in a bounded pool with the deflection wall with angles of 0° , 3° , 6° , and 9° . The numerical simulation agrees well with the experimental data. The studies show that the length of the potential core zone increases with the increase of the deflection angle. The velocity distribution is consistent with the Gaussian distribution and almost not affected by the deflection angle in potential core zone. The decay rates of flow velocity in the transition zone are 1.195, 1.281, 1.439, and 1.532 corresponding to the unilateral deflection angles, 0° , 3° , 6° , and 9° , respectively. The decay rates of velocity in the transition zone are 1.928 and 2.835 corresponding to the bilateral deflection angles 3° and 6° . It is also found that the spread of velocity is stronger in the vertical direction as the deflection angles become smaller. The spread rates of velocity with unilateral deflection wall are higher than those with bilateral deflection walls in the horizontal plane in the pool.

1. Introduction

Jet is an important motion type of fluid and it can be divided into the laminar jet and the turbulent jet according to its turbulent intensity. In hydraulic engineering, the jets almost belong to the turbulent jets [1]. In more detail, As shown in Figure 1, the jet can be divided into three regions: (I) core region or potential flow zone: the max velocity in this zone still maintains the velocity at the jet exit; (II) transition zone: the velocity in this zone decays rapidly; (III) fully development zone. When it moves into the limited pool, the flow is known as confined jets, such as hydraulics jump for energy dissipation. The flow is called wall jet when the main flow is closed to the boundary. The flow is called offset jet when the jet distances away from the boundary. Rajaratnam [2] has discussed these categories in detail. The hydraulic jump with sudden enlargement and drop was commonly used to be an energy dissipator in hydraulic engineering and it is actually a kind of submerged offset jet. According to the pressure in bottom, floor can be divided into three regions: ① recirculation region, where jet is not affected by the bottom floor, ② impingement region, where the jet attaches the

bottom floor due to the pressure, and ③ wall jet region, where the flow pattern is similar to the wall jet.

Submerged offset jets occur in many engineering applications, so submerged offset jet has received a lot of attention from researchers. However, there have been fewer investigations of jets with small offset ratios ($S/d < 5$) [3–5]. Nasr and Lai [5] determined the mean velocities and turbulence characteristics of a turbulent plane offset jet with a small offset ratio of 2.125 and a Reynolds number of 11,000 using LDA. Yang and Yeh [6] have numerically studied the field of an offset jet with Reynolds number of 15,000 for offset ratios of 3, 7, and 11. In their work, it was revealed that when the flow is fully developed near the exit and when the walls are far away from the region of concern, zero normal gradient boundary condition could be used at the entrainment and exit boundary. Agelin-Chaab and Tachie [7] reported that, in the early region of the flow development, the Reynolds number and the offset ratio have significant effects on the decay of the maximum mean velocity, but the decay and spread rates were found to be nearly independent of the offset ratio at larger downstream distances. Assoudi et al. [8] had investigated the mean velocity and turbulence characteristics of the turbulent

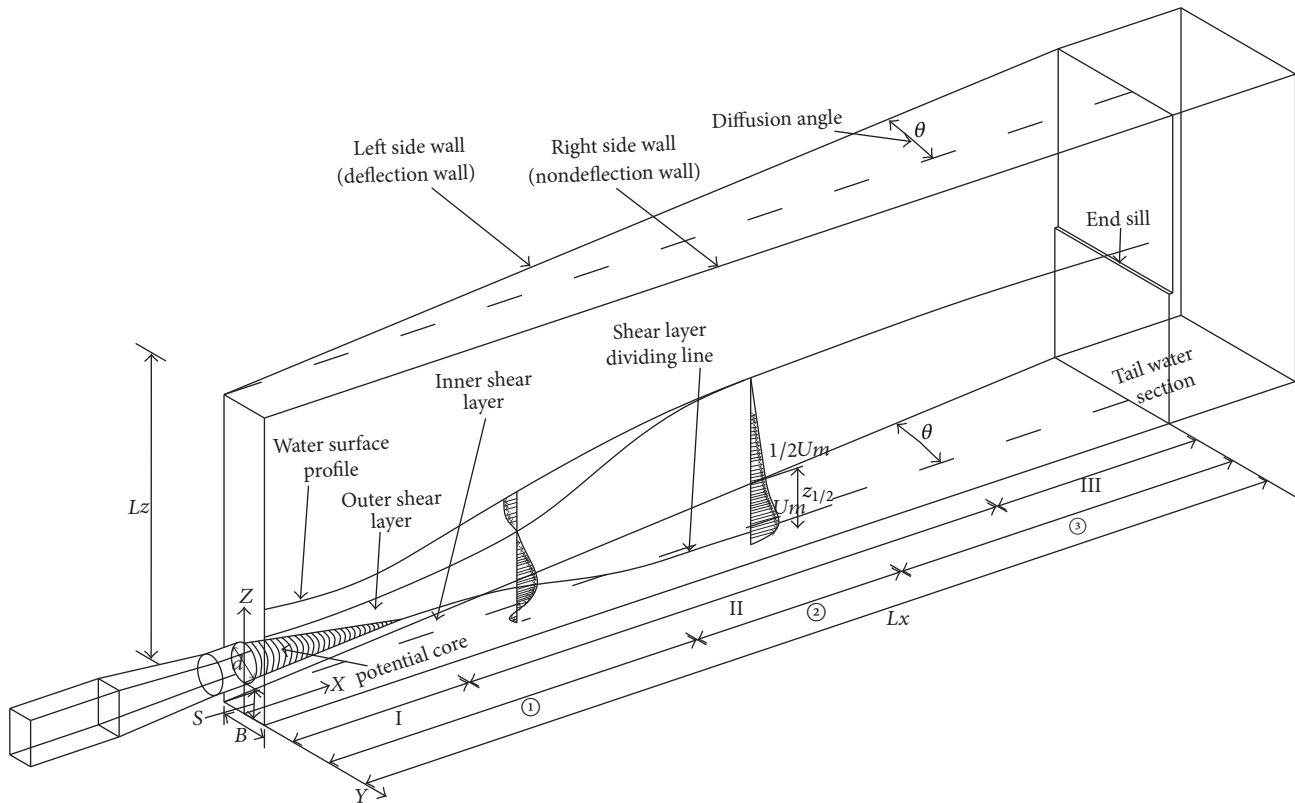


FIGURE 1: The sketch of submerged offset jet inside a unilateral deflection pool. *Note.* Divided by velocity decay rate in streamwise direction: (I) core region or potential flow zone, (II) transition zone, and (III) full development zone. Divided by pressure in bottom floor: ① recirculation region, ② impingement region, and ③ wall jet region.

offset jet using PIV technique at 3 velocity ratios and 2 offset ratios; their results indicated that increasing the offset ratio gives a better distribution of the jet within the flow field, giving rise to a better dynamic mixture. Nyantekyi-Kwakye et al. [9] studied experimentally the jet with different height ratios (0, 2 and 4); their work revealed that the large scale structures within the inner layer increase with wall normal distance from the pool bottom. Further, Rathore and Das [10] reported a numerical investigation for the turbulent offset jet and compared with results proposed by Launder and Sharma [11] and Yang and Shih [12]. They observed a similar profile in the wall jet region due to the resemblance of an offset jet with that of a wall jet flow in the wall jet region. Durand et al. [13] used ADV measuring the velocity of offset jet at the Reynold numbers of 34,000, 53,000, and 86,000; their results indicated the wall normal location of maximum mean velocity and jet spread to be independent of Reynold number. Kishore and Dey [14] provided an experimental investigation of hydraulic characteristics of submerged offset jets by ADV; the streamwise velocity profiles were measured at different sections. The work of Assoudi et al. [15] studied the mean flow behavior of a three-dimensional turbulent offset jet issuing into quiescent ambient; they reported high offset height and it is shown that reattachment point depends strongly on the jet form and the offset height.

In addition, most of the previous studies limit the jet pools to a rectangle. However, sometimes a deflection

stilling basin can easily be used to different upstream and downstream conditions; it is more economical than costly transitional structure. The gradually expanding hydraulic jump had been studied by Omid et al. [16]. Besides, Khalif and Moccroquodale [17] carried out a mathematical model of strip integral to investigate radiative hydraulic jump.

With the rapid development of computer power and numerical methods, it is more feasible to use numerical simulation to study the complex turbulent jets. Yue-Tzu Yang (1994), Gu [18], Karim and Ali [19], and Mohammad (2011) show that the $k-\epsilon$ turbulence model is an effective method to study the jet. In this paper, the standard $k-\epsilon$ turbulence model and VOF multiphase flow model were used to study the submerged offset jet in no deflection pool, unilateral deflection (deflection angle: 3° , 6° , and 9°), and bilateral deflection (deflection angle: 3° , 6°), so the understanding of the flow pattern of the submerged offset jet in a pool with unilateral and bilateral deflection wall can be deepened.

2. Numerical Model

2.1. Calculation Model. ANSYS 15.0 ICEM was used to carry out the numerical models for six types of the jet pools, as shown in Table 1. The computational area contained a circular jet exit, a pool, an end sill, and a tailwater section. The diameter of jet exit is $d = 5$ m, the offset height is $S = 4$ m (offset ratio is $S/d = 0.8$), the width of the start section of the

TABLE 1: The jet pool types parameters.

Case	Deflection pattern	Deflection angle θ
ND0	No deflection	0°
UD3	Unilateral deflection (left side wall)	3°
UD6	Unilateral deflection (left side wall)	6°
UD9	Unilateral deflection (left side wall)	9°
BD3	Bilateral deflection	3°
BD6	Bilateral deflection	6°

Note. The meanings of the abbreviations in the first column of the table are as follows: N is non, U is unilateral, B is bilateral, D is deflection, and the number is the deflection angle.

pool is $B = 8$ m (expansion ratio $d/B = 0.625$), the length of the pool is $Lx = 134.5$ m, the height of the pool is $Lz = 40$ m, and the height of the end sill is $He = 17$ m. All of cases were meshed using structural grids.

2.2. Governing Equations. The standard $k - \varepsilon$ model was considered to be useful when applied to offset jet flow, Mondal et al. [20], Kumar [21], and Mondal et al. [22]. In addition, Assoudi (2015) believed that the standard $k - \varepsilon$ model is more appropriate for the prediction of the turbulent offset jet with small offset ratio (the offset ratio is 0.8 in this paper). So the standard $k - \varepsilon$ turbulence model presented by Launder and Spalding (1972) was used. The equations of the turbulent kinetic energy, k , and its dissipation rate, ε , are as follows:

(1) k equation:

$$\frac{\partial(\rho k)}{\partial t} + \frac{\partial(\rho_i k)}{\partial x_i} = \frac{\partial}{\partial x_i} \left[\left(\mu + \frac{\mu_t}{\sigma_k} \right) \frac{\partial k}{\partial x_i} \right] + G_k - \rho \varepsilon. \quad (1)$$

(2) ε equation:

$$\begin{aligned} \frac{\partial(\rho \varepsilon)}{\partial t} + \frac{\partial(\rho u_i \varepsilon)}{\partial x_i} = & \frac{\partial}{\partial x_i} \left[\left(\mu + \frac{\mu_t}{\sigma_\varepsilon} \right) \frac{\partial \varepsilon}{\partial x_i} \right] + C_{1\varepsilon} \frac{\varepsilon}{k} G_k \\ & - C_{2\varepsilon} \rho \frac{\varepsilon^2}{k}. \end{aligned} \quad (2)$$

Here,

$$\begin{aligned} u_t &= \rho C_\mu \frac{k^2}{\varepsilon} \\ G_k &= \mu_t \left(\frac{\partial u_i}{\partial x_j} + \frac{\partial u_j}{\partial x_i} \right) \frac{\partial u_i}{\partial x_j}. \end{aligned} \quad (3)$$

When ρ is average density, u_i is the average velocity component in the i th direction; μ is the dynamic viscosity. $C_\mu = 0.09$, $\alpha_k = 1.0$, $\partial_\varepsilon = 1.3$, $C_{1\varepsilon} = 1.44$, and $C_{2\varepsilon} = 1.92$ are empirical constants; t is time, and P is pressure.

The volume of fluid (VOF) was used to track the air-water interface; ρ and u in (1) and (2) are given by the following equation:

$$\begin{aligned} \rho &= \alpha_w \rho_w + (1 - \alpha_w) \rho_a \\ \mu &= \alpha_w \mu_w + (1 - \alpha_w) \mu_a, \end{aligned} \quad (4)$$

where α_w is the volume fraction of water, ρ_w and ρ_a are the density of water and air, respectively, and μ_w and μ_a are the viscosities of water and air, respectively.

The governing equations were discretized based on the finite volume method using the SIMPLE algorithm for the pressure-velocity coupling. The gradient was calculated by least squares cell-based method. The pressure was discretized by PRESTO! and volume fraction was discretized by Geo-Reconstruct. The second-order upwind scheme was used for the momentum. The first-order upwind was selected for discretizing the turbulent kinetic energy and the dissipation rate.

2.3. Boundary Conditions

- Inlet boundary: the inlet is treated as an inlet velocity boundary, where the velocity is set to 30.66 m/s, so the mean velocity in the jet exit is 37.48 m/s.
- Outlet boundary: the outlet is treated as an outlet pressure boundary.
- Wall boundary: it is assumed that there is a no-slip velocity boundary condition; near-wall regions of the velocity are analyzed via the wall function.
- Free surface: at the free surface, the inlet pressure boundary is chosen; the pressure value is standard atmospheric pressure.

2.4. Grid Testing. In order to verify the accuracy of the numerical model, the grid convergence index (GCI) (Celik et al., 2008) was selected to test the uncertainty in the numerical results with different grid sizes. The procedure is summarized below.

Step 1. Define a representative grid size h .

$$h = \left[\frac{1}{N} \sum_{i=1}^N (\Delta V_i) \right]^{1/3}, \quad (5)$$

where ΔV_i is the volume and N is the total number of grids used for computations.

Step 2. Select three significantly different set of grids, N , and run simulations to determine the values of key variables, ϕ . It is desirable that refinement factor $r = h_{\text{coarse}}/h_{\text{fine}}$ be greater

TABLE 2: Sample calculations of discretization error using the GCI method.

	Velocity at $x/d = 0.4$	Velocity at $x/d = 6$	Velocity at $x/d = 7.6$
N_1, N_2, N_3	721854, 379432, 273439	721854, 379432, 273439	721854, 379432, 273439
r_{21}	1.9025	1.9025	1.9025
r_{32}	1.3876	1.3876	1.3876
ϕ_1	38.3747	29.4978	18.3938
ϕ_2	38.4487	28.7691	19.9773
ϕ_3	38.4645	31.9852	20.0786
p	1.0673	4.0300	2.4936
ϕ_{ext}^{21}	38.2997	29.5568	17.9951
e_a^{21}	0.19%	2.47%	8.61%
e_{ext}^{21}	0.20%	0.20%	2.22%
$\text{GCI}_{\text{fine}}^{21}$	0.24%	0.25%	2.71%

TABLE 3: The parameters of the experiment.

Case	Deflection type	Deflection angle θ	Mean velocity in jet exit (m/s)	Reynolds number (Re = vd/ν) at jet exit
UD6	Unilateral deflection	6°	37.48	1.85×10^8

than 1.3. Therefore, the sizes of the grids were N_1 (721,854), N_2 (379,432), and N_3 (273,439), giving r values of 1.90 and 1.39.

Step 3. Calculate the apparent order p of the method using the next equation. The equation was solved using fixed point iteration.

$$p = \frac{1}{\ln(r_1)} \left| \ln \left| \frac{\varepsilon_{32}}{\varepsilon_{21}} \right| + q(p) \right| \quad (6)$$

$$q(p) = \ln \left(\frac{r_{21}^p - [1 \cdot \text{sgn}(\varepsilon_{32}/\varepsilon_{21})]}{r_{32}^p - [1 \cdot \text{sgn}(\varepsilon_{32}/\varepsilon_{21})]} \right),$$

where $\varepsilon_{32} = \phi_3 - \phi_2$ and $\varepsilon_{21} = \phi_2 - \phi_1$.

Step 4. Calculate the extrapolated values from

$$\phi_{\text{ext}}^{21} = \frac{(r_{21}^p \phi_1 - \phi_2)}{(r_{21}^p - 1)}. \quad (7)$$

Step 5. Calculate the approximate relative error e_a^{21} , extrapolated relative error e_{ext}^{21} , and fine-grid convergence index $\text{CGI}_{\text{fine}}^{21}$:

$$\text{GCI}_{\text{fine}}^{21} = \frac{1.25e_a^{21}}{r_{21}^p - 1} \quad (8)$$

In this case, the streamwise mean velocity (U) at different positions on the x -axis was selected as the variable ϕ . The sampling point is selected on the jet exit axis, and the x/d range is 0 to 10 due to the high velocity flow in this range which is the focus of this study. Table 2 shows examples of the calculation procedure for the three selected grids. According to Table 1, the numerical uncertainty in the fine-grid solution for the velocity at $x/d = 7.6$ was 2.71% which corresponded to ± 0.50 m/s.

GCI index values are plotted in the form of error bars, as shown in Figure 2. Based on the grid convergence index, the maximum discretization uncertainty was 7.9% which corresponded to ± 1.73 m/s. the discretization uncertainty value ranged from 0.01% to 7.9%, with an average of 1.47%. Based on these results and considering the computational accuracy and time, the number of grids was reasonably set to 379,432.

2.5. Model Validation. In order to verify the numerical model, the physical model experiments were performed in the State Key Laboratory of Hydraulic and Mountain River Engineering, Sichuan University. The physical model consisted of an upper water tank, a circular tube, a circular jet exit, a pool, an end sill, a tailwater section, a measuring weir, and a reservoir. The physical model scale is 1/35. The size of a jet pool with unilateral 6° deflection angle was identical to that in the numerical model; other parameters are shown in Table 3. The time average pressure of the bottom floor and the height of water surface had been measured; the layout of the pressure measuring point is shown in Figure 3. It is evident from Figure 4(a) that the water surface height from computation agrees with the corresponding experimental results. Figures 4(b), 4(c), and 4(d) show the pressure values on the bottom of the pool. It can be seen that the numerical simulations were in good agreement with the experimental results; the maximum errors in the pressure were 8.01%. The numerical results thus produced acceptable error values.

3. Numerical Results and Analysis

3.1. Flow Pattern. When the jet enters the quiescent body of water, there is a velocity shear between the entering and the ambient water. The velocity shear is unavoidably disturbed during flow, loss of stability, and develops flow oscillations in the shear layer. These oscillations will roll up to form vortices with increase in size and strength with the axial

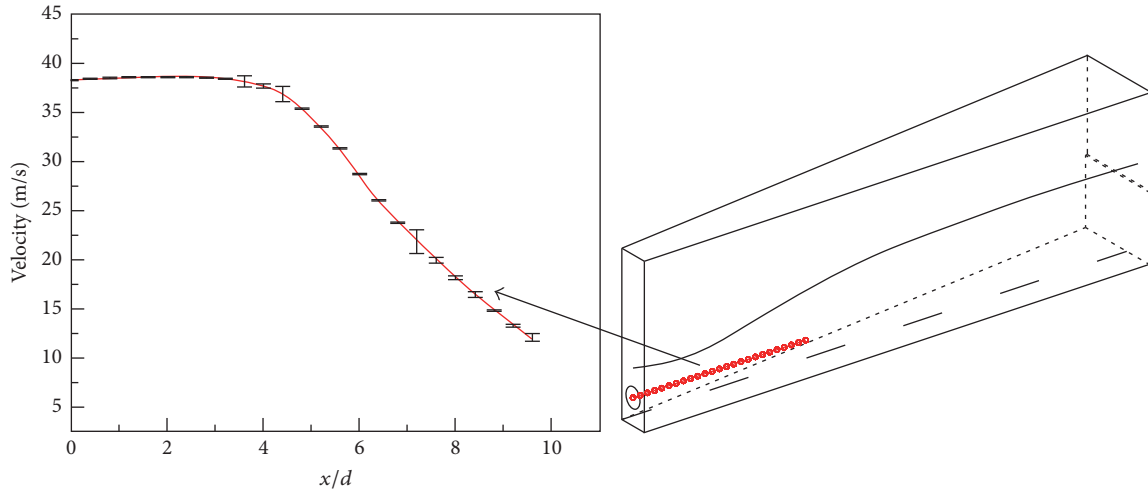


FIGURE 2: Fine-grid solution with discretization error bars computed using the GCI index.

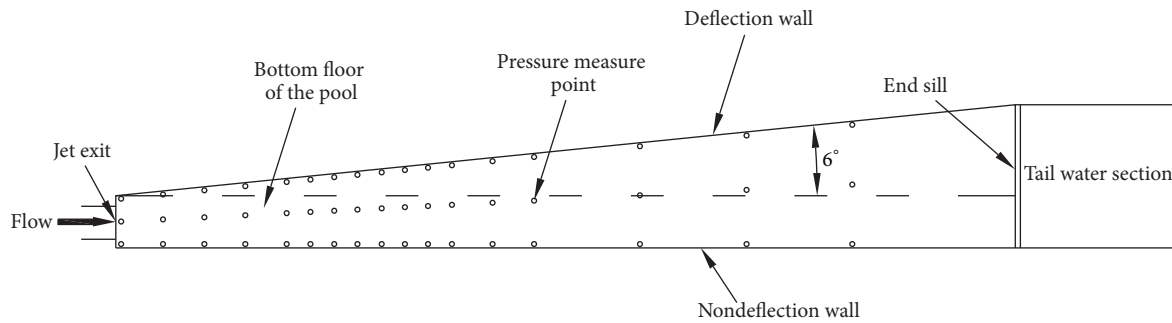


FIGURE 3: The measured point of time average pressure on the bottom floor in the pool.

distance. The vortices will influence the entrainment of the ambient water and the mixing of the ambient water and the jet water. (1) For the jet pool with no deflection, the volume of ambient water is relatively small due to the expansion ratio $d/B = 0.625$; the spread of the flow section is greatly restricted by the walls on both sides. From Figure 5(a), there is very small vertical axis vortex on both sides of the front part of the jet, then disappearing fast as the flow section spread to the side walls. (2) For the jet pool with unilateral deflection wall, the ambient water on both sides of the jet is asymmetrical; the restriction of the jet flow section on the side of the deflection wall is less compared to the side of the nondeflection wall; there are recirculation zone and the vertical axis vortex due to the jet flow interaction with the ambient water on the side of deflection wall. It is evident from Figures 5(b), 5(c), and 5(d) that the recirculation zone and vertical axis vortex are larger as the deflection angle increases. (3) For the jet pool with bilateral deflection, the process of mixing between flow jet and ambient water less affected by the side walls, the oscillations have enough conditions to produce vortices, if the deflection angle is large enough. As shown in Figures 5(e) and 5(f) the recirculation zone and vertical axis vortex are symmetrically dispersed on both sides of the jet; the size of the vortices increases as the deflection angle increases.

3.2. *The Velocity Attenuation of Mainstream.* Due to the lateral transmission of momentum, the entrained fluid gets momentum and flows forward with the original jet, and the original fluid momentum decreases and the velocities are lost to form a certain velocity gradient. The results of the mixing: the jet flow of section continues to expand, while the velocity is decreasing. In the mainstream direction, the velocity decay can be divided into three zones, including (I) potential core zone—the velocity in this zone still maintains the velocity at the jet exit; (II) transition zone—the velocity in this zone decays rapidly; (III) fully development zone—the velocity in this zone is small.

Figure 6 shows the attenuation of maximum mean velocity U_m for all types of jet pool. It can be found that, whether the jet pool is the unilateral deflection or bilateral deflection, the length of the potential core increases as the deflection angle increases. For the same deflection angle, the length of the potential core in the bilateral deflection jet pool is longer than that in unilateral deflection pool. The results show that if the deflection level of the jet pool is higher, flow is less affected by wall restrictions in the potential core zone, indicating that the turbulence intensity of the flow in potential core zone also is smaller, and the energy dissipation effect is worse.

Clark [23] reported that the decaying law of jet mean velocity in the transition zone is $U_m \propto (x/d)^{-\eta}$, where η

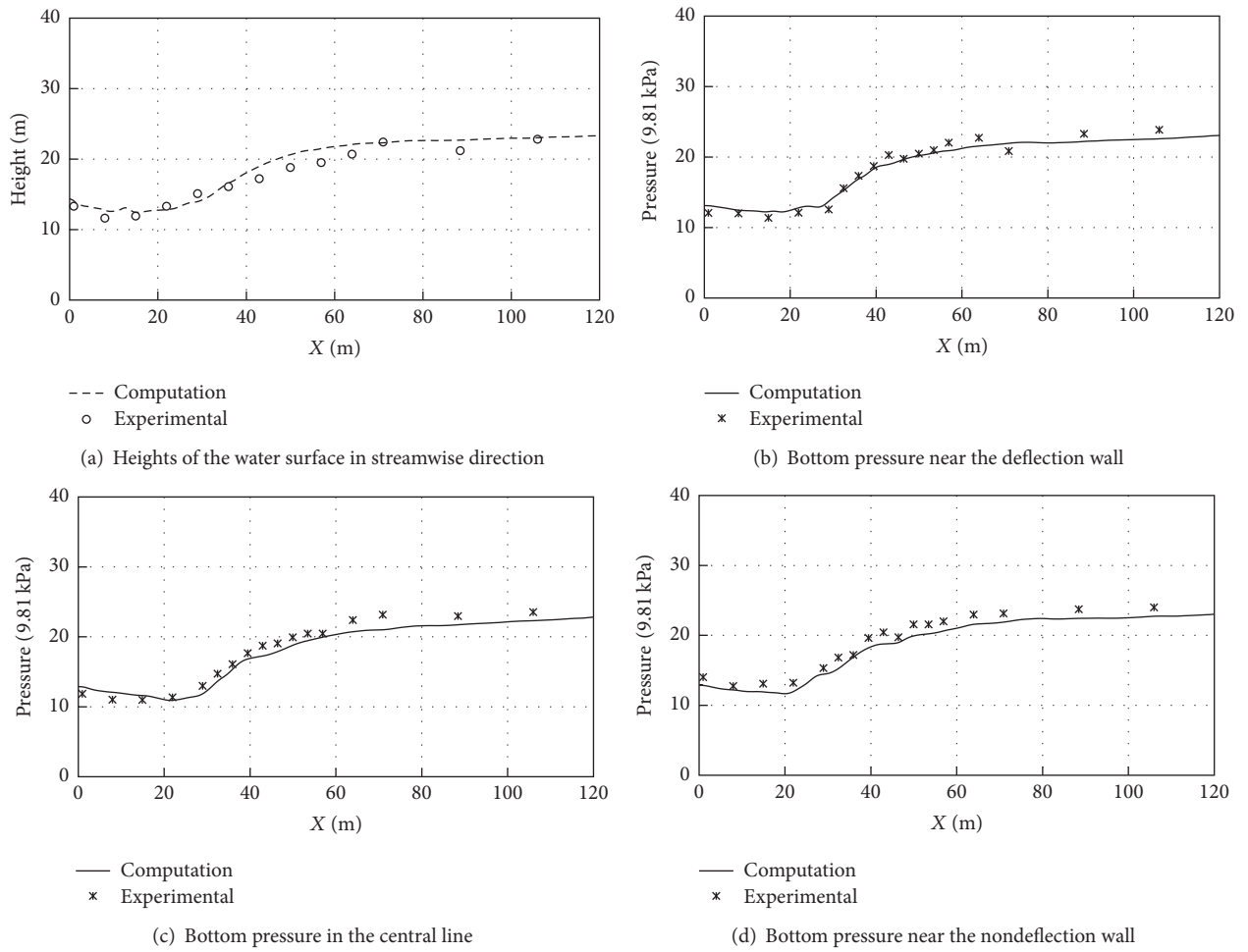


FIGURE 4: Comparison of numerical and experimental values.

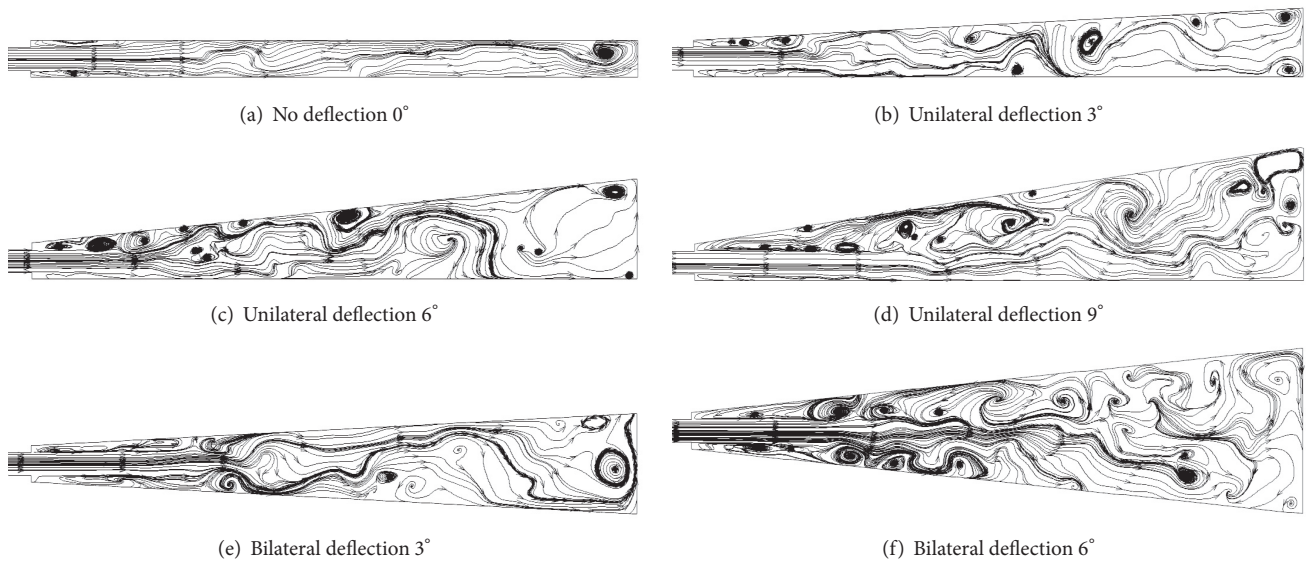


FIGURE 5: Instantaneous streamlines on different deflection patterns and deflection angle of the jet pool.

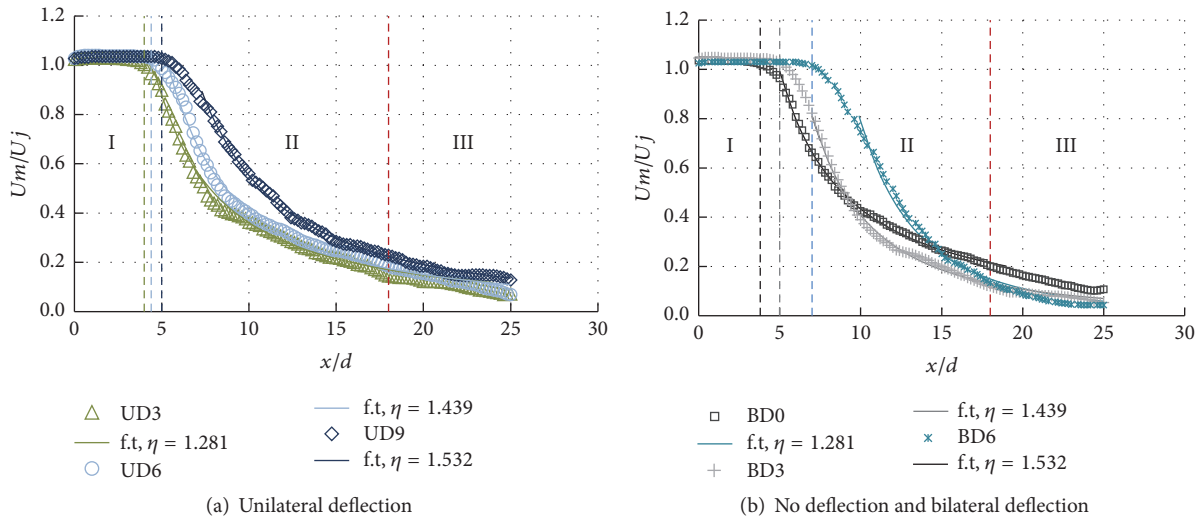


FIGURE 6: Distribution of maximum mean velocity for all types of jet pool. *Note.* The f.t. means fitting curve.

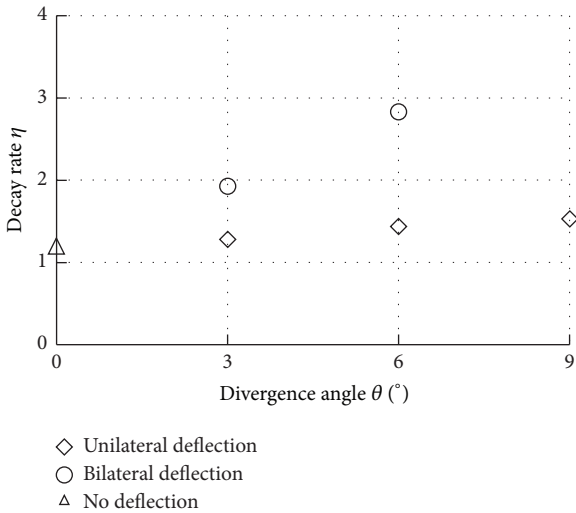


FIGURE 7: The decay rate of mean velocity in transition on different deflection pattern and deflection angle of jet pool.

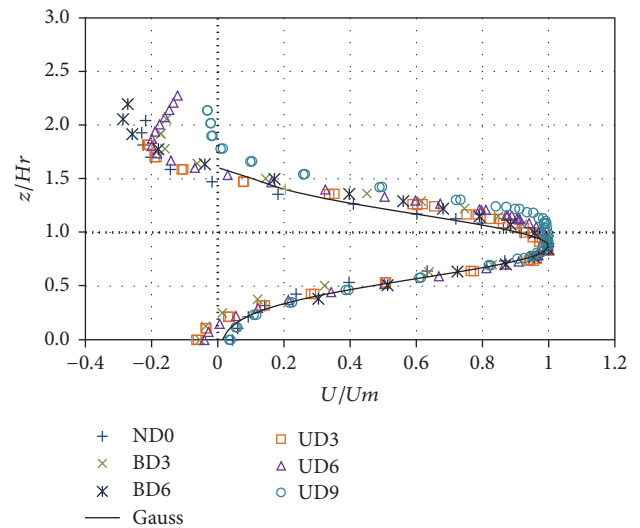


FIGURE 8: Velocity distribution in vertical direction at the end of the potential core. *Note.* $Hr = S + (1/2)d$.

is called decay rate. Figure 7 shows that, within transition zone, the deflection angle of the pool has significant effect on the decay rate. The decay rate, η , varies between 1.281~1.532 and 1.195~2.835 for unilateral deflection pool and bilateral deflection pool, respectively. The decay rate, η , is lowest at the no deflection pool and increases with increasing deflection level.

As the flow oscillations will roll up to form vortices, the kinetic energy from the jet flow is transferred to the turbulent vortices. As a result, the pool consists of vortices of different size. This energy is then handed down to smaller and smaller scales through an inviscid process called vortex stretching [24]. At the smallest scales, the vortices kinetic energy is dissipated by viscous action. For the transition zone, if the deflection level of the jet pool is higher, this indicates that the

deflection level of the pool is higher; the effect of mixing on the velocity decay is more pronounced.

3.3. Velocity Distribution on Vertical Plane. A jet spreads in the vertical directions as it entrains the surrounding fluid. The vertical spread was expanded in both the inner and outer shear layer. It was expected that the pool floor would limit the spread in the inner layer. The velocity distribution in vertical direction at the end of potential core zone with different deflection angles can be seen in Figure 8. It can be found that the velocity distribution in the vertical direction is basically the same at the end of the potential core zone; it conforms with the Gaussian distribution. The results show that the velocity distribution characteristics in the potential core zone have little difference.

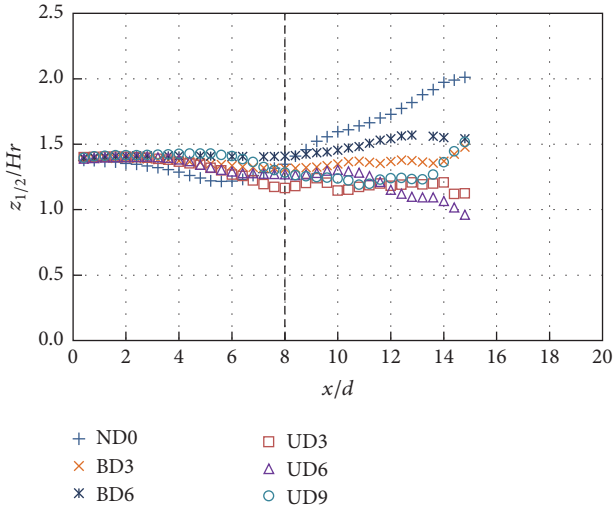


FIGURE 9: Vertical half-width ($Z_{1/2}$) distribution along the streamwise direction.

Vertical half-width ($Z_{1/2}$) distributions along the streamwise direction were shown in Figure 9 and it can be clearly seen that when $x/d \leq 8$, the deflection angle of the jet pool (no deflection, unilateral deflection, and bilateral deflection) has little effect on $Z_{1/2}$. Besides, in the potential core zone, the diffusion law of the velocity in the vertical direction is not affected by the deflection angle of the pool. In addition, Figure 9 also shows that when $x/d > 8$, the jet flow $Z_{1/2}$ (vertical half width) is higher when the pool is with no deflection or bilateral deflection.

Figure 10 shows the distribution of velocity on the bottom floor (U_s) of the pools in streamwise direction. It can be seen that U_s grows rapidly in $x/d = 5 \sim 13$. The max velocity and velocity gradient are shown in Table 4, for the cases of unilateral deflection; when the unilateral deflection angle is 3° , 6° , and 9° , the maximum U_s variation is very small, which is 0.29, 0.26, and 0.26, respectively, and these are similar to the value of pool with no deflection wall. For the cases of bilateral deflection, it is shown that as the deflection angle increases the maximum U_s decreases. In terms of gradients of velocity on bottom floor (U^*), for the jet pools with unilateral deflection wall, the maximum U^* decreases from 0.12 to 0.04 as the unilateral angle increased from 3° to 9° . U^* are 0.07 and 0.03, when the jet pools are with the bilateral deflection angle of 3° and 9° , respectively. U^* obtained in this paper is within the range of $0.03 \leq U^* \leq 0.16$.

The variation rules of maximum U_s and the maximum U^* reflect the jet flow spread in the vertical direction. The above results indicate that the deflection angle has significant effect on the decay rate. This indicates the deflection angle and the jet spread in the inner layer have strongly contact; the larger the deflection level, the higher the lateral spread rate of jet flow; the corresponding vertical spread rate is weakened.

3.4. Velocity Distribution on Horizontal Plane. The velocity in lateral distribution at the end of potential core zone with different deflection angle was shown on Figure 11(a). The

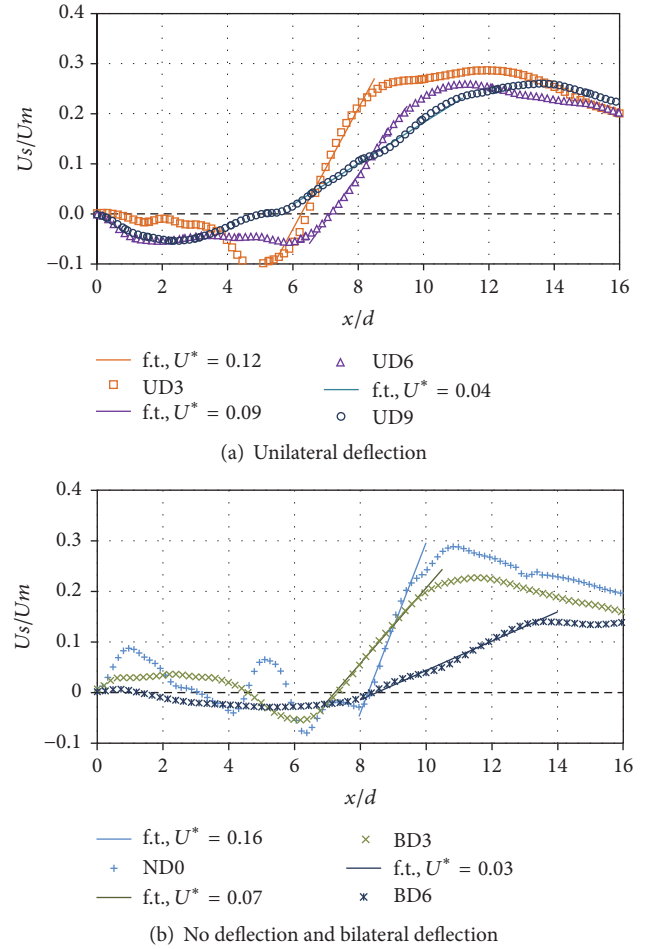


FIGURE 10: The distribution of velocity on the bottom floor (U_s) of the pools in streamwise direction. *Note.* The f.t. means fitting curve; and $U^* = d(U_s/U_m)/d(x/d)$.

velocity distribution in the horizontal direction for different cases is substantially the same at the end of the potential core zone and conforms to the Gaussian distribution. This indicates that the deflection wall has no significant effect on the jet spread in horizontal direction when the jet is still in the potential core zone.

Figure 11(b) shows the distribution of velocity on both side walls (U_w) of the pools in streamwise direction (unilateral deflection); Table 5 shows the maximum U_w and the corresponding location for all cases. The studies show that the jet pool is in the form of unilateral deflection; the maximum velocity U_w at the right side wall during the change of the deflection angle from 3° to 9° is always relatively higher than nondeflection wall. It is shown that the one side wall deflection of the pool has a little effect on the lateral spread rate of another side. Figure 11(c) shows the distribution of velocity on both side walls (U_w) of the pools in streamwise direction (bilateral deflection); it is obvious that the jet flows attach the wall which need more distance from jet exit as the deflection angle increases; at the same time, the maximum U_w decreases as the deflection angle increases. Figure 11(d) compared the velocity in the deflection wall

TABLE 4: The max velocity and the max velocity gradient on the bottom floor of pools.

Case	Max velocity on bottom floor (U_s/U_m)	Max velocity gradient U^*
ND0	0.30	0.16
UD3	0.29	0.12
UD6	0.26	0.09
UD9	0.26	0.04
BD3	0.23	0.07
BD6	0.14	0.03

TABLE 5: The maximum Uw and the corresponding location for all test cases.

Case	Right side wall		Left side wall	
	Max (Uw/Uj)	Location (x/d)	Max (Uw/Uj)	Location (x/d)
ND0	0.39	6.4	0.38	6.8
ND3	0.34	8.0	0.27	7.6
UD6	0.32	8.8	0.13	10.0
UD9	0.38	10.4	0.06	19.2
BD3	0.18	10.0	0.20	11.6
BD6	0.03	—	0.06	—

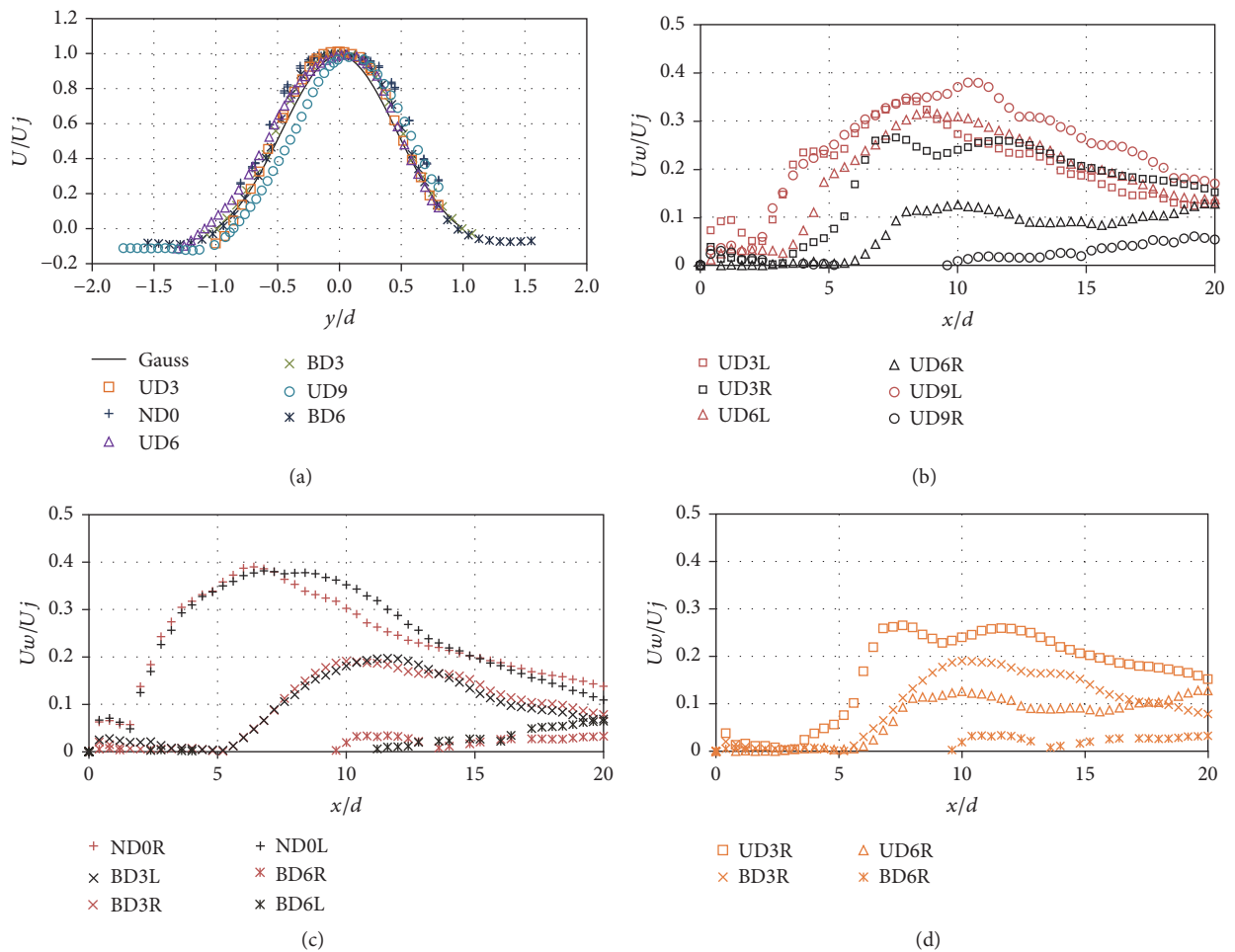


FIGURE 11: (a) Velocity U distribution in horizontal direction at the end of the potential core. (b) Distribution of velocity on the both side wall (U_s) of the pools in streamwise direction (unilateral deflection). (c) Distribution of velocity on both side walls (U_s) of the pools in streamwise direction (bilateral deflection). (d) Comparing the velocity in the deflection wall between unilateral deflection pool and bilateral deflection pools. *Note.* The R means the right side wall, and the L means the left side wall.

between unilateral deflection pools and bilateral deflection pools; when the deflection angles of unilateral deflection and bilateral deflection are the same, Uw in unilateral deflection pools is higher than that of bilateral deflection. It is clear that when the jet is in the bilateral deflection pool the surrounding water on both sides of the jet is about twice as much as water in the unilateral deflection pool. As a result, the jet section is larger in bilateral deflection pool and velocity decays faster. This indicates that the spread rates of velocity with unilateral deflection wall are higher than those with bilateral deflection walls in the horizontal plane in the pool.

4. Conclusions

The jets in the pool with nondeflection wall, unilateral deflection wall (3° , 6° , and 9°), and bilateral deflection wall (3° , 6°) had been studied in terms of decaying and spreading of the mean velocity. The main conclusions have been drawn as follows:

(1) For the unilateral deflection pool, there are vertical axis vortexes near the deflection wall. For the jet pool with bilateral deflection, the vertical axis vortexes symmetrically dispersed on both sides of the jet and the vertical axis vortexes process more symmetrical feature with the increase of angle. The sizes of these vortexes increase as the deflection angle increases.

(2) As the deflection angle of the jet pool increases, the potential core zone will become longer. For the same deflection angle, the potential core zone in the jet pools with bilateral deflection wall is longer than that in the pool with unilateral deflection angle. In the transition zone, the velocity decay rate η in the bilateral deflection pool is larger than that in the unilateral deflection pool.

(3) In the potential core zone, the velocity distributions in the vertical and horizontal directions are consistent with the Gaussian distribution and not affected by the deflection angle. When the jet pool is in the form of unilateral deflection, the flow velocity characteristics on the side of the nondeflection side wall cannot be improved. Compared to bilateral deflection, the jet spread rate of the unilateral deflection is higher in the horizontal direction.

For further understanding the characteristics of offset jet in bounded pool with deflection wall, the Reynolds number, offset ratios, expansion ratio, submergence ratios, and the shape of the jet exit should act as the variables to analyze. Furthermore, the fluctuating pressure of the floor and side walls should be studied through experiments to understand the vortexes characteristics in the pool.

Notation

B : The width of front part of the pool in Y direction
 d : Circular jet diameter (m)
 h : Representative grid size
 ht : Tailwater depth (m)
 p : The apparent order
 r : Refinement factor
 e : Error

He : The height of the end sill
 Lx : The length of the pool in X direction
 Lz : The height of the pool in Z direction
 V : The volume of computation domain
 U : Streamwise mean velocity (m/s)
 Uj : Average of mean jet exit velocity (m/s)
 Um : Local streamwise maximum mean velocity (m/s)
 Us : The streamwise velocity in the bottom floor of pool (m/s)
 Uw : The streamwise velocity in the wall of pool (m/s)
 U^* : The gradient of Us
 N : The total number of the grids
 X : Streamwise direction (m)
 Y : Horizontal direction (m)
 Z : Vertical direction (m)
 $Z_{1/2}$: Vertical half width (m)
 Zm : Lateral location of Um (m)
 S : Offset height for jet (m)
 Re : Reynolds number
 ϕ : Variables
 ν : Kinematic viscosity (cm^2/s)
 θ : Deflection angle
 η : Decay rate
 GCI_{fine}^{21} : Fine-grid convergence index.

Conflicts of Interest

The authors declare that they have no conflicts of interest.

Authors' Contributions

Xin Li and Yurong Wang contributed equally to this work.

Acknowledgments

This study was funded by the National Natural Science Foundation of China (Grant no. 51579165).

References

- [1] N. Rajaratnam, "The hydraulic jump as a wall jet," *Journal of Hydraulics Division*, vol. 91, no. 5, pp. 107–132, 1965.
- [2] N. Rajaratnam, "Turbulent jets," *Developments in Water Science*, vol. 5, no. 76, pp. 77–82, 1976.
- [3] N. Gao and D. Ewing, "Experimental investigation of planar offset attaching jets with small offset distances," *Experiments in Fluids*, vol. 42, no. 6, pp. 941–954, 2007.
- [4] T. S. Lund, "Augmented thrust and mass flow associated with two-dimensional jet reattachment," *AIAA Journal*, vol. 24, no. 12, pp. 1964–1970, 1986.
- [5] A. Nasr and J. C. S. Lai, "A turbulent plane offset jet with small offset ratio," *Experiments in Fluids*, vol. 24, no. 1, pp. 47–57, 1998.
- [6] Y.-T. Yang and Y.-Y. Yeh, "Numerical study of turbulent offset jets with entrainment boundary," *Journal of Thermophysics and Heat Transfer*, vol. 8, no. 1, pp. 182–184, 1994.

- [7] M. Agelin-Chaab and M. F. Tachie, "Characteristics and structure of turbulent 3D offset jets," *International Journal of Heat and Fluid Flow*, vol. 32, no. 3, pp. 608–620, 2011.
- [8] A. Assoudi, S. Habli, N. M. Saïd, H. Bournot, and G. L. Palec, "Experimental and numerical study of an offset jet with different velocity and offset ratios," *Engineering Applications of Computational Fluid Mechanics*, vol. 9, no. 1, pp. 490–512, 2015.
- [9] B. Nyantekyi-Kwakye, M. F. Tachie, S. P. Clark, J. Malenchak, and G. Y. Muluye, "Experimental study of the flow structures of 3D turbulent offset jets," *Journal of Hydraulic Research*, vol. 53, no. 6, pp. 773–786, 2015.
- [10] S. K. Rathore and M. K. Das, "Comparison of two low-Reynolds number turbulence models for fluid flow study of wall bounded jets," *International Journal of Heat and Mass Transfer*, vol. 61, no. 1, pp. 365–380, 2013.
- [11] B. E. Launder and B. I. Sharma, "Application of the energy-dissipation model of turbulence to the calculation of flow near a spinning disc," *International Communications in Heat and Mass Transfer*, vol. 1, no. 2, pp. 131–137, 1974.
- [12] Z. Yang and T. H. Shih, "New time scale based k-epsilon model for near-wall turbulence," *AIAA Journal*, vol. 31, no. 7, pp. 1191–1198, 1993.
- [13] Z. M. J. Durand, S. P. Clark, M. F. Tachie, J. Malenchak, and G. Muluye, "Experimental Study of Reynolds Number Effects on Three-Dimensional Offset Jets," in *Proceedings of the ASME 2014 4th Joint US-European Fluids Engineering Division Summer Meeting collocated with the ASME 2014 12th International Conference on Nanochannels, Microchannels, and Minichannels*, pp. V01C–15, 2014.
- [14] G. Kishore and S. Dey, "Hydraulics of submerged offset-jets," in *Proceedings of the Hydraulic Structures and Water System Management. 6th IAHR International Symposium on Hydraulic Structures*, B. Crookston and B. Tullis, Eds., pp. 407–416, 2016.
- [15] A. Assoudi, S. Habli, N. M. Saïd, P. Bournot, and G. L. Palec, "Numerical study of a turbulent offset jet flow," *Lecture Notes in Mechanical Engineering*, vol. 789, pp. 703–711, 2017.
- [16] M. H. Omid, M. Esmaeeli Varaki, and R. Narayanan, "Gradually expanding hydraulic jump in a trapezoidal channel," *Journal of Hydraulic Research*, vol. 45, no. 4, pp. 512–518, 2007.
- [17] A. A. M. Khalifa and J. A. McCorquodale, "Simulation of the radial hydraulic jump," *Journal of Hydraulic Research*, vol. 30, no. 2, pp. 149–163, 1992.
- [18] R. Gu, "Modeling two-dimensional turbulent offset jets," *Journal of Hydraulic Engineering*, vol. 122, no. 11, pp. 617–624, 1996.
- [19] O. A. Karim and K. H. M. Ali, "Prediction of flow patterns in local scour holes caused by turbulent water jets," *Journal of Hydraulic Research*, vol. 38, no. 4, pp. 279–287, 2000.
- [20] T. Mondal, A. Guha, and M. K. Das, "Computational study of periodically unsteady interaction between a wall jet and an offset jet for various velocity ratios," *Computers & Fluids*, vol. 123, pp. 146–161, 2015.
- [21] A. Kumar, "Mean flow characteristics of a turbulent dual jet consisting of a plane wall jet and a parallel offset jet," *Computers & Fluids*, vol. 114, pp. 48–65, 2015.
- [22] T. Mondal, A. Guha, and M. K. Das, "Effect of bottom wall proximity on the unsteady flow structures of a combined turbulent wall jet and offset jet flow," *European Journal of Mechanics - B/Fluids*, vol. 57, pp. 101–114, 2016.
- [23] S. P. Clark, "Flow characteristics within the recirculation region of three-dimensional turbulent offset jet," *Journal of Hydraulic Research*, vol. 53, no. 2, pp. 230–242, 2015.
- [24] S. B. Pope, *Modeling Mixing and Reaction in Turbulence Combustion*, May 2000, https://www.researchgate.net/publication/235185542_Modeling_Mixing_and_Reaction_in_Turbulence_Combustion.

Research Article

(2 + 1)-Dimensional Coupled Model for Envelope Rossby Solitary Waves and Its Solutions as well as Chirp Effect

Xin Chen,¹ Hongwei Yang,^{1,2} Min Guo,¹ and Baoshu Yin^{3,4}

¹Shandong University of Science and Technology, Qingdao, Shandong 266590, China

²Key Laboratory of Meteorological Disaster of Ministry of Education, Nanjing University of Information Science and Technology, Nanjing 210044, China

³Key Laboratory of Ocean Circulation and Waves, Institute of Oceanology, Chinese Academy of Sciences, Qingdao 266071, China

⁴Function Laboratory for Ocean Dynamics and Climate, Qingdao National Laboratory for Marine Science and Technology, Qingdao 266237, China

Correspondence should be addressed to Hongwei Yang; hwyang1979@163.com

Received 22 June 2017; Accepted 24 August 2017; Published 18 October 2017

Academic Editor: Jian G. Zhou

Copyright © 2017 Xin Chen et al. This is an open access article distributed under the Creative Commons Attribution License, which permits unrestricted use, distribution, and reproduction in any medium, provided the original work is properly cited.

Using the method of multiple scales and perturbation method, a set of coupled models describing the envelope Rossby solitary waves in (2 + 1)-dimensional condition are obtained, also can be called coupled NLS (CNLS) equations. Following this, based on trial function method, the solutions of the NLS equation are deduced. Moreover, the modulation instability of coupled envelope Rossby waves is studied. We can find that the stable feature of coupled envelope Rossby waves is decided by the value of S . Finally, learning from the concept of chirp in the optical soliton communication field, we study the chirp effect caused by nonlinearity and dispersion in the propagation of Rossby waves.

1. Introduction

Wave phenomenon exists widely in nature. As a special and important branch of waves, Rossby solitary waves have important theoretical significance and research value. Meanwhile, with the intercross and penetration of different knowledge, the Rossby solitary waves theory has applied to many other fields successfully, such as physical oceanography, atmospheric physics, hydraulic engineering, communication engineering, and thermal power engineering. In the case of application of solitary waves in engineering, the application of optical soliton in communication engineering is the most representative. Meanwhile, the Rossby waves theory was widely used in the study of mesoscale eddies and the interaction of large and medium scale motions. Rossby solitary waves in the westerly shear flow were first found by Long [1]. Afterward, Benny [2] amplified this research and found that velocity and amplitude of Rossby waves were proportional and depicted the importance of nonlinearity. In view of the barotropic fluid and stratified fluid model, the KdV and

mKdV equation are also generated to describe the generation and evolution of Rossby solitary waves by Redekopp [3]. Compared to KdV equation, the mKdV equation is more suitable to express the condition with stronger perturbation. With the development of solitary waves, a variety of equation models for describing the Rossby solitary waves such as ILW-Burgers equation and ZK-Burgers equation were discussed by Yang et al. [4, 5]. Moreover, the generation and evolution of solitary waves in different topography condition and different fluid depths were discussed. Recently, the Rossby parameters β along with the changes of latitude were discussed by Luo [6] and β plane approximation was obtained. These Rossby solitary waves are called classical solitary waves which related to the KdV-type equations. Later, many researchers have studied the Rossby wave equation in many aspects [7, 8], such as integrable system [9, 10], the integrable coupling of equations [11], and Hamiltonian structures [12]. Unlike the KdV-type equation, the nonlinear Schrödinger equations were used to study the evolution of envelope classical Rossby solitary waves. From the end of the 70's to the 80's, driven

by the study of atmospheric blocking dynamics [13], nonlinear Rossby wave theory had been developing rapidly and gradually formed Rossby solitary waves theory and dipole waves theory. In addition, beside the above two theories, envelope Rossby solitary waves also dropped in the research scope of the theme. The envelope Rossby solitons in the barotropic shear and uniform flows were first investigated by Benney [14] and Yamagata [15]. Afterward, Luo [16] tried to use this envelope Rossby solitons to explain atmospheric blocking phenomenon. Later, dissipative NLS equation in rotational stratified fluids and its solution were obtained by Shi et al. [17]. As we all know, using the nonlinear Schrödinger equation describing the Rossby solitary waves, we can introduce the concept of chirp in optical soliton communication [18], to study the influence of dispersion and nonlinearity on solitary waves propagation process. In the optical soliton communication field, the concept of chirp [19, 20] is the phenomenon that the central wavelength shifts when the pulse is transmitted. It is helpful to analyze the propagation characteristics and the formation mechanism of solitary waves.

In the domain of solitary wave models, it is necessary to obtain the exact solutions of solitary wave models by all kinds of solving methods and analyze the feature of solitary waves in propagation process based on the exact solutions. Many methods to solve the equations are proposed, such as traveling wave method [21], Darboux transformation method [22–24], Hirota method [25, 26], homogeneous balance method [27], Jacobi elliptic function method [28], Symmetry method [29, 30], Rational solutions [31–33]; meanwhile the features of equations are also discussed [34–36]. In this paper, we plan to adopt the trial function method and derive the exact solution of model. The difference between the two-dimensional and three-dimensional model will be given and some features of three-dimensional NLS equation will be discussed.

We note that the above researches commonly considered two-dimensional model or single (2 + 1)-dimensional model to reflect the evolution of envelope Rossby solitary waves. There are two disadvantages:

- (1) The two-dimensional model can only be applied to describe the evolution of envelope Rossby solitary waves in a line.
- (2) The velocity of the KdV-type soliton is larger than the real observation.

While, as we know, the (2 + 1)-dimensional model can be applied to reflect the evolution of envelope Rossby solitary waves in a plane, which is more suitable for the real ocean and atmosphere, in this paper, by using the method of multiple scales and perturbation method, starting from the barotropic atmospheric vorticity equation, we will derive the coupled (2 + 1)-dimensional nonlinear Schrödinger equations for envelope Rossby solitary waves in Section 2. Not only is the model (2 + 1)-dimensional and more suitable to describe the feature of two envelope Rossby solitary waves in a plane, particularly, but also it is a coupled model and can show the interaction process between two waves. Then, based on

trial function method, we will deduce the solution of the CNLS equations group and the envelope solitary waves characteristics in Section 3. Thirdly, we study the modulation instability of Rossby waves trains in (2 + 1)-dimensional condition in Section 4. Finally, the concept of chirp in optical soliton communication is introduced, and the chirp effect caused by dispersion and nonlinearity is also discussed in Section 5.

2. Derivation of the (2 + 1)-Dimensional CNLS Equations

The tropical atmospheric motion is quasihorizontal and quasiconvergent. The governing equation is the quasigeostrophic barotropic vorticity equation [37].

$$\begin{aligned} \left(\frac{\partial}{\partial t} + \bar{U}(y) \frac{\partial}{\partial x} \right) \nabla^2 \psi + (\beta - \bar{U}'') \frac{\partial \psi}{\partial x} \\ = -\epsilon J(\psi, \nabla^2 \psi), \end{aligned} \quad (1)$$

and the boundary condition is

$$\frac{\partial \psi}{\partial x} = 0, \quad \text{as } y = 0, L_y, \quad (2)$$

where x and y are the local Cartesian coordinates pointing east and north. In this $\beta = \beta^* L^2/U$, β^* is Rossby parameter. U is characteristic velocity, L is characteristic length, and L_y is the width of the beta-channel. ϵ is small parameter, on behalf of nonlinear strength. J is the Jacobian of (A, B) .

$$J(A, B) = \frac{\partial A}{\partial x} \frac{\partial B}{\partial y} - \frac{\partial A}{\partial y} \frac{\partial B}{\partial x}, \quad (3)$$

and ∇^2 is Laplace operator

$$\nabla^2 = \frac{\partial^2}{\partial x^2} + \frac{\partial^2}{\partial y^2}. \quad (4)$$

In general, it is difficult to get analytic solution of (1). But, because of the nonlinear term with a small parameter ϵ , we use the multiple scales method and perturbation method to obtain the nonlinear solution of it. As a preliminary study, we will consider two waves.

Let us introduce the slow time and space variables

$$\begin{aligned} T_1 &= \epsilon t, \\ T_2 &= \epsilon^2 t, \\ X_1 &= \epsilon x, \\ X_2 &= \epsilon^2 x, \\ Y &= \epsilon y, \end{aligned} \quad (5)$$

so long time and space scales are defined as

$$\begin{aligned}\frac{\partial}{\partial x} &\longrightarrow \frac{\partial}{\partial x} + \epsilon \frac{\partial}{\partial X_1} + \epsilon^2 \frac{\partial}{\partial X_2}, \\ \frac{\partial}{\partial y} &\longrightarrow \frac{\partial}{\partial y} + \epsilon \frac{\partial}{\partial Y}, \\ \frac{\partial}{\partial t} &\longrightarrow \frac{\partial}{\partial t} + \epsilon \frac{\partial}{\partial T_1} + \epsilon^2 \frac{\partial}{\partial T_2}.\end{aligned}\quad (6)$$

Substituting (6) into (1), we obtain

$$\begin{aligned}&\left[\frac{\partial}{\partial t} + \epsilon \frac{\partial}{\partial T_1} + \epsilon^2 \frac{\partial}{\partial T_2} \right. \\ &\quad \left. + \bar{U}(y) \left(\frac{\partial}{\partial x} + \epsilon \frac{\partial}{\partial X_1} + \epsilon^2 \frac{\partial}{\partial X_2} \right) \right] \left[\frac{\partial^2 \psi}{\partial x^2} + \frac{\partial^2 \psi}{\partial y^2} \right. \\ &\quad \left. + 2\epsilon \left(\frac{\partial^2 \psi}{\partial x \partial X_1} + \frac{\partial^2 \psi}{\partial y \partial Y} \right) \right. \\ &\quad \left. + \epsilon^2 \left(\frac{\partial^2 \psi}{\partial X_1^2} + 2 \frac{\partial^2 \psi}{\partial x \partial X_2} + \frac{\partial^2 \psi}{\partial Y^2} \right) + 2\epsilon^3 \frac{\partial^2 \psi}{\partial X_1 \partial X_2} \right. \\ &\quad \left. + \epsilon^4 \frac{\partial^2 \psi}{\partial X_2^2} \right] + (\beta - \bar{U}'') \left(\frac{\partial \psi}{\partial x} + \epsilon \frac{\partial \psi}{\partial X_1} + \epsilon^2 \frac{\partial \psi}{\partial X_2} \right) \\ &\quad + \epsilon \left(\frac{\partial \psi}{\partial x} \frac{\partial \nabla^2 \psi}{\partial y} - \frac{\partial \psi}{\partial y} \frac{\partial \nabla^2 \psi}{\partial x} \right) = 0, \\ &\quad \frac{\partial \psi}{\partial x} = 0, \quad y = 0, L_y.\end{aligned}\quad (7)$$

Further

$$\begin{aligned}&\left[\frac{\partial}{\partial t} + \bar{U} \frac{\partial}{\partial x} \right] \left(\frac{\partial^2 \psi}{\partial x^2} + \frac{\partial^2 \psi}{\partial y^2} \right) + (\beta - \bar{U}'') \frac{\partial \psi}{\partial x} \\ &\quad + \epsilon \left[\left(\frac{\partial}{\partial T_1} + \bar{U} \frac{\partial}{\partial X_1} \right) \left(\frac{\partial^2 \psi}{\partial x^2} + \frac{\partial^2 \psi}{\partial y^2} \right) + \left(\frac{\partial}{\partial t} \right. \right. \\ &\quad \left. \left. + \bar{U} \frac{\partial}{\partial x} \right) \left(2 \frac{\partial^2 \psi}{\partial x \partial X_1} + 2 \frac{\partial^2 \psi}{\partial y \partial Y} \right) + (\beta - \bar{U}'') \frac{\partial \psi}{\partial X_1} \right. \\ &\quad \left. + \frac{\partial \psi}{\partial x} \left(\frac{\partial^3 \psi}{\partial y \partial x^2} + \frac{\partial^3 \psi}{\partial y^3} \right) - \frac{\partial \psi}{\partial y} \left(\frac{\partial^3 \psi}{\partial x^3} + \frac{\partial^3 \psi}{\partial x \partial y^2} \right) \right] \\ &\quad + \epsilon^2 \left[\left(\frac{\partial}{\partial T_2} + \bar{U} \frac{\partial}{\partial X_2} \right) \left(\frac{\partial^2 \psi}{\partial x^2} + \frac{\partial^2 \psi}{\partial y^2} \right) + \left(\frac{\partial}{\partial T_1} \right. \right. \\ &\quad \left. \left. + \bar{U} \frac{\partial}{\partial X_1} \right) \left(2 \frac{\partial^2 \psi}{\partial x \partial X_1} + 2 \frac{\partial^2 \psi}{\partial y \partial Y} \right) + \left(\frac{\partial}{\partial t} + \bar{U} \frac{\partial}{\partial x} \right) \right. \\ &\quad \left. \cdot \left(\frac{\partial^2 \psi}{\partial X_1^2} + \frac{\partial^2 \psi}{\partial Y^2} \right) + (\beta - \bar{U}'') \frac{\partial \psi}{\partial X_2} \right. \\ &\quad \left. + \frac{\partial \psi}{\partial x} \left(2 \frac{\partial^3 \psi}{\partial y \partial x \partial X_1} + 3 \frac{\partial^3 \psi}{\partial y^2 \partial Y} + \frac{\partial^3 \psi}{\partial x^2 \partial Y} \right) \right]\end{aligned}$$

$$\begin{aligned}&+ \frac{\partial \psi}{\partial X_1} \left(\frac{\partial^3 \psi}{\partial y \partial x^2} + \frac{\partial^3 \psi}{\partial y^3} \right) - \frac{\partial \psi}{\partial y} \left(2 \frac{\partial^3 \psi}{\partial x^2 \partial X_1} \right. \\ &\quad \left. + 2 \frac{\partial^3 \psi}{\partial y \partial x \partial Y} + \frac{\partial^3 \psi}{\partial y^2 \partial X_1} \right) - \frac{\partial \psi}{\partial Y} \left(\frac{\partial^3 \psi}{\partial x^3} + \frac{\partial^3 \psi}{\partial x \partial y^2} \right) \Big] \\ &\quad + \epsilon^3 \left[\left(\frac{\partial}{\partial t} + \bar{U} \frac{\partial}{\partial x} \right) \frac{\partial^2 \psi}{\partial X_1 \partial X_2} + \frac{\partial \psi}{\partial x} \left(\frac{\partial^3 \psi}{\partial y \partial X_1^2} \right. \right. \\ &\quad \left. \left. + \frac{\partial^3 \psi}{\partial y \partial x \partial X_2} + 2 \frac{\partial^3 \psi}{\partial x \partial Y \partial X_1} + 3 \frac{\partial^3 \psi}{\partial y \partial Y^2} \right) \right. \\ &\quad \left. + \frac{\partial \psi}{\partial X_1} \left(2 \frac{\partial^3 \psi}{\partial y \partial x \partial X_1} + 2 \frac{\partial^3 \psi}{\partial y^2 \partial Y} + \frac{\partial^3 \psi}{\partial Y \partial x^2} \right. \right. \\ &\quad \left. \left. + \frac{\partial^3 \psi}{\partial Y \partial y^2} \right) \right] + o(\epsilon^3) = 0,\end{aligned}\quad (8)$$

and the boundary condition is

$$\frac{\partial \psi}{\partial x} = 0, \quad \text{as } y = 0, L_y. \quad (9)$$

The stream function ψ is expanded according to the small parameter ϵ

$$\psi = \psi^{(0)} + \epsilon \psi^{(1)} + \epsilon^2 \psi^{(2)} + \epsilon^3 \psi^{(3)} + \dots, \quad (10)$$

and, substituting (9) into (8), we get the multiple order questions of the stream function ψ .

First, one introduces an operator

$$L = \left[\frac{\partial}{\partial t} + \bar{U} \frac{\partial}{\partial x} \right] \nabla^2 + (\beta - \bar{U}'') \frac{\partial}{\partial x}, \quad (11)$$

so that

$$\begin{aligned}o(\epsilon^0): &L(\psi^{(0)}) \\ &= \left(\frac{\partial}{\partial t} + \bar{U} \frac{\partial}{\partial x} \right) \nabla^2 \psi^{(0)} + (\beta - \bar{U}'') \frac{\partial \psi^{(0)}}{\partial x}, \\ o(\epsilon^1): &L(\psi^{(1)}) \\ &= \left(\frac{\partial}{\partial T_1} + \bar{U} \frac{\partial}{\partial X_1} \right) \left(\frac{\partial^2 \psi^{(0)}}{\partial x^2} + \frac{\partial^2 \psi^{(0)}}{\partial y^2} \right) \\ &\quad + \left(\frac{\partial}{\partial t} + \bar{U} \frac{\partial}{\partial x} \right) \left(2 \frac{\partial^2 \psi^{(0)}}{\partial x \partial X_1} + 2 \frac{\partial^2 \psi^{(0)}}{\partial y \partial Y} \right) \\ &\quad + (\beta - \bar{U}'') \frac{\partial \psi^{(0)}}{\partial X_1} + \frac{\partial \psi^{(0)}}{\partial x} \left(\frac{\partial^3 \psi^{(0)}}{\partial y \partial x^2} + \frac{\partial^3 \psi^{(0)}}{\partial y^3} \right) \\ &\quad - \frac{\partial \psi^{(0)}}{\partial y},\end{aligned}$$

$$\begin{aligned}
o(\epsilon^2): L(\psi^{(2)}) &= \left(\frac{\partial}{\partial T_2} + \bar{U} \frac{\partial}{\partial X_2} \right) \left(\frac{\partial^2 \psi^{(0)}}{\partial x^2} + \frac{\partial^2 \psi^{(0)}}{\partial y^2} \right) \\
&+ \left(\frac{\partial}{\partial T_1} + \bar{U} \frac{\partial}{\partial X_1} \right) \left(2 \frac{\partial^2 \psi^{(0)}}{\partial x \partial X_1} + 2 \frac{\partial^2 \psi^{(0)}}{\partial y \partial Y} \right) \\
&+ \left(\frac{\partial}{\partial t} + \bar{U} \frac{\partial}{\partial x} \right) \left(\frac{\partial^2 \psi^{(0)}}{\partial X_1^2} + \frac{\partial^2 \psi^{(0)}}{\partial Y^2} \right) \\
&+ (\beta - \bar{U}'') \frac{\partial \psi^{(0)}}{\partial X_2} \\
&+ \frac{\partial \psi^{(0)}}{\partial x} \left(2 \frac{\partial^3 \psi^{(0)}}{\partial y \partial x \partial X_1} + 3 \frac{\partial^3 \psi^{(0)}}{\partial y^2 \partial Y} + \frac{\partial^3 \psi^{(0)}}{\partial x^2 \partial Y} \right) \\
&+ \frac{\partial \psi^{(0)}}{\partial X_1} \left(\frac{\partial^3 \psi^{(0)}}{\partial y \partial x^2} + \frac{\partial^3 \psi^{(0)}}{\partial y^3} \right) \\
&- \frac{\partial \psi^{(0)}}{\partial y} \left(2 \frac{\partial^3 \psi^{(0)}}{\partial x^2 \partial X_1} + 2 \frac{\partial^3 \psi^{(0)}}{\partial y \partial x \partial Y} + \frac{\partial^3 \psi^{(0)}}{\partial y^2 \partial X_1} \right) \\
&+ \frac{\partial \psi^{(0)}}{\partial Y} \left(\frac{\partial^3 \psi^{(0)}}{\partial x^3} + \frac{\partial^3 \psi^{(0)}}{\partial x \partial y^2} \right) \\
&- \left(\frac{\partial}{\partial T_1} + \bar{U} \frac{\partial}{\partial X_1} \right) \left(\frac{\partial^2 \psi^{(1)}}{\partial x^2} - \frac{\partial^2 \psi^{(1)}}{\partial y^2} \right) \\
&- \left(\frac{\partial}{\partial t} + \bar{U} \frac{\partial}{\partial x} \right) \left(2 \frac{\partial^2 \psi^{(1)}}{\partial x \partial X_1} + 2 \frac{\partial^2 \psi^{(1)}}{\partial y \partial Y} \right) \\
&+ (\beta - \bar{U}'') \frac{\partial \psi^{(1)}}{\partial X_1} - \frac{\partial \psi^{(1)}}{\partial x} \left(\frac{\partial^3 \psi^{(1)}}{\partial y \partial x^2} + \frac{\partial^3 \psi^{(1)}}{\partial y^3} \right) \\
&+ \frac{\partial \psi^{(1)}}{\partial y} \left(\frac{\partial^3 \psi^{(1)}}{\partial x^3} + \frac{\partial^3 \psi^{(1)}}{\partial x \partial y^2} \right) \\
&\frac{\partial \psi}{\partial x} = 0, \quad y = 0, L_y.
\end{aligned} \tag{12}$$

Assume

$$\begin{aligned}
\psi^{(0)} &= \sum_{j=1}^2 A_j (T_1, T_2, X_1, X_2, Y) \phi_j(y) e^{i(K_j x - \omega_j t)} \\
&+ c.c.,
\end{aligned} \tag{13}$$

and, substituting (13) into $L(\psi^{(0)})$, we have

$$\begin{aligned}
L(\psi^{(0)}) &= \left(\frac{\partial}{\partial t} + \bar{U} \frac{\partial}{\partial x} \right) \left[- \sum_{j=1}^2 A_j \phi_j K_j^2 e^{i(K_j x - \omega_j t)} \right. \\
&\left. + \sum_{j=1}^2 A_j \frac{d^2 \phi_j}{dy^2} e^{i(K_j x - \omega_j t)} \right] + (\beta - \bar{U}'')
\end{aligned}$$

$$\begin{aligned}
&\cdot \sum_{j=1}^2 A_j \phi_j i K_j e^{i(K_j x - \omega_j t)} = \sum_{j=1}^2 A_j e^{i(K_j x - \omega_j t)} \left[i \omega_j K_j^2 \phi_j \right. \\
&- \omega_j \frac{d^2 \phi_j}{dy^2} - i \bar{U} K_j^3 \phi_j + i \bar{U} K_j \frac{d^2 \phi_j}{dy^2} \\
&\left. + i K_j (\beta - \bar{U}'') \phi_j \right] \equiv 0,
\end{aligned} \tag{14}$$

and further

$$- (i \omega_j - i \bar{U} K_j) \frac{d^2 \phi_j}{dy^2} \tag{15}$$

$$- [i \bar{U} K_j^3 - i \omega_j K_j^2 - i K_j (\beta - \bar{U}'')] \phi_j = 0,$$

$$\frac{d^2 \phi_j}{dy^2} - \left[K_j^2 - \frac{\beta - \bar{U}''}{\bar{U} - C_j} \right] \phi_j = 0, \tag{16}$$

and the boundary condition is

$$\frac{\partial \psi}{\partial x} = 0, \quad \text{as } y = 0, L_y, \tag{17}$$

where

$$C_j = \frac{\omega_j}{K_j}. \tag{18}$$

From (15), we can get the solution of ϕ_j :

$$\phi_j(y) = \sqrt{\frac{2}{Ly_j}} \sin(my), \tag{19}$$

$$m = \frac{n_1 \pi}{Ly_j} \quad (n_1 = \pm 1, 2, 3, \dots).$$

Formula (15) under the boundary condition poses a standard Sturm-Liouville problem. The effects of zonal flows on linear equation trapped waves were treated in detail by many researchers. The analytic solution of (15) can be obtained when $\bar{U}(y)$ takes some specific functions. Under normal circumstance one can only seek numerical solution, so we consider the higher order question

$$\begin{aligned}
o(\epsilon^1): L(\psi^{(1)}) &= - \left(\frac{\partial}{\partial T_1} + \bar{U} \frac{\partial}{\partial X_1} \right) \left(\frac{\partial^2 \psi}{\partial x^2} + \frac{\partial^2 \psi}{\partial y^2} \right) \\
&- \left(\frac{\partial}{\partial t} + \bar{U} \frac{\partial}{\partial x} \right) \left(2 \frac{\partial^2 \psi}{\partial x \partial X_1} + 2 \frac{\partial^2 \psi}{\partial y \partial Y} \right) \\
&- (\beta - \bar{U}'') \frac{\partial \psi}{\partial X_1} - \frac{\partial \psi}{\partial x} \left(\frac{\partial^3 \psi}{\partial y \partial x^2} + \frac{\partial^3 \psi}{\partial y^3} \right) \\
&+ \frac{\partial \psi}{\partial y} \left(\frac{\partial^3 \psi}{\partial x^3} + \frac{\partial^3 \psi}{\partial x \partial y^2} \right), \quad \frac{\partial \psi}{\partial x} = 0, \quad y = 0, L_y,
\end{aligned} \tag{20}$$

and, further, we get

$$L(\psi^{(1)}) = -\sum_{j=1}^2 g_{1j} e^{2i(K_j x - \omega_j t)} - \sum_{j=1}^2 g_{2j} e^{2i(K_j x - \omega_j t)} A_j^2 - i g_3 e^{i[(K_1 + K_2)x - (\omega_1 + \omega_2)t]} A_1 A_2 - i g_4 e^{i[(K_1 - K_2)x - (\omega_1 - \omega_2)t]} A_1 A_2, \quad (21)$$

where

$$g_{1j} = \frac{\beta - \bar{U}''}{\bar{U} - C_j} \phi_j \left(\frac{\partial A_j}{\partial T_1} + C_{gj} \frac{\partial A_j}{\partial X_1} \right) - 2i K_j (\bar{U} - C_j) \frac{d\phi_j}{dy} \frac{\partial A_j}{\partial Y},$$

$$g_{2j} = K_j \left(\phi_j \frac{d}{dy} - \frac{d\phi_j}{dy} \right) \frac{d^2 \phi_j}{dy^2},$$

$$g_3 = \left(K_1 \phi_1 \frac{d}{dy} - K_2 \frac{d\phi_1}{dy} \right) \left(\frac{d^2 \phi_2}{dy^2} - K_2^2 \phi_2 \right) + \left(K_2 \phi_2 \frac{d}{dy} - K_1 \frac{d\phi_2}{dy} \right) \left(\frac{d^2 \phi_1}{dy^2} - K_1^2 \phi_1 \right), \quad (22)$$

$$g_4 = \left(K_1 \phi_1 \frac{d}{dy} + K_2 \frac{d\phi_1}{dy} \right) \left(\frac{d^2 \phi_2}{dy^2} - K_2^2 \phi_2 \right) - \left(K_2 \phi_2 \frac{d}{dy} + K_1 \frac{d\phi_2}{dy} \right) \left(\frac{d^2 \phi_1}{dy^2} - K_1^2 \phi_1 \right).$$

$$C_{gj} = C_j + \frac{2K_j^2 (\bar{U} - C_j)^2}{\beta - \bar{U}''},$$

and the special solution corresponding to the second, third, and fourth item of (21) right side is

$$\psi_{2j}^{(1)} = A_j^2 \phi_{2j} e^{2i(K_j x - \omega_j t)} + c.c.,$$

$$\psi_3^{(1)} = A_1 A_2 \phi_3 e^{i[(K_1 + K_2)x - (\omega_1 + \omega_2)t]} + c.c., \quad (23)$$

$$\psi_4^{(1)} = A_1 A_2 \phi_4 e^{i[(K_1 - K_2)x - (\omega_1 - \omega_2)t]} + c.c.,$$

where ϕ_{2j} , ϕ_3 , and ϕ_4 satisfied

$$\frac{d^2 \phi_{2j}}{dy^2} - \left(4K_j^2 - \frac{\beta - \bar{U}''}{\bar{U} - c_j} \right) \phi_{2j} = \frac{g_{2j}}{2(\bar{U}K_j - \omega_j)},$$

$$\frac{d^2 \phi_3}{dy^2} - \left[(K_1 + K_2)^2 - \frac{(\beta - \bar{U}'') (K_1 + K_2)}{\bar{U} (K_1 + K_2) - (\omega_1 + \omega_2)} \right] \phi_3 = \frac{g_3}{\bar{U} (K_1 + K_2) - (\omega_1 + \omega_2)},$$

$$\frac{d^2 \phi_4}{dy^2} - \left[(K_1 - K_2)^2 - \frac{(\beta - \bar{U}'') (K_1 - K_2)}{\bar{U} (K_1 - K_2) - (\omega_1 - \omega_2)} \right] \phi_4 = \frac{g_4}{\bar{U} (K_1 - K_2) - (\omega_1 - \omega_2)}, \quad (24)$$

and boundary condition

$$\phi_{2j}|_{y=0} = \phi_{2j}|_{y=L_y} = \phi_3|_{y=0} = \phi_3|_{y=L_y} = \phi_4|_{y=0} = \phi_4|_{y=L_y} = 0, \quad (25)$$

We assume the special solution corresponding to the first item of the right side of (20) is

$$\psi_{1j}^{(1)} = \bar{\psi}_{1j}^{(1)} e^{i(K_j x - \omega_j t)} + c.c.,$$

$$\bar{\psi}_{1j}^{(1)}|_{y=0} = \bar{\psi}_{1j}^{(1)}|_{y=L_y} = 0, \quad (26)$$

where $\psi_{1j}^{(1)}$ satisfied

$$\frac{d^2 \psi_{1j}^{(1)}}{dy^2} - \left(K_j^2 - \frac{\beta - \bar{U}''}{\bar{U} - C_j} \right) \psi_{1j}^{(1)} = \frac{\beta - \bar{U}''}{\bar{U} - C_j} \phi_j \left(\frac{\partial A_j}{\partial T_1} + C_{gj} \frac{\partial A_j}{\partial X_1} \right) - 2i K_j (\bar{U} - C_j) \frac{d\phi_j}{dy} \frac{\partial A_j}{\partial Y}. \quad (27)$$

The following operators are introduced:

$$\xi = X_1 - C_{gj} T_1, \quad (28)$$

$$T_2 = \varepsilon T_1.$$

Substituting (28) into (27) and because ε is infinitesimal, we can ignore the first item

$$(\bar{U} - C_{gj}) \frac{\partial}{\partial \xi} \left(\frac{\partial \bar{\psi}_{1j}}{\partial y^2} \right) + \beta \frac{\partial \bar{\psi}_{1j}}{\partial \xi} = -\frac{4K_j^2 m}{Ly_j} (\sin 2m_j y) \frac{\partial |A_j|^2}{\partial \xi}, \quad (29)$$

$$\bar{\psi}_{1j}|_{y=0} = \bar{\psi}_{1j}|_{y=L_y} = 0.$$

Obviously the solution for ψ_{1j} may be expressed in the following form:

$$\bar{\psi}_{ij} = \frac{4K_j^2 (K_j^2 + m^2)^2 m \sin(2my) |A_j|^2}{[3m^2 (m^2 - 2K_j^2) - k_j^4] \beta Ly_j}. \quad (30)$$

So we obtained the solution of (20):

$$\psi^{(1)} = \psi_{1j}^{(1)} + \psi_{2j}^{(1)} + \psi_{3j}^{(1)} + \psi_{4j}^{(1)} + \phi(y, T_1, X_1). \quad (31)$$

So as to obtain the solution of A , we continue to consider the question of $o(\varepsilon^2)$. Substituting (19) and (30) into $o(\varepsilon^2)$ and collecting the secular-producing items proportional to $e^{i(Kx - \omega t)}$, we have

$$\begin{aligned} L(\psi^{(2)}) = & -\sum_{j=1}^2 \left\{ \left(\frac{\partial A_j}{\partial T_2} + \bar{U} \frac{\partial A_j}{\partial X_2} \right) \left(\frac{d^2 \phi_j}{dy^2} - K_j^2 \phi_j \right) \right. \\ & + i\phi_j (3\bar{U}K_j - \omega_j) \frac{\partial^2 A_j}{\partial X_1^2} + i\phi_j (\bar{U}K_j - \omega_j) \frac{\partial^2 A_j}{\partial Y^2} \\ & + 2iK_j \phi_j \frac{\partial^2 A_j}{\partial T_1 \partial X_1} + 2 \frac{d\phi_j}{dy} \left(\frac{\partial^2 A_j}{\partial T_1 \partial Y} + \bar{U} \frac{\partial^2 A_j}{\partial X_1 \partial Y} \right) \\ & \left. + (\beta - \bar{U}'') \frac{\partial A_j}{\partial X_2} \phi_j + 8iK_j^3 m^2 (K_j^2 + m^2)^2 \right. \\ & \left. \cdot \frac{|A_j^2| A_j \cos(2my)}{[3m^2(m^2 - 2K_j^2) - K_j^4] \beta L y_j} \right\}, \\ & \frac{\partial \psi}{\partial x} = 0, \quad y = 0, L_y. \end{aligned} \quad (32)$$

For the sake of obtaining the evolution equation of A_j , we consider another class of nonhomogeneous solutions, assuming

$$L(\psi^{(2)}) = \sum_{j=1}^2 F_j(T_1, T_2, X_1, X_2, Y) e^{i(K_j x - \omega_j t)} + c.c., \quad (33)$$

introducing (33) into (32), where

$$\begin{aligned} F_1 = & f_1 \frac{\partial A_1}{\partial T_2} + \alpha_1 \frac{\partial A_1}{\partial X_2} + \beta_1 \frac{\partial^2 A_1}{\partial Y^2} + f_{10} \frac{\partial^2 A_1}{\partial X_1^2} \\ & + f_{11} |A_1|^2 A_1 + f_{12} |A_2|^2 A_1 + f_{13} A_1, \\ F_2 = & f_2 \frac{\partial A_2}{\partial T_2} + \alpha_2 \frac{\partial A_2}{\partial X_2} + \beta_2 \frac{\partial^2 A_2}{\partial Y^2} + f_{20} \frac{\partial^2 A_2}{\partial X_1^2} \\ & + f_{21} |A_1|^2 A_2 + f_{22} |A_2|^2 A_2 + f_{23} A_2. \end{aligned} \quad (34)$$

We assume two special nonhomogeneous solutions of (33) are

$$\begin{aligned} \psi_1^{(2)} = & \Phi_1^{(2)} e^{i(K_1 x - \omega_1 t)} + c.c., \\ \psi_2^{(2)} = & \Phi_2^{(2)} e^{i(K_2 x - \omega_2 t)} + c.c., \end{aligned} \quad (35)$$

and, substituting (35) into (34), we get

$$\frac{d^2 \Phi_j^{(2)}}{dy^2} - \left(K_j - \frac{\beta - \bar{U}''}{\bar{U} - c_j} \right) \Phi_j^{(2)} = \frac{F_j}{K_j (\bar{U} - c_j)}, \quad (36)$$

multiplying (35) by ϕ_j , and integrating on y from 0 to L_y . The two sides of (35) are equal to zero, so we get the solution conditions:

$$\begin{aligned} & \left(\frac{\partial}{\partial T_2} + c_{g1} \frac{\partial}{\partial X_2} \right) A_1 - i\alpha_1 \frac{\partial^2 A_1}{\partial X_1^2} - i\beta_1 \frac{\partial^2 A_1}{\partial Y^2} \\ & - i(\sigma_1 |A_1|^2 + \gamma_{12} |A_2|^2 + \lambda_{1j}(X_1, Y, T_1)) A_1 = 0, \\ & \left(\frac{\partial}{\partial T_2} + c_{g2} \frac{\partial}{\partial X_2} \right) A_2 - i\alpha_2 \frac{\partial^2 A_2}{\partial X_1^2} - i\beta_2 \frac{\partial^2 A_2}{\partial Y^2} \\ & - i(\sigma_2 |A_2|^2 + \gamma_{21} |A_1|^2 + \lambda_{2j}(X_1, Y, T_1)) A_2 = 0. \end{aligned} \quad (37)$$

We get the evolution equations group of wave amplitude, that is, the coupled equations group. To simplify, we introduce the following transformation:

$$X = \frac{1}{\varepsilon} (X_2 - C_g T_2) = X_1 - C_g T_1, \quad T = T_2, \quad (38)$$

and then (37) can be written as

$$\begin{aligned} & i \frac{\partial A_1}{\partial T} + \alpha_1 \frac{\partial^2 A_1}{\partial X^2} + \beta_1 \frac{\partial^2 A_1}{\partial Y^2} \\ & + (\sigma_1 * |A_1|^2 + r_{12} * |A_2|^2) A_1 = 0, \\ & i \left(\frac{\partial A_2}{\partial T} + C_{g2} * \frac{\partial A_2}{\partial X} \right) + \alpha_2 \frac{\partial^2 A_2}{\partial X^2} + \beta_2 \frac{\partial^2 A_2}{\partial Y^2} \\ & + (\sigma_2 * |A_2|^2 + r_{21} * |A_1|^2) A_2 = 0, \end{aligned} \quad (39)$$

where

$$\begin{aligned} C_{g2}^* = & \frac{1}{\varepsilon} (C_{g1} - C_{g2}), \\ \sigma_1^* = & \sigma_1 + \lambda_{11}, \\ \sigma_2^* = & \sigma_2 + \lambda_{22}, \\ \gamma_{12}^* = & \gamma_{12} + \lambda_{12}, \\ \gamma_{21}^* = & \gamma_{21} + \lambda_{21}. \end{aligned} \quad (40)$$

In (38), coefficients α_1 , α_2 , β_1 , and β_2 are dispersion coefficients, σ_1^* , σ_2^* are Landau coefficients, γ_{12}^* , γ_{21}^* are interaction coefficients, and from their expressions it can be seen that

their values are related to the base flow function $\bar{U}(y)$. The (38) is called CNLS equations group.

3. The Solutions of the (2 + 1)-Dimensional CNLS Equations

In this chapter, we will discuss the solutions of the (2 + 1)-dimensional CNLS equation. Based on our experience, we should transform the coupled equations into two independent equations. Inspired by [38, 39], (39) can be written with the following form:

$$iA_{j,T} + \alpha_j A_{j,XX} + \beta_j A_{j,YY} + \gamma_j |A_j|^2 A_j = 0, \quad (41)$$

$j = 1, 2,$

where α_j, β_j represent the coefficients of dispersion term. γ_j is the nonlinear coupling term coefficient, which can be positive or negative. In order to obtain the traveling wave solutions of the CNLS equations, we define the transformation which is the complex number envelope solution:

$$A_j(T, X, Y) = \bar{A}_j(T, X, Y) \exp^{i\varphi(T, X, Y)}, \quad (42)$$

where $\bar{A}_j(T, X, Y)$ is the amplitude portion of the soliton solutions and $\varphi(T, X, Y)$ is the phase portion of the soliton solution, which is given as

$$\varphi(T, X, Y) = \omega T + KX + MY. \quad (43)$$

Substituting (42) into (41), let real part and imaginary part be zero, and we can get the following coupled equations:

$$\begin{aligned} & \frac{\partial \bar{A}_j}{\partial T} + \alpha_j \left(2 \frac{\partial \bar{A}_j}{\partial X} \frac{\partial \varphi}{\partial X} + \bar{A}_j \frac{\partial^2 \varphi}{\partial X^2} \right) \\ & + \beta_j \left(2 \frac{\partial \bar{A}_j}{\partial Y} \frac{\partial \varphi}{\partial Y} + \bar{A}_j \frac{\partial^2 \varphi}{\partial Y^2} \right) = 0, \\ & - \bar{A}_j \frac{\partial \varphi}{\partial T} + \alpha_j \left[\frac{\partial^2 \bar{A}_j}{\partial X^2} - \bar{A}_j \left(\frac{\partial \varphi}{\partial X} \right)^2 \right] \\ & + \beta_j \left[\frac{\partial^2 \bar{A}_j}{\partial Y^2} - \bar{A}_j \left(\frac{\partial \varphi}{\partial Y} \right)^2 \right] + \gamma_j \bar{A}_j^3 = 0. \end{aligned} \quad (44)$$

Further, replacing φ with (43)

$$\frac{\partial \bar{A}_j}{\partial T} + 2\alpha_j K \frac{\partial \bar{A}_j}{\partial X} + 2\beta_j M \frac{\partial \bar{A}_j}{\partial Y} = 0,$$

$$\begin{aligned} & -\omega \bar{A}_j + \alpha_j \left(\frac{\partial^2 \bar{A}_j}{\partial X^2} - K^2 \bar{A}_j \right) + \beta_j \left(\frac{\partial^2 \bar{A}_j}{\partial Y^2} - M^2 \bar{A}_j \right) \\ & + \gamma_j \bar{A}_j^3 = 0. \end{aligned} \quad (45)$$

Using the traveling wave transformation, this pair of equations will be analyzed further, let

$$\bar{A}_j(T, X, Y) = F_j(\zeta), \quad \text{as } \zeta = \omega' T + K' X + M' Y, \quad (46)$$

and we have

$$\begin{aligned} & [-\omega' + 2(KK'\alpha_j + MM'\beta_j)] \frac{dF_j}{d\zeta} = 0, \\ & (\alpha_j K'^2 + \beta_j M'^2) \frac{d^2 F_j}{d\zeta^2} - (\alpha_j K^2 + \beta_j M^2 + \omega) F_j + \gamma_j F_j^3 \\ & = 0. \end{aligned} \quad (47)$$

From the first term of (47), we get

$$\omega' = 2(KK'\alpha + MM'\beta). \quad (48)$$

Further, according to the balance principle in trial function method, we will balance F_j'' with F_j^3 . Using the solution procedure of the trial function method, we will obtain the system of algebraic equations as follows:

$$\begin{aligned} & F^3: 2(\alpha_j K'^2 + \beta_j M'^2) a_4 + \gamma_j = 0, \\ & F^2: \frac{3}{2}(\alpha_j K'^2 + \beta_j M'^2) a_3 = 0, \\ & F^1: (\alpha_j K'^2 + \beta_j M'^2) a_2 - (\alpha_j K^2 + \beta_j M^2 + \omega_j) = 0, \\ & F^0: \frac{1}{2}(\alpha_j K'^2 + \beta_j M'^2) a_1 = 0. \end{aligned} \quad (49)$$

From the equations above, we have the results of the system

$$\begin{aligned} & a_4 = -\frac{\gamma_j}{\alpha_j K'^2 + \beta_j M'^2}, \\ & a_3 = 0, \\ & a_2 = \frac{\alpha_j K^2 + \beta_j M^2 + \omega}{\alpha_j K'^2 + \beta_j M'^2}, \\ & a_1 = 0. \end{aligned} \quad (50)$$

Therefore, we know that F satisfied

$$\pm(\zeta - \zeta_0) = \int \frac{1}{\sqrt{a_0 + ((\alpha_j K^2 + \beta_j M^2 + \omega) / (\alpha_j K'^2 + \beta_j M'^2)) F_j^2 - (\gamma_j / (\alpha_j K'^2 + \beta_j M'^2)) F_j^4}} dF_j. \quad (51)$$

If we set $a_0 = 0$ in (51) and integrating with respect to F_j , we will obtain the following soliton solutions of (41) as follows:

$$\begin{aligned} \bar{A}_1 &= \pm \sqrt{\frac{\alpha_1 K^2 + \beta_1 M^2 + \omega}{\gamma_1}} \\ &\cdot \operatorname{sech} \left\{ \sqrt{\frac{\alpha_1 K^2 + \beta_1 M^2 + \omega}{\alpha_1 K'^2 + \beta_1 M'^2}} [K'X + M'Y \right. \\ &\quad \left. - 2(KK'\alpha_1 + MM'\beta_1)t - \zeta_0] \right\} \times \exp \{i(KX \\ &\quad + MY + \omega T)\}, \\ \bar{A}_2 &= \pm \sqrt{\frac{\alpha_2 K^2 + \beta_2 M^2 + \omega}{\gamma_2}} \\ &\cdot \operatorname{csch} \left\{ \sqrt{\frac{\alpha_2 K^2 + \beta_2 M^2 + \omega}{\alpha_2 K'^2 + \beta_2 M'^2}} [K'X + M'Y \right. \\ &\quad \left. - 2(KK'\alpha_2 + MM'\beta_2)t - \zeta_0] \right\} \times \exp \{i(KX \\ &\quad + MY + \omega T)\}, \end{aligned} \quad (52)$$

and these solutions are the soliton solutions for CNLS equations, when $KK'\alpha_j + MM'\beta_j + \omega > 0$.

4. Modulation Instabilities of Coupled Envelope Rossby Waves

For coupled envelope nonlinear Rossby waves, they meet the CNLS equations (39). We set the NLS equation of the (2 + 1)-dimension with constant coefficients as

$$\begin{aligned} i \frac{\partial A_1}{\partial T} + \alpha \frac{\partial^2 A_1}{\partial X^2} + \beta \frac{\partial^2 A_1}{\partial Y^2} \\ + (\sigma_1 * |A_1|^2 + r_{12} * |A_2|^2) A_1 = 0, \\ i \frac{\partial A_2}{\partial T} + \alpha \frac{\partial^2 A_2}{\partial X^2} + \beta \frac{\partial^2 A_2}{\partial Y^2} \\ + (\sigma_2 * |A_2|^2 + r_{21} * |A_1|^2) A_2 = 0. \end{aligned} \quad (53)$$

Further, introducing

$$Z = X \cos \theta + Y \sin \theta, \quad (54)$$

(53) reduces to

$$\begin{aligned} i \frac{\partial A_1}{\partial T} + \gamma_1 \frac{\partial^2 A_1}{\partial Z^2} + (\sigma_1 * |A_1|^2 + r_{12} * |A_2|^2) A_1 = 0, \\ i \frac{\partial A_2}{\partial T} + \gamma_2 \frac{\partial^2 A_2}{\partial Z^2} + (\sigma_2 * |A_2|^2 + r_{21} * |A_1|^2) A_2 = 0, \end{aligned} \quad (55)$$

where $\gamma_1 = \gamma_2 = \alpha^2 \cos^2 \theta + \beta^2 \sin^2 \theta$.

From Section 3, we know the exact periodic wave solutions, taking the simple form as follows:

$$\begin{aligned} A_1 &= a \exp i(m_1 Z - \Omega_1 T), \\ A_2 &= b \exp i(m_2 Z - \Omega_2 T), \end{aligned} \quad (56)$$

where m_1, Ω_1, m_2 , and Ω_2 satisfy

$$\begin{aligned} \Omega_1 &= \gamma_1 m_1^2 - (\sigma_1 a^2 + \gamma_{12} b^2), \\ \Omega_2 &= \gamma_2 m_2^2 - (\sigma_2 b^2 + \gamma_{21} a^2). \end{aligned} \quad (57)$$

We assume that a, b are real numbers and m_1, m_2 represent wave number. Equation (54) shows that each nonlinear Rossby wave dispersion not only contains itself wave number and amplitude, but also contains another wave amplitude, which is characteristic of the interaction between wave and wave.

Next, we will analyze the stability of waves solution below. Assume the solutions for the disturbance as follows:

$$\begin{aligned} A_1 &= \exp i(m_1 Z - \Omega_1 T) (a + \epsilon \phi_1(Z, T)), \\ A_2 &= \exp i(m_2 Z - \Omega_2 T) (b + \epsilon \phi_2(Z, T)). \end{aligned} \quad (58)$$

Substituting (58) into (53), we can get the linear equations as follows:

$$\begin{aligned} i \frac{\partial \phi_1}{\partial T} + \gamma_1 \left(2m_1 i \frac{\partial \phi_1}{\partial Z} + \frac{\partial^2 \phi_1}{\partial Z^2} \right) + \sigma_1 a^2 (\phi_1 + \phi_1^*) \\ + \gamma_{12} ab (\phi_2 + \phi_2^*) = 0, \end{aligned} \quad (59)$$

$$\begin{aligned} i \frac{\partial \phi_2}{\partial T} + \gamma_2 \left(2m_2 i \frac{\partial \phi_2}{\partial Z} + \frac{\partial^2 \phi_2}{\partial Z^2} \right) + \sigma_2 b^2 (\phi_2 + \phi_2^*) \\ + \gamma_{21} ab (\phi_1 + \phi_1^*) = 0. \end{aligned}$$

Further, assume

$$\begin{aligned} \phi_1 &= p_1 \exp(i\lambda Z + \sigma T) + q_1 \exp(-i\lambda Z + \sigma^* T), \\ \phi_2 &= p_2 \exp(i\lambda Z + \sigma T) + q_2 \exp(-i\lambda Z + \sigma^* T), \end{aligned} \quad (60)$$

and, substituting (60) into (59), we can get

$$\begin{aligned} [(\sigma_1 a^2 - \gamma_1 \lambda^2) + (i\sigma - 2\gamma_1 m_1 \lambda)] p_1 + \gamma_{12} ab p_2 \\ + \sigma_1 a^2 q_1^* + \gamma_{12} ab q_2^* = 0, \\ \sigma_1 a^2 p_1^* + \gamma_{12} ab p_2^* \\ + [(\sigma_1 a^2 - \gamma_1 \lambda^2) - (i\sigma^* + 2\gamma_1 m_1 \lambda)] q_1 \\ + \gamma_{12} ab q_2 = 0, \\ \gamma_{21} ab p_1 + [(\sigma_2 b^2 - \gamma_2 \lambda^2) + (i\sigma - 2\gamma_2 m_2 \lambda)] p_2 \\ + \gamma_{21} ab q_1^* + \sigma_2 b^2 q_2^* = 0, \\ \gamma_{21} ab p_1^* - \sigma_2 b^2 p_2^* + \gamma_{21} ab q_1 \\ + [(\sigma_2 b^2 - \gamma_2 \lambda^2) + (i\sigma - 2\gamma_2 m_2 \lambda)] q_2 = 0. \end{aligned} \quad (61)$$

The above equations are linear homogeneous equations for p_1 , p_2 , q_1 , and q_2 . If there are nonzero solutions, the coefficients determinant must be zero. So we can get the next type:

$$\begin{aligned} & [(\gamma_1^2 \lambda^4 - 2\gamma_1 \sigma_1 \lambda^2 a^2) - (i\sigma - 2\gamma m_1 \lambda)^2] \\ & \cdot [(\gamma_2^2 \lambda^4 - 2\gamma_2 \sigma_2 \lambda^2 b^2) - (i\sigma - 2\gamma_2 m_2 \lambda)^2] \quad (62) \\ & = 4\gamma_1 \gamma_2 \gamma_{12} \gamma_{21} a^2 b^2 \lambda^4, \end{aligned}$$

and these are the four algebraic equations of $i\sigma$. When the parameters are certain, the value of λ makes $\text{Re}\sigma > 0$. But, for the influence of the interaction between wave and wave on the stability of wave, we will give a special case for discussion. Assume the number of waves satisfies

$$\gamma_1 m_1 = \gamma_2 m_2, \quad (63)$$

and, moreover, set

$$\begin{aligned} \Delta_1 &= \gamma_1^2 \lambda^2 \left(\lambda^2 - \frac{2\sigma_1 a^2}{\gamma_1} \right), \\ \Delta_2 &= \gamma_2^2 \lambda^2 \left(\lambda^2 - \frac{2\sigma_2 b^2}{\gamma_2} \right), \quad (64) \\ S &= 4\gamma_1 \gamma_2 \gamma_{12} \gamma_{21} a^2 b^2 \lambda^4. \end{aligned}$$

Clearly, when $\Delta_1 \geq 0$ the first wave is stable and there is no interaction and the contrary occurs when $\Delta_1 < 0$ is instable. Similarly, when $\Delta_2 \geq 0$ the second wave is stable and there is no interaction, and the contrary occurs when $\Delta_2 < 0$ is instable. From (62), we get

$$\begin{aligned} \sigma &= \text{Im} \left\{ \gamma_1 m_1 \lambda \right. \\ & \left. \pm \left[\frac{(\Delta_1 + \Delta_2) \pm \sqrt{(\Delta_1 - \Delta_2)^2 + 4S}}{2} \right]^{1/2} \right\}, \quad (65) \end{aligned}$$

where σ represents the gain for the frequency shift, which has been described in Figure 1. Equation (65) shows that when $\Delta_1 < 0$ and $\Delta_2 < 0$, that is, $\Delta_1 + \Delta_2 < 0$, no matter what value S takes, at least there is one which satisfies $\text{Re}\sigma > 0$; therefore, the waves have instability. This conclusion shows that when $\gamma_1 m_1 = \gamma_2 m_2$, two modulated unstable waves, the interaction of the two waves is still unstable.

When $\Delta_1 > 0$, $\Delta_2 > 0$, that is, $\Delta_1 + \Delta_2 > 0$, corresponding to no interaction, the two waves are stable. If $S > 0$, when $S \leq \Delta_1 \Delta_2$, two waves are stable after interaction. When $S > \Delta_1 \Delta_2$, two waves are unstable after interaction. If $S < 0$, when $-(1/4)(\Delta_1 - \Delta_2)^2 \leq S \leq \Delta_1 \Delta_2$, the two waves are stable. When $S < -(1/4)(\Delta_1 - \Delta_2)^2$ or $S > \Delta_1 \Delta_2$ two waves are unstable after interaction. From the above analysis, we can find that when $\Delta_1 > 0$ and $\Delta_2 > 0$, even with two

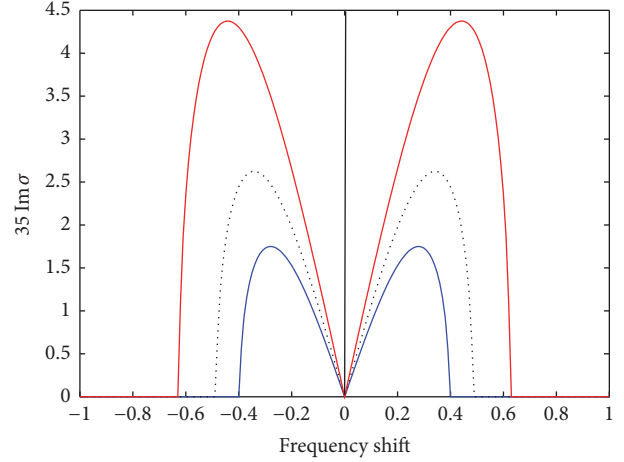


FIGURE 1: Gain spectra for frequency shift.

stable nonlinear waves through interaction, the stable feature is decided by the value of S .

When $\Delta_1 < 0$ and $\Delta_2 > 0$, corresponding to no interaction, the first wave is stable, but the second wave is unstable, while when $\Delta_1 > 0$, $\Delta_2 < 0$, the condition is opposite.

5. Chirp Effect

With summary of previous studies on Rossby waves, it is not hard to find that nonlinearity and dispersion are important factors affecting the propagation of Rossby waves. In this section, we use the concept of chirp in the field of optical soliton communication to study the chirp effect caused by nonlinearity and dispersion in the propagation of Rossby waves.

when $\alpha = \beta$, the NLS equation (41) for describing the characteristics of Rossby wave propagation transforms to

$$i \frac{\partial A}{\partial T} + \alpha \left(\frac{\partial^2 A}{\partial X^2} + \frac{\partial^2 A}{\partial Y^2} \right) + \gamma |A|^2 A = 0, \quad (66)$$

where α is the coefficient of dispersion and γ is the nonlinear coefficient. Here, based on the soliton solution of the NLS equation, we take the initial wave form of (2+1)-dimensional Rossby solitary waves as follows, setting $K = M = K' = M' = 1$:

$$A = \sqrt{\frac{2\alpha + \omega}{\gamma}} \text{sech} \left[\sqrt{\frac{2\alpha + \omega}{2\alpha}} (X + Y) \right]. \quad (67)$$

5.1. Chirp Effect Caused by Dispersion. Let us consider the dispersion effect of chirp, and (66) becomes

$$A_T = -i\alpha (A_{XX} + A_{YY}). \quad (68)$$

Reviewing the time T from $0 \rightarrow \Delta T$, where ΔT is an infinitesimal variable, and introducing (67) into (68), we can get the approximate solution of (68) as follows:

$$A(\Delta T, X, Y) = \sqrt{\frac{2\alpha + \omega}{\gamma}} \operatorname{sech} \left[\sqrt{\frac{2\alpha + \omega}{2\alpha}} (X + Y) \right] \cdot \exp \left\{ -i(2\alpha + \omega) \Delta T \right. \\ \left. \times \operatorname{sech}^2 \left[\sqrt{\frac{2\alpha + \omega}{2\alpha}} (X + Y) \right] \right\}, \quad (69)$$

so that the phase of the wave meets

$$\varphi_D = -i(2\alpha + \omega) \Delta T \operatorname{sech}^2 \left[\sqrt{\frac{2\alpha + \omega}{2\alpha}} (X + Y) \right], \quad (70)$$

and, based on (70), we can obtain the chirp effect caused by the dispersion

$$\Delta v_D = -\nabla \varphi_D = \sqrt{2} (2\alpha + \omega)^{3/2} \cdot \Delta T \left\{ \operatorname{sech}^2 \left[\sqrt{\frac{2\alpha + \omega}{2\alpha}} (X + Y) \right] \cdot \tanh \left[\sqrt{\frac{2\alpha + \omega}{2\alpha}} (X + Y) \right] \right\}. \quad (71)$$

5.2. Chirp Effect Caused by Nonlinearity. Separately considering the nonlinear effect of chirp, the NLS equation (66) becomes

$$A_T = -i\gamma |A|^2 A, \quad (72)$$

and, investigating the condition of time T from $0 \rightarrow \Delta T$, where ΔT is an infinitesimal variable, and introducing (67) into (72), we can get the approximate solution of (72) as follows:

$$A(\Delta T, X, Y) = \sqrt{\frac{2\alpha + \omega}{\gamma}} \operatorname{sech} \left[\sqrt{\frac{2\alpha + \omega}{2\alpha}} (X + Y) \right] \cdot \exp \left\{ -i(2\alpha + \omega) \Delta T \right. \\ \left. \times \operatorname{sech}^2 \left[\sqrt{\frac{2\alpha + \omega}{2\alpha}} (X + Y) \right] \right\}, \quad (73)$$

and the phase of the wave meets

$$\varphi_N = -(2\alpha + \omega) \Delta T \times \operatorname{sech}^2 \left[\sqrt{\frac{2\alpha + \omega}{2\alpha}} (X + Y) \right], \quad (74)$$

and, based on (74), we can get the chirp effect caused by the nonlinear

$$\Delta v_N = -\nabla \varphi_N = -4(2\alpha + \omega)^{3/2} \cdot \sqrt{2\alpha} \Delta T \left\{ \operatorname{sech}^2 \left[\sqrt{\frac{2\alpha + \omega}{2\alpha}} (X + Y) \right] \cdot \tanh \left[\sqrt{\frac{2\alpha + \omega}{2\alpha}} (X + Y) \right] \right\}. \quad (75)$$

5.3. Discussion of Total Chirp. According to (71) and (75), the total chirp is

$$\Delta v_s = \Delta v_D + \Delta v_N = (\sqrt{2} - 4\sqrt{2\alpha}) (2\alpha + \omega)^{3/2} \cdot \Delta T \left\{ \operatorname{sech}^2 \left[\sqrt{\frac{2\alpha + \omega}{2\alpha}} (X + Y) \right] \cdot \tanh \left[\sqrt{\frac{2\alpha + \omega}{2\alpha}} (X + Y) \right] \right\}. \quad (76)$$

(1) When the dispersion and nonlinear effects cancel each other, as follows:

$$\Delta v_s = \Delta v_D + \Delta v_N = 0, \quad (77)$$

we can get $\alpha = 1/16$.

(2) When the dispersion effect is greater than the nonlinear effect, as follows:

$$|\Delta v_D| > |\Delta v_N|, \quad (78)$$

we get $\alpha < 1/16$.

(3) When the dispersion is less than the nonlinear effect, as follows:

$$|\Delta v_D| < |\Delta v_N|, \quad (79)$$

we get $\alpha > 1/16$. As we know, the total chirp effect is related to the sea conditions in the propagation region and the amplitude of the initial wave. If the propagation area and the sea condition parameter is determined, the total chirp effect is only related to the initial amplitude. The chirp effect caused by dispersion and nonlinearity is described in Figures 2 and 3. The above calculation shows that the magnitude of the initial amplitude is determined by the parameter α . Combining Figure 2, Figure 3, and calculation, we can get the following conclusions.

(1) When $\alpha = 1/16$, the dispersion and nonlinear effects cancel each other, and solitary waves propagate over long distances and keep waveforms constant.

(2) When $\alpha > 1/16$, the nonlinear effect is greater than the dispersion effect, so that the total chirp is not zero. In this case, the isolated waves present nonlinear characteristics, and the amplitude of isolated waves is changed periodically.

(3) When $\alpha < 1/16$, the dispersion effect is greater than the nonlinear effect, so that the total chirp is not zero. In this case, the isolated waves present dispersion property, and the amplitude of isolated waves is changed periodically.

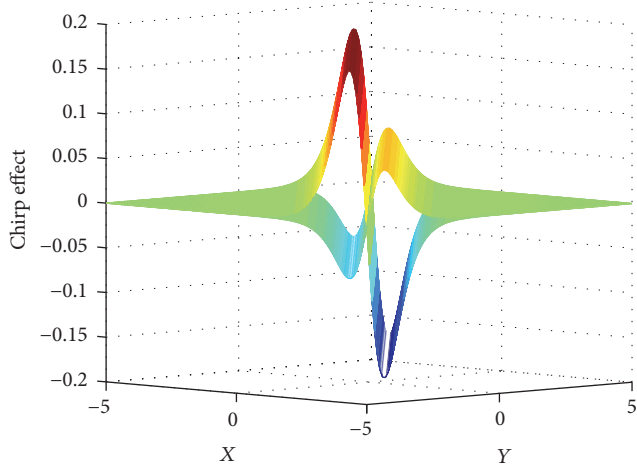


FIGURE 2: Three-dimensional waveform with dispersion and nonlinear effects.

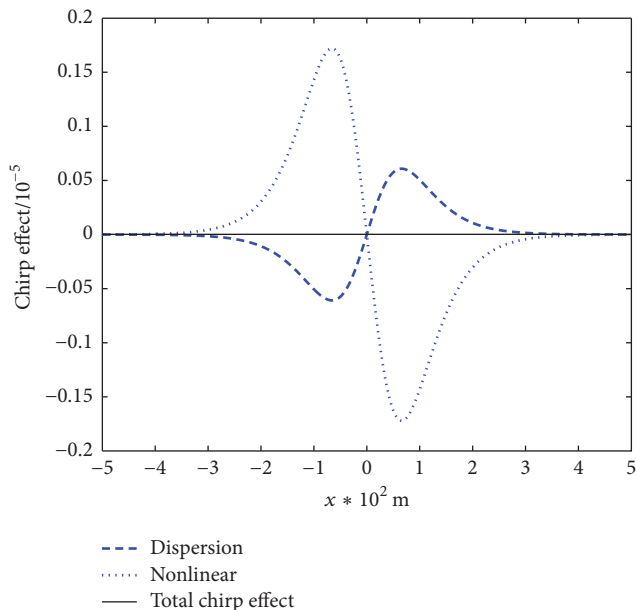


FIGURE 3: The variation of the chirp effect under the dispersion and nonlinearity.

6. Conclusions

In this paper, we obtained the $(2 + 1)$ -dimensional coupled NLS (CNLS) equations and discussed the solutions of the single nonlinear Schrödinger equation. In addition, we know that, for two nonlinear Rossby waves, they can be described by CNLS equations. The equations show that no matter the two waves' interaction process, their respective energy and momentum are conserved. Furthermore, modulational instability of coupled envelope Rossby waves in $(2 + 1)$ -dimensional condition is also discussed. we can find that the stable feature of coupled envelope Rossby waves is decided by the value of S , which implies that the instability condition depends not only on the prescribed perturbation wave numbers p, q , but also on the amplitude of the Rossby

waves. Finally, introducing the concept of chirp in the optical soliton communication field we study the chirp effect caused by nonlinearity and dispersion in the propagation of Rossby waves.

Conflicts of Interest

The authors declare that there are no conflicts of interest regarding the publication of this paper.

Acknowledgments

The project is supported by the Scientific and Technological Innovation Project Financially Supported by Qingdao National Laboratory for Marine Science and Technology (no. 2016ASKJ12), China Postdoctoral Science Foundation Funded Project (2017M610436), Open Fund of the Key Laboratory of Meteorological Disaster of Ministry of Education (Nanjing University of Information Science and Technology) (no. KLME1507), and Open Fund of the Key Laboratory of Ocean Circulation and Waves, Chinese Academy of Sciences (no. KLOCAW1401).

References

- [1] R. R. Long, "Solitary waves in one and two-fluids system," *Journal of the Atmospheric Sciences*, vol. 21, pp. 197–200, 1964.
- [2] D. J. Benny, "Long non-linear waves in fluid flows," *Journal of Mathematical Physics*, vol. 45, pp. 52–63, 1966.
- [3] L. G. Redekopp, "On the theory of solitary Rossby waves," *Journal of Fluid Mechanics*, vol. 82, no. 4, pp. 725–745, 1977.
- [4] H. Yang, Q. Zhao, B. Yin, and H. Dong, "A new integro-differential equation for rossby solitary waves with topography effect in deep rotational fluids," *Abstract and Applied Analysis*, vol. 2013, Article ID 597807, 2013.
- [5] H. Yang, B. Yin, Y. Shi, and Q. Wang, "Forced ILW-Burgers equation as a model for Rossby solitary waves generated by topography in finite depth fluids," *Journal of Applied Mathematics*, vol. 2012, Article ID 491343, 2012.
- [6] D. H. Luo, "The nonlinear schrödinger equation rotating barotropic atmosphere and atmospheric blocking," *Acta Meteor. Sinica*, vol. 48, p. 265, 1990.
- [7] X.-X. Xu, "A deformed reduced semi-discrete Kaup-Newell equation, the related integrable family and Darboux transformation," *Applied Mathematics and Computation*, vol. 251, pp. 275–283, 2015.
- [8] H. Li, Y. Li, and Y. Chen, "Bi-Hamiltonian structure of multi-component Yajima-Oikawa hierarchy," *Zeitschrift für Naturforschung - Section A Journal of Physical Sciences*, vol. 70, no. 11, pp. 929–934, 2015.
- [9] Q. L. Zhao and X. Z. Wang, "The integrable coupling system of a 3×3 discrete matrix spectral problem," *Applied Mathematics and Computation*, vol. 216, no. 3, pp. 730–743, 2010.
- [10] Q.-L. Zhao and X.-Y. Li, "A Bargmann system and the involutive solutions associated with a new 4-order lattice hierarchy," *Analysis and Mathematical Physics*, vol. 6, no. 3, pp. 237–254, 2016.

- [11] X.-X. Xu, "An integrable coupling hierarchy of the MkdV-Integrable systems, its hamiltonian structure and corresponding nonisospectral integrable hierarchy," *Applied Mathematics and Computation*, vol. 216, no. 1, pp. 344–353, 2010.
- [12] W.-X. Ma, "Variational identities and applications to Hamiltonian structures of soliton equations," *Nonlinear Analysis. Theory, Methods & Applications. An International Multidisciplinary Journal*, vol. 71, no. 12, pp. e1716–e1726, 2009.
- [13] L. G. Redekopp and P. D. Weidman, "Solitary rossby waves in zonal shear flows and their interactions," *Journal of the Atmospheric Sciences*, vol. 35, no. 5, pp. 790–804, 1978.
- [14] D. J. Benney, "The perturbed plane-wave solutions of the cubic Schrödinger equation," *Studies in Applied Mathematics*, vol. 60, p. 1, 1979.
- [15] T. Yamagata, "The stability, modulation and long wave resonance of a planetary wave in a rotating, two-layer fluid on a channel β -plane," *Journal of the Meteorological Society of Japan*, vol. 58, no. 3, pp. 160–171, 1980.
- [16] D. Luo, "Envelope solitary Rossby waves and modulational instabilities of uniform Rossby wave trains in two space dimensions," *Wave Motion. An International Journal Reporting Research on Wave Phenomena*, vol. 24, no. 3, pp. 315–325, 1996.
- [17] Y. Shi, B. Yin, H. Yang, D. Yang, and Z. Xu, "Dissipative nonlinear Schrödinger Equation for envelope solitary Rossby waves with dissipation effect in stratified fluids and its solution," *Abstract and Applied Analysis*, Article ID 643652, Art. ID 643652, 9 pages, 2014.
- [18] S. Y. Song, J. Wang, J. M. Meng, J. B. Wang, and P. X. Hu, "Nonlinear Schrödinger equation for internal waves in deep sea," *Acta Physica Sinica*, vol. 59, no. 2, pp. 1123–1129, 2010.
- [19] H. W. Yang, Z. H. Xu, D. Z. Yang, X. R. Feng, B. S. Yin, and H. H. Dong, "ZK-Burgers equation for three-dimensional Rossby solitary waves and its solutions as well as chirp effect," *Advances in Difference Equations*, 2016:167, 22 pages, 2016.
- [20] J. Wang and Y. M. Shi, "Study of chirps induced by the higher-order nonlinear effects in the photonic crystal fiber," *Acta Physica Sinica*, vol. 55, no. 6, pp. 1000–3290, 2006.
- [21] L. G. Yang, C. J. Da, J. Song, H. Zhang, H. Yang, and Y. Hou, "Rossby waves with linear topography in barotropic fluids," *Chinese Journal of Oceanology and Limnology*, vol. 26, no. 3, pp. 334–338, 2008.
- [22] T. Xu and Y. Chen, "Localized waves in three-component coupled nonlinear Schrödinger equation," *Chinese Physics B*, vol. 25, no. 9, Article ID 090201, 2016.
- [23] Y. Li, W.-X. Ma, and J. E. Zhang, "Darboux transformations of classical Boussinesq system and its new solutions," *Physics Letters. A*, vol. 275, no. 1-2, pp. 60–66, 2000.
- [24] Q.-L. Zhao, X.-Y. Li, and F.-S. Liu, "Two integrable lattice hierarchies and their respective Darboux transformations," *Applied Mathematics and Computation*, vol. 219, no. 10, pp. 5693–5705, 2013.
- [25] D.-Y. Chen, D.-J. Zhang, and S.-F. Deng, "The novel multi-soliton solutions of the MKdV-sine Gordon equations," *Journal of the Physical Society of Japan*, vol. 71, no. 2, pp. 658–659, 2002.
- [26] X. Guo, "On bilinear representations and infinite conservation laws of a nonlinear variable-coefficient equation," *Applied Mathematics and Computation*, vol. 248, pp. 531–535, 2014.
- [27] E. G. Fan and H. Q. Zhang, "Homogeneous balance method for nonlinear soliton equations," *Chinese Journal of Physics*, vol. 47, no. 3, pp. 353–363, 1998.
- [28] S. D. Liu, Z. T. Fu, S. K. Liu, and Q. Zhao, "Jacobi elliptic function envelope periodic solutions for nonlinear wave equations," *Chinese Physics*, vol. 51, no. 4, pp. 718–723, 2002.
- [29] W. X. Ma and R. G. Zhang, "Adjoint symmetry constraints of multi-component AKNS equations," *Chinese Annals of Mathematics*, vol. 349, pp. 153–163, 2006.
- [30] L. Huang and Y. Chen, "Nonlocal symmetry and similarity reductions for the Drinfeld-Sokolov-SATsuma-Hirota system," *Applied Mathematics Letters. An International Journal of Rapid Publication*, vol. 64, pp. 177–184, 2017.
- [31] Y. Zhang, H. Dong, X. Zhang, and H. Yang, "Rational solutions and lump solutions to the generalized (3 + 1)-dimensional Shallow Water-like equation," *Journal of Computers & Mathematics with Applications*, vol. 73, no. 2, pp. 246–252, 2017.
- [32] Y. Zhang and W.-X. Ma, "Rational solutions to a KdV-like equation," *Applied Mathematics and Computation*, vol. 256, pp. 252–256, 2015.
- [33] H. Dong, K. Zhao, H. Yang, and Y. Li, "Generalised (2+1)-dimensional super MKdV hierarchy for integrable systems in soliton theory," *East Asian Journal on Applied Mathematics*, vol. 5, no. 3, pp. 256–272, 2015.
- [34] X.-Y. Li, Y.-X. Li, and H.-X. Yang, "Two families of Liouville integrable lattice equations," *Applied Mathematics and Computation*, vol. 217, no. 21, pp. 8671–8682, 2011.
- [35] H. H. Dong, B. Y. Guo, and B. S. Yin, "Generalized fractional supertrace identity for Hamiltonian structure of NLS-MKdV hierarchy with self-consistent sources," *Analysis and Mathematical Physics*, vol. 6, no. 2, pp. 199–209, 2016.
- [36] X. Li and Q. Zhao, "A new integrable symplectic map by the binary nonlinearization to the super AKNS system," *Journal of Geometry and Physics*, vol. 121, pp. 123–137, 2017.
- [37] B. Tan and J. P. Boyd, "Coupled-mode envelope solitary waves in a pair of cubic Schrödinger equations with cross modulation: Analytical solution and collisions with application to Rossby waves," *Chaos, Solitons & Fractals*, vol. 11, no. 7, pp. 1113–1129, 2000.
- [38] R. Hirota, *The Direct Method in Soliton Theory*, Cambridge University Press, Cambridge, UK, 2004.
- [39] R. Xiang, L. M. Ling, and X. Lü, "Some novel solutions for the two-coupled nonlinear Schrödinger equations," *Applied Mathematics Letters*, vol. 68, pp. 163–170, 2017.

Research Article

Development of Embedded Element Technique for Permeability Analysis of Cracked Porous Media

Peng Qian and Qianjun Xu

State Key Laboratory of Hydrosience and Engineering, Department of Hydraulic Engineering, Tsinghua University, Beijing 100084, China

Correspondence should be addressed to Qianjun Xu; qxu@tsinghua.edu.cn

Received 27 June 2017; Accepted 14 September 2017; Published 17 October 2017

Academic Editor: Haifei Liu

Copyright © 2017 Peng Qian and Qianjun Xu. This is an open access article distributed under the Creative Commons Attribution License, which permits unrestricted use, distribution, and reproduction in any medium, provided the original work is properly cited.

The widely used approach of mesoscale finite element modeling for permeability analysis is to simulate the matrix and cracks with continuum elements (CE), whereas this process brings technical difficulties in generating a satisfying mesh conformity at the interface. In this work, an alternative method based on embedded element (EE) technique is developed for the prediction of water pressure field and effective permeability in the numerical simulation. Based on the mathematical similarity between elasticity and seepage problems, water pressure can derive from the corresponding displacement through “elastic analogy.” To assess the capability of the EE technique, different cases are simulated and compared with the CE model. The results show that there is a satisfactory agreement in water pressures and velocities between the CE and EE modeling. In the CE model, different factors, such as permeability contrast between matrix and cracks ($K_{\text{crack}}/K_{\text{matrix}}$) and mesh size, are considered. It is obvious to find that results will become stable when $K_{\text{crack}}/K_{\text{matrix}}$ reaches 10^4 , and the mesh size has little impact. The effective permeability of 3D porous media with random cracks is evaluated and the results show that the differential method is accurate for 3D permeability analysis when the crack density is not large.

1. Introduction

During the period of services, porous media like concrete and rocks are often subjected to various loads caused by mechanical, thermal, or physicochemical factors; the damage process generates new microcracks [1–3]. If the microcracks continue clustering and connecting, the permeability of porous media will certainly increase, accelerating the deterioration process and threatening the safety of structures. The cracked porous media are usually regarded as a two-phase composite which includes a porous matrix and a large number of cracks for permeability problems [4, 5]. The X-ray CT scan images of porous media have shown that the crack distribution varies with locations, influencing mechanical and permeability properties [6–8]. The geometrical information of individual cracks, such as orientation and connectivity, should be considered on cracked porous media.

The two main categories of models used in permeability analysis are the equivalent continuum model (ECM) and

the discrete fracture model (DFM) [9, 10]. The ECM is widely used in field-scale studies, and it contains a limited number of subdomains in which permeability is assumed to be uniform [11]. Under this assumption, the effective permeability is an average value over the subdomains that reflects the comprehensive effects of cracks and matrix [12, 13]. Although the ECM is simple to implement and requires low computational resources, it is difficult to present a reasonable representative volume elementary volume for permeability [14, 15]. Whereas, in small-scale studies, the influence of the individual cracks cannot be neglected, the DFM are quite suitable on this condition. In this approach cracks are represented by line elements or surface elements for 2D problems, and for 3D problems cracks are simulated with surface elements or body elements [5, 16–18]. Although this method considers real crack geometry, it is computationally intensive for models containing large number of cracks. The most commonly used numerical approaches in three-dimensional DFM are conventional solid or continuum elements [19, 20].

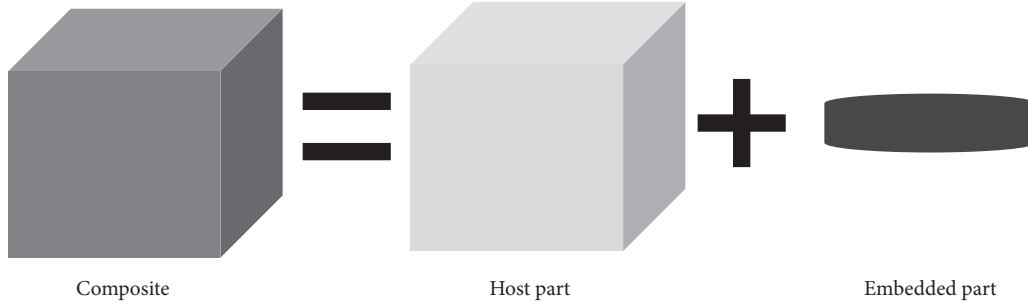


FIGURE 1: The relationship between host and embedded part.

This approach not only describes the actual crack distribution but also considers water transportation between the matrix and the cracks. Unfortunately, this process brings technical difficulties in generating a satisfying mesh conformity at the interface; therefore software is not able to mesh a geometry with more than 100 fractures when both the matrix and fractures must be mesh [21].

Noncontinuous meshing techniques present a practical solution for the meshing problems in finite element models applied in DFM [22]. Fish [23] introduced a mesh superposition technique to modeling of laminated composites and stress-stain fields. Takano et al. [24] proposed an enhanced mesh superposition method for multiscale finite element analysis of porous materials. They discretized the domain into three parts: global, local, and pores parts. Based on automatic image-based modeling and FE mesh superposition method, Kawagai et al. [25] study the multiscale modeling strategy for complex and heterogeneous microstructures of real materials. The embedded element of the commercial software ABAQUS can be applied in DFM as a mesh superposition technique [22]. Under the EE technique, the host and embedded parts can be meshed separately and independently, resolving difficulties in meshing complex geometry of the matrix.

Some noncontinuous methods like s-version FE model are developed and implemented by some authors, which makes it difficult for other researchers to use and develop them further. In this case, this paper adopts the EE technique to simulate pressure fields of cracked porous media. The results of meso-FE simulations of different cases using the CE and EE models are investigated and discussed to verify the EE technique. Meanwhile, some factors such as permeability ratio between matrix and cracks and mesh size which could influence results are also taken into consideration. Finally, effective permeability of 3D porous media with random distributed cracks are evaluated.

2. Embedded Element Technique

In the EE model, the reinforced part is placed inside the matrix part. The host is the main part, which is considered an independent model from the point of view of translational degrees of freedom (DOFs). The simple form of embedded element technique is shown in Figure 1. The host part and the embedded part can be meshed separately.

The weight functions in the famous finite element analysis software ABAQUS are used to create the geometric relationship between the nodes of embedded and host elements [26], which is illustrated as follows:

$$\mathbf{U}_{i(\text{Emb})} = \sum_{j=1}^N W_j \mathbf{U}_{j(H)}, \quad (1)$$

where $\mathbf{U}_{i(\text{Emb})}$ and $\mathbf{U}_{j(H)}$ denote the DOF of the embedded and host nodes and W_j denotes the weight function. The value of the weight function is determined by the distance between the embedded node and the corresponding host node. A short distance will lead to a large weight function. If an embedded node is located within a host element, then the translational DOFs at the node are eliminated and the node becomes an “embedded node.” The translational DOFs of the embedded node are constrained to the interpolated values of the corresponding DOF of the host element.

The host and embedded strain are set to have the equivalent in the superposition regions, which is called the principal of strain equivalence. Therefore, the composite stiffness \mathbf{S}_C can be calculated as follows [27]:

$$[\mathbf{S}_C] = [\mathbf{S}_H] + [\mathbf{S}_E], \quad (2)$$

where \mathbf{S}_H and \mathbf{S}_E represent the stiffness for the host and embedded part separately. Finally, the stress in the embedded region $\boldsymbol{\sigma}_E$ can be calculated as

$$[\boldsymbol{\sigma}_E] = [\mathbf{D}_E] \{\boldsymbol{\varepsilon}_E\}, \quad (3)$$

where $\boldsymbol{\varepsilon}_E$ is strain matrix and \mathbf{D}_E is the elastic matrix. The relationships between stresses of different parts are shown in Figure 2 in a concise way.

Even with the possibility of applying the EE technique in permeability analysis for cracked porous media, the following limitations must be eliminated first. Firstly, the EE techniques are allowed to have rotational DOF, but these rotations are not constrained by embedding. Secondly, some DOFs such as rotational, temperature, pore pressure, acoustic pressure, and electrical potential at an embedded node are not constrained [28]. Therefore, the direct application of the EE does not work. In this case, an indirect approach called “elastic analogy” is adopted as an auxiliary method combined with the EE technique.

TABLE 1: Correspondence between elastic and conductive problems.

Problem	Elasticity	Heat conduction	Seepage
Corresponding parameters	Displacement \mathbf{u}	Temperature T	Water head H
	Stress $\boldsymbol{\sigma}$	Heat flux \mathbf{s}	Flow velocity \mathbf{v}
	Strain $\boldsymbol{\varepsilon}$	Temperature gradient \mathbf{p}	Hydraulic gradient \mathbf{J}
	$\boldsymbol{\varepsilon} = \frac{(\nabla\mathbf{u} + \mathbf{u}\nabla)}{2}$	$\mathbf{p} = -\nabla T$	$\mathbf{J} = -\nabla H$
	External force \mathbf{f}	Heat source q	Water source g
Physical equation	Elastic tensor \mathbf{E}	Thermal conductivity tensor \mathbf{M}	Hydraulic conductivity tensor \mathbf{K}
Equilibrium equation	$\boldsymbol{\sigma} = \mathbf{E} : \boldsymbol{\varepsilon}$	$\mathbf{s} = -\mathbf{M} \cdot \mathbf{p}$	$\mathbf{v} = -\mathbf{K} \cdot \mathbf{J}$
	$\nabla \cdot \boldsymbol{\sigma} + \mathbf{f} = \mathbf{0}$	$\nabla \cdot \mathbf{s} + q = 0$	$\nabla \cdot \mathbf{v} + g = 0$

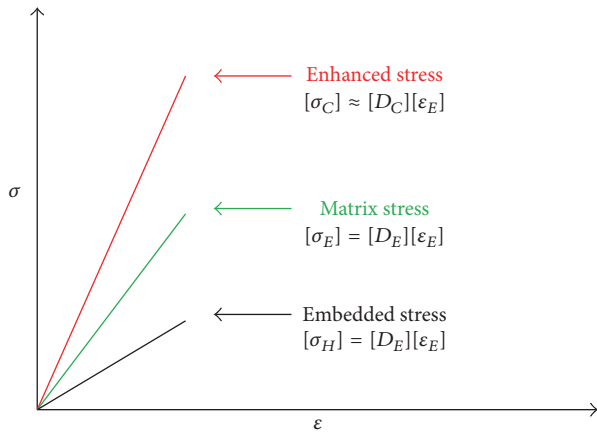


FIGURE 2: The relationship between stresses of different parts.

3. Elastic Analogy

Heat conduction, mass diffusion, and seepage can be described by very similar mathematical equations [29]. The mathematical similarity also exists between elasticity and seepage problems, which is illustrated in Table 1. For 3D problems, the displacement vector has three components, and the water head is merely a scalar. So a seepage field can be obtained through an analogy of the corresponding elastic field in the case of constrained DOF. Hence EE technique for elastic problems can be extended to the corresponding seepage problems by “elastic analogy” because of such correspondence.

In steady-state seepage analysis, the flow rate \mathbf{q} and water head H obey the generalized Darcy law in Cartesian coordinate system as follows:

$$\mathbf{q} = -\mathbf{K} \cdot \nabla H, \quad (4)$$

where \mathbf{K} is the hydraulic conductivity tensor, which is expressed as follows:

$$\mathbf{K} = \begin{bmatrix} k_x & k_{xy} & k_{xz} \\ k_{yx} & k_y & k_{yz} \\ k_{zx} & k_{zy} & k_z \end{bmatrix}. \quad (5)$$

And \mathbf{K} is a second-order tensor with six independent elements. The equilibrium equation can be expressed as follows:

$$\nabla H^T \cdot \mathbf{K} \cdot \nabla H + g = 0, \quad (6)$$

where g denotes the water source. If the principal axes of the materials coincide with the coordinate axes, then (6) can be rewritten as follows:

$$\frac{\partial}{\partial x} \left(k_x \frac{\partial H}{\partial x} \right) + \frac{\partial}{\partial y} \left(k_y \frac{\partial H}{\partial y} \right) + \frac{\partial}{\partial z} \left(k_z \frac{\partial H}{\partial z} \right) + g = 0. \quad (7)$$

Strain $\boldsymbol{\varepsilon}$ and stress $\boldsymbol{\sigma}$ in the elasticity problems obey Hooke’s law as follows:

$$\boldsymbol{\varepsilon} = \mathbf{C} : \boldsymbol{\sigma}, \quad (8)$$

where flexibility tensor \mathbf{C} is a fourth-order tensor with 21 independent elements. In an orthotropic material, \mathbf{C} becomes

$$\mathbf{C} = \begin{bmatrix} \frac{1}{E_{11}} & -\frac{\nu_{12}}{E_{22}} & -\frac{\nu_{13}}{E_{33}} & 0 & 0 & 0 \\ -\frac{\nu_{21}}{E_{11}} & \frac{1}{E_{22}} & -\frac{\nu_{23}}{E_{33}} & 0 & 0 & 0 \\ -\frac{\nu_{31}}{E_{11}} & -\frac{\nu_{32}}{E_{22}} & \frac{1}{E_{33}} & 0 & 0 & 0 \\ 0 & 0 & 0 & \frac{1}{G_{23}} & 0 & 0 \\ 0 & 0 & 0 & 0 & \frac{1}{G_{31}} & 0 \\ 0 & 0 & 0 & 0 & 0 & \frac{1}{G_{12}} \end{bmatrix}, \quad (9)$$

where E_{ij} and G_{ij} ($i, j = 1, 2, 3$) denote the elastic and shear moduli and ν denotes Poisson’s ratio. In the case of $\nu = 0$, \mathbf{C} becomes a diagonal matrix.

Furthermore, if the principal axes of the materials coincide with the coordinate axes but the displacements in the X and Y directions are constrained to be zero, then the elastic equilibrium equation in the Z direction can be simplified as follows:

$$\frac{\partial}{\partial x} \left(G_{13} \frac{\partial w}{\partial x} \right) + \frac{\partial}{\partial y} \left(G_{23} \frac{\partial w}{\partial y} \right) + \frac{\partial}{\partial z} \left(E_{33} \frac{\partial w}{\partial z} \right) + f_z = 0, \quad (10)$$

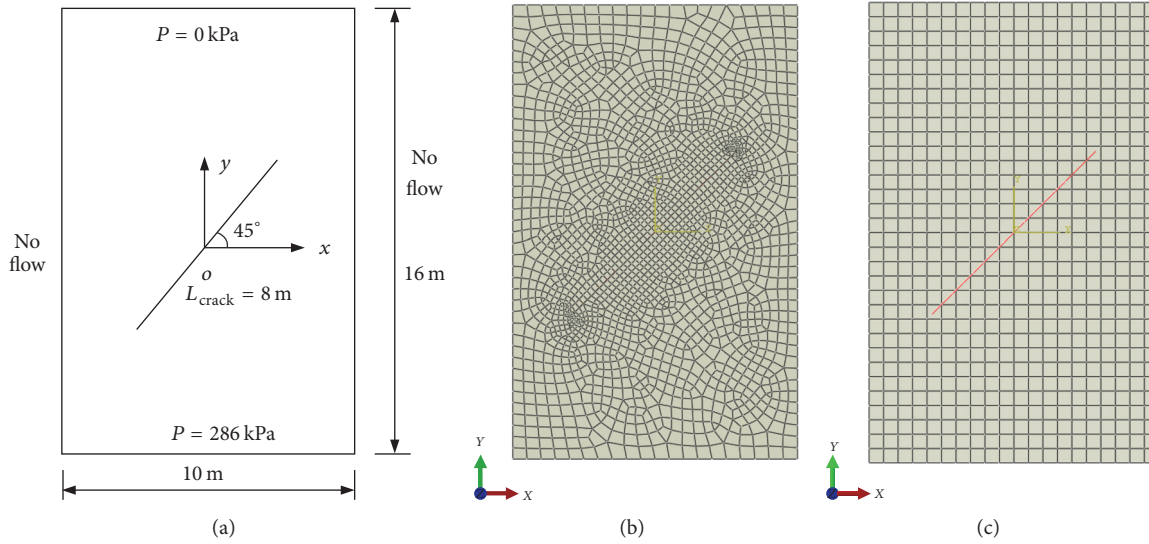


FIGURE 3: Two-dimensional cracked domain with a single crack: boundary condition (a); mesh of CE method (b); mesh of EE method (c).

where w and f_z are the displacement and body force in the Z -direction, respectively. This equation is similar to (7). By equating G_{13} , G_{23} , and E_{33} to k_x , k_y , and k_z , the water head and flow velocity can be obtained from the values of displacement w and stress components σ_{13} , σ_{23} , and σ_{33} , which are determined by (10). This equation is used as the basis for a seepage field to be obtained by the “degradation” of a corresponding elasticity field.

4. Numerical Application

This section presents the numerical results obtained using EE methods described in the previous sections. First, two examples which contain a single crack are addressed as the reference problems to verify the validity of the EE method by comparing with the results obtained from CE method. In the first one, a single crack in a 2D infinite matrix is modelled. Similarly, a 3D example with a single rectangular crack in a porous domain is presented in the second case. Moreover, an example with eight intersecting cracks is also presented to illustrate the capacities of the EE method. Finally, the effective permeability of 3D cracked porous media with hundreds of random distributed cracks is evaluated and compared with various analytical effective medium predictions.

4.1. 2D Example of a Single Crack. In this part, an inclined crack located in a rectangular matrix is shown in Figure 3 [10]. The matrix has an isotropic permeability, and a constant conductivity is supposed for the crack along its direction. Two constant values of pressure are applied on the bottom and up edges, and a zero normal flux is prescribed on the left and right edges. The CE and EE methods are used to generate meshes for this case (Figure 3). It is obvious to find that the EE modeling has independent meshes between crack and matrix, and the grid around the single crack seems intensive as expectation. The pressure fields determined by

the CE method and EE method are compared as shown in Figure 4. The contours obtained from these two methods have similar general characteristics which vary rapidly near the crack tips. However, unlike the displacements, water head varies continuously through the crack. The pressure profiles along two vertical sections ($x = 0$ and $x = 3$) through the domain were also created to compare the pressure change (shown in Figure 5). The results show that there is an excellent agreement between the two models, which proves the validity of EE method.

4.2. 3D Example of a Single Crack in a Cubic Domain. The 3D example contains a single square crack with 20 m long inside the cubic matrix, and the dimension of the matrix is $100 \text{ m} \times 100 \text{ m} \times 100 \text{ m}$ (shown in Figure 6). The center of the square crack is located at the position (60, 60, and 60), and its normal direction is $\vec{n} = (0.63, -0.45, 0.63)$. The matrix and crack are both isotropic and their relative permeability coefficients are 1 and 10,000, respectively. On faces $abcd$ ($Z = 100$) and $efgh$ ($Z = 0$), the water heads are set to be 1.0 and 0.0, and other faces are set to be impermeable.

4.2.1. Validation of the EE Technique. In this model, eight special positions in the matrix around the square crack were selected as reference points for comparing the difference between the CE and EE models (shown in Figure 7). The coordinates of these reference points are A (60, 57, 32), B (60, 62, 33), C (60, 67, 38), D (60, 67, 46), E (60, 53, 33), F (60, 53, 38), G (60, 57, 45), and H (60, 63, 48).

Figure 8 presents the water head fields at the section $x = 60$, and the contour distributions in both models are similar, except for a slight difference near tips of the crack.

The values of water heads at eight reference points are listed in Table 2; meanwhile the flow velocities are summarized in Table 3. The results shown in Table 2 reveal that difference of water head between the two methods is quite small, and the maximal relative error is less than 3%.

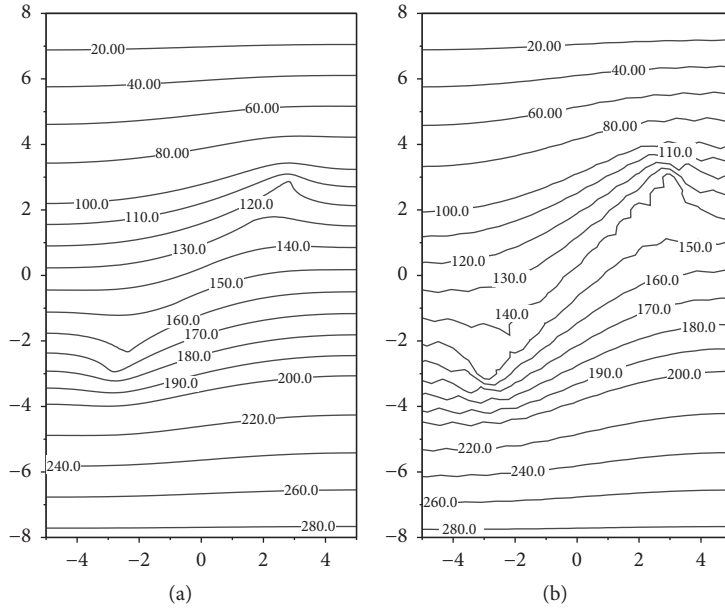


FIGURE 4: Pressure and displacement fields obtained from CE (a) and EE method for a single crack domain (b).

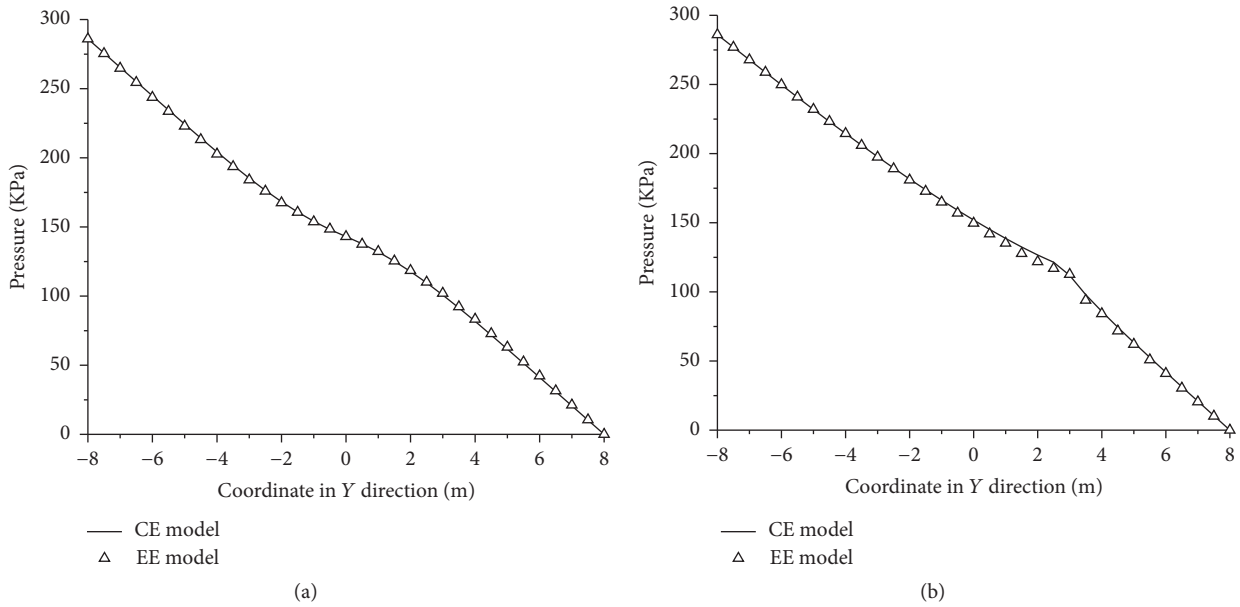


FIGURE 5: Pressure profile taken through the center of the cracked domain at $x = 0$ (a) and at $x = 3$ (b).

In Table 3, the flow velocities in the Z -direction of the two methods are nearly the same; in addition the velocity components in X and Y directions are so small that they can be omitted. However, what needs to be emphasized is that the relative errors of flow velocity at different reference points are all rather small except the point D , which is very close to the crack tip. The accuracy of water head filed is excellent on the whole domain, and the accuracy of flow velocity field is good enough except the limited area near the crack tip. The good agreement between the EE and CE modeling indicates the EE model is accurate.

4.2.2. Effect of the Relative Permeability Ratio. In order to examine the effect of permeability ratio between crack and matrix (K_{crack}/K_{matrix}) upon the flow properties, the 3D single crack model is studied. The variation of water pressure (water head) is plotted in Figure 9.

With the increase of K_{crack}/K_{matrix} , water heads at different locations converge to constant values. When the ratio is larger than 10^4 , the water heads at the reference points reach stability. This result is attributed to the fact that when the opening of the crack is sufficiently large, the crack becomes a superconductor and the head losses that occur almost reach

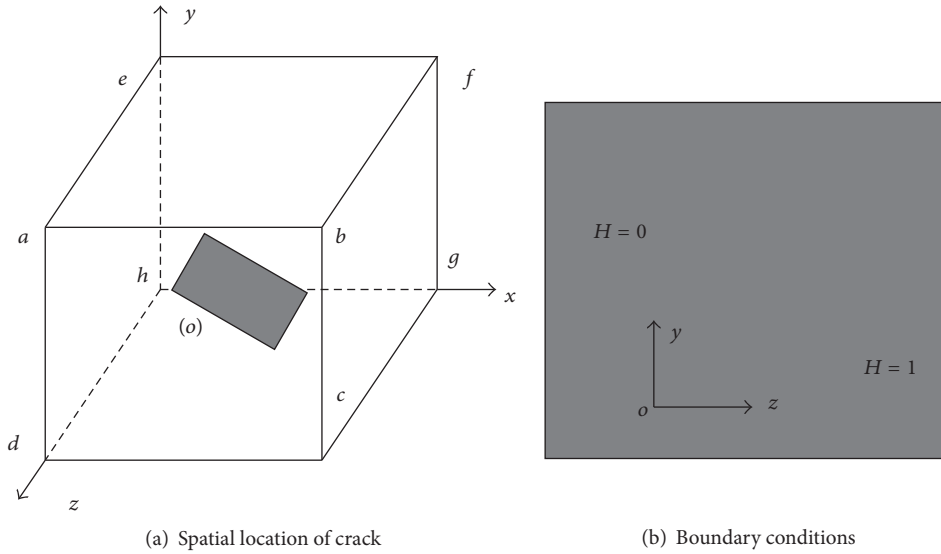
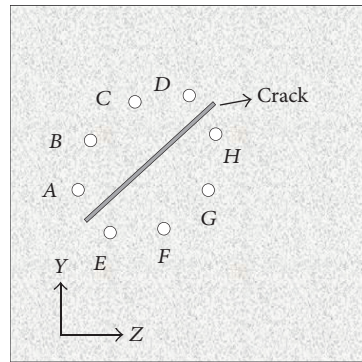


FIGURE 6: Three-dimensional cracked domain with a single crack.



Coordinates of the reference points:

A (60, 57, 32) D (60, 67, 46) G (60, 57, 45)
 B (60, 62, 33) E (60, 53, 33) H (60, 63, 48)
 C (60, 67, 38) F (60, 53, 38)

FIGURE 7: Locations of the reference points (section $X = 60$).

TABLE 2: Water heads at different reference points.

Reference point	A	B	C	D	E	F	G	H
EE model	0.3886	0.3660	0.3734	0.3898	0.4043	0.4109	0.4243	0.4081
CE model	0.3877	0.3601	0.3758	0.3987	0.3969	0.4046	0.4250	0.4114
Relative error	0.23%	1.64%	0.65%	2.22%	1.86%	1.57%	0.17%	0.80%

TABLE 3: Flow velocities at different reference points.

Reference point	A	B	C	D	E	F	G	H	
X direction	EE	$-9.10E-5$	$-1.63E-5$	$-1.15E-5$	$-2.89E-6$	$-4.14E-5$	$-1.03E-5$	$-2.13E-6$	$-5.00E-6$
	CE	$6.81E-7$	$-1.19E-5$	$2.11E-5$	$-3.10E-4$	0	$-3.18E-5$	$-2.61E-6$	$-4.08E-5$
Y direction	EE	$7.36E-5$	$6.60E-6$	$1.26E-5$	$5.22E-5$	$1.31E-4$	$-5.24E-5$	$5.29E-6$	$-5.28E-5$
	CE	$2.96E-6$	$6.70E-6$	$1.19E-5$	$-1.97E-4$	0	$-1.52E-5$	$6.25E-4$	$2.07E-6$
Z direction	EE	$-1.03E-2$	$-1.04E-2$	$-1.04E-2$	$-1.02E-2$	$-1.04E-2$	$-1.04E-2$	$-1.01E-2$	$-1.03E-2$
	CE	$-9.98E-3$	$-9.97E-3$	$-9.94E-3$	$-8.63E-3$	$-1.01E-2$	$-1.01E-2$	$-1.00E-2$	$-1.00E-2$
Relative error	3.21%	4.31%	4.63%	18.08%	2.97%	2.97%	1.00%	3.00%	

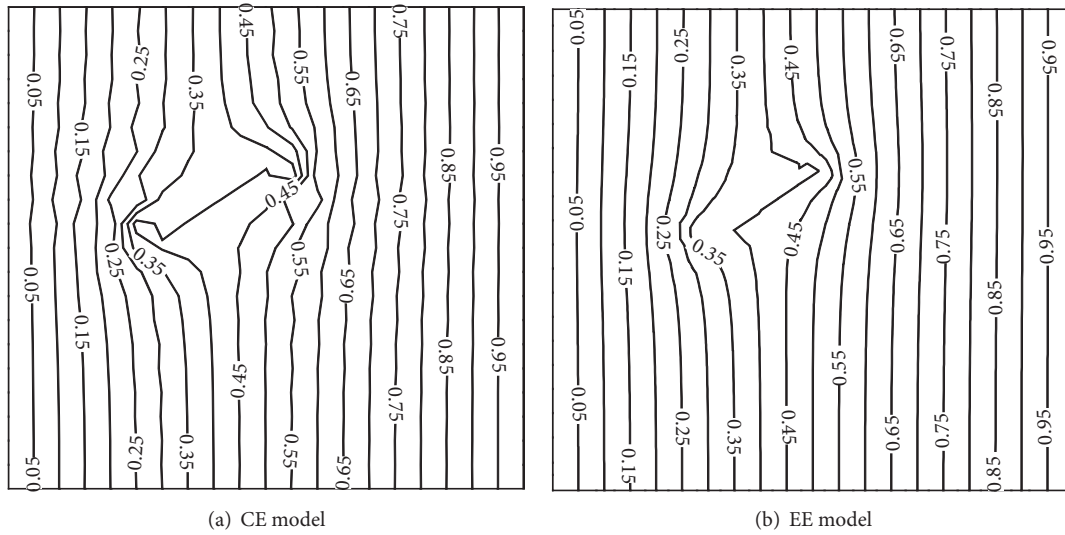


FIGURE 8: Water pressure fields calculated for the single crack model.

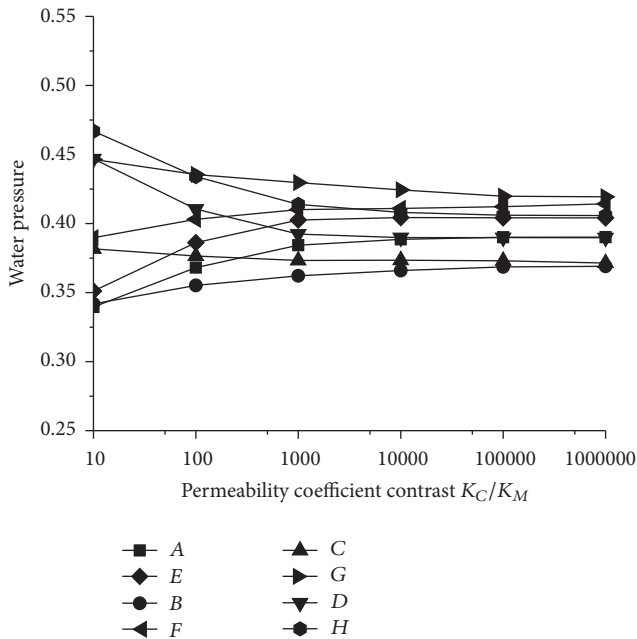


FIGURE 9: Effect of permeability coefficient on water pressure.

zero as water flows through. In general, for crack-matrix composites such as cracked porous media, cracks usually can be regarded as superpermeable compared with the matrix [5].

4.2.3. Mesh Sensitivity. Different mesh sizes of EE were investigated in the single crack model of the same 3D case to evaluate mesh sensitivity in EE modeling. The element size of the matrix remains constant ($L_M = 5$), and the mesh size of crack has three different values ($L_C = 10, 5, 1$). Therefore, mesh sensitivity analysis is investigated under three different mesh size ratios ($R_{\text{matrix/crack}} = 0.5, 1, 5$). Figure 10 shows the water head fields with different mesh size ratios, and Table 4

provides the values of water heads at the eight different reference points. The very small differences among different results conclude that the influence of mesh size upon water head can be ignored, which are similar to results presented by Tabatabaei et al. [22].

4.3. Multiple Intersecting Cracks. The case of intersecting cracks might be more interesting to us. Here consider a 6 m long square domain with nine intersecting cracks [30]. The model boundary condition and its corresponding CE and EE meshes are shown in Figure 11. The permeability of matrix and cracks is $1 \times 10^{-15} \text{ m}^2$ and $1 \times 10^{-9} \text{ m}^2$, respectively. Both the lower and the upper boundary are impermeable. The left boundary has a constant pressure of 100 kPa, while the right boundary has a constant pressure of 0 Pa.

Figure 12 shows that the displacement field from the EE method is similar to the pressure field from the CE method. In the center part of the domain, both fields have a relatively flat change, and the contour lines vary rapidly around different crack tips. The pressure values at different intersecting points are also investigated and Table 5 presents the results obtained from these two methods. It is found that the EE model provides a little higher values than the results obtained from the CE model, and the maximal relative error is less than 2%. The results conclude the EE technique is also feasible for intersecting cracks.

4.4. Effective Permeability of 3D Cracked Porous Media. To study the effective permeability of 3D cracked porous media, cracks are supposed to be isodiametric discs and follow unclustered random distribution. With such assumptions, the permeability of the cracked porous media is evaluated for different crack densities. Since the crack radius is kept constant, the crack density or volume fraction only depends on the number of cracks. The permeability contrast of crack to matrix is set to be 10000 to represent the great permeability

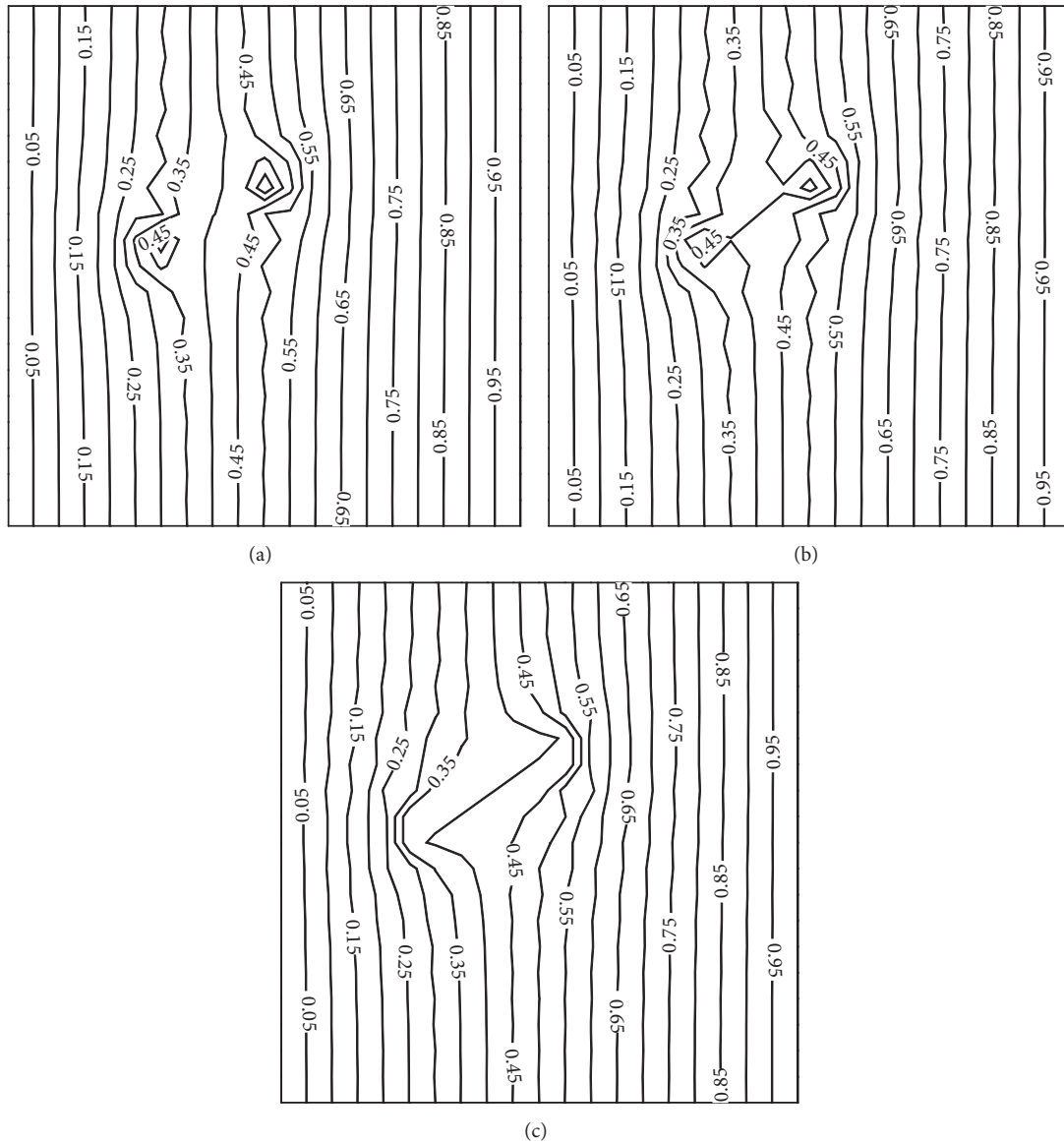


FIGURE 10: Water pressure fields of $R_{\text{matrix/crack}} = 0.5$ (a), $R_{\text{matrix/crack}} = 1$ (b), and $R_{\text{matrix/crack}} = 5$ (c) at section $X = 60$.

TABLE 4: Water head results under different mesh sizes.

Mesh	$R_{\text{matrix/crack}}$	Reference points near the crack							
		A	B	C	D	E	F	G	H
1	0.5	0.3912	0.3550	0.3733	0.4101	0.3895	0.3997	0.4285	0.3935
2	1	0.3982	0.3544	0.3693	0.3965	0.4018	0.4085	0.4294	0.3928
3	5	0.3899	0.3680	0.3742	0.3902	0.4038	0.4108	0.4203	0.4063

TABLE 5: Pressure at different intersecting points.

Intersecting point	1	2	3	4	5	6	7	8
CE model	52.6339	52.5069	52.27433	52.0081	52.2668	52.0307	52.5781	52.9278
EE model	53.6094	53.3770	53.1042	52.9307	52.9644	52.5680	53.4228	53.6258
Relative error	1.85%	1.66%	1.59%	1.77%	1.33%	1.03%	1.61%	1.32%

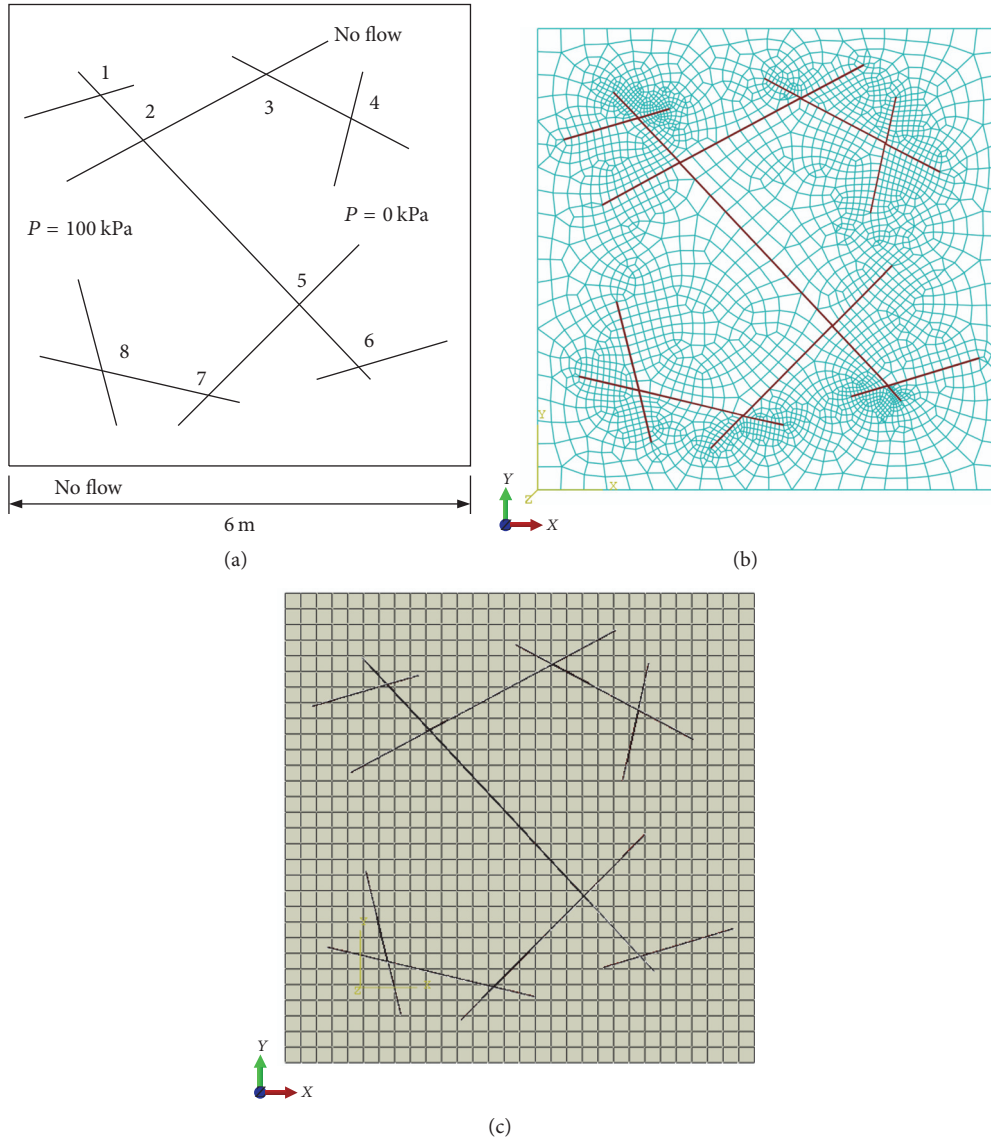


FIGURE 11: Two-dimensional cracked domain with multiple intersecting cracks: boundary condition (a); mesh of CE method (b); mesh of EE method (c).

gap between crack and matrix in the real situation. Constitutive equations of flow are given by Darcy's law, and this law is based on the establishment of a uniform water gradient along the domain as a result of applied external water flux. The side length of the cubic matrix and the radius of all cracks are taken as $l = 100$ and $r = 10$. In the modeling, two different water heads are given on two opposite sides of the matrix, and other sides are impermeable. The mesh schematic with the EE technique is displayed in Figure 13, where the matrix and the cracks are meshed separately and independently. Meanwhile, the crack density adopts definition of volume fraction of cracks with respect to the reference volume [5, 21]:

$$\rho = \frac{\sum a_i^3}{V}, \tag{11}$$

where the crack volume is denoted by the cubic of its radius, and the reference volume is the cubic of the side length. The predicted results obtained from effective medium models, such as the dilute schemes, the differential scheme, and self-consistent method, are compared with numerical results to investigate the potential application of the EE technique in DFM (shown in Figure 14).

The results shows that different approximations fit numerical results very well for crack density $\rho \leq 0.04$. As crack density increases, the dilute and difference methods seem to deviate the numerical solutions. On the other hand, the self-consistent approach still provides a relatively accurate fit to the numerical data. The effective medium methods are based on the assumption of a single inclusion in an infinite domain, so the effect of intersecting could not be

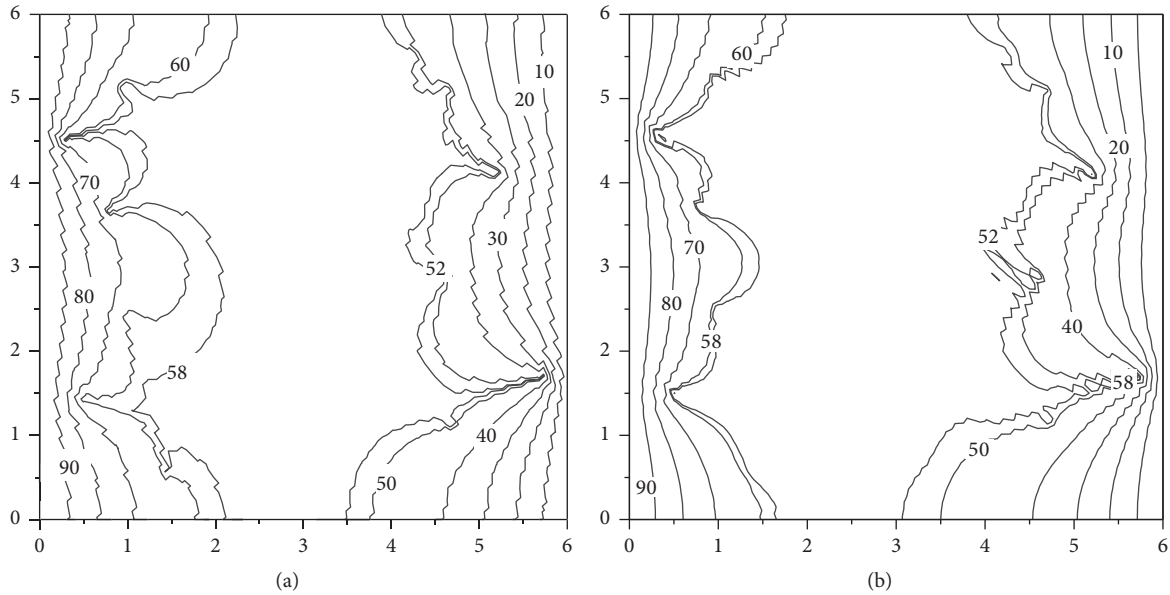


FIGURE 12: Pressure and displacement fields obtained from CE and EE method for multiple intersecting cracks domain.

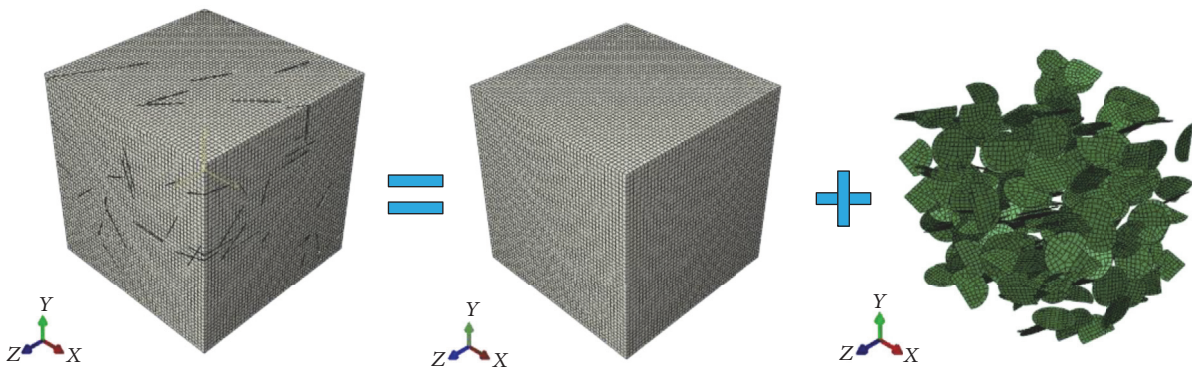


FIGURE 13: Schematic diagram of three-dimensional random cracks: mesh of composite (left); mesh of the matrix (middle); mesh of the cracks (right).

taken into consideration. It is generally accepted that self-consistent approach overestimates the effective property for nonintersecting cracks. However, self-consistent approach might be more reasonable when cracks comes intersecting.

5. Conclusion and Discussion

In this paper, we have developed a novel numerical method to calculate permeability of cracked porous media. The EE technique, combined with elastic analogy, can be utilized in the permeability modeling for crack-matrix composites like concrete or rocks. Compared to pressure (water head) and flow velocity fields obtained from the conventional CE method, the reliability of the EE technique is evaluated with different cases, and the results prove its validity and accuracy. Furthermore, some factors that influence the EE modeling are also taken into account. Further examinations indicate that stable calculation results can be induced if the relative

permeability ratio reaches 10^4 . What is more, the influence of mesh size upon water pressure is not significant.

For the case of 3D cracks densely and randomly distributed, the EE technique consequently reduces the computational cost since matrix and cracks can be meshed separately and independently. The numerical results show that the EE method can be applied to simulate the effective permeability of cracked porous media, and the self-consistent approach has a good analytical estimation when cracks come intersecting.

Conflicts of Interest

The authors declare that they have no conflicts of interest.

Acknowledgments

The research work was funded by the National Key Research and Development Program during the 13th Five-Year Plan

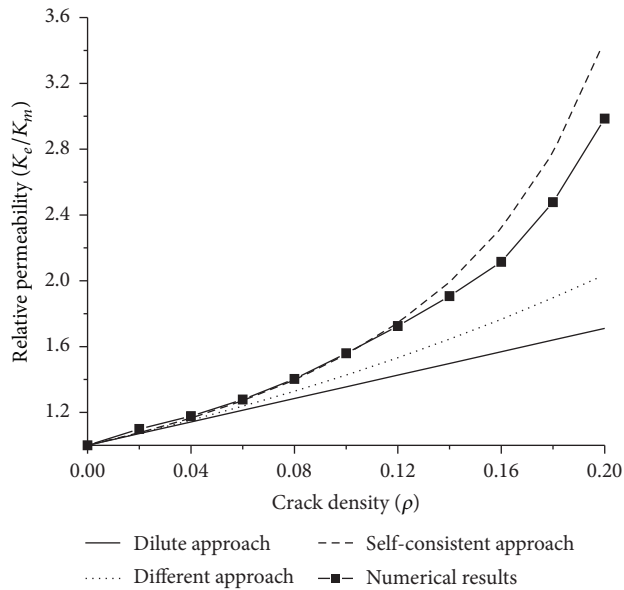


FIGURE 14: Effective permeability of cracked porous media with 3D random cracks.

of China (2017YFC0804602), National Basic Research Program of China (2013CB035902), National Natural Science Foundation of China (51339003), and State Key Laboratory of Hydrosience and Engineering (2016-KY-05).

References

- [1] S. Jacobsen, J. Marchand, and B. Gerard, "Concrete cracks I: durability and self healing—a review," in *Proceedings of the Second International Conference On Concrete Under Severe Conditions, Environment and Loading*, vol. 2, pp. 217–231, Tromsø, Norway, 1998.
- [2] D. Krajcinovic, "Damage mechanics: accomplishments, trends and needs," *International Journal of Solids and Structures*, vol. 37, no. 1-2, pp. 267–277, 1999.
- [3] C. Qian, B. Huang, Y. Wang, and M. Wu, "Water seepage flow in concrete," *Construction and Building Materials*, vol. 35, pp. 491–496, 2012.
- [4] G. Chatzigeorgiou, V. Picandet, A. Khelidj, and G. Pijaudier-Cabot, "Coupling between progressive damage and permeability of concrete: analysis with a discrete model," *International Journal for Numerical and Analytical Methods in Geomechanics*, vol. 29, no. 10, pp. 1005–1018, 2005.
- [5] C. Zhou, K. Li, and X. Pang, "Effect of crack density and connectivity on the permeability of microcracked solids," *Mechanics of Materials*, vol. 43, no. 12, pp. 969–978, 2011.
- [6] C. Kawaragi, T. Yoneda, T. Sato, and K. Kaneko, "Microstructure of saturated bentonites characterized by X-ray CT observations," *Engineering Geology*, vol. 106, no. 1-2, pp. 51–57, 2009.
- [7] Y. Nara, P. G. Meredith, T. Yoneda, and K. Kaneko, "Influence of macro-fractures and micro-fractures on permeability and elastic wave velocities in basalt at elevated pressure," *Tectonophysics*, vol. 503, no. 1-2, pp. 52–59, 2011.
- [8] X. Qin and Q. Xu, "Statistical analysis of initial defects between concrete layers of dam using X-ray computed tomography," *Construction and Building Materials*, vol. 125, pp. 1101–1113, 2016.
- [9] S. H. Lee, M. F. Lough, and C. L. Jensen, "Hierarchical modeling of flow in naturally fractured formations with multiple length scales," *Water Resources Research*, vol. 37, no. 3, pp. 443–455, 2001.
- [10] A. R. Lamb, *Coupled deformation, fluid flow and fracture propagation in porous media [Ph.D. thesis]*, Imperial College, London, UK, 2011.
- [11] H. Jourde, P. Fenart, M. Vinches, S. Pistre, and B. Vayssade, "Relationship between the geometrical and structural properties of layered fractured rocks and their effective permeability tensor. A simulation study," *Journal of Hydrology*, vol. 337, no. 1-2, pp. 117–132, 2007.
- [12] J. C. Long and P. A. Witherspoon, "The relationship of the degree of interconnection to permeability in fracture networks," *Journal of Geophysical Research: Atmospheres*, vol. 90, no. B4, pp. 3087–3097, 1985.
- [13] P. A. Hsieh, S. P. Neuman, G. K. Stiles, and E. S. Simpson, "Field Determination of the Three-Dimensional Hydraulic Conductivity Tensor of Anisotropic Media: 2. Methodology and Application to Fractured Rocks," *Water Resources Research*, vol. 21, no. 11, pp. 1667–1676, 1985.
- [14] P. H. S. W. Kulatilake and B. B. Panda, "Effect of block size and joint geometry on jointed rock hydraulics and REV," *Journal of Engineering Mechanics*, vol. 126, no. 8, pp. 850–858, 2000.
- [15] P. H. S. W. Kulatilake, B. Malama, and J. Wang, "Physical and particle flow modeling of jointed rock block behavior under uniaxial loading," *International Journal of Rock Mechanics and Mining Sciences*, vol. 38, no. 5, pp. 641–657, 2001.
- [16] O. Bour and P. Davy, "Connectivity of random fault networks following a power law fault length distribution," *Water Resources Research*, vol. 33, no. 7, pp. 1567–1583, 1997.
- [17] J.-R. De Dreuzy, P. Davy, and O. Bour, "Hydraulic properties of two-dimensional random fracture networks following a power law length distribution 1. Effective connectivity," *Water Resources Research*, vol. 37, no. 8, pp. 2065–2078, 2001.
- [18] A. Ebigbo, P. S. Lang, A. Paluszny, and R. W. Zimmerman, "Inclusion-based effective medium models for the permeability of a 3D fractured rock mass," *Transport in Porous Media*, vol. 113, no. 1, pp. 137–158, 2016.
- [19] I. I. Bogdanov, V. V. Mourzenko, J. F. Thovert, and P. M. Adler, "Effective permeability of fractured porous media in steady state flow," *Water Resources Research*, vol. 39, no. 1, pp. 1–16, 2003.
- [20] V. V. Mourzenko, I. I. Bogdanov, J.-F. Thovert, and P. M. Adler, "Three-dimensional numerical simulation of single-phase transient compressible flows and well-tests in fractured formations," *Mathematics and Computers in Simulation*, vol. 81, no. 10, pp. 2270–2281, 2011.
- [21] P. I. Sævik, I. Berre, M. Jakobsen, and M. Lien, "A 3D computational study of effective medium methods applied to fractured media," *Transport in Porous Media*, vol. 100, no. 1, pp. 115–142, 2013.
- [22] S. A. Tabatabaei, S. V. Lomov, and I. Verpoest, "Assessment of embedded element technique in meso-FE modelling of fibre reinforced composites," *Composite Structures*, vol. 107, pp. 436–446, 2014.
- [23] J. Fish, "The s-version of the finite element method," *Computers & Structures*, vol. 43, no. 3, pp. 539–547, 1992.
- [24] N. Takano, M. Zako, and Y. Okuno, "Multi-scale finite element analysis of porous materials and components by asymptotic homogenization theory and enhanced mesh superposition method," *Modelling and Simulation in Materials Science and Engineering*, vol. 11, no. 2, pp. 137–156, 2003.

- [25] M. Kawagai, A. Sando, and N. Takano, "Image-based multi-scale modelling strategy for complex and heterogeneous porous microstructures by mesh superposition method," *Modelling and Simulation in Materials Science and Engineering*, vol. 14, no. 1, pp. 53–69, 2006.
- [26] F. Tahmasebinia, G. Ranzi, and A. Zona, "Beam tests of composite steel-concrete members: A three-dimensional finite element model," *International Journal of Steel Structures*, vol. 12, no. 1, pp. 37–45, 2012.
- [27] M. W. Joosten, M. Dingle, A. Denmead et al., "Simulation of progressive damage in composites using the enhanced embedded element technique," in *Proceedings of the Composites Australia and CRC-ACS 2015 Conference and Trade Exhibition*, pp. 1–17, DEStech, 2015.
- [28] Abaqus 6.10 Documentation, 2010.
- [29] F. Deng and Q. Zheng, "Interaction models for effective thermal and electric conductivities of carbon nanotube composites," *Acta Mechanica Solida Sinica*, vol. 22, no. 1, pp. 1–17, 2009.
- [30] M.-N. Vu, A. Pouya, and D. M. Seyedi, "Theoretical and numerical study of the steady-state flow through finite fractured porous media," *International Journal for Numerical and Analytical Methods in Geomechanics*, vol. 38, no. 3, pp. 221–235, 2014.

Research Article

Flood Risk Zoning by Using 2D Hydrodynamic Modeling: A Case Study in Jinan City

Tao Cheng,^{1,2} Zongxue Xu,^{1,2} Siyang Hong,^{1,2} and Sulin Song³

¹College of Water Sciences, Beijing Normal University, Beijing 100875, China

²Beijing Key Laboratory of Urban Hydrological Cycle and Sponge City Technology, Beijing 100875, China

³Jinan Hydrology Bureau, Jinan 250014, China

Correspondence should be addressed to Zongxue Xu; zongxuexu@vip.sina.com

Received 30 June 2017; Accepted 6 September 2017; Published 12 October 2017

Academic Editor: Jian G. Zhou

Copyright © 2017 Tao Cheng et al. This is an open access article distributed under the Creative Commons Attribution License, which permits unrestricted use, distribution, and reproduction in any medium, provided the original work is properly cited.

Climate change and rapid urbanization have aggravated the rainstorm flood in Jinan City during the past decades. Jinan City is higher in the south and lower in the north with a steep slope inclined from the south to the north. This results in high-velocity overland flow and deep waterlogging, which poses a tremendous threat to pedestrians and vehicles. Therefore, it is vital to investigate the rainstorm flood and further perform flood risk zoning. This study is carried out in the “Sponge City Construction” pilot area of Jinan City, where the InfoWorks ICM 2D hydrodynamic model is utilized for simulating historical and designed rainfall events. The model is validated with observations, and the causes for errors are analyzed. The simulated water depth and flow velocity are recorded for flood risk zoning. The result shows that the InfoWorks ICM 2D model performed well. The flood risk zoning result shows that rainfalls with larger recurrence intervals generate larger areas of moderate to extreme risk. Meanwhile, the zoning results for the two historical rainfalls show that flood with a higher maximum hourly rainfall intensity is more serious. This study will provide scientific support for the flood control and disaster reduction in Jinan City.

1. Introduction

During the past decades, Jinan City has experienced prosperity in social economy. However, a series of urban water problems such as water pollution, water shortage, and urban flooding have arisen and posed a great challenge to the continued healthy development of social society [1, 2]. Severe climate change and rapid urbanization augment the probability of urban rainstorm flood and cause a large number of casualties and economic losses [3, 4]. Urban rainstorm flood has become one of the most concerning problems [5, 6]. In order to strengthen the work of flood control and disaster reduction and reduce the casualty and property losses caused by urban floods, it has become an increasingly common method to use the urban flood model to simulate the flooding situation and perform flood risk zoning which provides technical support for flood control and disaster reduction [7–10]. At present, many Chinese scholars have used hydrological and hydraulic models to carry out a lot of researches on

the urban flooding problem and have accumulated abundant theoretical and practical experience for flood prevention and reduction work in our country [8, 11]. Since the 1980s, a group of Chinese scholars have developed urban rain-flood models with independent intellectual property rights, but these models are usually codes or programs used within a number of research teams. These models are not easy to operate or interface friendly, and they are not widely used for the lack of commercial promotion [8]. In comparison, the SWMM model from the United States is broadly used because its codes are open-source and it is free to use [12]. MIKE series (Denmark), InfoWorks ICM (UK), and PCSWMM (Canada) also have a good number of users due to their strong hydrodynamic ability and preprocessing and postprocessing capacity [4, 13]. Yu et al. [14] developed an urban flood model of city scale in Jinan City by using the SWMM model. The results are good and the work has provided scientific and technological support for flood control and disaster reduction in Jinan City. Huang et al. [15] used the

InfoWorks ICM model to develop an integrated catchment model of urban scale in Haikou City. The model has been verified with monitoring data and the results have shown that the model has good accuracy and reliability. Wu and Huang [16] used the PCSWMM model to develop a rain-flood model which has been verified with observed data and used for analyzing the risk for designed rainfalls of different recurrence intervals. Qi et al. [17] developed a one-dimensional and a two-dimensional hydrodynamic model in the lower reaches of Tiantang River of Beijing based on MIKE 11 and MIKE 21. Then, these models have been coupled using MIKE FLOOD to simulate the regional flood under different rainstorm scenarios. The flood risk has been analyzed and has provided scientific support for the rational selection of the detention area and the development of a proper dam control scheme.

Jinan City has repeatedly suffered extreme rainstorms in history. Its flood problem is very severe due to its special geography. The city is higher in the south and lower in the north, so road flood and waterlogging have become a main threat to pedestrians and vehicles [1, 14]. This paper intends to use InfoWorks ICM to develop a model coupling hydrological with hydrodynamic process in the "Sponge City Construction" pilot area of Jinan City. Several historical rainstorm events are modeled and verified with the flood monitoring records. Then, the verified model is used for designed rainfalls of different recurrence intervals. The water depth and velocity are recorded and used to perform flood risk zoning. This work will provide scientific and technological support for flood prevention and mitigation work of the study area and Jinan City as well.

2. Methodologies

2.1. Coupled Hydrological and Hydrodynamic Model. The coupled hydrological and hydrodynamic model based on InfoWorks ICM consists of a hydrological process and a hydrodynamic process and their coupled process. As we know, the hydrodynamic modeling, especially the two-dimensional hydrodynamic modeling, is very time-consuming and always a bottleneck for fast and detailed modeling. The InfoWorks ICM can solve this problem with its parallel computation based on GPUs. Moreover, table handling, SQL query, and GIS function are available in the InfoWorks ICM, which make it easier for data preprocessing and result postprocessing.

The processes included in the InfoWorks ICM are the runoff calculation and flow convergence for the hydrological model, the one-dimensional hydrodynamic simulation for the underground pipe networks, and the two-dimensional hydrodynamic simulation for surface inundation. The hydrological model adopts a distributed method to simulate the rainfall-runoff process by dividing the study area into detailed subcatchment areas which may have various runoff surfaces of different flow characteristics. The runoff calculation and flow convergence process of the hydrological model can employ various models. In this paper, the fixed runoff model and SWMM flow convergence model are employed, respectively, as the object of our study is the urban area.

The hydrodynamic simulation for the underground pipe networks is implemented by solving the Saint-Venant equations. The flow in the underground pipes has two states, that is, surface flow and pressurized flow, and the Preissmann Slot is used to handle both kinds of flow and their transition. The mathematical expressions of the Saint-Venant equations are shown in

$$\begin{aligned} \frac{\partial A}{\partial t} + \frac{\partial Q}{\partial x} &= 0, \\ \frac{\partial Q}{\partial t} + \frac{\partial}{\partial x} \left(\frac{Q^2}{A} \right) + gA \left(\cos \theta \frac{\partial h}{\partial x} - S_0 + \frac{Q|Q|}{K^2} \right) &= 0, \end{aligned} \quad (1)$$

where A is the cross-sectional area of the pipe (m^2); Q is the flow rate of the pipe ($\text{m}^3 \cdot \text{s}^{-1}$); t is time (s); x is the length along the x direction (m); h is water depth (m); g is gravity ($\text{m} \cdot \text{s}^{-2}$); θ is the angle between the pipe line and horizontal line (degree); K is the conveyance and is calculated with Colebrook-White formula or Manning formula; S_0 is the bed slope.

The two-dimensional hydrodynamic simulation of the surface inundation is implemented by solving the shallow water equations (SWE), which are based on the depth-averaged Navier-Stokes equations. The assumption of these equations is that the flow is mainly in the horizontal direction, while flow rate changes in the vertical direction are negligible. The mathematical expressions of the shallow water equations are shown in

$$\begin{aligned} \frac{\partial h}{\partial t} + \frac{\partial (hu)}{\partial x} + \frac{\partial (hv)}{\partial y} &= q_{1D}, \\ \frac{\partial (hu)}{\partial t} + \frac{\partial}{\partial x} \left(hu^2 + \frac{gh^2}{2} \right) + \frac{\partial (huv)}{\partial y} &= S_{0,x} - S_{f,x} + q_{1D}u_{1D}, \\ \frac{\partial (hv)}{\partial t} + \frac{\partial}{\partial y} \left(hv^2 + \frac{gh^2}{2} \right) + \frac{\partial (huv)}{\partial x} &= S_{0,y} - S_{f,y} + q_{1D}v_{1D}, \end{aligned} \quad (2)$$

where u and v are the velocity component in the x and y directions ($\text{m} \cdot \text{s}^{-1}$); $S_{0,x}$ and $S_{0,y}$ are the bed slope component in the x and y directions ($\text{m}^2 \cdot \text{s}^{-2}$); $S_{f,x}$ and $S_{f,y}$ are the friction component in the x and y directions ($\text{m}^2 \cdot \text{s}^{-2}$); q_{1D} is the outflow per unit area ($\text{m} \cdot \text{s}^{-1}$); u_{1D} and v_{1D} are the velocity component of q_{1D} in the x and y directions ($\text{m} \cdot \text{s}^{-1}$); other variables not stated here are the same as above.

2.2. Flood Risk Zoning. There is a broad consensus that the degree of flood risk that flood poses to people (as well as vehicles, buildings, etc.) is a function of velocity and depth. Other physical factors such as water temperature, land surface type, and objects that may cause slippage or fall (e.g., "blown" manhole), are likely to have an impact on the risk for people or objects in the flood. Xia et al. [18, 19] and Milanese et al. [20, 21] developed risk calculation methods

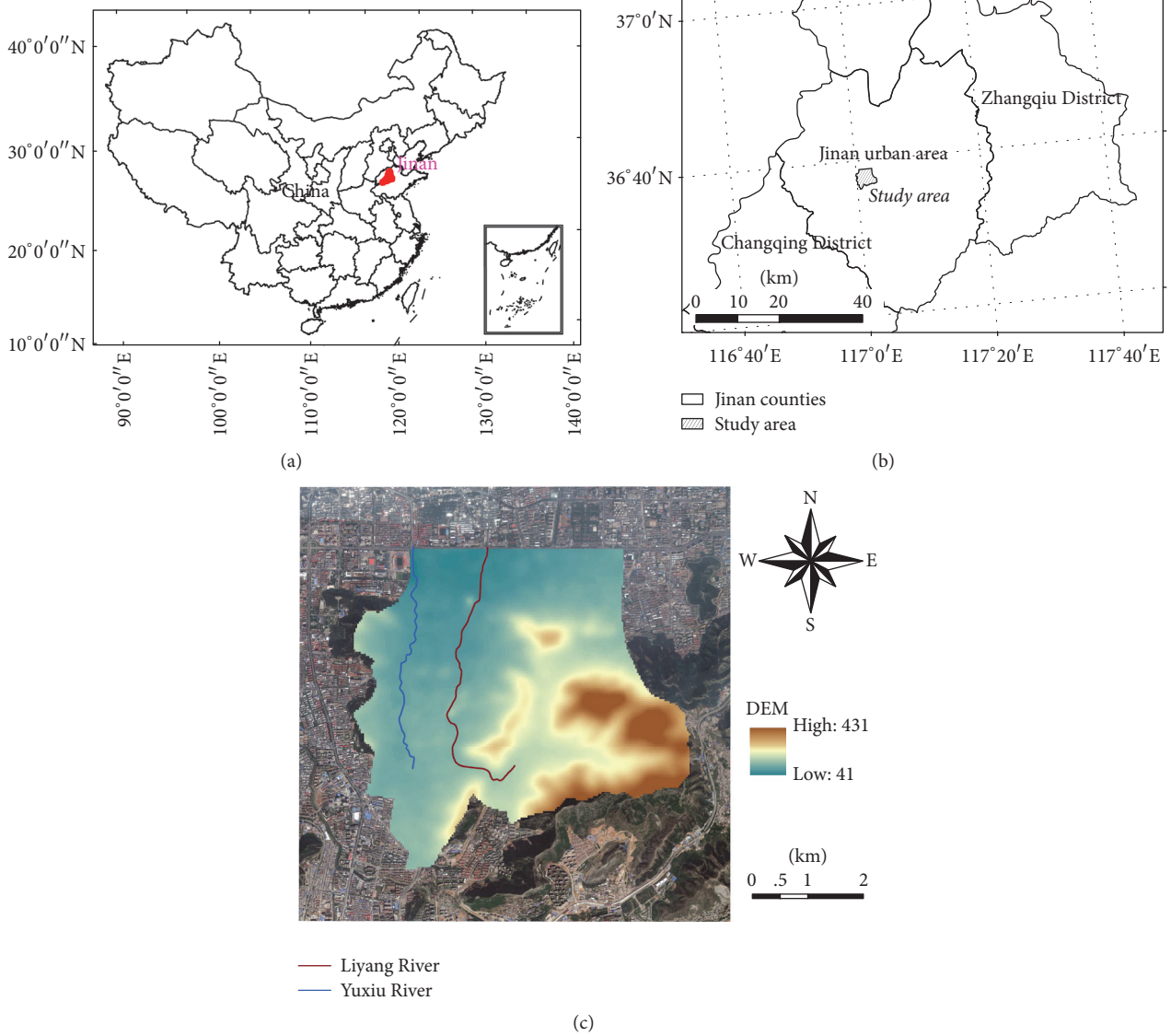


FIGURE 1: Location of the study area. (a) The overall location of Jinan City in China. (b) The location of the study area in Jinan City. (c) The layout of the study area where two rivers and the DEM are shown.

of the human body or vehicles through rigorous mechanical analyses and human engineering. However, these methods are based on complicated theoretical formula deduction, restricting their convenient and efficient applications. In this paper, the empirical method of calculating the flood risk recommended by Defra/Environment Agency of the United Kingdom [22] will be used, and the corresponding formula is shown as

$$HR = h \times (U + 0.5) + DF, \quad (3)$$

where HR is the flood risk value; h is water depth (m); U is the velocity of floodwater ($m \cdot s^{-1}$); DF is the debris factor ($=0, 0.5, \text{ or } 1$ depending on the probability that debris will lead to a significantly greater hazard, shown in Table 1).

The risk values calculated with the above formula will be classified and a detailed classification is shown in Table 2.

TABLE 1: Debris factors for different flood depths, velocities, and dominant land uses.

Depth (m) & velocity ($m \cdot s^{-1}$)	Pasture/arable	Woodland	Urban
$0 < h \leq 0.25$	0	0	0
$0.25 < h \leq 0.75$	0	0.5	1
$h > 0.75$ or $v > 2$	0.5	1	1

3. Model Application

3.1. Study Area Description. Jinan is the political, economic, and cultural center of Shandong Province of China. The study area (as shown in Figure 1) is situated in the south of the main urban area of Jinan City, where the Liyang River and the Yuxiu River go through and the “Sponge City Construction” pilot area is located. The eastern, western, and southeastern

TABLE 2: Classification of risk levels.

HR	Degree of flood risk	Description
[0, 0.75)	Low	<i>Caution</i> Flood zone with shallow flowing water or deep standing water
[0.75, 1.25]	Moderate	<i>Dangerous for some (i.e., children)</i> “Danger: flood zone with deep or fast flowing water”
(1.25, 2.5]	Significant	<i>Dangerous for most people</i> “Danger: flood zone with deep fast flowing water”
[2.5, ∞)	Extreme	<i>Dangerous for all</i> “Extreme danger: flood zone with deep fast flowing water”

TABLE 3: Parameter attributes for three kinds of surfaces.

Number	Surface type	Runoff model	Runoff coefficient	Surface type	Initial losses type	Initial losses (mm)	Routine model	Routine type	Routine parameter	Area (ha)
1	Road	Fixed PR model	0.95	Impervious	Constant	2	SWMM	Relative	0.018	127.1
2	Roof	Fixed PR model	0.90	Impervious	Constant	1	SWMM	Relative	0.020	231.1
3	Others	Fixed PR model	0.60	Pervious	Constant	5	SWMM	Relative	0.025	2014.5

parts of the study area are characterized by mountains and hills. The area inclines from the south to the north, with a maximum slope of 35.77% and an average slope of 6.8%. This area has been planned and constructed ages ago, and the drainage capacity of the underground drainage pipe networks is insufficient. The huge body of water from the southern mountainous area in the fluvial season will easily form a rapid flood in the study area. Jinan is characterized by a semihumid continental monsoon climate, and so is the study area. Rainfall averages at 500 and 600 mm and is unevenly distributed during the year. Heavy rain events usually occur from July to August in the summer. The distribution of a rain event is concentrated and mainly happens in 12 hours, which generally accounts for more than 80% of the total amount.

3.2. Setup of InfoWorks ICM. The Thiessen polygon method is used to divide the subcatchments of which the runoff will flow into the nearest manholes. Through this way, the hydrological model for surface runoff is connected with the one-dimensional hydrodynamic model for the pipe network. Meanwhile, the hydrodynamic model for the underground pipe network is connected with the two-dimensional hydrodynamic model for surface inundation by setting the flood type of manholes as “2D.” This means the water exchange between the surface and manholes is calculated using standard weir equations, where the weir width is taken as the circumference of the manholes. When the drainage capacity is insufficient, the surface is flooded by overflow from the manholes, and in turn the water on the ground will return to the pipe network through the manholes if the drainage network capacity is restored. This way, the coupled model simulates the water exchange between these simulation processes.

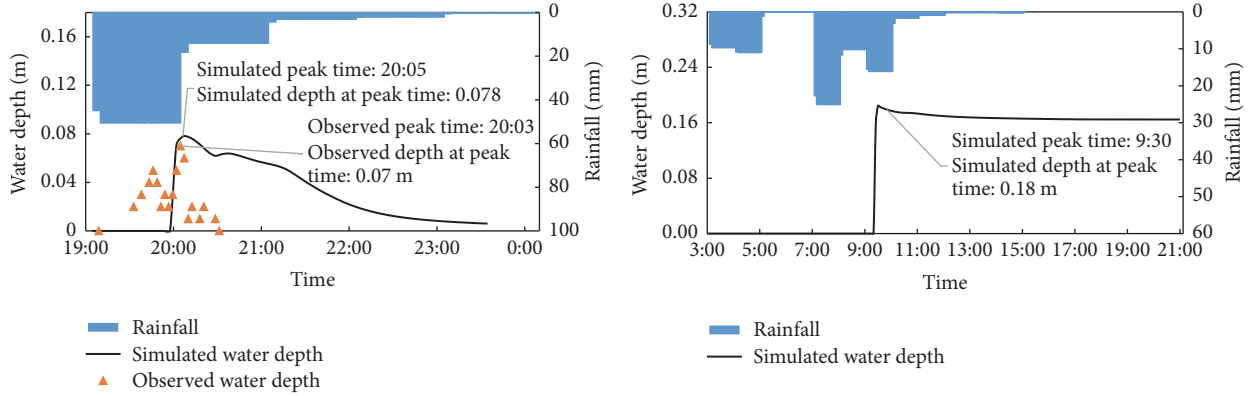
The cell size of the two-dimensional hydrodynamic model is set to be less than 50 m² for road areas and between 50 and 100 m² for other areas. The exact cell size for each mesh is decided by the boundary and topography and is generated with a grid generator embedded in the InfoWorks ICM.

The hydrological model mainly contains parameters for the runoff process and flow convergence process. The parameter is the roughness of the pipe walls for the one-dimensional pipe network model and the roughness of the surfaces for the two-dimensional hydrodynamic model. These parameters are set and adjusted mainly referring to the InfoWorks ICM help document [23] and other related researches [1, 24–26].

4. Result Analysis and Discussion

4.1. Model Calibration and Validation. We have gathered historical rainfalls and surface inundation records only for 2013-07-23 and 2015-08-03 rainfall events, of which the inundation record for 2015-08-03 is comparatively complete. Therefore, the record for 2015-08-03 is used for parameter calibration, and the record for 2013-07-23 is used for parameter validation. As the InfoWorks ICM cannot perform parameters autoverification and is not feasible for secondary development, the parameters are adjusted manually. Through parameter calibration and validation, the rational parameters values are finally obtained. The roughness of the pipe walls is 0.013, and the roughness of the surface is 0.025. Parameters values of the hydrological model are shown in Table 3.

Figures 2(a) and 2(b), respectively, show the hydrograph of surface inundation for parameters calibration and validation. It can be seen from Figure 2(a) that the simulated maximum water depth for 2015-08-03 rainfall event is 0.078 m and occurs at 20:05, well in accord with the observed record.



(a) The simulated water depth hydrograph for 2015-08-03 rainfall event (b) The simulated water depth hydrograph for 2013-07-23 rainfall event

FIGURE 2: Hydrograph of water depth at the road station for historical rainfall events.

TABLE 4: Characteristics and areas for different risk levels of historical and designed rainfall events, respectively.

Designed rainfall & historical rainfall	Total rainfall (mm)	Maximum hourly rainfall intensity (mm·h ⁻¹)	Flood risk area (hm ²)			
			Low	Moderate	Significant	Extreme
$P = 1$	26.7	–	98.9	0.3	0.7	0.2
$P = 5$	38.84	–	97.6	0.5	1.6	0.5
$P = 10$	44.06	–	96.8	0.6	2.2	0.5
$P = 20$	49.29	–	95.9	0.6	3.1	0.6
2013-07-23	71.3	22.9	99.0	0.3	0.7	0.2
2015-08-03	62.1	39.6	97.5	0.5	1.7	0.4

Owing to the instrument problem, only the maximum water depth (0.13 m) and the corresponding occurrence time (9:06) have been recorded for 2013-07-23 rainfall event; those of the simulation are 0.18 m and 9:30 (see Figure 2(b)). It can be noticed that the difference of the maximum water depth and the occurrence time between simulation and observation is small. Through calibration and validation, it is concluded that the model has well represented the historical rainfall events with reasonable accuracy and confidence.

4.2. Road Flood Risk Zoning. Now that the model shows good performance, it can be applied for urban flood simulation and risk zoning. The model is used for running with four designed rainfall scenarios (rainfall duration is 120 min and recurrence intervals are 1, 5, 10, and 20 years) generated with the InfoWorks ICM (as shown in Figure 3). The time-variable water depth and velocity for every calculating grid are obtained and used to calculate flood risk with the formula in Section 2. And the maximum risk value for each grid along the simulating period is obtained. The risk level for each risk value can be calculated referring to Table 2 with which the risk zoning maps are generated and shown in Figures 4 and 5. Areas with low, moderate, significant, and extreme risk are summarized in Table 4.

Table 4 shows that, with the increase of rainfall recurrence intervals, the total area of low risk gradually decreases while the total area of the risk above moderate gradually increases

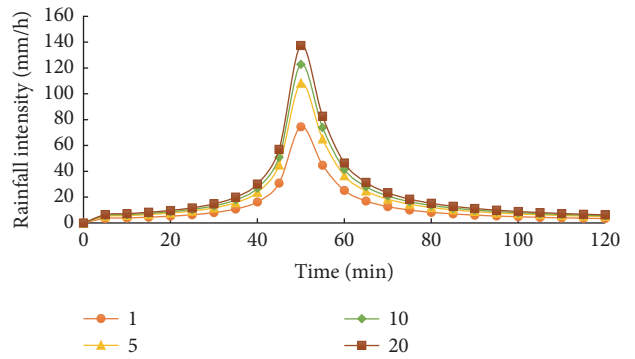


FIGURE 3: Hydrograph of the designed rainfall events.

on the contrary. The total rainfall of 2013-07-23 event is greater than that of 2015-08-03 event, whereas the latter has a larger maximum hourly rainfall than the former. It can be found that the area of low risk for the former is larger than the latter while the former has a larger area of risk above moderate.

4.3. Discussion. (1) It can be seen from Figure 2 that the simulation shows some discrepancy with the observation. The simulation results of the two historical rainfall events show that almost no water accumulates before about 9:20

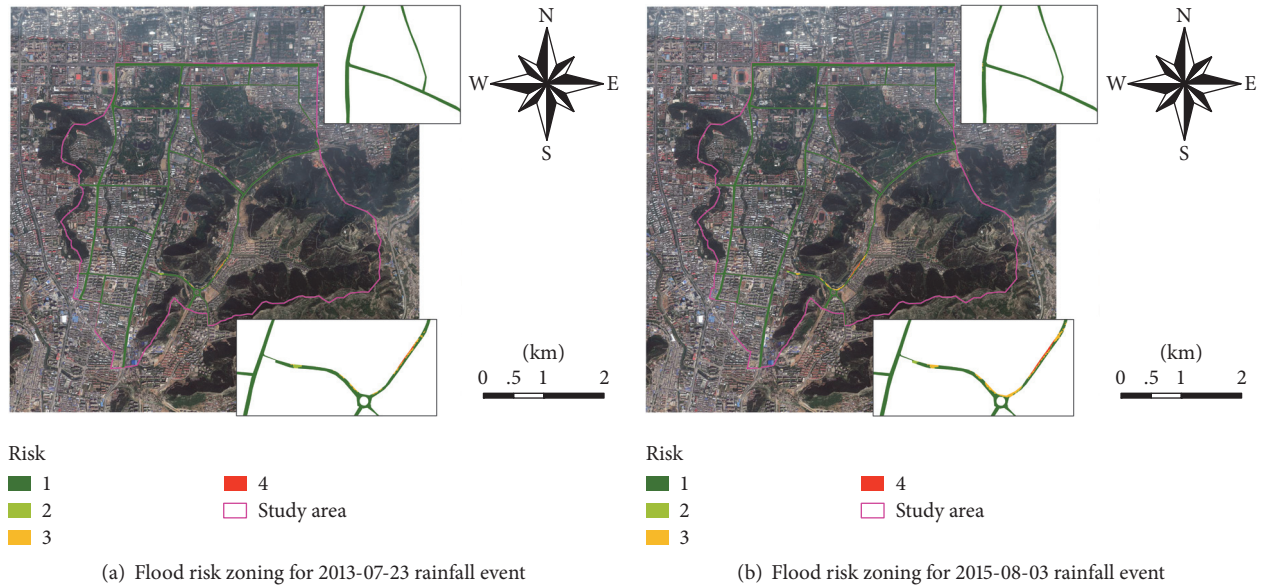


FIGURE 4: Flood risk zoning for historical rainfalls.

and 19:50, respectively, whereas the water depth quickly rises afterwards. The observed water depth for 2015-08-03 rainfall event shows a fluctuation before reaching the peak and then inclines quickly (as depicted in Figure 2(a)). There are two reasons accounting for this phenomenon. First, the runoff of the subcatchments converges into manholes without flowing through the surface in the early time. As a consequence, no water will accumulate on the surface before the pipe networks become surcharged. Second, the interval of the rainfall data used here is one hour, which means the rainfall intensity is constant from 19:00 to 20:00. Therefore, the simulated surface inundation depth increases gradually. However, the actual rainfall intensity for historical rainfall events varies along time, which generates the fluctuated dash-dotted line in Figure 2(a). It is deduced that if fully two-dimensional hydrodynamic simulation is carried out with computationally powerful computers and the rainfall data intervals are smaller (such as 5 min intervals), the simulation results will be better in line with the observations.

(2) It can be noted from Section 4.2 that the flood risk zoning results show that the area of risk above moderate for 2013-07-23 rainfall event (more rainfalls) is smaller than that for 2015-08-03 rainfall event (fewer rainfalls). This is mainly because the latter has a larger maximum hourly rainfall intensity. Moreover, the former has two rainfall peaks and the distribution is more even, while the latter has only one rainfall peak which is centralized. Owing to the limited capacity of the underground drainage system, surcharged water will induce surface inundation if excessive rains flow into the drainage system within a short time. For the 2013-07-23 rainfall event, the light rain after the first rainfall peak makes it easier for drainage capacity restoration, while the 2015-08-03 rainfall event has an earlier rainfall peak which is relatively concentrated. For the 2015-08-03 event, the drainage pipes are overloaded all the time without enough time for their

capacity restoration, and therefore the surface is flooded by the excessive water from manholes.

5. Conclusions

This paper presents a study on urban flood risk in the “Sponge City Construction” pilot area of Jinan City. In this study, the InfoWorks ICM model is used to simulate two historical rainfall events and four designed rainfalls with different recurrence intervals. The surface water depth and flood velocity are recorded. The model is verified with flood monitoring records and its applicability is proved. Possible causes resulting in model errors are analyzed. Then, the recorded water depth and flood velocity are utilized to estimate the flood risk and perform flood risk zoning. Through analysis and discussion on the results, the following conclusions are drawn:

- (1) The coupled model developed in this study well simulates the historical rainstorm events with good confidence and accuracy. Although the simulated water depth and occurrence time of the peak for 2013-07-23 rainfall event show a little discrepancy with the observed record, the result is reasonable. The simulating maximum water depth and the occurrence time for 2015-08-03 rainfall event are almost entirely the same as the observed records, although the hydrographs of water depth are not completely consistent.
- (2) There are two main reasons accounting for the inconsistency of the hydrograph between simulation and observation for 2015-08-03 rainfall event. First, the hydrological modeling cannot simulate the surface inundation, so the surface will not get flooded until the pipes become overloaded. Second, the rainfall data used in this study is hourly interval and the

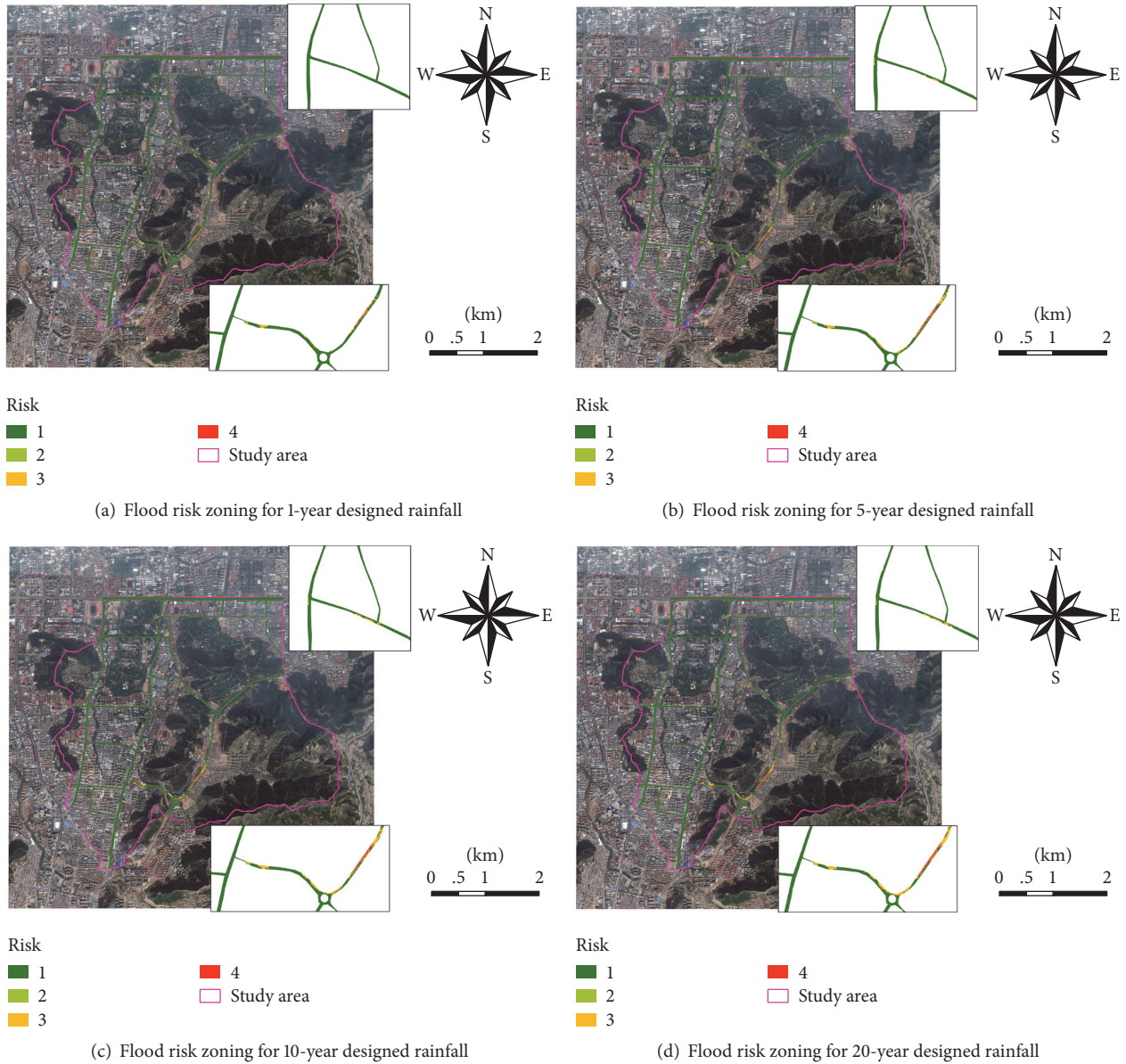


FIGURE 5: Flood risk zoning for designed rainfalls.

rainfall intensity is even in an hour, which results in the gradual increase and decrease of the hydrograph. However, the actual rainfall may change frequently and rapidly, resulting in the fluctuation of the observed surface water depth.

- (3) The flood risk zoning results of the historical and designed rainfall events show that rainfall with larger recurrence intervals will produce larger areas of risk above moderate. The simulation results of the two historical rainfall events indicate that if the maximum hourly rainfall intensity is smaller and the rainfall distribution is more even, the area of risk above moderate is smaller. This is mainly because the pipes

will not easily get surcharged to make manholes overflow under this condition. This conclusion is very constructive to the flood control work. Water storage devices (e.g., pond, valley dam) can be set up at the mountain fronts, and water collecting devices such as Rain Barrels can be placed in the residential area. These measures will help collect rainwater in the early raining time, which alleviates drainage pressure, thereby avoiding urban flooding.

Conflicts of Interest

The authors declare that they have no conflicts of interest.

Acknowledgments

This work was financially supported by the National Natural Science Foundation of China (Grant no. 51579007). The authors would also like to acknowledge the financial support of the project named Water Cycle and Hydrological Process Modeling of Jinan “Sponge City.”

References

- [1] T. Cheng, Z. Xu, and S. Song, “Rainfall-runoff simulations for Xinglong sponge city pilot area of Jinan,” *Journal of Hydroelectric Engineering*, vol. 36, no. 6, pp. 1–11, 2017.
- [2] J. Liu and C. Zhang, “Identification of risks and estimation of flood storage in ponds,” *Mathematical Problems in Engineering*, vol. 2017, pp. 1–9, 2017.
- [3] M. J. Hammond, A. S. Chen, S. Djordjević, D. Butler, and O. Mark, “Urban flood impact assessment: A state-of-the-art review,” *Urban Water Journal*, vol. 12, no. 1, pp. 14–29, 2015.
- [4] E. Salvatore, J. Bronders, and O. Batelaan, “Hydrological modelling of urbanized catchments: A review and future directions,” *Journal of Hydrology*, vol. 529, no. 1, pp. 62–81, 2015.
- [5] J. Yin, D. Yu, Z. Yin, M. Liu, and Q. He, “Evaluating the impact and risk of pluvial flash flood on intra-urban road network: A case study in the city center of Shanghai, China,” *Journal of Hydrology*, vol. 537, pp. 138–145, 2016.
- [6] J. Yin, D. Yu, and R. Wilby, “Modelling the impact of land subsidence on urban pluvial flooding: A case study of downtown Shanghai, China,” *Science of the Total Environment*, vol. 544, pp. 744–753, 2016.
- [7] J. Xie, H. Chen, Z. Liao, X. Gu, D. Zhu, and J. Zhang, “An integrated assessment of urban flooding mitigation strategies for robust decision making,” *Environmental Modelling & Software*, vol. 95, pp. 143–155, 2017.
- [8] W. Hu, W. He, G. Huang, and J. Feng, “Review of urban storm water simulation techniques,” *Advances in Water Science*, vol. 21, no. 1, pp. 137–144, 2010 (Chinese).
- [9] X. Wu, Z. Wang, S. Guo, W. Liao, Z. Zeng, and X. Chen, “Scenario-based projections of future urban inundation within a coupled hydrodynamic model framework: A case study in Dongguan City, China,” *Journal of Hydrology*, vol. 547, pp. 428–442, 2017.
- [10] Q. Huang, J. Wang, M. Li, M. Fei, and J. Dong, “Modeling the influence of urbanization on urban pluvial flooding: a scenario-based case study in Shanghai, China,” *Natural Hazards*, vol. 87, no. 2, pp. 1035–1055, 2017.
- [11] Y. Fan, T. Ao, H. Yu, G. Huang, and X. Li, “A coupled 1D-2D hydrodynamic model for urban flood inundation,” *Advances in Meteorology*, vol. 2017, pp. 1–12, 2017.
- [12] W. Huber, J. Heaney, M. Medina, W. Peltz, and H. Sheikh, *Storm Water Management Model: User’s Manual*, 2nd edition, 1975.
- [13] J. Teng, A. J. Jakeman, J. Vaze, B. F. W. Croke, D. Dutta, and S. Kim, “Flood inundation modelling: A review of methods, recent advances and uncertainty analysis,” *Environmental Modelling & Software*, vol. 90, pp. 201–216, 2017.
- [14] H. Yu, G. Huang, and C. Wu, “Application of the stormwater management model to a piedmont city: A case study of Jinan City, China,” *Water Science and Technology*, vol. 70, no. 5, pp. 858–864, 2014.
- [15] G. Huang, X. Wang, and W. Huang, “Simulation of rainstorm water logging in urban area based on InfoWorks ICM model,” *Water Resources and Power*, vol. 34, no. 2, pp. 66–70, 2017.
- [16] H. Wu and G. Huang, “Risk assessment of urban waterlogging based on PCSWMM model,” *Water Resources Protection*, vol. 32, no. 5, pp. 11–16, 2016.
- [17] Q. Chu, D. Peng, Z. Xu, D. Meng, T. Zhen, and Q. Jiang, “Risk analysis of urban flooding by using MIKE11 and MIKE21,” *Journal of Beijing Normal University (Natural Science)*, vol. 50, no. 5, pp. 446–451, 2014.
- [18] J. Xia, R. A. Falconer, Y. Wang, and X. Xiao, “New criterion for the stability of a human body in floodwaters,” *Journal of Hydraulic Research*, vol. 52, no. 1, pp. 93–104, 2014.
- [19] J. Xia, Q. Chen, R. A. Falconer, S. Deng, and P. Guo, “Stability criterion for people in floods for various slopes,” in *Institution of Civil Engineers-Water Management*, Thomas Telford Ltd., UK, 2015.
- [20] L. Milanese, M. Pilotti, and R. Ranzi, “A conceptual model of people’s vulnerability to floods,” *Water Resources Research*, vol. 51, no. 1, pp. 182–197, 2015.
- [21] L. Milanese, M. Pilotti, and B. Bacchi, “Using web-based observations to identify thresholds of a person’s stability in a flow,” *Water Resources Research*, vol. 52, no. 10, pp. 7793–7805, 2016.
- [22] H. Wallingford, *R&D outputs: flood risks to people: phase 2: the flood risks to people methodology*, 2006.
- [23] H. Wallingford, *Innovyze. InfoWorks ICM Help v3.0*. 2012: UK.
- [24] G. Huang, “Urban Storm Water Model and its Application,” in *China Water & Power Press*, Beijing, 2013.
- [25] C. Song, H. Wang, and J. Shang, “Study on application of InfoWorks CS to Xiangshan area in Beijing,” *Water Resources and Hydropower Engineering*, vol. 45, no. 7, pp. 13–17, 2014.
- [26] G. Zhao, R. Shi, B. Pang, Z. Xu, L. Du, and X. Chang, “Impact of rapid urbanization on rainfall-runoff processes in urban catchment case study for Liangshui river basin,” *Journal of Hydroelectric Engineering*, vol. 35, no. 5, pp. 55–64, 2016.

Research Article

A One-Dimensional Hydrodynamic and Water Quality Model for a Water Transfer Project with Multihydraulic Structures

Yujun Yi,¹ Caihong Tang,² Zhifeng Yang,¹ Shanghong Zhang,³ and Cheng Zhang³

¹State Key Joint Laboratory of Environment Simulation and Pollution Control, Ministry of Education Key Laboratory of Water and Sediment Science, Beijing Normal University, No. 19, Xijiekouwai St., Haidian District, Beijing 100875, China

²Ministry of Education Key Laboratory of Water and Sediment Science, School of Environment, Beijing Normal University, No. 19, Xijiekouwai St., Haidian District, Beijing 100875, China

³Renewable Energy School, North China Electric Power University, No. 2, Beinong Road, Changping District, Beijing 102206, China

Correspondence should be addressed to Yujun Yi; yiyujun@bnu.edu.cn

Received 3 May 2017; Accepted 21 August 2017; Published 1 October 2017

Academic Editor: Jian G. Zhou

Copyright © 2017 Yujun Yi et al. This is an open access article distributed under the Creative Commons Attribution License, which permits unrestricted use, distribution, and reproduction in any medium, provided the original work is properly cited.

The long Middle Route of the South to North Water Transfer Project is composed of complex hydraulic structures (aqueduct, tunnel, control gate, diversion, culvert, and diverted siphon), which generate complex flow patterns. It is vital to simulate the flow patterns through hydraulic structures, but it is a challenging work to protect water quality and maintain continuous water transfer. A one-dimensional hydrodynamic and water quality model was built to understand the flow and pollutant movement in this project. Preissmann four-point partial-node implicit scheme was used to solve the governing equations in this study. Water flow and pollutant movement were appropriately simulated and the results indicated that this water quality model was comparable to MIKE II and had a good performance and accuracy. Simulation accuracy and model uncertainty were analyzed. Based on the validated water quality model, six pollution scenarios ($Q_1 = 10 \text{ m}^3/\text{s}$, $Q_2 = 30 \text{ m}^3/\text{s}$, and $Q_3 = 60 \text{ m}^3/\text{s}$ for volatile phenol (VOP) and contaminant mercury (Hg)) were simulated for the MRP. Emergent pollution accidents were forecasted and changes of water quality were analyzed according to the simulations results, which helped to guarantee continuously transferring water for a large water transfer project.

1. Introduction

Water resource is an important natural source for supporting and maintaining human health and social sustainable development [1]. Population growth, urban expansion, industrialization, consumption pattern, and energy structure changes result in the increased demand for freshwater resources [2]. According to the China Water Resources Bulletin 2014, the national average rainfall was 622.3 mm, while the average rainfall was 316.9 mm in the Haihe basin and 1100.63 mm in the Yangtze River basin. The corresponding surface water resources were $26,263.9 \times 10^8 \text{ m}^3$, $98 \times 10^8 \text{ m}^3$ and $10,020.3 \times 10^8 \text{ m}^3$, respectively. This extremely uneven distribution of water resources pushed China to build the Middle Route of the South to North Water Transfer Project (MRP) to alleviate the shortage of water resources in the north and fully utilize the water resources in the Yangtze River basin.

The MRP consists of open channel and six types of hydraulic structures. Complex structures are the typical characteristics of this project. The transferred water needs to meet the requirement of the Class II water quality standards of the Environmental Quality Standards for Surface Water of China (GB3838-2000). Open channel is the main way to transfer water in south of the Beijing territory for this project. Meanwhile, transferred water in the open channel has a high risk of water pollution resulting from atmosphere deposition, groundwater pollution, discharged polluted water, and sudden pollution accidents [3]. Therefore, protecting water quality is still an emphasis on water transfer and water resources management [4].

To ensure water quality of the transferred water to meet the Class II standards of water quality, it is vital to make clear the movement rules of flow and pollutant. Especially for the MRP, water flow is disturbed by lots of complex

hydraulic structures in the channel. Figuring out the flow patterns and transfer process of pollutants are difficult to be observed at structures. Thus, water quality simulation can be utilized in water quality protection and water resources management [5]. From the original Streeter-Phelps equation to now integrated water quality models, from zero-dimensional model to multidimensional model, water quality models have achieved great progress. The typical representatives include WASP [6], QUAL2E [7], Environmental Fluid Dynamics Code (EFDC) [8], Computational Fluid Dynamics (CFD) [9], and DHI MIKE (Danish Hydraulic Institute) [10]. These models were widely applied to rivers, lakes, estuaries, and water transfer projects with large amount of hydraulic structures (gates, culverts, dams, and bridges) [10–13]. Although water flow was difficult to be determined when it gets through hydraulic structures, hydraulic regulation was crucial for water resources management and water quality control [14]. In simulating complex water flow, DHI MIKE II is a widely used tool of simulating complex flows [10]. It was employed to simulate the water flow and pollutant movement in an open channel of the Middle Route of the South to North Water Transfer Project (MRP) with complex hydraulic structures [13]. The hydrodynamic module (HD) of MIKE II was coupled with MIKE FLOOD, MIKE SHE, and reservoir scheduling module to expose the influence of hydraulic structures on hydrological regime and benefit water resources management and flood forecasting [10, 12, 15].

Although the above-mentioned dominating water quality models have been constantly improving, for the complicated MRP, there is no existing model that could directly be used for this project. Another model WHYSWESS (watershed hydrology, hydraulic, sediment transport, water quality, and ecology simulation system) integrates distributed hydrological model, water quality module, and habitat simulation modules of benthos, fish, and vegetation [16, 17]. Additionally, it is capable of simulating flows through complex hydraulic structures. A one-dimensional water quality module was built on WHYSWESS platform, which simulated the pollutant movement in the complex MRP.

This paper focuses on a one-dimensional water quality model (WHYSWESS-WQ) for the long distance water transfer project (MRP) with complex hydraulic structures. This model included a hydrodynamic module (WHYSWESS-HD) and an advection-dispersion module (WHYSWESS-AD). Flows in open channel and six types of hydraulic structures were simulated based on this model. Simulation results based on the WHYSWESS indicated that it was a good water quality model when compared with that relying on MIKE II. The validated model was then applied to simulate and predicate sudden pollution accidents for the MRP. Six scenarios were presented to provide suggestions for water resources management and forecasting of emergent pollution accidents in large water transfer projects.

2. Study Area

The MRP stretches across the North China Plain and has a length of approximately 1277 km. The whole MRP is a combination of open channel and 1750 hydraulic structures

[13]. It is a magnificent project in China and results in a total submerged land area of 30,800 hm² [19]. This project transfers water from Danjiangkou Reservoir to Tuancheng Lake and is constructed mainly to supply drinking water for cities in North China, including the capital city Beijing. Since December 12, 2014, the MRP has transferred water 5,000 million m³ and more than 40 million people have used it (http://www.nsb.gov.cn/zz/mtgz/201608/t20160829_446841.html). Besides, the MRP has a strict requirement for water quality on the basis of Environmental Quality Standards for Surface Water of China (GB3838-2002). Its long distance, complex hydraulic structures, and strict water quality requirement push researchers to study the processes of hydrodynamics and water quality from planning to construction and finally operation [13, 20].

This study was conducted for the approximate 42 km canal from the starting point Xishi to the ending point Beijuma River nearby Beijing (Figure 1). Averaged bottom width ranges from 7.5 m to 11 m in this reach. The slope and longitudinal gradient are approximately 2.5 and 1/25000, respectively. The largest discharge should be less than 70 m³/s. Six types of hydraulic structures (inverted siphons, culverts, gates, diversions, tunnels, and aqueduct) were considered in this reach. All these hydraulic structures are vital to successfully transferring and diverting water from south to north, but it is tough to accurately simulate the flow field around the structure (Figure 1 and Table 1).

3. Method

3.1. Governing Equations

3.1.1. Hydrodynamic Module. The Saint-Venant equations, classical unsteady open channel flow governing equations, describe the flow of one-dimensional rivers or channels based on the following three hypotheses: (1) distribution of velocity along cross section is uniform and water pressure is regarded as the hydrostatic pressure; (2) as a result of the small river slope, $\sin \alpha \approx \tan \alpha$; (3) water flow is described by the gradually varied flow [21]. Saint-Venant equations are still employed to indicate water flow in this WHYSWESS-HD and are represented as follows [13]:

Continuity equation is

$$B \frac{\partial h}{\partial t} + \frac{\partial Q}{\partial x} = q. \quad (1)$$

Momentum equation is

$$\begin{aligned} \frac{\partial Q}{\partial t} + 2 \frac{Q}{A} \frac{\partial Q}{\partial x} + \left(gA - B \frac{Q^2}{A^2} \right) \frac{\partial h}{\partial x} - \left(\frac{Q}{A} \right)^2 \frac{\partial A}{\partial x} \Big|_h \\ + \frac{gQ|Q|}{C^2 AR} = 0, \end{aligned} \quad (2)$$

where x and t denote the spatial and temporal coordinates, respectively; Q and h denote the cross-sectional discharge and water level, respectively; A

TABLE 1: List of hydraulic structures of study canal.

Structure (Abbreviation)	Symbol	Name	Distance from initial section (km)
Aqueduct (Aq)	Aq1	Shuibegou aqueduct	32.133
Culvert (C)	C1	Leizixi culvert	20.374
	C2	Leizidong culvert	20.944
Diversion (D)	D1	Jingkeshan diversion	3.697
	D2	Xiacheting diversion	27.994
Check gate (G)	G1	Beiyishui check gate	4.87
	G2	Fenzhuang River check gate	19.575
Inverted siphon (INS)	INS1	Beiyishui inverted siphon	4.39
	INS2	Qilizhuanggou inverted siphon	10.437
	INS3	Matougou inverted siphon	17.077
	INS4	Fenzhuang River inverted siphon	19.352
	INS5	Nanjuma River inverted siphon	38.348
	INS6	Beijuma River inverted siphon	41.25
Tunnel (T)	T1	Xishi tunnel	0.045
	T2	Xiacheting tunnel	26.375

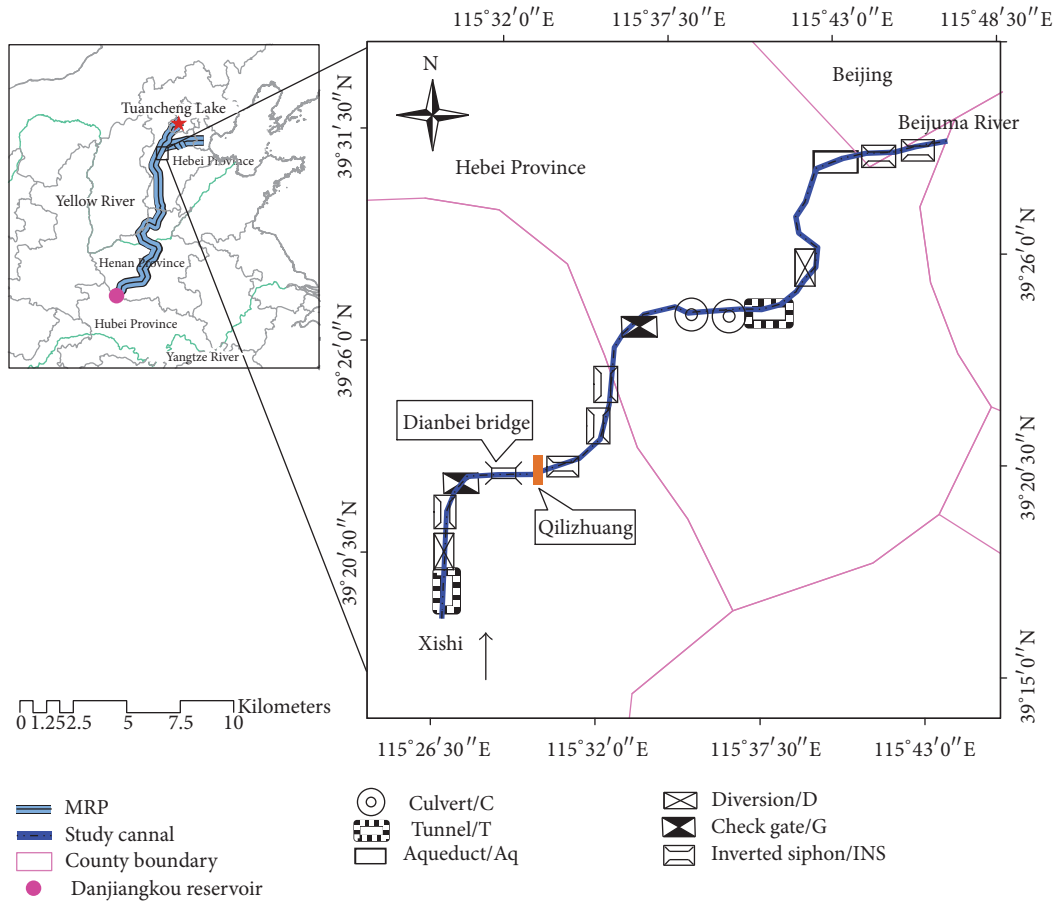


FIGURE 1: Map of study canal.

and R denote the cross-sectional area and hydraulic radius, respectively; B denotes the width of the river; q denotes the lateral inflow; C denotes the Chezy coefficient; and g denotes the gravitational acceleration.

3.1.2. *Water Quality Module.* One-dimensional river advection-dispersion equation was used to analyze the movement

patterns of pollutant in this WHYWESS-AD. The specific equation of mass conservation was used to describe the one-order degradation process of pollutant in open channel and represented as follows [22]:

$$\frac{\partial C_1 A}{\partial t} + \frac{\partial C Q}{\partial x} = \frac{\partial}{\partial x} \left[E \frac{\partial C_1 A}{\partial x} \right] - AK_d C_1 + C_2 q, \quad (3)$$

TABLE 2: Solution methods of hydraulic structures in two water quality models.

Items	WHYSWESS-WQ	MIKE 11
Aqueduct	Open channel flow with branches	Open channel flow
Tunnel	Open channel flow with branches	Open channel flow
Control gate	Discrete gate flow formula is coupled with discrete Saint-Venant equations. Initial water level, discharge, and process of control gate opening are provided to automatically select corresponding flow calculation formula	Discharge point, single setting; three controlling modes (H/Q , dH/dQ , sum Q); appropriate discrete solution is coupled
Diversion	Lateral outflow, source-sink term in continuity equation	Lateral outflow, inner boundary
Culvert	According to the water level, flow contains open flow; half-pressure flow and pressure flow	Culvert module includes zero flow, upstream controlled flow, downstream controlled flow for different computational purposes. Above flow modes consists of many flow situations and equation. Discrete equations are solved with Saint-Venant equations
Inverted siphon	Discrete pressure flow equation is coupled with discrete Saint-Venant equations to solve together	As a culvert with fully submerged flow

where C_1 is the concentration of pollutant; E is the river longitudinal dispersion coefficient; K_d is the first-order decay coefficient; and C_2 is the concentration of pollutant from point-source pollution.

3.2. Solution of Equations. The Saint-Venant equations are first-order quasilinear hyperbolic partial differential equations and are difficult to directly get the analytical solutions. Therefore, numerical methods, such as finite difference method, finite element method, finite volume method, and characteristic line method, are common ways to solve them [23].

The Preissmann four-point partial-node implicit scheme is a representative implicit difference scheme and has fast convergence, high efficiency, and good stability [24]. It was used in WHYSWESS-HD. Water level h and discharge Q were treated as dependent variables. The form of Preissmann four-point partial-node implicit scheme was shown in Figure 2. The discrete Saint-Venant equations are presented as follows:

$$\begin{aligned} a_{1i}h_i^{j+1} - c_{1i}Q_i^{j+1} + a_{1i}h_{i+1}^{j+1} + c_{1i}Q_{i+1}^{j+1} &= e_{1i} \\ a_{2i}h_i^{j+1} + c_{2i}Q_i^{j+1} - a_{2i}h_{i+1}^{j+1} + d_{2i}Q_{i+1}^{j+1} &= e_{2i}, \end{aligned} \quad (4)$$

where $a_{1i} = 1$, $c_{1i} = 2\theta(\Delta t/\Delta s_i)(1/B_{i+1/2}^{j+\theta})$, $e_{1i} = h_i^j + h_{i+1}^j - ((1-\theta)/\theta)c_{1i}(Q_{i+1}^j - Q_i^j) + 2\Delta t q_{i+1/2}^{j+\theta}/B_{i+1/2}^{j+\theta}$, $a_{2i} = 2\theta(\Delta t/\Delta s_i)[(Q_{i+1/2}^{j+\theta}/A_{i+1/2}^{j+\theta})^2 B_{i+1/2}^{j+\theta} - gA_{i+1/2}^{j+\theta}]$, $c_{2i} = 1 - 4\theta(\Delta t/\Delta s_i)(Q_{i+1/2}^{j+\theta}/A_{i+1/2}^{j+\theta})$, $d_{2i} = 1 + 4\theta(\Delta t/\Delta s_i)(Q/A)_{i+1/2}^{j+\theta}$, $e_{2i} = ((1-\theta)/\theta)a_{2i}(h_{i+1}^j - h_i^j) + [1-4(1-\theta)(\Delta t/\Delta s_i)(Q/A)_{i+1/2}^{j+\theta}]Q_{i+1}^j + [1 + 4(1-\theta)(\Delta t/\Delta s_i)(Q/A)_{i+1/2}^{j+\theta}]Q_i^j + 2\Delta t(Q_{i+1/2}^{j+\theta}/A_{i+1/2}^{j+\theta})^2 \times (A_{i+1}(h_{i+1/2}^{j+\theta}) - A_i(h_{i+1/2}^{j+\theta}))/\Delta s_i - 2\Delta t(gm^2 Q_{i+1/2}^{j+\theta}/Q_{i+1/2}^{j+\theta})|B_{i+1/2}^{j+\theta}/(A_{i+1/2}^{j+\theta})^2 (A_{i+1/2}^{j+\theta}/B_{i+1/2}^{j+\theta})^{1/3} + 2\Delta t Q_{i+1/2}^{j+\theta} q_{i+1/2}^{j+\theta}/A_{i+1/2}^{j+\theta}$, $\varphi_{i+1/2}^{j+1} = \theta((\varphi_i^{j+1} + \varphi_{i+1}^{j+1})/2) + (1-\theta)((\varphi_i^j + \varphi_{i+1}^j)/2)$. φ refers to the coefficient of A , B , Q , h , and so on. $A_{i+1}(h_{i+1/2}^{j+\theta})$ and $A_i(h_{i+1/2}^{j+\theta})$ represent the sectional areas A_{i+1} and A_i at the water level of $h_{i+1/2}^{j+\theta}$, respectively; i is the cross section number.

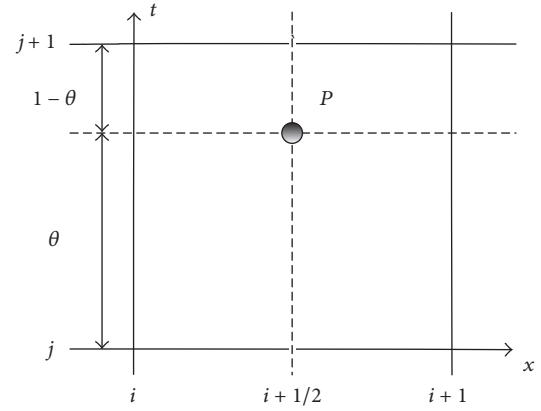


FIGURE 2: Sketch of the Preissmann four-point implicit scheme of WHYSWESS-HD.

3.3. Hydraulic Structures. The main canal of the MRP is made up of open channel and complex hydraulic structures. Movement of flows and pollutants around structures were accurately simulated using WHYSWESS-WQ model. The specific description of hydraulic structures was listed in Table 2. Flows in aqueduct and tunnel were rectangular free surface flow in the MRP, so aqueduct and tunnel were set as open channels in WHYSWESS-WQ. Flows in gate were calculated according to the gate outflow formula. Water flows in diversion were regarded as the lateral outflow through adding source-sink term in continuity equation. Flows in culvert were calculated based on the water flow patterns. Flows in inverted siphon were regarded as the pressure flow. Discrete pressure flow equation was coupled with discrete Saint-Venant equations to be solved (Table 2).

4. Results and Discussion

4.1. Calibration and Validation

4.1.1. Hydrodynamic Model. The MRP is a long artificial canal, which has a uniform roughness coefficient and regular

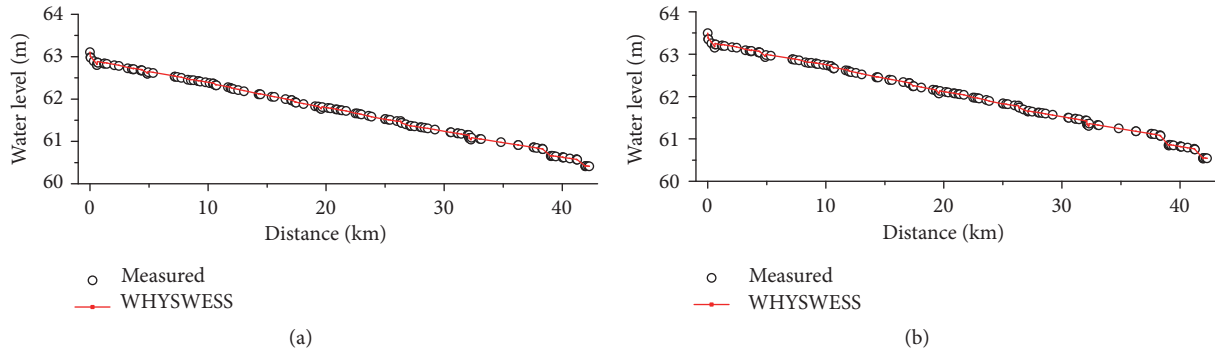


FIGURE 3: Calibration and validation results of WHYSWESS-HD ((a) is the calibration results at $Q = 60 \text{ m}^3/\text{s}$ and (b) is the validation results at $Q = 70 \text{ m}^3/\text{s}$).

TABLE 3: Comparison of parameters between WHYSWESS-WQ and MIKE 11.

Parameters	WHYSWESS-WQ	MIKE 11
Hydrodynamic module		
Validation		
Absolute error (m)	-0.009~0.022	-0.147~0.356
Relative error (%)	-0.015~0.034	-0.24~0.56
Water quality module		
Dispersion coefficient (m^2/s)	3.47	4
Decay coefficient (/h)		
TP	0.26	0.24
COD_{Mn}	0.097	0.084
$\text{NH}_3\text{-N}$	0.21	0.24
F	0.083	0.072
Water quality prediction		
Dispersion coefficient (m^2/s)	3.47	4
Decay coefficient (/h)		
Toxic organic		
Hg		0
Indissoluble heavy metal		
VOP	0.00417 ^a	

Note. ^aBased on Zhang [18].

shape. Therefore, steady flow was chose to test the models. Water levels at discharge of $Q = 60 \text{ m}^3/\text{s}$ were employed to calibrate and that of $Q = 70 \text{ m}^3/\text{s}$ at Qilizhuang section were used to validate the WHYSWESS-HD. Discharges and water levels were, respectively, set as the upstream and downstream boundaries in this hydrodynamic module. Calibrated and validated results were shown in Figure 3.

According to the calibration and validation results of WHYSWESS-HD, the error range was relatively low (Figure 3). Maximum absolute error of water levels was 0.022 m and the maximum relative error was 0.034% (Table 3). A knee point appeared at this section (Xiacheting tunnel) away from the initial section of 28 km (Table 1). The big disturbance might be resulted from the flow around tunnel.

A one-dimensional water quality model based on MIKE 11 was built for the study canal in Tang et al. [13]. Method,

calibration, and validation of this model were specifically described there.

4.1.2. *Water Quality Model.* Based on the WHYSWESS-HD, WHYSWESS-AD for Total Phosphorus (TP), Potassium Permanganate Index (COD_{Mn}), Fluoride (F), and Ammonia Nitrogen ($\text{NH}_3\text{-N}$) were established. Concentrations of these four pollutants from October 13, 2008, to August 9, 2009, were simulated and simulation results were used to validate the WHYSWESS-WQ. Validation results indicated that the water quality model adequately reflected change trend of concentrations of these four pollutants.

Only the first-order decay processes of TP, COD_{Mn} , $\text{NH}_3\text{-N}$, and F have been considered in this paper. Water quality simulation results based on MIKE 11 were closer to the measured data than simulation results based on WHYSWESS, which had a larger dispersion coefficient (Figure 4 and Table 3). When comparing the calibration and validation results referenced from Tang et al. [13] with that of WHYSWESS-WQ, WHYSWESS-WQ had a smaller longitudinal dispersion coefficient and decay coefficient of $\text{NH}_3\text{-N}$ and had a larger decay coefficient of TP, COD_{Mn} , and F (Table 3).

4.2. *Parameter Settings.* Longitudinal dispersion coefficient was a crucial parameter in water pollution accidents, and it was easily affected by hydrodynamic and geometrical parameters [25]. According to model calibration and validation results, WHYSWESS-WQ had a smaller longitudinal dispersion coefficient than MIKE 11, which showed that a larger water flow velocity gradient indicated a larger pollutant transport capacity. Same constant boundaries and initial conditions were adopted in two water quality models. The dispersion coefficient of WHYSWESS-WQ was less than that of MIKE 11. This result showed that a discrete degree of water body simulated by WHYSWESS-WQ was more intense than that by MIKE 11. The first-order degradation coefficients of TP and COD_{Mn} in WHYSWESS were slightly larger than those in MIKE 11 and were smaller than those of $\text{NH}_3\text{-N}$ and F. Different equation solutions of the Saint-Venant equations and flow patterns through structures lead to the different degradation coefficients. Therefore, the two water quality

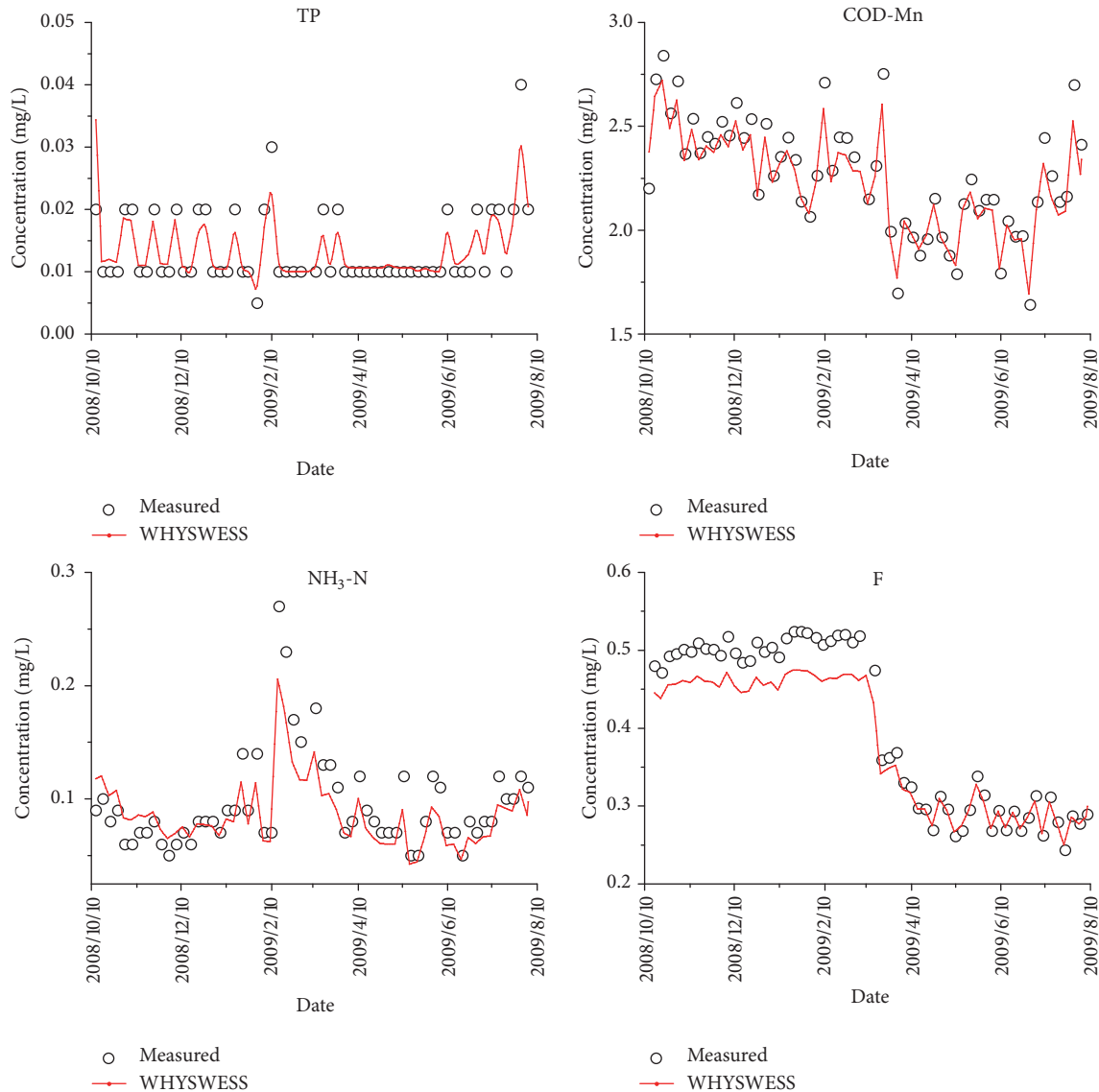


FIGURE 4: Validation results of water quality model based on the WHYSWESS (the point is the measured data; the red line is the simulated results).

models presented here are reasonable and WHYSWESS is an effective tool of simulating the long canal with complex hydraulic structures. The first-order decay was considered in WHYSWESS for COD_{Mn} and F. Respirations of algae and benthos, oxidation of NH_3-N , and transformation between resolvable P and released P from sediment were considered in WHYSWESS. Yet sediment in channel is neglected in this paper. Only the first-order decay for all materials was considered in MIKE 11.

4.3. Simulation Accuracy. From Table 3 and Figure 3, WHYSWESS-HD had higher calculation accuracy than MIKE 11. Maximum absolute error and maximum relative error of water levels were, respectively, 0.022 m and 0.034% in WHYSWESS-HD. Validation results in MIKE 11 also showed the same trend and had an averaged water depth of 4.3 m. From validation results of hydrodynamic module in MIKE 11,

the maximum absolute error was 0.356 m, and the maximum relative error was 0.56%. These error ranges represented an acceptable simulation error (Table 3).

The MRP had characteristics of regular trapezoidal section, uniform longitudinal slope, and gradually decreased discharges from south to north. The study canal was divided into 143 sections in this paper. Calculation results indicated that WHYSWESS had higher simulation accuracy than MIKE 11. Two main aspects lead the different accuracy between models: setting of hydraulic structures and the solution formats of governing equations.

Hydraulic structures were considered differently in governing equations between WHYSWESS-WQ and MIKE 11. Except aqueducts and tunnels, other structures such as control gate, diversion, culvert, and inverted siphon were treated differently in WHYSWESS-WQ and MIKE 11 (Table 2). Although hydrodynamic module of MIKE 11 could directly

set hydraulic structures (weir, bridge, culvert, and pump), there was a lack of modules for diversion, inverted siphon, and aqueduct. Therefore, diversions, inverted siphons, and aqueducts were appropriately adjusted in MIKE 11 to achieve better simulation results. Aqueducts and tunnels were solved as open channel just the same as the WHYSWESS-WQ. Flow through inverted siphons was pressure flow and was generalized into culverts in MIKE 11 (Table 2).

For the solution formats of Saint-Venant equations, WHYSWESS-HD is based on the Preissmann four-point partial-node implicit scheme, while MIKE 11 is based on the six-point Abbott-Ionescu implicit scheme. Other than the Preissmann four-point partial-node implicit scheme, main idea of the latter was using staggered computational grid of alternating Q (discharge) and h (water level). In momentum equation, Q was the center point, and forward difference scheme was used to deal with time t . Water level h was conducted as the central point. Central difference for space was used to achieve the discrete x in continuity equation (Danish Hydraulic Institute). MIKE 11 has higher simulation accuracy than HEC-RAS for a 43 km long river [26]. The same rule was derived in by Bennett et al. [27]. Four-point operators Preissmann implicit finite difference scheme was used in HEC-RAS [28, 29]. In the case of the same river roughness, boundaries, and initial conditions, different simulation results originated from the solution of equations. According to the comparison of HEC-RAS and MIKE 11, six-point Abbott-Ionescu implicit scheme was more accurate than Preissmann implicit finite difference scheme in calculating the river water flow. From this perspective, more accurate results of WHYSWESS-WQ than MIKE 11 benefited from the calculation of hydraulic structures, which reversely explained and supported that solution formats of governing equations were the main reason for different calculation results in the two models.

4.4. Model Uncertainty. Model uncertainty in river water quality modeling mainly results from parameter estimations, input data and model structure [30]. River cross section and river bed roughness coefficient used in this study were the theory data and did not consider the virtual conditions for the artificial canal. This difference can lead to model uncertainty, and also, the initial water level and boundary conditions result in model uncertainty [31]. The measured water levels, discharges, and concentrations of pollutant can result in model uncertainty, because of monitoring methodology and subjective judgment of staff [32]. Additionally, model structure is another main reason for inconsistent coefficients and calculation accuracy. As commercial software, MIKE 11 had a more mature model framework and a wider application in hydrodynamic simulation and water quality prediction than WHYSWESS which later appeared. In summary, the calculation precision and simulation efficiency of model established by the WHYSWESS-WQ were acceptable. As an open-source water quality model, WHYSWESS-WQ would provide more references and suggestions for further studies and be more meaning.

4.5. Water Quality Prediction. Sudden pollution accidents were simulated to provide early warning and emergency

response for water quality conservation and eutrophication control [6, 33]. One single or one type of pollutant is not enough to forecast pollution accidents and give advice for water resources management and regulation [18]. Water quality of Danjiangkou Reservoir (the water source region of the MRP) has to meet the requirement of the Environmental Quality Standards for Surface Water of China. Due to clean water sources and artificial channels of the MRP, alga and sediments in canals were neglected. The MRP stretches across the Hebei Province from south to north, and 697 bridges have been built to recover transportation along the canal [13]. These bridges had potential pollution risk for transferred water [3].

Volatile phenol (VOP), as a high toxic organic compound, was widely used in the cooking wastewater at present, and its solution had a serious effect on human health [34]. Except organics, heavy metals are also the main pollutants that are capable of being accumulated in human bodies and other aquatic organisms and even resulting in deadly hazard [35]. Heavy metal pollution has been attracting more attentions [36]. Road transport of raw materials made an increased emergent pollution risks for the MRP under influences of weather, road, and environmental factors [3]. To forecast water quality changes and provide suggestions for water resources regulation, typical nonconservative contaminant VOP and conservation contaminant mercury (Hg) were chosen as the emergent pollutants for the MRP in this study. Point-source pollution occurred in the MRP which was simulated using the WHYSWESS-WQ. The Dianbei bridge is located at the place away from the starting section 9.17 km in the study canal (Figure 1). As a national second-class bridge, it is busy to be an important traffic artery in the Hebei Province, China. Therefore, Dianbei bridge is selected as the accidental place of emergent pollution.

In order to compare the accuracy of the WHYSWESS-WQ, sudden pollution accidents were also simulated by MIKE 11. Point-source pollution was directly added to the initial conditions in WHYSWESS, while it was treated as the inner boundary in MIKE 11. Based on WHYSWESS-WQ and MIKE 11, six scenarios (two pollutants (volatile phenol (VOP) and contaminant mercury (Hg)) under three upstream discharges ($Q_1 = 10 \text{ m}^3/\text{s}$, $Q_2 = 30 \text{ m}^3/\text{s}$, and $Q_3 = 60 \text{ m}^3/\text{s}$) were simulated in this research (Figures 5 and 6). Leakage concentration C_1 was supposed to be 100 mg/L and the emission speed (q') was $1 \text{ m}^3/\text{s}$. Longitudinal dispersion coefficients were achieved from the calibration results of water quality modules and decay coefficients were derived from previous research (Table 3).

Simulated concentrations of Hg at three discharges had the same change trend in WHYSWESS-WQ and MIKE 11. Larger discharges lead to quicker diffusion and dispersion of Hg and VOP. When pollutants arrived at the end section, the arrival time decreased gradually (Figures 5 and 6). Although Hg and VOP had the same leakage concentration, Hg could be only diffused and VOP could be diffused and dispersed. The maximum concentration of Hg was the same as VOPs, which was also reasonable. The pollution area was mainly controlled by the pollutant load. When incoming discharge was close to Q_1 , enough time was needed to remove Hg

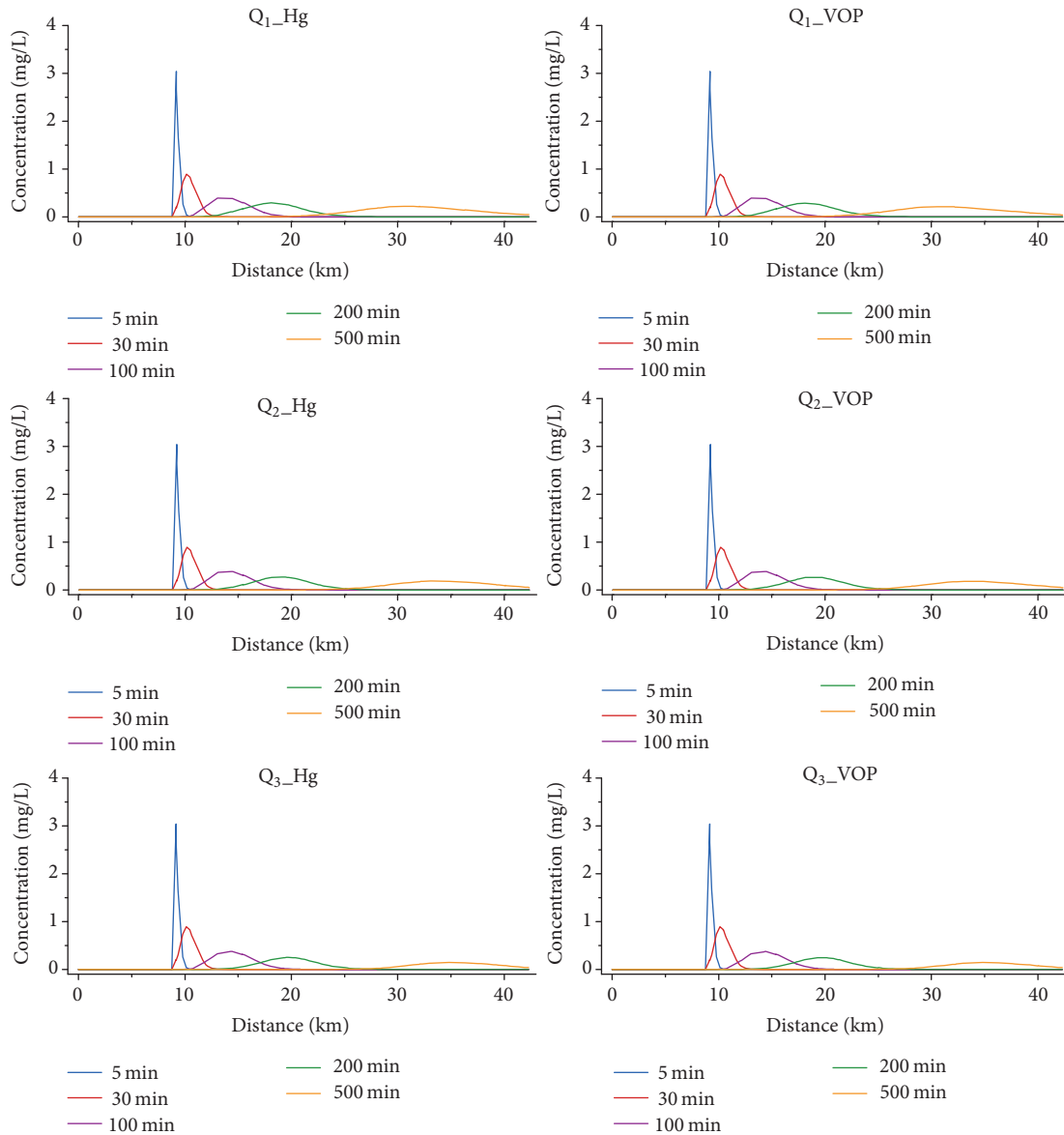


FIGURE 5: Water quality simulation based on WHYSWESS at Dianbei bridge ($Q_1 = 10 \text{ m}^3/\text{s}$, $Q_2 = 30 \text{ m}^3/\text{s}$, and $Q_3 = 60 \text{ m}^3/\text{s}$).

and VOP in the reach. Pollutants were dissolved and carried in water, which resulted in the coincidence of simulation results of hydrodynamic and water quality module. Therefore, pollutant concentrations based on WHYSWESS had a more change than that based on MIKE 11 due to the larger hydrodynamic simulation errors of MIKE 11. The water standard Class II (GB3838-2000) indicated that concentrations of Hg and VOP should not exceed 0.005 mg/L and 0.002 mg/L , respectively, for transferred water. Simulation results showed when the peak concentration arrived at the end of the study reach, all concentrations of organic pollutants and heavy metals exceeded the standard values even at the lowest discharge of Q_1 . Under this serious pollution, it is indispensable to strengthen the monitoring and management of water quality for the MRP. Large transfer projects (for an example of the MRP) cost amount of manpower and public finance; relative

policy and laws should be established and perfected to protect water resources safety and make full use of the transferred water.

5. Conclusions

A one-dimensional hydrodynamic and water quality model (WHYSWESS-WQ) was built for simulating the flow field and pollutants movement through the MRP, a long distance water transfer project with multiple types of hydraulic structures. The Preissmann four-point partial-node implicit scheme was chosen to solve the governing equations in this study. Validation results of water quality represented that this model could well describe transport regularities of flow and pollutants with a maximum relative error of 0.034% , and it was capable of simulating and providing reference

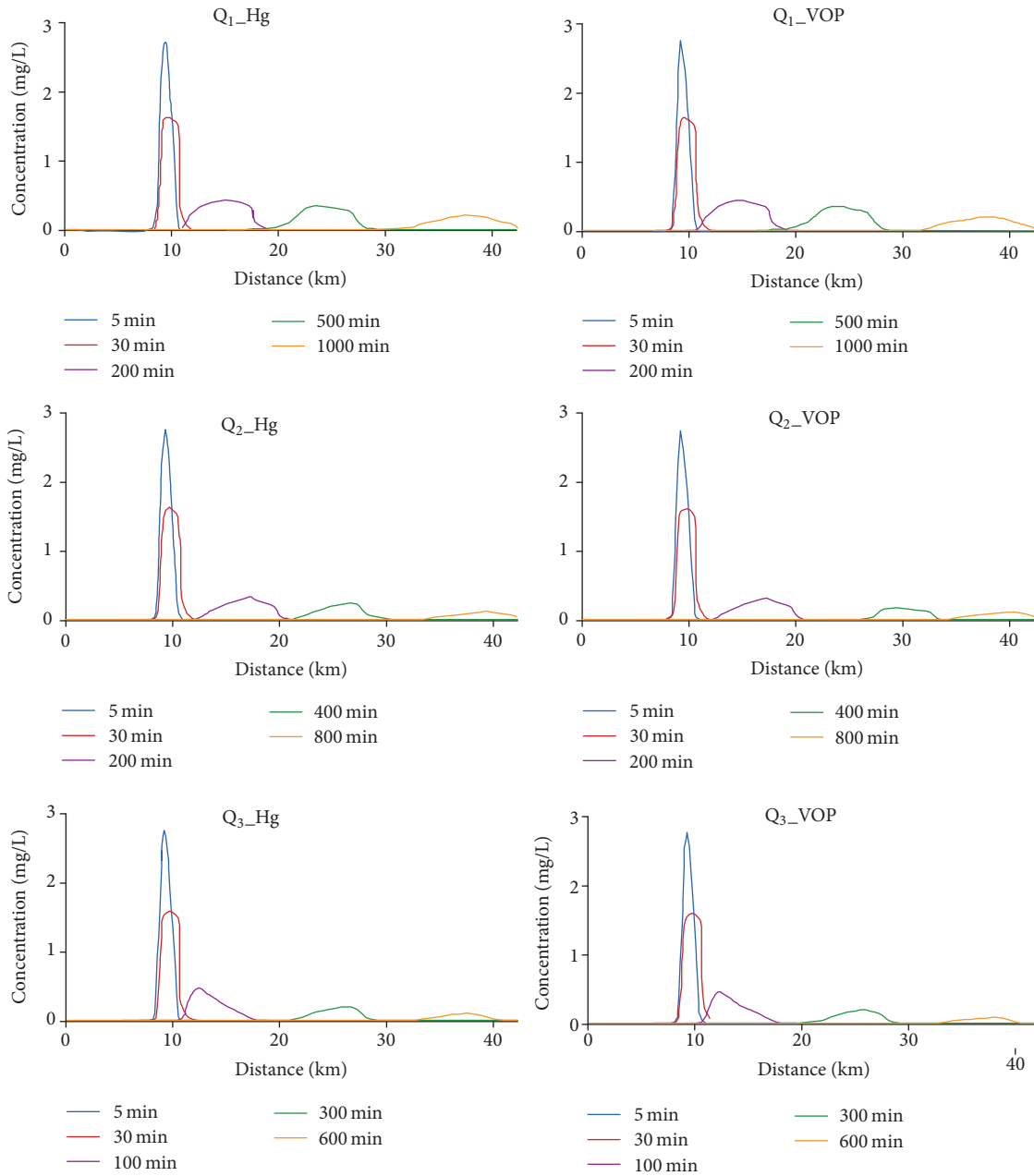


FIGURE 6: Water quality simulation based on MIKE 11 at Dianbei bridge ($Q_1 = 10 \text{ m}^3/\text{s}$, $Q_2 = 30 \text{ m}^3/\text{s}$, and $Q_3 = 60 \text{ m}^3/\text{s}$).

for pollution simulations in large water transfer projects with complex hydraulic structures. Simulation results were compared with those simulated by MIKE 11. Comparison showed WHYSWESS-WQ had higher simulation accuracy than MIKE 11 when water flow was calculated in a long water transfer project with complex hydraulic structures. Six water quality prediction scenarios (discharge of $Q_1 = 10 \text{ m}^3/\text{s}$, $Q_2 = 30 \text{ m}^3/\text{s}$, and $Q_3 = 60 \text{ m}^3/\text{s}$) results showed that concentrations of VOP and Hg at the last section of the study's reach exceeded Class II standard when the discharge was more than $Q_1 = 10 \text{ m}^3/\text{s}$. This suggestion would be helpful for the water quality protection and water resources management,

and relative policy and laws should be established to protect the water quality.

Notations

- A: Cross-sectional area
- B: Width of river
- C: Chezy coefficient
- C_1 : Concentration of pollutants
- C_2 : Concentration of point source
- E: Longitudinal dispersion coefficient
- g: Gravitational acceleration
- h: Cross-sectional water level

i : Number of cross sections
 j : Space step
 K_d : First-order decay coefficient
 n : Time step
 Q : Cross-sectional discharge
 q : Lateral inflow
 q' : Pollution emission speed
 R : Hydraulic radius
 t : Temporal coordinate
 x : Spatial coordinate
 φ : Coefficient
 θ : Time weighting factor.

Conflicts of Interest

The authors declare that they have no conflicts of interest.

Acknowledgments

This study was supported by the National Natural Science Foundation of China (no. 51439001 and no. 51279220) and National Key R&D Program (Grant no. 2016YFC0502209).

References

- [1] Y. Sun, Z. Chen, G. Wu et al., "Characteristics of water quality of municipal wastewater treatment plants in China: Implications for resources utilization and management," *Journal of Cleaner Production*, vol. 131, pp. 1–9, 2016.
- [2] R. Bagatin, J. J. Klemeš, A. P. Reverberi, and D. Huisinigh, "Conservation and improvements in water resource management: A global challenge," *Journal of Cleaner Production*, vol. 77, pp. 1–9, 2014.
- [3] C. Tang, Y. Yi, Z. Yang, and J. Sun, "Risk analysis of emergent water pollution accidents based on a Bayesian Network," *Journal of Environmental Management*, vol. 165, pp. 199–205, 2016.
- [4] N. C. Kunz, C. J. Moran, and T. Kastle, "Implementing an integrated approach to water management by matching problem complexity with management responses: A case study of a mine site water committee," *Journal of Cleaner Production*, vol. 52, pp. 362–373, 2013.
- [5] K. W. Chau, "Integrated water quality management in Tolo Harbour, Hong Kong: a case study," *Journal of Cleaner Production*, vol. 15, no. 16, pp. 1568–1572, 2007.
- [6] S. Liang, H. Jia, C. Yang, C. Melching, and Y. Yuan, "A pollutant load hierarchical allocation method integrated in an environmental capacity management system for Zhushan Bay, Taihu Lake," *Science of the Total Environment*, vol. 533, pp. 223–237, 2015.
- [7] V. Palmieri and R. J. de Carvalho, "Qual2e model for the Corumbataí River," *Ecological Modelling*, vol. 198, no. 1-2, pp. 269–275, 2006.
- [8] G. Wu and Z. Xu, "Prediction of algal blooming using EFDC model: Case study in the Daoxiang Lake," *Ecological Modelling*, vol. 222, no. 6, pp. 1245–1252, 2011.
- [9] V. T. Nguyen, C. S. Moreno, and S. Lyu, "Numerical simulation of sediment transport and bedmorphology around Gangjeong Weir on Nakdong River," *KSCE Journal of Civil Engineering*, vol. 19, no. 7, pp. 2291–2297, 2014.
- [10] J. R. Thompson, H. R. Sørensen, H. Gavin, and A. Refsgaard, "Application of the coupled MIKE SHE/MIKE 11 modelling system to a lowland wet grassland in southeast England," *Journal of Hydrology*, vol. 293, no. 1–4, pp. 151–179, 2004.
- [11] F. Cheng, U. Zika, K. Banachowski, D. Gillenwater, and T. Granata, "Modelling the effects of dam removal on migratory walleye (*Sander vitreus*) early life-history stages," *River Research and Applications*, vol. 22, no. 8, pp. 837–851, 2006.
- [12] S. Förster, C. Chatterjee, and A. Bronstert, "Hydrodynamic simulation of the operational management of a proposed flood emergency storage area at the Middle Elbe River," *River Research and Applications*, vol. 24, no. 7, pp. 900–913, 2008.
- [13] C. Tang, Y. Yi, Z. Yang, and X. Cheng, "Water pollution risk simulation and prediction in the main canal of the South-to-North Water Transfer Project," *Journal of Hydrology*, vol. 519, pp. 2111–2120, 2014.
- [14] O. Fovet, G. Belaud, X. Litrico et al., "A model for fixed algae management in open channels using flushing flows," *River Research and Applications*, vol. 28, no. 7, pp. 960–972, 2012.
- [15] L. Wen, R. Macdonald, T. Morrison, T. Hameed, N. Saintilan, and J. Ling, "From hydrodynamic to hydrological modelling: Investigating long-term hydrological regimes of key wetlands in the Macquarie Marshes, a semi-arid lowland floodplain in Australia," *Journal of Hydrology*, vol. 500, pp. 45–61, 2013.
- [16] Y. Yi, C. Tang, Z. Yang, and X. Chen, "Influence of Manwan Reservoir on fish habitat in the middle reach of the Lancang River," *Ecological Engineering*, vol. 69, pp. 106–117, 2014.
- [17] S. Zhang, Z. Xia, and T. Wang, "A real-time interactive simulation framework for watershed decision making using numerical models and virtual environment," *Journal of Hydrology*, vol. 493, pp. 95–104, 2013.
- [18] H. J. Zhang, *Study on prediction model of Volatile Phenol pollution accidents in natural river of Dalian city*, Dalian University of Technology, China, 2009.
- [19] H. J. Zhai, L. Chen, and J. Zhang, "Study on environmental protection of the resettlement and reconstruction around danjiangkou reservoir in the first-stage middle route of the south-to-north water diversion project," *South-to-North Water Diversion and Water Science & Technology*, vol. 10, pp. 477–485, 2011.
- [20] S. Li, J. Li, and Q. Zhang, "Water quality assessment in the rivers along the water conveyance system of the Middle Route of the South to North Water Transfer Project (China) using multivariate statistical techniques and receptor modeling," *Journal of Hazardous Materials*, vol. 195, pp. 306–317, 2011.
- [21] F. Saleh, A. Ducharne, N. Flipo, L. Oudin, and E. Ledoux, "Impact of river bed morphology on discharge and water levels simulated by a 1D Saint-Venant hydraulic model at regional scale," *Journal of Hydrology*, vol. 476, pp. 169–177, 2013.
- [22] K. El Kadi Abderrezzak, R. Ata, and F. Zaoui, "One-dimensional numerical modelling of solute transport in streams: The role of longitudinal dispersion coefficient," *Journal of Hydrology*, vol. 527, pp. 978–989, 2015.
- [23] S. N. Kuiry, W. Wu, and Y. Ding, "A hybrid finite-volume/finite-difference scheme for one-dimensional boussinesq equations to simulate wave attenuation due to vegetation," in *Proceedings of the World Environmental and Water Resources Congress 2011: Bearing Knowledge for Sustainability*, pp. 2114–2124, USA, May 2011.
- [24] D. A. Lyn and P. Goodwin, "Stability of a general preissmann scheme," *Journal of Hydraulic Engineering*, vol. 113, no. 1, pp. 16–28, 1987.

- [25] Y. H. Zeng and W. X. Huai, "Estimation of longitudinal dispersion coefficient in rivers," *Journal of Hydro-Environment Research*, vol. 8, no. 1, pp. 2–8, 2014.
- [26] S. W. Jiang and W. U. Yong-Xin, "A comparison and analysis of flood control capacity of the nandu river based on MIKE 11 and HEC-RAS model," *China Rural Water & Hydropower*, vol. 2, pp. 46–49, 2014.
- [27] T. H. Bennett, R. Walton, P. D. Dickerson, and J. W. Howard, "Comparison of HEC-RAS and MIKE11 unsteady flow modeling for the Tillamook Valley," *In Critical Transitions in Water and Environmental Resources Management*, vol. 128, pp. 1–8, 2004.
- [28] B. N. Bockelmann, E. K. Fenrich, B. Lin, and R. A. Falconer, "Development of an ecohydraulics model for stream and river restoration," *Ecological Engineering*, vol. 22, no. 4-5, pp. 227–235, 2004.
- [29] USACE, 2010. HEC-RAS, River Analysis System. US Army Corps of Engineers. Hydrologic Engineering Center, v4.1, CPD-68.
- [30] K.-E. Lindenschmidt, K. Fleischbein, and M. Baborowski, "Structural uncertainty in a river water quality modelling system," *Ecological Modelling*, vol. 204, no. 3-4, pp. 289–300, 2007.
- [31] Y. P. Li, C. Y. Tang, Z. B. Yu, and K. Acharya, "Uncertainty and sensitivity analysis of large shallow lake hydrodynamic models," *Advances in Water Science*, vol. 2, pp. 271–227, 2012.
- [32] A. F. Blumberg and N. Georgas, "Quantifying uncertainty in estuarine and coastal ocean circulation modeling," *Journal of Hydraulic Engineering*, vol. 134, no. 4, pp. 403–415, 2008.
- [33] Y. Rui, D. Shen, S. Khalid, Z. Yang, and J. Wang, "GIS-based emergency response system for sudden water pollution accidents," *Physics and Chemistry of the Earth*, vol. 79-82, pp. 115–121, 2015.
- [34] T. Chen, X. Huang, M. Pan, S. Jin, S. Peng, and P. H. Fallgren, "Treatment of coking wastewater by using manganese and magnesium ores," *Journal of Hazardous Materials*, vol. 168, no. 2-3, pp. 843–847, 2009.
- [35] Y. Yi, Z. Yang, and S. Zhang, "Ecological risk assessment of heavy metals in sediment and human health risk assessment of heavy metals in fishes in the middle and lower reaches of the Yangtze River basin," *Environmental Pollution*, vol. 159, no. 10, pp. 2575–2585, 2011.
- [36] X. Wei, B. Gao, P. Wang, H. Zhou, and J. Lu, "Pollution characteristics and health risk assessment of heavy metals in street dusts from different functional areas in Beijing, China," *Ecotoxicology and Environmental Safety*, vol. 112, pp. 186–192, 2015.

Research Article

Comparison of Three Different Parallel Computation Methods for a Two-Dimensional Dam-Break Model

Shanghong Zhang,¹ Wenda Li,¹ Zhu Jing,¹ Yujun Yi,² and Yong Zhao³

¹Renewable Energy School, North China Electric Power University, Beijing 102206, China

²School of Environment, Beijing Normal University, Beijing 100875, China

³China Institute of Water Resources and Hydropower Research, Beijing 100038, China

Correspondence should be addressed to Shanghong Zhang; zhangsh928@126.com

Received 22 May 2017; Revised 31 July 2017; Accepted 22 August 2017; Published 28 September 2017

Academic Editor: Alistair Borthwick

Copyright © 2017 Shanghong Zhang et al. This is an open access article distributed under the Creative Commons Attribution License, which permits unrestricted use, distribution, and reproduction in any medium, provided the original work is properly cited.

Three parallel methods (OpenMP, MPI, and OpenACC) are evaluated for the computation of a two-dimensional dam-break model using the explicit finite volume method. A dam-break event in the Pangtoupao flood storage area in China is selected as a case study to demonstrate the key technologies for implementing parallel computation. The subsequent acceleration of the methods is also evaluated. The simulation results show that the OpenMP and MPI parallel methods achieve a speedup factor of 9.8× and 5.1×, respectively, on a 32-core computer, whereas the OpenACC parallel method achieves a speedup factor of 20.7× on NVIDIA Tesla K20c graphics card. The results show that if the memory required by the dam-break simulation does not exceed the memory capacity of a single computer, the OpenMP parallel method is a good choice. Moreover, if GPU acceleration is used, the acceleration of the OpenACC parallel method is the best. Finally, the MPI parallel method is suitable for a model that requires little data exchange and large-scale calculation. This study compares the efficiency and methodology of accelerating algorithms for a dam-break model and can also be used as a reference for selecting the best acceleration method for a similar hydrodynamic model.

1. Introduction

Floods are an example of the main types of disaster in the world; they occur frequently and have extensive influence. As the main engineering measure for flood prevention, dams play an important role in flood control. However, along with its protective benefits, a dam itself brings the potential risk of collapse. The damage caused by a dam-break flood is far more than that caused by a general flood; it is enough to take thousands of lives [1]. Therefore, to reduce the risk of a dam project and draw up a disaster emergency treatment plan, it is necessary to establish a precise dam-break model to simulate the flood evolution.

Many methods have been used to simulate dam-break flood behavior, and they are broadly classified into simplified methods and hydrodynamic methods. Simplified methods [2–5] have the advantage of fast simulation. However, the results of some processes are not calculated and the predictions are less accurate because these models either have

low-resolution grids or use simplified shallow water equations. To obtain more accurate results, two-dimensional hydrodynamic models are usually applied to simulate dam-break flooding [6].

The simulation accuracy depends mainly on the resolution of the terrain and the methods of solution. In recent years, with the development of telemetry technology, the terrain accuracy has reached the 1 m resolution and is no longer a constraint on the accuracy of model calculations. However, at the same time, the cost of high-resolution 2D dam-break model computation has risen sharply. Taking a 1 m resolution terrain as an example, according to the Courant–Friedrichs–Lewy (CFL) condition, it is necessary that the Courant number should be less than 1.0 so that time step is small enough for stability and convergence of the model. For a time step of 0.1 s, there are about 10^6 meshes per square kilometer. With roughly 10^{12} operations per km^2 per day, it is not acceptable to work with general study areas [7]. To solve the challenges of high-precision models, the use of

parallel methods is very important and extremely necessary [7–11].

The parallel computation algorithms of mathematical models fall into three categories: message-passing interface (MPI) models, shared memory models (OpenMP), and GPU general computing models. In a shared memory model, communication between threads is achieved by reading and writing directly from shared memory, and it is easy to solve the traditional programming problem of load balancing. Models developed under this standard have the advantages of simplicity, good extensibility, and portability [12]. The LISFLOOD-FP explicit storage cell model was parallelized using OpenMP [13], and Neal et al. [14] tested the OpenMP version of the LISFLOOD-FP for a range of test cases with grid sizes that varied from 3 km to 3 m. The latter study showed that such test cases had a significant effect on acceleration. Zhang et al. [15] applied OpenMP to the parallel computation of the dam-break model and gained a speedup factor of 8.64× on a 16-core computer. In the MPI parallel applications, TRENT [16, 17], CalTWiMS [18], RMA [19], and Oger et al. [20] used MPI and regional decomposition in the parallel simulation cases. Pau and Sanders [18] achieved a speedup factor of 1.5–2× on four cores in an implicit total-variation-diminishing finite volume scheme. Villanueva and Wright [17] obtained speedup factors up to 6×, 12×, and 30× on 6, 18, and 32 processors, respectively, in a coupled 1D-2D full shallow water model. Among all the parallel algorithms, GPU models obtain the best acceleration [21–23]. The multistreaming processors and powerful computational capabilities of GPUs are vitally important for efficient parallel computation with large amounts of data and high-precision requirements [24–28]. Bradbrook et al. [29] rewrote the two-dimensional diffusive wave model JFLOW using general-purpose GPUs and achieved substantially faster computation on single-accelerator processors. However, it has the limitations of single precision and having to be completely recoded in a graphics-oriented language. Lamb et al. [30] reported a speedup factor of 112× for a GPU code run on a NVIDIA GeForce 8800GTX over the serial JFLOW code. Zhang et al. [31, 32] applied a GPU-based parallel method, OpenACC, to the parallel calculation of the flow field and the dam-break model. Rueda et al. [33] performed parallel experiments on OpenACC and CUDA based on an algorithm for simulating flood storage area and on the DEM dataset of Africa. The single core CPU simulation took 234 s, whereas OpenACC and CUDA took only 45 s and 11 s, respectively, to complete the model operation. Although there have been many studies on parallel computation, most of them focused on special methods for implementing parallel algorithms and on the associated acceleration effects. There are relatively few examples of comprehensive comparisons among multiple parallel methods. Moreover, there is no clear parallel optimization method for the dam-break model because of the limited cases of different parallel methods being used for different models and applications.

To compare the advantages and disadvantages of various parallel methods for dam-break simulations, the most common way is to use different parallel algorithms for the same dam-break model and simulation cases. Thus, the

novel task undertaken here is to build a two-dimensional hydrodynamic dam-break model and compare the three main parallel methods, OpenMP, MPI, and OpenACC. The serial version of the dam-break model is used as a benchmark for the three parallel versions solving the same problem, which means that there are four models to be compared: (1) the serial version of the model; (2) a version of the model that uses the OpenMP application programming interface and shared memory; (3) a version of the model that uses MPI and distributed memory; (4) a version of the model that uses OpenACC and cooperates with the CPU. To compare their performances, the four models are run in different context configurations and the run time for each model version is recorded separately. In addition to the acceleration effect, the environmental requirements, the difficulty of rewriting, and the trend in technological development are taken into consideration. Finally, recommendations are made for selecting a parallel algorithm for a dam-break model.

2. Method

2.1. Dam-Break Flow Model

2.1.1. Control Equation. The three-dimensional Navier–Stokes equation can reasonably describe the mechanism of dam-break flow, but it is too complex and expensive to be used for a large range of flood simulations. Because changes in the dam-break flow characteristics in the depth direction are less pronounced than those in the horizontal direction, they can be regarded as planar and the Navier–Stokes equation can be simplified by averaging in the depth direction. The conservative form of the planar 2D shallow water equations is as follows:

$$\frac{\partial U}{\partial t} + \nabla \cdot G = \frac{\partial U}{\partial t} + \frac{\partial E}{\partial x} + \frac{\partial F}{\partial y} = S.$$

$$U = \begin{bmatrix} h \\ hu \\ hv \end{bmatrix},$$

$$G = (E, F),$$

$$E = \begin{bmatrix} hu \\ hu^2 + \frac{gh^2}{2} \\ huv \end{bmatrix},$$

$$F = \begin{bmatrix} hv \\ huv \\ hv^2 + \frac{gh^2}{2} \end{bmatrix},$$

$$S = \begin{bmatrix} 0 \\ gh(S_{ox} + S_{fx}) \\ gh(S_{oy} + S_{fy}) \end{bmatrix},$$

$$\begin{aligned}
S_{ox} &= -\frac{\partial Z_b}{\partial x}, \\
S_{oy} &= -\frac{\partial Z_b}{\partial y}, \\
S_{fx} &= -\frac{n^2 u \sqrt{u^2 + v^2}}{h^{4/3}}, \\
S_{fy} &= -\frac{n^2 v \sqrt{u^2 + v^2}}{h^{4/3}}
\end{aligned} \tag{1}$$

Here, U is the conservation vector, G is the flux vector, E is the x -direction flux, F is the y -direction flux, and S is the source term vector. Terms u and v are the water velocities in the x and y directions, respectively; g is the gravitational acceleration, S_{ox} and S_{oy} describe the bottom slope and S_{fx} and S_{fy} give the friction gradients in the x and y directions, respectively. Finally, Z_b is the river bottom elevation, and n is the Manning coefficient.

2.1.2. Model Solving Method. A quadrilateral unstructured grid is used in the dam-break flow model. A cell-centered format control volume in which all physical variables are defined in the centroid of the grid cell is used in model solving, for which a single grid cell gives the control volume.

Planar 2D shallow water equation (1) is integrated over the control volume A :

$$\int_{A_j} \frac{\partial U}{\partial t} dA + \int_{A_j} \nabla \cdot G dA = \int_{A_j} S dA. \tag{2}$$

Gauss's formula is used to convert (2) to

$$\frac{\partial U_i}{\partial t} \Delta S_i = - \oint_{L_i} G \cdot n dl + \int_{A_j} S dA, \tag{3}$$

where U_i is the average value of the control unit, L_i is the boundary of control volume k , n is a unit normal vector on the boundary, and ΔS_i is the area of each calculation unit. The line integral of (3) is then discretized as

$$\Delta U = -\frac{\Delta t}{\Delta S_i} \sum_{j=1}^4 (G_{ij} \cdot n_{ij}) \Delta l_{ij} + \frac{\Delta t}{\Delta S_i} \int_{A_j} S dA, \tag{4}$$

where Δl_{ij} is the length of each side, G_{ij} is the numerical flux via edge I , and n_{ij} is the unit outer normal vector passing through the unit boundary j .

For the Riemann problem at the interface, the Roe scheme is used to solve the normal flux of the computation unit. The detailed process of solving a Roe scheme has been described by Toro [34]. The expression is as follows:

$$G \cdot n = \frac{1}{2} [(E, F)_R \cdot n + (E, F)_L \cdot n - |\tilde{J}| (U_R - U_L)], \tag{5}$$

where $\tilde{J} = \partial(G \cdot n) / \partial U$ is a Roe-formatted Jacobian matrix and U_R and U_L are conserved variables on both sides of the cell.

The source term solution plays a role in stabilizing the computational format and improving the computational accuracy in the model. Using the bottom slope characteristic decomposition method to obtain a reasonable solution for the bottom slope source term is realistic for complex terrain conditions. The upwind interface fluxes for upwind treatment of the bottom slope source term are

$$\begin{aligned}
\bar{S}_0 &= \sum_{i=1}^4 \sum_{j=1}^3 \left[\frac{1}{2} (1 - \text{sign}(\bar{\lambda}^j)) \beta^j \bar{e}^j l_i \right]^i, \\
\beta^1 &= -\frac{1}{2} \bar{c} \bar{z}_b, \\
\beta^2 &= 0, \\
\beta^3 &= \frac{1}{2} \bar{c} \bar{z}_b,
\end{aligned} \tag{6}$$

where \bar{e}^j ($j = 1, 2, 3$) is the eigenvector corresponding to the three eigenvalues of the Jacobian matrix, $\text{sign}()$ is the sign function, \bar{z}_b is the average that calculates the left and right bottom elevations, and \bar{c} is the average velocity given by the Roe scheme.

With a completely explicit discretization to deal with the friction source term in order to further discretize (4), the following expression for ΔU is obtained:

$$\begin{aligned}
\Delta U &= \frac{\Delta t}{\Delta S_j} \left[\left(-\sum_{i=1}^4 G_i n_i l_i \right) \right. \\
&\quad \left. + \sum_{i=1}^4 \sum_{j=1}^3 \left(\frac{1}{2} (1 - \text{sign}(\bar{\lambda}^j)) \beta^j \bar{e}^j l_i \right)^i + \Delta t S_f^n \right]. \tag{7}
\end{aligned}$$

The flow chart for solving the serial model is shown in Figure 1.

2.2. Model Parallelism Analysis. From the above method for solving the flow, we can see that the variable ΔU at the next time step requires only the flow characteristics of the previous time step. As there is no association with the grid, this provides the basic conditions for parallelism. Hence, at the time T of entering the grid cycle, all mesh cycles can be cut to form a few smaller grid cycle blocks. The tasks including the interface flux calculation, the bottom slope and friction source term calculation, and the simulation data update, which belongs to different grid blocks, will be assigned to all the computing resources. Hence, the grid block can calculate at the same time and the overall simulation process can be accelerated.

The FORTRAN language was used to implement the dam-break model calculation, and the OpenMP, MPI, and OpenACC parallel methods were used to realize parallel computing. Of these methods, OpenMP is an implicit parallel method; it is a shared storage and CPU thread granularity parallel method. The MPI method is an explicit parallel method; it is a distributed storage and CPU process granularity parallel method. The OpenACC method is implicitly parallel; it is a single address storage and GPU parallel method.

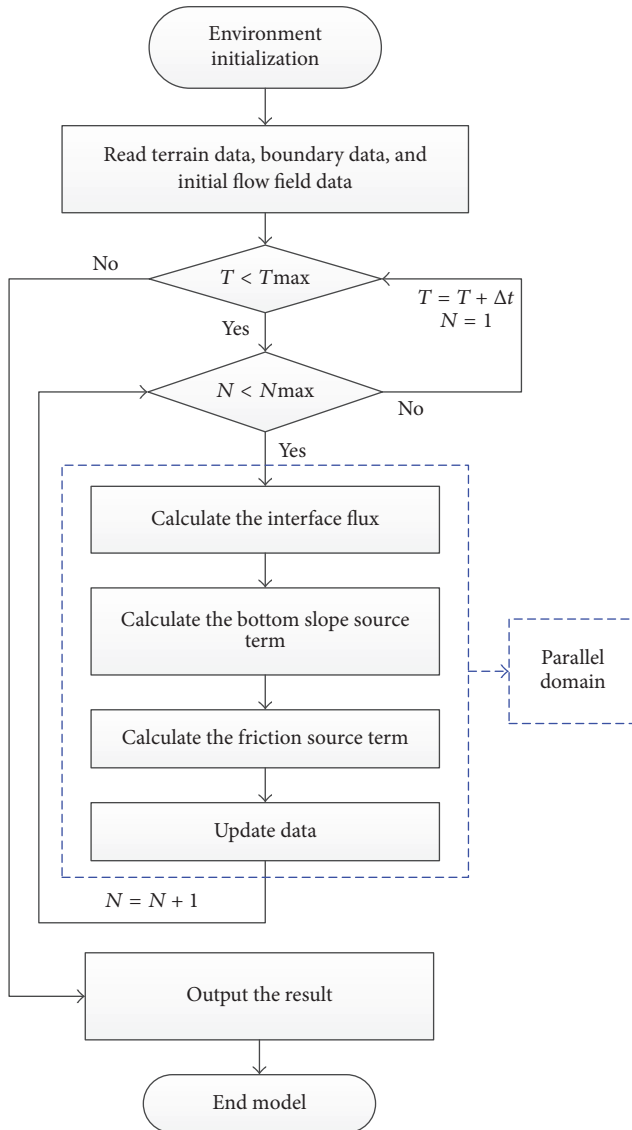


FIGURE 1: Flow diagram for solving the serial dam-break model.

2.3. Dam-Break Model Based on OpenMP. The general realization method of the OpenMP interface is that the calculation task should be allocated to all virtual threads of the CPU according to the OpenMP directives given to the compiler, wherein each thread completes part of the grids' calculation task. There is no difference with the serial model outside the OpenMP parallel part. In the OpenMP parallel part, OpenMP directives are used to convey information. Shared memory is applied for the shared parameters of the threads and independent storage space is applied for the private variables of the independent thread. The information exchange speed between threads is the memory-level exchange speed.

Rewriting the dam-break model with OpenMP includes the following four steps.

(1) *Determine the Scope of the Parallel Domain.* All of the parallel operations need to be carried out in their respective

parallel domains. The overall range of parallelism is the grid loop part according to the dam-break model flow diagram and the model parallelism analysis. Thus, the whole model can be set up with a whole parallel domain. The specific implementation is as follows: use the `$ OMP PARALLEL` directive above the grid loop of the 2D hydrodynamic model to turn on the parallel domain, and add the `$ OMP END PARALLEL` directive at the end of the grid loop to end the parallel field.

(2) *Set the Type of Parallel Data Access within the Domain and the Number of Threads.* This is the most critical part of the parallel process; identifying the data type of each variable determines the shared boundary within the parallel domain, and it can save compiler stack space and increase the efficiency of acceleration. The realization method is as follows: add the directive word `SHARED()` and add the shared variables in it; then call the `DEFAULT (PRIVATE)` directive to set the remaining parallel domain variables to the private-variable properties by default. Using the `NUM.THREADS` directive to define a reasonable number of threads for the model, the maximum number of threads is the number of host virtual threads.

(3) *Model Task Division.* The grid cycle of the dam-break model is the main part for parallel computation. The `$OMP DO` directive is used before the grid loop to dispatch all grid computing tasks to different threads in order to maximize the acceleration effect of the model.

(4) *Parallel Protection Measures and Optimization.* When the private variables in the parallel domain are turned on, they apply storage memory according to the number of threads; the applied memory will increase along with the increasing amount of threads opened. Because the applied memory for parallel computing will be used when the model runs the `PARALLEL` directive, if the compiler stack space is insufficient, the compiler can compile the program successfully, but the running program will exit because of a shortage of memory. To solve this problem, one method is to increase the compiler stack storage; another is to redetermine the shared storage variables in the parallel domain so as to decrease the memory needed. The `DYNAMIC` directive should be added after the `$OMP DO` directive to ensure that the task allocation is sufficiently reasonable, so that more calculation tasks can be assigned to faster threads.

The solving flow chart of the OpenMP parallel dam-break model is shown in Figure 2. The program directive statements are used to provide parallel purposes to the compiler, and the specific implementation of the parallel computation is completed by the compiler itself. If the directives added in the program are ignored, the program will automatically degenerate to the serial version, so this type of parallel method has good reversibility.

2.4. Dam-Break Model Based on MPI. The thinking behind the MPI interface takes the following steps. Firstly, the calculation tasks are divided manually according to their parallel computation characteristics, and then each divided

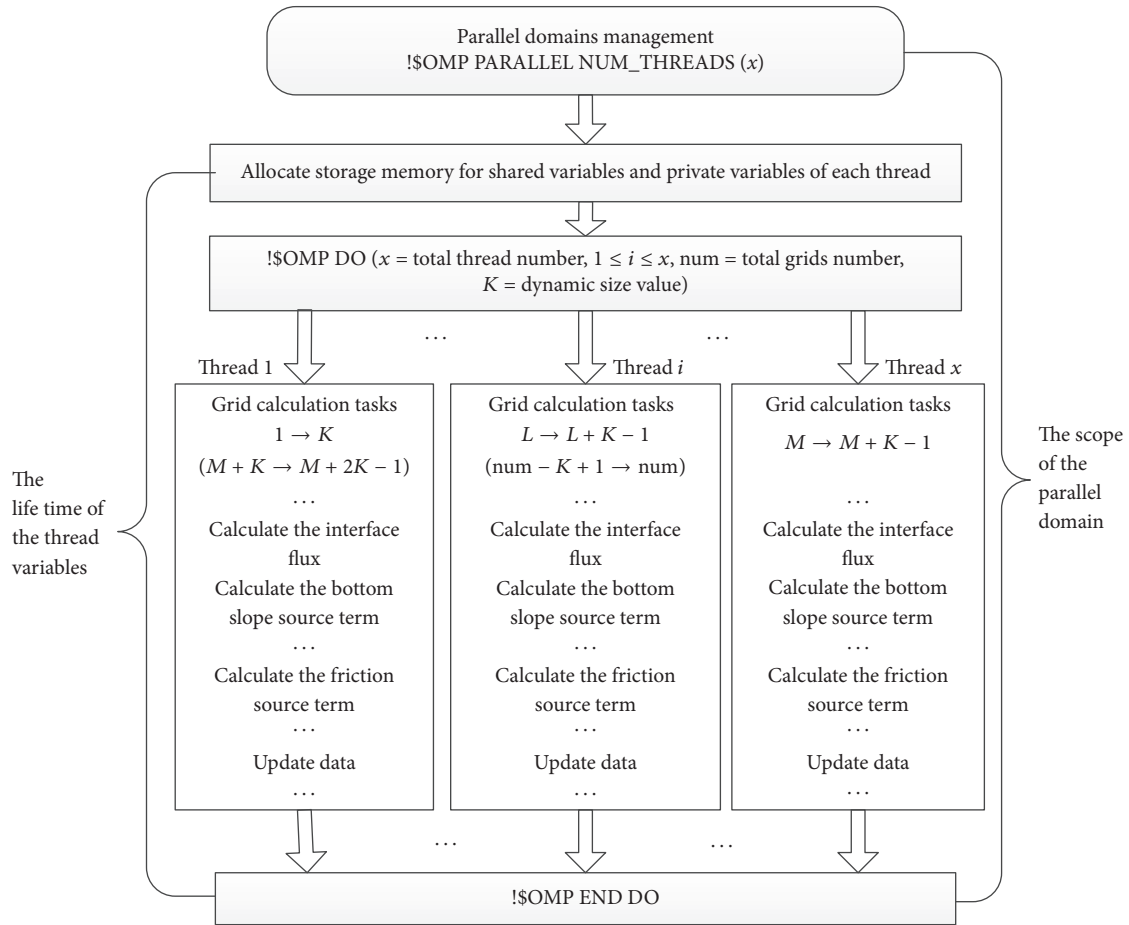


FIGURE 2: Flow diagram for solving the OpenMP dam-break model.

part is sent to a different process to run. The data exchanges between the processes are achieved by calling the MPI library. All the processes run synchronously and apply their own space, as in the serial program. The data exchange is transmitted internally on the same computer, and the transmission efficiency depends on the means of transmission between different processes under different computers. Unlike the thread-opening method in the OpenMP parallel model, the number of opening processes, including the number of hosts and the opening process number of each host, should be controlled by the mpich2 software in MPI. MPI itself does not provide a parallel guidance statement; its main roles are message communication, data management, and input and output. Thus, it is impossible to add MPI directives directly in the 2D hydrodynamic model to achieve parallelism; the model should be reconstructed based on the serial code. The key points of the reconstruction are the task division and the control of message communication.

Rewriting the dam-break model based on MPI can be divided into the following steps.

(1) *MPI Initialization and Environment Identification.* Firstly, the MPI environment should be opened by calling the MPI_INIT (ierr) function after the data input part of the

model. The current process number and the number of total opening processes should then be obtained by calling the MPI_COMM_RANK (MPI_COMM_WORLD myid ierr) and MPI_COMM_SIZE (MPI_COMM_WORLD proc ierr) functions; the values will be stored in the *myid* and *proc* variables.

(2) *Calculate the Offset Array and Data Receiving Array.* Data and calculation task division of the model require two key arrays: the offset array and the data receiving array. Setting up these arrays is a key step in the MPI rewriting. The two arrays are used throughout the MPI parallel model, named *displs* and *recvcounts*, respectively, and apply memory space according to the total number of processes. The average number of meshes per process (*num*) can be calculated by dividing the total number of grids (*nelem*) by the total number of processes (*proc*). Hence, the last item of the *recvcounts* array is the sum of *num* and the remainder, and the remaining items are *num*. The first item of *displs* is 0, and the following item value can be calculated by accumulating the *num* value. The main purpose of task division is to consider multiple grid computing units as a whole; the calculation task is distributed manually to each process according to the offset array and data receiving array.

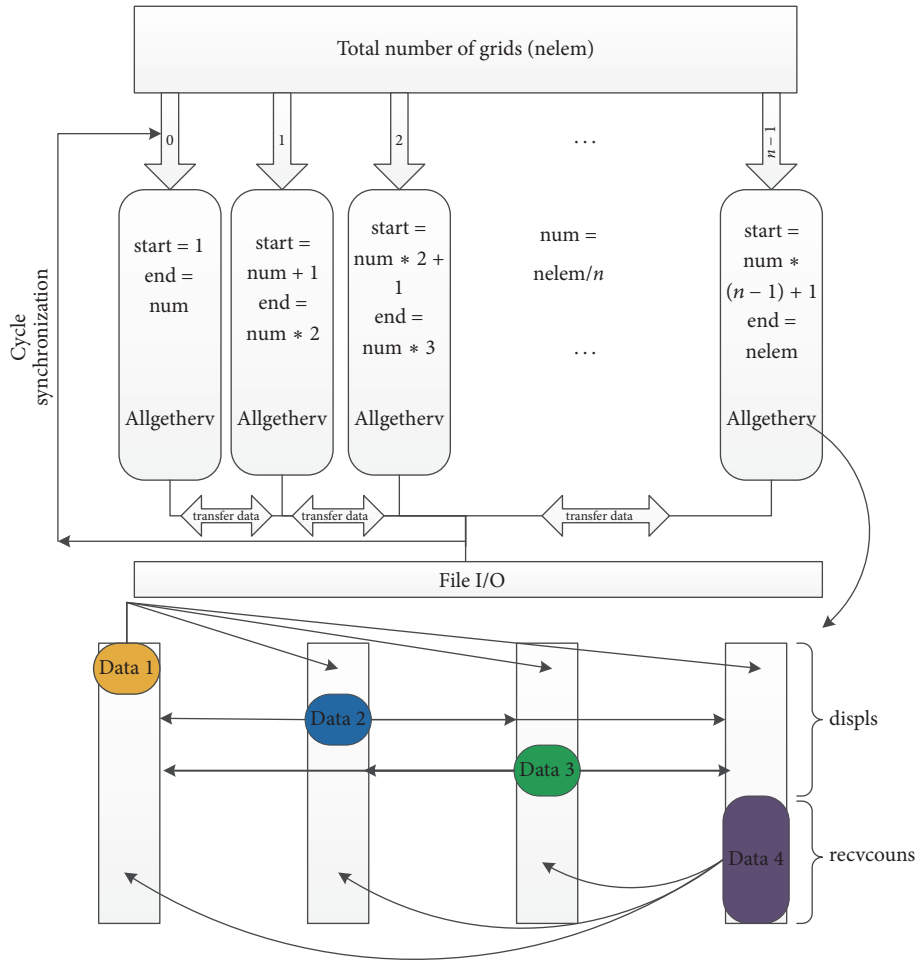


FIGURE 3: Flow chart for solving the dam-break model based on MPI.

(3) *Data Communications and Synchronization.* When the grid calculations of all processes are completed, the results from different processes need to be exchanged with each other to enter the next time step of the calculation. The method of broadcast communication is used to exchange data because of the large amount of data exchange. This performs an all-gather collection operation of variable length and uses the in place mechanism of the intergroup communication communicator. To realize data exchange, the start and end points of the calculation process can firstly be used to determine the sizes of the data receiving array and storage location offset array. The MPI_ALLGATHERV function can then be used to realize data transmission. The send port uses MPI_IN_PLACE and the value is zero, and the receiver port should set the array name that needs to be received and then put the offset array and data receiving array into the function to complete the operation. Thus, the model result in the process has been completed in exchange between different processes when the model runs into the next round of cycle time.

At this point, the manual task allocation and data communication of the dam-break model are complete. However,

the average distribution of tasks cannot guarantee that the end time was the same. Therefore, the MPI_Barrier function is called after each grid cycle; the communicator identifies the processes that run the program at the same time and that maintain interprocess synchronization. The solving flow chart of the dam-break model based on MPI is shown in Figure 3.

2.5. Dam-Break Model Based on OpenACC. The OpenACC interface is similar to OpenMP in that all operations are done through directive statements. Firstly, the memory is applied in the graphics memory, and then data are transmitted to the GPU and the model calculations are completed on the accelerator. Finally, the results are sent back to the host. The task division on the accelerator has different accelerating effects according to the directive. In this paper, the KERNELS directive is used to realize parallel computing, and this directive can make each accelerator core obtain a basic calculation unit. The data transmission between the GPU and the CPU depends on the data bandwidth between the GPU and the host's external interface. Generally, because of the impact of data packets, the real transmission efficiency is slightly lower than the bandwidth.

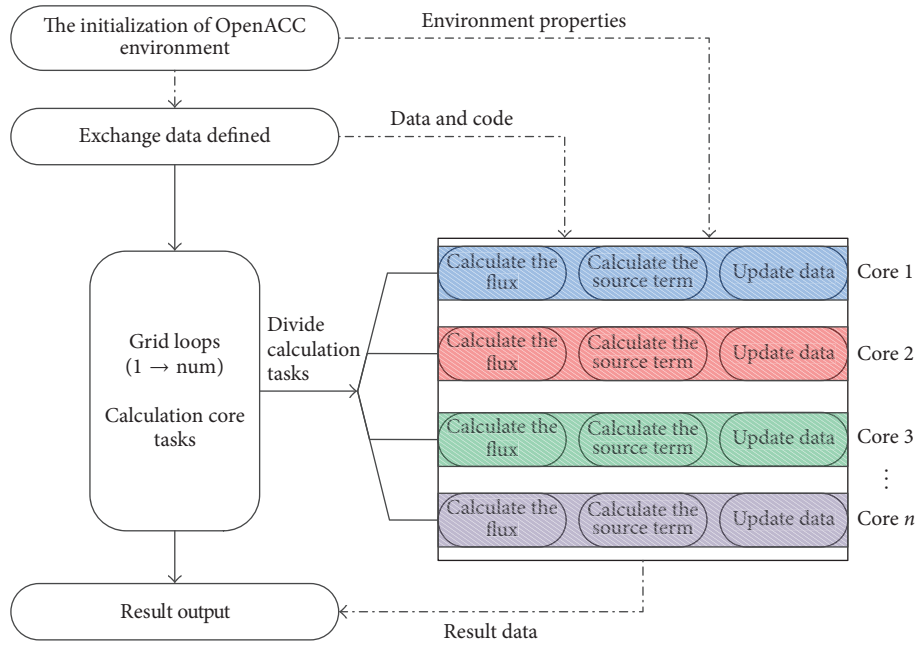


FIGURE 4: Flow chart for solving the dam-break model based on OpenACC.

There are three steps to implement the dam-break model based on OpenACC.

(1) *Subroutine Processing.* A number of functions of the dam-break model are realized through the FORTRAN subroutine, such as the functions of interpolation and the bottom slope source calculation. Unlike OpenMP, these subroutines cannot be loaded directly into the GPU. Modularity is used in OpenACC to realize the usage of subroutines. On the one hand, this method maintains the readability of the model, and on the other hand, it reduces the workload of the parallel model modification. The concrete realization is as follows: all of the functions and subroutines are written in front of the main program, the directives MODULE and END MODULE are used to modularize them, and finally the ROUTINE directive is used to transmit information to the GPU. The SEQ directive is used to ensure that the functions and subroutines are calling in single-thread mode.

(2) *Environment Setting and Data Copying.* Before the dam-break model runs to the time loop and uses the parallel computing, the *acc_init* function should be called firstly to turn on the OpenACC environment, and then the *acc_set_device_num* function should be called to determine which graphics card is to be used in the following calculation. In order to reduce the data exchange between the GPU and CPU, the directives DATA, COPYIN, and COPY should be used to define the exchanged variables and transmission method. The simulated value cannot be used in the CPU if the variable is transmitted to the GPU by the COPYIN directive. In addition, if some temporary variables need not be transmitted between the CPU and GPU, the CREATE directive will be used to define them. The directives DATA and END DATA define all the variables used to exchange between the CPU and GPU.

(3) *Task Division.* The directive KERNELS LOOP is used to set the parallel instructions at each loop. In order to further optimize the data management of the hydrodynamic model, the directive PRIVATE is used to privatize the variables that are calculated repeatedly, and the INDEPENDENT directive is used to extract the data dependency of KERNELS LOOP.

There are many differences between the OpenACC and OpenMP models; the choice of KERNELS is also important in addition to the above differences in steps. OpenACC also has a PARALLEL directive; multiple GANGs can be created and multiple WORKS can be distributed in the parallel domain to maintain the accelerated state. The solving flow chart of the dam-break model based on OpenACC is shown in Figure 4.

3. Case Study

3.1. *Study Area.* The Pangtoupao flood storage area is located in the Songhua River basin of China (Figure 5); it undertakes flood control tasks for Harbin City and has a direct impact on the safety of the lives and property of the city's residents. The elevation of the Pangtoupao flood storage area drops gradually from northwest to southeast, and its average east-west width and north-south length are 46 km and 58 km, respectively. It covers an area of 1,994 km² and its volume is about 5.5 billion cubic meters. According to flood data measured in 1998, flooding caused multiple levee breaches on the Songhua Rivers, with the Pangtoupao dam being breached on August 15. Outburst floods spread rapidly to the northeast and caused a huge flooded area.

3.2. *Dam-Break Event Simulation.* A DEM (resolution of 10 m) of Pangtoupao and the flood data for the Songhua River in 1998 were used to build the hydrodynamic model. In total, 337,084 quadrilateral unstructured meshes were partitioned

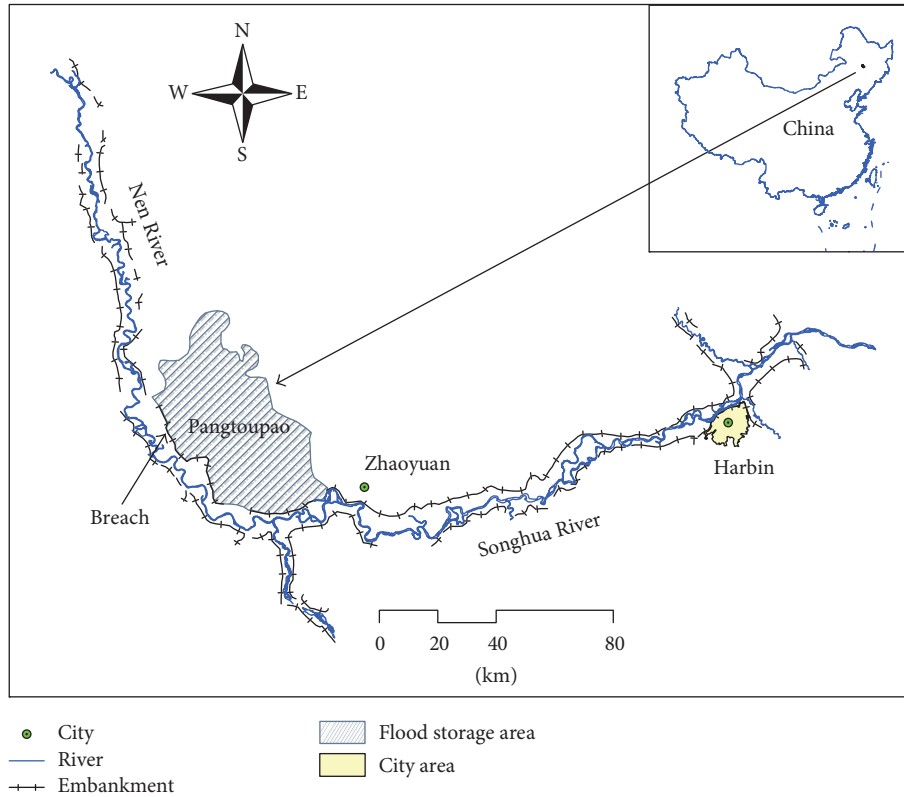


FIGURE 5: Location of the Pangtoupao flood storage area.

by the gambit software; the average grid length is 80 m. The Manning roughness value of the study area is 0.055. The measured flood occurred on August 15, 1998. The breach expanded rapidly to 530 m, and therefore this breach width is used for the dam-break simulation. The time from the levee breaches to reaching the maximum inundated area of the flood was 320 h, so the simulation time is chosen as 320 h. To examine the accuracy of the model, the maximum inundated area is calculated and compared with the measured value.

3.3. Parallel Efficiency Comparison Scheme. The simulation of the 320 h flood process takes approximately 170 h, which would be too long to compare the efficiencies of different parallel methods if the whole flood process was to be simulated. Instead, here 6,000 time steps (2,988 s) are used to compare the efficiencies of the different parallel computing methods.

The model operating environment of OpenMP and MPI is as follows: a Windows 7 64-bit operating system with Intel Parallel Studio XE 2016 compiler, an Intel Xeon E5-2640v3 CPU with a basic frequency of 2.6 GHz, 16 GB of memory, and a dual processor with 32 virtual cores. The model operating environment of OpenACC is as follows: a Windows 7 64-bit operating system with the PGI PVF version 14.9 compiler, an Intel Xeon E5-2603 CPU with a basic frequency of 1.8 GHz, 4 GB of memory, and an NVIDIA Tesla k20c graphics card. The CPU gap did not affect the consistency of the results because OpenACC mainly uses the GPU to realize acceleration.

Even-numbered threads from 2 to 24 were selected to test the calculation time of the OpenMP parallel model. Even-numbered processes from 2 to 24 were selected to test the calculation time of the MPI parallel model. For the OpenACC parallel model, the calculation time was tested on the computer with the NVIDIA Tesla k20c graphics card.

4. Results and Discussion

4.1. Calculation Results. The results of the model show that the maximum inundation area is 1,180 km², which is close to the measured value of 1,160 km². Figure 6 shows the flow field and inundation area of the dam-break flood. The parallel results are consistent with the serial results, and the calculation times used to simulate 2,988 s of the dam-break flood are given in Table 1. For this, the speedup ratio S is calculated as follows:

$$S = \frac{T_S}{T_P}, \quad (8)$$

where T_S is the serial computation time and T_P is the parallel computation time. The time-saving ratio δT is calculated as follows:

$$\delta T = \frac{(T_S - T_P)}{T_S}. \quad (9)$$

The speedup ratios of OpenMP and MPI in different threads/processes are shown in Figure 7. From Table 1 and Figure 7, we can see that the OpenACC parallel method

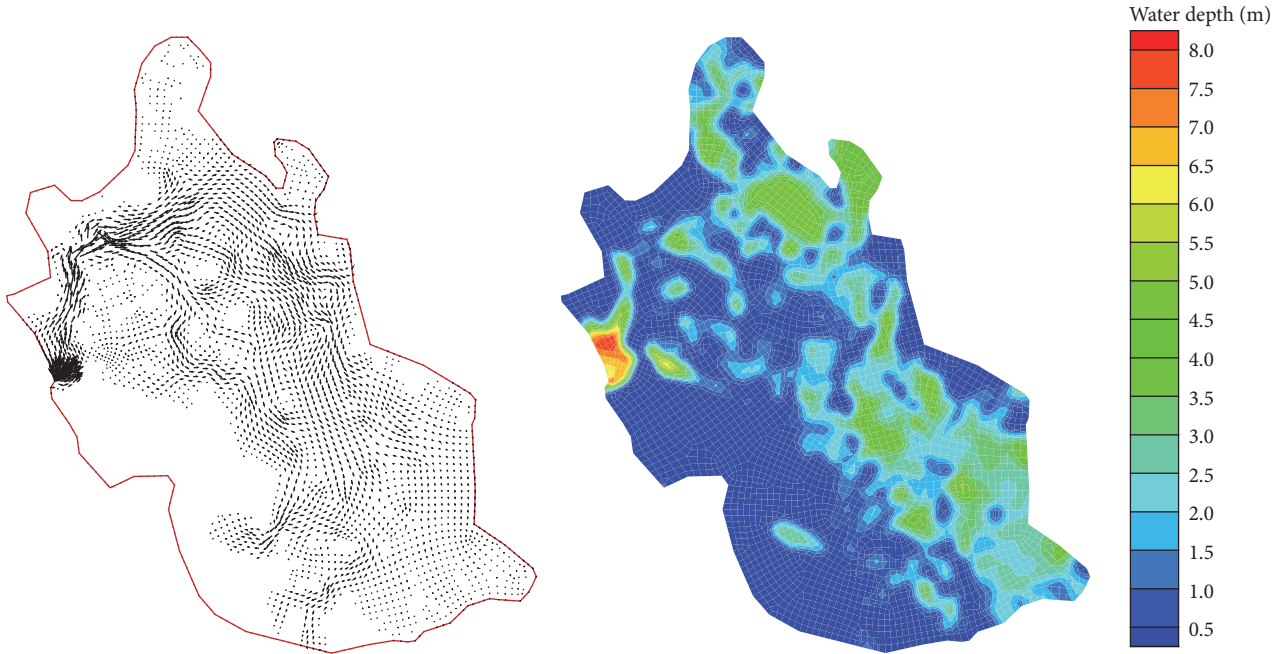


FIGURE 6: Flow field and inundation area of the dam-break flow in the Pangtoupao flood storage area.

TABLE 1: Calculation time and acceleration effect of different models (total simulation time: 2,988 s).

	Shortest time (s)	Speedup ratio	Time-saving ratio (%)
Serial model	1,639	1	0
OpenACC model	79	20.7	95
OpenMP model	168	9.8	90
MPI model	324	5.1	80

achieved the best acceleration effect. The OpenMP parallel model achieved the biggest speedup ratio of 9.8 and was better than the MPI parallel model when the number of threads was greater than 12. The MPI parallel method was slightly better than the OpenMP acceleration effect for fewer than 12 threads (processes) and it achieved the biggest speedup ratio of 5.1.

As two of the more mature parallel approaches, the performance comparison between OpenMP and MPI is well known, although fine-grained OpenMP is not necessarily more efficient than MPI. For the dam-break model, the number of atomic operations is very small, with no extra mutex overhead, so OpenMP gets the upper hand. In the case of low computational resource consumption (fewer than 12 processes and threads), the task allocation overhead of the OpenMP directive is significantly higher than the message delivery cost in MPI, so the MPI acceleration efficiency is higher at the beginning. Along with more allocation of computing resources, MPI will be slightly weaker than OpenMP because of load balancing.

Because only the total amount of the loop (not the amount of calculation) can be divided in MPI, we cannot

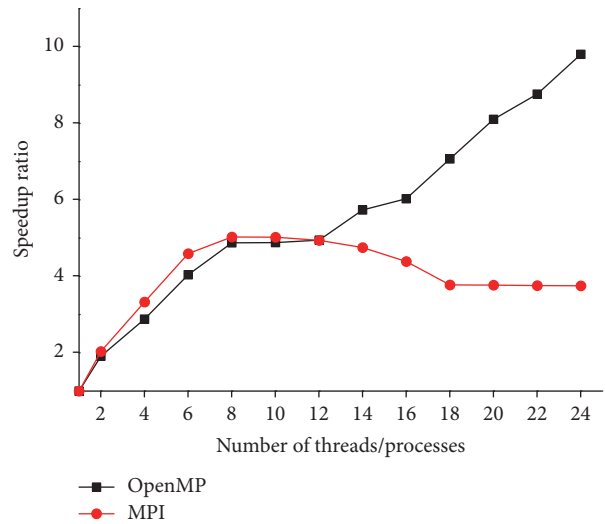


FIGURE 7: Speedup ratios of OpenMP and MPI parallel methods for different numbers of threads or processes.

determine which process is more efficient in order to obtain more computation; the main program has to wait for the slowest process to complete the calculation task before the next round of time cycle. At the same time, the MPI data communication costs are also increasing with the number of processes. This is because each process has to broadcast to all the other processes in order to exchange results when the calculation task has been completed in each time step. In addition, the means of communication are related directly to the communication consumption. In this paper, a single server was used to test the MPI model. The internal transmission speed between different processes is equal to the

memory exchange speed, which is close to twice the speed of universal optical fibre transmission. Even so, the benefits of an increment in computing resources is still counteracted by the data exchange and other expenses. A linear increment in the amount of data exchange locks the speedup ratio of MPI to 5.1, which then declines smoothly.

The OpenACC parallel model realizes its acceleration based on the graphics card, whose computational capability is much higher than that of the CPU. Although it is not as flexible as the CPU parallel mode, which can adjust the amount of calculation resources, the overall acceleration capability of the GPU is considerable. In addition, the development of GPU technology has been very fast in recent years, including the graphics card and the GPU parallel language. Hence, the GPU acceleration mode has great potential in parallel computing.

4.2. Implementation Method Discussion. In order of implementation difficulty from high to low, the three parallel methods are listed as OpenACC, MPI, and OpenMP. Despite the fact that OpenMP requires the least rewrite work, developer has to understand the calculation flow and variables of the program clearly in order to find the correct variables to set as shared variables. The program can still run and achieve correct results with different shared- and private-variable conditions, but the acceleration efficiencies are different. For example, setting the constant variables to private variables, the acceleration effect still exists, but the cost of the error significantly reduces the speed of the original OpenMP model. Overall, OpenMP parallelization has the lowest degree of rewrite difficulty, good reversibility, and high fault tolerance. It is easy to debug and its acceleration efficiency is middling.

The rewrite workload of MPI is large because the serial code should be rewritten totally, and it is difficult to reverse. However, the rewrite difficulty level is low because the data division and transmission of the MPI model are clear. The MPI model can be debugged and tested easily in a single computer, whereas it is more difficult to debug on a multimachine cluster. It is suitable for conditions with less data exchange and sufficiently large amounts of calculation. The OpenACC parallel model has hard rewrite difficulty and is difficult to debug, but its reversibility and fault tolerance are good, and its acceleration effect is the best.

From the point of view of hardware requirements, the OpenACC model needs a high-performance graphics card. With the development of graphics cards, their price is likely to decrease continually; the price of a common graphics card used in parallel computing is now the same as a personal computer. The MPI model generally needs to be run on a computer cluster. The requirement of a single calculation node is low; a common personal computer could be used as a calculation node, although the CPU frequency and memory size will influence the acceleration efficiency. Of course, a huge amount of calculation requires a sufficient number of calculation nodes, which would increase the hardware costs. In addition, because the data transmission method is one of the most important factors influencing the acceleration efficiency, the general recommendation is to use fibre-optic cable or high-efficiency wireless to undertake

the transmission. The OpenMP model requires a multicore computer, so the number of cores, the basic frequency, and the memory size are the factors that influence the acceleration efficiency.

5. Conclusion

In this paper, high-performance dam-break flow simulation models based on the finite volume method were established. An explicit scheme was used to discretize the 2D shallow water control equations, and Roe's approximate Riemann solution for the finite volume method was adopted for the interface flux of the grid cells. For the dam-break flow observed in 1998 in the Pangtoupao flood storage area, three parallel computing methods, OpenMP, MPI, and OpenACC, were used to accelerate the dam-break model calculation. The characteristics of these three methods and their acceleration effects were compared and analysed. The conclusions are as follows.

(1) To obtain more accurate results, hydrodynamic models are usually used to simulate dam-break flooding instead of simplified methods. To speed up the calculation, an explicit discrete technique was used to solve the governing equations. Moreover, there is no correlation between the grid calculations in a single time step, so the 2D hydrodynamic dam-break model can be calculated in parallel using the loop structure of the grid calculations. This modification does not substantially change the original program code, so it is easy to convert the original serial model into one that can be computed in parallel.

(2) In the acceleration effect, the OpenACC method was the best. It achieved a 20.7 speedup ratio, with OpenMP and MPI achieving 9.8 and 5.1, respectively. The simulation time for the Pangtoupao dam-break event (320 h) was shortened from 170 h to 8.2 h with parallel computing, which effectively improved the simulation speed of the dam-break model.

(3) In the implementation method, the OpenMP parallel method had the lowest degree of difficulty, good reversibility, and high fault tolerance; it was easy to debug but it was difficult to achieve the best acceleration effect. The code rewrite of the OpenACC model was more difficult, and it was also difficult to debug, but its reversibility and fault tolerance were good. The code rewrite workload of MPI was very large, although the work was not very difficult because data division and transmission could be realized manually. Its reversibility was poor and it was difficult to debug on a multicomputer cluster. It is suitable for calculation cases with less data exchange and sufficiently large calculation tasks.

(4) In the case of small-scale calculations, if the memory of a single computer is enough to calculate the task, the OpenMP parallel method is recommended as a simple and effective method to achieve a better effect. If higher acceleration performance is required, the OpenACC parallel method should be considered. In the case of large-scale calculation, because of the single-machine memory bottleneck, the MPI method is a better choice. In addition, a combination of parallel methods, such as MPI + OpenMP or MPI + OpenACC, would also be effective for large-scale computing acceleration.

Conflicts of Interest

The authors declare that there are no conflicts of interest regarding the publication of this paper.

Acknowledgments

This study was supported by the National Key Research and Development Program of China (2016YFC0401407) and the National Natural Science Foundation of China (51379076).

References

- [1] Sichuan Seismological Bureau, *The 1933 Diexi Earthquake*, Sichuan Science and Technology Press, Chengdu, China, 1983.
- [2] M. Krupka, S. Wallis, S. Pender, and S. Neélz, "Some practical aspects of flood inundation modelling, transport phenomena in hydraulics, publications of the institute of geophysics," *Polish Academy of Sciences*, vol. 7, no. 401, pp. 129–135, 2007.
- [3] P. Samuels, S. Huntington, W. Allsop, and J. Harrop, *Recent development and application of a rapid flood spreading model*, River Flow 2008, CRC Press, 2008, http://eprints.hrwallingford.co.uk/223/1/HRPP361-Recent_development_and_application_of_a_rapid_flood_spreading_method.pdf.
- [4] B. Ghimire, A. S. Chen, M. Guidolin, E. C. Keedwell, S. Djordjević, and D. A. Savić, "Formulation of a fast 2D urban pluvial flood model using a cellular automata approach," *Journal of Hydroinformatics*, vol. 15, no. 3, pp. 676–686, 2013.
- [5] S. Zhang, T. Wang, and B. Zhao, "Calculation and visualization of flood inundation based on a topographic triangle network," *Journal of Hydrology*, vol. 509, pp. 406–415, 2014.
- [6] J. Singh, M. S. Altinakar, and Y. Ding, "Two-dimensional numerical modeling of dam-break flows over natural terrain using a central explicit scheme," *Advances in Water Resources*, vol. 34, no. 10, pp. 1366–1375, 2011.
- [7] B. F. Sanders, J. E. Schubert, and R. L. Detwiler, "ParBreZo: A parallel, unstructured grid, Godunov-type, shallow-water code for high-resolution flood inundation modeling at the regional scale," *Advances in Water Resources*, vol. 33, no. 12, pp. 1456–1467, 2010.
- [8] J. C. Neal, T. J. Fewtrell, P. D. Bates, and N. G. Wright, "A comparison of three parallelisation methods for 2D flood inundation models," *Environmental Modelling and Software*, vol. 25, no. 4, pp. 398–411, 2010.
- [9] E. R. Vivoni, G. Mascaro, S. Mniszewski et al., "Real-world hydrologic assessment of a fully-distributed hydrological model in a parallel computing environment," *Journal of Hydrology*, vol. 409, no. 1-2, pp. 483–496, 2011.
- [10] A. R. Brodtkorb, M. L. Sætra, and M. Altinakar, "Erratum to 'Efficient shallow water simulations on GPUs: implementation, visualization, verification and validation' [Comp Fluids 55 (2012) 1-12] [MR2979690]," *Computers & Fluids. An International Journal*, vol. 59, 125 pages, 2012.
- [11] J. M. Kelly, E. A. Divo, and A. J. Kassab, "Numerical solution of the two-phase incompressible Navier-Stokes equations using a GPU-accelerated meshless method," *Engineering Analysis with Boundary Elements*, vol. 40, pp. 36–49, 2014.
- [12] A. Amritkar, D. Tafti, R. Liu, R. Kufirin, and B. Chapman, "OpenMP parallelism for fluid and fluid-particulate systems," *Parallel Computing*, vol. 38, no. 9, pp. 501–517, 2012.
- [13] P. D. Bates and A. P. J. De Roo, "A simple raster-based model for flood inundation simulation," *Journal of Hydrology*, vol. 236, no. 1-2, pp. 54–77, 2000.
- [14] J. Neal, T. Fewtrell, and M. Trigg, "Parallelisation of storage cell flood models using OpenMP," *Environmental Modelling and Software*, vol. 24, no. 7, pp. 872–877, 2009.
- [15] S. Zhang, Z. Xia, R. Yuan, and X. Jiang, "Parallel computation of a dam-break flow model using OpenMP on a multi-core computer," *Journal of Hydrology*, vol. 512, pp. 126–133, 2014.
- [16] I. Villanueva and N. G. Wright, "Linking Riemann and storage cell models for flood prediction," *Proceedings of the Institution of Civil Engineers: Water Management*, vol. 159, no. 1, pp. 27–33, 2006.
- [17] I. Villanueva and N. G. Wright, *An Efficient Multi-processor Solver for the 2D Shallow Water Equations*. Hydroinformatics, France, Nice, 2006.
- [18] J. C. Pau and B. F. Sanders, "Performance of parallel implementations of an explicit finite-volume shallow-water model," *Journal of Computing in Civil Engineering*, vol. 20, no. 2, pp. 99–110, 2006.
- [19] P. Rao, "A parallel RMA2 model for simulating large-scale free surface flows," *Environmental Modelling and Software*, vol. 20, no. 1, pp. 47–53, 2005.
- [20] G. Oger, D. Le Touzé, D. Guibert et al., "On distributed memory MPI-based parallelization of SPH codes in massive HPC context," *Computer Physics Communications*, vol. 200, pp. 1–14, 2016.
- [21] M. De La Asunción, J. M. Mantas, and M. J. Castro, "Simulation of one-layer shallow water systems on multicore and CUDA architectures," *Journal of Supercomputing*, vol. 58, no. 2, pp. 206–214, 2011.
- [22] L. Grillo, F. De Sande, J. J. Fumero, and R. Reyes, "Programming for GPUs: The directive-based approach," in *Proceedings of the 2013 8th International Conference on P2P, Parallel, Grid, Cloud and Internet Computing*, 3PGCIC 2013, pp. 612–617, fra, October 2013.
- [23] B. P. Pickering, C. W. Jackson, T. R. Scogland, W.-C. Feng, and C. J. Roy, "Directive-based GPU programming for computational fluid dynamics," *Computers & Fluids. An International Journal*, vol. 114, pp. 242–253, 2015.
- [24] A. Hart, R. Ansaloni, and A. Gray, "Porting and scaling OpenACC applications on massively-parallel, GPU-accelerated supercomputers," *The European Physical Journal: Special Topics*, vol. 210, no. 1, pp. 5–16, 2012.
- [25] T. Hoshino, N. Maruyama, S. Matsuoka, and R. Takaki, "CUDA vs OpenACC: Performance case studies with Kernel benchmarks and a memory-bound CFD application," in *Proceedings of the 13th IEEE/ACM International Symposium on Cluster, Cloud, and Grid Computing*, CCGrid 2013, pp. 136–143, nld, May 2013.
- [26] R. Reyes, I. López-Rodríguez, J. J. Fumero, and F. de Sande, "accULL: an OpenACC implementation with CUDA and OpenCL support," in *Euro-Par 2012 Parallel Processing*, vol. 7484 of *Lecture Notes in Computer Science*, pp. 871–882, Springer, Berlin, Germany, 2012.
- [27] X. Wang, Y. Shangguan, N. Onodera, H. Kobayashi, and T. Aoki, "Direct numerical simulation and large eddy simulation on a turbulent wall-bounded flow using lattice Boltzmann method and multiple GPUs," *Mathematical Problems in Engineering*, Article ID 742432, Art. ID 742432, 10 pages, 2014.
- [28] X. Xia and Q. Liang, "A GPU-accelerated smoothed particle hydrodynamics (SPH) model for the shallow water equations," *Environmental Modelling and Software*, vol. 75, pp. 28–43, 2016.

- [29] K. F. Bradbrook, S. N. Lane, S. G. Waller, and P. D. Bates, “Two dimensional diffusion wave modelling of flood inundation using a simplified channel representation,” *International Journal of River Basin Management*, vol. 2, no. 3, pp. 211–223, 2004.
- [30] R. Lamb, M. Crossley, and S. Waller, “A fast two-dimensional floodplain inundation model,” *Proceedings of the Institution of Civil Engineers: Water Management*, vol. 162, no. 6, pp. 363–370, 2009.
- [31] S. Zhang, R. Yuan, Y. Wu, and Y. Yi, “Parallel computation of a dam-break flow model using OpenACC applications,” *Journal of Hydraulic Engineering*, vol. 143, no. 1, Article ID 04016070, 2017.
- [32] S. Zhang, R. Yuan, Y. Wu, and Y. Yi, “Implementation and efficiency analysis of parallel computation using OpenACC: a case study using flow field simulations,” *International Journal of Computational Fluid Dynamics*, vol. 30, no. 1, pp. 79–88, 2016.
- [33] A. J. Rueda, J. M. Noguera, and A. Luque, “A comparison of native GPU computing versus OpenACC for implementing flow-routing algorithms in hydrological applications,” *Computers and Geosciences*, vol. 87, pp. 91–100, 2016.
- [34] E. F. Toro, *Riemann Solvers and Numerical Methods for Fluid Dynamics*, Springer, Berlin, Germany, 3rd edition, 2009.

Research Article

Two-Dimensional Simulation of Flows in an Open Channel with Groin-Like Structures by iRIC Nays2DH

Md. Shahjahan Ali, Md. Milon Hasan, and Masuma Haque

Department of Civil Engineering, Khulna University of Engineering & Technology, Khulna 9203, Bangladesh

Correspondence should be addressed to Md. Shahjahan Ali; bablu41@yahoo.com

Received 19 February 2017; Accepted 6 August 2017; Published 14 September 2017

Academic Editor: Jian G. Zhou

Copyright © 2017 Md. Shahjahan Ali et al. This is an open access article distributed under the Creative Commons Attribution License, which permits unrestricted use, distribution, and reproduction in any medium, provided the original work is properly cited.

This study presents the results obtained from the numerical simulation on turbulent flows around a single groin for different orientations. Here iRIC Nays2DH, which is based on 2D model, is used to simulate the flows in a straight open channel with groin of 45° , 90° , and 135° angled with the approaching flow. A depth-averaged $k-\varepsilon$ model is used as turbulence closure model with finite differential advectations as upwind scheme. The numerical results of velocity and bed shear stress profiles are compared with the available experimental data. Good agreements are found between experimental and calculated results. From the simulation, it is observed that the peak of velocity and bed shear stress is maximum at the position of head of groin when lateral distance $y/l = 1$, where l is the groin length. The position of maximum velocity and bed shear stress is found to be shifted towards downstream with increasing y/l . The maximum velocity and bed shear stress for 135° groin are found lower than the other two cases for all the sections of y/l .

1. Introduction

The simulation of water flow and sediment transport in rivers has been the subject of many researches in the field of hydraulics and river engineering [1]. In hydraulics and coastal engineering, groins are very important structures for river navigation, coastal protection, and beach reclamation [2]. It is an elongated obstruction having one end on the bank of the stream and the other end projecting into the current. Groins have been used extensively all over the world as river training and bank protection structure to reduce the current along the stream bank, thus reducing the erosive capacity of the stream and in some cases inducing sedimentation between two groins. It can be built at right angles to the bank or current (normal/deflecting groin) or angled towards upstream (repelling groin) or angled towards downstream (attracting groin). The obstructed flow field in the downstream of a single groin or the flow field enclosed by two consecutive groynes is low velocity region compared to mainstream. This type of zone is generally termed as dead zone [3]. Flow velocity inside

such kind of arrangement is lower than main channel. In addition to engineering applications, such structures increase the biodiversity of aquatic species by creating habitat and providing shelter for them. The main stream of a river, where the velocity is high, is not suitable for weak and small fishes. That is why the dead zone is a suitable shelter for them.

Many experimental and numerical researches have been performed to investigate the flow pattern and scouring around groins [4–7]. Those studies were carried out in different conditions in terms of groin length, groin inclination angle to the flow direction, permeable or impermeable states, submerged and nonsubmerged states, flow separation, recirculating length, and number of groins. The groin which is placed perpendicular to the river approaching flow causes narrowing and deviation of the flow and consequently this gives a complex three-dimensional form to flow around a groin [4, 5]. However, dealing with the practical engineering problems, such as alluvial geomorphic processes, it is computationally efficient to use 2D models compared to 3D. In this study, 2D software called iRIC Nays2DH (available

in <http://www.i-ric.org>) has been used which is based on Navier-Stokes equations to simulate the flows in an open channel with groin-like structures.

It is well known that the RANS (Reynolds Averaged Navier-Stokes) type turbulence models, such as two-equation model or Reynolds stress model, are the most popular tool used for practical engineering applications [8–10]. Because it requires less CPU time and computer memory compared to LES and DNS. Therefore, the clarification of the possibility, the limitation, and areas of improvement of RANS models should be still paid attention to. To resolve the Reynolds stress term which appeared in the averaged Navier-Stokes equations, the k - ϵ model is one of the most frequently adopted ones [10, 11]. However, the standard k - ϵ model cannot produce satisfactory results for the flow field having high rate of strain and rotation [12, 13]. In iRIC Nays2DH, a nonlinear k - ϵ model is used to predict the turbulent flow field by capturing the anisotropic turbulence.

2. Basic Equations of the Model

iRIC (International River Interface Cooperative), pre- and postprocessing software application and framework for computational models of flow and sediment transport in rivers, is used in this study. The application is a Graphical User Interface (GUI) that allows the model user to build, run, and visualize the results of the system's computational models. The GUI provides tools for building both structured and unstructured grids, defining topography and other boundary conditions on the grid, and defining grid-dependent values such as grain size, vegetation, and obstacles by mapping measured values to the grid or by creating user-defined polygons with attributes of grid-dependent value. It combines the functionality of MD_SWMS, developed by the USGS (U.S. Geological Survey), and RIC-Nays, developed by the Foundation of Hokkaido River Disaster Prevention Research Center. The details of the model can be found in iRIC [14] and Jang and Shimizu [15].

For the analysis, the general curvilinear coordinate system is adopted, allowing direct consideration of complex boundaries and riverbed shapes. Basic equations of two-dimensional plane flow at orthogonal coordinates (x, y) are transformed into general coordinates (ξ, η) . By transforming the equations into general coordinates, it becomes possible to set a calculation mesh of any shape (in keeping with the boundary conditions). The basic equations in an orthogonal coordinate system (x, y) are as follows [16].

Equation of Continuity

$$\frac{\partial h}{\partial t} + \frac{\partial(hu)}{\partial x} + \frac{\partial(hv)}{\partial y} = 0. \quad (1)$$

Equations of Motion

$$\begin{aligned} \frac{\partial(hu)}{\partial t} + \frac{\partial(hu^2)}{\partial x} + \frac{\partial(huv)}{\partial y} &= -hg \frac{\partial H}{\partial x} - \frac{\tau_x}{\rho} + D^x, \\ \frac{\partial(hv)}{\partial t} + \frac{\partial(huv)}{\partial x} + \frac{\partial(hv^2)}{\partial y} &= -hg \frac{\partial H}{\partial y} - \frac{\tau_y}{\rho} + D^y, \end{aligned} \quad (2)$$

where h is water depth, t is time, u is velocity in the x direction, v is velocity in the y direction, g is gravitational acceleration, and H is the total water depth. Here, the bed shear stresses in x and y directions (τ_x and τ_y) are expressed by using coefficient of riverbed shearing force C_f as

$$\begin{aligned} \frac{\tau_x}{\rho} &= C_f u \sqrt{u^2 + v^2}, \\ \frac{\tau_y}{\rho} &= C_f v \sqrt{u^2 + v^2}. \end{aligned} \quad (3)$$

In the model, the bottom friction is set using Manning's roughness parameter. The coefficient of riverbed shearing force C_f is estimated by Manning's roughness parameter n_m as follows:

$$C_f = \frac{gn_m^2}{\sqrt[3]{h}}. \quad (4)$$

The diffusion terms in x and y directions are expressed as (5) and (6), respectively. Here, ν_t is the eddy viscosity coefficient.

$$D^x = \frac{\partial}{\partial x} \left[\nu_t \frac{\partial(hu)}{\partial x} \right] + \frac{\partial}{\partial y} \left[\nu_t \frac{\partial(hu)}{\partial y} \right], \quad (5)$$

$$D^y = \frac{\partial}{\partial x} \left[\nu_t \frac{\partial(hv)}{\partial x} \right] + \frac{\partial}{\partial y} \left[\nu_t \frac{\partial(hv)}{\partial y} \right]. \quad (6)$$

2.1. Depth-Averaged k - ϵ Model. The eddy viscosity coefficient ν_t in the standard k - ϵ model is expressed by the following equation:

$$\nu_t = C_\mu \frac{k^2}{\epsilon}, \quad (7)$$

where C_μ is a model constant. k and ϵ are obtained by the following equations [16]:

$$\begin{aligned} \frac{\partial k}{\partial t} + u \frac{\partial k}{\partial x} + v \frac{\partial k}{\partial y} &= \frac{\partial}{\partial x} \left(\frac{\nu_t}{\sigma_k} \frac{\partial k}{\partial x} \right) + \frac{\partial}{\partial y} \left(\frac{\nu_t}{\sigma_k} \frac{\partial k}{\partial y} \right) + P_h \\ &\quad + P_{kv} - \epsilon, \\ \frac{\partial \epsilon}{\partial t} + u \frac{\partial \epsilon}{\partial x} + v \frac{\partial \epsilon}{\partial y} &= \frac{\partial}{\partial x} \left(\frac{\nu_t}{\sigma_\epsilon} \frac{\partial \epsilon}{\partial x} \right) + \frac{\partial}{\partial y} \left(\frac{\nu_t}{\sigma_\epsilon} \frac{\partial \epsilon}{\partial y} \right) \\ &\quad + C_{1\epsilon} \frac{\epsilon}{k} P_h + P_{\epsilon v} - C_{2\epsilon} \frac{\epsilon^2}{k}, \end{aligned} \quad (8)$$

where $C_{1\epsilon}$, $C_{2\epsilon}$, σ_k , and σ_ϵ are model constants whose respective values are shown in Table 1. Note that P_{kv} and $P_{\epsilon v}$ are calculated with the following equations:

$$\begin{aligned} P_{kv} &= C_k \frac{u_*^3}{h}, \\ P_{\epsilon v} &= C_\epsilon \frac{u_*^4}{h^2}. \end{aligned} \quad (9)$$

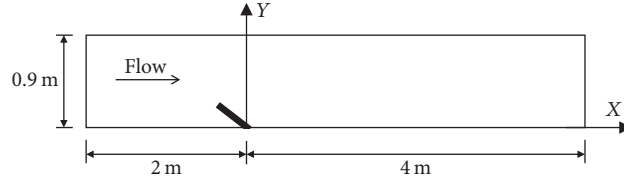


FIGURE 1: Groin orientation for 45° angled to the direction of flow (case 1).

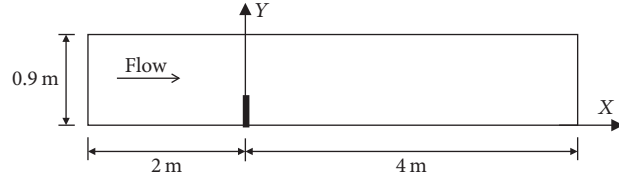


FIGURE 2: Groin orientation for 90° angled to the direction of flow (case 2).

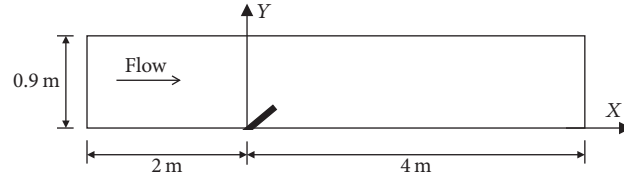


FIGURE 3: Groin orientation for 135° angled to the direction of flow (case 3).

TABLE 1: Model constants for nonlinear k - ϵ model [16].

C_μ	$C_{1\epsilon}$	$C_{2\epsilon}$	σ_k	σ_ϵ
0.09	1.44	1.92	1.0	1.3

3. Numerical Tests

3.1. Flow Domain and Hydraulic Parameters. The hydraulic parameters for different test cases that were simulated are shown in Table 2. The parameters for case 2 of flows in a straight open channel with groin of 90° angle to the direction of flow were taken the same as the experiments by Rajaratnam and Nwachukwu [7]. In their experiments, a 37 m long, 0.9 m wide, and 0.76 m deep flume with smooth bed and sides were used. The groin was an aluminum plate with 3 mm thickness and 152 mm length and was projected partly above the water surface. The hydraulic parameters for the 45° and 135° angled groin are the same as case 2.

Figure 2 shows the sketch of the flow domain for flows in a straight open channel with groin of 90° angled to the direction of flow which was performed under the same conditions of the experiments conducted by Rajaratnam and Nwachukwu [7]. Figures 1 and 3 show the sketch of the flow domain for 45° and 135° which were performed under the same conditions as case 2. For all these cases, 120 × 20 grids were used considering fixed bed condition. Figure 4 shows a

sample of computational mesh that consists of 120 grids in the longitudinal direction and 20 grids in transverse directions.

For all the cases of numerical simulation, the computational domain was 6 m in length and 0.9 m in width. The upstream and downstream boundaries were located at 2 m and 4 m away from the groin, respectively. The constant discharge at upstream was 0.043 m³/s, and at the downstream the constant flow depth was 0.189 m. Manning's roughness coefficient $n = 0.01$ and the time step $\Delta t = 0.003$ sec are assigned in the present computation. The simulations are performed in fixed bed condition with bottom slope, $S_o = 0.001$.

Quanhong and Pengzhi [17] also used the same experimental data of Rajaratnam and Nwachukwu [7] to validate their model. Governing equations of their model were shallow water equations and depth-averaged k - ϵ model as the turbulence model. According to Quanhong and Pengzhi [17] model, the computational domain was 6 m in length and 0.9 m in width. Flow flux of 0.047817 m²/s and water depth of 0.189 m are specified at the upstream and downstream boundaries, respectively. For the same flow geometry and hydraulic conditions, Sarveram et al. [2] also simulated the flow field around 90° groin using semi-implicit semi-Lagrangian method and compared their computed results with the Rajaratnam and Nwachukwu's experimental result. In the present study, the simulated flow field is compared with previous experimental results of Rajaratnam and

TABLE 2: Hydraulic parameters for the simulated cases.

Cases	Groin position	L (m)		W (m)	Q _o (m ³ /s)	h _o (m)	S _o	n
		U/S	D/S					
Case 1	45°	2	4	0.9	0.043	0.189	0.001	0.01
Case 2	90°	2	4	0.9	0.043	0.189	0.001	0.01
Case 3	135°	2	4	0.9	0.043	0.189	0.001	0.01

Here, L = length of the straight channel, W = width of channel, Q_o = upstream discharge, h_o = water depth at downstream, S_o = channel slope, and n = Manning's roughness coefficient.

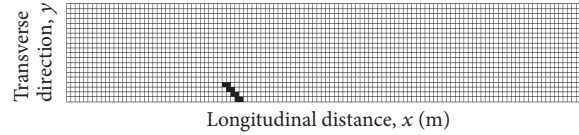


FIGURE 4: Plan of input grid for simulation of flow around groin with 45° angle (case 1).

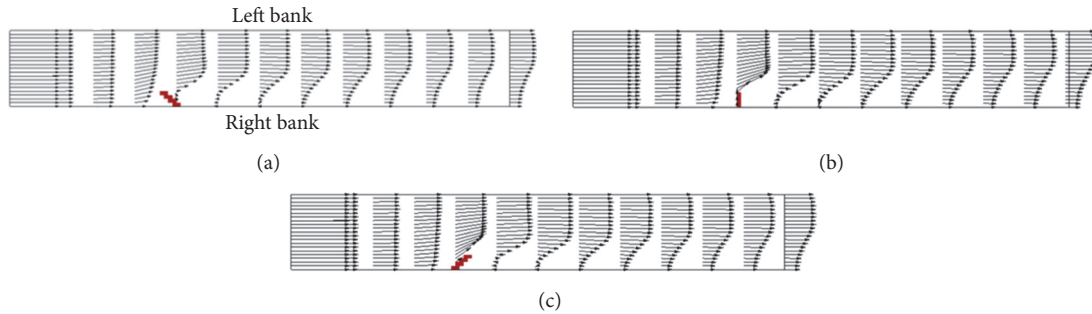


FIGURE 5: Computed velocity vector for (a) case 1, (b) case 2, and (c) case 3 developed by iRIC Nays2DH.

Nwachukwu [7] as well as previous simulation results of Quanhong and Pengzhi [17] and Sarveram et al. [2].

3.2. Computational Scheme. The governing equations for mean velocities and turbulent flows were discretized with the finite difference method based on full staggered boundary fitted coordinate system. The basic equations are discretized as fully explicit forms and solved successively with the time increment step by step. It is solved using iterative procedure at each time step. Constant discharge at upstream and constant depth with zero velocity gradients were given as downstream boundary conditions. Finite difference scheme was used for the solution of the equations, where the nonlinear convection terms were discretized with the upwind scheme.

4. Simulated Flow Field

Figures 5 and 6 show the predicted velocity vector of the flow field around the groin for different angles with the flow. For all the cases, the model is found to reproduce the general flow features of the flow field around the groin successfully. From the simulated results, it is seen that at the upstream

boundary the flow is uniform and hence the flow vectors are straight and parallel to bank. However, when the flow approaches the groin, the flow is deviated towards the left bank compared to the right due to obstruction of flow by the groin. A recirculation zone is observed just downstream region of the groin for all the cases.

Figure 7 shows the streamline around a groin, which is obtained by the present study. From the streamline contour, it is also found that at the position of groin head the flow is deviated towards the opposite bank and at the downstream of the groin there is a circulation. Figures 6 and 7 depict that for case 1 (45° groin) the deviations of vectors and streamlines are higher compared to case 2 (90° groin). 135° groin for case 3 shows the least deviation compared to other cases. The length of circulation zone at downstream of the groin is also higher for case 1 and lower in case 3.

5. Comparison of Simulated Results with Previous Studies

Simulated results such as computed velocity profiles and bed shear stress profiles for 90° groins (case 2) are compared with

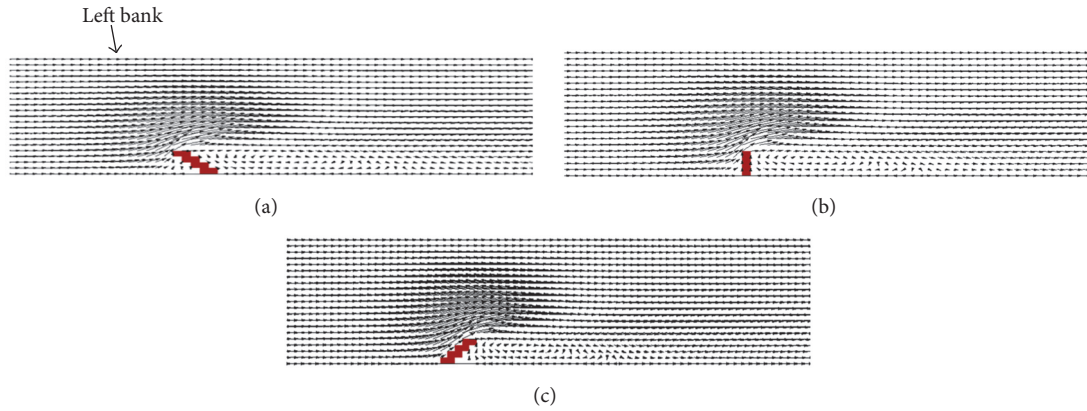


FIGURE 6: Computed velocity vector and recirculation zone around groin for (a) case 1, (b) case 2, and (c) case 3 developed by iRIC Nays2DH.

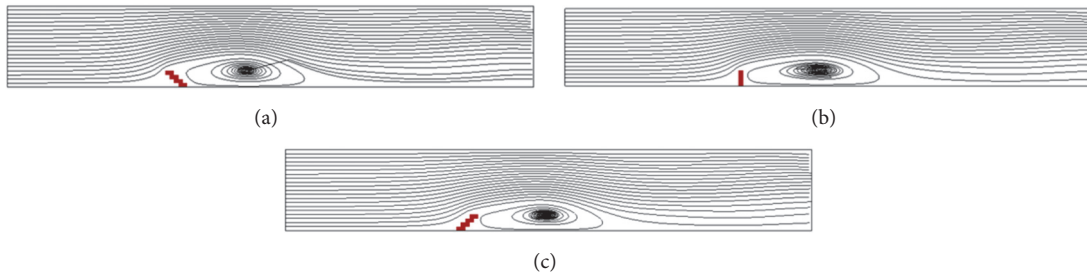


FIGURE 7: Streamline around a groin for (a) case 1, (b) case 2, and (c) case 3 developed by iRIC Nays2DH.

previous experimental as well as available previous simulation results. The comparison is described in the following sections.

5.1. Velocity Profiles. For 90° groins, the resultant velocity profiles are compared with available experimental results measured at $y/l = 1.0, 1.5, 2.0, 3.0,$ and 4.0 , where $l = 152$ mm is the length of the groin. Figure 8 shows the comparison of velocity profiles for different lateral distances (y/l). Here, the initial flow velocity and water depth were $U_o = 0.253$ m/s and $H = 0.189$ m, respectively. In the figure, all the velocities were normalized by U_o . In the figure, $x/l = 0$ indicated the groin position along flume direction.

Good agreements are found between experimental and calculated results. For the velocity profiles, the only large discrepancy occurs at $y/l = 2$, where the calculated results underpredict the experimental data in the downstream zone of the groin. It is noticed that the numerical results reported by Quanhong and Pengzhi [17] and Sarveram et al. [2] also underpredicted the experimental data largely in this region. This may be due to the very high velocity gradient arising in this region which makes the depth-averaged model inapplicable. Otherwise, the possible reason may come from the experimental measurement errors in this region [17].

5.2. Bed Shear Stress Profiles. Figure 9 shows comparison of bed shear stress profiles (τ) of predicted results with the available previous studies. In the figure, all the shear stresses are normalized by $\tau_o = 0.1293$ N/m². The comparison between the numerical results and experimental data shows reasonable agreement. For the lateral sections up to $y/l = 2$, the simulated results underpredict the downstream shear stress slightly. The numerical results reported by Quanhong and Pengzhi [17] also show similar prediction. It may be the deficiency of the depth-averaged model to account for the high velocity gradient arising very near to the groin.

6. Simulation Results for Different Cases

6.1. Predicted Velocity Profiles. Figure 10 shows the comparison among predicted velocity profiles (W) for case 1, case 2, and case 3. For each case, the longitudinal velocity profiles are compared at a lateral position of $y/l = 1.0, 1.5, 2.0, 3.0,$ and 4.0 . In the figure, all the velocities are normalized by $U_o = 0.253$ m/s and here $x/l = 0$ indicates the groin position in the longitudinal direction. The comparisons among the three cases show reasonable differences. Along line $y/l = 1$, the peak of velocities is found at longitudinal distances of $x/l = -0.28, 0.0,$ and 0.56 for case 1, case 2, and case 3, respectively. For $y/l = 1.0$, in all the cases, the velocity is found to be

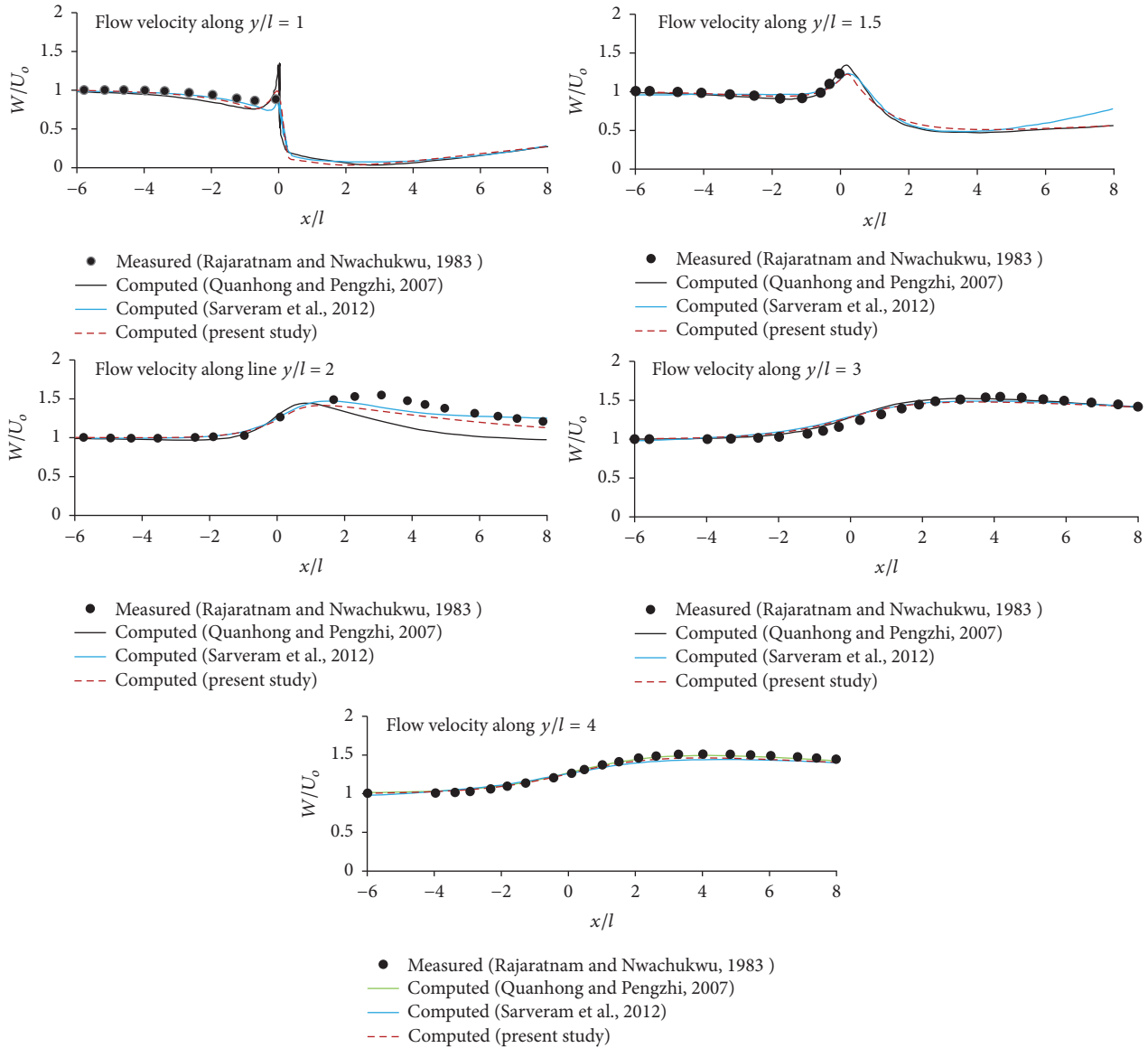


FIGURE 8: Comparison of resultant velocity profiles (W) with the available previous studies for 90° groin (case 2).

decreased from upstream velocity just before the position of groin head. In other words, in addition to the circulation zone at downstream of groin, a small low velocity zone is observed just upstream of groin at right bank. Along the line $y/l = 1.5$, the peak of velocities is found at longitudinal distances of $x/l = -1.0, 0.22,$ and 0.67 for case 1, case 2, and case 3, respectively. These peak velocities are found to be decayed with the longitudinal distance x/l . For $y/l = 2$, the peaks of velocities are found at a distance of $x/l = -0.11, 1.22,$ and 2.54 for case 1, case 2, and case 3, respectively. For $y/l \geq 2$, the decay of velocity along the downstream is found to be slower compared to the region $y/l \leq 1.5$. Along the line $y/l = 3$, the peak of velocities is found at longitudinal distances of $x/l = 2.87, 3.53,$ and 3.88 for case 1, case 2, and case 3, respectively. Along the line $y/l = 4$, the peak of velocities is

found at longitudinal distances of $x/l = 3.33, 3.89,$ and 4.44 for case 1, case 2, and case 3, respectively.

From the figures, it is observed that the peak of velocity is found maximum at the position of head of groin when $y/l = 1$. However, this position of maximum velocity is found to be shifted towards downstream with increasing y/l . The maximum velocity for case 3 is found lower than the other two cases for all the sections of y/l . However, W/U_0 for 90° groin is found maximum for $y/l \leq 2$; and for $y/l > 2$, the velocity is maximum for 45° angled groin.

6.2. Predicted Bed Shear Stress Profiles. Figure 11 shows the predicted bed shear stress profiles (τ) of the proposed model for case 1, case 2, and case 3. For each case, the longitudinal

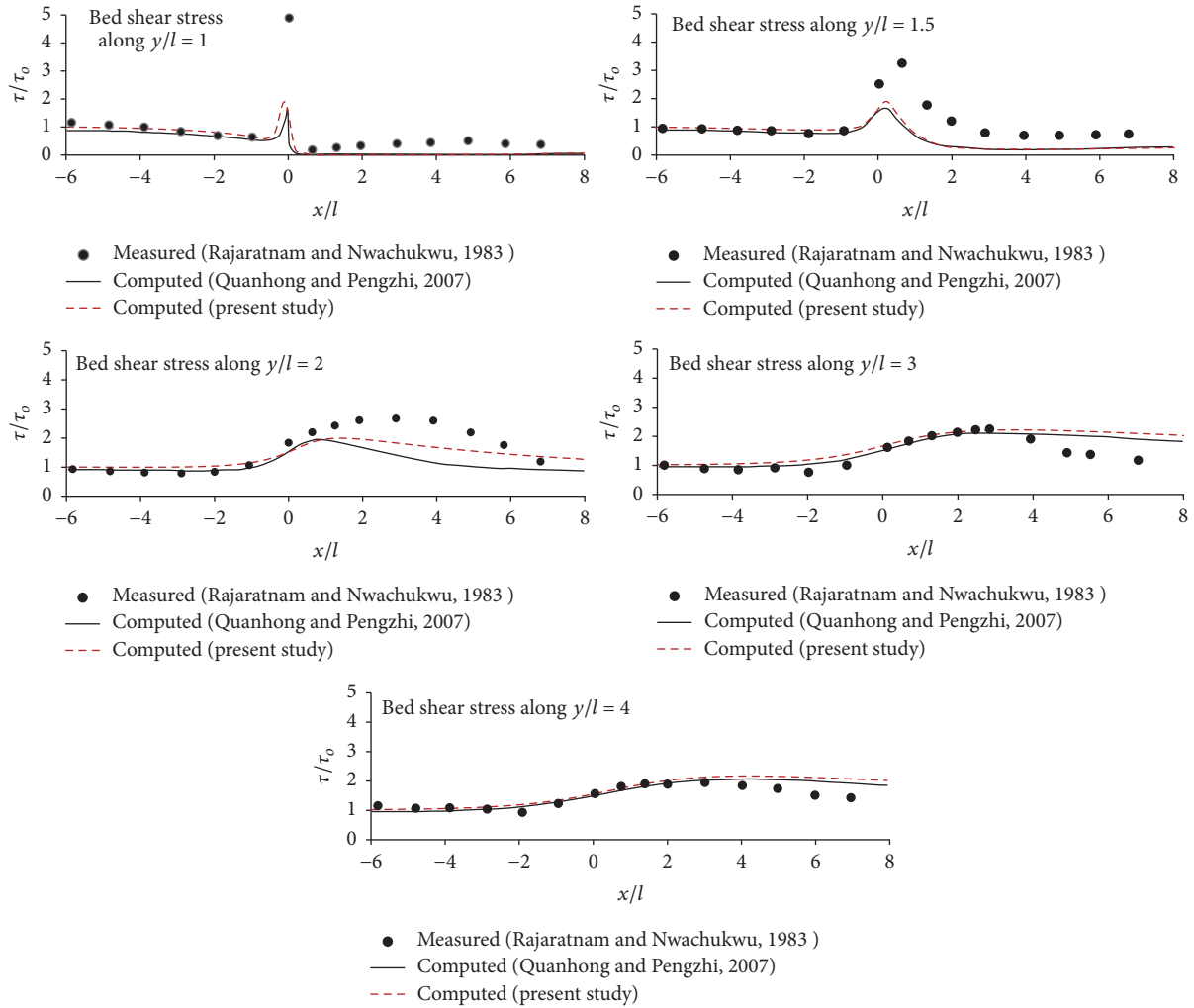


FIGURE 9: Comparison of bed shear stress profiles (τ) with the available previous studies for 90° groin (case 2).

shear stress profiles are compared at a lateral position of $y/l = 1.0, 1.5, 2.0, 3.0,$ and 4.0 . In the figure, all the shear stresses are normalized by $\tau_o = 0.1293 \text{ N/m}^2$, which is the value of upstream region. Here, $x/l = 0$ is the groin position along longitudinal direction. The profiles of bed shear stress are found in similar pattern of velocity profiles. For different values of y/l , the peak of shear stresses is found at the same longitudinal distances (x/l) as reported in velocity profiles. For $y/l = 1.0$, in all the cases, the shear stress is found to be decreased from its upstream value just before the position of groin head.

From the figures, it is observed that the peak of bed shear stress is found maximum at the position of head of groin when $y/l = 1$. However, this position of maximum bed shear stress is found to be shifted towards downstream with increasing y/l . These peak shear stresses are found to be decayed with the longitudinal distance x/l . However, for $y/l \geq 2$, the decay of shear stress along the downstream is found to be slower compared to the region $y/l \leq 1.5$. The

maximum bed shear stress for case 3 is found lower than the other two cases for all the sections of y/l . However, τ/τ_o for 90° groin is found maximum for $y/l \leq 1.5$, and for $y/l \geq 2$, the velocity is maximum for 45° angled groin.

6.3. Velocity and Bed Shear Stress Contour. Figure 12 shows the simulated velocity contour in shaded color for case 1, case 2, and case 3, respectively. The results are found to be similar in nature. For all the cases, the velocity contour along the left bank is higher than the right bank at the downstream region of the groin; it indicates the deflection of flow towards right bank and sheltering of flow by groin at east bank. The downstream circulation zone is found to be larger for 45° groin compared to 90° groin; similarly the circulation zone for 90° groin is found to be larger compared to 135° groin.

In the figure, the flow field is seen to be divided into four distinct regions: (i) the uniform flow at upstream end, (ii) big circulation of low velocity zone at the downstream of the groin created due to sheltering of groin where the velocity

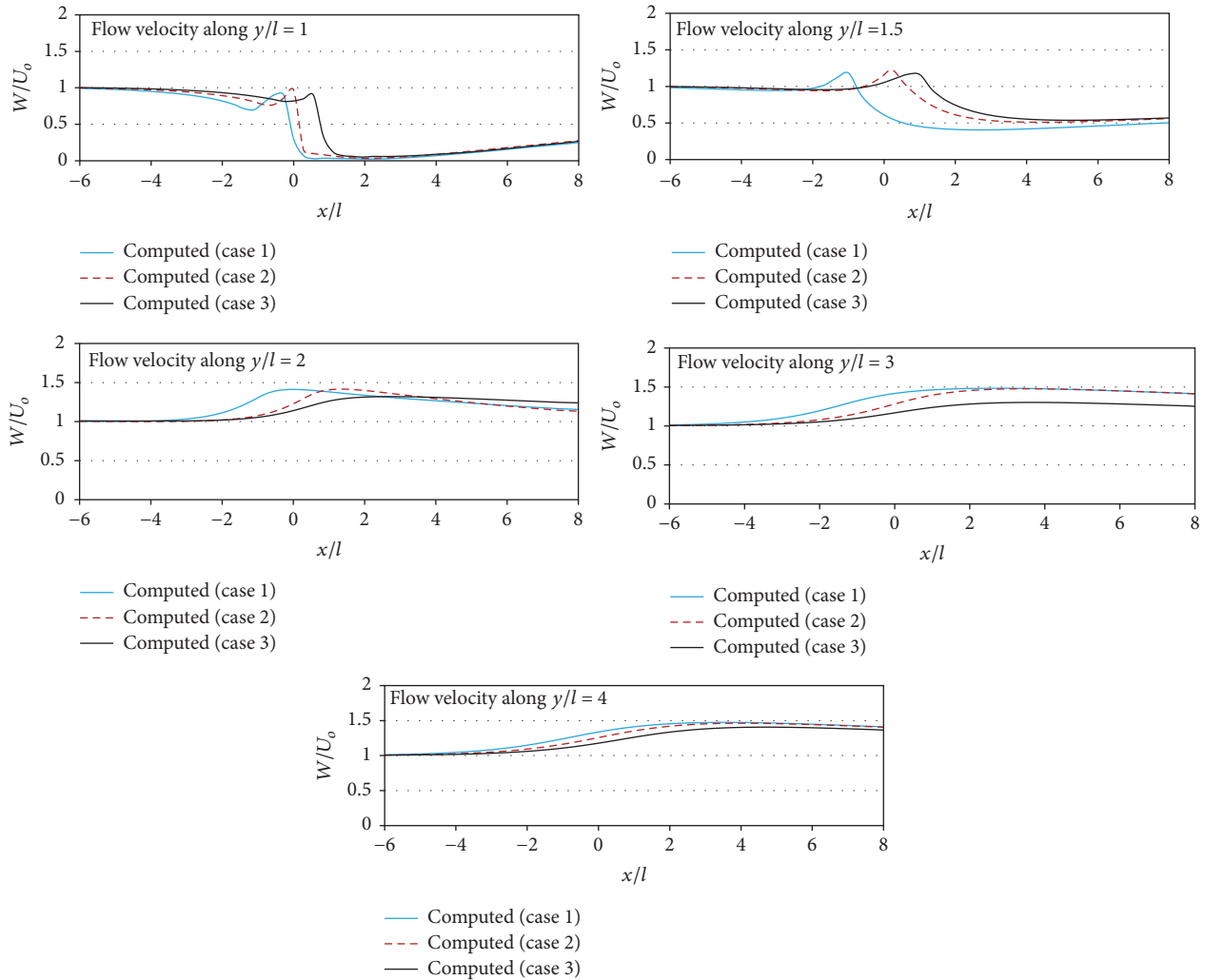


FIGURE 10: Comparison between resultant velocity profiles (W) of present study for case 1, case 2, and case 3 along lateral distance, $y/l = 1, 1.5, 2, 3,$ and 4 .

is zero in the center of the circulation zone, (iii) a small low velocity zone near the foot at the upstream of groin, and (iv) high velocity zone opposite to the circulation zone created due to the deflected flow. The high velocity zone is found to be decayed towards downstream and the low velocity in circulating zone is found to be regained.

Figure 13 shows the simulated bed shear stress contour in shaded color for case 1, case 2, and case 3, respectively. The results are found to be similar in nature. Like the velocity contour, for all the cases, the shear stress contour along the left bank is higher than the right bank at the downstream region of the groin. Four distinct flow regions as described in velocity contour are also clearly visible in the contour of shear stress.

7. Conclusions

This simulation has provided us with detailed information regarding the flow pattern, the velocity, and bed shear stress profiles of a groin. This adds to the effort of work done by others on different types of groins. In the simulation,

the general flow features around a groin is reproduced successfully. The flow field is found to be divided into four distinct regions: (i) the uniform flow at upstream end, (ii) big circulation of low velocity zone at the downstream of the groin created due to sheltering of groin where the velocity is zero in the center of the circulation zone, (iii) a small low velocity zone near the foot at the upstream of groin, and (iv) high velocity zone opposite to the circulation zone created due to the deflected flow. The high velocity zone is found to be decayed towards downstream and the low velocity in circulating zone is found to be regained.

The computed velocity and bed shear stress profiles of present study are compared among case 1, case 2, and case 3. From the simulation, it is observed that the peak of velocity and bed shear stress is found maximum at the position of head of groin when lateral distance $y/l = 1$, where l is the groin length. The position of maximum velocity and bed shear stress is found to be shifted towards downstream with increasing y/l . The maximum velocity and bed shear stress for 135° groin are found lower than the other two cases for all

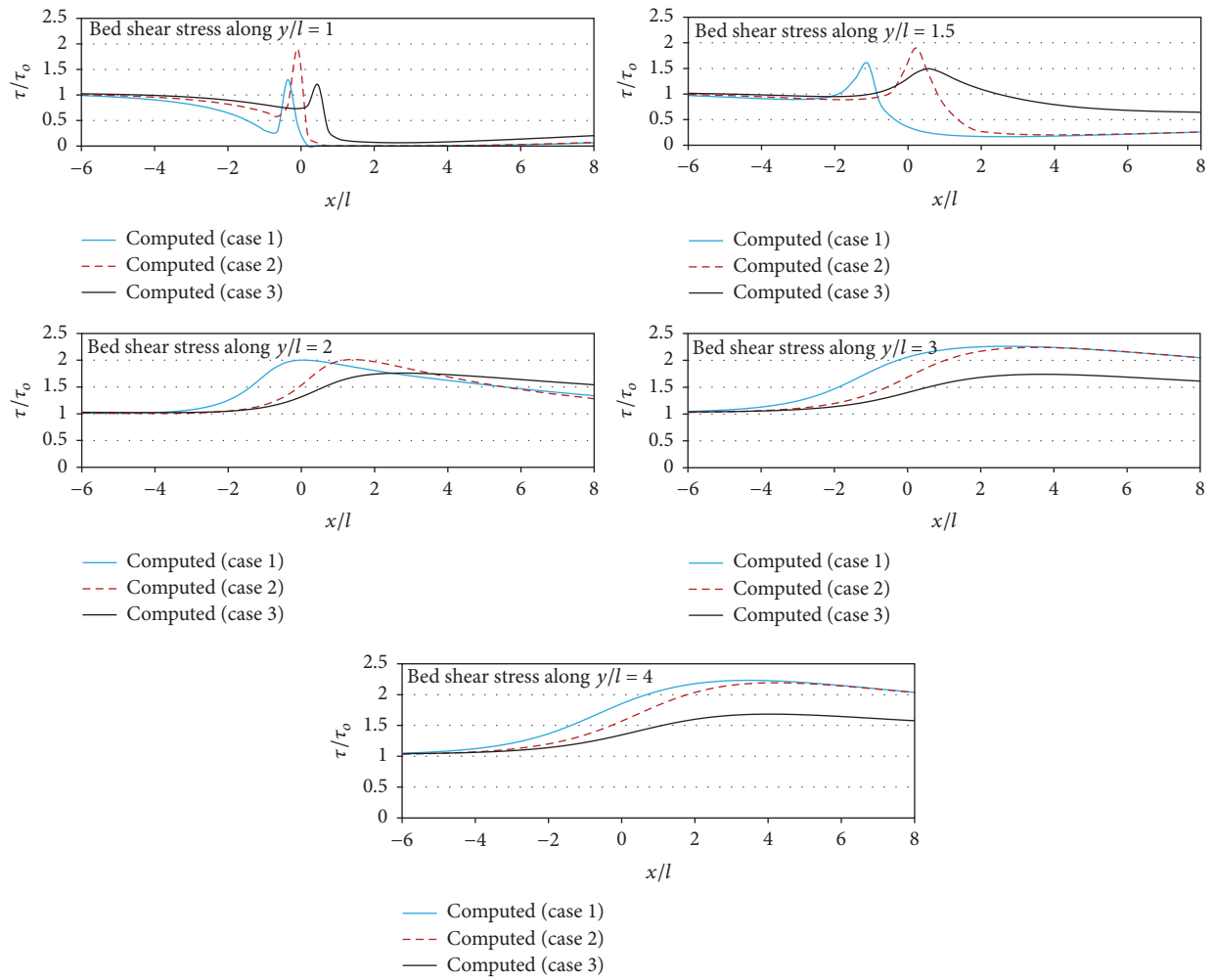


FIGURE 11: Comparison between computed bed shear stress profiles (τ) of proposed model for case 1, case 2, and case 3 along lateral distance, $y/l = 1, 1.5, 2, 3,$ and 4 .

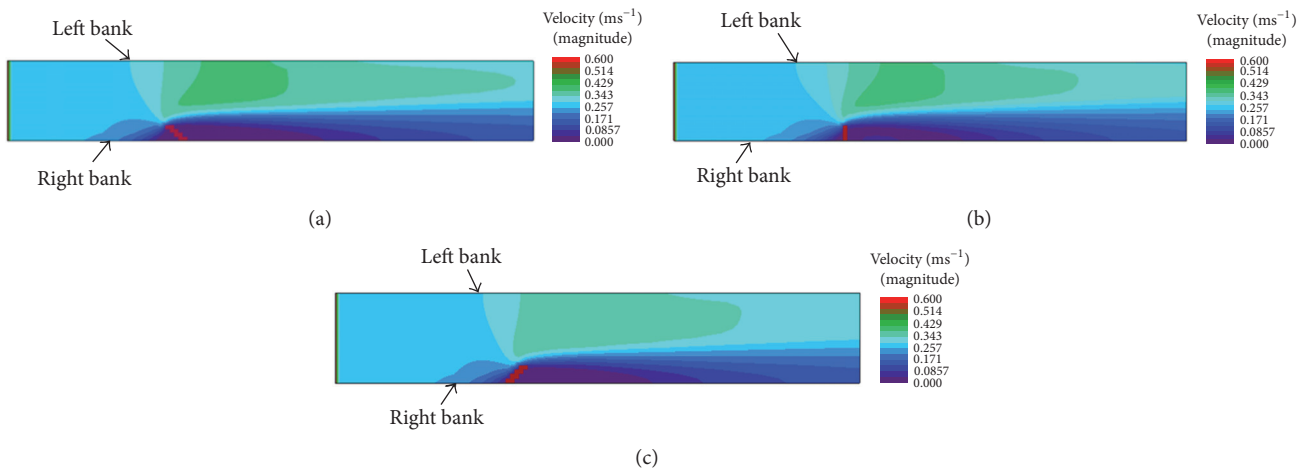


FIGURE 12: Velocity contoured around a groin for (a) case 1, (b) case 2, and (c) case 3 at the end of simulation by iRIC Nays2DH.

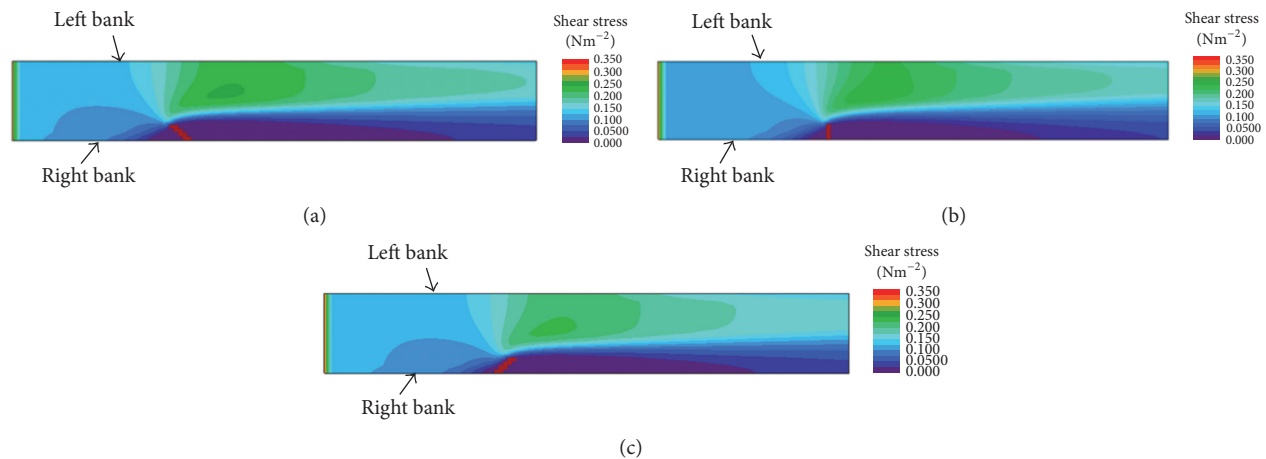


FIGURE 13: Bed shear stress contour around a groin for test (a) case 1, (b) case 2, and (c) case 3 at the end of simulation by iRIC Nays2DH.

the sections of y/l , W/U_o and τ/τ_o for 90° groin are found maximum for $y/l \leq 2$, and for $y/l > 2$, the velocity and bed shear stress are maximum for 45° angled groin. The downstream circulation zone is found to be larger for 45° groin compared to 90° groin; similarly, the circulation zone for 90° groin is found larger compared to 135° groin.

In order to validate the present model, the computed results are compared with previous numerical and experimental results. The comparison between numerical and experimental results showed that except in areas where strong downward flow is observed there are good agreements between experimental and calculated results.

Conflicts of Interest

The authors declare that there are no conflicts of interest regarding the publication of this paper.

References

- [1] L. G. T. De Azevedo, T. K. Gates, D. G. Fontane, J. W. Labadie, and R. L. Porto, "Integration of water quantity and quality in strategic river basin planning," *Journal of Water Resources Planning and Management*, vol. 126, no. 2, pp. 85–97, 2000.
- [2] H. Sarveram, A. Shamsai, and M. A. Banihashemi, "Two-dimensional simulation of flow pattern around a groyne using semi-implicit semi-Lagrangian method," *International Journal of the Physical Sciences*, vol. 7, no. 20, 2012.
- [3] T. YiQun, Z. Hua, and W. YuanDong, "Characteristics of strain accumulation of reinforced soft clay around tunnel under subway vibration loading," *Journal of Tongji University. Natural Science*, vol. 39, no. 7, pp. 972–977, 2011.
- [4] M. Vaghefi, M. Ghodsian, and S. A. A. S. Neyshabouri, "Experimental study on scour around a T-shaped spur dike in a channel bend," *Journal of Hydraulic Engineering*, vol. 138, no. 5, pp. 471–474, 2012.
- [5] M. J. Uddin, M. M. Hossain, and M. S. Ali, "Local scour around submerged bell mouth groin for different orientations," *Journal of Civil Engineering*, vol. 39, no. 1, pp. 1–18, 2011.
- [6] H. K. Yeo, J. G. Kang, and S. J. Kim, "An experimental study on tip velocity and downstream recirculation zone of single groynes of permeability change," *KSCE Journal of Civil Engineering*, vol. 9, no. 1, pp. 29–38, 2005.
- [7] N. Rajaratnam and B. A. Nwachukwu, "Flow near groin-like structures," *Journal of Hydraulic Engineering*, vol. 109, no. 3, pp. 463–480, 1983.
- [8] M. S. Ali, T. Hosoda, and I. Kimura, "Unsteady RANS and les simulation of an ideal Rankine vortex decay," *Advances in Civil Engineering*, vol. 2012, Article ID 523839, 8 pages, 2012.
- [9] M. S. Ali, *Model Refinements of Unsteady RANS and Its Practical Applications in the Field of Hydraulic Engineering [Ph.D. thesis]*, Department of Urban Management, Kyoto University, Japan, 2008.
- [10] S. Y. Jaw and C. J. Chen, "Present status of second-order closure turbulence models. I: overview," *Journal of Engineering Mechanics*, vol. 124, no. 5, pp. 485–501, 1998.
- [11] M. S. Ali, T. Hosoda, and I. Kimura, "Development of a nonlinear $k-\epsilon$ model incorporating strain and rotation parameters for prediction of complex turbulent flows," *International Journal of Partial Differential Equations*, Art. ID 105809, 15 pages, 2015.
- [12] I. Kimura, W. S. J. Uijtewaal, T. Hosoda, and M. S. Ali, "URANS computations of shallow grid turbulence," *Journal of Hydraulic Engineering*, vol. 135, no. 2, pp. 118–131, 2009.
- [13] W. Rodi, *Turbulence models for environmental problems, Prediction Methods for Turbulent Flows*, (1979).
- [14] iRIC (2013) Nays 2D, International River Interface Cooperative, Hokkaido Univ., Japan, <http://i-ric.org/en/introduction>.
- [15] C.-L. Jang and Y. Shimizu, "Numerical simulation of relatively wide, shallow channels with erodible banks," *Journal of Hydraulic Engineering*, vol. 131, no. 7, pp. 565–575, 2005.
- [16] I. Kimura and T. Hosoda, "A non-linear $k-\epsilon$ model with realizability for prediction of flows around bluff bodies," *International Journal for Numerical Methods in Fluids*, vol. 42, no. 8, pp. 813–837, 2003.
- [17] L. Quanhong and L. Pengzhi, "Numerical simulation of recirculating flow near a groyne," in *Proceedings of the The 2nd International Conference on Marine Research and Transportation*, pp. 61–68, Ischia, Naples, Italy, 2007.

Research Article

Comparison of Different Turbulence Models for Numerical Simulation of Pressure Distribution in V-Shaped Stepped Spillway

Zhaoliang Bai and Jianmin Zhang

State Key Laboratory of Hydraulics and Mountain River Engineering, Sichuan University, Chengdu 610065, China

Correspondence should be addressed to Jianmin Zhang; zhangjianmin@scu.edu.cn

Received 23 March 2017; Accepted 1 August 2017; Published 7 September 2017

Academic Editor: Alistair Borthwick

Copyright © 2017 Zhaoliang Bai and Jianmin Zhang. This is an open access article distributed under the Creative Commons Attribution License, which permits unrestricted use, distribution, and reproduction in any medium, provided the original work is properly cited.

V-shaped stepped spillway is a new shaped stepped spillway, and the pressure distribution is quite different from that of the traditional stepped spillway. In this paper, five turbulence models were used to simulate the pressure distribution in the skimming flow regimes. Through comparing with the physical value, the realizable k - ϵ model had better precision in simulating the pressure distribution. Then, the flow pattern of V-shaped and traditional stepped spillways was given to illustrate the unique pressure distribution using realizable k - ϵ turbulence model.

1. Introduction

The unique structure of the stepped spillways causes abundant vortices near the steps [1–3], which results in high energy dissipation and aeration than that of smooth spillways [4, 5]. For these reasons, the stepped spillways have been widely used [6, 7].

Considering that the flow pattern of the stepped spillway reflects the hydraulic characteristics of the flow, many scholars have also studied the flow regimes. The flow regimes of a stepped spillway can be divided into nappe flow, transition flow, and skimming flow [8–10]. Pressure distribution in stepped spillways also became a research focus for negative pressure on the step surface which may lead to cavitation damage. Many scholars have studied the pressure distributions of stepped spillways through physical models, such as Zhang et al. [11], Fratino et al. [12], Sánchez-Juny et al. [13, 14], Amador et al. [15], Zhang et al. [16], and Dhattrak and Tatewar [17] and so on. With the development of computer science and computational technology, the numerical method has become an efficient method to study the pressure distribution of stepped spillways. Chen et al. [2] studied the pressure distribution of traditional stepped spillway using k - ϵ turbulence model and satisfactory results were obtained. Qian et al.

[18] compared four turbulence models (realizable k - ϵ model, SST k - ϵ model, v^2 - f model and LES model) and found that the realizable k - ϵ model was the most efficient in simulating flow overstepped spillways which involves rotation. And the pressure field was studied using the realizable k - ϵ model. Chakib [19] also got the contours of pressure distribution in simulating air-water interaction using k - ϵ turbulence model and VOF model. Daneshfaraz et al. [20] adopted standard k - ϵ , renormalization group k - ϵ , and standard k - ω turbulence model to simulate the four step arrangements stepped spillways. And pressure distribution was studied by RNG k - ϵ turbulence model, which was regarded as the optimal turbulence model through comparing the physical value and numerical value of water level.

In this paper, the stepped spillways of $\theta = 120^\circ$ and $\theta = 180^\circ$ are named as V-shaped and traditional stepped spillway, respectively (shown in Figure 1). V-shaped stepped spillway is a new type of stepped spillways, which has distinguished three-dimensional flow program and greater aerated characteristic. In this paper, the pressure distribution along the V-shaped stepped spillway in the skimming flow regime was studied through numerical simulations with five kinds of turbulence models and the unique pressure distribution was

analyzed through the comparison of the flow pattern between traditional and V-shaped stepped spillways. These results can be used to choose a better turbulence model to study the pressure distribution of V-shaped stepped spillway.

2. Numerical Simulation

Fluent software was used to perform these simulations using the finite volume method (FVM). The numerical model of the stepped spillway (shown in Figure 1) consists of a press slope section, a smooth section, a stepped section, and tail water section. The chute width is $B = 0.4$ m, the height of the model inlet is $h = 0.12$ m, and the outlet of the press slope section is 0.08 m. The step section consists of 56 steps, which were numbered #1 to #56. The first 28 steps are transitional steps for improving the flow patterns; then there are 28 uniform steps (6 cm high, 12 cm long). The slope of the stepped spillway is 1V:2H.

2.1. Fluid Volume Model. The volume of fluid (VOF) was used to track the air-water interface, which was presented by Hirt and Nichols [21]. In each computational cell, the sum of the volume fractions of air, α_a , and water, α_w , is unity and can be given as

$$\alpha_w + \alpha_a = 1; \quad 0 \leq \alpha_w, \alpha_a \leq 1. \quad (1)$$

In this approach, the tracking interface between air and water was accomplished by the solution of the continuity equation for the volume fraction of water:

$$\frac{\partial \alpha_w}{\partial t} + \frac{\partial \alpha_w u_i}{\partial x_i} = 0. \quad (2)$$

2.2. Turbulence Models

2.2.1. ST k - ε Model for the VOF Flow. The standard (ST) k - ε turbulence model presented by Launder and Spalding [22] was useful in practical engineering flow calculations for the advantages of economy and reasonable accuracy. The equations of turbulent kinetic energy, k , and its dissipation rate, ε , are as follows:

$$\begin{aligned} \frac{\partial (\rho k)}{\partial t} + \frac{\partial}{\partial x_i} (\rho k u_i) &= \frac{\partial}{\partial x_j} \left[\left(\mu + \frac{\mu_t}{\sigma_k} \right) \frac{\partial k}{\partial x_j} \right] + G_k \\ &+ G_b - \rho \varepsilon - Y_M + S_k \\ \frac{\partial (\rho \varepsilon)}{\partial t} + \frac{\partial}{\partial x_i} (\rho \varepsilon u_i) &= \frac{\partial}{\partial x_j} \left[\left(\mu + \frac{\mu_t}{\sigma_\varepsilon} \right) \frac{\partial \varepsilon}{\partial x_j} \right] \\ &+ C_{1\varepsilon} \frac{\varepsilon}{k} (G_k + C_{3\varepsilon} G_b) \\ &- C_{2\varepsilon} \rho \frac{\varepsilon^2}{k} + S_\varepsilon, \end{aligned} \quad (3)$$

where G_k , G_b are the generation of turbulence kinetic energy due to the mean velocity gradients and buoyancy, respectively; Y_M is the contribution of the fluctuating dilatation in compressible turbulence to the overall dissipation rate; u_i is

the mean velocity component in the i th direction; μ_t is the turbulent viscosity and calculated by $\mu_t = \rho C_\mu (k^2/\varepsilon)$; C_μ , $C_{1\varepsilon}$, $C_{2\varepsilon}$, σ_k , and σ_ε are model constants which are specified as follows: $C_\mu = 0.09$, $C_{1\varepsilon} = 1.44$, $C_{2\varepsilon} = 1.92$, $\sigma_k = 1.0$, and $\sigma_\varepsilon = 1.3$. S_k and S_ε are user-defined source terms.

This model is a semiempirical model based on transport equations for turbulence kinetic energy and turbulence kinetic energy dissipation rate. For its assumption of fully turbulent, it is valid only for fully turbulent flows.

2.2.2. RNG k - ε Model for the VOF Flow. The renormalization group (RNG) k - ε turbulence model was presented by Yakhot and Orszag [23]. The equations of turbulent kinetic energy, k , and its dissipation rate, ε , are as follows:

$$\begin{aligned} \frac{\partial (\rho k)}{\partial t} + \frac{\partial}{\partial x_i} (\rho u_i k) &= \frac{\partial}{\partial x_j} \left[\alpha_k \mu_{\text{eff}} \frac{\partial k}{\partial x_j} \right] + G_k + G_b \\ &- \rho \varepsilon - Y_M + S_k \\ \frac{\partial (\rho \varepsilon)}{\partial t} + \frac{\partial}{\partial x_i} (\rho u_i \varepsilon) &= \frac{\partial}{\partial x_j} \left[\alpha_\varepsilon \mu_{\text{eff}} \frac{\partial \varepsilon}{\partial x_j} \right] \\ &+ C_{1\varepsilon} \frac{\varepsilon}{k} (G_k + C_{3\varepsilon} G_b) \\ &- C_{2\varepsilon} \rho \frac{\varepsilon^2}{k} - R_\varepsilon + S_\varepsilon, \end{aligned} \quad (4)$$

where α_k , α_ε are the inverse effective Prandtl numbers; $C_{1\varepsilon} = 1.42$, $C_{2\varepsilon} = 1.68$ are model constants; $R_\varepsilon = C_\mu \rho \eta^3 (1 - \eta/\eta_0) \varepsilon^2 / (k(1 + \beta \eta^3))$, where $\eta \equiv Sk/\varepsilon$, $\eta_0 = 4.38$, and $\beta = 0.012$.

This model was derived using a rigorous statistical technique. Although it is similar in form to the ST k - ε turbulence model, there are some refinements: (1) adding an additional term in turbulence kinetic energy dissipation rate equation which improves the accuracy for rapidly strained flows; (2) the effect of swirl is included to enhance accuracy for swirling flows; (3) the turbulent Prandtl numbers are got by analytical formula.

2.2.3. RI k - ε Model for the VOF Flow. The realizable (RI) k - ε turbulence model was presented by Shih et al. [24]. The equations of turbulent kinetic energy, k , and its dissipation rate, ε , are as follows:

$$\begin{aligned} \frac{\partial (\rho k)}{\partial t} + \frac{\partial}{\partial x_j} (\rho u_j k) &= \frac{\partial}{\partial x_j} \left[\left(\mu + \frac{\mu_t}{\sigma_k} \right) \frac{\partial k}{\partial x_j} \right] + G_k \\ &+ G_b - \rho \varepsilon - Y_M + S_k \\ \frac{\partial (\rho \varepsilon)}{\partial t} + \frac{\partial}{\partial x_j} (\rho u_j \varepsilon) &= \frac{\partial}{\partial x_j} \left[\left(\mu + \frac{\mu_t}{\sigma_\varepsilon} \right) \frac{\partial \varepsilon}{\partial x_j} \right] \\ &+ \rho C_1 S_\varepsilon - \rho C_2 \frac{\varepsilon^2}{k + \sqrt{\nu \varepsilon}} \\ &+ C_{1\varepsilon} \frac{\varepsilon}{k} C_{3\varepsilon} G_b + S_\varepsilon, \end{aligned} \quad (5)$$

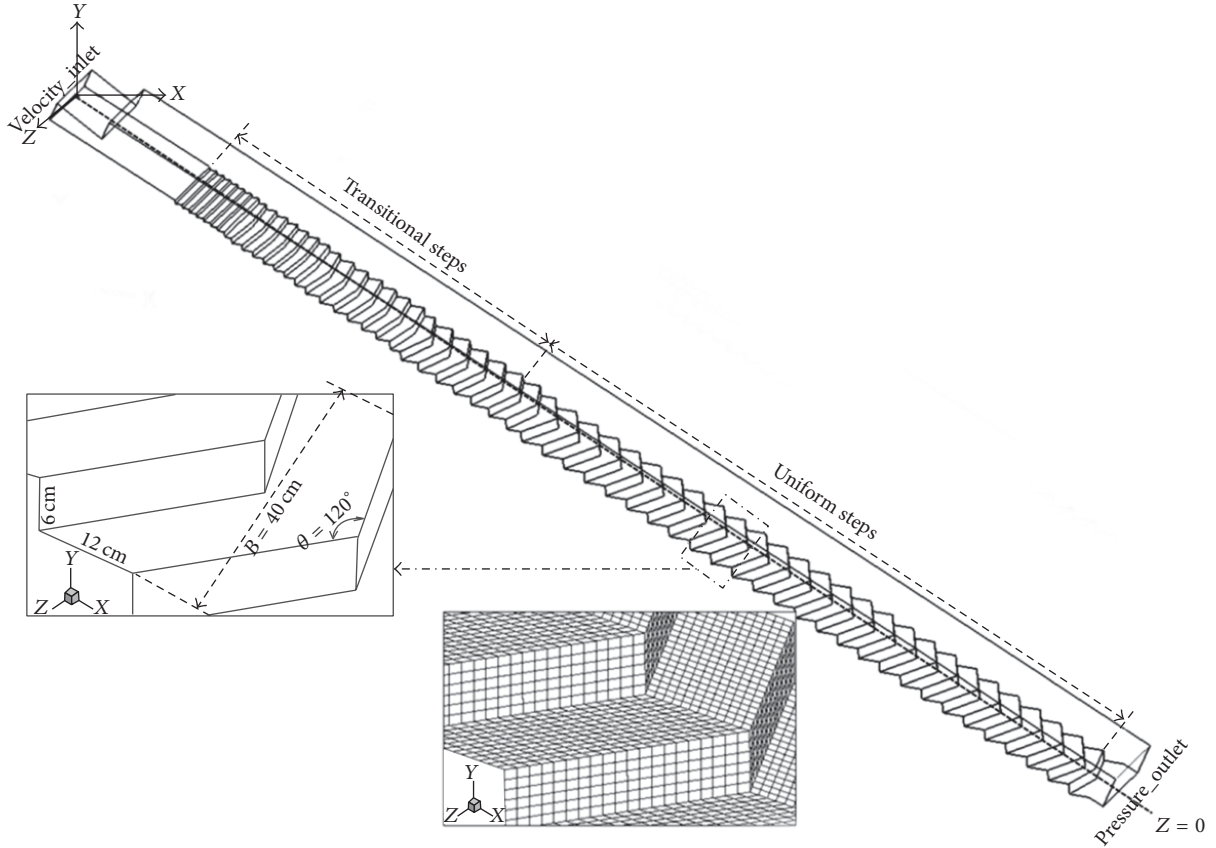


FIGURE 1: The numerical model layout.

where $C_1 = \max[0.43, \eta/(\eta + 5)]$ and $\eta = Sk/\varepsilon$, $S = \sqrt{2S_{ij}S_{ij}}$, where $S_{ij} = 0.5(\partial u_j/\partial x_i + \partial u_i/\partial x_j)$; ν is the turbulent kinematic viscosity; $C_{1\varepsilon} = 1.44$, $C_2 = 1.9$, $\sigma_k = 1.0$, and $\sigma_\varepsilon = 1.2$ are the empirical constants.

This model can accurately simulate the spreading rate of both planar and round jets and the flows involving rotation, boundary layers under strong adverse pressure gradients, separation, and recirculation.

2.2.4. ST k - ω Model for the VOF Flow. The standard (ST) k - ω turbulence model was presented by Wilcox [25], which incorporates modifications for low-Reynolds-number effects, compressibility, and shear flow spreading. The equations of turbulent kinetic energy, k , and its dissipation rate, ω , are as follows:

$$\begin{aligned} \frac{\partial(\rho k)}{\partial t} + \frac{\partial}{\partial x_i}(\rho u_i k) &= \frac{\partial}{\partial x_j} \left(\Gamma_k \frac{\partial k}{\partial x_j} \right) + G_k - Y_k + S_k \\ \frac{\partial(\rho \omega)}{\partial t} + \frac{\partial}{\partial x_i}(\rho u_i \omega) &= \frac{\partial}{\partial x_j} \left(\Gamma_\omega \frac{\partial \omega}{\partial x_j} \right) + G_\omega - Y_\omega \\ &+ S_\omega, \end{aligned} \quad (6)$$

where G_ω is the generation of ω ; Γ_k and Γ_ω are the effective diffusivity of k and ω , respectively; Y_k and Y_ω are the dissipation of k and ω , respectively; S_ω is the user-defined source term.

This model is an empirical model based on model transport equations for the turbulence kinetic energy and turbulence kinetic energy dissipation rate.

2.2.5. SST k - ω Model for the VOF Flow. The shear-stress transport (SST) k - ω turbulence model was developed by Menter [26]. The equations of turbulent kinetic energy, k , and its dissipation rate, ω , are as follows:

$$\begin{aligned} \frac{\partial(\rho k)}{\partial t} + \frac{\partial}{\partial x_i}(\rho u_i k) &= \frac{\partial}{\partial x_j} \left(\Gamma_k \frac{\partial k}{\partial x_j} \right) + G_k - Y_k + S_k \\ \frac{\partial(\rho \omega)}{\partial t} + \frac{\partial}{\partial x_i}(\rho u_i \omega) &= \frac{\partial}{\partial x_j} \left(\Gamma_\omega \frac{\partial \omega}{\partial x_j} \right) + G_\omega - Y_\omega \\ &+ D_\omega + S_\omega, \end{aligned} \quad (7)$$

where D_ω is the cross-diffusion term.

2.3. Boundary Conditions

(1) *Inlet Boundary.* At the inlet, velocity inlet was used and the velocity was 2.61–4.08 m/s according to the unit discharges;

(2) *Outlet Boundary.* At the outlet, the pressure outlet boundary was chosen and the normal gradient of all variables were 0.

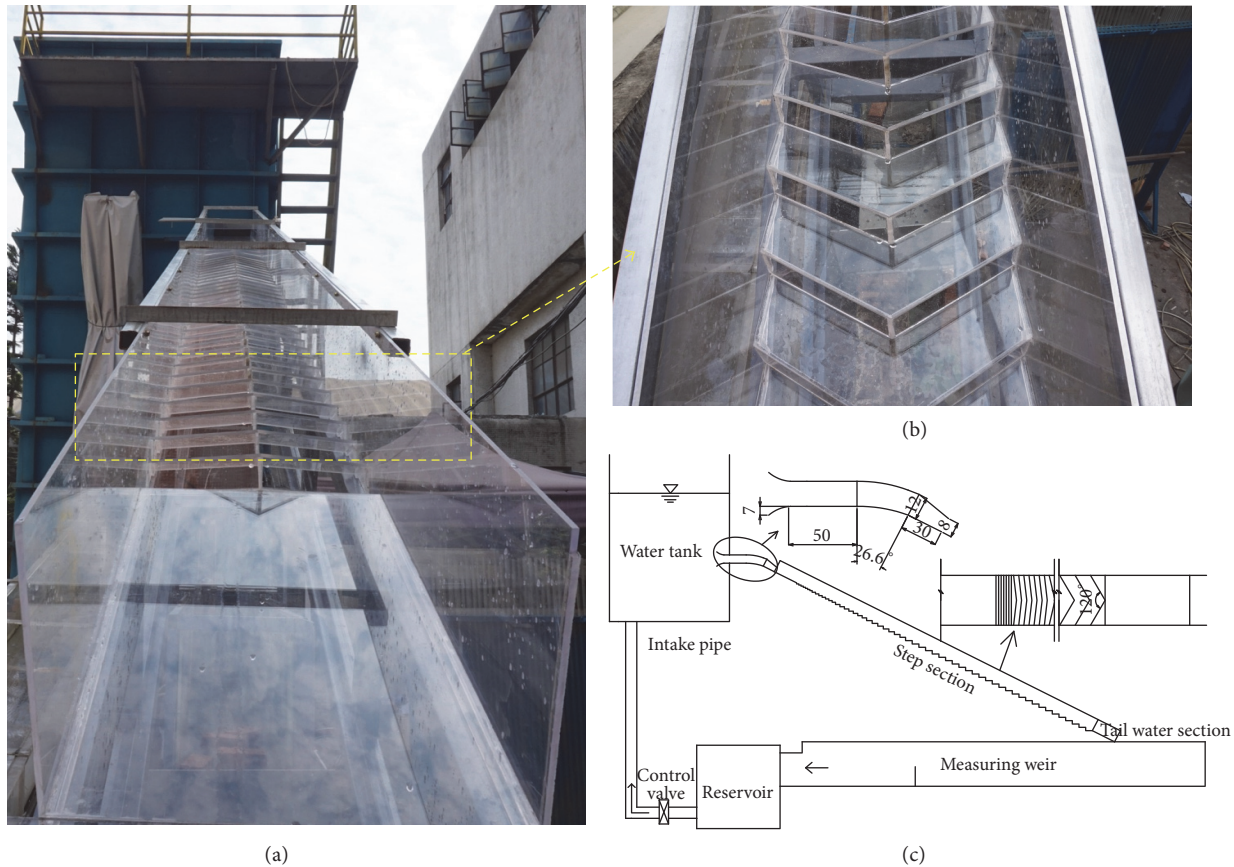


FIGURE 2: The physical model layout.

(3) *Free Surface*. Pressure inlet was presented at the free surface;

(4) *Wall Boundary*. The no-slip velocity boundary condition was used on the wall surface and the standard wall function was chosen to specify the near-wall regions of the flow.

2.4. Validation Model. A physical model of V-shaped stepped spillway is shown in Figure 2, which was performed in the State Key Laboratory of Hydraulics and Mountain River Engineering, Sichuan University, Chengdu. The total model height was 5.4 m and the size of the stepped spillway was identical to that in the numerical model, as shown in Figure 1. Piezometer tube was used to measure the time-averaged pressure.

3. Results and Analysis

3.1. Pressure Distribution. Figure 3 shows the pressure distribution on steps, where L represents the width of the step and H represents the height of the step. The figure shows that (1) for traditional stepped spillway, the pressure does not change along the cross section, but there are obvious changing at different profiles of V-shaped stepped spillway; (2) the extreme values of pressure locate at the sidewalls in V-shaped stepped spillway, but they locate along the cross section in traditional stepped spillway; (3) the maximum

pressure on horizontal step surface of V-shaped stepped spillway is larger than that of on traditional stepped spillway and the minimum pressure on vertical step surface of V-shaped stepped spillway is smaller than that of on traditional stepped spillway.

3.2. Pressure Distribution of the Profiles. Since the pressure distribution changed along the cross section in V-shaped stepped spillway, three rows of pressure measurement points were adopted, and the position of rows was in $Z/B = 0$, $Z/B = 0.25$, and near the $Z/B = 0.5$, respectively. The interval of pressure measurement points was 1 cm in each row, which means that each step horizontal surface had 11 points and 5 points on vertical surface in each row, as shown in Figure 4.

In this section, we take the pressure distribution on one step (#43) when $Fr = 5.99$ as an example to illustrate. Figure 5 shows the pressure distributions of physical model and five turbulence models on #43 step. Note from Figure 5 that (1) the numerical values at all pressure measurement points show a good agreement with the physical values at each profile; (2) it also can be regarded as an S-shaped variation on horizontal step surface, but the fluctuation decreases from both sidewalls to the axial plane; (3) on vertical step surface, from the step's lower edge to its upper edge ($Y/H = 1.0$), the pressure gradually decreases at all the profiles and at the same step height, from the axial plane to sidewalls,

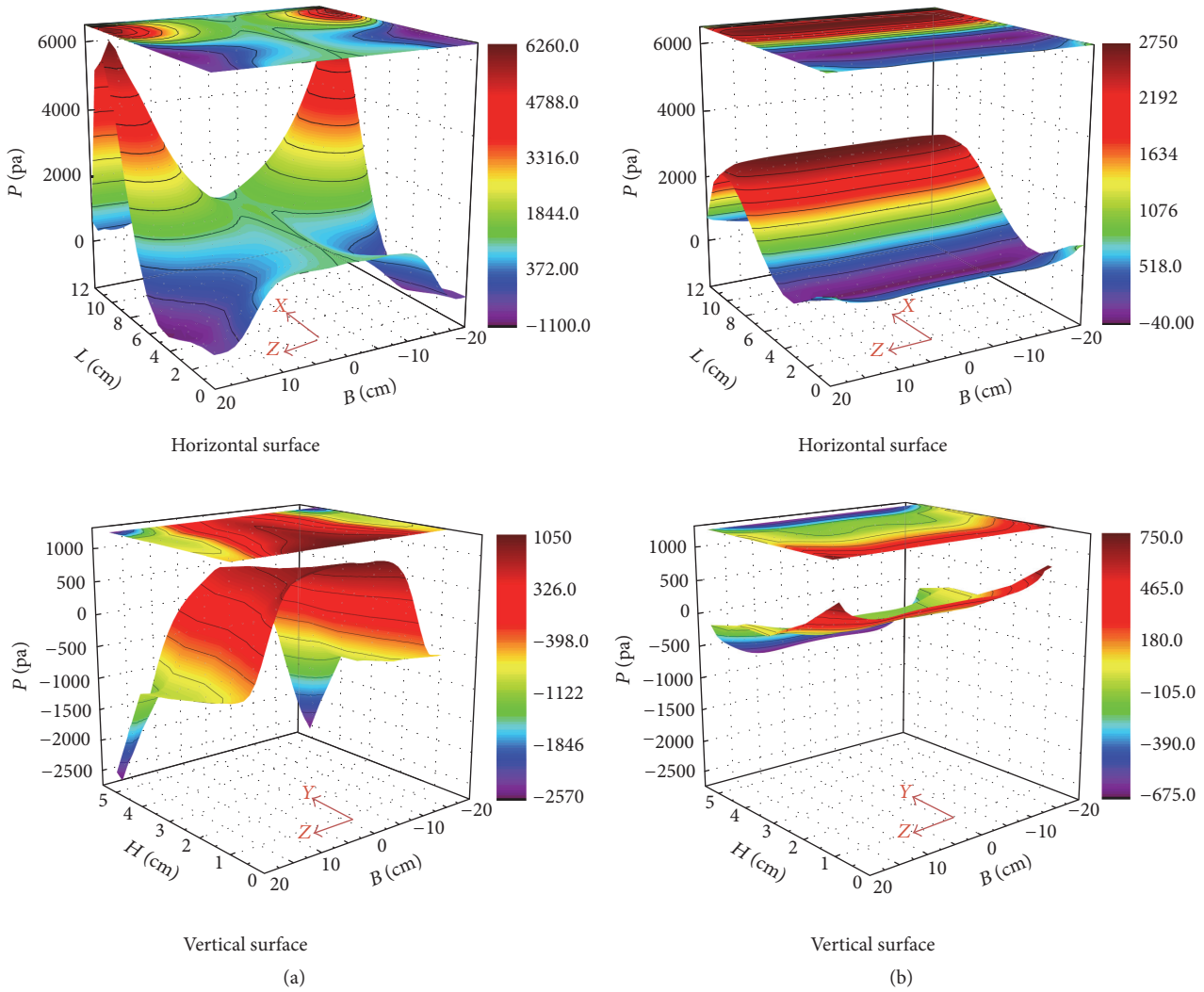


FIGURE 3: The pressure distribution on steps ((a) on V-shaped step, (b) on traditional step).

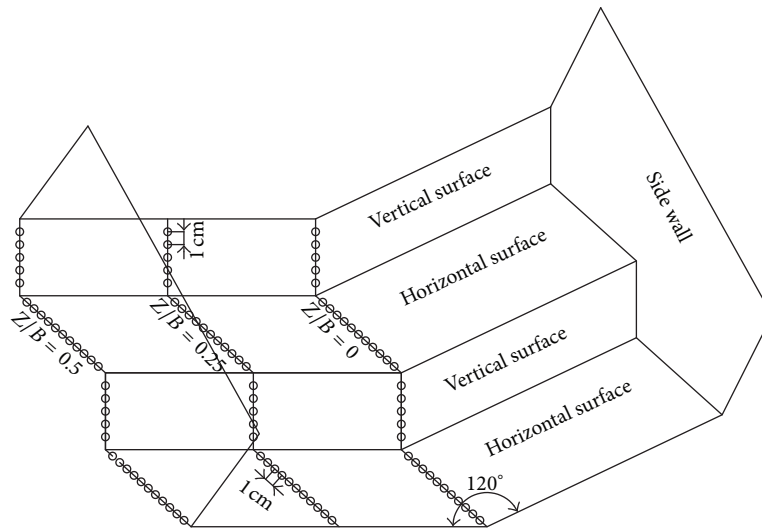


FIGURE 4: Pressure measurement points on steps.

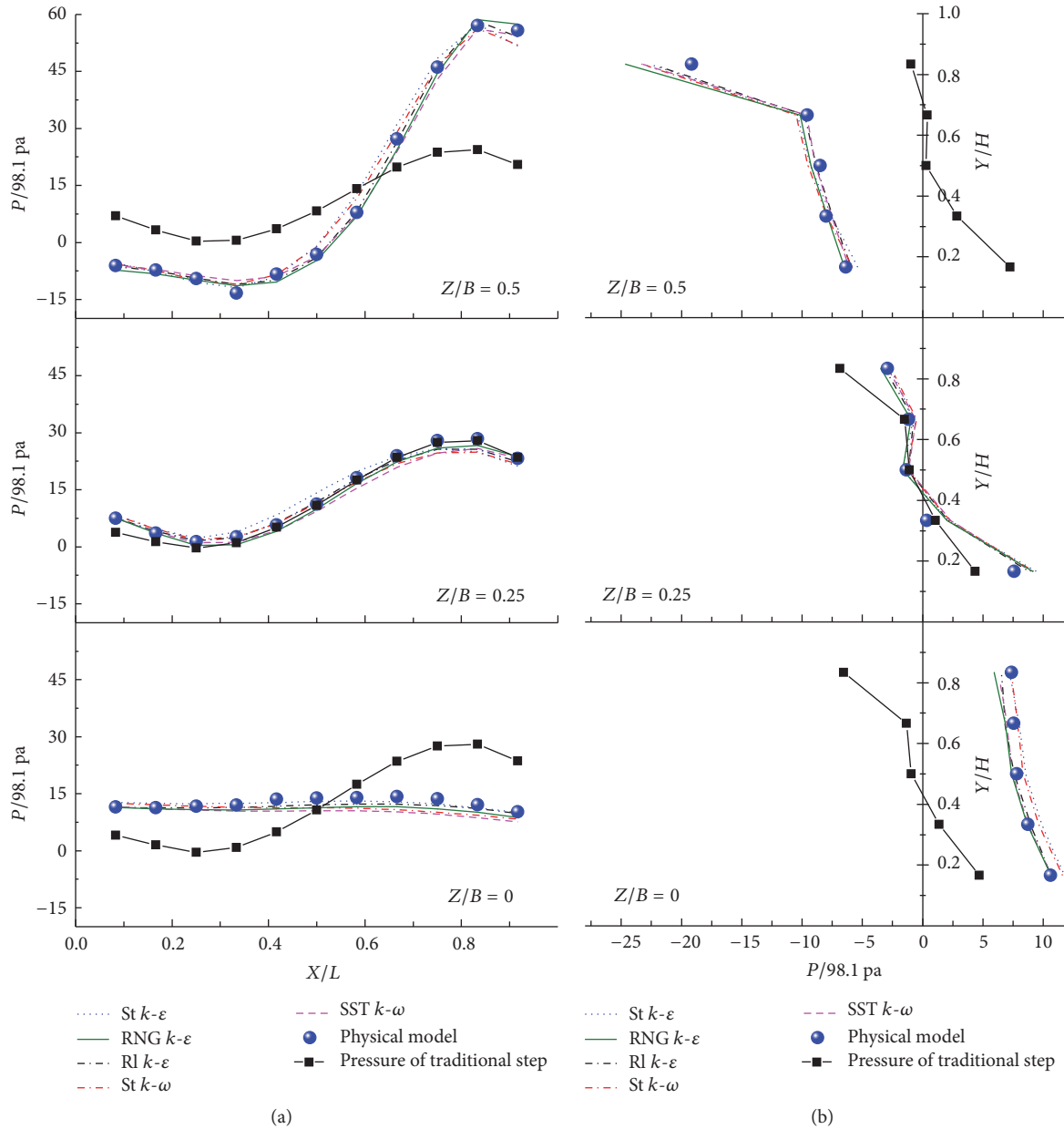


FIGURE 5: The pressure distribution of profiles on step ((a) on horizontal surface, (b) on vertical surface, $Fr = 5.997$).

pressure also gradually decreases; (4) at $Z/B = 0.25$, the pressure distributions of V-shaped and traditional stepped spillways are nearly the same; from the profile of $Z/B = 0.25$ to sidewalls, the fluctuation of pressure distribution is larger on the horizontal step surface and the pressure is lower at the same position on vertical step surface than those of in traditional stepped spillway; otherwise, from the profile of $Z/B = 0.25$ to axial plane, the fluctuation of pressure distribution is smaller on the horizontal step surface and the pressure is larger at the same position on the vertical step surface than those of in traditional stepped spillway; finally, at $Z/B = 0$, the pressure is nearly the same on the horizontal step surface and the pressure is positive on the vertical step surface.

For comparing the turbulence models performance statistically, the root mean square error (RMSE) criterion was estimated using

$$RMSE = \sqrt{\frac{1}{n} \sum_{i=1}^n (\text{Pressure}_{\text{physical}} - \text{Pressure}_{\text{numerical}})^2}, \quad (8)$$

where n is the number of pressure measurement points in each profile, $\text{pressure}_{\text{physical}}$ and $\text{pressure}_{\text{numerical}}$ are the physical and numerical values of the pressure, respectively. According to the definition of RMSE, the lower the RMSE value is, the more accurate the model is.

TABLE 1: The RMSE values of different turbulence models.

Step surface	Profile	St $k-\epsilon$	RNG $k-\epsilon$	RI $k-\epsilon$	St $K-\omega$	SST $K-\omega$
Horizontal surface	$Z/B = 0$	0.98	1.93	1.30	2.25	2.81
	$Z/B = 0.25$	2.00	1.39	1.20	1.71	1.93
	$Z/B = 0.5$	2.56	1.63	1.11	1.98	1.80
Vertical surface	$Z/B = 0$	0.82	0.75	0.53	0.67	0.59
	$Z/B = 0.25$	1.15	1.06	0.99	1.15	1.12
	$Z/B = 0.5$	1.70	2.49	1.51	1.96	1.85

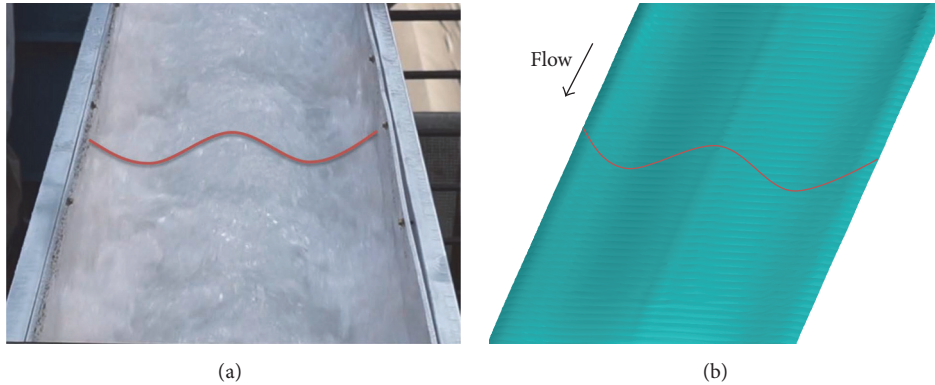
FIGURE 6: The free water surface of physical model and numerical model ((a) physical model, (b) RI $k-\epsilon$ model).

Table 1 presents the RMSE values of five turbulence models. It can be seen that (1) all the numerical turbulence models show satisfactory results at each profile; (2) the RI $k-\epsilon$ model can be regarded as a better model to simulate the pressure distribution of V-shaped stepped spillway according all the RMSE values.

3.3. The Flow Pattern. Figure 6 is the free water surface of the physical model and numerical model. It can be seen that (1) the results of the free water surfaces of numerical model and physical model are similar; (2) the free water surfaces of the axial plane and near sidewall were higher, and it is lower in other places, like a “W” shape, which is different from that of the traditional stepped spillway.

For stepped spillway, when the flow transitions from one step to the next step, a part of the flow travels in the downstream direction, and the other part changes direction because of the collision between the water and the steps. The flow that changes direction forms a reflux and collides with the vertical step surface. Then, the flow is forced to climb and blocked by the mainstream, forming stable vortices.

To clearly show the spiral flow and downstream flow, the streamlines are shown in different steps in Figure 7(d). From Figure 7(a), we can see that the velocity vectors are parallel to the axial plane, so the vortices are parallel to the axial plane (as shown in Figure 7(c)) and the flow pattern can be regarded as a two-dimensional flow, so the pressure distribution of traditional stepped spillway does not change along the cross section. However, from Figure 7(b), we can see that the velocity vectors are not parallel to the axial plane in V-shaped stepped spillway, and there is transverse velocity which is from the sidewall to the axial plane. So the water is

nearly void at the sidewalls and causes the minimum pressure at the upper ledge of vertical step surface at sidewall profiles. And the collision is formed through the vortex flow from the sidewall to the axial plane at near the axial plane, so the water surface is high at near the axial plane and the flow pattern can be regarded as a three-dimensional flow (as shown in Figure 7(d)). For this kind of unique flow field, the pressure distribution of V-shaped stepped spillway is obviously different at different profiles.

This flow field in V-shaped stepped spillway increases the turbulence intensity; therefore, there will be better energy dissipation rate and aeration properties and this will be studied in the future.

4. Conclusions

In this paper, the pressure distribution of V-shaped stepped spillway was studied using five turbulence models. The following conclusions can be drawn:

(1) Although all the numerical results show a good agreement with physical values, the realizable $k-\epsilon$ model is slightly better than other turbulence models in simulating the pressure distribution of V-shaped stepped spillway.

(2) Compared to traditional steps, the negative pressure is greater than the traditional steps, but the order of magnitude has not changed. So near the sidewalls, compared to the V-shaped steps, although the traditional steps are more resistant to cavitation damage, there is no obvious difference between them. Considering better energy dissipation rate and aeration properties, there are broad application prospects, especially in ecological water conservancy and aeration tanks.

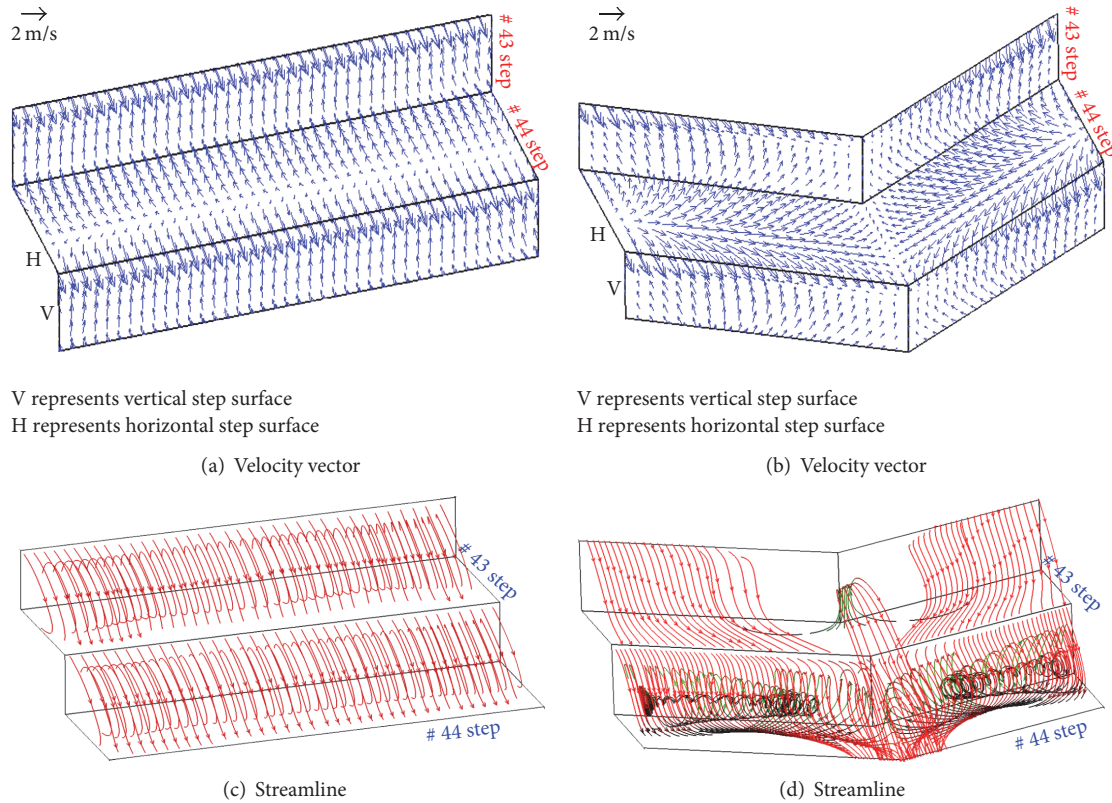


FIGURE 7: The velocity vectors and streamlines on steps ((a, c) traditional steps, (b, d) V-shaped steps; RI k - ϵ model).

Notation

B :	Chute width
h :	Inlet height of the model
k :	Turbulent kinetic energy
ϵ :	Turbulent kinetic energy dissipation rate
α_a :	Volume fractions of air
α_w :	Volume fractions of water
G_k :	Generation of turbulence kinetic energy due to the mean velocity gradients
G_b :	Generation of turbulence kinetic energy due to buoyancy
u_i :	Mean velocity component in the i th direction
μ_t :	Turbulent viscosity
S_k, S_ϵ :	User-defined source terms
$\alpha_k, \alpha_\epsilon$:	Inverse effective Prandtl numbers
ν :	Turbulent kinematic viscosity
G_ω :	Generation of ω
Γ_k, Γ_ω :	Effective diffusivity of k and ω , respectively
Y_k, Y_ω :	Dissipation of k and ω , respectively
S_ω :	User-defined source term
D_ω :	Cross-diffusion term
L :	Width of the step
H :	Height of the step
Fr :	Froude number.

Conflicts of Interest

The authors declare that they have no conflicts of interest.

Acknowledgments

This project was supported by the National Key Research and Development Program of China (no. 2016YFC0401707), the National Natural Science Foundation of China (no. 51579165), and the National Science Fund for Distinguished Young Scholars (no. 51625901). The authors acknowledge the working of Dr. Yong Peng.

References

- [1] A. Amador, M. Sánchez-Juny, and J. Dolz, "Characterization of the nonaerated flow region in a stepped spillway by PIV," *Journal of Fluids Engineering*, vol. 128, no. 6, pp. 1266–1273, 2006.
- [2] Q. Chen, G. Dai, and H. Liu, "Volume of fluid model for turbulence numerical simulation of stepped spillway overflow," *Journal of Hydraulic Engineering*, vol. 128, no. 7, pp. 683–688, 2002.
- [3] R. M. Sorensen, "Stepped spillway hydraulic model investigation," *Journal of Hydraulic Engineering*, vol. 111, no. 12, pp. 1461–1472, 1985.
- [4] S. Terrier, M. Pfister, and A. J. Schleiss, "Comparison of chute aerator effect on stepped and smooth spillways," in *Proceedings of the 36th IAHR World Congress*, vol. 15, pp. 1–5, Hague, The Netherlands, 2015.
- [5] E. Aras and M. Berkun, "Comparison of stepped and smooth spillway effects on stream reaeration," *Journal of Water SA*, vol. 36, no. 3, pp. 309–314, 2010.
- [6] M. E. Emiroglu and A. Baylar, "An investigation of effect of stepped chutes with end sill on aeration performance," *Water*

- Quality Research Journal of Canada*, vol. 38, no. 3, pp. 527–539, 2003.
- [7] H. Chanson, “Historical development of stepped cascades for the dissipation of hydraulic energy,” *Trans. Newcomen Soc.*, vol. 72, no. 2, pp. 295–318, 2001.
- [8] H. Chanson and L. Toombes, “Energy dissipation and air entrainment in stepped storm waterway: Experimental study,” *Journal of Irrigation and Drainage Engineering*, vol. 128, no. 5, pp. 305–315, 2002.
- [9] N. O. S. Alghazali and S. M. Jasim, “Experimental study on the limits of flow regimes for different configurations of stepped spillway,” *Civil Environmental Research*, vol. 6, no. 6, pp. 30–39, 2014.
- [10] O. Kisi, M. E. Emiroglu, and A. Baylar, “Flow regime prediction in stepped channels using neural computing technique,” *The International Journal of Science & Technology*, vol. 3, no. 1, pp. 109–121, 2008.
- [11] Z. C. Zhang, D. Y. Zeng, and A. M. Zheng, “Experimental investigation on the pressure characteristics of skimming flow on stepped chutes,” *Journal of Hydrodynamics*, vol. 18, no. 5, pp. 652–659, 2003.
- [12] U. Fratino, M. Sánchez-Juny, B. Valenzano, and M. Sánchez-Juny, “Air inception and pressure fields in transition flow regime over a stepped spillway,” *XXX IAHR Congress*.
- [13] M. Sánchez-Juny, E. Bladé, and J. Dolz, “Analysis of pressures on a stepped spillway,” *Journal of Hydraulic Research*, vol. 46, no. 3, pp. 410–414, 2008.
- [14] M. Sánchez-Juny, E. Bladé, and J. Dolz, “Pressures on a stepped spillway,” *Journal of Hydraulic Research*, vol. 45, no. 4, pp. 505–511, 2007.
- [15] A. Amador, M. Sánchez-Juny, and J. Dolz, “Developing flow region and pressure fluctuations on steeply sloping stepped spillways,” *Journal of Hydraulic Engineering*, vol. 135, no. 12, pp. 1092–1100, 2009.
- [16] J. M. Zhang, J. G. Chen, and Y. R. Wang, “Experimental study on time-averaged pressures in stepped spillway,” *Journal of Hydraulic Research*, vol. 50, no. 2, pp. 236–240, 2012.
- [17] A. I. Dhattrak and S. P. Tatewar, “Air entrainment and pressure fields over stepped spillway in skimming flow regime,” *Journal of Power and Energy Engineering*, vol. 2, no. 4, pp. 53–57, 2014.
- [18] Z. D. Qian, X. Q. Hu, W. X. Huai, and A. António, “Numerical simulation and analysis of water flow over stepped spillways,” *Science China Technological Sciences*, vol. 52, no. 7, pp. 1958–1965, 2009.
- [19] B. Chakib, “Numerical Computation of inception point location for flat-sloped stepped spillway,” in *Proceeding of the ASME 2013 Heat Transfer Summer Conference Collocated with the ASME 2013, International Conference on Energy Sustainability and the ASME 2013, International Conference on Fuel Cell Science, Engineering and Technology*, vol. 2, 2013.
- [20] R. Daneshfaraz, A. R. Joudi, A. Ghahramanzadeh, and A. Ghaderi, “Investigation of flow pressure distribution over a stepped spillway,” *Advances and Applications in Fluid Mechanics*, vol. 19, no. 4, pp. 811–822, 2016.
- [21] C. W. Hirt and B. D. Nichols, “Volume of fluid (VOF) method for the dynamics of free boundaries,” *Journal of Computational Physics*, vol. 39, no. 1, pp. 201–225, 1981.
- [22] B. E. Launder and D. B. Spalding, *Lectures in mathematical models of turbulence*, Academic Press, London, UK, 1972.
- [23] V. Yakhot and S. A. Orszag, “Renormalization group analysis of turbulence. I. basic theory,” *Journal of Scientific Computing*, vol. 1, no. 1, pp. 1–51, 1986.
- [24] T.-H. Shih, W. W. Liou, A. Shabbir, Z. Yang, and J. Zhu, “A new $k-\epsilon$ eddy viscosity model for high reynolds number turbulent flows,” *Computers and Fluids*, vol. 24, no. 3, pp. 227–238, 1995.
- [25] D. C. Wilcox, *Turbulence Modeling for CFD*, DCW Industries, Inc, La Canada, Calif, USA, 1993.
- [26] F. R. Menter, “Two-equation eddy-viscosity turbulence models for engineering applications,” *AIAA Journal*, vol. 32, no. 8, pp. 1598–1605, 1994.

Research Article

A New Mathematical Method for Solving Cuttings Transport Problem of Horizontal Wells: Ant Colony Algorithm

Liu Yongwang,¹ Liu Yu-ming,² Qiu Heng-bin,³ and Bai Yan-feng⁴

¹School of Petroleum Engineering, China University of Petroleum, Qingdao 266580, China

²College of Energy Engineering, Yulin University, Yulin 719000, China

³Drilling Technology Research Institute, Shengli Petroleum Engineering Corporation, Sinopec, Dongying 257000, China

⁴Laojunmiao Oil Production Plant, Yumen Oilfield, Jiuquan 735000, China

Correspondence should be addressed to Liu Yongwang; liuyongwang2003@163.com

Received 19 March 2017; Revised 1 July 2017; Accepted 16 July 2017; Published 29 August 2017

Academic Editor: Jian G. Zhou

Copyright © 2017 Liu Yongwang et al. This is an open access article distributed under the Creative Commons Attribution License, which permits unrestricted use, distribution, and reproduction in any medium, provided the original work is properly cited.

Cuttings transport problem has long been recognized as one of the key difficulties in drilling horizontal wells, and the models in cuttings transport research are usually formulated with highly nonlinear equations set. When using Newton methods to solve real engineering problems with nonlinear equations set, the problems of result dependence on initial values, Jacobian matrix singularity, and variable outflow of its definition domain in iterations are three of the often-encountered difficulties. In this paper, the ant colony algorithm is applied to solve the two-layer cuttings transport model with highly nonlinear equations set. The solution-searching process of solving nonlinear equations set is transformed into an optimization process of searching the minimum value of an objective function by applying ant colony algorithm. Analyzing the results of the example, it can be concluded that ant colony algorithm can be used to solve the highly nonlinear cuttings transport model with good solution accuracy; transforming the solution-searching process of solving nonlinear equations set into an optimization process of searching the minimum value of the objective function is necessary; the real engineering problem should be simplified as much as possible to decrease the number of unknown variables and facilitate the use of ant colony algorithm.

1. Introduction

Cuttings transport problem has long been recognized as one of the key difficulties in drilling horizontal wells. Over the past 30 years, considerable effort has been expended on solving cuttings transport problem in drilling horizontal wells. Many researchers developed various models [1–10] to investigate this problem, among which the two-layer model is one of the analytical research models and is formulated with highly nonlinear equations set.

Nevertheless, solving the complicated highly nonlinear model to get a reasonable and stable solution has long been a challenge to researchers. Usually, the Newton methods, including the Newton iteration method, Discrete Newton method, and Newton Downhill method, are used in solving nonlinear equations set. However, the result solved by using the Newton methods is highly dependent on the initial values, and finding proper initial values for nonlinear equations

set is not an easy job. Meanwhile, since the gradient or the Jacobian matrix has to be calculated and updated in the iteration, singularity problem of Jacobian matrix often occurs in the computation, and this problem will probably make the iteration prematurely terminated. In addition, when these Newton methods are applied to solve real engineering problems in which the variables usually have to fall within their specific definition domain, the solution-searching process often causes the variable outflow of its definition domain, which often leads to failure of getting reasonable results. Obviously, the result dependence on initial values, Jacobian matrix singularity, and variable outflow of its definition domain in iterations are three of the often-encountered difficulties when using Newton methods to solve real engineering problems.

Recently, some researchers [11–19] used artificial intelligence algorithms, such as Genetic Algorithm, Simulated Annealing Algorithm, and Artificial Fish-Swarm Algorithm,

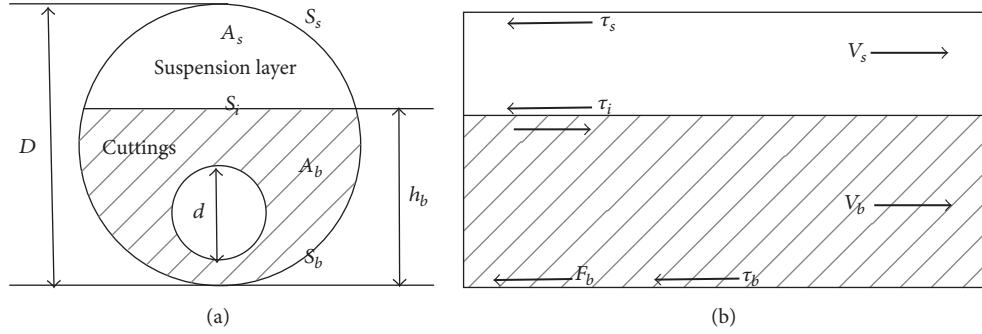


FIGURE 1: Schematic of cuttings condition under two-layer model [1].

to solve nonlinear equations set and obtained satisfactory results. The artificial intelligence algorithms search solutions in the whole definition domain and the result does not depend on the initial values. Moreover, the artificial intelligence algorithm does not need to calculate the Jacobian matrix and the variable definition domain can be artificially preset according to real problems requirements. Therefore, the initial values sensitivity problem, the singularity problem in calculating Jacobian matrix, and the variable outflow of its definition domain problem can be effectively avoided when using artificial intelligence algorithms to solve problems with nonlinear equations set. Ant colony algorithm is one of the artificial intelligence algorithms and has been widely used in optimizing engineering problems. Since solving real engineering problems needs much more work on model formulation, model simplification, variable definition domain determination, model solution, and so on, it is much more complicated than solving pure mathematical nonlinear equations set. Some researchers [18, 19] tried to solve pure mathematical nonlinear equations set with ant colony algorithm, but few applications of ant colony algorithm in solving real engineering problems with nonlinear equations set have been reported.

The objective of this paper is to apply the ant colony algorithm to solve the cuttings transport problem with highly nonlinear equations set so as to simplify the process of solving cutting transport model and provide a new way to solve nonlinear engineering problems.

2. Formulation of Cuttings Transport Problem

2.1. Model Formulation. In order to formulate the model of cuttings transport problem, material and momentum balance analysis are needed. In the formulation of material and momentum balance equations, A , C , v , S , and τ refer to area, cuttings concentration, velocity, wetted perimeter, and shear stress, respectively. The subscripts, s , b , i , and t , refer to suspension layer, cuttings bed, suspension-bed interface, and total quantity, respectively.

Under steady flow conditions, assuming no slip between the liquid and solid phases, the material balances can be expressed as follows.

For solid phase [1],

$$A_s C_s v_s + A_b C_b v_b = A_t C_t v_t. \quad (1)$$

For liquid phase,

$$A_s (1 - C_s) v_s + A_b (1 - C_b) v_b = A_a (1 - C_t) v_t, \quad (2)$$

where A_a is the annular area. In Figure 1, D is the hole diameter and d is the drill pipe diameter. SI units are adopted if units are not specially indicated.

Under steady flow conditions, the forces acting on the cuttings bed and suspension layer must equal zero. Therefore, the momentum balances can be written as follows.

For cuttings bed,

$$-A_b \left(\frac{\Delta p}{L} \right) - \tau_b S_b + \tau_i S_i - G_b - F_b = 0. \quad (3)$$

For suspension layer,

$$-A_s \left(\frac{\Delta p}{L} \right) - \tau_s S_s - \tau_i S_i - G_s = 0, \quad (4)$$

where Δp is the pressure loss, L is the length for one particular section, G_b and G_s are the gravitational forces on the cuttings bed and the suspension layer in the flow direction, respectively, and F_b is the frictional force on the cuttings bed at the wellbore-bed interface.

The cuttings concentration in the suspension layer is assumed to submit to the diffusion law, which can be expressed as follows:

$$\frac{C_s}{C_b} = \frac{1}{A_s} \int_{A_s} \exp \left(\frac{v_{\text{hin}} \sin \alpha}{\varepsilon_p} (y - h_b) \right) dA, \quad (5)$$

where v_{hin} is the hindered cutting falling velocity due to cuttings collision in the suspension layer, α is the well inclination angle, h_b is the cuttings bed height, and ε_p is the diffusion coefficient of cuttings in the suspension layer.

In (1)–(5), h_b , v_s , v_b , C_s , and $\Delta p/L$ are the unknown variables. Once these unknowns are determined, all the other variables can be calculated. The detailed derivations of the model equations are documented in [1].

2.2. Model Simplification. From Figure 1, it can be seen that the values of A_s , A_b , S_s , S_b , and S_i are all dependent on the cuttings bed h_b (see reference [20]). For the other variables, the shear stresses τ_s , τ_i , and τ_b are functions of variables v_s or v_b . The gravitational forces G_s and G_b are functions of A_s and

A_b , respectively, and hence they are functions of h_b . Cuttings hindered falling velocity v_{hin} and diffusion coefficient ε_p are functions of v_s .

The analysis above shows that (1)–(5) are highly nonlinear. The main challenge in solving this cuttings transport problem is to solve this set of highly nonlinear equations and obtain a stable and reliable solution. In solving nonlinear equations set, it is much better to simplify the equations set and reduce the number of unknown variables. Therefore, this set of nonlinear equations in cuttings transport problem will be analyzed to reduce the number of equations in order to decrease the solution difficulty.

When solving the cuttings transport problem in horizontal section (i.e., $\alpha = 90^\circ$), the cuttings bed does not move at the lower side of the wellbore and thus $v_b = 0$. Equation (3) can be eliminated for it is meaningless to analyze the force balance on a static cuttings bed.

Adding (1) and (2) gives

$$A_s v_s = A_a v_t \quad (6)$$

which is

$$A_s v_s = Q, \quad (7)$$

where Q is the flow rate, which is a known variable.

Comparing (6) with the simplified (1), we can get

$$C_s = C_t \quad (8)$$

in which C_t is the cuttings supply concentration, which can be determined by the rate of penetration.

The pressure loss per unit length $\Delta p/L$ is only shown in (4), so it can be obtained using the value of other variables after the other equations are solved. Therefore, the nonlinear equations' set to be solved only consists of (7) and (5).

Through the analysis above, it can be seen that solving the five nonlinear equations set can be simplified into two steps.

First, solve the equations set of (7) and (5) to get the value of v_s and h_b , and then substitute the values of v_s and h_b to (4) to get the value of $\Delta p/L$.

2.3. Formulation of the Objective Function. In order to apply the ant colony algorithm to the cuttings transport problem, an objective function has to be formulated before the calculation. Transforming (7) and (5), define the objective function F as

$$F = |A_s v_s - Q| + \left| C_s - \frac{C_b}{A_s} \int_{A_s} \exp\left(\frac{v_{\text{hin}} \sin \alpha}{\varepsilon_p} (y - h_b)\right) dA \right|. \quad (9)$$

If F reaches its minimum value (i.e., close to zero), the values of v_s and h_b can be recognized as the solution of (7) and (5).

3. Two-Dimensional Continuous-Domains Ant Colony Algorithm

3.1. Ant Colony Algorithm Mechanism. Ant colony algorithm (ACA) is a heuristic algorithm initially proposed by Marco

Dorigo in 1992 and has been widely used in many areas [21–32], such as fuzzy predictive control, behavior learning and reproduction by robots, and mobile ad hoc network optimization. The general idea of ACA is to mimic the process of ants seeking an optimum path between their colony and a source of food. The ants will leave pheromones on the path when they are searching food. There are the most pheromones accumulated on the shortest path. The ants exchange information through the pheromones on the path and finally all the ants seek food along the shortest path. This is a path optimization process.

The initial design of ant colony algorithm is only applicable to discrete domains, such as in TSP problems. When the algorithm is applied in continuous domains, it should be modified. For example, the selection probability is calculated by the fitness value which is related to the objective function value rather than the distance between two discrete cities in the TSP problem.

In this paper, F is set as the optimization objective, and $2 - F$ is used as the pheromone accumulation value (i.e., fitness value), and the selection probability of one ant for one particular path in one generation is defined as

$$\text{prob} = \left| \frac{\tau_{\text{best}}^p - \tau_i^p}{\tau_{\text{best}}^p} \right|. \quad (10)$$

The pheromone update rule is calculated as

$$\tau_i^p = (1 - \text{Rho}) * \tau_i^{p-1} + T_i^p, \quad (11)$$

where τ_{best}^p is the largest value of pheromone accumulation among all ants in the p th generation, τ_i^p is the value of pheromone accumulation for the i th ant in the p th generation, τ_i^{p-1} is the value of pheromone accumulation for the i th ant in the $(p - 1)$ th generation, Rho is the pheromone evaporation coefficient, and T_i^p is the newly added pheromone value, that is, the function value for the i th ant in the p th generation.

For the formulation of the fitness value of each ant, choose arbitrary values within their definition domain (e.g., 1.53 m/s, 0.059 m) and then calculate the value of F (e.g., 0.0171). The fitness value can be set as $2 - F$ in order to get a higher value as the objective function F goes lower. The fitness value represents the pheromone accumulation, and all the ants are designed to move towards the position where the accumulated pheromone is the largest. The ants will select moving paths according to the selection probability calculated based on the fitness value. After sufficient generations, all the ants will gather at the position where the pheromone accumulation (i.e., fitness value) is the largest.

3.2. Problem Description. Objective function:

$$\begin{aligned} \min F &= |A_s v_s - Q| \\ &+ \left| C_s - \frac{C_b}{A_s} \int_{A_s} \exp\left(\frac{v_{\text{hin}} \sin \alpha}{\varepsilon_p} (y - h_b)\right) dA \right|. \end{aligned} \quad (12)$$

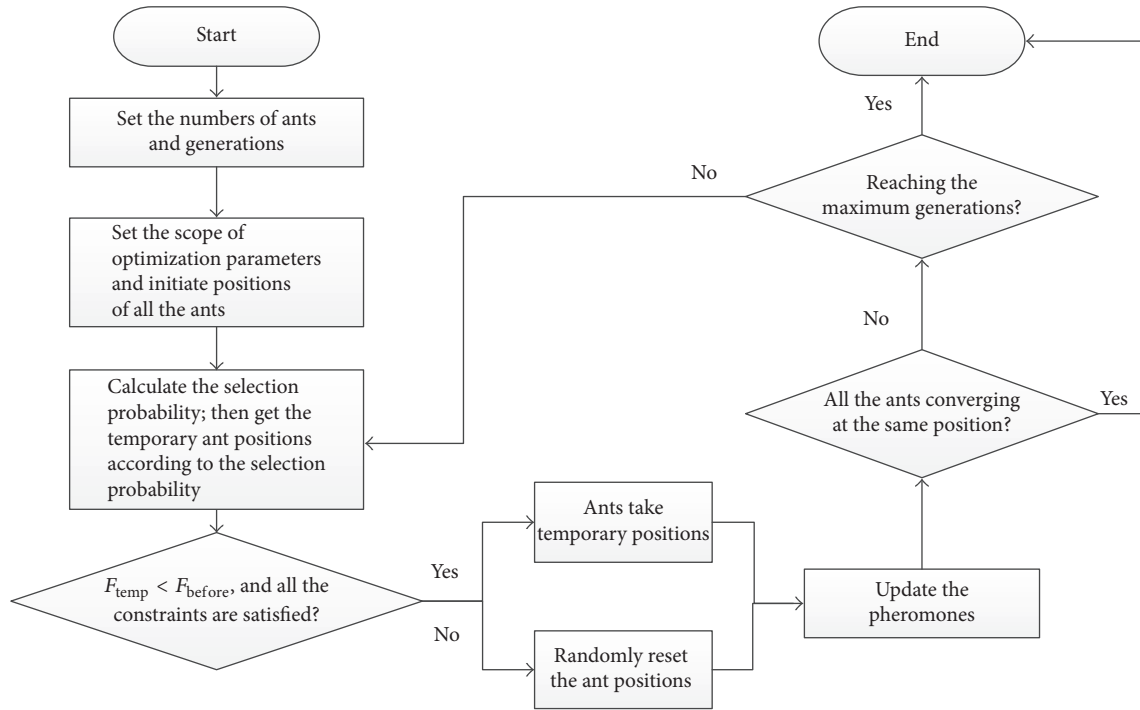


FIGURE 2: Flow loop of equation solving with ant colony algorithm.

Fitness value: $2 - F$.

Variables: v_s, h_b .

Definition domain: $v_s > 0, h_b \in (0, D)$.

3.3. Solution-Searching Procedure. The solution-searching procedure with ant colony algorithm is shown in Figure 2. The ant colony algorithm is solved by Matlab programming and the detailed process of solving the problem is as follows.

(1) Set the numbers of ants and iteration generations.

In the ant colony algorithm, the ants will search solutions within the preset generations. If the ants could not find solution with the preset generations, probably, more ants and generations are necessary. The quantity of ants and iteration generations can be adjusted by doing tests for different problems. Generally, 6–10 ants and 300–700 generations are sufficient for a common optimization.

(2) Set the scopes of optimization parameters, which are the cuttings bed height and the suspension layer velocity.

When using the ant colony algorithm to solve the cuttings transport model, it only needs setting the scopes of optimization parameters, which are the cuttings bed height and the suspension layer velocity, rather than providing accuracy-sensitive initial values. The two parameters will change within the preset scope, and the ant will find solution within their preset scope. This successfully avoids the difficulty of providing the result-sensitive initial value selection problem. The scopes of optimization parameters can be set according to common drilling experiences.

(3) Conduct the optimization and obtain the optimum cuttings bed height and suspension layer velocity.

The detailed solution-searching process with ant colony algorithm is as follows.

First, the ant colony algorithm randomly assigns positions (i.e., cuttings bed height and suspension layer velocity) within the two preset optimization scopes for each ant to initiate the ant positions. After doing this, each ant has an initial position with two parameters (i.e., cuttings bed height and suspension layer velocity). Then, these chosen parameters for each ant are sent to evaluate the objective function (i.e., (12)) and the fitness value (i.e., the pheromone accumulation in (11)). In the whole optimization process, the ants tend to find the position with the largest fitness value, which mathematically means the smallest error for solving the nonlinear equations set (i.e., the smallest objective function value in (12)). Next, use the fitness value to calculate the selection probability by (10). The selection probability represents the distance between each ant position and the optimum ant position (i.e., ant position with the largest fitness value). The ants with higher selection probability, which means they are comparatively farer from the ant with the largest fitness value, are designed to move faster towards the ant with the largest fitness value. According to the value of selection probability for each ant, all the ants will be accordingly assigned a temporary position at each generation. If the fitness value at the temporary position is higher than the fitness value at the previous position, those ants will take the temporary positions as their new positions. The ant positions (i.e., cuttings bed height and suspension layer velocity), at which their fitness values do not increase, are sent to reset their values randomly. At each generation, all

TABLE 1: Parameters used in the model.

Parameters	Values
Hole size, m	0.127
Drill pipe size, m	0.04826
Consistency coefficient, Pa. s ⁿ	0.295
Flow index	0.698
Drilling fluid density, kg/m ³	1.102 × 10 ³
Well inclination angle	90°

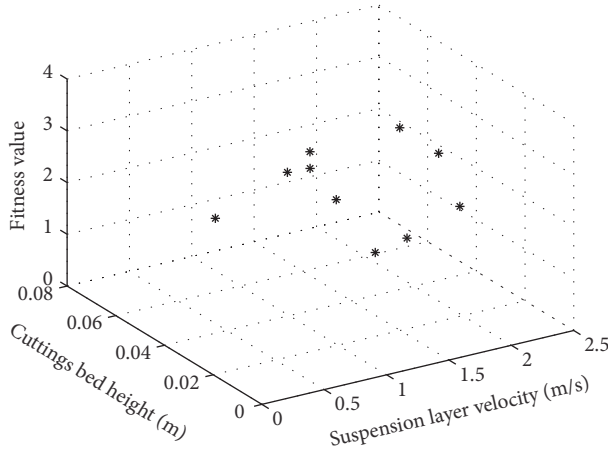


FIGURE 3: Initial distribution of ants.

the ants tend to move towards the position where the fitness value is the largest, and the fitness values (i.e., pheromones) are updated by (11). Therefore, it can be expected that after certain generations, all the ants will gather at the position with the largest fitness value, and the optimum ant position (i.e., the optimum cuttings bed height and suspension layer velocity) is obtained.

4. Example

4.1. Example Data. The parameters used in the cuttings transport model are shown in Table 1.

The ant population size, maximum generations, and the pheromones evaporation coefficient are taken as 10, 700, and 0.8, respectively.

4.2. Result and Discussion. Figures 3–5 demonstrate the process of how the ants find the solution at flow rate 0.014 m³/s. First, the ants dispersed randomly in the scopes of suspension layer velocity v_s and cuttings bed height h_b as shown in Figure 3. After 55 generations shown in Figure 4, it can be apparently seen that the ants tend to gather towards the positions where the fitness value is higher. When the 550 generations pass, shown in Figure 5, all the ants stay at around (1.3303 m/s, 0.0070 m), where the fitness value is the highest (i.e., 1.9999). The highest fitness value means that objective function value reaches the lowest, very close to zero (i.e., 0.000063), which mathematically corresponds to the solution of the nonlinear equations set. Therefore, the value

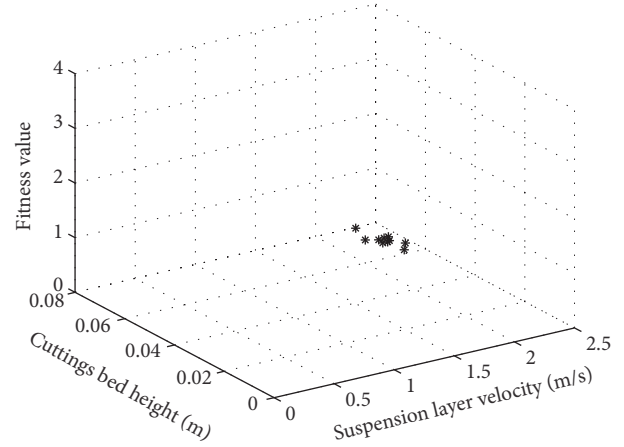


FIGURE 4: Distribution of ants at generation = 55.

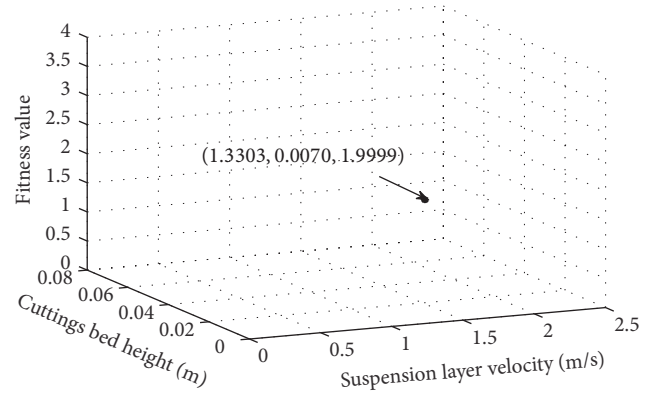


FIGURE 5: Final distribution of ants at generation = 550.

(1.3303 m/s, 0.0070 m) can be taken as the solution for v_s and h_b .

The relationship between the average objective function value and iteration generations is shown in Figure 6. It can be seen from Figure 6 that the objective function value decreases quickly as the generation increases. At generation 550, the objective function value is very close to zero (0.000063), and the values of v_s and h_b (1.3303 m/s, 0.0070 m) in Figure 5 can be used as the solution of the nonlinear equations set.

The cuttings transport problem is also solved with Discrete Newton method. When using Discrete Newton method, one should be very careful with dealing with the singularity problem of the Jacobian matrix and try to keep the variation of variables in the reasonable scope in the iteration. If the values of variables go beyond the reasonable scope, it can lead to obtain unreasonable results or possibly failure to converge. However, when using ant colony algorithm, there is no need to calculate the gradient and Jacobian matrix, so the singularity problem of the Jacobian matrix is avoided. Moreover, the scope of variable variation can be artificially set within the reasonable scope. For instance, the cuttings bed height should vary within the limit of hole diameter, so the variation range of cuttings bed height can be artificially set within the scope (0, 0.127 m), so the variable outflow of its

TABLE 2: Comparison of results calculated by Discrete Newton method and ant colony algorithm.

Flow rate, m ³ /s	Variables	Discrete Newton method	Ant colony algorithm	Error
Q = 0.010	v_s , m/s	1.0282	1.0270	0.12%
	h_b , m	0.0178	0.0179	0.56%
Q = 0.012	v_s , m/s	1.1688	1.1663	0.21%
	h_b , m	0.0111	0.0110	0.90%
Q = 0.014	v_s , m/s	1.3285	1.3303	0.14%
	h_b , m	0.0070	0.0070	0.00%

TABLE 3: The values of all the variables at flow rate 0.014 m³/s.

Flow rates, m ³ /s	Suspension layer velocity, m/s	Cuttings bed height, m	Pressure loss per unit length, Pa/m	Cuttings concentration in suspension layer	Velocity of cuttings bed, m/s
0.014	1.3303	0.007	756.23	0.0025	0

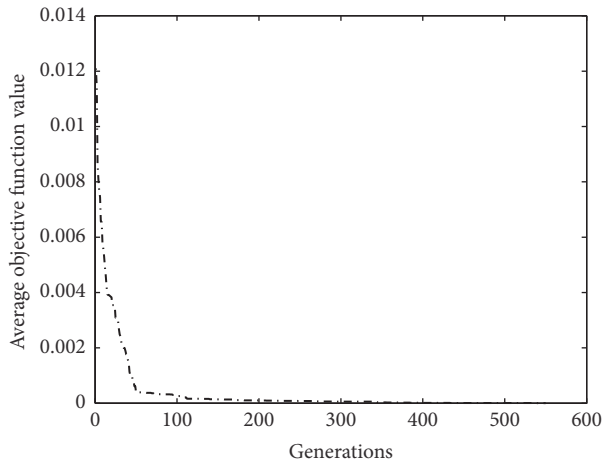


FIGURE 6: Relationship between the average objective function values and generations.

definition domain problem is avoided. Meanwhile, since the ant colony algorithm initiates values of variables randomly in the optimization domain, the optimization result has no dependence on the initial values. Therefore, using ant colony algorithm can avoid the result dependence on initial values problem, Jacobian matrix singularity problem, and variable outflow of its definition domain problem. The solution result comparison between the Discrete Newton method and ant colony algorithm is presented in Table 2. As can be seen from Table 2, the error between these two methods is below 1%, which proves the effectiveness of using ant colony algorithm to solve the cuttings transport problem.

The values of pressure loss per unit length $\Delta p/L$ can be calculated after the values of v_s and h_b are obtained. One group of values for 5 unknown variables in the cuttings transport model is presented in Table 3.

4.3. Advances of Using the New Method. The cuttings transport model is formulated with nonlinear equations set, and traditionally it is solved by the Newton methods. When the Newton methods are used to solve the nonlinear equations

set, the result dependence on initial values, Jacobian matrix singularity, and variable outflow of its definition domain are three of the often-encountered difficulties. These problems will lead to the failure of getting reasonable results when Newton methods are used to solve real engineering problems.

Compared to the Newton methods, the ant colony algorithm method does not need the selection of result-sensitive initial values but only needs a comparatively large solution-included scope, which greatly decreases the difficulty of providing result-sensitive initial values. Since there is no Jacobian matrix in the ant colony algorithm, the new method avoids the Jacobian matrix singularity problem which often occurs when using Newton methods. The ant colony algorithm searches solution in the preset scope, so there is no problem such as variable outflow of its definition domain. Therefore, compared to Newton methods, using ant colony algorithm makes solving the nonlinear cuttings transport model easier and more stable and provides a new way of solving cuttings transport problem.

The present study mainly focuses on proposing a new method of using ant colony algorithm to solve the cuttings transport model. The new method effectively avoids the initial values selection, the singularity problem of Jacobian matrix, and the variable outflow of its definition domain problem in solving the model and meanwhile does not decrease the accuracy, which greatly simplifies the process of solving the nonlinear equations model. The application of using the ant colony algorithm to solve the cuttings transport problem in the field will be further explored in the future research.

5. Conclusions

- (1) The ant colony algorithm can be used to solve cuttings transport model with highly nonlinear equations set, and the solutions solved by ant colony algorithm and Discrete Newton method show good agreement with each other.
- (2) Transforming the solution-searching process of solving nonlinear equations set into an optimization process of searching the minimum value of the objective

function is necessary in applying the ant colony algorithm to real nonlinear engineering problems.

- (3) The real engineering problem should be simplified according to its physical characteristics as much as possible in order to decrease the number of unknown variables and facilitate the use of ant colony algorithm.

Conflicts of Interest

The authors declare that they have no conflicts of interest.

Acknowledgments

This work is supported by the Qingdao Independent Innovation Project (no. 16-5-1-23-jch); the Fundamental Research Funds for the Central Universities (no. 16CX02025A); Program for Changjiang Scholars and Innovative Research Team in University of Ministry of Education of China (no. IRT_14R58).

References

- [1] Z.-M. Wang and Z. Zhang, "Model for two-layer cutting transport in horizontal wells," *Journal of the University of Petroleum China*, vol. 28, no. 4, pp. 63–66, 2004.
- [2] D. Nguyen and S. Rahman, "A Three-Layer Hydraulic Program for Effective Cuttings Transport and Hole Cleaning in Highly Deviated and Horizontal Wells," in *Proceedings of the SPE/IADC Asia Pacific Drilling Technology*, Kuala Lumpur, Malaysia, 1996.
- [3] R.-C. Cheng and R.-H. Wang, "A three-segment hydraulic model for annular cuttings transport with foam in horizontal drilling," *Journal of Hydrodynamics*, vol. 20, no. 1, pp. 67–73, 2008.
- [4] Y. Masuda, Q. Doan, M. Oguztoreli et al., "Critical cuttings transport velocity in inclined annulus: experimental studies and numerical simulation," in *Proceedings of the SPE/CIM International Conference on Horizontal Well Technology*, Calgary, Alberta, Canada, 2000.
- [5] X. Song, Z. Guan, and S. Chen, "Mechanics Model of Critical Annular Velocity for Cuttings Transport in Deviated Well," *Journal of China University of Petroleum*, vol. 33, no. 1, pp. 53–63, 2009.
- [6] N. Wei, Y. Meng, G. Li et al., "Cuttings transport models and experimental visualization of underbalanced horizontal drilling," *Mathematical Problems in Engineering*, vol. 2013, Article ID 764782, 6 pages, 2013.
- [7] A. Ramadan, P. Skalle, S. T. Johansen, J. Svein, and A. Saasen, "Mechanistic model for cuttings removal from solid bed in inclined channels," *Journal of Petroleum Science and Engineering*, vol. 30, no. 3-4, pp. 129–141, 2001.
- [8] M. Duan, S. Z. Miska, M. Yu, N. E. Takach, R. M. Ahmed, and C. M. Zettner, "Transport of small cuttings in extended-reach drilling," *SPE Drilling & Completion*, vol. 23, no. 03, pp. 258–265, 2013.
- [9] T. I. Lasen, A. A. Pilehvari, and J. J. Azar, "Development of a new cuttings-transport model for high-angle wellbores including horizontal wells," *SPE Drilling Completion*, vol. 122, pp. 129–135, 1997.
- [10] M. Sorgun, "Simple correlations and analysis of cuttings transport with newtonian and non-newtonian fluids in horizontal and deviated wells," *Journal of Energy Resources Technology, Transactions of the ASME*, vol. 135, no. 3, article 032903, 2013.
- [11] H. Guo, X. Jin, and X. Hu, "Research on the solving of nonlinear equation group based on swarm particle optimization," *Computer Engineering and Applications*, vol. 15, 2006.
- [12] D. Wang and Y. Zhou, "Artificial Fish-Swarm Algorithm for Solving Nonlinear Equation," *Application Research of Computers*, vol. 24, no. 6, pp. 242–244, 2007.
- [13] L. W. Yan and S. H. Chen, "Solving nonlinear equations based on an improved genetic algorithm," *Acta Scientiarum Naturalium Universitatis Sunyatseni*, vol. 50, no. 1, pp. 9–13, 2011.
- [14] L. L. Wu, Z. R. Wang, and C. J. Zhu, "Evolutionary strategy based on a simulated annealing algorithm to solve a system of nonlinear equations," *Journal of Hefei University of Technology*, vol. 31, no. 2, pp. 301–304, 2008.
- [15] Y. Luo, D. Yuan, and G. Tang, "Hybrid genetic algorithm for solving systems of nonlinear equations," *Chinese Journal of Computation Mechanics*, vol. 22, no. 1, pp. 109–114, 2005.
- [16] Q. Tian, Z. Gu, and X. Zhou, "Solving systems of nonlinear equations with hybrid genetic algorithm," *Computer Technology And Development*, vol. 173, pp. 10–12, 2007.
- [17] A. Ouyang, L. Liu, and G. Yue, "Hybrid particle swarm optimization for solving systems of nonlinear functions," *Computer Engineering And Applications*, vol. 47, no. 9, pp. 33–36, 2011.
- [18] B. Zhang and H. Zhang, "Ant colony algorithm for solving nonlinear equations," *Industrial Control Computer*, vol. 26, no. 1, pp. 63–64, 2013.
- [19] X. Wu, *Solving TSP Problem and Systems of Nonlinear Equations with Ant Colony Algorithm*, Masters Thesis [Master, thesis], Shanxi Normal University, 2008.
- [20] A. A. Gavignet and I. J. Sobey, "Model aids cuttings transport prediction," *JPT, Journal of Petroleum Technology*, vol. 41, no. 9, pp. 916–15417, 1989.
- [21] A. Rashno, B. Nazari, S. Sadri, and M. Saraee, "Effective pixel classification of Mars images based on ant colony optimization feature selection and extreme learning machine," *Neurocomputing*, vol. 226, pp. 66–79, 2017.
- [22] F. Zhao, Z. Yao, J. Luan, and X. Song, "A novel fused optimization algorithm of genetic algorithm and ant colony optimization," *Mathematical Problems in Engineering*, vol. 2016, Article ID 2167413, 10 pages, 2016.
- [23] H. Ismikhani, "Effective heuristics for ant colony optimization to handle large-scale problems," *Swarm and Evolutionary Computation*, vol. 32, pp. 140–149, 2017.
- [24] M. Maboudi, J. Amini, M. Hahn, and M. Saati, "Object-based road extraction from satellite images using ant colony optimization," *International Journal of Remote Sensing*, vol. 38, no. 1, pp. 179–198, 2017.
- [25] S. Bououden, M. Chadli, and H. R. Karimi, "An ant colony optimization-based fuzzy predictive control approach for nonlinear processes," *Information Sciences. An International Journal*, vol. 299, pp. 143–158, 2015.
- [26] S. Chatterjee and S. Das, "Ant colony optimization based enhanced dynamic source routing algorithm for mobile ad-hoc network," *Information Sciences. An International Journal*, vol. 295, pp. 67–90, 2015.
- [27] O. Castillo, H. Neyoy, J. Soria, P. Melin, and F. Valdez, "A new approach for dynamic fuzzy logic parameter tuning in ant colony optimization and its application in fuzzy control of a

- mobile robot,” *Applied Soft Computing Journal*, vol. 28, pp. 150–159, 2015.
- [28] B. Fonooni, A. Jevtić, T. Hellström, and L.-E. Janlert, “Applying ant colony optimization algorithms for high-level behavior learning and reproduction from demonstrations,” *Robotics and Autonomous Systems*, vol. 65, pp. 24–39, 2015.
- [29] Q. Ni, H. Xing, Z. Zhang, and alet., “Ant colony algorithm and its applications: review and progress,” in *Computer applications and software*, vol. 25, pp. 12–16, 6 edition, 2008.
- [30] Y. Hajizadeh, M. A. Christie, and V. Demyanov, “Ant Colony Optimization Algorithm for History Matching,” in *Proceedings of the EUROPEC/EAGE Conference and Exhibition*, Amsterdam, The Netherlands, 2009.
- [31] J. Yang, *Research of Ant Colony Algorithm and Its Applications*, [Ph.D. thesis], Zhejiang University, Hangzhou, 2007.
- [32] H. Duan, D. Wang, and X. Yu, “Ant colony algorithm: survey and prospect,” *Engineering science*, vol. 9, no. 2, pp. 98–102, 2007.

Research Article

Multispeed Lattice Boltzmann Model with Space-Filling Lattice for Transcritical Shallow Water Flows

Y. Peng,¹ J. P. Meng,² and J. M. Zhang¹

¹State Key Laboratory of Hydraulics and Mountain River Engineering, Sichuan University, Chengdu 610065, China

²Scientific Computing Department, STFC Daresbury Laboratory, Warrington WA4 4AD, UK

Correspondence should be addressed to J. M. Zhang; zhangjianmin@scu.edu.cn

Received 21 February 2017; Revised 7 June 2017; Accepted 5 July 2017; Published 24 August 2017

Academic Editor: Ling Qian

Copyright © 2017 Y. Peng et al. This is an open access article distributed under the Creative Commons Attribution License, which permits unrestricted use, distribution, and reproduction in any medium, provided the original work is properly cited.

Inspired by the recent success of applying multispeed lattice Boltzmann models with a non-space-filling lattice for simulating transcritical shallow water flows, the capabilities of their space-filling counterpart are investigated in this work. Firstly, two lattice models with five integer discrete velocities are derived by using the method of matching hydrodynamics moments and then tested with two typical 1D problems including the dam-break flow over flat bed and the steady flow over bump. In simulations, the derived space-filling multispeed models, together with the stream-collision scheme, demonstrate better capability in simulating flows with finite Froude number. However, the performance is worse than the non-space-filling model solved by finite difference scheme. The stream-collision scheme with second-order accuracy may be the reason since a numerical scheme with second-order accuracy is prone to numerical oscillations at discontinuities, which is worthwhile for further study.

1. Introduction

The shallow water equations (SWEs) have been used to model free surface flows in rivers and coastal areas under the assumption of the hydrostatic pressure [1]. Numerically, the SWEs can be solved by using conventional numerical method such as finite difference methods [2], finite element methods [3], and finite volume methods [4]. Alternatively, the lattice Boltzmann method (LBM) [5–8] can be used to model SWEs at mesoscopic level [1, 9–18]. In particular, one-dimensional shallow water flows have been studied by Frandsen [19], Thang et al. [20], and Chopard et al. [21].

A major limitation of LBM is its inability to model supercritical flows. For this reason, Chopard et al. [21] developed an asymmetric lattice Boltzmann model for one-dimensional flow flows which can simulate flows with Froude numbers larger than 1. La Rocca et al. [22] proposed a multispeed model with a non-space-filling lattice which is solved by finite difference scheme and successfully simulated supercritical flows. Here, by using the word “multispeed,” it means lattices that have more than one nonzero speed in one dimension; see, for example, La Rocca et al. [22] and Brownlee et al. [23]. For instance, the commonly used D1Q3, D2Q9, and

D3Q19 lattices are not classified as multispeed lattice. Also, “non-space-filling”/“space-filling” means a lattice model that cannot/can fit into the standard stream-collision scheme.

Inspired by the success of the non-space-filling multispeed model, the capability of their space-filling counterpart will be investigated on simulating flows with finite Froude number. Specifically, two space-filling models will be derived by matching hydrodynamic moments (see, e.g., [1, 22, 24]) and then tested by using two typical shallow water problems.

2. Multispeed Lattice Boltzmann Models for 1D Shallow Water Equation

The one-dimensional SWEs read

$$\begin{aligned} \frac{\partial h}{\partial t} + \frac{\partial(hu)}{\partial x} &= 0, \\ \frac{\partial(hu)}{\partial t} + \frac{\partial(hu^2)}{\partial x} &= -g \frac{\partial}{\partial x} \left(\frac{h^2}{2} \right) + \nu \frac{\partial^2(hu)}{\partial x^2} - gh \frac{\partial z_b}{\partial x} \quad (1) \\ &+ F, \end{aligned}$$

which describe the evolution of water depth h and depth-averaged velocity u . The force term F is used to model various interesting effects such as wind-induced surface stress and the bed gradient.

SWEs can be modelled by using a mesoscopic evolution rule

$$\begin{aligned} & f_\alpha(x + e_\alpha \Delta t, t + \Delta t) - f_\alpha(x, t) \\ &= -\frac{1}{\tau} (f_\alpha - f_\alpha^{\text{eq}}) + \Delta t S_\alpha \left(x + \frac{1}{2} e_\alpha \Delta t, t \right) \end{aligned} \quad (2)$$

which describes the fluid motion using a distribution function f . Important factors, such as wind-induced surface stress, are also modelled by a force term at the right hand side; that is, $S_\alpha = w_\alpha e_{\alpha i} F_i / (cs)^2$ and $F_i = F_i(x + (1/2)e_\alpha \Delta t, t)$. The weight factor is denoted by w_α for a discrete velocity e_α , and the sound speed cs can be calculated by using e/λ , where λ is a reference quantity varying with lattice.

To successfully simulate shallow water flows, the key is to define an appropriate local equilibrium function f_α^{eq} and the associated lattice. Here, the equilibrium distribution function in Zhou [1] is generalized to

$$f_\alpha^{\text{eq}} = \begin{cases} w_0 h \left(\frac{1}{w_0} - A \frac{gh}{e^2} - \frac{u_i u_i}{2cs^2} \right) & \alpha = 0, \\ w_\alpha h \left(B \frac{gh}{e^2} + \frac{e_{\alpha i} u_i}{cs^2} + \frac{1}{2} \left[\frac{e_{\alpha i} e_{\alpha j} u_i u_j}{cs^4} - \frac{u_i u_i}{cs^2} \right] \right) & \alpha \neq 0, \end{cases} \quad (3)$$

where the coefficients A and B can be adjusted to satisfy the conservation of mass and momentum, i.e.,

$$\begin{aligned} h &= \sum_\alpha f_\alpha^{\text{eq}}, \\ hu^2 + \frac{gh^2}{2} &= \sum_\alpha e_\alpha e_\alpha f_\alpha^{\text{eq}}. \end{aligned} \quad (4)$$

By substituting (3) into (4), the following equations can be obtained:

$$\begin{aligned} w_0 A &= \sum_\alpha w_\alpha B \quad (\alpha \neq 0), \\ \sum_\alpha \frac{e_\alpha e_\alpha w_\alpha B}{e^2} &= \frac{1}{2} \quad (\alpha \neq 0). \end{aligned} \quad (5)$$

The weights w_α in (3) will depend on the choice of lattice. Here two sets of velocity lattices will be adopted, that is, discrete velocities $(0, \pm 1, \pm 2)$ derived by Qian and Zhou [25] and $(0, \pm 1, \pm 3)$ derived by Chikatamarla and Karlin [26]. They are named as DIQ5A and DIQ5B, respectively, and the relevant parameters are listed in Table 1. For convenience, the standard $(0, \pm 1)$ (DIQ3) lattice also is listed and it will be used for comparison in the following simulations.

3. Case 1: 1D Dam-Break Flow

To test the ability of the derived space-filling models, firstly a simple but challenging 1D dam-break flow over flat bed

TABLE 1: Parameters of three lattice Boltzmann models. The reference quantity and the weights for DIQ5A and DIQ5B are adopted from Qian and Zhou [25] and Chikatamarla and Karlin [26], respectively.

	DIQ3	DIQ5A	DIQ5B
A	3/4	1/2	$(110 + 23\sqrt{10})/48$
B	3/2	1/2	$(5 - \sqrt{10})/6$
λ	$\sqrt{3}$	1	$\sqrt{(5 - \sqrt{10})/3}$
$w(0)$	2/3	1/2	$(16 - 4\sqrt{10})/45$
$w(\pm 1)$	1/6	1/6	$(24 + 3\sqrt{10})/80$
$w(\pm 2)$ or $w(\pm 3)$	—	1/12	$(16 + 5\sqrt{10})/720$

is used. Initially, the water is stationary but there is a discontinuity in the middle of computational region ($x = 1000$ m), described as follows:

$$h(x) = \begin{cases} h_1, & 0 \leq x \leq 1000 \text{ m} \\ h_2, & 1000 \text{ m} < x \leq 2000 \text{ m}. \end{cases} \quad (6)$$

The discontinuity will then propagate stream-wise and change its shape. The sharp gradient at the wave front is difficult to be captured smoothly.

In simulations, 2000 cells are used and therefore Δx is 1 m and Δt is 0.1 s. The initial upstream water depth is set to be 5 m for all tests. Firstly, in order to verify the two multispeed lattice models, the water depth of 3 m is specified in the downstream, where the maximum Froude (Fr) number is 0.26. In Figure 1, the predictions of water depth and velocity of two models and the DIQ3 model are compared with the corresponding analytical solutions [27]. It is shown that all three models are satisfactory, which is as expected since the Fr is relatively low.

To examine the capability of simulating flow with higher Froude number, a series of tests will be carried out by adjusting the downstream depth. It is found, as shown in Figure 2, that the DIQ5B model can simulate flows with $Fr = 1.14$ if the relaxation time is set to be 1.99, although there are errors near the discontinuity perhaps due to the numerical oscillations. The DIQ5A is able to simulate flows with $Fr = 1.07$, while the DIQ3 model fails to simulate Froude number beyond unity. The difference between two multispeed models shows that the capability can also be impacted by the lattice structure.

4. Case 2: 1D Steady Flow over Bump

A steady flow over a bump bed will be utilized to further test the multispeed models. For this flow problem, the subcritical flow over the same bump has been studied by Goutal and Maurel [28], Zhou [1], and Peng et al. [18].

For testing, the bed bottom is defined as

$$Z_b(x) = \begin{cases} 0.2 - 0.05(x - 6)^2, & 8 \text{ m} < x < 12 \text{ m} \\ 0, & \text{else.} \end{cases} \quad (7)$$

The inlet boundary condition is specified by setting a constant discharge of $Q = 4.42 \text{ m}^2/\text{s}$. The length of channel is 25 m.

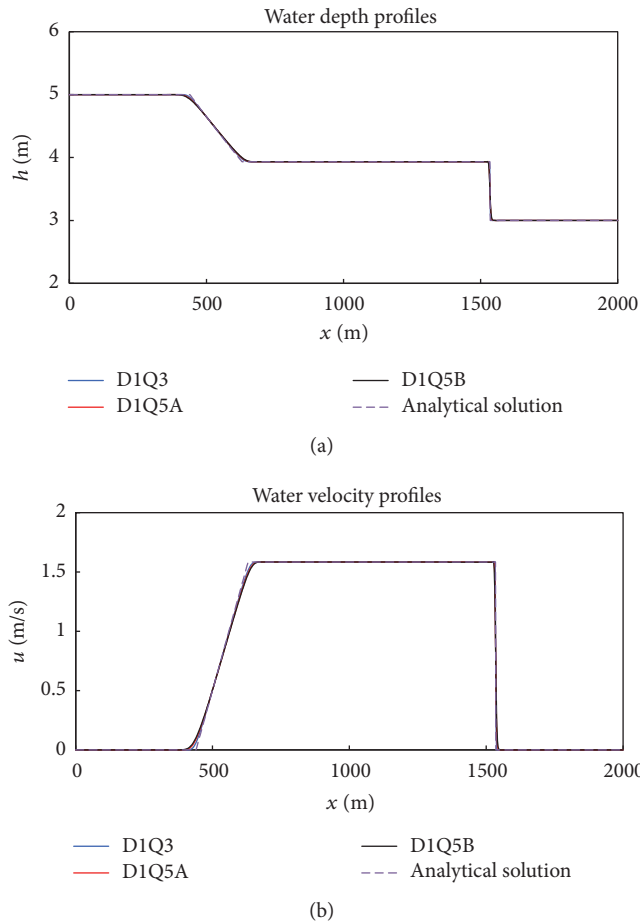


FIGURE 1: Water depth and velocity profiles predicted by D1Q3, D1Q5A, and D1Q5B models at $t = 80$ s ($h_1 = 5$ m and $h_2 = 3$).

A fixed water depth h_0 will be used at the outlet boundary, which will be reduced gradually to find the maximum Fr that can be simulated. The space step Δx is set to be 0.1 m to get the grid-independent solution according to Peng et al. [18] and the time step $\Delta t = 0.002$ s. A relaxation time of 1.99 is employed for all simulations except for the cases shown in Figure 3. Besides, the bed friction is ignored here.

First, the case with a downstream water depth of 2 m is tested to verify the multispeed models. As shown in Figure 3, all models agree well with the analytical solution, which again confirms capability of multispeed model in the relative low Froude number.

Then the downstream water depth is adjusted to test the capability of higher Froude number, that is, to find the minimal downstream water depth. The corresponding results are presented in Figure 4. It is found that the maximum Fr for D1Q3 is 0.69, which is consistent with the previous findings by Zhou [1]. The D1Q5B model can simulate flows with a Froude number of 1.09, while the D1Q5A model fails to simulate Froude number beyond 0.91, which also shows the importance of lattice structure.

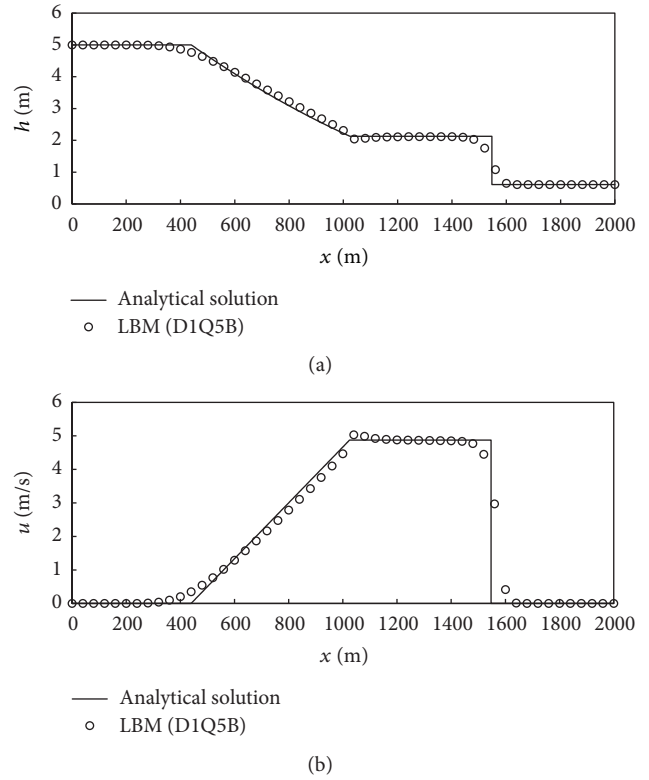


FIGURE 2: Water depth and velocity profiles predicted by D1Q5B models at $t = 80$ s with $h_2 = 0.61$ m and maximum Fr = 1.14 [(a) water depth, (b) water velocity].

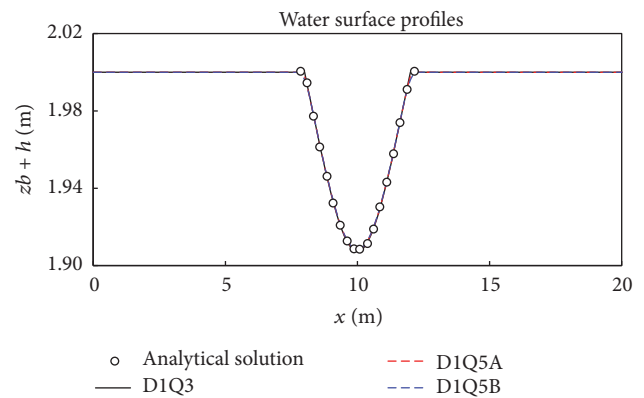


FIGURE 3: Water surface profiles with $h_0 = 2$ m.

5. Concluding Remarks

In this study, the space-filling multispeed lattice Boltzmann model has been investigated to simulate the transcritical shallow water flows. By matching hydrodynamics moments, two lattice models with five integer lattice velocities have been derived, which are tested together with the standard model with three discrete velocities for a 1D dam-break and a 1D steady flow over bump.

It is encouraging to find that the space-filling multispeed model can improve the capability of simulating flows with

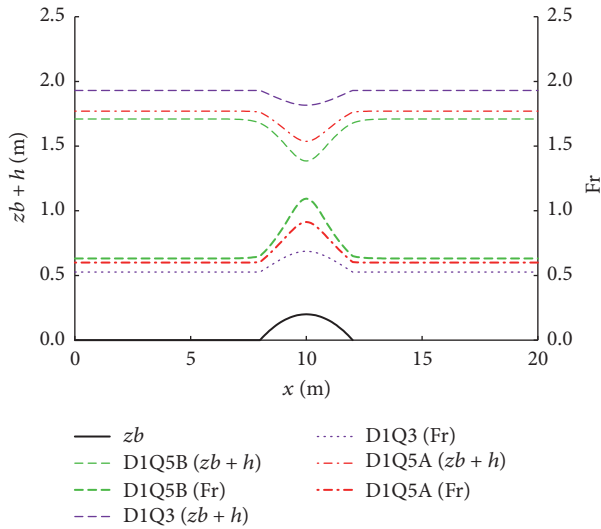


FIGURE 4: Water surface and Froude number profiles with minimum water depth for three models ($h_0 = 1.93, 1.77, \text{ and } 1.71$ and $Fr = 0.69, 0.91, \text{ and } 1.09$ for D1Q3, D1Q5A, and D1Q5B models, resp.).

higher Fr , particularly compared with the standard D1Q3 model. The different performances between two multispeed models show that capability can be impacted by the lattice structure.

In comparison with the non-space-filling model proposed by La Rocca et al. [22], the space-filling versions here demonstrate limited capability in terms of finite Froude number although similar numbers of discrete velocities are used in these two studies. This is potentially due to the fact that the stream-collision scheme is a second-order scheme. It is well known that a numerical scheme of second-order accuracy is prone to numerical oscillations at discontinuities. The impact of the stream-collision scheme will be studied further in the future.

Conflicts of Interest

The authors declare that they have no conflicts of interest.

Acknowledgments

Y. Peng would like to acknowledge the financial support of National Natural Science Foundation of China (Grant nos. 51409183, 51579166, and 51611130203). J. P. Meng is grateful to the support of the Open Fund from the State Key Laboratory of Hydraulics and Mountain River Engineering in Sichuan University, China (Grant no. SKHL1410). Both Y. Peng and J. P. Meng would like to acknowledge the support of International Exchange Programme of Royal Society, UK (IE151119) and NSFC, China (51611130203).

References

- [1] J. G. Zhou, *Lattice Boltzmann Methods for Shallow Water Flows*, Springer, Berlin, Germany, 2004.

- [2] V. Casulli and R. T. Cheng, "Semi-implicit finite difference methods for three-dimensional shallow water flow," *International Journal for Numerical Methods in Fluids*, vol. 15, no. 6, pp. 629–648, 1992.
- [3] T. W. H. Sheu and C. C. Fang, "High resolution finite-element analysis of shallow water equations in two dimensions," *Computer Methods in Applied Mechanics and Engineering*, vol. 190, no. 20–21, pp. 2581–2601, 2001.
- [4] A. H. Daoud, K. A. Rakha, and A. G. Abul-azm, "A two-dimensional finite volume hydrodynamic model for coastal areas: model development and validation," *Ocean Engineering*, vol. 35, no. 1, pp. 150–164, 2008.
- [5] F. J. Higuera and S. Succi, "Simulating the flow around a circular cylinder with a lattice boltzmann equation," *Europhysics letters*, vol. 8, no. 6, pp. 517–521, 1989.
- [6] R. Benzi, S. Succi, and M. Vergassola, "The lattice Boltzmann equation: theory and applications," *Physics Reports*, vol. 222, no. 3, pp. 145–197, 1992.
- [7] S. Chen and G. D. Doolen, "Lattice Boltzmann method for fluid flows," *Annual Review of Fluid Mechanics*, vol. 30, pp. 329–364, 1998.
- [8] C. K. Aidun and J. R. Clausen, "Lattice-boltzmann method for complex flows," *Annual Review of Fluid Mechanics*, vol. 42, pp. 439–472, 2010.
- [9] R. Salmon, "The lattice Boltzmann method as a basis for ocean circulation modeling," *Journal of Marine Research*, vol. 57, no. 3, pp. 503–535, 1999.
- [10] P. J. Dellar, "Nonhydrodynamic modes and a priori construction of shallow water lattice Boltzmann equations," *Physical Review E—Statistical, Nonlinear, and Soft Matter Physics*, vol. 65, no. 3, Article ID 036309, pp. 1–12, 2002.
- [11] H. Liu, J. G. Zhou, and R. Burrows, "Numerical modeling of turbulent compound channel flow using the lattice Boltzmann method," *International Journal for Numerical Methods in Fluids*, vol. 59, no. 7, pp. 753–765, 2009.
- [12] H. Liu, J. G. Zhou, and R. Burrows, "Multi-block lattice Boltzmann simulations of subcritical flow in open channel junctions," *Computers and Fluids*, vol. 38, no. 6, pp. 1108–1117, 2009.
- [13] C. Biscarini, S. D. Francesco, and M. Mencattini, "Application of the lattice Boltzmann method for large-scale hydraulic problems," *International Journal of Numerical Methods for Heat and Fluid Flow*, vol. 21, no. 5, pp. 584–601, 2011.
- [14] K. R. Tubbs and F. T. Tsai, "GPU accelerated lattice Boltzmann model for shallow water flow and mass transport," *International Journal for Numerical Methods in Engineering*, vol. 86, no. 3, pp. 316–334, 2011.
- [15] C. Biscarini, S. D. Francesco, F. Nardi, and P. Manciola, "Detailed simulation of complex hydraulic problems with macroscopic and mesoscopic mathematical methods," *Mathematical Problems in Engineering*, vol. 2013, Article ID 928309, 14 pages, 2013.
- [16] Y. Peng, J. G. Zhou, and R. Burrows, "Modelling solute transport in shallow water with the lattice Boltzmann method," *Computers and Fluids*, vol. 50, pp. 181–188, 2011.
- [17] Y. Peng, J. G. Zhou, J. M. Zhang, and H. Liu, "Lattice Boltzmann modeling of shallow water flows over discontinuous beds," *International Journal for Numerical Methods in Fluids*, vol. 75, no. 8, pp. 608–619, 2014.
- [18] Y. Peng, J. M. Zhang, and J. G. Zhou, "Lattice boltzmann model using two relaxation times for shallow-water equations," *Journal*

- of Hydraulic Engineering*, vol. 142, no. 2, Article ID 06015017, 2015.
- [19] J. B. Frandsen, "A simple LBE wave runup model," *Progress in Computational Fluid Dynamics*, vol. 8, no. 1-4, pp. 222–232, 2008.
- [20] P. V. Thang, B. Chopard, L. Lefèvre, D. A. Ondo, and E. Mendes, "Study of the 1D lattice Boltzmann shallow water equation and its coupling to build a canal network," *Journal of Computational Physics*, vol. 229, no. 19, pp. 7373–7400, 2010.
- [21] B. Chopard, P. V. Thang, and L. Lefèvre, "Asymmetric lattice Boltzmann model for shallow water flows," *Computers and Fluids*, vol. 88, pp. 225–231, 2013.
- [22] M. La Rocca, A. Montessori, P. Prestininzi, and S. Succi, "A multispeed Discrete Boltzmann Model for transcritical 2D Shallow water flows," *Journal of Computational Physics*, vol. 284, pp. 117–132, 2015.
- [23] R. A. Brownlee, A. N. Gorban, and J. Levesley, "Stable multi-speed lattice Boltzmann methods," Tech. Rep. MA-06-026, University of Leicester, Leicester, UK, 2006, <https://arxiv.org/abs/cond-mat/0611616>.
- [24] H. W. Zheng, C. Shu, Y. T. Chew, and J. Qiu, "A platform for developing new lattice Boltzmann models," *International Journal of Modern Physics C. Computational Physics and Physical Computation*, vol. 16, no. 1, pp. 61–84, 2005.
- [25] Y.-H. Qian and Y. Zhou, "Complete Galilean-invariant lattice BGK models for the Navier-Stokes equation," *Europhysics Letters*, vol. 42, no. 4, pp. 359–364, 1998.
- [26] S. S. Chikatamarla and I. V. Karlin, "Entropy and Galilean invariance of lattice Boltzmann theories," *Physical Review Letters*, vol. 97, no. 19, Article ID 190601, 2006.
- [27] O. Delestre, C. Lucas, P.-A. Ksinant et al., "SWASHES: a compilation of shallow water analytic solutions for hydraulic and environmental studies," *International Journal for Numerical Methods in Fluids*, vol. 72, no. 3, pp. 269–300, 2013.
- [28] N. Goutal and F. Maurel, Proceedings of the 2nd Workshop on Dam-break Wave Simulation, Tech. Rep. HE-43/97/016/B, Département Laboratoire National d'Hydraulique, Groupe Hydraulique Fluviale, Electricité de France, France, 1997.

Research Article

Numerical Study for Near-Bed Variables in Velocity-Skewed Oscillatory Sheet Flow Transport

Xin Chen,¹ Zichao Zhang,² Yong Li,³ and Xiaoyan Shi¹

¹Beijing Engineering Research Center of Safety and Energy Saving Technology for Water Supply Network System, China Agricultural University, Beijing 100083, China

²School of Electric Power, North China University of Water Resources and Electric Power, Zhengzhou 450045, China

³Tianjin Centre, China Geological Survey, Tianjin 300170, China

Correspondence should be addressed to Xin Chen; chenx@cau.edu.cn

Received 14 April 2017; Revised 2 July 2017; Accepted 11 July 2017; Published 22 August 2017

Academic Editor: Alistair Borthwick

Copyright © 2017 Xin Chen et al. This is an open access article distributed under the Creative Commons Attribution License, which permits unrestricted use, distribution, and reproduction in any medium, provided the original work is properly cited.

The near-bed sediment concentration and vertical sediment flux are important in sediment transport mechanics, but they are known much less than the horizontal sediment flux, especially for fine sediment in unsteady flows. A developed two-phase model is applied to study the near-bed sediment concentration, vertical sediment flux, and the relevant total sediment amount for the velocity-skewed oscillatory sheet flow transport. With the sediment concentration hindered fall velocity, the classical reference concentration formulas conducted by Engelund and Fredsoe (1976) and Zyserman and Fredsoe (1994) are utilized for the comparison with the two-phase model and illustration of the phase-lag and sediment size effects in near-bed sediment concentration and vertical sediment flux. The concentration and vertical flux predicted by the two-phase model agree well with experimental data and are better than empirical formulas. Furthermore, the sediment size effect for pick-up flux function over starved bed is shown to be quite different from that containing sufficient sediment in oscillatory flows.

1. Introduction

The phenomenon of sediment entrainment and settlement is universal in river and coastal environment and extraordinarily important in the subaquatic geomorphology. The vertical sediment fluxes consist of pick-up flux due to turbulence, settling flux due to gravity, and their summation denoting the variation rate of total sediment amount. Associated with the sediment concentration, they represent the vertical sediment exchange strength and are important for the study of sediment settling down to deposition and picked up into suspension. Most sediment models need a type of near-bed condition associated with vertical sediment flux for bottom boundary conditions. So the predictions of near-bed concentration, vertical sediment flux, pick-up flux, and settling flux are very fundamental for such sediment models.

In fully developed steady flows, the pick-up flux and settling flux are in balance and the total vertical flux is zero. Numerous steady flow formulas have been carried out to

predict the vertical sediment flux over loose sediment bed in developed equilibrium steady flows. Generally, some are straight driven by the pick-up function based on clear water flow over starved bed without considering the influence of suspended sediment [1, 2], so they are not appropriate in the flow already containing large amount of suspended sediment. The others are evaluated by the balance of pick-up and settling down according to the concentration and sediment fall velocity [3], and the relevant concentration denotes the vertical sediment flux strength.

The near-bed sediment concentration and vertical sediment fluxes in unsteady flows are much more complicated than that in steady flows due to the phase-lag effect, and formulas in unsteady flows are lacking. So the near-bed concentrations denoting vertical flux strength in steady flows [4–6] are applied and widely used in unsteady numerical models for sediment transport [7–9], and even their concentrations drop to zero near the flow reversal when the bottom shear stress is under a threshold. The knowledge of vertical

sediment flux in unsteady flow is still necessary for numerical models' boundary conditions in engineering.

In unsteady flows, the vertical sediment flux can be derived from the variation rate of sediment amount in movement [10], which can be obtained by single phase models or two-phase models. The single phase numerical models are dependent on the reference concentration or vertical flux as the bottom boundary conditions and cannot describe the vertical flux below reference height. The two-phase models [11–13] can obtain the details of reference concentration and vertical flux as a result of the turbulent upward effect and gravitational settlement. Yu et al. [12] study the vertical flux for medium and coarse sediment, but the model is not valid for fine sediment (diameter $D < 0.2$ mm) when the phase-lag is obvious due to the sediment stress. In addition, the vertical sediment fluxes have not been extracted accurately enough due to the noise or error of modelling high concentration. Very little is known about the near-bed concentration and vertical flux for fine sediment and the phase-lag effects, which are important in the generation of net sediment transport, especially in velocity-skewed oscillatory flows with a sharp wave crest and gentle wave trough.

Present study utilizes a two-phase model to study the near-bed sediment concentration and vertical fluxes in velocity-skewed oscillatory sheet flows containing sufficient amount of sediment. The results mainly exhibit and explain the phase-lag characteristics in concentration and vertical flux at the reference height, near-immobile bed, and very low concentration area for difference sediment sizes.

2. Applied Models

Chen and Yu [13] two-phase model is utilized to obtain the sediment concentration and vertical fluxes. For comparison, several steady flow empirical formulas are also applied.

2.1. Two-Phase Flow Model. The two-phase model includes Reynolds averaged continuity and momentum equations:

$$\begin{aligned} \frac{\partial [(1-\alpha)u_{f,j} + \alpha u_{s,j}]}{\partial x_j} &= 0, \\ \frac{\partial \alpha}{\partial t} + \frac{\partial (\alpha u_{s,j})}{\partial x_j} &= \frac{\partial}{\partial x_j} \left(\frac{\nu_{st}}{\delta_s} \frac{\partial \alpha}{\partial x_j} \right), \\ \frac{\partial [(1-\alpha)u_{f,i}]}{\partial t} + \frac{\partial [(1-\alpha)u_{f,i}u_{f,j}]}{\partial x_j} &= -\frac{1-\alpha}{\rho_f} \frac{\partial p}{\partial x_i} + \frac{\partial \tau_{fj}}{\partial x_j} + (1-\alpha)g_i - \frac{F_i}{\rho_f}, \\ \frac{\partial (\alpha u_{s,i})}{\partial t} + \frac{\partial (\alpha u_{s,i}u_{s,j})}{\partial x_j} &= -\frac{\alpha}{\rho_s} \frac{\partial p}{\partial x_i} + \frac{\partial \tau_{sj}}{\partial x_j} + \alpha g_i + \frac{F_i}{\rho_s}, \end{aligned} \quad (1)$$

where α is the sediment volumetric concentration; u is the velocity; x is the Cartesian coordinate; t is the time; the subscripts f and s stand for the fluid and the sediment

phases; the indices $i, j = 1, 2$ represent horizontal and vertical components and obey summation convention; ν_{st} is the sediment turbulent viscosity confirmed by fluid turbulent viscosity ν_{ft} ; $\delta_s = 1$ is the Schmidt number; p is the pressure; τ is the stress; ρ is the density; g is the body force; F is the interaction force. ν_{st} , ν_{ft} , τ , and F can be seen in Chen and Yu [13]. Equations (1) are closed by k - ε turbulent equations:

$$\begin{aligned} \frac{\partial [(1-\alpha)k]}{\partial t} + \frac{\partial [(1-\alpha)ku_{fj}]}{\partial x_j} &= \frac{\partial}{\partial x_j} \left[(1-\alpha)\nu_{fk} \frac{\partial k}{\partial x_j} \right] + (1-\alpha)(G-\varepsilon), \\ \frac{\partial [(1-\alpha)\varepsilon]}{\partial t} + \frac{\partial [(1-\alpha)\varepsilon u_{fj}]}{\partial x_j} &= \frac{\partial}{\partial x_j} \left[(1-\alpha)\nu_{f\varepsilon} \frac{\partial \varepsilon}{\partial x_j} \right] + \frac{1-\alpha}{k} (C_1 G \varepsilon - C_2 \varepsilon^2), \end{aligned} \quad (2)$$

where k is the turbulent kinetic energy (TKE); ε is the turbulent kinetic energy dissipation rate (DTKE); $\nu_{fk} = \nu_{ft}$, $\nu_{f\varepsilon} = \nu_{ft}/1.33$, $C_1 = 1.44$, and $C_2 = 1.92$; G is the turbulence generation term [13].

Equations (1) and (2) are applied for sheet flows happening at maximum Shields parameter $\theta > 0.8$ – 1.0 when large amounts of sediment are in movement. The computation domain covers the immobile bed and the water tunnel top. The initial bed is located at $x_2 = 0$. The still water condition is assumed to be the initial condition. At the time $t = 0$, all flow variables are zero, while $\alpha = 0$ at $x_2 > 0$ and $\alpha = 0.6$ at $x_2 \leq 0$.

At the tunnel top, $u_{f,1} = U(t) = U_0\{0.8 \cos[2\pi(t/T - 0.21)] + 0.2 \cos[4\pi(t/T - 0.21)]\}$, where U is the free stream (Figure 1); $A = dU/dt$; U_0 and A_0 are the amplitudes of U and A ; T is the period; subscripts a and d denote acceleration and deceleration stages; scripts c and t denote the crest and trough durations. Positive ($t/T = 0$ – 0.42) and negative ($t/T = 0.42$ – 1) U denote onshore and offshore durations, respectively. The vertical gradient of all variables vanished, and the sediment flux is

$$\frac{\nu_{st}}{\delta_s} \frac{\partial \alpha}{\partial x_2} - u_{s,2} \alpha = 0. \quad (3)$$

Nonslip condition is assumed at the bottom that $\alpha = 0.6$ and the other variables are set to be zero.

In the lateral boundaries, the horizontal gradients of α , u , k , and ε are all zero. The flow is driven by a horizontal pressure gradient:

$$\frac{\partial p}{\partial x_1} = -\rho_f \frac{dU}{dt}. \quad (4)$$

2.2. Flux Definition and Empirical Formulas. The sediment amount in movement is defined by Nielsen et al. [10]:

$$Q(x_2, t) = \int_{x_2}^{\infty} \alpha(y, t) dy. \quad (5)$$

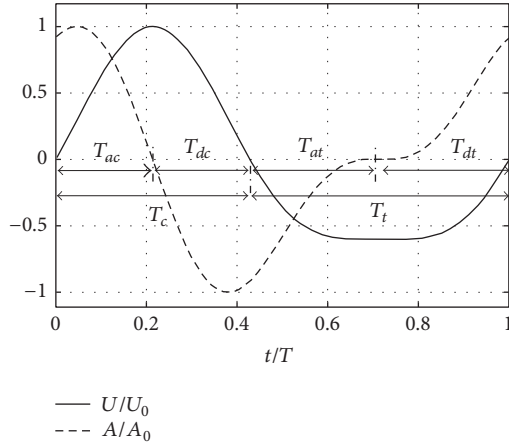


FIGURE 1: Free stream velocity and acceleration.

The total vertical flux is

$$q_t(x_2, t) = \frac{\partial Q(x_2, t)}{\partial t}, \quad (6)$$

and the downward settling flux is

$$q_d(x_2, t) = -\alpha(x_2, t) w(x_2, t), \quad (7)$$

where w is the fall velocity equal to $-u_{s,2}$. The pick-up flux is

$$q_u(x_2, t) = q_t(x_2, t) - q_d(x_2, t). \quad (8)$$

The dimensionless equations (10)–(12) are $\Phi = q[(S - 1)gD^3]^{-0.5}$, where the specific gravity $S = 2.65$. In the two-phase model, α and w are straight given by (1), and $q_u = -v_{st}/\delta_s(\partial\alpha/\partial x_2)$.

For q_d comparison, the classical Engelund and Fredsoe [4] formula (EF76) and Zyserman and Fredsoe [5] formula (ZF94) for reference α defined at $x_2/D = 2$ and $w = w_0(1 - \alpha)^n$ are applied. w_0 is the single sediment fall velocity in still water [14] and n is the same as Yu et al. [12]. The EF76 formula is

$$\alpha(2D, t) = \frac{0.6}{(1 + \lambda)^3}, \quad (9)$$

λ

$$= \kappa c_r \sqrt{\frac{\theta - \theta_c}{0.013S\theta} \left\{ 1 - \frac{\pi\mu}{6} \left[(\theta - \theta_c)^4 + \left(\frac{\pi\mu}{6} \right)^4 \right]^{-1/4} \right\}}, \quad (10)$$

where D is the sediment diameter; λ is the linear concentration; $\kappa = 0.4$ is the Karman constant; $c_r = 2$ is associated with the bed roughness; $\theta_c = 0.05$ is the critical Shields parameter; $\mu = 0.6$ is the dynamic friction coefficient. The ZF94 formula is

$$\alpha(2D, t) = \frac{0.331(\theta - \theta_c)^{1.75} c_m}{c_m + 0.331(\theta - \theta_c)^{1.75}}, \quad (11)$$

where $c_m = 0.46$. Figure 2 shows the reference α against θ for the two empirical formulas. The EF76 considers the dispersive

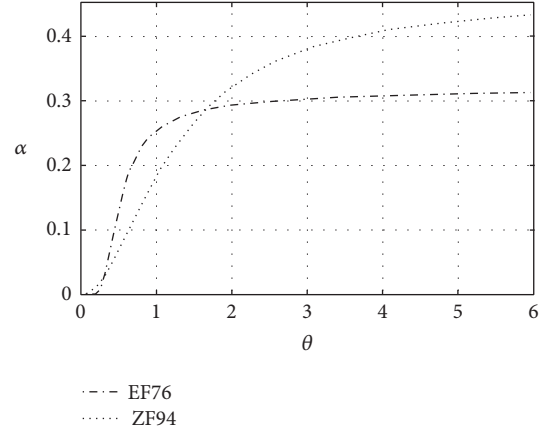
FIGURE 2: Reference α against θ in steady flow.

TABLE 1: Computation conditions.

Test case	U_0	D (mm)	T (s)	w_0 (m/s)
Fine: FA5010	1.5	0.13	5.0	0.0126
Medium: MA5010	1.5	0.27	5.0	0.0387
Coarse: CA5010	1.5	0.46	5.0	0.0672

stress from suspended sediment and drag of moving bed, so the reference α is mildly increased when $\theta > 1$ and is hindered mildly to be a constant. ZF94 is based on Garcia and Parker's [3] prohibiting a particular trend toward a limitation for high sediment concentration. So the ZF94 also has a limitation of α and keeps a mild increment after $\theta > 6$ (Figure 2).

For q_u comparison, van Rijn [1] pick-up function over a starved bed is applied:

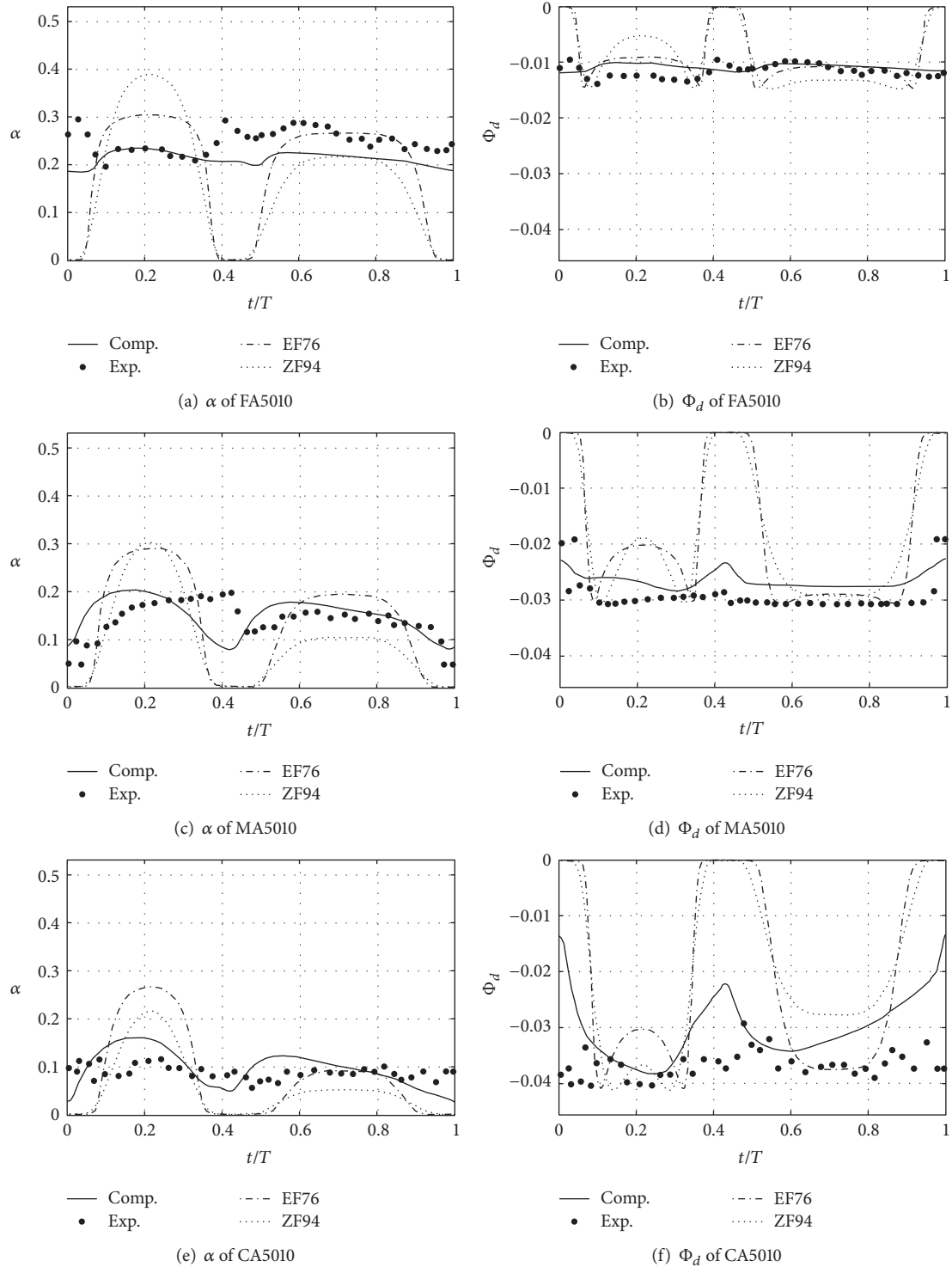
$$\begin{aligned} \Phi_u &= \frac{q_u}{\sqrt{(S - 1)gD^3}} \\ &= 3.3 \times 10^{-4} \left(\frac{\theta}{\theta_c} - 1 \right)^{1.5} \left[\frac{(S - 1)gD^3}{\nu_{f0}^2} \right]^{0.1}, \end{aligned} \quad (12)$$

where ν_{f0} is the fluid molecular viscosity. q_d in EF76 and ZF94 formulas and q_u in van Rijn [1] drop to zero when $\theta < \theta_c$ without phase-lag effect.

3. Results

Computations are based on the O'Donoghue and Wright [15] experiments in Table 1, where the phase-lag effect increases with the decrement of D . Results are shown for the classical reference height $x_2/D = 2$ first and second the near-immobile bed and low concentration areas.

3.1. Reference Vertical Flux. The references α and Φ_d are shown in Figure 3. The absolute locations of $x_2/D = 2$ are slightly different and are very close to each other, so they can be treated as an approximation to the initial bed. The α distribution pivot, around which α is almost constant in a wave period, exists at the location a little below the initial bed

FIGURE 3: Reference α and Φ_d .

[15]. In Figures 3(a), 3(c), and 3(e), the location $x_2/D = 2$ is very close to the pivots, and both the maximum free stream flow and flow reversal would probably lead to α peaks. For the experiment (dot), the α difference between flow crest ($t/T = 0.21$) and flow trough ($t/T = 0.71$) is not obvious and even the crest flow strength is much larger than that at flow trough

(Figure 3), because many sediments picked up at the flow crest are still in movement at the flow trough. Large D corresponds to small concentration magnitude due to the large fall velocity. α never decrease to zero in a period due to the phase-lag effect. The results of two-phase model exhibit clearly the decrement of concentration magnitude when D increases,

TABLE 2: Root-mean-square (RMS) errors at $x_2/D = 2$.

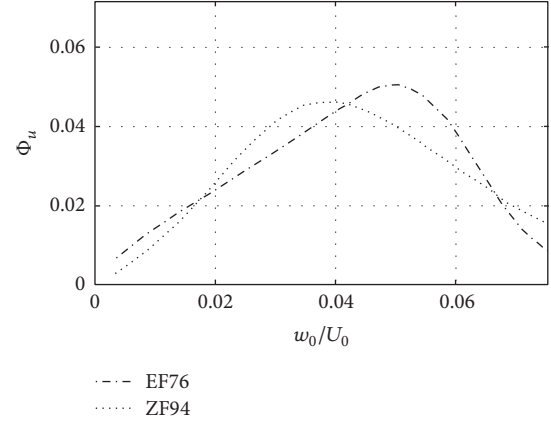
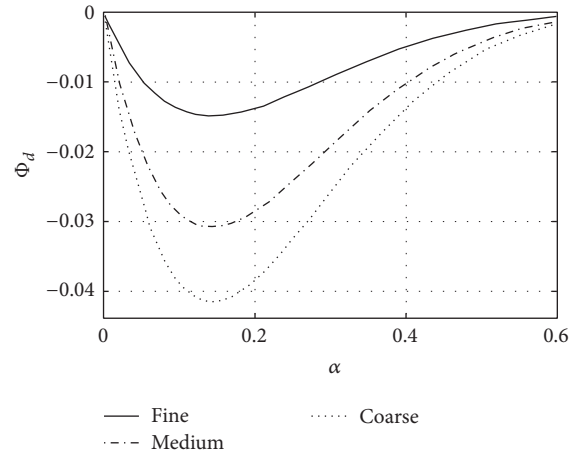
Cases	α			Φ_d		
	FA5010	MA5010	CA5010	FA5010	MA5010	CA5010
Two-phase model	0.051	0.039	0.042	0.037	0.038	0.053
EF76	0.138	0.094	0.086	0.091	0.100	0.118
ZF94	0.148	0.094	0.068	0.095	0.102	0.106

and the computed α is also always above a proper nonzero value (Figures 3(a), 3(c), and 3(e)) due to the phase-lag. Some differences between two-phase model and experimental data exist from a qualitative perspective, probably due to the high concentration measurement uncertainties [15] without mass conservation.

The EF76 and ZF94 are strictly in phase with U without any phase-shift. Mild increment at large shear stress (Figure 2) leads to a small concentration variation near onshore flow peak around $t/T = 0.21$ (Figures 3(a) and 3(c)). There are also small concentration variations for EF76 and ZF94 near the offshore flow peak ($t/T = 0.6\sim 0.8$) caused by the nearly constant U (Figure 1). When θ is less than a critical level, EF76 and ZF94 predicted α are unrealistic zero (Figure 2), because the formulas are derived without the phase-lags. Predicted concentrations of EF76 and ZF94 increase rapidly in the acceleration stage and decrease fast in the deceleration stage (Figures 3(a), 3(c), and 3(e)). Furthermore, their prediction between onshore and offshore are quite different because of the large different flow strength and bottom shear stress. Although both EF76 and ZF94 can predict the experiments near the flow trough ($t/T = 0.6\sim 0.8$), they much overestimate the experiments near the flow crest ($t/T = 0.21$). Generally, the EF76 and ZF94 are weaker than the two-phase model results at the flow reversal and flow crest. RMS errors in Table 2 for two-phase model are much less than EF76 and ZF94 formulas.

Corresponding to the concentration due to phase-lag, the experimental Φ_d never decreases to zero near the flow reversal in Figure 3, and the value near the flow crest is close to that near the flow trough. The two-phase model predicted computed Φ_d agree very well with the experiments for nonzero duration and the magnitude increment with D . Although the α magnitude decreases with the increment of D , the magnitude of Φ_d increases with the increment of D in Figure 3, because the flux is hindered by high concentration at small sediment size. Based on the same $U_0 = 1.5$ m/s, the pick-up flux ($\Phi_u = -\Phi_d$) against D for ZF94 and ZF76 in steady flow is shown in Figure 4, where the dimensionless D is represented by w_0/U_0 . The flux increases first and then decreases with D (w_0/U_0). The Φ_d magnitude would decrease with small α when D is large enough as the balanced pick-up flux ($\Phi_u = -\Phi_d$) in Figure 4, and finally it decreases to zero when reference α magnitude reduces to zero.

Near the flow crest, there are hollows in EF76 and ZF94 that predicted Φ_d which are far from the experiments (Figures 3(b), 3(d), and 3(f)) with overestimation of α (Figures 3(a), 3(c), and 3(e)), because the maximum Φ_d and optimal α exist in the two empirical formulas when we applied $w = w_0(1 - \alpha)^n$, as seen in Figure 5. The maximum Φ_d

FIGURE 4: Φ_u in steady flow.FIGURE 5: Φ_d of different D in steady flow.

approximately corresponds to optimal $\alpha = 0.14$, after which Φ_d decreases with the increment of α by the hindered fall velocity. Near the flow trough, both EF76 and ZF94 can predict Φ_d well due to the agreement of concentration. At flow reversal, both the EF76 and ZF94 predicted Φ_d drop to zero because of unrealistic zero α (Figures 3(a), 3(c), and 3(e)) when θ is less than a critical value. Predicted Φ_d of EF76 and ZF94 changes rapidly near flow reversal with rapid change of α . Generally, the RMS errors for EF76 and ZF94 are much larger than two-phase model for Φ_d (Table 2).

Against the settling down induced by gravity, the pick-up effect induced by turbulence maintains the suspension of sediment, and the total vertical sediment flux (Φ_t) is the balance of pick-up flux (Φ_u) and settling flux (Φ_d). Figure 6

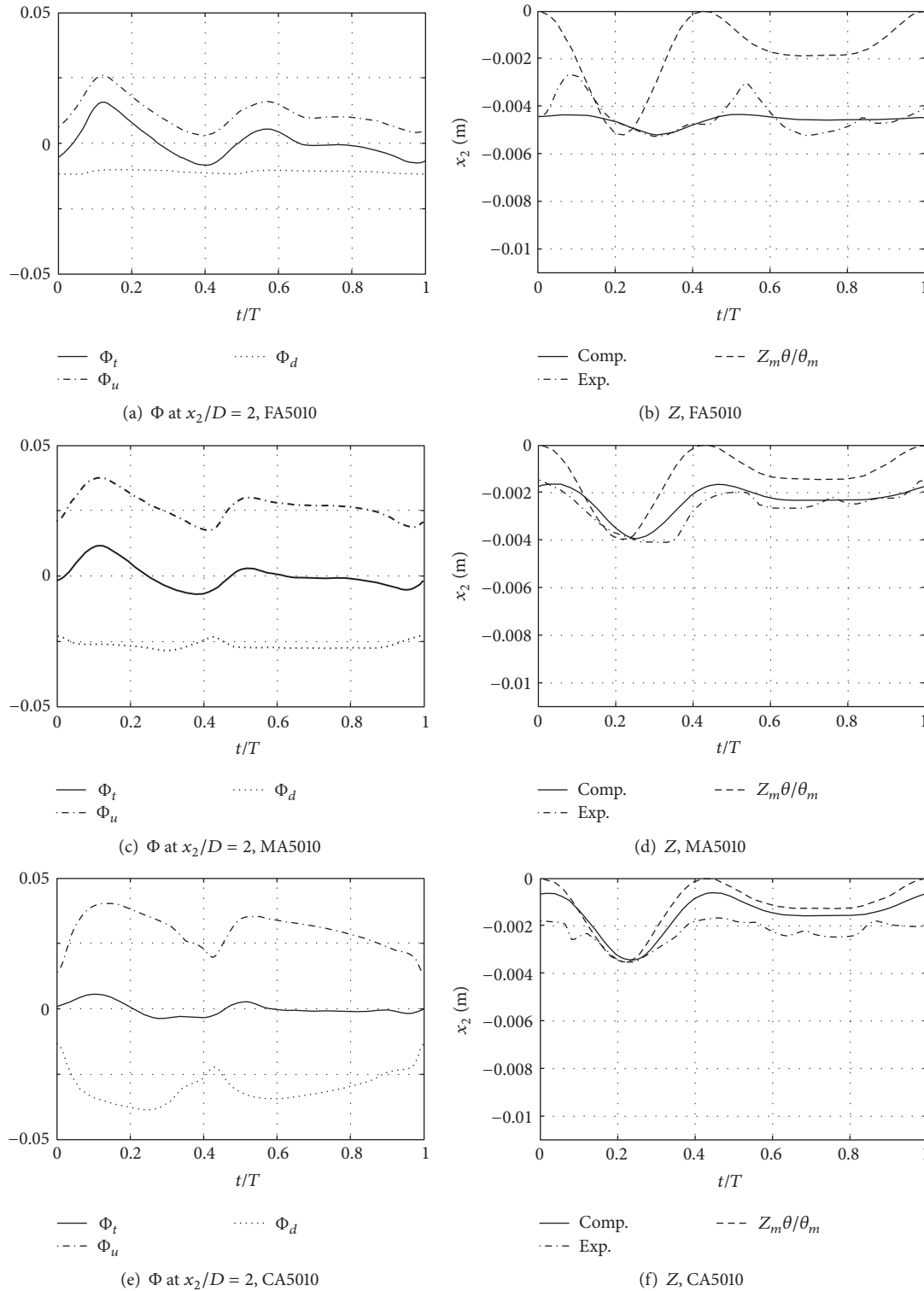


FIGURE 6: Vertical sediment flux and immobile bed surface.

shows the two-phase model computed Φ_t and Φ_u at $x_2/D = 2$ and the immobile bed surface level denoted by Z ($\alpha = 0.594$). To illustrate their relationships available and validate Φ_u indirectly, Φ_d in Figure 3 is included again. Magnitudes of Φ_u and Φ_d are around each other with opposite direction,

and they are in periodic averaged balance with averaged $\Phi_t = 0$. As the difference of Φ_u and Φ_d , Φ_t is almost one magnitude smaller than Φ_u and Φ_d . Φ_u increases and reaches a local maximum value before flow crest ($t/T = 0.21$) or flow trough ($t/T = 0.71$) and decreases to a local minimum

value before flow reversal both in the onshore and in the offshore durations. Correspondingly, Φ_t almost follows the same variation tendency as Φ_u . Similar process can be seen in Ribberink et al. [16], Nielsen et al. [10], Li et al. [17], and Bakhtyar et al. [11]. Onshore magnitudes of Φ_u and Φ_t are larger than that at offshore, and the onshore variations are more rapid than offshore.

Z almost varies together with Φ_t which decided the bed morphology in the present three cases in Figure 6. The bed morphology repeats periodically in oscillatory sheet flow conditions without horizontal variation. When $\Phi_t > 0$, Z decreases because sediment below the initial bed is picked up. Z decreases to minimum ($t/T = 0.25-0.3$) almost after Φ_t decreases to zero. While $\Phi_t < 0$, Z increase because sediment above the initial bed settles down. Z increases to local maximum ($t/T = 0.45-0.5$) almost after Φ_t increases to zero. Z never drops to zero due to the phase-lag effect. For comparison, $Z_m\theta/\theta_m$ is shown considering theoretical $Z/Z_m = \theta/\theta_m$ in steady flow, where Z_m is the maximum Z . The difference between Z and $Z_m\theta/\theta_m$ denotes the phase-lag. There is a time phase-shift between Z and $Z_m\theta/\theta_m$. For fine 0.13 mm, the phase-lag effect is the largest with the most obvious difference between Z and $Z_m\theta/\theta_m$, while the phase-lag effect for 0.46 mm is the smallest because present Z almost coincides with $Z_m\theta/\theta_m$.

Corresponding to Φ_d , the Φ_u magnitude also increases with the increment of D for the three sizes. But it does not increase with the increment of D monotonously, which is similar to Figure 4. In the two-phase model, Φ_u is obtained from the turbulence diffusion term $-\nu_{st}/\delta_s(\partial\alpha/\partial x_2)$ modelled by the classical gradient transport assumption. There are two reasons for the smallest Φ_u amplitude with fine $D = 0.13$ mm in Figure 6: the concentration gradient and the turbulence intensity. With $D = 0.13$ mm, much sediment is picked up for suspension and $\partial\alpha/\partial x_2$ at $x_2/D = 2$ becomes smaller than $D = 0.27-0.46$ mm. When much sediment is already in suspension in the boundary layer, much turbulence energy is dissipated [15, 18] corresponding to small ν_{st} and restrains other sediments to be picked up.

For comparison without the effect of suspended hindered sediment, van Rijn [1] pick-up flux function is shown in Figure 7 under the same $U_0 = 1.5$ m/s. van Rijn [1] pick-up function decreases with the increment of D , which is opposite to the flows containing sufficient sediment amount in Figures 4 and 5. The onshore magnitude is much larger than offshore magnitude without the effect of suspended hindered sediment. In the experiment [15], Φ_u did not drop to zero due to the shear (velocity overshoot) and turbulence that exist near flow reversal. But van Rijn [1] function based on steady flow drops to zero around flow reversal. Comparing the van Rijn pick-up function (Figure 7) with Φ_u given by two-phase model (Figure 6), their Φ_u magnitudes are the closest only for $D = 0.46$ mm when the suspension sediment amount is the smallest (Figure 8). Over all, the van Rijn [1] pick-up function is not valid for the oscillatory sheet flow when the maximal $\theta > 0.8-1.0$ and sufficient sediment is in suspension.

In developed oscillatory sheet flow, the averaged Φ_t is zero, and suspended sediment is quasi-steady saturated and

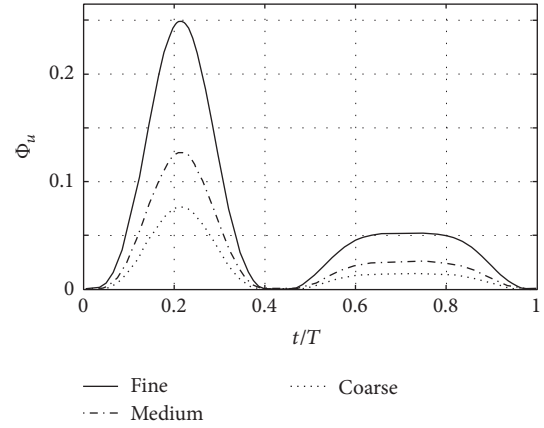


FIGURE 7: Pick-up function of van Rijn.

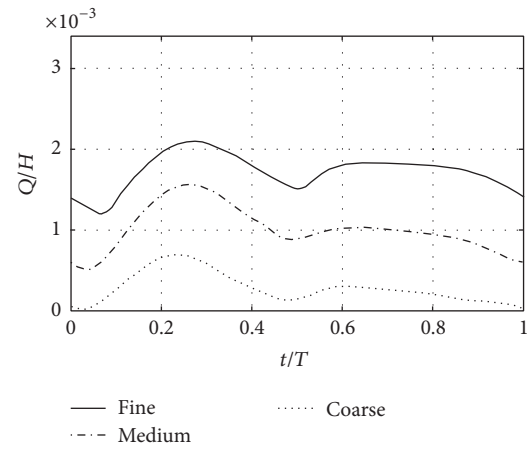


FIGURE 8: Sediment amount above $x_2/D = 2$.

hinders the pick-up process. The vertical fluxes display the sediment exchange in vertical direction, but they can not be used as the index for the sediment-laden capacity of oscillatory sheet flow. The sediment amount Q is in a quasi-steady status in the developed stage and can be used to estimate the sediment-laden capacity. Q above $x_2/D = 2$ is shown in Figure 8, where $H = 0.5$ m is the water depth. Q increases with the decrement of D . The variation rate of Q is Φ_t (see (6)), so Q reaches a local maximum value when positive Φ_t decreases to zero near the flow peak and reaches a local minimum value when negative Φ_t increases to zero near the flow reversal. Due to large phase-lag, the Q magnitude's ratio between onshore ($t/T = 0-0.42$) and offshore ($t/T = 0.42-1$) for 0.13 mm case is 0.87, much larger than 0.41 for 0.46 mm case.

3.2. Other Vertical Fluxes. The near-bed flux at the locations above or below the reference height is essential for better understanding of the near-bed sediment exchange. Figure 9 shows the two-phase model computed vertical fluxes at $x_2 = 10$ mm and $x_2 = -3.5$ mm. -3.5 mm is in the main eroded area with high concentration and almost fully hindered w_0 . 10 mm is out of the sheet flow layer where particle interactions

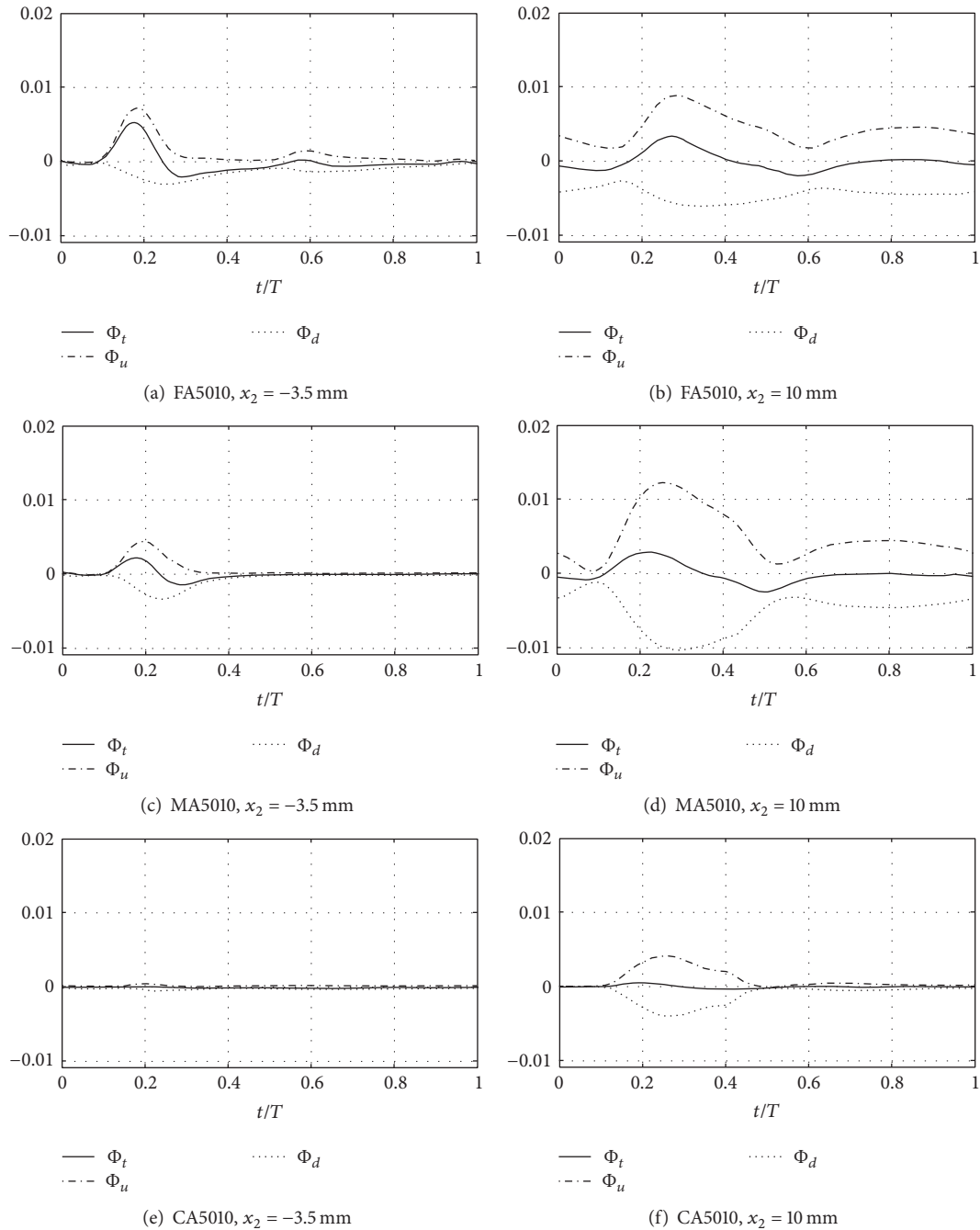
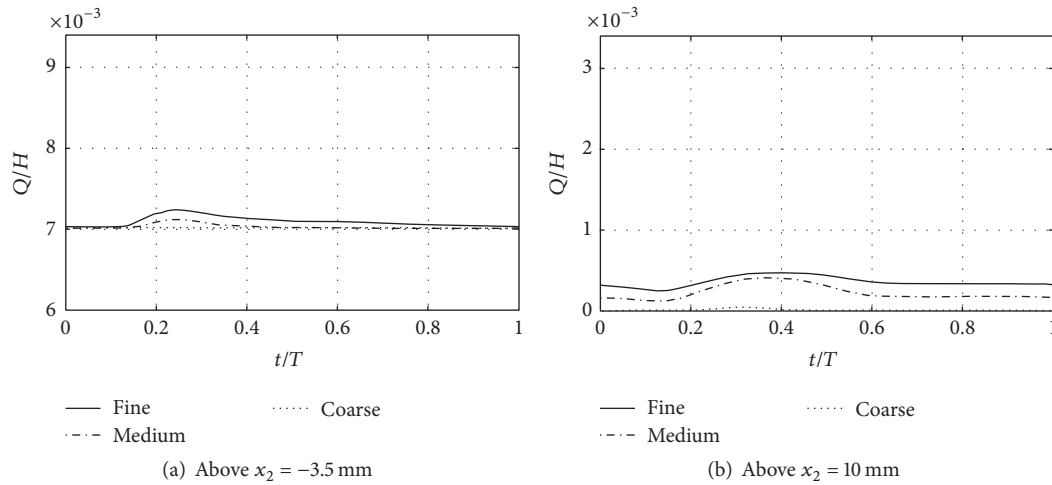


FIGURE 9: Computed vertical flux at $x_2 = -3.5$ mm and $x_2 = 10$ mm.

can be negligible and is still in the oscillatory boundary layer with small concentration and unhindered w_0 . Because the absolute locations of x_2/D in the main eroded area or low concentration area for three sizes are far from each other, the vertical locations in Figure 9 are in absolute millimetres rather than as a function of the diameter. At $x_2 = -3.5$ mm, Φ_u , Φ_d , and Φ_t decrease with the increment of D . Two peak values exist in Figure 9(a) and onshore magnitude is larger than offshore, but only one peak value exists near the onshore flow crest in Figure 9(c), while in Figure 9(e) almost zero

fluxes exist because -3.5 mm is nearly located at the immobile bed for $D = 0.46$ mm. At $x_2 = 10$ mm, obvious phases for all the fluxes are shifted after $x_2/D = 2$. Both the maximum Φ_u and Φ_d are around 0.01, which are much larger than Φ_t . For fine and medium sediment (Figures 9(b) and 9(d)), their magnitudes of Φ_u , Φ_d , and Φ_t are similar to and larger than coarse sediment (Figure 9(f)). For coarse sediment, both Φ_u and Φ_d only exist near the onshore flow peak, and Φ_t almost disappear compared to the fine and medium sediment cases. Comparing the results in Figure 9 to that in Figure 6, all Φ_t ,


 FIGURE 10: Sediment amount above $x_2 = -3.5$ mm and $x_2 = 10$ mm.

Φ_u , and Φ_d decrease from the initial bed toward the immobile bed and the top of tunnel. The decrement is also seen in Li et al. [17] and Bakhtyar et al. [11]. All the fluxes finally decrease to zero when the location is down into the immobile bed or up to the top of tunnel.

Also, Q above the locations -3.5 mm and 10 mm are shown (Figure 10). At $x_2 = -3.5$ mm and $x_2 = -10$ mm, the variation amplitudes of each sediment sizes are much smaller than that at $x_2/D = 2$ (Figure 8) due to smaller Φ_t in Figure 9. Finally, the Q variation amplitudes decrease to zero in the immobile bed or tunnel top corresponding to $\Phi_t = 0$ (Figure 9).

4. Conclusions

The present work studies the near-bed conditions in velocity-skewed oscillatory sheet flows with a two-phase model and classical empirical formulas. The phase-lag and sediment size effects in concentration, vertical sediment flux, and sediment amount are focused on the area near the initial bed, the immobile bed, and the low concentration area.

Due to the phase-lag, the reference concentration and the settling flux never drop to zero in a period even at the flow reversal, and the relevant magnitudes between onshore and offshore are similar. The two-phase model computed reference concentration and settling flux by two-phase model agree with experiment very well and are better than empirical formulas. Under the same flows, reference concentration magnitudes decrease with the increment of sediment size due to the increment of fall velocity. While, for settling flux, as the product of concentration and fall velocity, the magnitude increases first and then decreases with the increment of sediment size.

The pick-up flux and settling flux are in periodic averaged balance in oscillatory sheet flow, and their magnitudes are around each other with opposite direction. The pick-up flux increases and reaches a local maximum value before flow peak and decreases to a local minimum value before flow reversal both in the onshore and in the offshore durations.

Corresponding to the settling flux, the pick-up flux also increases first and then decreases with the increment of sediment size.

The sediment amount magnitude increases with the decrement of sediment size. Phase-lag effect increases the sediment amount magnitude's ratio between onshore and offshore. As the sediment amount variation rate, the total vertical flux is much smaller than the pick-up flux and varies almost following the pick-up flux. The vertical sediment flux magnitude decreases from the initial bed toward immobile bed and top of tunnel.

Conflicts of Interest

The authors declare that they have no conflicts of interest.

Acknowledgments

This work was supported by the National Natural Science Foundation of China (Grants no. 51609244 and no. 11472156) and National Science-Technology Support Plan of China (Grant no. 2015BAD20B01).

References

- [1] L. C. van Rijn, "Sediment pick-up functions," *Journal of Hydraulic Engineering*, vol. 110, no. 10, pp. 1494–1502, 1984.
- [2] D. Zhong, G. Wang, and Y. Ding, "Bed sediment entrainment function based on kinetic theory," *Journal of Hydraulic Engineering*, vol. 137, no. 2, pp. 222–233, 2011.
- [3] M. Garcia and G. Parker, "Entrainment of bed sediment into suspension," *Journal of Hydraulic Engineering*, vol. 117, no. 4, pp. 414–435, 1991.
- [4] F. Engelund and J. Fredsoe, "A sediment transport model for straight alluvial channels," *Nordic Hydrology*, vol. 7, pp. 295–324, 1976.
- [5] J. A. Zyserman and J. Fredsoe, "Data analysis of bed concentration of suspended sediment," *Journal of Hydraulic Engineering*, vol. 120, no. 9, pp. 1021–1042, 1994.

- [6] S. Wright and G. Parker, "Flow resistance and suspended load in sand-bed rivers: Simplified stratification model," *Journal of Hydraulic Engineering*, vol. 130, no. 8, pp. 796–805, 2004.
- [7] M. Li, P. T. Fernando, S. Pan, B. A. O'Connor, and D. Chen, "Development of a quasi-3d numerical model for sediment transport prediction in the coastal region," *Journal of Hydro-Environment Research*, vol. 1, no. 2, pp. 143–156, 2007.
- [8] B. G. Ruessink, T. J. J. Van Den Berg, and L. C. Van Rijn, "Modeling sediment transport beneath skewed asymmetric waves above a plane bed," *Journal of Geophysical Research: Oceans*, vol. 114, no. 11, article C11021, 2009.
- [9] W. N. M. Hassan and J. S. Ribberink, "Modelling of sand transport under wave-generated sheet flows with a RANS diffusion model," *Coastal Engineering*, vol. 57, no. 1, pp. 19–29, 2010.
- [10] P. Nielsen, K. Van Der Wal, and L. Gillan, "Vertical fluxes of sediment in oscillatory sheet flow," *Coastal Engineering*, vol. 45, no. 1, pp. 61–68, 2002.
- [11] R. Bakhtyar, A. Yeganeh-Bakhtiary, D. A. Barry, and A. Ghaheri, "Two-phase hydrodynamic and sediment transport modeling of wave-generated sheet flow," *Advances in Water Resources*, vol. 32, no. 8, pp. 1267–1283, 2009.
- [12] X. Yu, T.-J. Hsu, J. T. Jenkins, and P. L.-F. Liu, "Predictions of vertical sediment flux in oscillatory flows using a two-phase, sheet-flow model," *Advances in Water Resources*, vol. 48, pp. 2–17, 2012.
- [13] X. Chen and X. Yu, "A numerical study on oscillatory flow-induced sediment motion over vortex ripples," *Journal of Physical Oceanography*, vol. 45, no. 1, pp. 228–246, 2015.
- [14] L. C. van Rijn, *Principles of Sediment Transport in Rivers, Estuaries and Coastal Seas*, Aqua Publications, 1993.
- [15] T. O'Donoghue and S. Wright, "Concentrations in oscillatory sheet flow for well sorted and graded sands," *Coastal Engineering*, vol. 50, no. 3, pp. 117–138, 2004.
- [16] J. S. Ribberink, C. M. Dohmen-Janssen, D. M. Hanes, S. R. McLean, and C. Vincent, "Near-bed sand transport mechanisms under waves," in *Proceedings of the 27th International Conference on Coastal Engineering, ICCE 2000*, pp. 3263–3276, Sydney, Australia, July 2000.
- [17] M. Li, S. Pan, and B. A. O'Connor, "A two-phase numerical model for sediment transport prediction under oscillatory sheet flows," *Coastal Engineering*, vol. 55, no. 12, pp. 1159–1173, 2008.
- [18] K. C. Wilson, "Friction of wave-induced sheet flow," *Coastal Engineering*, vol. 12, no. 4, pp. 371–379, 1989.

Research Article

Lattice Boltzmann Method of a Flooding Accident at Gopeng, Perak, Malaysia

Siti Habibah Shafiai, Diana Bazila Shahruzzaman, Goh Juin Xien, and Mohamed Latheef

Department of Civil and Environmental Engineering, Universiti Teknologi PETRONAS, 32610 Bandar Seri Iskandar, Perak, Malaysia

Correspondence should be addressed to Siti Habibah Shafiai; sitihabibah.shafiai@utp.edu.my

Received 20 April 2017; Accepted 31 May 2017; Published 16 August 2017

Academic Editor: Jian G. Zhou

Copyright © 2017 Siti Habibah Shafiai et al. This is an open access article distributed under the Creative Commons Attribution License, which permits unrestricted use, distribution, and reproduction in any medium, provided the original work is properly cited.

The extraordinary flood had hit the residential area at Taman Raia Mesra, Gopeng, Perak, Malaysia, in November 2016. The event illustrated how the river basin had been fully inundated due to the heavy rainfall and caused the overflow to this affected area. It was reported that the occurrence became worst as the outlet of retention pond which connects to the river is unsuitable for the water outflow. Henceforth, this paper attempts to evaluate the causal factor of this recent disaster by using a model developed from Lattice Boltzmann Method (LBM). The model also incorporated with the rainfall and stormwater in LABSWE™. The simulation was commenced with the basic tests for model validation comprising turbulent and jet-forced flow in a circular channel, which resulted in a good agreement for both models. The simulation continued by using LABSWE model to reveal the water depth and velocity profile at the study site. These results had proven the incompatibility size of the outlet pond which is too small for the water to flow out to the river. The study is capable of providing the authorities with a sustainable design of proper drainage system, especially in Malaysia which is constantly receiving the outrageous heavy rainfall.

1. Introduction

A flood is well defined as the overflow of high water from the occupied water basin system including river and stream [1]. Flood is ranked as a third largest of the disastrous events among the Asian countries after wave surge and wind storm [2]. The occurrence can be dangerous to life and can lead to economic and properties loss. In Malaysia, a flood is not a new occasion especially for those who settled at the northeast of Peninsular Malaysia. Generally, the area will be flooded during northeast monsoon season held between October and March almost every year.

Perak which is located nearby the northeast state of Peninsular Malaysia is not exempted from the flood attacks. In December 2014, the state of Perak was affected by the astonishing flood on a scale that has never been experienced before. It is reported that more than 50 relief centres have been operated due to this event, with Perak Tengah as the most affected district. Typically, the cause of flood is a heavy continuous rainfall; however, the major triggering factor for the flood is the improper drainage system [3]. Yoon et al.

(2010) investigated that almost 30% of the flood is contributed by the improper setup of a drainage system, followed by pollution and urbanization management with 20% and 18%, respectively [3]. The flood can affect one's life (death) and health including psychological or physiological problems [4].

Recognizing the adverse consequence of the flood, there is a need to demonstrate such a natural phenomenon by using a model or device that provides an accurate prediction. The Computational Fluid Dynamics (CFD) model applied in the water sector is a prevailing device to simulate the condition of the fluid especially in urban hydrology and water management field [5]. The ability to investigate the real situation by using a device can help to predict the future condition [6]. Hence, we benefit by comparing and improvising both theory and the real-life situations. There are numerous numbers of computer models for simulating the water sector including WEST, SIMBA, and MIKE. The evolution in technology enables the researchers to study their scope up to the microscopic scale, and today it is even possible to formulate the complex system.

Lattice Boltzmann Method (LBM) is a modern computer model using High-Performance Computing (HPC) efficiently for fluid simulation within the complex geometries [7]. LBM is an advanced technique evolved from the Lattice Gas Automata (LGA) method. LGA method represents the macroscopic physical variables; meanwhile, LBM is able to solve the flow problem up to the microscopic equation [8]. LBM is proposed to allow an easy program and can be used for simulating the complex flow in complex geometries. The LBM comprised three criteria including lattice Boltzmann equation, lattice pattern, and local equilibrium distribution function. These tasks are responsible for forming a lattice Boltzmann equation for shallow water flows known as LABSWE.

The LABSWE had been applied in various conditions of water flow by many scientists including steady and unsteady flows, tidal flows, and turbulent flows in different dimensions [7]. The findings were compared with the physical modelling or analytical solutions in order to demonstrate their validation. The result shows that the accuracy of the LABSWE is very promising, hence proving the efficiency and capabilities of the method in simulating fluids.

The flood study by using the numerical approached had been explored by many researchers [9, 10]. However, these studies focus on the scope of macroscopic result only. On the other hand, the study on flood is by using the LABSWE providing a microscopic outcome. The research may involve several variables including river profile, water flow direction, and water depth profile which help to estimate the future occurrence of the flood, hence reducing the risk of flood [11].

Taman Raia Mesra located at Gopeng, Perak, is under construction for the residential area. The project site is about 30 acres of land with the presence of retention pond located nearby the housing area. The retention pond is attached with the adjacent river by an outlet. In November 2016, the area was flooded which caused a major loss to the developer. The area received about 821 mm rainfall intensity throughout the event. The continuous heavy rainfall is causing the water from the nearby river, Sg Tekah, to overflow at the site. It is mentioned that the housing area was inundated by flood for about three days. The ground visit observed that one of the factors that may cause the flood is the size of outlet drainage of the retention pond which is too small.

The study was then started immediately after the event to overcome the problem. The LABSWE is used in this study to analyse the flood at Taman Raia Mesra. The model also incorporates in the LABSWE the rainfall and stormwater parameters that lead to the flood. The few basic tests were investigated for the model validation including turbulent flow and jet-forced flow in a circular channel. The simulation results of the study area are capable of providing the authorities with a sustainable design of proper drainage system at Taman Raia Mesra, Gopeng, Perak, hence, preventing the occurrence of a future flood at the site.

2. Materials and Methods

2.1. Lattice Boltzmann Model for Shallow Water Equation with Turbulent Flow (LABSWE). The LBM for shallow water

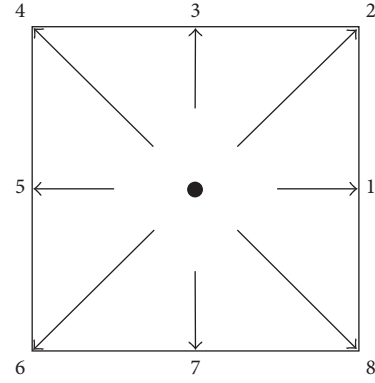


FIGURE 1: Lattice pattern with a 9-velocity square [12].

equation (LABSWE) based on the 9-velocity square lattice pattern is approached. The lattice pattern indicated the movement of the particle on a lattice unit at its velocity along one of the eight links specified 1–8 (Figure 1). Meanwhile, the zero value means the particle is at resting phase with zero speed.

The Lattice Boltzmann equation (LBE) can be determined as

$$f'_a(x + e_a \Delta t, t + \Delta t) = f_a(x, t) + \frac{\Delta t}{N_\alpha e^2} e_{ai} F_i(x, t), \quad (1)$$

where f_a is the particle distribution function; $e = \Delta x / \Delta t$, where Δx is the lattice size and Δt is the time. N_α is a constant determined by

$$N_\alpha = \frac{1}{e^2} \sum_\alpha e_{ax} e_{ax} = \frac{1}{e^2} \sum_\alpha e_{ay} e_{ay}. \quad (2)$$

There are two steps in LBM including streaming and collision. If the particles move at their own velocities towards their nearest neighbours, it is called streaming step. On the other hand, collision step occurs when the particles arrive at lattice point and have interaction with one another. This interaction, according to the scattering rules, will affect their velocities and direction. Hence, the new distribution function is expressed as

$$f_\alpha(x, t) = f'_\alpha(x, t) - \Omega_\alpha [f'_\alpha(x, t) - f_\alpha^{\text{eq}}(x, t)], \quad (3)$$

where Ω_α is the collision operator and f_α^{eq} is the local equilibrium distributions function. The combination of streaming and collision steps in a 9-velocity square lattice modified the lattice Boltzmann equation as

$$f'_a(x + e_a \Delta t, t + \Delta t) = f_a(x, t) - \frac{1}{\tau_t} [f_a(x, t) - f_a^{\text{eq}}(x, t)] + \frac{\Delta t}{6e^2} e_{ai} F_i, \quad (4)$$

where τ_t is the total relaxation time for modelling flow turbulence and can be calculated from

$$\tau_t = \tau + \tau_e,$$

$$\tau_e = \frac{-\tau \sqrt{\tau^2 + 18C_S^2 / (e^2 h)} \sqrt{\Pi_{ij} \Pi_{ij}}}{2}. \quad (5)$$

In the equation above, τ_e is the eddy relaxation time, and Π_{ij} is defined as

$$\Pi_{ij} = \sum_{\alpha} e_{\alpha i} e_{\alpha j} (f_{\alpha} - f_{\alpha}^{\text{eq}}). \quad (6)$$

$$f_{\alpha}^{\text{eq}} = \begin{cases} h - \frac{5gh^2}{6e^2} - \frac{2h}{3e^2} u_i u_i, & \alpha = 0, \\ \frac{gh^2}{6e^2} - \frac{h}{3e^2} e_{\alpha i} u_i + \frac{h}{2e^4} e_{\alpha i} e_{\alpha j} u_i u_j - \frac{h}{6e^2} u_i u_i, & \alpha = 1, 3, 5, 7, \\ \frac{gh^2}{24e^2} - \frac{h}{12e^2} e_{\alpha i} u_i + \frac{h}{8e^4} e_{\alpha i} e_{\alpha j} u_i u_j - \frac{h}{24e^2} u_i u_i, & \alpha = 2, 4, 6, 8, \end{cases} \quad (8)$$

where h is water depth and u_i is flow velocity which can be obtained through

$$h = \sum_{\alpha} f_{\alpha},$$

$$u_i = \frac{1}{h} \sum_{\alpha} e_{\alpha i} f_{\alpha}. \quad (9)$$

2.2. Flood Model. There are a few parameters taken into account for the flood model in this study. The discharge rainfall (Q) was focusing on the data on November 2016 with the catchment area located in a nearby city; Ipoh is taken as a reference. The discharge can be calculated by using the Rational Formula based on urban Stormwater Management Manual for Malaysia (MSMA 2):

$$Q = \frac{C \times i \times A}{360}, \quad (10)$$

where Q is a peak flow (m^3/s), i is the average intensity of rainfall, and A is site area. C is the coefficient of a rainfall that can be obtained from the table provided by MSMA 2.

The discharge of a domestic waste usage is derived from the continuity equation

$$Q = AV, \quad (11)$$

where Q is a peak flow (m^3/s), A is an average intensity of rainfall, and V is the water velocity. The velocity of the water flow is obtained by using Manning's equation

$$V = \frac{1}{n} R^{2/3} S^{1/2}. \quad (12)$$

In (12), V is defined as the velocity of water in the drain (m/s), n is Manning's Roughness coefficient obtained from

In order to identify the velocity vector of particles in the square lattice, the equation that follows will be approached:

$$e_{\alpha} = \begin{cases} (0, 0), & \alpha = 0, \\ e \left[\cos \frac{(\alpha - 1)\pi}{4}, \sin \frac{(\alpha - 1)\pi}{4} \right], & \alpha = 1, 3, 5, 7, \\ \sqrt{2}e \left[\cos \frac{(\alpha - 1)\pi}{4}, \sin \frac{(\alpha - 1)\pi}{4} \right], & \alpha = 2, 4, 6, 8. \end{cases} \quad (7)$$

Hence, to solve the shallow water equations using LBM, a local equilibrium function is defined as

the MSMA 2. R (m) is referred as a hydraulic radius and S (mm/hr) is a drain slope.

For the simulation process, the inlet drainage to the river is set up with a rectangular channel with dimension and slope of $300 \text{ mm} \times 600 \text{ mm}$ and $S_a = 0.002$, respectively. Meanwhile, the river nearby is defined to be rectangular stream channel with a flatbed bathymetry. The layout plan of the river is developed by integrating the AutoCAD system into LABSWE.

3. Results and Discussion

3.1. Turbulent Flow within a Channel with a Circular Cavity. The flow in a channel with a circular cavity is simulated to demonstrate the ability of the model in simulating the effect of the turbulent flow in a river attached to a lake [12]. The shape of the model prediction for the simulation is prepared as illustrated in Figure 2. The model is designed with a rectangular channel 1.89 m wide and 18.9 m long. The channel is attached to a circular sidewall cavity on the right side of the channel with a radius of 3.15 m .

The simulation is set up to a constant value of flow velocity components, $u = 0.25 \text{ m/s}$ and $v = 0 \text{ m/s}$. The water depth is maintained at $h = 0.25 \text{ m}$. A 190×70 lattice with grid space of $\Delta x = 0.1 \text{ m}$ applied. A semislip boundary condition has a surface roughness coefficient $C_f = 0.0045$ and is used at the solid walls. The relaxation time and Smagorinsky constant are applied with $\tau = 0.6$ and $C_S = 0.3$, respectively. A time step of $\Delta t = 0.03 \text{ s}$ is applied in this model.

The model reached its steady state after 10000th iteration with relative error $E_R = 5.24 \times 10^{-9}$. The fully convergence flow of velocity vectors and streamlines are generated in the cavity by the model as illustrated in Figures 3 and 4, respectively.

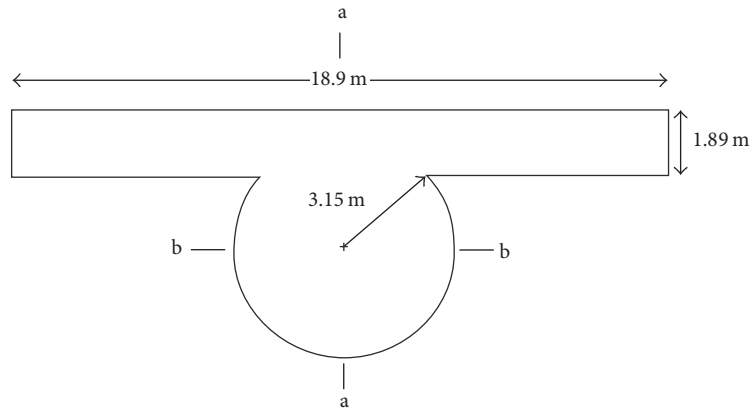


FIGURE 2: Dimension of the open channel with circular sidewall cavity [12].

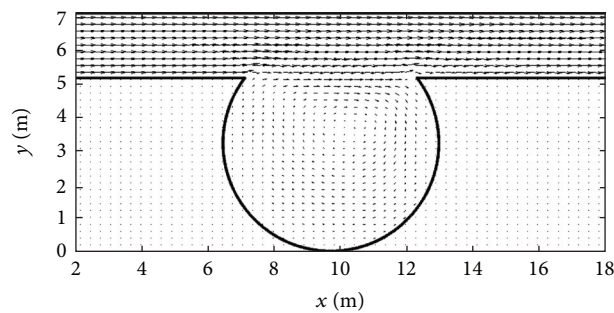


FIGURE 3: Velocity vectors in the circular sidewall cavity [12].

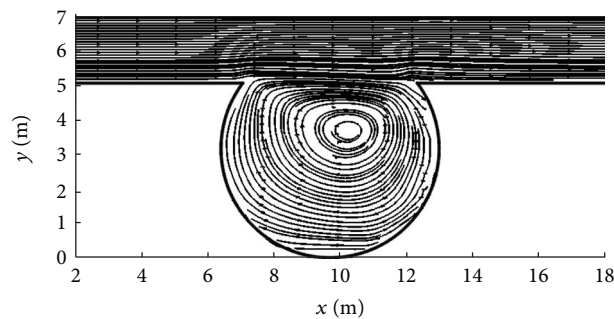


FIGURE 4: Streamlines flow in the circular sidewall cavity [12].

The u and v velocity components along the vertical (a-a) and horizontal (b-b) cross section were validated (Figures 5 and 6) by comparing the data with data from Kuipers and Vreugdenhill (1973) [13]. The evaluation demonstrates that the model used in this study generates a better outcome than the previous data.

3.2. Turbulent Jet-Forced Flow in Circular Basin. The jet-forced flow in the circular basin was simulated by using the LABSWE [12]. The model of the simulation is designed in the symmetrical shape which is a standard profile of the circular basin. The dimensions and flow parameters for the model are shown in Figure 7.

The simulation flow is prepared with the radius of a basin $r = 1.0$ m with an opening of inlet and outlet is at an angle of $\pi/16$ rad. The outlet position is separated by $7\pi/8$ rad from the inlet. The model is utilized with 280×160 lattice grid spacing $\Delta x = \Delta y = 0.0125$ m with time step $\Delta t = 0.00625$ s. For boundary conditions, there is a similar set up at upstream and downstream channel. The model is arranged with a water depth of $h = 0.1$ m and velocity components of $u = 0.1$ m/s and $v = 0$ m/s.

The simulations of the turbulent jet-forced flow show that the model reached a steady state condition at 10000th iteration, with a relative error $E_R = 1.54 \times 10^{-7}$. The optimum streamline with the required circulation length and pattern

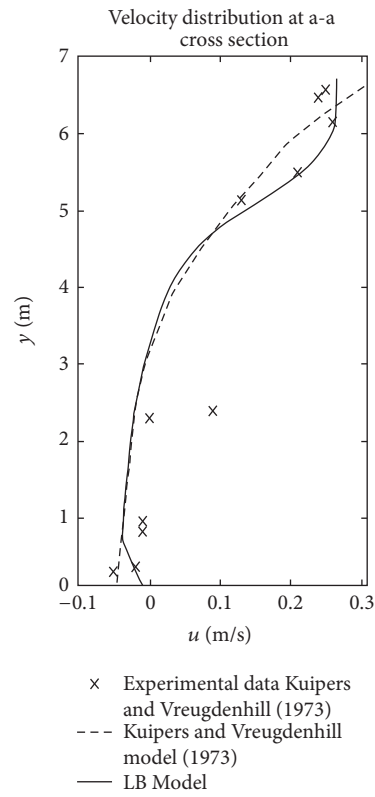


FIGURE 5: Velocity components u at the vertical (a-a) cross section [12].

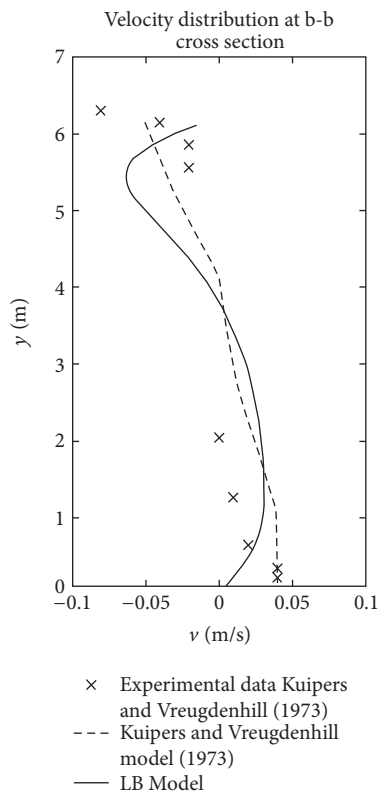


FIGURE 6: Velocity components v at the horizontal (b-b) cross section [12].

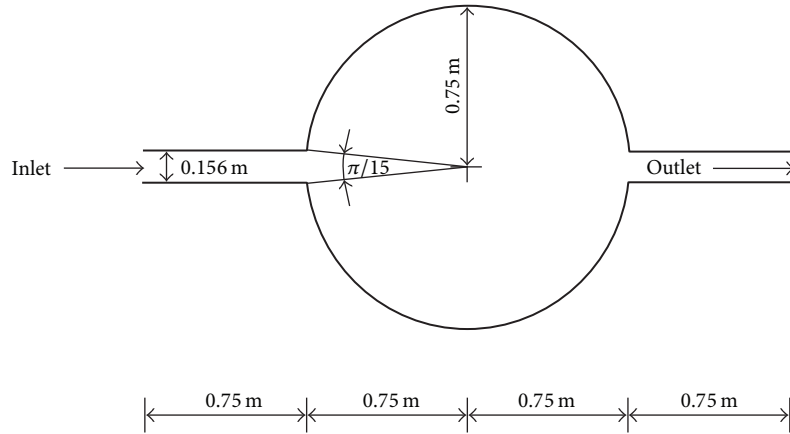


FIGURE 7: Dimension of the jet-forced flow for the symmetrical circular basin [12].

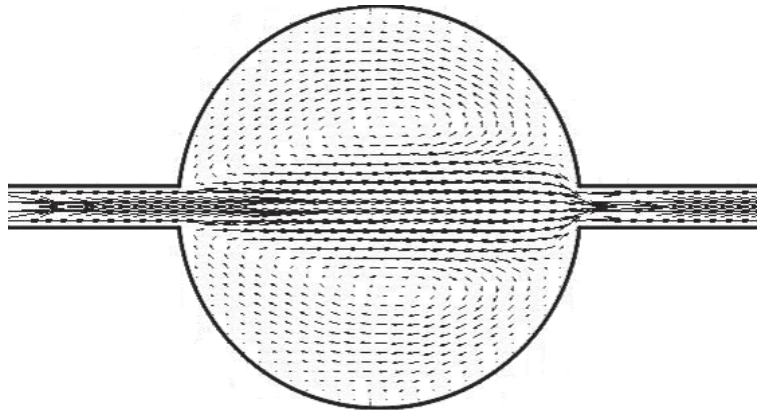


FIGURE 8: Velocity vectors of jet-forced flow in the symmetrical circular basin [12].

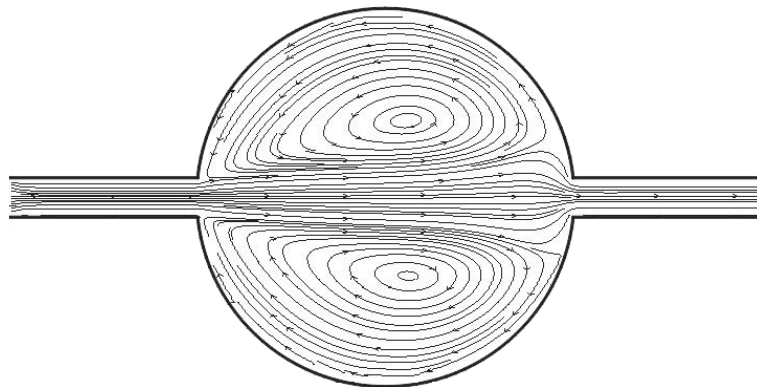


FIGURE 9: Streamline contours of jet-forced flow in the symmetrical circular basin [12].

is obtained from $\tau = 0.55$ and $C_S = 0.25$. The symmetrical channel model also generated velocity vectors of eddy and well-developed circulation flows as illustrated in Figures 8 and 9, respectively.

The validation is done by comparing the LBM data with the numerical result by Barber's model. Figure 10 shows the velocity component, u profile across the mid-section for LBM, and Barber's model. It is suggested that the LBM and

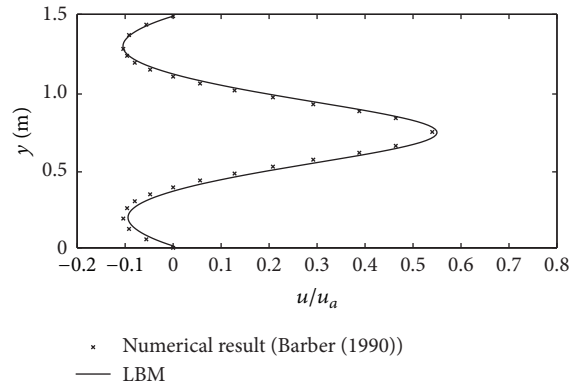


FIGURE 10: Comparison of LBM and numerical result in a circular basin [12].

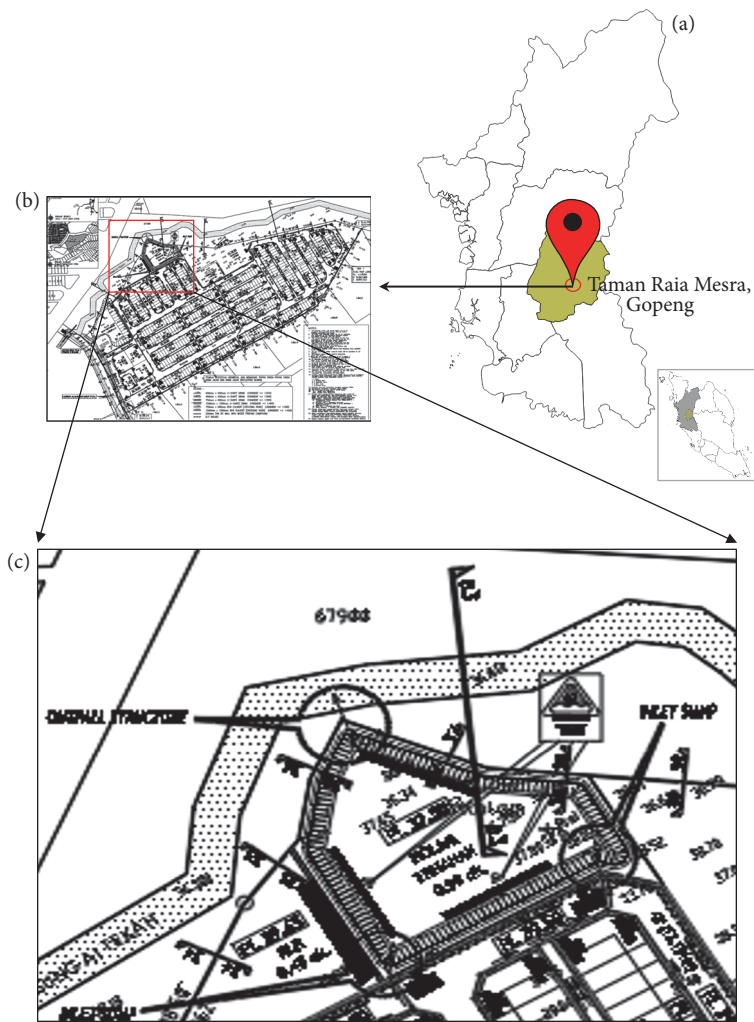


FIGURE 11: Location of the case study; Taman Raia Mesra, Gopeng, Perak. (a) Map showing the location of the study area in Perak, Malaysia. (b) Project plan at the study area. (c) Retention pond attached with the nearby river at the site.

the boundary-fitted primitive variable scheme results are in good agreement especially in the recirculation zones.

3.3. Case Study: Flood at Taman Raia Mesra, Gopeng, Perak, Malaysia. Taman Raia Mesra, Gopeng, is located at the

district of Kampar, Perak, within a Peninsular Malaysia (Figure 11). This 30-acre land is a project site for the residential area. The area was flooded at the end of 2016 and is believed to occur due to the overflow of water from the nearby river basin. The retention pond found nearby the area

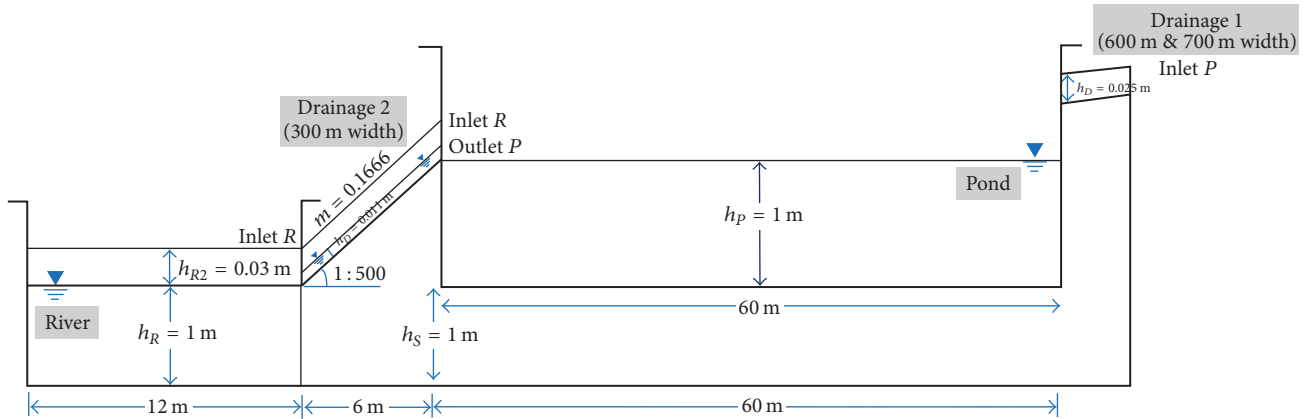


FIGURE 12: Cross section of the layout.

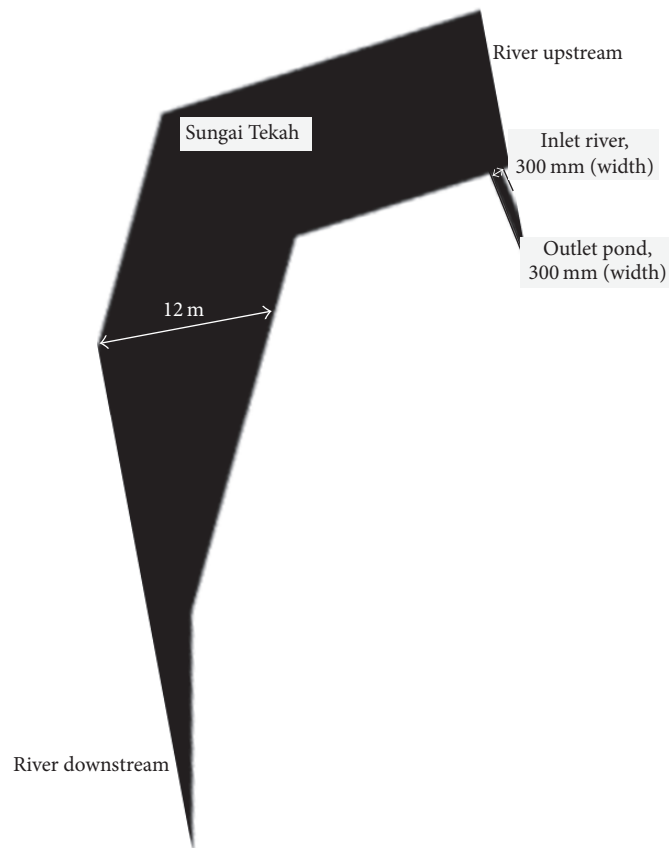


FIGURE 13: Data input for simulation showing the outlet of the pond to the river.

is a function to hold the excess water from the land and is attached to the river by a small outlet.

The cross section layout for the focusing area including a pond, outlet pond, and river is illustrated in Figure 12. The 60 m pond is attached with a drainage 1 as inlet pond and drainage 2 as outlet pond and inlet river in unison. In simulation test, the inlet pond is set up with a peak flow of $Q = 0.0036 \text{ m}^3/\text{s}$, the height of $h_d = 0.025 \text{ m}$, and velocity in the x direction of $u = 0.5 \text{ m/s}$. Meanwhile, both outlet pond

and inlet river are arranged with $Q = 0.74 \text{ m}^3/\text{s}$, $h_D = 0.011 \text{ m}$, and $u = 0.5 \text{ m}$. The simulation was done in a domain area of $63.5 \text{ m} \times 30.7 \text{ m}$.

The LABSWE model is used to investigate the behaviour of the water flow. The simulation test was carried out by using a model resulted from a conversion of AutoCAD file into PNG image comprising a grid lattice size of 396×154 (Figure 13). The time step used is $dt = 0.01$ with an iteration of 10,000. The kinematic viscosity is set up with $\tau = 1.1$ and $dx = 1.0$.

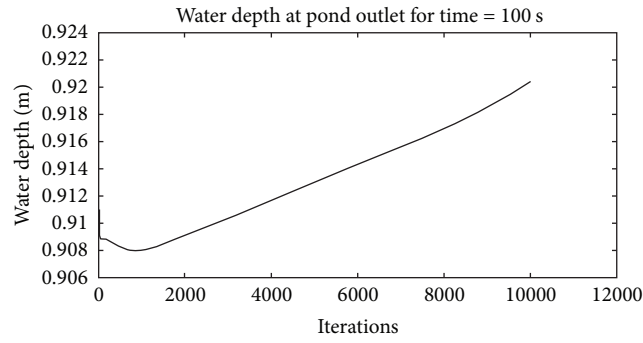


FIGURE 14: Water depth at an outlet of the pond at 100 s.

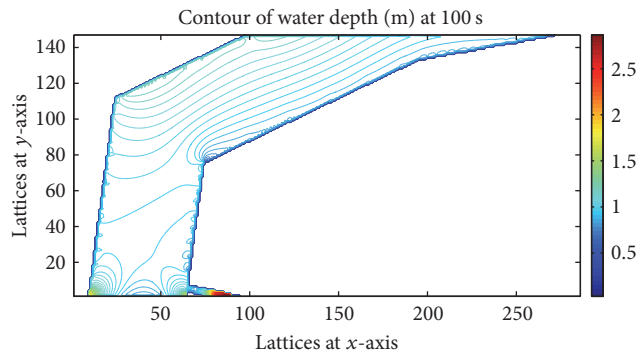


FIGURE 15: Contour of water depth at the domain area for 100 s.

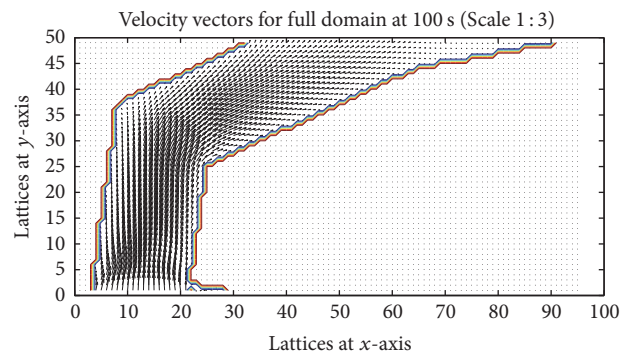


FIGURE 16: Velocity vectors for a whole domain area at 100 s with the scale of 1 : 3.

The simulation results were observed for every 5 seconds starting from 0 s up to 100 s. The analysis revealed the water depth at the outlet of the pond and velocity profile of the domain area as plotted in Figures 14–18.

The water depth at the outlet of the pond has been recorded for 100 sec. The result shown in Figure 14 illustrated that the water depth in the outlet increased from 0.9 m until 0.92 m. There are no significant changes of water profile observed during the simulation. However, it is noticed that a hydraulic jump profile had occurred within the channel. The occurrence can be related to a steep slope and high velocity.

Figure 15 shows a contour of water depth in the domain area. The highest water depth is observed at the beginning of the channel due to the very steep slope for the outlet. The water depth will increase with time due to the size of the outlet channel that is too small for capturing the water flow.

In order to understand the flow directions in the domain area, the figure of velocity vectors has been produced as shown in Figures 16 and 17. Figure 16 is the velocity vectors for the whole domain area. It is observed that there are no anomalies in the simulation result. However, a close-up view has been done near to the outlet pond area such as in Figure 17 shows that the water is flooding from the river into the outlet

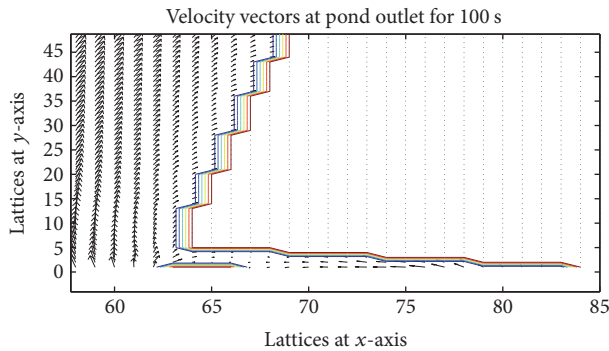


FIGURE 17: Velocity vectors for the outlet pond at 100 s.

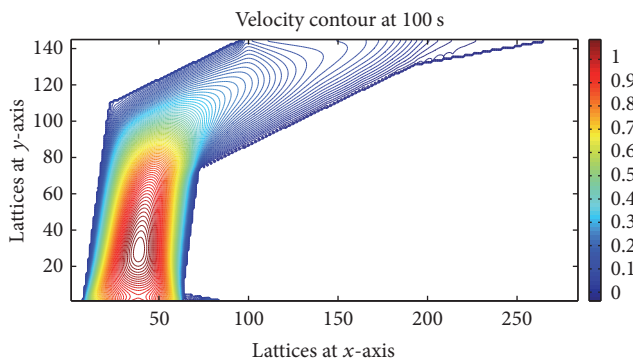


FIGURE 18: Velocity contour of water flow at 100 s.

pond channel. This is a very significant effect that can cause flooding to the residential area.

In addition, towards the results analysis, a velocity contour of the domain area has been produced and studied as illustrated in Figure 18. The water velocity in the stream has increased from 0.5 m/s to 1.09 m/s due to the heavy rainfall event.

4. Conclusions

The LABSWE is used for simulating a flood event at Taman Raia Mesra, Gopeng, Perak. The turbulent flow and jet force flow in a circular channel had been tested for a model validation. The outcome for both validations shows a very satisfactory result. The LABSWE also has been incorporated with rainfall and storm water parameters for November 2016. The investigation had proven the incompatibility of the size of the outlet pond which is too small for the water to flow out to the river. The situation then can cause a flood to the pond area and will finally overflow to the residential area. In order to overcome this problem, equatorial countries like Malaysia should consider the heavy rainfall and stormwater discharge when designing an outlet as the country is always receiving the heavy rainfall continuously.

Conflicts of Interest

The authors declare that there are no conflicts of interest regarding the publication of this paper.

Acknowledgments

The authors appreciate the full support by research grant from MOSTI Science fund (04-02-13-SF0022). It is a pleasure to also acknowledge the Centre of Postgraduate Studies and Department of Civil and Environmental Engineering, Universiti Teknologi PETRONAS, for their support and encouragement.

References

- [1] S. G. Diya, M. E. Gazim, M. E. Toriman, and M. G. Abdullahi, "Floods in Malaysia: historical reviews, causes, effects and mitigations approach," *International Journal of Interdisciplinary Research and Innovations*, pp. 59–65, 2014.
- [2] WMO, "Role of WMO and national meteorological and hydrological services in disaster risk reduction," *World Meteorological Organization*, 2009.
- [3] K. Y. Yoon, N. A. Bahrun, and Y. Kum, *A study on the urban flooding*, Universiti Malaysia Pahang, Pahang, Malaysia, 2010.
- [4] S. N. Jonkman and I. Kelman, "An analysis of the causes and circumstances of flood disaster deaths," *Disasters*, vol. 29, no. 1, pp. 75–95, 2005.
- [5] J. Janssen and R. Mayer, "Computational fluid dynamics (CFD)-based droplet size estimates in emulsification equipment," *Processes*, vol. 4, no. 4, pp. 1–14, 2016.
- [6] D. Bigoni, A. P. Engsig-Karup, and C. Eskilsson, "Efficient uncertainty quantification of a fully nonlinear and dispersive water wave model with random inputs," *Journal of Engineering Mathematics*, vol. 101, pp. 87–113, 2016.
- [7] J. G. Zhou, *Lattice Boltzmann Methods for Shallow Water Flows*, Springer, Heidelberg, Germany, 2004.
- [8] S. H. Shafai, "A lattice Boltzmann model for the 2D solitary wave run-up around a conical island," in *Proceedings of the Coasts, Marine Structures and Breakwaters*, pp. 1–10, Edinburgh, UK, September 2013.
- [9] M. Delphi, M. M. Shooshtari, and H. H. Zadeh, "Application of diffusion wave method for flood routing in Karun river," *International Journal of Environmental Science and Development*, pp. 432–434, 2010.
- [10] A. A. Mahessar, A. L. Qureshi, and A. Baloch, "Numerical study on flood routing in Indus river," *International Water Technology Journal*, pp. 3–12, 2013.
- [11] N. Liu, J. Feng, and J. Zhu, "Flood routing based on diffusion wave equation using lattice Boltzmann method," *Procedia Engineering*, vol. 28, pp. 190–195, 2012.
- [12] S. H. Shafai, *Lattice Boltzmann Method for Simulating Shallow Free Surface Flows involving Wetting and Drying [Ph.D. dissertation]*, Liverpool University, Liverpool, UK, 2011.
- [13] J. Kuipers and C. B. Vreugdenhil, "Calculations of two-dimensional horizontal flow," *Hydraulics Laboratory Report*, Delft, The Netherlands, 1973.

Research Article

Comprehensive Numerical Investigations of Unsteady Internal Flows and Cavitation Characteristics in Double-Suction Centrifugal Pump

Xuelin Tang,^{1,2} Mingde Zou,¹ Fujun Wang,^{1,2} Xiaoqin Li,^{1,2} and Xiaoyan Shi^{1,2}

¹College of Water Resources and Civil Engineering, China Agricultural University, Beijing 100083, China

²Beijing Engineering Research Center of Safety and Energy Saving Technology for Water Supply Network System, China Agricultural University, Beijing 100083, China

Correspondence should be addressed to Xuelin Tang; xl-tang@mail.tsinghua.edu.cn

Received 27 April 2017; Accepted 5 July 2017; Published 14 August 2017

Academic Editor: Ling Qian

Copyright © 2017 Xuelin Tang et al. This is an open access article distributed under the Creative Commons Attribution License, which permits unrestricted use, distribution, and reproduction in any medium, provided the original work is properly cited.

The RNG k - ϵ turbulence model combined with cavitation model was used to simulate unsteady cavitating flows inside a double-suction centrifugal pump under different flow rate conditions based on hexahedral structured grid. The numerical external characteristic performances agree well with the experimental performances. The predicted results show that the turbulence kinetic energy and the turbulence dissipation rate inside the impeller at design flow rate are lower than those at other off-design flow rates, which are caused by various vortices. Based on frequency-domain analyses in the volute casing, the blade passing frequency is the dominant one of the pressure fluctuations except the vicinity of volute tongue for all operating cases, and the dominant frequency near the volute tongue ranges from 0 to 0.5 times the blade passing frequency for other off-design points, while the blade passing one near the volute tongue is the dominant one of the pressure fluctuations at design point. The increase of flow rate reduces the pressure fluctuations amplitude. For cavitation cases, the blade loading of the middle streamline increases a bit during the initial stage, but, for serious cavitation, the blade loading near the blade inlet reduces to 0 and even negative values, and the serious cavitation bubbles block the blade channels, which results in a sharp drop in pump head. Under noncavitation condition, the predicted power related to the pressure in the impeller channels increases from the inlet to the exit, while, under different cavitation conditions at the design flow rate, these power-transformation distributions in the impeller channels show that these power conversions are affected by the available $NPSH_a$ and the corresponding work in leading regions of the blades increases gradually a bit, and then it increases sharply in the middle regions, but it decreases in the blade trailing regions and is greatly influenced by secondary flows.

1. Introduction

Centrifugal pumps are the most commonly used type among various pumps, where double-suction centrifugal pumps have advantages of large flow rate, high efficiency, high head, and so forth, which occupies a large proportion of the pump products. The internal flow inside a double-suction centrifugal pump is unsteady and extremely complex. There are some possible phenomena in the flow, such as rotor-stator interaction, rotating stalling, and cavitation [1–3]. With rapid development in computer technology and computational fluid dynamics (CFD), the CFD method is a good tool to investigate complex turbulent flows inside pumps [4]. In

numerical simulation of a centrifugal pump, blade angles, blade number, and turbulence model have great effect on the predicted performances of centrifugal pump [5]. Shigemitsu et al. [6] numerically studied three types of impellers with different outlet angles in the mini turbo-pumps and found that the change of the blade outlet angle has effect on performance and internal flows in mini turbo-pumps. Chakraborty et al. [7] analyzed the static pressure distribution and characteristics of the two-dimensional (2D) incompressible flow inside a centrifugal pump's impellers with different blade numbers, and the predicted results displayed that the head and static pressures of the pump increase with the increase of the blade number, while the efficiency with seven-blade

pump is optimal. González et al. [8] investigated numerically the internal flow inside a double-suction centrifugal machine in the pump operation mode and found that the flow in the double-suction chamber is uniform at design flow rate but has a strong unsteady characteristic at off-design flow rates. At the same time, the cavitation is a common phenomenon in centrifugal pumps. When the pressure inside the pump is below the saturation water vapor pressure, cavitation may occur. It will cause noise, performance breakdown, and costly damage to hydraulic machineries [9]. Liu et al. [10] used the standard RNG $k-\varepsilon$ model and two modified RNG $k-\varepsilon$ models, that is, density correction based model (DCM) and filter-based model (FBM), to simulate the unsteady attached sheet-cavitating flows in centrifugal pumps, and the studies suggested that all the turbulence models rarely affect the evolution of cavitation bubbles, but the advanced turbulence model can significantly improve the prediction precision of head coefficients and critical cavitation numbers. Thai and Lee [11] predicted the cavitation characteristics of the centrifugal pump with two types of short and long blades at on-design and off-design points, respectively. The numerical results showed that the pump can safely operate without cavitation at design point, but the cavitation develops inhomogeneously in the blade channels at off-design points.

The main focus of our work is to investigate the hydraulic performance and the cavitation performance of a double-suction centrifugal pump. Firstly, based on ANSYS CFX solver, the RNG $k-\varepsilon$ turbulence model was used to calculate the unsteady flow fields inside the pump without cavitation at different flow rates. The predicted external characteristics of the pump were in good agreement with the experimental ones. For different $NPSH_a$, the blade loading and the vapor volume fraction for cavitation flows in the impeller were simulated numerically and analyzed systematically at design point, and the studies on the influence of the cavitation and secondary flows on power distributions were carried out.

2. Basic Parameters and Computational Grids

The flow characteristics inside a double-suction centrifugal pump with a specific speed n_s of $160 \text{ (r/min} \cdot \text{(m}^3/\text{s)}^{1/2} \cdot \text{m}^{-3/4}\text{)}$ was investigated here, and the main hydraulic components of the pump include a suction chamber, an impeller, and volute casing. The basic geometric parameters of this pump are the pump inlet diameter D_{in} of 300 mm, the pump outlet diameter D_{out} of 250 mm, the 355 mm cutwater diameter D_3 of the volute, the impeller inlet diameter D_1 of 200 mm, and the impeller outlet diameter D_2 of 348 mm. The blades on the two sides of the impeller are arranged in a staggered angle of 30 degrees shown in Figure 1, and the blade number N on each side is 6. In addition, the rated rotating speed n is 1480 r/min and the design flow rate Q_d is $808.38 \text{ m}^3/\text{h}$. The experimental performance parameters are listed in Table 1, where Q , H , P , and η represent the flow rate, the pump head, the shaft power, and the pump efficiency, respectively.

Based on 3D CAD software, the computational domain of the pump was constructed as shown in Figure 2. The

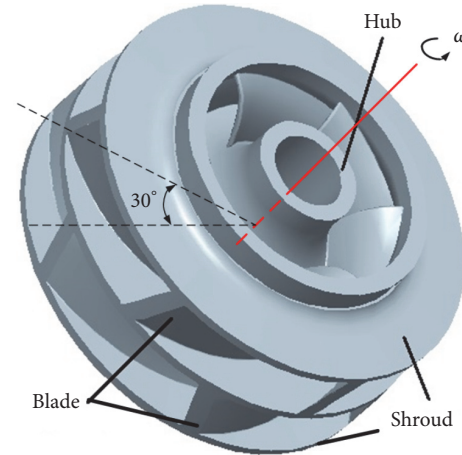


FIGURE 1: Pump impeller.

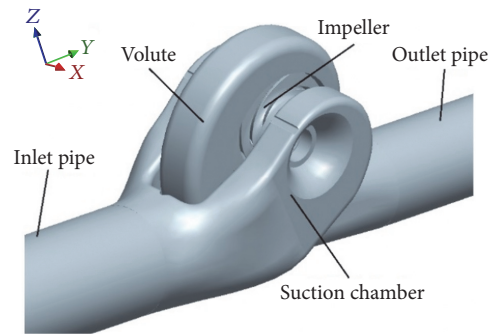


FIGURE 2: Computational domain.

Cartesian x , y , and z coordinate system is adopted here; the x axis is the rotating one of the impeller and $x = 0$ m for the $y-z$ symmetry plane of the suction chamber. The computational grids based on the hexahedral structured grid were generated as shown in Figure 3, and the grid quality value calculated based on determinant $3 \times 3 \times 3$ method is above 0.4. A localized refinement of grids was employed near the volute tongue and the blade leading and trailing edges of the impeller to capture accurately the flow field structure. Also, 4 different grid systems were used to perform the independent-grid verification at design flow rate as shown in Figure 4. It can be seen that when the grid number is more than 2.39×10^6 , the predicted head will not change apparently and its increase rates are less than 0.2%. So the final grid number for the computation was selected as 2.39×10^6 , and the node and grid numbers of each hydraulic component are listed in Table 2. This computation was done on a PC (configuration: Intel (R) Core (TM) 2 Quad CPUs; memory, 8 G).

3. Turbulence and Cavitation Models

3.1. Turbulence Model. The RNG $k-\varepsilon$ turbulence model proposed by Yakhot and Orszag [12] has its unique advantages

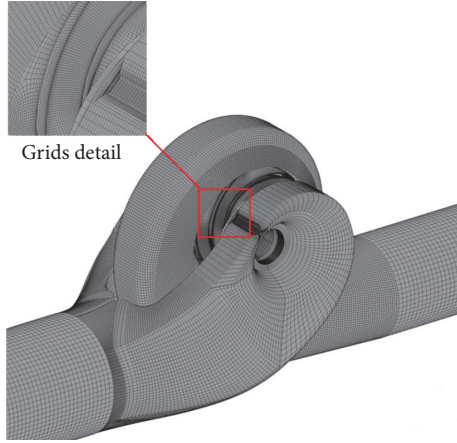


FIGURE 3: Computational grids.

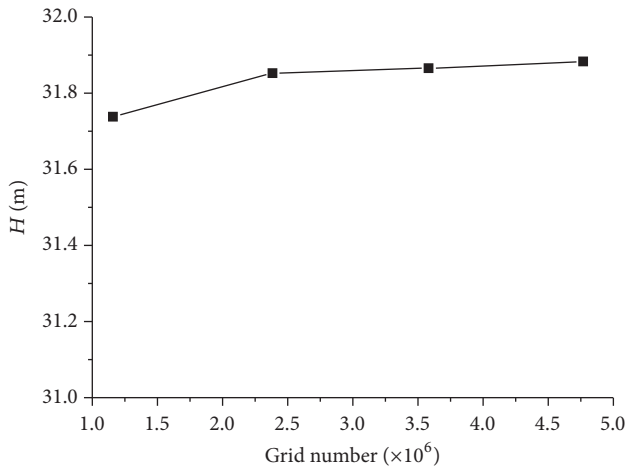


FIGURE 4: Head variation with grid number of pump grid system at design flow rate.

TABLE 1: The experimental performance parameters of pump at different flow rates.

Flow rates	Q (m^3/h)	n (r/min)	H (m)	P (kW)	η (%)
$0.57Q_d$	459.48	1480	39.17	63.792	76.84
$0.72Q_d$	583.38	1480	37.22	69.411	85.2
$0.82Q_d$	659	1480	35.57	73.276	87.11
$0.91Q_d$	738.74	1480	33.44	76.16	88.33
$1.00Q_d$	808.38	1480	31.5	77.757	89.18
$1.07Q_d$	861.4	1480	29.65	79.772	87.18
$1.16Q_d$	936.4	1480	26.71	82.157	82.91
$1.20Q_d$	971.7	1480	24.55	81.495	79.73

of turbulent viscosity modified based on standard k - ε turbulence model and allowing high curvature and strain rate for the rotation and the swirl flow of the average flow. So the turbulence model was adopted to investigate the complex turbulence flows in double-suction centrifugal pump in this

TABLE 2: The node and grid numbers of each of the hydraulic components.

Hydraulic components	Suction chamber	Impeller	Volute casing
Node number ($\times 10^6$)	1.01	0.99	0.59
Grid number ($\times 10^6$)	0.96	0.87	0.56

paper. The RNG k - ε turbulence model is as follows:

$$\begin{aligned} \frac{\partial(\rho k)}{\partial t} + \frac{\partial(\rho k u_i)}{\partial x_i} &= \frac{\partial}{\partial x_j} \left[\alpha_k (\mu + \mu_t) \frac{\partial k}{\partial x_j} \right] + G_k \\ &+ \rho \varepsilon, \\ \frac{\partial(\rho \varepsilon)}{\partial t} + \frac{\partial(\rho \varepsilon u_i)}{\partial x_i} &= \frac{\partial}{\partial x_j} \left[\alpha_\varepsilon (\mu + \mu_t) \frac{\partial \varepsilon}{\partial x_j} \right] + C_{1\varepsilon}^* \frac{\varepsilon}{k} G_k \\ &- C_{2\varepsilon} \rho \frac{\varepsilon^2}{k}, \\ \mu_t &= \rho C_\mu \frac{k^2}{\varepsilon}, \\ G_k &= \mu_t \left(\frac{\partial u_i}{\partial x_j} + \frac{\partial u_j}{\partial x_i} \right) \frac{\partial u_i}{\partial x_j}, \\ C_{1\varepsilon}^* &= C_{1\varepsilon} - \frac{\eta(1 - \eta/\eta_0)}{1 + \beta \eta^3}, \\ \eta &= \frac{\sqrt{2}}{2} \left(\frac{\partial u_i}{\partial x_j} + \frac{\partial u_j}{\partial x_i} \right) \frac{k}{\varepsilon}, \end{aligned} \quad (1)$$

where μ_t stands for the turbulent viscosity and G_k represents the turbulence production due to turbulent forces. The model coefficients are taken as $C_{1\varepsilon} = 1.42$, $C_{2\varepsilon} = 1.68$, $C_\mu = 0.0845$, $\alpha_k = \alpha_\varepsilon = 1.39$, $\eta_0 = 4.377$, and $\beta = 0.012$.

3.2. Cavitation Model. It is necessary to introduce a two-phase mixture model and a cavitation model in cavitating flow calculation. The basic governing equations of the two-phase mixture are based on the Navier-Stokes equations [13], and the continuity equation of the two-phase mixture is given as

$$\frac{\partial \rho_m}{\partial t} + \nabla \cdot (\rho_m \mathbf{u}) = 0; \quad (2)$$

the momentum equation is as follows:

$$\begin{aligned} \frac{\partial(\rho_m \mathbf{u})}{\partial t} + \nabla \cdot (\rho_m \mathbf{u}) &= -\nabla p + \frac{1}{3} \nabla [(\mu_m + \mu_t) \nabla \cdot \mathbf{u}] \\ &+ \nabla [(\mu_m + \mu_t) \nabla \cdot \mathbf{u}]. \end{aligned} \quad (3)$$

The cavitation model used is the transport equation deduced from the Rayleigh-Plesset equation [14]. Considering the growth and collapse of cavitation bubbles, the mass transport equation is expressed as

$$\begin{aligned} \frac{\partial (\alpha_v \rho_v)}{\partial t} + \nabla \cdot (\alpha_v \rho_v \mathbf{u}) &= m_{\text{eva}} - m_{\text{con}}, \\ m_{\text{eva}} &= C_{\text{eva}} \frac{3\alpha_v \rho_v}{R_b} \sqrt{\frac{2 \max(p_v - p, 0)}{3 \rho_l}}, \\ m_{\text{con}} &= C_{\text{con}} \frac{3\alpha_v \rho_v}{R_b} \sqrt{\frac{2 \max(p - p_v, 0)}{3 \rho_l}}, \end{aligned} \quad (4)$$

where ρ_m represents the mass density of the two-phase mixture; \mathbf{u} represents the velocity vector of the two-phase mixture; μ_m represents the dynamic viscosity coefficient of the two-phase mixture; α_v represents the volume fraction of bubbles; ρ_v and ρ_l represent the mass densities of vapor and liquid, respectively; m_{eva} and m_{con} represent the evaporation rate and condensation rate of water vapor in unit volume, respectively; C_{eva} and C_{con} represent the evaporation rate coefficient and condensation rate coefficient of water vapor in unit volume, respectively; the saturated vapor pressure p_v of water is 3170 Pa at the temperature of 25°C, and the average diameter of the bubbles R_b is 2×10^{-6} m.

4. Numerical Methods and Boundary Conditions

The ANSYS CFX solver was selected in this study. In the discrete process of governing equations, the time-dependent terms were discretized with the second-order backward Euler scheme, the second-order central scheme was used for the diffusive terms, and the high resolution was used to solve the convection terms. In the ANSYS CFX solver, the high resolution is a special discrete scheme for the convection terms. When dealing with the convection terms, the convective fluxes at the integral points are approximated by those of the adjacent nodes, which can be expressed as

$$\varphi_p = \varphi_n + \beta \nabla \varphi \cdot \Delta \vec{r}, \quad (5)$$

where φ_p and φ_n denote the convective fluxes at the integral points and the upwind nodes, respectively; $\nabla \varphi$ denotes the convective flux gradients within the control volumes; β represents the coefficient of the numerical convection correction; $\Delta \vec{r}$ is the vector from the upwind node to the integral point. Different discrete schemes differ in choices for β and $\nabla \varphi$. In the high resolution scheme, β at each node is computed to be as close to 1 (not exceed 1) as possible by using a special nonlinear recipe that is based on the boundedness principles used by Barth and Jespersen [15]. Obviously, (5) indicates that the high resolution scheme preferentially uses the second-order backward Euler scheme and reverts to the first-order backward Euler scheme only when the convective flux gradients are very small somewhere within the control volumes.

The solving process was based on the fully implicit grid coupling solution technique. The rotating period T of the impeller was 0.0405 s. The time step was set to 2.252×10^{-4} s in the transient calculation. Number of periods per time step was set to 10 to achieve the periodic unsteady solution convergence, and the convergence criterion was set to RMS residuals of 10^{-5} . The steady solution was used to initialize the unsteady calculation.

In order to minimize edge effects and to improve numerical stability, two extension domains were added upstream and downstream. The normal velocity condition was used at the inlet. The static pressure condition was used at the outlet and the pressure values were given by the experimental data. The dynamic-static coupling between the suction chamber and the impeller was realized by setting the rotor frozen interface and the same setting was also used for the dynamic-static coupling between the impeller and the volute casing. Simultaneously, the no-slip boundary condition was used on the solid wall, and the near-wall region was treated by using scalable wall function. The cavitating flow was simulated by gradually reducing the static pressure at the outlet, and the reference pressure value of fluid domain was set to 0. Besides, the cavitating flow calculation was initialized by the solution of single-phase noncavitating flow calculation. At the beginning of cavitating flow calculation, the volume fraction of vapor phase was set to 0, and that of liquid phase was set to 1.

5. Analyses of Internal Flow in Noncavitation Condition

5.1. The External Characteristics Curves. The numerical efficiency is only the hydraulic efficiency η_h . In fact, there are also mechanical loss and volumetric loss in the pump operation. In order to do comparisons between the numerical results and the experimental data, the total pump efficiency η must be considered, which is actually composed of the hydraulic efficiency η_h , the mechanical efficiency η_m , and the volumetric efficiency η_v [16], expressed as

$$\eta = \eta_h \eta_m \eta_v. \quad (6)$$

The mechanical efficiency η_m is calculated by the empirical formula as follows:

$$\eta_m \approx 1 - 0.07 \frac{1}{(n_s/100)^{7/6}}. \quad (7)$$

The volumetric efficiency η_v caused by volumetric loss is calculated by the following empirical formula:

$$\eta_v \approx \frac{1}{1 + 0.68 n_s^{-2/3}}. \quad (8)$$

It can be seen from Figure 5 that, with the increase of flow rate, the pump head drops gradually, while the pump shaft power rises. The calculated pump head is larger than the experimental data at large flow rates but smaller than the experimental data at small flow rates. The trends between the

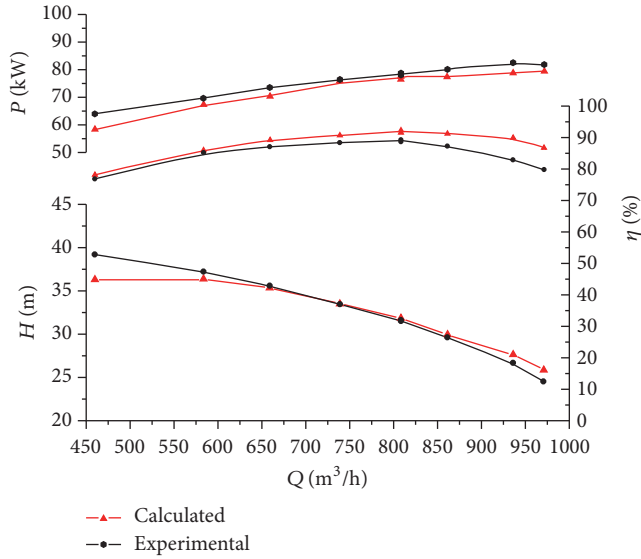


FIGURE 5: Comparison between performance curves.

calculated pump shaft power and the experimental data are roughly identical, and the calculated value is lower than the experimental one. The efficiency increases with the increase of flow rate at first, and it reaches the highest point at design flow rate; then as the flow rate continues to increase, it begins to decline gradually. The calculated efficiency is higher a little than the experimental one. Overall, the calculated results agree well with the experimental data.

5.2. Static Pressure Distribution in the Impeller. Viewed from the pump inlet, the pump is divided by the y - z symmetry plane of the suction chamber into two parts, that is, left part and right one. Figure 6 shows the static pressure distributions on the hubs of the right part and the left one at different flow rates. It can be seen that the static pressure increases gradually from the impeller inlet to the outlet, and the fluid flows inside the left and right parts are symmetric. An obvious low-pressure region appears near the impeller inlet and near the blade suction surface; the static pressure reaches the lowest and cavitation may happen here as shown in Figure 7. When the fluid enters into the impeller channel, it can get the energy due to the work done by the impeller. It is shown in Figure 7 that the static pressure on pressure surface is higher than that on suction surface, and the pressure difference causes the moment of resistance on rotating impeller.

5.3. Analysis of Pressure Fluctuations in the Volute Casing. There is dynamic-static coupling between the volute casing and the impeller, which may cause the pressure fluctuations and affects the stability of the pump. The pressure fluctuations characteristics are usually characterized by pressure coefficient C_p [17], which is defined as

$$C_p = \frac{p - \bar{p}}{0.5\rho u_2^2}, \quad (9)$$

where p represents the transient pressure, \bar{p} is the average value of all the transient pressure at all monitoring points for

8 rotor revolutions, u_2 represents the circumferential velocity at the impeller outlet, and ρ is the fluid mass density.

In order to monitor the pressure fluctuations in the volute casing, 6 monitoring points (namely, V0, V1, V2, V3, V4, V5) are set on the symmetric plane of the volute casing, as illustrated in Figure 8. The sampling frequency f_s is 4440 Hz ($f_s = 1/T$) and the results for $8T$ sampling time are selected for analysis. The blade passing frequency f_b is 296 Hz.

At design flow rate, the dominant frequency of the pressure fluctuations at monitoring point V0 is mainly caused by the blade passing frequency shown in Figure 9, followed by the frequencies that are 0~0.5 times the blade passing frequency. However, at monitoring points from V1 to V5, the blade passing frequency is the dominant frequency of the pressure fluctuations, followed by the second harmonic of the blade passing frequency. At off-design flow rates, the dominant frequency of the pressure fluctuations at monitoring point V0 is 0~0.5 times the blade passing frequency, and, in contrast, the dominant frequency of the pressure fluctuations at monitoring points from V1 to V5 is mainly brought about by the blade passing frequency, followed by the frequencies that are 0~0.5 times the blade passing frequency. Besides, the pressure fluctuations amplitudes at all monitoring points in volute casing decrease gradually with the increase of the flow rate.

5.4. Distributions of the Relative Velocity and Streamline in the Hydraulic Components. Figure 10 shows the relative velocity and streamline distributions in the impeller and the volute casing at different flow rates. At the flow rate of $0.72Q_d$, the relative velocity distribution in the impeller is nonaxisymmetric; there is an obvious low-velocity region in the impeller channel near the volute tongue and an axial vortex appears in the low-velocity region. In most regions of the impeller channels, the relative velocity is higher near the suction surface than that near pressure surface of the blade. The relative velocity and the streamlines in the volute casing distribute nonsmoothly. At the flow rate of $1.0Q_d$, the relative velocity distribution in the impeller appears axisymmetric and uniform, and the axial vortex in blade channel disappears at flow rate of $0.72Q_d$. What is more, the relative velocity and the streamlines in the volute casing distribute much more smoothly. The relative velocity and streamline distributions in the impeller and volute casing at the flow rate of $1.2Q_d$ are roughly similar to those at the flow rate of $1.0Q_d$, but the flow in the impeller at the flow rate of $1.2Q_d$ is less axisymmetric than that at flow rate of $1.0Q_d$. In addition, it can be concluded from Figure 10 that, under the off-design conditions, a low-velocity region will appear in the vicinity of volute outlet, which is caused by the reverse flow.

Relative velocity and streamline distributions on the plane of $x = 0.16$ m in the suction chamber are shown in Figure 11. It can be found that the relative velocity increases along the streamwise direction and reaches the highest value at the regions near the outlet. The mean relative velocity in the whole channel increases with the increase of the flow rate. The semivolute spiral streamlines distribute smoothly and finally surround the impeller inlet. It is obvious that some vortexes appear in the vicinity of baffle tongue, which is because

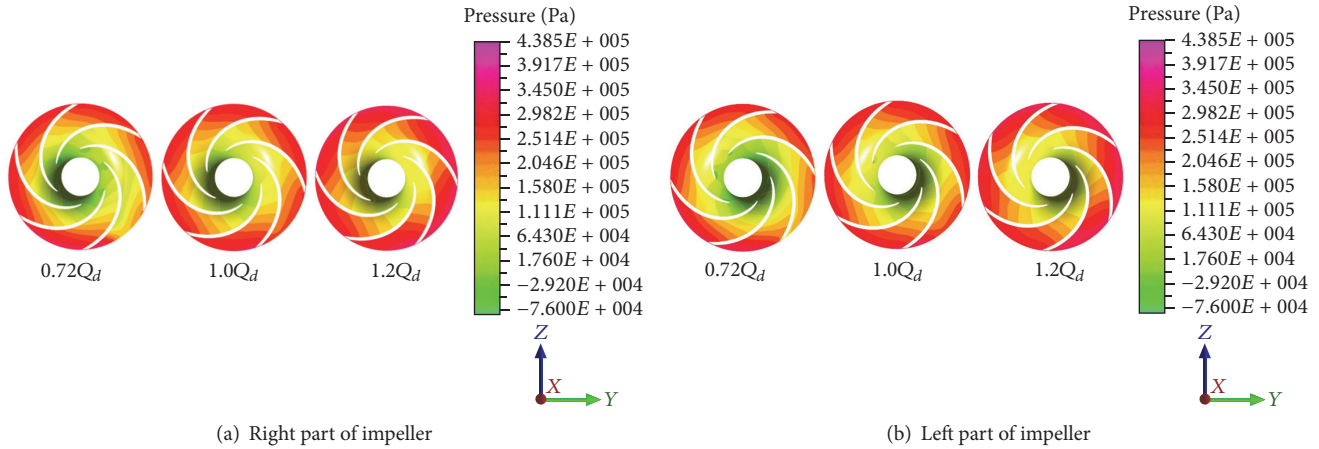


FIGURE 6: Static pressure distributions on impeller hub at different flow rates.

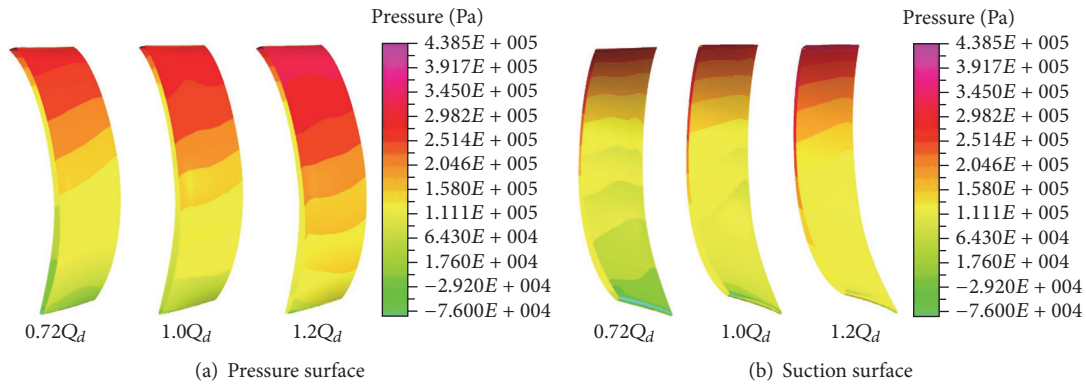


FIGURE 7: Static pressure distribution on blade surfaces.

the liquid flow is blocked here. All the calculated results show that these vortexes gradually evolve, shedding from the vicinity of baffle tongue into the impeller, and bring velocity circulation here, which affects the hydraulic efficiency and the anticavitation performance of the impeller.

5.5. Distributions of Turbulence Kinetic Energy and Dissipation Rate in the Impeller. The distributions of turbulence kinetic energy k and turbulence dissipation rate ε in impeller from the inlet to the outlet are shown in Figures 12 and 13, respectively. In the figures, R_1 is the inlet radius of impeller, R_2 stands for the outlet radius, and R represents the radial distance between a point in the blade channels and the rotating center. It can be seen that the variation tendencies between k and ε are very similar. At different flow rates, k and ε increase at first and then decrease until reaching the minimum values in the middle of the flow channels and finally increase again. At the flow rate of $0.72Q_d$, there is a sharp increase in k and ε near the point of $(R-R_1)/(R_2-R_1) = 0.2$ due to the existence of axial vortexes here, which enlarge the energy dissipation. However, at the flow rates of $1.0Q_d$ and $1.2Q_d$, the changes of k and ε are relatively slow. On the whole, k and ε are lowest at design flow rate, which indicates that the efficiency is highest.

6. Analyses of Cavitation Characteristics

Normally, to avoid cavitation, the static pressure head at the pump inlet must be higher than the saturated vapor pressure by some margin, which is defined as the cavitation margin and is expressed as [18]

$$NPSH_a = \frac{p_{in} - p_v}{\rho g}, \quad (10)$$

where p_{in} and p_v represent the static pressure head at the pump inlet and the saturated vapor pressure, respectively. Figure 14 shows the predicted cavitation characteristic curve at design flow rate. If the point on the curve where the head drops by 3% is regarded as the critical cavitation point, $NPSH_c$ of this pump at design flow rate is about 4.7 m.

6.1. Blade Loading Distribution in the Impeller. The blade loading is defined by the pressure difference between the pressure surface and the suction surface of one blade at the same radius location. The blade loading distribution of the middle streamlines on the blade surfaces under different cavitation margin conditions is shown in Figure 15, where L is the total length of the middle streamlines on the blade surfaces and l represents the distance from the blade inlet

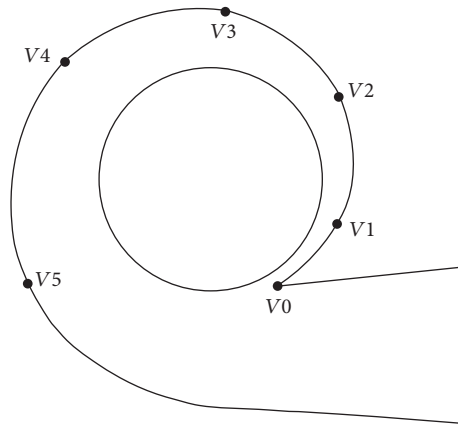


FIGURE 8: Monitoring points in volute wall.

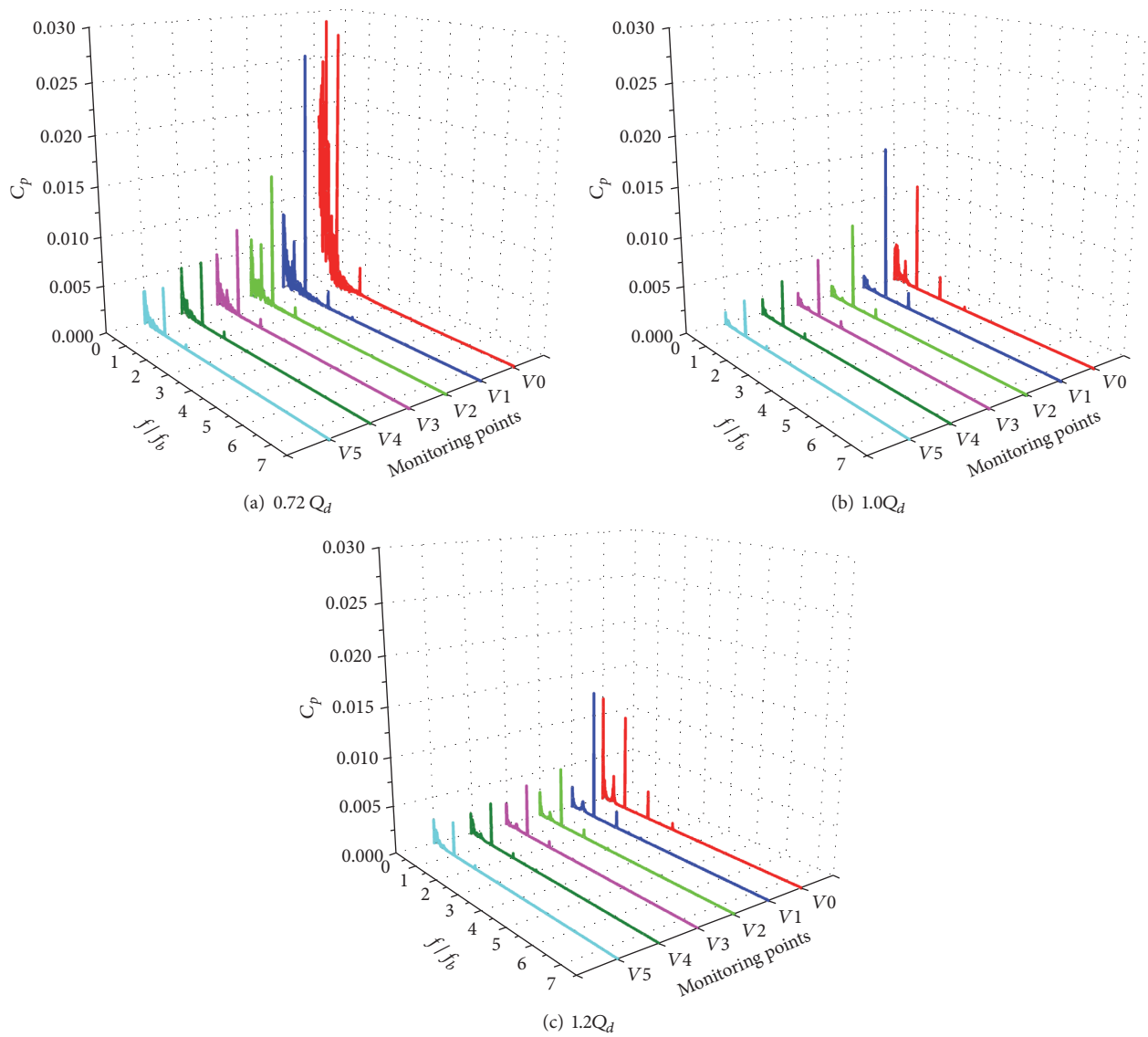


FIGURE 9: Frequency domain of pressure fluctuations in volute casing at different flow rates.

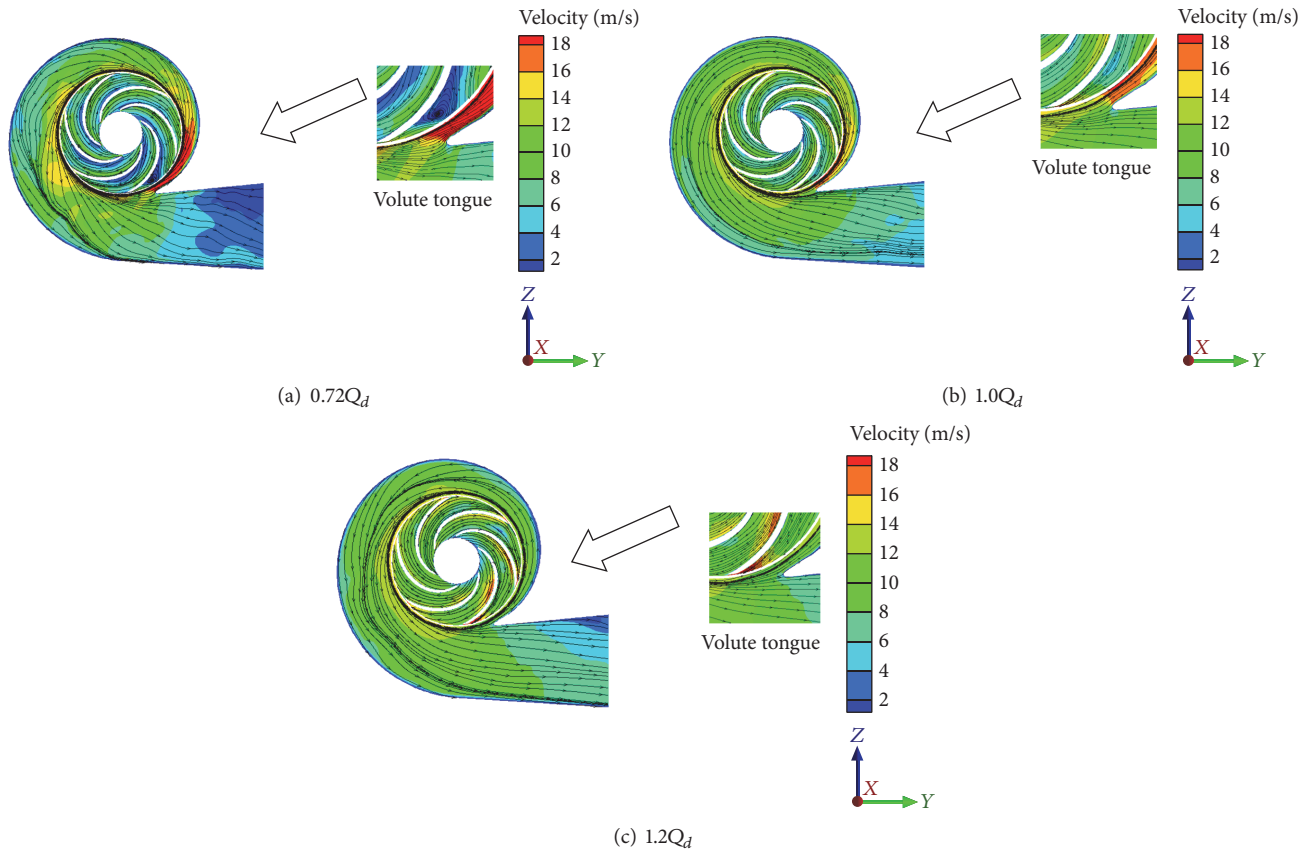


FIGURE 10: Relative velocity and streamline distributions in the impeller and volute casing.

edge to a point of the middle streamlines on the blade surfaces along the streamlines. It can be found that when $NPSH_a = 11.4$ m and 6.33 m, the cavitation does not occur and the blade loading is not affected. Under the condition of $NPSH_a = 4.27$ m, the pressure distribution of the middle streamline on the pressure surface does not change, but it obviously reduces on the suction surface, and thus it increases the blade loading. When $NPSH_a$ drops to 3.94 m, the cavitation is more serious, which makes the pressure in the middle streamlines on both the suction surface and the pressure surface of blade reduce a lot. In the positions from $l/L = 0$ to $l/L = 0.3$, the blade loading is almost 0 and even reaches negative values.

6.2. Vapor-Phase Volume Fraction Distribution in the Impeller. Figures 16 and 17 show the distribution of the vapor-phase volume fraction in the impeller under conditions of different $NPSH_a$. It can be concluded that the vapor-phase volume fraction increases with the decrease in $NPSH_a$, and the cavitation bubbles gradually spread from the impeller inlet to the outlet. And the bubbles mainly concentrate around the blade suction surfaces near the inlet, which is because of the low pressure appearing near the suction surfaces. When $NPSH_a = 11.4$ m and 6.33 m, the vapor-phase volume fraction is almost 0 from the impeller inlet to the outlet, which indicates that the cavitation phenomenon does not appear and the pump head is not affected, which can be confirmed from the pump cavitation characteristic curves

shown in Figure 14. But when $NPSH_a = 4.27$ m and 3.94 m, a large number of cavitation bubbles appear in the impeller; particularly when $NPSH_a = 3.94$ m, the cavitation is more serious. The bubbles have blocked the blade channels, and the pump head drops by more than 20%. In addition, the distribution of vapor-phase volume fraction in the blade channels is nonaxisymmetric, which may be caused by the dynamic-static coupling between the tongue of the volute casing and the impeller.

6.3. Streamline Distribution in the Impeller. The streamlines in the impeller distribute smoothly under noncavitation condition as shown in Figure 18(a), while the streamline distribution in impeller channels is relatively disordered under cavitation condition as shown in Figure 18(b), which is caused by the secondary flows near the exit of the impeller. These vortices have great effects on the pump head, as is shown in Figure 14.

6.4. Power Distribution in the Impeller. The impeller is the key component of the pump for energy conversions. In addition, because the cavitation occurrence is closely related to the pressure, the power related to the pressure plays an important role in the impeller channels; the power P_{sec} on the cross section of the passage is defined as

$$P_{sec} = \int_S p_t \mathbf{v} \cdot \mathbf{n} dS, \quad (11)$$

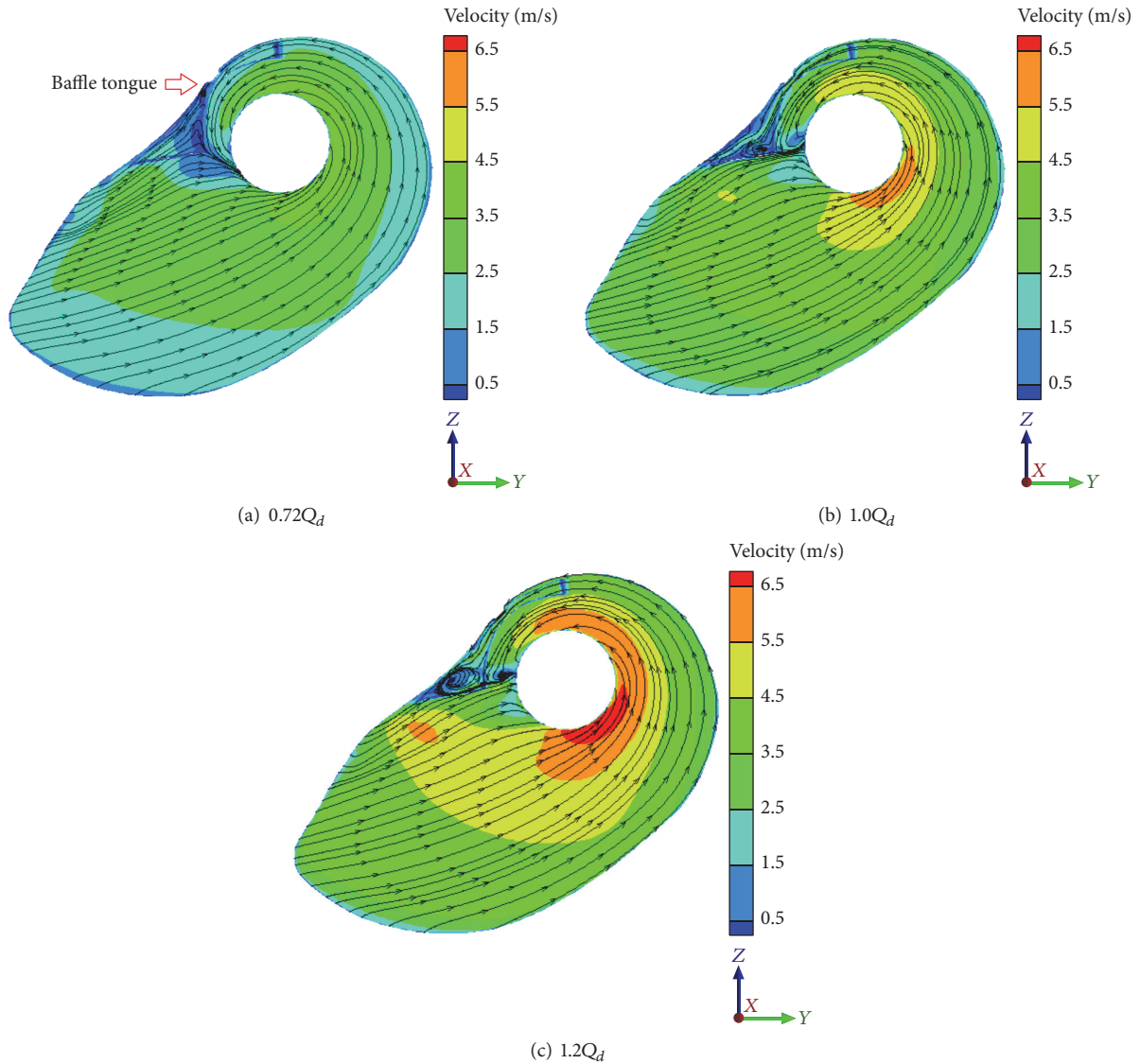


FIGURE 11: Relative velocity and streamline distributions in the suction chamber at different flow rates.

where p_t represents the total pressure of the fluid based on the absolute coordinate system, \mathbf{v} represents the fluid absolute velocity, and \mathbf{n} represents the unit vector normal to the cross section. And the integral term $p_t \mathbf{v} \cdot \mathbf{n}$ represents the power density on the cross section. 7 cross sections in each impeller channel are selected to investigate the power distribution, and these cross sections in impeller channels are located on the cylinders, the radii of which range from 60 mm to 174 mm as shown in Figure 19.

It can be seen from Figure 20 that the power in the impeller channels increases with the increase of the radius because the fluid obtains the work done by blades. In the blade leading regions, the power is very low and increases slowly for different $NPSH_a$ and its growth rate decreases as $NPSH_a$ decreases, which is related to the cavitation. In the blade middle regions, a sharp increase in the power occurs because a large proportion of energy conversion happens here, and

the energy conversion becomes worse for serious cavitation. In the blade trailing regions, the power increases slowly when $NPSH_a = 11.4$ m and 6.33 m, and, in contrast, the secondary backflows cause drop in the power for $NPSH_a = 4.27$ m and even sudden drop for $NPSH_a = 3.94$ m, which can be confirmed by Figure 18. Overall, the power distribution in the left part of the impeller is the same as that in the right part of the impeller.

The power density distributions on the cylindrical cross sections in the impeller under noncavitation and cavitation conditions are shown in Figure 21. It can be seen that the power density on each cross section distributes nonuniformly, and the averaged power density on the cross sections in the impeller under noncavitation condition is larger than that under cavitation condition. In the same impeller channel, the averaged power density increases gradually from the inlet to the exit.

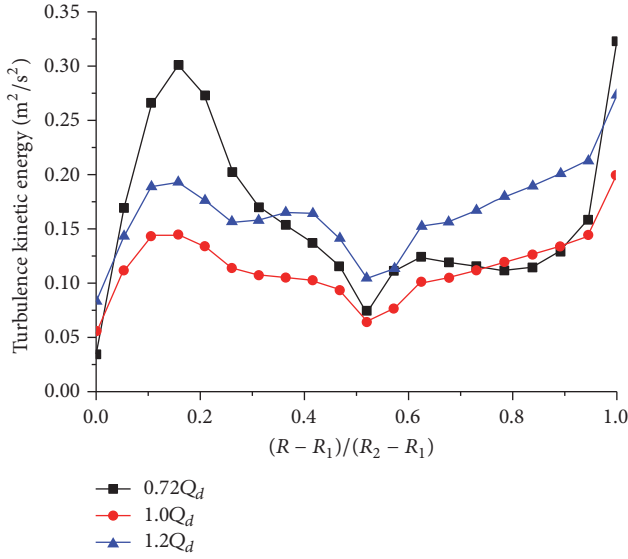


FIGURE 12: The distribution of the turbulence kinetic energy k in the impeller at different flow rates.

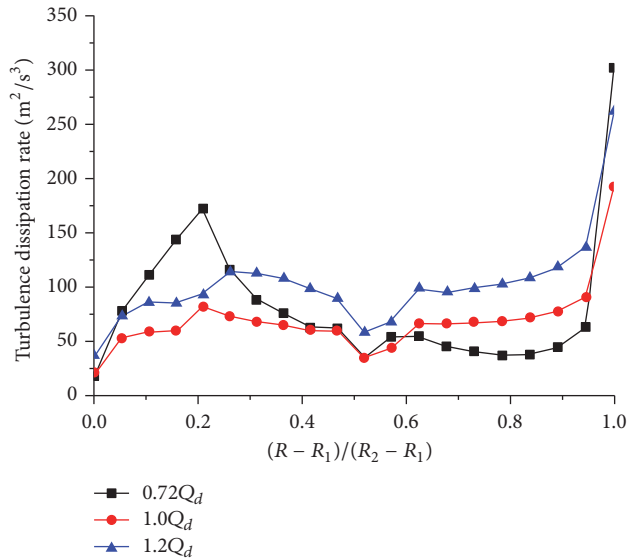


FIGURE 13: The distribution of the turbulence dissipation rate ϵ in the impeller at different flow rates.

7. Conclusions

Based on the RNG $k-\epsilon$ turbulence model and the hexahedral structured grid, the unsteady flow inside a double-suction centrifugal pump was numerically investigated under different flow rate conditions. In addition, the blade loading and power distributions related to the cavitation at design flow rate were analyzed systematically. The results are listed and discussed as follows:

- (1) The external and internal flow characteristics of the pump obtained by numerical simulation are in accord with the general law and agree well with the experimental results.

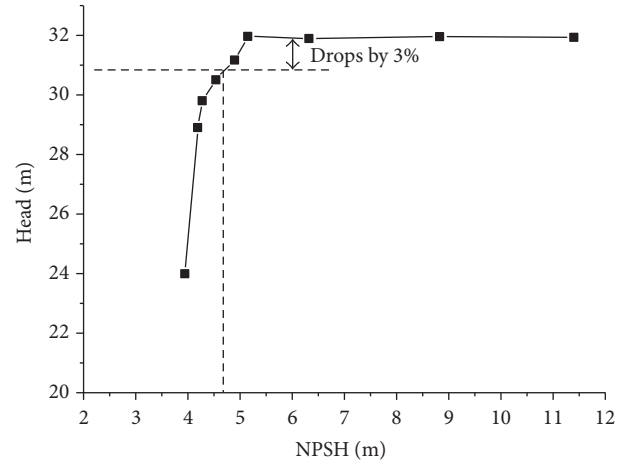


FIGURE 14: Predicted cavitation characteristics curve.

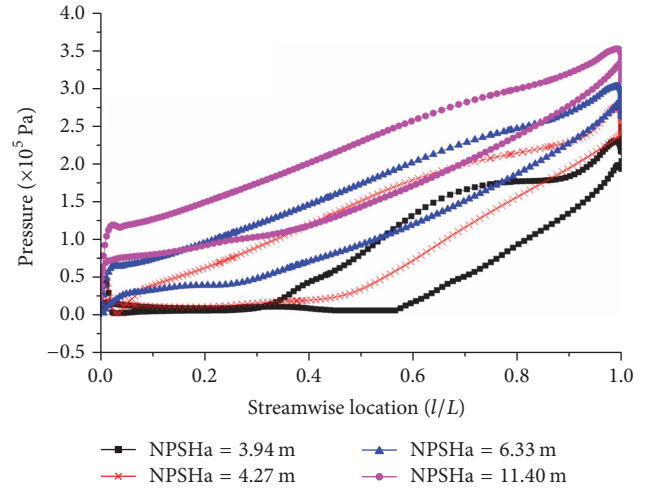


FIGURE 15: Blade loading distribution on middle streamlines.

- (2) The predicted variation tendencies of the turbulence kinetic energy k and the turbulence dissipation rate ϵ are very similar under different flow rate conditions, but k and ϵ at design flow rate are lower than those at other off-design flow rates.
- (3) The blade passing frequency is the dominant frequency of the pressure fluctuations in the volute casing except the vicinity of the volute tongue for all operating cases, and the dominant one near the volute tongue is the blade passing frequency at the design point and 0~0.5 times the blade passing frequency at other off-design points.
- (4) At the design flow rate, the cavitation causes the blade loading of the middle streamline to increase a bit during the initial stage, and serious cavitation causes the blade loading near the blade inlet to reduce to 0 and even negative values, which results in a sharp drop in the pump head.
- (5) The power obtained from the impeller increases with the increase of radius in the whole impeller

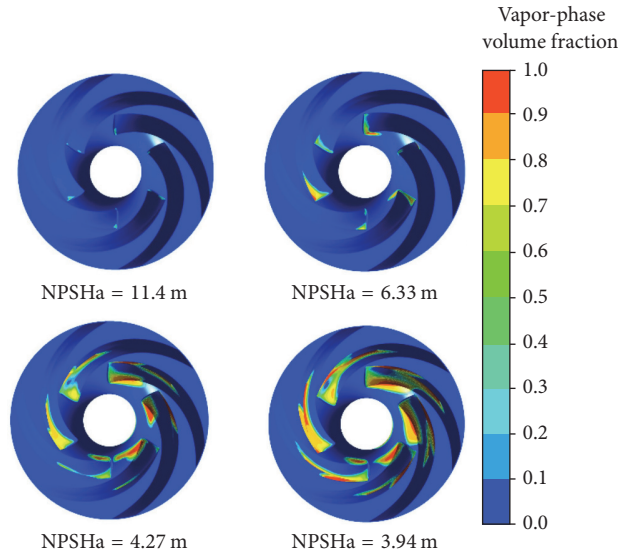


FIGURE 16: Vapor-phase volume fraction distribution in the impeller.

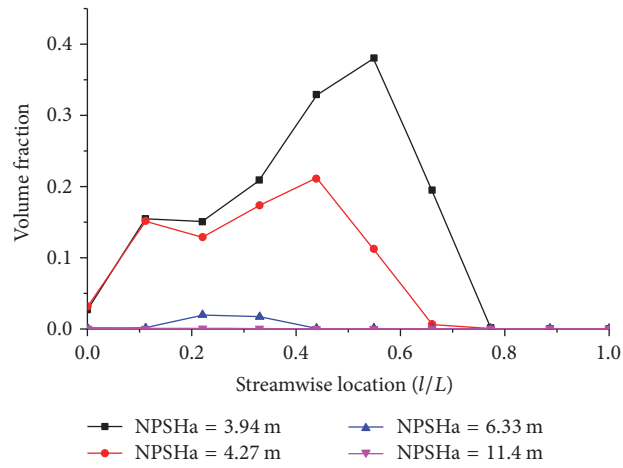


FIGURE 17: The volume fraction curves of vapor phase in the impeller from inlet to outlet.

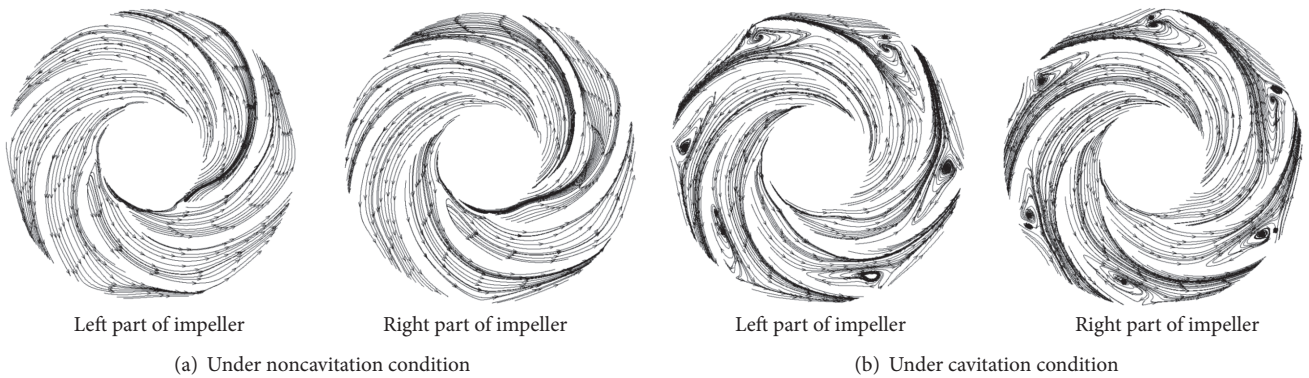


FIGURE 18: Streamline distribution in the impeller.

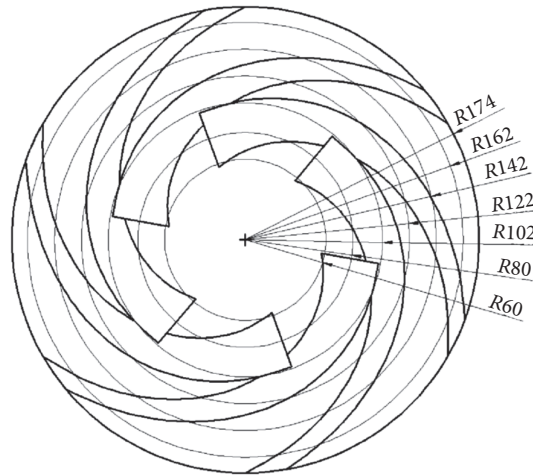


FIGURE 19: Sketch of impeller sections.

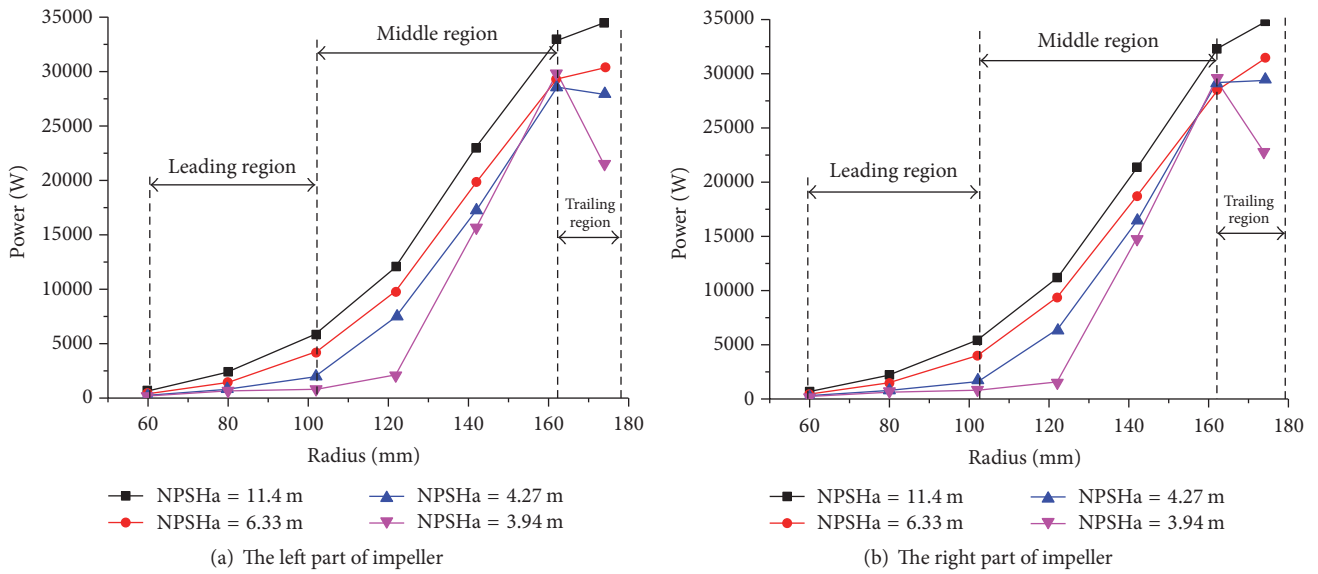


FIGURE 20: Power curves of the impeller sections.

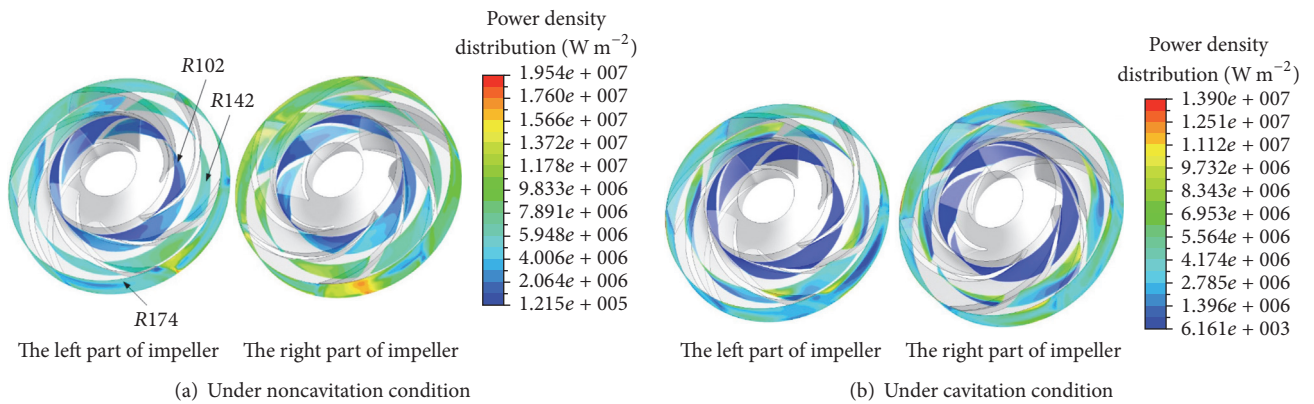


FIGURE 21: Power density contour of cross section ($R = 102, 142, 174$ mm).

channels, but the power in leading regions of the blades increases gradually a bit, and then it increases sharply in the middle regions. In the blade leading regions, the power increases slowly for non-cavitation cases, while it decreases for cavitation cases; in particular, it suddenly drops for serious cavitation, which is caused by the secondary flows.

Nomenclature

D_{in} :	Pump inlet diameter
D_{out} :	Pump outlet diameter
D_1 :	Inlet diameter of impeller
D_2 :	Outlet diameter of impeller
D_3 :	Cutwater diameter of volute casing
N :	Blade number
n_s :	Specific speed of the pump
H :	Pump head
P :	Pump shaft power
P_{sec} :	The power on the cross section of impeller
Q :	Flow rate
η :	Pump efficiency
η_m :	Mechanical efficiency
η_v :	Volumetric efficiency
η_h :	Hydraulic efficiency
ρ :	Fluid mass density
ρ_v :	Mass density of vapor phase
p_v :	Saturated vapor pressure of water
p :	Transient pressure
C_p :	Pressure coefficient
k :	Turbulence kinetic energy
ε :	Turbulence dissipation rate
$NPSH_a$:	Available net positive suction head
$NPSH_r$:	Required net positive suction head
m_{eva} :	Evaporation rate of water vapor
m_{con} :	Condensation rate of water vapor
C_{eva} :	Evaporation rate coefficient of water vapor
C_{con} :	Condensation rate coefficient of water vapor
T :	The rotating period of the impeller
f_s :	Sampling frequency
f_b :	Blade passing frequency.

Conflicts of Interest

The authors declare that they have no conflicts of interest.

Acknowledgments

This work was supported by the National Natural Science Foundation of China (Grants nos. 51479196, 51179192, and 51139007) and the Program for New Century Excellent Talents in University (NCET) (Grant no. NETC-10-0784).

References

- [1] R. Barrio, J. Parrondo, and E. Blanco, "Numerical analysis of the unsteady flow in the near-tongue region in a volute-type centrifugal pump for different operating points," *Computers & Fluids*, vol. 39, no. 5, pp. 859–870, 2010.
- [2] N. Krause, K. Zähringer, and E. Pap, "Time-resolved particle imaging velocimetry for the investigation of rotating stall in a radial pump," *Experiments in Fluids*, vol. 39, no. 2, pp. 192–201, 2005.
- [3] X. Luo, W. Wei, B. Ji, Z. Pan, W. Zhou, and H. Xu, "Comparison of cavitation prediction for a centrifugal pump with or without volute casing," *Journal of Mechanical Science and Technology*, vol. 27, no. 6, pp. 1643–1648, 2013.
- [4] S. Shah, S. Jain, R. Patel, and V. Lakhera, "CFD for centrifugal pumps: a review of the state-of-the-art," *Procedia Engineering*, vol. 51, pp. 715–720, 2013.
- [5] N. P. Jaiswal, "CFD analysis of centrifugal pump: a review," *Journal of Engineering Research and Applications*, vol. 4, pp. 175–178, 2014.
- [6] T. Shigemitsu, J. Fukutomi, R. Nasada, and K. Kaji, "The effect of blade outlet angle on performance and internal flow condition of mini turbo-pump," *Journal of Thermal Science*, vol. 20, no. 1, pp. 32–38, 2011.
- [7] S. Chakraborty, K. Choudhuri, P. Dutta, and B. Debbarma, "Performance prediction of Centrifugal Pumps with variations of blade number," *Journal of Scientific and Industrial Research*, vol. 72, no. 6, pp. 373–378, 2013.
- [8] J. González, J. M. F. Oro, and K. M. Argüelles-Díaz, "Flow analysis for a double suction centrifugal machine in the pump and turbine operation modes," *International Journal for Numerical Methods in Fluids*, vol. 61, no. 2, pp. 220–236, 2009.
- [9] X.-L. Tang, L.-Y. Bian, F.-J. Wang, X.-Q. Li, and M. Hao, "Numerical investigations on cavitating flows with thermodynamic effects in a diffuser-type centrifugal pump," *Journal of Mechanical Science and Technology*, vol. 27, no. 6, pp. 1655–1664, 2013.
- [10] H. Liu, Y. Wang, D. Liu, S. Yuan, and J. Wang, "Assessment of a turbulence model for numerical predictions of sheet-cavitating flows in centrifugal pumps?" *Journal of Mechanical Science and Technology*, vol. 27, no. 9, pp. 2743–2750, 2013.
- [11] Q. Thai and C. Lee, "The cavitation behavior with short length blades in centrifugal pump," *Journal of Mechanical Science and Technology*, vol. 24, no. 10, pp. 2007–2016, 2010.
- [12] V. Yakhot and S. A. Orszag, "Renormalization group analysis of turbulence. I. Basic theory," *Journal of Scientific Computing*, vol. 1, no. 1, pp. 3–51, 1986.
- [13] R. B. Medvitz, R. F. Kunz et al., "Performance analysis of cavitating flow in centrifugal pumps using multiphase CFD," *Journal of Fluids Engineering*, vol. 124, no. 2, pp. 377–383, 2002.
- [14] A. K. Singhal, M. M. Athavale, H. Li, and Y. Jiang, "Mathematical basis and validation of the full cavitation model," *Journal of Fluids Engineering*, vol. 124, no. 3, pp. 617–624, 2002.
- [15] T. Barth and D. Jespersen, "The design and application of upwind schemes on unstructured meshes," in *Proceedings of the 27th Aerospace Sciences Meeting*, Reno, NV, USA, 1989.
- [16] G. Xingfan, *Modern Pumps Theory and Design*, Astronautics Press, Beijing, China, 2011.
- [17] J. L. Parrondo-Gayo, J. González-Pérez, and J. Fernández-Francos, "The effect of the operating point on the pressure fluctuations at the blade passage frequency in the volute of a centrifugal pump," *Journal of Fluids Engineering*, vol. 124, no. 3, pp. 784–790, 2002.
- [18] B. Ji, X. W. Luo, R. E. Arndt, X. Peng, and Y. Wu, "Large eddy simulation and theoretical investigations of the transient cavitating vortical flow structure around a NACA66 hydrofoil," *International Journal of Multiphase Flow*, vol. 68, pp. 121–134, 2015.

Research Article

Shallow-Water-Equation Model for Simulation of Earthquake-Induced Water Waves

Hongzhou Ai,^{1,2} Lingkan Yao,^{1,3,4} Haixin Zhao,^{1,5} and Yiliang Zhou¹

¹*School of Civil Engineering, Southwest Jiaotong University, Chengdu 610031, China*

²*Civil Aviation Flight University of China, Guanghan, Sichuan 618307, China*

³*Road and Railway Engineering Research Institute, Sichuan Key Laboratory of Seismic Engineering and Technology, Chengdu 610031, China*

⁴*MOE Key Laboratory of High-Speed Railway Engineering, Chengdu 610031, China*

⁵*Key Laboratory of Mountain Surface Process and Hazards, CAS, Chengdu 610041, China*

Correspondence should be addressed to Lingkan Yao; yaolk@swjtu.edu.cn

Received 13 April 2017; Accepted 7 June 2017; Published 7 August 2017

Academic Editor: Ling Qian

Copyright © 2017 Hongzhou Ai et al. This is an open access article distributed under the Creative Commons Attribution License, which permits unrestricted use, distribution, and reproduction in any medium, provided the original work is properly cited.

A shallow-water equation (SWE) is used to simulate earthquake-induced water waves in this study. A finite-difference method is used to calculate the SWE. The model is verified against the models of Sato and of Demirel and Aydin with three kinds of seismic waves, and the numerical results of earthquake-induced water waves calculated using the proposed model are reasonable. It is also demonstrated that the proposed model is reliable. Finally, an empirical equation for the maximum water elevation of earthquake-induced water waves is developed based on the results obtained using the model, which is an improvement on former models.

1. Introduction

Strong earthquakes shake the banks of reservoirs and can consequently generate large water waves that may result in a geohazard in mountainous earthquake-prone areas [1]. Hydrodynamic pressures in dam reservoirs during earthquakes were first rigorously analyzed by Westergaard in 1933 [2]. In his study, the hydrodynamic equations were derived in terms of the theory of elasticity of solids, and an analytical solution was obtained. Later, Sato modeled a seismic wave as a simple sine wave and proposed a formula for an earthquake-induced water wave using analytical calculations based on linearized shallow-water equations (SWEs) [3]. Chopra and coworkers provided a revised solution to account for the effects of water compressibility on pressure distribution and to investigate dam-water interaction using a finite-element method [4, 5]. They found that the effects of water compressibility for most dams should be considered in their earthquake-response analysis. Hung and Chen analyzed the variation of the water surface and the hydrodynamic pressures of dam-reservoir systems during the El Centro

Earthquake, solving Euler equations by a finite-element method [6]. Chen et al., solving three-dimensional coupling Euler equations and incompressible continuity equations with a complete three-dimensional (3D) finite-difference scheme, calculated the hydrodynamic pressures and water-level increase for nonlinear conditions, including the non-vertical dam face and the nonhorizontal reservoir bottom. They concluded that the geometry effects of reservoir shape on hydrodynamic pressures were significant and the effects of surface wave and convective acceleration on hydrodynamic pressure were about the same [7–9]. C.-H. Zee and R. Zee assumed that water was incompressible and modeled the water flow in reservoirs with a Laplace equation. They studied the hydrodynamic pressure on dams during a horizontal earthquake with a computer program [10]. Demirel and Aydin developed a wave-absorption filter for the far-end boundary of semi-infinite large reservoirs and computed the earthquake-excited surface waves and nonlinear hydrodynamic pressures in a dam-reservoir system based on solving the Navier-Stokes equations and a depth-integrated continuity equation. They used the numerical model to compute

the maximum wave run-up height on the dam face during earthquakes. Based on the data obtained from numerical simulations for nine selected earthquake ground motions, they presented a relationship between dimensionless run-up height and the Froude number that was defined in terms of maximum ground velocity and water depth [11, 12].

Earthquake-excited reservoir systems have been modeled as a shaking-wave tank by many researchers. Faltinsen studied shaking-wave-tank problems with the boundary-element method, solving the Laplace equation based on potential-flow theory [13]. Cooker used linearized SWEs to model a horizontal rectangular wave tank. The free-surface boundary conditions were linearized by potential-flow theory [14]. They found that time-periodic solutions existed for the system. Liu and Lin developed a numerical model to study 3D nonlinear liquid sloshing with broken free surfaces under 6-degree-of-freedom excitations [15]. Godderidge et al. developed an inhomogeneous multiphase model for the computational-fluid-dynamics (CFD) analysis of violent sloshing flows [16]. Chen et al. solved the Reynolds-averaged Navier-Stokes (RANS) equations in both water and air regions to study the sloshing-tank problems [17]. Du et al. approached the characteristics of seismic surges using a shaking-water-tank experiment. They proposed two empirical relationships between the maximum water wave height and the peak ground acceleration for low- and high-frequency seismic waves, respectively [18].

Given the above, investigations of earthquake-induced water waves may apply three methods: analytical calculations, numerical simulations, and experimental studies. In the present study, for an inviscid and incompressible fluid, SWE is developed to simulate earthquake-induced water waves based on Chen's hydrodynamic model [9]. A finite-difference method is used to discretize the SWE. The accuracy and applicability of our method were verified by the results of several classical models, which include analytical solutions of Sato [3] and numerical solutions of Demirel and Aydin [12]. Finally, we propose an empirical equation to predict the maximum water elevation of earthquake-induced water waves based on the calculated results of the proposed model.

2. Mathematical and Numerical Model

2.1. Basic Equations. Figure 1 is a sketch of the dam-reservoir system studied in this paper. As seen in the figure, x , y , and z are space coordinates; L , W , and H are the length, width, and height of the reservoir, respectively; h is the water depth; h_0 is the still water depth; and η is the free-surface displacement. The 3D equations of motion of fluid in this dam-reservoir system during an earthquake, proposed by Chen and Yuan [9], can be written as

$$\begin{aligned} \frac{\partial(u_0 + u)}{\partial t} + u \frac{\partial u}{\partial x} + v \frac{\partial u}{\partial y} + w \frac{\partial u}{\partial z} &= -\frac{1}{\rho} \frac{\partial p}{\partial x}, \\ \frac{\partial(v_0 + v)}{\partial t} + u \frac{\partial v}{\partial x} + v \frac{\partial v}{\partial y} + w \frac{\partial v}{\partial z} &= -\frac{1}{\rho} \frac{\partial p}{\partial y}, \\ \frac{\partial(w_0 + w)}{\partial t} + u \frac{\partial w}{\partial x} + v \frac{\partial w}{\partial y} + w \frac{\partial w}{\partial z} &= -\frac{1}{\rho} \frac{\partial p}{\partial z} - g. \end{aligned} \quad (1)$$

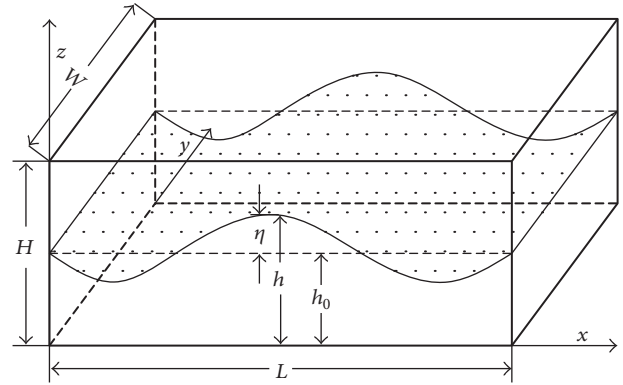


FIGURE 1: Sketch of the dam-reservoir system studied.

The corresponding continuity equation of an incompressible fluid is

$$\frac{\partial u}{\partial x} + \frac{\partial v}{\partial y} + \frac{\partial w}{\partial z} = 0, \quad (2)$$

where u , v , and w are the fluid velocity components in the x , y , and z directions, respectively; u_0 , v_0 , and w_0 are the instantaneous ground-velocity components in the x , y , and z directions, respectively; ρ is the fluid density; g is the gravity acceleration; and p is the hydrodynamic pressure.

The 3D hydrodynamic model proposed by Chen focuses on the nonlinear hydrodynamic pressures on the banks during earthquakes and is calculated by a complete 3D finite-difference scheme. This work described in this paper focused on the maximum water elevation on the reservoir bank during earthquakes, which can be used for the critical hydrologic condition of geohazards such as a moraine-lake burst with overflow [19]. In order to simplify the calculation, we operated under the following hypotheses.

(1) For the external seismic excitation, we assume that there is only the horizontal vibration without the vertical seismic motion, so

$$w_0 = 0. \quad (3)$$

(2) As there is only the horizontal vibration, the vertical acceleration of the fluid is far smaller than that of the gravity acceleration, so the assumption of nearly uniform vertical distribution of the hydrostatic pressure distribution is reasonable [20]; then,

$$\frac{\partial p}{\partial z} = \rho g. \quad (4)$$

(3) The reservoir banks are vertical and rigid. There is no wave absorption and the water waves are totally reflected at the reservoir banks.

Based on the above assumptions, by depth integration of (1) and (2), the basic equations of the SWE model for simulation of earthquake water waves can be written as

$$\frac{\partial h}{\partial t} + \frac{\partial hu}{\partial x} + \frac{\partial hv}{\partial y} = 0,$$

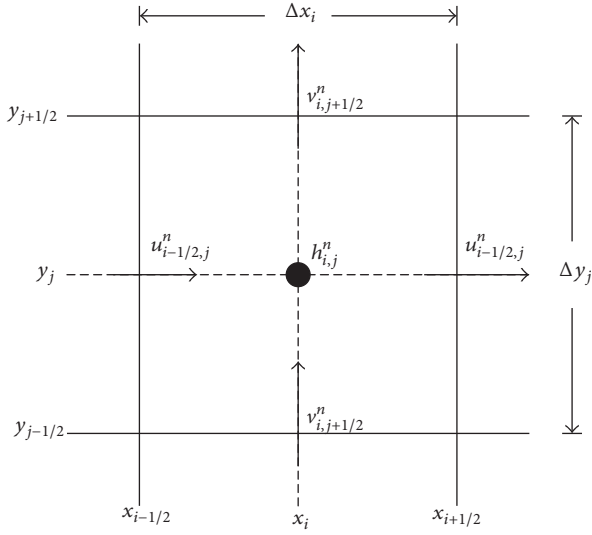


FIGURE 2: Single cell of the staggered grid and the locations of variables.

$$\begin{aligned} \frac{\partial h(u + u_0)}{\partial t} + \frac{\partial hu^2}{\partial x} + \frac{\partial huv}{\partial y} &= -gh \frac{\partial h}{\partial x}, \\ \frac{\partial h(v + v_0)}{\partial t} + \frac{\partial hvu}{\partial x} + \frac{\partial hv^2}{\partial y} &= -gh \frac{\partial h}{\partial y}. \end{aligned} \quad (5)$$

2.2. Numerical Implementation. In this study, a finite-difference method was used to calculate (5). As shown in Figure 2, the parameters u , v , and h are defined in the cell. The continuity equation and the momentum equations in the x and y directions, respectively, are discretized in the center of the cell at the $(n + 1)$ th time step. The derivative terms of (5) can be discretized as shown in the following.

(1) *Time-Derivative Terms*

$$\begin{aligned} \left(\frac{\partial h}{\partial t} \right)_{i,j}^n &= \frac{h_{i,j}^{n+1} - h_{i,j}^n}{\Delta t}, \\ \left(\frac{\partial h(u + u_0)}{\partial t} \right)_{i,j}^n &= \frac{h_{i,j}^{n+1} (u_{i,j}^{n+1} + u_0^{n+1}) - h_{i,j}^n (u_{i,j}^n + u_0^n)}{\Delta t}, \\ \left(\frac{\partial h(v + v_0)}{\partial t} \right)_{i,j}^n &= \frac{h_{i,j}^{n+1} (v_{i,j}^{n+1} + v_0^{n+1}) - h_{i,j}^n (v_{i,j}^n + v_0^n)}{\Delta t}. \end{aligned} \quad (6)$$

(2) *Spatial-Derivative Terms*

$$\begin{aligned} \left(\frac{\partial hu}{\partial x} \right)_{i,j}^n &= \frac{(h_{i+1/2,j}^n u_{i+1/2,j}^n - h_{i-1/2,j}^n u_{i-1/2,j}^n)}{\Delta x_i}, \\ \left(\frac{\partial hv}{\partial y} \right)_{i,j}^n &= \frac{(h_{i,j+1/2}^n v_{i,j+1/2}^n - h_{i,j-1/2}^n v_{i,j-1/2}^n)}{\Delta y_j}, \\ \left(\frac{\partial hu^2}{\partial x} \right)_{i,j}^n &= \frac{(u_{i+1/2,j}^n)^2 h_{i+1/2,j}^n - (u_{i-1/2,j}^n)^2 h_{i-1/2,j}^n}{\Delta x_i}, \\ \left(\frac{\partial huv}{\partial x} \right)_{i,j}^n &= \frac{u_{i+1/2,j}^n v_{i+1/2,j}^n h_{i+1/2,j}^n - u_{i-1/2,j}^n v_{i-1/2,j}^n h_{i-1/2,j}^n}{\Delta x_i}, \\ \left(\frac{\partial huv}{\partial y} \right)_{i,j}^n &= \frac{u_{i,j+1/2}^n v_{i,j+1/2}^n h_{i,j+1/2}^n - u_{i,j-1/2}^n v_{i,j-1/2}^n h_{i,j-1/2}^n}{\Delta y_j}, \\ \left(\frac{\partial hv^2}{\partial y} \right)_{i,j}^n &= \frac{(v_{i,j+1/2}^n)^2 h_{i,j+1/2}^n - (v_{i,j-1/2}^n)^2 h_{i,j-1/2}^n}{\Delta y_j}, \\ \left(gh \frac{\partial h}{\partial x} \right)_{i,j}^n &= gh_{i,j}^n \frac{h_{i+1/2,j}^n - h_{i-1/2,j}^n}{\Delta x_i}, \\ \left(gh \frac{\partial h}{\partial y} \right)_{i,j}^n &= gh_{i,j}^n \frac{h_{i,j+1/2}^n - h_{i,j-1/2}^n}{\Delta y_j}. \end{aligned} \quad (7)$$

(3) *The Middle Terms*

$$\begin{aligned} h_{i+1/2,j}^n &= \frac{1}{2} (h_{i,j}^n + h_{i+1,j}^n), \\ h_{i,j+1/2}^n &= \frac{1}{2} (h_{i,j}^n + h_{i,j+1}^n), \\ u_{i+1/2,j}^n &= \frac{1}{2} (u_{i,j}^n + u_{i+1,j}^n), \\ u_{i,j+1/2}^n &= \frac{1}{2} (u_{i,j}^n + u_{i,j+1}^n), \\ v_{i+1/2,j}^n &= \frac{1}{2} (v_{i,j}^n + v_{i+1,j}^n), \\ v_{i,j+1/2}^n &= \frac{1}{2} (v_{i,j}^n + v_{i,j+1}^n), \end{aligned} \quad (8)$$

where superscript n denotes the time step, Δt represents the time-step size, subscript (i, j) denotes the spatial node, and Δx_i and Δy_j represent the spatial step sizes in the x and y directions, respectively. Considering (6)–(8), the continuity

equation and the momentum equations can be discretized as follows:

$$h_{i,j}^{n+1} = h_{i,j}^n - \frac{\Delta t}{\Delta x_i} \left(h_{i+1/2,j}^n u_{i+1/2,j}^n - h_{i-1/2,j}^n u_{i-1/2,j}^n \right) - \frac{\Delta t}{\Delta y_j} \left(h_{i,j+1/2}^n v_{i,j+1/2}^n - h_{i,j-1/2}^n v_{i,j-1/2}^n \right), \quad (9)$$

$$u_{i,j}^{n+1} = \frac{h_{i,j}^n}{h_{i,j}^{n+1}} \left(u_{i,j}^n + u_0^n \right) - u_0^{n+1} - \frac{\Delta t \left[\left(u_{i+1/2,j}^n \right)^2 h_{i+1/2,j}^n - \left(u_{i-1/2,j}^n \right)^2 h_{i-1/2,j}^n \right]}{\Delta x_i h_{i,j}^{n+1}} - \frac{\Delta t \left(u_{i,j+1/2}^n v_{i,j+1/2}^n h_{i,j+1/2}^n - u_{i,j-1/2}^n v_{i,j-1/2}^n h_{i,j-1/2}^n \right)}{\Delta y_j h_{i,j}^{n+1}} - \frac{gh_{i,j}^n \Delta t \left(h_{i+1/2,j}^n - h_{i-1/2,j}^n \right)}{\Delta x_i h_{i,j}^{n+1}}, \quad (10)$$

$$v_{i,j}^{n+1} = \frac{h_{i,j}^n}{h_{i,j}^{n+1}} \left(v_{i,j}^n + v_0^n \right) - v_0^{n+1} - \frac{\Delta t \left(u_{i+1/2,j}^n v_{i+1/2,j}^n h_{i+1/2,j}^n - u_{i-1/2,j}^n v_{i-1/2,j}^n h_{i-1/2,j}^n \right)}{\Delta x_i h_{i,j}^{n+1}} - \frac{\Delta t \left[\left(v_{i,j+1/2}^n \right)^2 h_{i,j+1/2}^n - \left(v_{i,j-1/2}^n \right)^2 h_{i,j-1/2}^n \right]}{\Delta y_j h_{i,j}^{n+1}} - \frac{gh_{i,j}^n \Delta t \left(h_{i,j+1/2}^n - h_{i,j-1/2}^n \right)}{\Delta y_j h_{i,j}^{n+1}}. \quad (11)$$

2.3. Boundary Conditions. In this paper, we have assumed rigid and totally reflective boundary conditions. In order to treat these boundary conditions, one extra ghost grid is introduced outside the computational space domain [21]. The parameters of the boundary cell, namely, h_B , u_B , and v_B , are defined at the center of the boundary cell. The boundary conditions in the x direction are then updated using

$$\begin{aligned} h_B^{n+1} &= h_B^n, \\ u_B^{n+1} &= -u_B^n, \\ v_B^{n+1} &= v_B^n, \end{aligned} \quad (12)$$

and the boundary conditions in the y direction are updated by using

$$\begin{aligned} h_B^{n+1} &= h_B^n, \\ u_B^{n+1} &= u_B^n, \\ v_B^{n+1} &= -v_B^n, \end{aligned} \quad (13)$$

where superscript n denotes the time step.

2.4. Stability Condition. The stability and accuracy of the numerical results significantly depend on the spatial step sizes and the selected time step. In this paper, the continuity equation and the momentum equations are discretized by an explicit difference scheme using a sequential iteration. Thus, the Courant-Friedrichs-Lewy (CFL) stability criterion is used [22], and the joint stability conditions for the time step Δt are as follows:

$$\Delta t = \text{CFL} \min \left(\frac{\Delta x_i}{|u_{i,j}| + (gh_{i,j})^{1/2}}, \frac{\Delta y_j}{|v_{i,j}| + (gh_{i,j})^{1/2}} \right). \quad (14)$$

2.5. Computational Cycle. With a chosen finite-difference mesh, and given initial conditions and ground acceleration for each time step, the complete cycle for the explicit iterative procedure can be summarized as follows.

(1) Compute all the variables at the n th time step, including variables at the center of the cell, such as $h_{i,j}^n$, $u_{i,j}^n$, and $v_{i,j}^n$, and variables at the faces of the cell, such as $h_{i+1/2,j}^n$, $u_{i+1/2,j}^n$, and $v_{i+1/2,j}^n$.

(2) Compute the continuity equation (9) and the momentum equations (10) and (11) at the $(n+1)$ th time step to obtain the new water depths $h_{i,j}^{n+1}$ and the new water velocities $u_{i,j}^{n+1}$ and $v_{i,j}^{n+1}$.

(3) Update the boundary conditions with (12) and (13).

(4) Now all of the new variables at the $(n+1)$ th time step have been obtained, so repeat Steps (1)–(3) and enter the next cycle.

3. Numerical Validation

To demonstrate the accuracy and applicability of the present model for earthquake-induced water waves, the calculated results of two classical models, which include analytical solutions of Sato and numerical solutions of Demirel and Aydin, will be used to facilitate a comparison to the results obtained using the present model. Three different seismic waves, namely, a Wolong wave, Mexicali wave, and Tongmai wave, having varied peak ground acceleration (PGA), are used in the comparison of calculated results.

3.1. Comparative Models. Two models of earthquake-induced water waves are used to facilitate the comparison to the present model.

(1) *Sato's Model (1967).* Sato modeled the seismic wave as a simple sine wave and assumed that the earthquake-induced water waves were generated by horizontal movement of a vertical wall, and then proposed a formula for the earthquake-induced water wave using analytical calculations as follows:

$$\eta = \frac{a_0 \sqrt{gh_0}}{2\pi f}, \quad (15)$$

where $a_0 = a/g$ is nondimensional, a is the peak ground acceleration of the earthquake, and f is the dominant frequency of the earthquake.

TABLE 1: Details of seismic waves used in the comparison of calculated results.

Seismic wave types		Dominant frequency (Hz)					
Wolong wave	PGA (g)	0.1	0.2	0.3	0.4	0.5	2.34
	PGV (m/s)	0.051	0.102	0.1535	0.2048	0.256	
Mexicali wave	PGA (g)	0.05	0.1	0.15	0.2	0.25	0.38
	PGV (m/s)	0.0353	0.0706	0.1059	0.1412	0.1857	
Tongmai wave	PGA (g)	0.05	0.25	0.4	—	—	0.39
	PGV (m/s)	0.0518	0.1969	0.448	—	—	

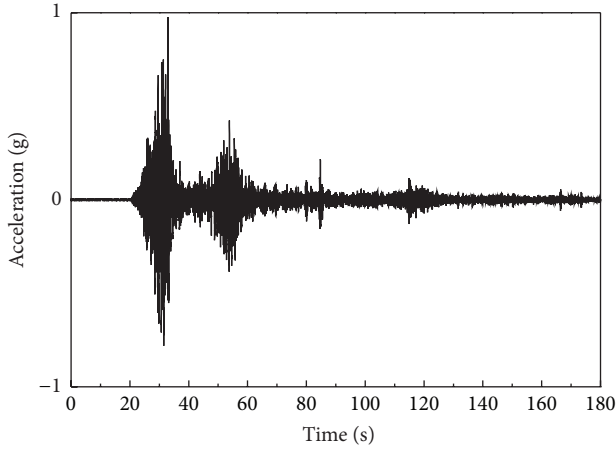


FIGURE 3: Wolong earthquake.

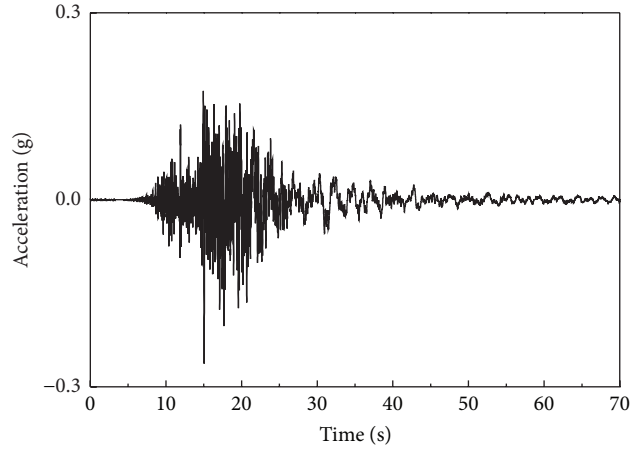


FIGURE 4: Mexicali earthquake.

(2) *Demirel-Aydin's Model (2016)*. Demirel and Aydin used a numerical simulation method to compute breaking surface waves in the reservoir and to predict the maximum height of an earthquake-induced water wave. On the basis of these numerical simulation results, they presented the following equation for predicting the maximum wave height:

$$\frac{\eta}{h_0} = 0.55F^{0.72}, \tag{16}$$

where $F = v/\sqrt{gh_0}$ is the earthquake Froude number and v is the peak ground velocity (PGV).

3.2. Earthquake Excitations. Three kinds of earthquake excitations are used in the comparison of calculated results. A Wolong seismic wave was recorded in the Wenchuan Ms 8.0 earthquake on 12 May 2008 at Wolong Station, as shown in Figure 3; a Mexicali seismic wave was recorded in the California Ms 7.2 earthquake on 4 April 2010 at Mexicali, as shown in Figure 4; and Tongmai seismic waves were the synthetic waves that were based on rock-response spectra (supplied by the Institute of Crustal Dynamic China and CCCC First Highway Consultants Co., Ltd., 2005), as shown in Figure 5. Details of the seismic waves and corresponding PGA and PGVs are shown in Table 1.

3.3. Calculated Results and Analysis. Before the numerical validation of the present model, the reservoir system is assumed to be a rectangular tank with a length of 300 m,

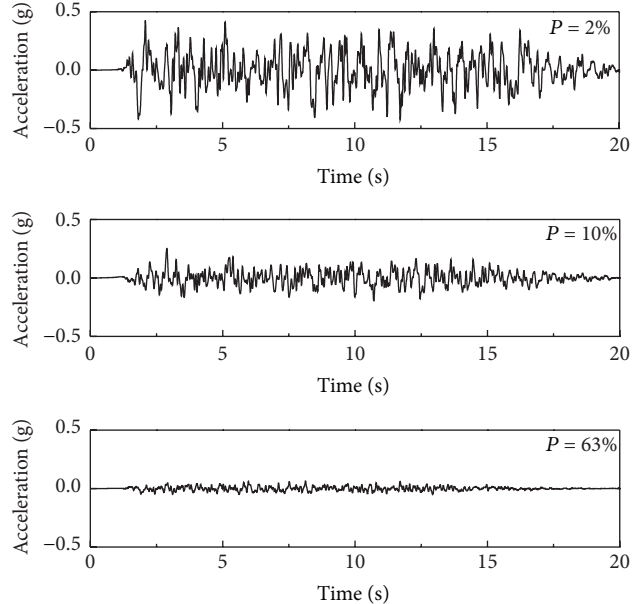


FIGURE 5: Tongmai earthquake with different exceeding probabilities.

a width of 150 m, and an initial water depth of 30 m. The simulations of earthquake-induced water waves based on the present model were then carried out with varied seismic waves at different output times, as seen in Figures 6(a)–6(f).

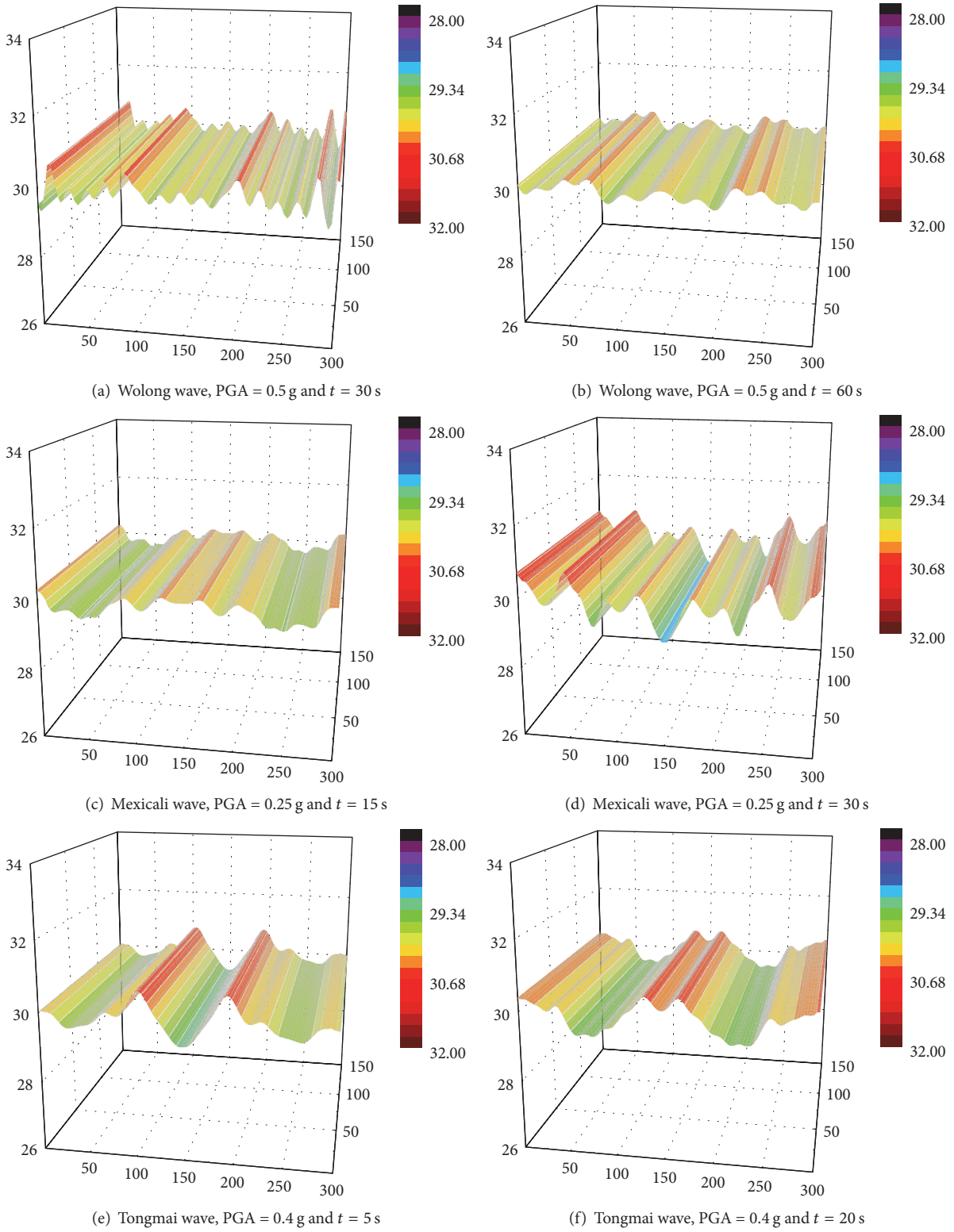


FIGURE 6: Earthquake-induced water waves with varied seismic waves at different output times.

Figures 6(a) and 6(b) show the numerical water waves at different output times ($t = 30$ and 60 s) generated by a Wolong seismic wave with a 0.5 G horizontal acceleration. It can be seen in Figure 3 that the peak value of the acceleration of the Wolong seismic wave appeared at approximately $t = 30$ s and the main quake ended at approximately $t = 60$ s. Figures 6(c) and 6(d) show the numerical water waves at different output times ($t = 15$ and 30 s) generated by a Mexicali seismic wave with a 0.25 G horizontal acceleration. It can be seen in Figure 4 that the peak value of the acceleration of the Mexicali seismic wave appeared at approximately $t = 15$ s and the main quake ended at approximately $t = 30$ s. Figures 6(e) and 6(f) show the numerical water waves at different output times ($t = 5$ and 20 s) generated by a Tongmai seismic wave with a 0.25 G horizontal acceleration. It can be seen in Figure 5 that the peak value of the acceleration of the Tongmai seismic wave appeared at approximately $t = 5$ s and the main quake ended at approximately $t = 20$ s.

By comparing the water waves generated by the three kinds of seismic waves, it can be seen that, compared to the other two seismic waves, the wavelength of water waves generated by a Wolong seismic wave is shorter, the amplitude of water waves is smaller, and the water waves generated by a Wolong seismic wave calm down faster. These numerical results are reasonable. On one hand, the dominant frequency of a Wolong seismic wave is higher than the other two. During earthquakes, water waves are generated by the shaking bank, which is a kind of forced-vibration problem, and the frequency of water waves depends on the dominant frequency of the seismic wave. On the other hand, the dominant frequencies of all of the seismic waves are higher than the natural frequencies of reservoir water, which are very low. Then, for higher excitation frequency, the amplitude of water waves is smaller and decays faster [23].

3.4. Comparison to Former Models. The value of the present model, which will be used for comparison with former models, is the maximum water elevation at the right-hand side of the rectangular tank, as shown in Figure 6. In order to obtain the calculated results of the other models, the data of seismic waves in Table 1 and (15) and (16) are used. The initial water depth varies from 20 to 40 m at intervals of 5 m. Figure 7 depicts the comparison of the maximum water elevations under varied conditions obtained in the present model, in Sato's model, and in the Demirel-Aydin model. As seen in Figure 7, the calculated values of the present model are all between the calculated results of the other two models [except in Figure 7(1)]. The results indicate that the calculated results of the present model are within the scope of the results of previous models, so the present model is reliable. The calculated results of the present model are closer to the results of the Demirel-Aydin model in most cases. This is because the present model and the Demirel-Aydin model both consider the time-history curve of an earthquake wave's acceleration and use the seismic wave data more sufficiently. However, Sato's model takes the seismic wave as a simple sine wave, may ignore more information, and could become more sensitive to the dominant frequency of an earthquake and to the PGA.

3.5. Prediction of the Maximum Water Elevation. By comparing the calculated results of the three models, it can be seen that the calculated results of the present model are closer to those of the Demirel-Aydin model in most cases. However, while the dominant frequency of an earthquake is lower, the calculated results of the present model are also close to the results of Sato's model. The Demirel-Aydin model considers that the PGV and the initial water depth are the main factors that influence the maximum water elevation of earthquake-induced water waves, while ignoring the influence of the PGA and the dominant frequency of the earthquake. Sato's model simplified the seismic wave, which may increase the influence of the PGA and the dominant frequency of an earthquake.

In this paper, the PGA, PGV, dominant frequency of an earthquake, and initial water depth are considered to be the main factors that influence the maximum water elevation of earthquake-induced water waves. As there is a significant correlation among the PGA, PGV, and the dominant frequency of an earthquake [24], the PGA, PGV, and initial water depth are finally selected as the factors influencing the maximum water elevation. The three factors can be combined into two dimensionless parameters that can be calculated as follows:

$$\begin{aligned} F &= \frac{v}{\sqrt{gh_0}}, \\ a_0 &= \frac{a}{g}. \end{aligned} \quad (17)$$

The dimensionless wave height η^+ for the maximum water elevation of earthquake-induced water waves is defined by

$$\eta^+ = \frac{\eta}{h_0}. \quad (18)$$

In Section 3.4, we described the 65 group tests with varied conditions for earthquake-induced water waves that were carried out using the present model; the calculated results for the maximum water elevations are given in Table 2.

An empirical equation can then be developed for the dimensionless wave height by means of nondimensional multiple linear regression analysis. The relationship between the dimensionless wave height and the two dimensionless factors is expressed as follows:

$$\eta^+ = 0.7305a_0^{-0.2105}F^{0.8233}. \quad (19)$$

In Figure 8, we compare the results calculated using the present model and those using (19) for the 65 group tests. The correlation coefficient between the two sets of calculated results is 0.9045 . Therefore, (19) can be used to estimate the maximum water elevation of earthquake-induced water waves if no better method is available.

4. Conclusions

In this study, a 2D SWE model was used to simulate earthquake-induced water waves. We used two former classical models to verify the accuracy and reasonability of our new

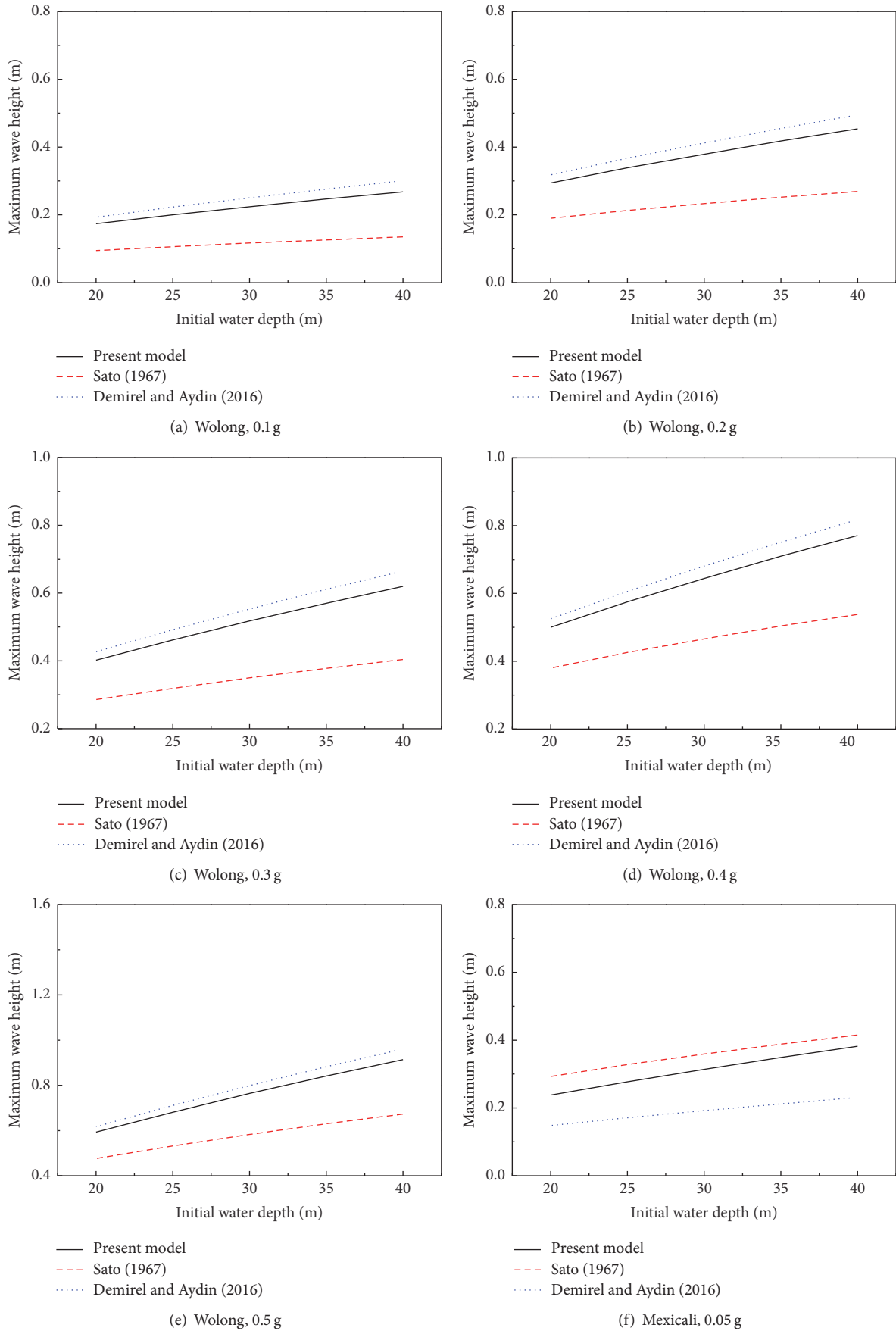
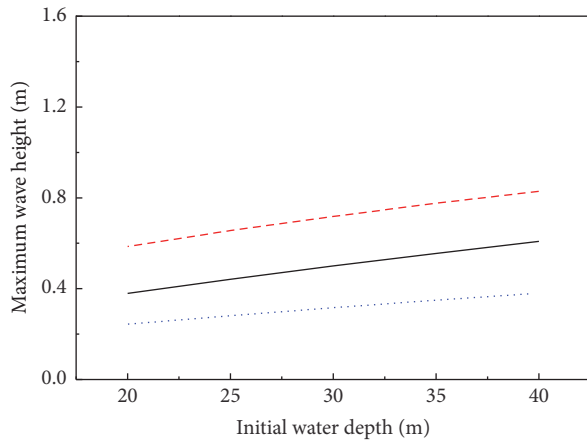
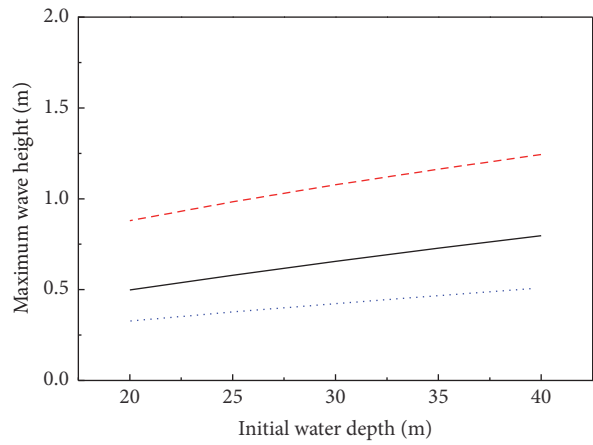


FIGURE 7: Continued.



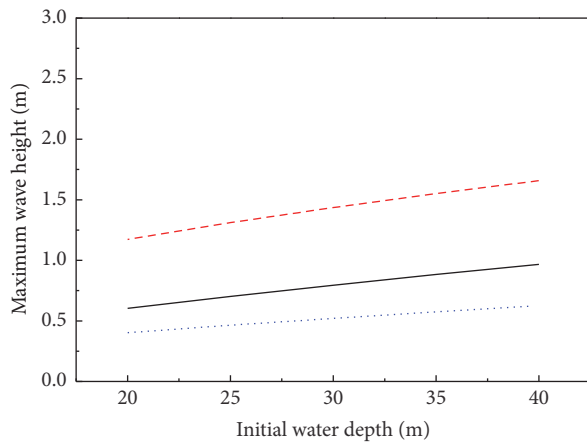
— Present model
 - - - Sato (1967)
 Demirel and Aydin (2016)

(g) Mexicali, 0.1 g



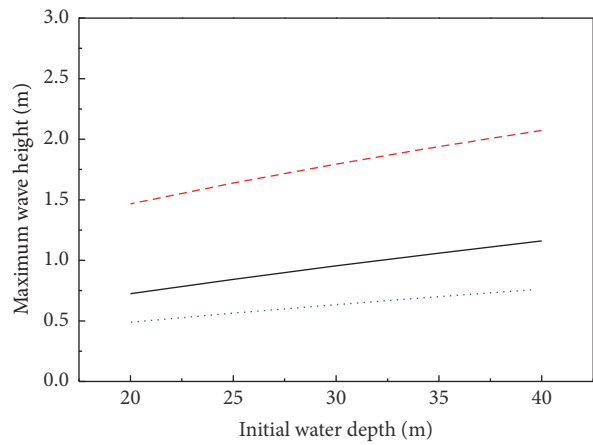
— Present model
 - - - Sato (1967)
 Demirel and Aydin (2016)

(h) Mexicali, 0.15 g



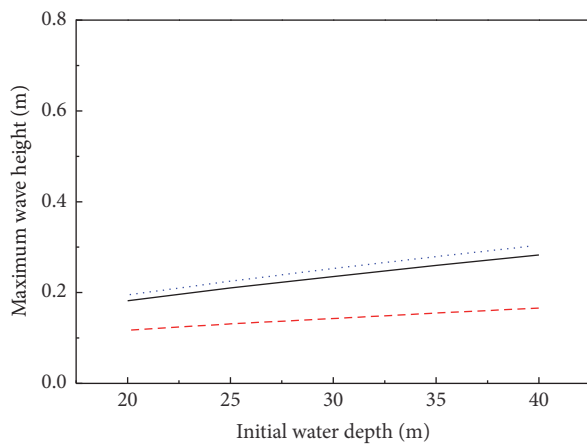
— Present model
 - - - Sato (1967)
 Demirel and Aydin (2016)

(i) Mexicali, 0.2 g



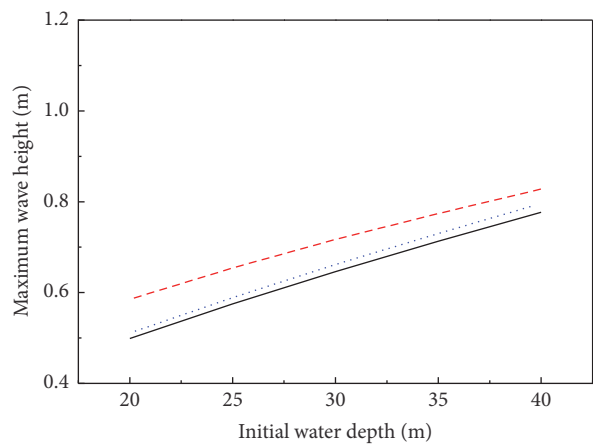
— Present model
 - - - Sato (1967)
 Demirel and Aydin (2016)

(j) Mexicali, 0.25 g



— Present model
 - - - Sato (1967)
 Demirel and Aydin (2016)

(k) Tongmai, 0.05 g



— Present model
 - - - Sato (1967)
 Demirel and Aydin (2016)

(l) Tongmai, 0.25 g

FIGURE 7: Continued.

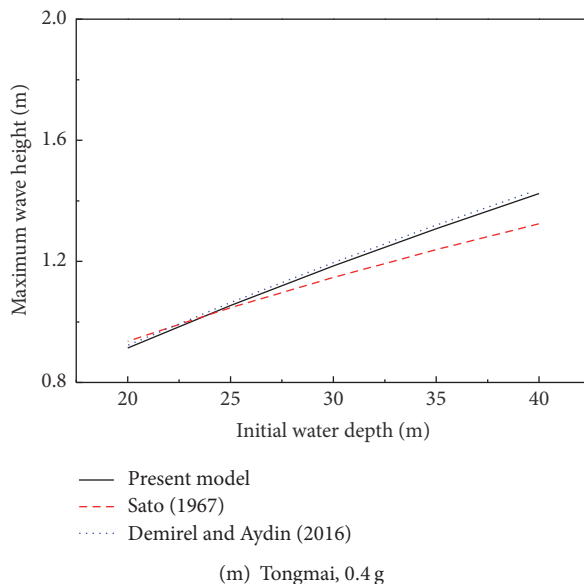


FIGURE 7: Comparison of the maximum water elevations predicted by the present, Sato, and Demirel-Aydin models.

TABLE 2: Results of the maximum water elevation calculated using the present model.

Seismic waves	PGA (g)	Initial water depth (m)				
		20	25	30	35	40
Wolong wave	0.1	0.174	0.200	0.224	0.247	0.268
	0.2	0.294	0.339	0.379	0.418	0.454
	0.3	0.402	0.462	0.518	0.570	0.620
	0.4	0.500	0.575	0.644	0.710	0.771
	0.5	0.593	0.681	0.764	0.841	0.914
Mexicali wave	0.05	0.238	0.277	0.314	0.349	0.382
	0.1	0.379	0.441	0.500	0.555	0.608
	0.15	0.498	0.579	0.656	0.728	0.797
	0.2	0.603	0.702	0.795	0.883	0.967
	0.25	0.724	0.842	0.954	1.059	1.160
Tongmai wave	0.05	0.182	0.210	0.235	0.260	0.283
	0.25	0.499	0.575	0.646	0.713	0.777
	0.4	0.914	1.054	1.185	1.308	1.424

model and drew the following conclusions from the results of our study.

(1) It can be seen from the numerical results of the present model that, for a higher dominant frequency of an earthquake, the wavelength of water waves induced by an earthquake is shorter and their amplitude is smaller and decays faster.

(2) The results calculated using the present model are within the scope of the results of previous models, which indicates that the present model is reliable. Furthermore, they are closer to results calculated using the Demirel-Aydin model in most cases. This is because the present model and the Demirel-Aydin model both consider the time-history curve of the earthquake wave's acceleration and use the seismic wave data more sufficiently.

(3) An empirical equation for the maximum water elevation of earthquake-induced water waves was developed based on the results calculated using the present model. The empirical equation selects the PGA, PGV, and initial water depth as factors influencing the maximum water elevation, which is an improvement to both Sato's and the Demirel-Aydin model.

Ultimately, we have provided a new numerical model to calculate earthquake-induced water waves, and its calculation method is reliable. An empirical equation for the maximum water elevation of earthquake-induced water waves was developed that is an improvement to the former models. Moreover, our calculation method can greatly improve preventive engineering and provide references for disaster prevention and mitigation engineering.

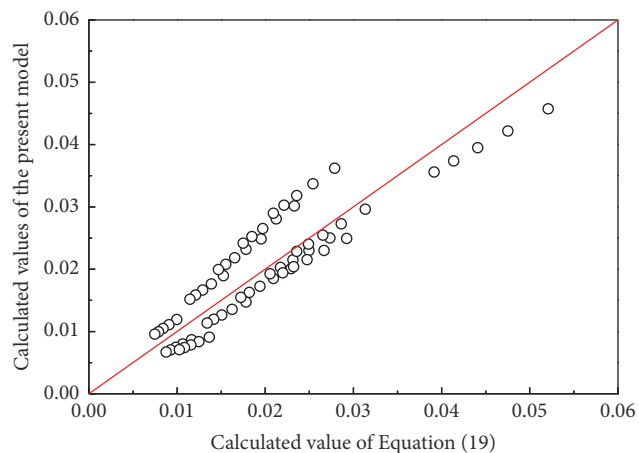


FIGURE 8: Verification of (19) for calculating maximum water elevation.

Conflicts of Interest

The authors declare that they have no conflicts of interest.

Acknowledgments

This research was supported by the National Natural Science Foundation of China (Grant no. 41571004), National Program on Key Research Project of China (Grant no. 2016YFC0802206), and Key Laboratory Foundation of Mountain Hazards and Earth Surface Processes, Chinese Academy of Sciences (Grant no. KLMHESP-17-03).

References

- [1] P. Cui, Y.-Y. Zhu, Y.-S. Han, X.-Q. Chen, and J.-Q. Zhuang, "The 12 May Wenchuan earthquake-induced landslide lakes: distribution and preliminary risk evaluation," *Landslides*, vol. 6, no. 3, pp. 209–223, 2009.
- [2] H. M. Westergaard, "Water pressures on dams during earthquakes," *Transactions of the American Society of Civil Engineers*, vol. 98, no. 2, pp. 418–432, 1933.
- [3] Q. Sato, "Seismic waves in reservoirs generated by earthquake," *Civil Engineering Materials*, vol. 9, pp. 480–482, 1967 (Japanese).
- [4] C. S. Porter and A. K. Chopra, "Hydrodynamic effects in dynamic response of simple arch dams," *Earthquake Engineering and Structural Dynamics*, vol. 10, no. 3, pp. 417–431, 1982.
- [5] K.-L. Fok and A. K. Chopra, "Water compressibility in earthquake response of arch dams," *Journal of Structural Engineering (United States)*, vol. 113, no. 5, pp. 958–975, 1987.
- [6] T.-K. Hung and B.-F. Chen, "Nonlinear hydrodynamic pressure on dams," *Journal of Engineering Mechanics*, vol. 116, no. 6, pp. 1372–1391, 1990.
- [7] B.-F. Chen, "Nonlinear hydrodynamic pressures by earthquakes on dam faces with arbitrary reservoir shapes," *Journal of Hydraulic Research*, vol. 32, no. 3, pp. 401–413, 1994.
- [8] B.-F. Chen, Y.-S. Yuan, and J.-F. Lee, "Three-dimensional nonlinear hydrodynamic pressures by earthquakes on dam faces with arbitrary reservoir shapes," *Journal of Hydraulic Research*, vol. 37, no. 2, pp. 163–187, 1999.
- [9] B.-F. Chen and Y.-S. Yuan, "Hydrodynamic Pressures on Arch Dam during Earthquakes," *Journal of Hydraulic Engineering*, vol. 137, no. 1, pp. 34–44, 2011.
- [10] C.-H. Zee and R. Zee, "Earthquake hydrodynamic pressure on dams," *Journal of Hydraulic Engineering*, vol. 132, no. 11, pp. 1128–1133, 2006.
- [11] I. Aydin and E. Demirel, "Hydrodynamic modeling of dam-reservoir response during earthquakes," *Journal of Engineering Mechanics*, vol. 138, no. 2, pp. 164–174, 2012.
- [12] E. Demirel and I. Aydin, "Numerical simulation and formulation of wave run-up on dam face due to ground oscillations using major earthquake acceleration records," *Journal of Engineering Mechanics*, vol. 142, no. 6, 2016.
- [13] O. M. Faltinsen, "A numerical nonlinear method of sloshing in tanks with two-dimensional flow," *Journal of Ship Research*, vol. 22, no. 3, pp. 193–202, 1978.
- [14] M. J. Cooker, "Water waves in a suspended container," *Wave Motion*, vol. 20, no. 4, pp. 385–395, 1994.
- [15] D. Liu and P. Lin, "A numerical study of three-dimensional liquid sloshing in tanks," *Journal of Computational Physics*, vol. 227, no. 8, pp. 3921–3939, 2008.
- [16] B. Godderidge, S. Turnock, M. Tan, and C. Earl, "An investigation of multiphase CFD modelling of a lateral sloshing tank," *Computers and Fluids*, vol. 38, no. 2, pp. 183–193, 2009.
- [17] Y. G. Chen, K. Djidjeli, and W. G. Price, "Numerical simulation of liquid sloshing phenomena in partially filled containers," *Computers and Fluids*, vol. 38, no. 4, pp. 830–842, 2009.
- [18] C. Du, L. Yao, Y. Huang, J. Yan, and S. Shakya, "Effects of seismic surge waves and implications for moraine-dammed lake outburst," *Frontiers of Earth Science*, vol. 10, no. 3, pp. 570–577, 2016.
- [19] Z.-X. Jiang, P. Cui, and L.-W. Jiang, "Critical hydrologic conditions for overflow burst of moraine lake," *Chinese Geographical Science*, vol. 14, no. 1, pp. 39–47, 2004 (Chinese).
- [20] W. Y. Tan, *Shallow Water Hydrodynamics*, Elsevier, New York, NY, USA, 1992.
- [21] Y. Zhang and P. Lin, "An improved SWE model for simulation of dam-break flows," *Proceedings of the Institution of Civil Engineers: Water Management*, vol. 169, no. 6, pp. 260–274, 2016.
- [22] Q. H. Lin, *Numerical Simulation of Sediment Transport and Morphological Evolution [Ph.D. thesis]*, National University of Singapore, Singapore, 2009.
- [23] G. X. Wu, Q. W. Ma, and R. Eatock Taylor, "Numerical simulation of sloshing waves in a 3D tank based on a finite element method," *Applied Ocean Research*, vol. 20, no. 6, pp. 337–355, 1998.
- [24] M. Brun, J. M. Reynouard, L. Jezequel, and N. Ile, "Damaging potential of low-magnitude near-field earthquakes on low-rise shear walls," *Soil Dynamics and Earthquake Engineering*, vol. 24, no. 8, pp. 587–603, 2004.

Research Article

Numerical Investigation of the FSI Characteristics in a Tubular Pump

Shuo Wang, Liaojun Zhang, and Guojiang Yin

College of Water Conservancy and Hydropower Engineering, Hohai University, Nanjing 210098, China

Correspondence should be addressed to Shuo Wang; qqwang@hhu.edu.cn

Received 18 January 2017; Revised 12 May 2017; Accepted 29 May 2017; Published 13 July 2017

Academic Editor: Haifei Liu

Copyright © 2017 Shuo Wang et al. This is an open access article distributed under the Creative Commons Attribution License, which permits unrestricted use, distribution, and reproduction in any medium, provided the original work is properly cited.

Flow condition was simulated in a shaft tubular pump by using the Shear-Stress Transport (SST) $k-\omega$ turbulence model with high quality structured grids in design condition. Corresponding structural vibration characteristics were then analyzed based on two-way coupled Fluid-Structure Interaction (FSI) method. Fluid results showed that flow in the outlet flow passage was a combination of the axial flow and circumferential rotation motion. Time and frequency domain analysis of pressure pulsation of typical measure points indicated that larger pulsation amplitudes appeared in the tip of the blades and the main vibration source was the pressure pulsation induced by rotation of the blades. The fluid pulsation amplitudes decreased gradually along the flow direction, which can be ascribed to the function of fixed guide vane. Structural analysis of the blades in both pressure and suction side indicated that significant stress concentration was formed at the blade and hub connection near the leading edge. Maximum effective stress of the blades varied periodically, so prevention measures of the fatigue of blades should be taken. This research can provide important reference for the design of the tubular pump.

1. Introduction

Rapid development of the industry and agriculture puts great demand on the water conservancy facilities, which gives rise to more pumping stations. Because of its less hydraulic loss, high efficiency, and compact structure, convenient installation, and maintenance, tubular pump, a kind of axial flow pump, presents wide popularity and development potential worldwide. Nevertheless, it is a bit difficult for the design and performance prediction of the tubular pump. Experimental model testing is one of the solutions for performance prediction but it is costly and time-consuming [1]. By contrast, numerical simulation is a powerful tool to provide information of the fluid flow behavior accurately, thus helping the scholars to obtain a thorough performance evaluation of a specific design [2–4].

Numerous CFD simulations were performed to analyze the flow features of the pump and then corresponding optimization design was provided. Jafarzadeh et al. [3] presented a general three-dimensional simulation of a high-speed centrifugal pump to predict velocity and pressure field. The optimum pumping operation was explored in terms of turbulence models and the number of blades. Shojaeefard

et al. [5] investigated the effects of the blade outlet angle and passage width on the centrifugal pump performance during the pumping of water and oil, and they found pump head and efficiency can be increased with a proper modification of the original geometry. Zhu et al. [6] applied a multiobjective optimization design system to the design of a middle-high-head pump-turbine runner and concluded that the choice of blade loading and the meridional channel shape is crucial to efficiency and operation stability. All their researches have beneficial enlightenment, but without taking the coupled effect of the fluid and solid into account, their concern is mainly the fluid feature.

Analysis of the stress distribution characteristics of a centrifugal pump was conducted in [7, 8]. Results showed that the maximum stress on the blade appeared on the pressure side near the hub, and the maximum static stress increased with the decreasing of the flow rate. However, like previously mentioned researches, they focused on the centrifugal pump, and enough importance was not attached to the axial flow pump.

Shi and Wang [9], Tang et al. [10], and Zhang et al. [11] calculated the stress and deformation of the axial impeller and

found similar law of stress and deformation distribution. But guide vanes and tip clearance were omitted for simplification in their structure simulation, which could not reflect the actual characteristics of the pump. There is tremendous need for the detailed study of the axial flow pump based on two-way coupled Fluid-Structure Interaction approach [12].

On account of the scarcities above, this research performed simulation of the actual flow in a shaft tubular pump to acquire the general features of the fluid flow and vibration characteristics of the blades in design condition. Based on two-way coupled FSI approach, a three-dimensional unified model for a shaft tubular pump was established, including the whole flow passage, the structure of the impeller, and the fixed guide vane. Analysis of flow pattern was performed using the SST k - ω turbulence model to obtain the general law in the flow passage. Time and frequency domain analysis of the fluid pressure pulsation was conducted to explore its vibration characteristics. For the structure, features of effective stress, strain, deformation, and velocity distribution in both pressure and suction sides of the blades were analyzed and the property of maximum dynamic stress was evaluated. Note that the whole calculation was performed with the commercial software ADINA.

2. Basic Theory and Method

2.1. Basic Equations. For the fluid flow analysis, the continuity equation and Reynolds-Averaged Navier–Stokes equation for an incompressible flow have been used in the following form [13]:

$$\begin{aligned} \frac{\partial u_j}{\partial x_j} &= 0, \\ \frac{\partial u_i}{\partial t} + u_j \frac{\partial u_i}{\partial x_j} &= -\frac{1}{\rho} \frac{\partial p}{\partial x_i} + \nu \frac{\partial^2 u_i}{\partial x_j \partial x_j} - \frac{\partial}{\partial x_j} (\overline{u'_i u'_j}) + f_i, \end{aligned} \quad (1)$$

where u_i is an average velocity component, and $\overline{u'_i u'_j}$ is the turbulent stress. In this research Shear-Stress Transport (SST) k - ω turbulence model proposed by Menter is used to acquire the features of unsteady flow in CFD calculation. SST k - ω turbulence model can yield more accurate and reliable results for simulating flows with adverse pressure gradient [14], flows around complex geometry [15], transonic flows [16], and so forth. Equation for SST k - ω turbulence model is expressed as follows [17–19]:

$$\begin{aligned} \rho \frac{\partial k}{\partial t} + \rho \frac{\partial}{\partial x_j} (k u_j) &= \frac{\partial}{\partial x_j} \left(\Gamma_k \frac{\partial k}{\partial x_j} \right) + \overline{G}_k - Y_k + S_k, \\ \rho \frac{\partial \omega}{\partial t} + \rho \frac{\partial}{\partial x_j} (\omega u_j) &= \frac{\partial}{\partial x_j} \left(\Gamma_\omega \frac{\partial \omega}{\partial x_j} \right) + G_\omega - Y_\omega + D_\omega \\ &\quad + S_\omega, \end{aligned} \quad (2)$$

where k and ω are turbulent kinetic and turbulence dissipation rate, respectively, \overline{G}_k is a productive term of the turbulent kinetic, G_ω is a productive term of the turbulence dissipation rate, Γ_k and Γ_ω are the effective diffusion coefficients of k and

ω , respectively, Y_k and Y_ω are the dissipation terms of k and ω , respectively, D_ω is the cross-diffusion term, and S_k and S_ω are source terms.

The fundamental conditions applied to the FSI [20] are the kinematic condition (or displacement compatibility) and the dynamic condition (or traction equilibrium), and corresponding equations are expressed in (3) and (4), respectively.

$$\underline{d}_f = \underline{d}_s, \quad (3)$$

$$n \cdot \underline{\tau}_f = n \cdot \underline{\tau}_s, \quad (4)$$

where \underline{d}_f and \underline{d}_s are, respectively, the fluid and solid displacements, and $\underline{\tau}_f$ and $\underline{\tau}_s$ are, respectively, the fluid and solid stresses. The underlining denotes that the values are defined on the fluid-structure interfaces only.

When no-slip or slip condition is applied separately, the fluid velocity condition that resulted from the kinematic condition is expressed in (5) and (6), respectively.

$$\underline{v} = \underline{\dot{d}}_s, \quad (5)$$

$$n \cdot \underline{v} = n \cdot \underline{\dot{d}}_s. \quad (6)$$

Fourier analysis is employed in vibration analysis of the pressure pulsation in fluid domain and dynamic stress in solid domain. Given a time history $f(t)$, defined from t_0 to t_1 , the Fourier series corresponding to $f(t)$ is expressed as follows:

$$f(t) = a_0 + \sum_{n=1}^{\infty} (a_n \cos n\omega_1 t + b_n \sin n\omega_1 t), \quad (7)$$

where $\omega_1 = 2\pi/t_p$, $t_p = t_1 - t_0$, $a_0 = (1/t_p) \int_{t_0}^{t_1} f(t) dt$, $a_n = (2/t_p) \int_{t_0}^{t_1} f(t) \cos n\omega_1 t dt$, $b_n = (2/t_p) \int_{t_0}^{t_1} f(t) \sin n\omega_1 t dt$.

Equation (7) could be rewritten as (8) due to sine and cosine transforms:

$$f(t) = c_0 + \sum_{n=1}^{\infty} c_n \cos(n\omega_1 t - \Phi_n), \quad (8)$$

where $c_n = \sqrt{a_n^2 + b_n^2}$, $\Phi_n = \tan^{-1}(b_n/a_n)$.

Conceptually, the function $f(t)$ is considered to contain the frequencies $0, \omega_1, 2\omega_1, \dots$. The constants c_n and Φ_n are the amplitude and phase angle of that portion of $f(t)$ which oscillates at frequency $n\omega_1$.

2.2. Numerical Model. A unified finite element model was established to analyze the coupled vibration of the pump. The fluid domain, as shown in Figure 1, is composed of inlet flow passage, an impeller chamber, a guide vane chamber, a water-guide cone, and outlet flow passage. The solid domain, as shown in Figure 2, contains impeller, guide vanes, water-guide cone, and shaft. The geometric parameters of the pump model are as follows: impeller diameter $D_2 = 3.25$ m, flow rate in design condition $Q = 30$ m³/s, rated head $H = 1.96$ m, rated rotation speed $n = 105$ rpm, and rotation frequency $f_n = 105/60 = 1.75$ Hz. The number of impeller blades is 3, and the number of guide vanes is 5. Tip clearance is

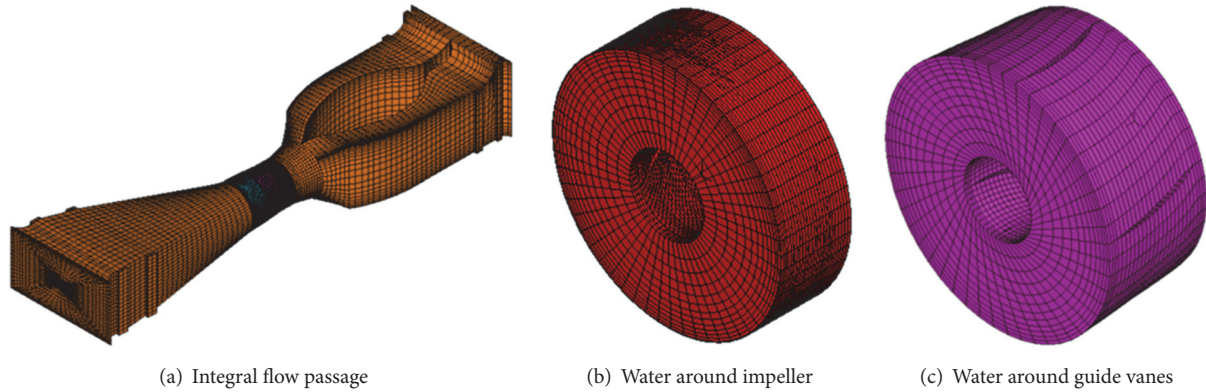


FIGURE 1: Structured grids for fluid domain.

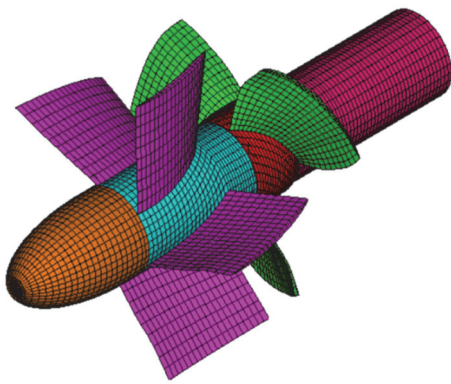


FIGURE 2: Structured grids for solid domain.

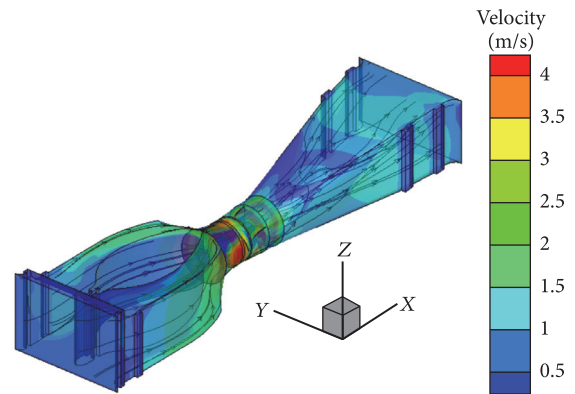


FIGURE 3: Three-dimension distribution of velocity magnitude and streamlines.

considered and the value is 5 mm. Density for fluid and solid is 1000 and 7850 kg/m³, respectively. Structured grids are chosen and designed on the basis of different topology and finer grids are applied to the rotational zone and field near the wall to ensure high-accuracy results. For most of the first cells near the wall, the y^+ values are in the variation of 30 to 500 to ensure correct utilization of the model. Mass convergence criteria are adopted in equation residual with a tolerance of 0.0001. For this study, the chosen computation is comprised of 123519 grid nodes and 106892 elements in fluid domain, including 25536 elements in inlet flow passage, 23964 elements in an impeller chamber, 15600 elements in the guide vane chamber, 16192 elements in the water-guide cone, and 25600 elements in outlet flow passage, and 24690 grid nodes and 18230 elements in solid domain, including 4680 elements in impeller, 6320 elements in guide vanes, 3000 elements in water-guide cone, and 4230 elements in shaft.

The FSI simulation is carried out in design condition with blades rotating under dynamic operation. The inlet boundary condition is set as a uniform velocity of 0.575 m/s in terms of the flow rate 30 m³/s, normal to the inlet. Fully developed turbulent flow is supposed at the outlet and outflow is defined as the outlet boundary condition. The rotational speed of 105 rpm is assigned to the impeller, where the sliding mesh boundary condition is employed to satisfy the

compatibility, continuity, and completeness conditions along the nonconforming interfaces. Wall boundary condition is imposed on the outmost layer of the flow body with no-slip velocity assumed. For the interface between fluid and structure, FSI boundary condition is assigned to make the mutual transmission of velocity and pressure.

The commercial software ADINA is adopted to study the performance of the pump under transient state in ADINA CFD module and dynamic-implicit analysis in ADINA structure module. The entire fluid domain of the pump is formed by combining the components with an interface between impeller and guide vanes. Total calculation time is set as 10 seconds to obtain reliable simulation results. There are 2000 steps calculated and the time step is 0.005 seconds.

3. Analysis of the Results

3.1. Fluid Vibration Analysis

3.1.1. Analysis of Flow Pattern. Figure 3 presents the velocity distribution band and three-dimensional streamlines in the flow passage at $t = 10$ s and Figure 4 is close look in typical sections. With steady flow pattern, there is no reflux in the inlet flow passage during the pump operation. The velocity increased greatly and the flow pattern remains steady as

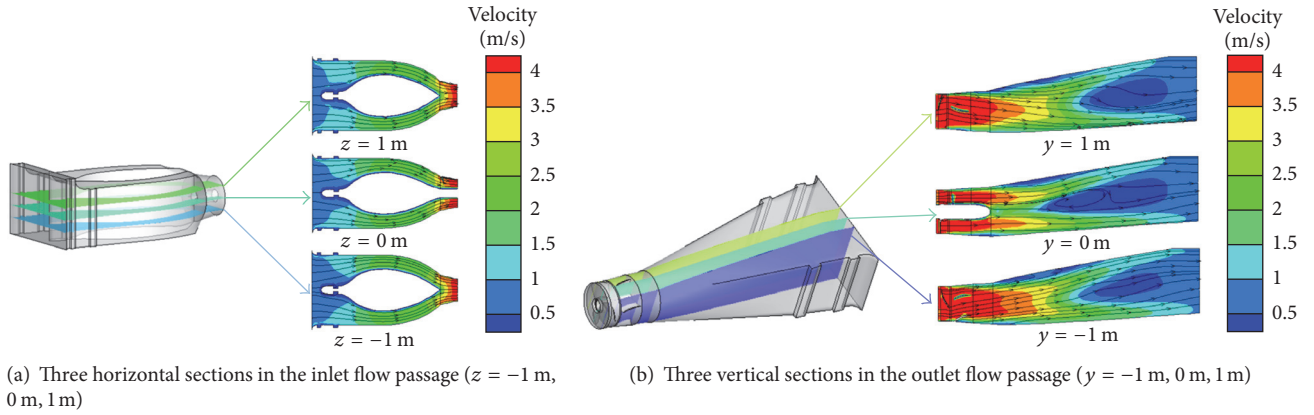


FIGURE 4: Distribution of velocity magnitude and streamlines in typical sections.

TABLE 1: First main frequency and amplitude of measure points.

Measure points	Before impeller				Between impeller and guide vanes				Behind water-guide cone			
	P11	P12	P13	P14	P21	P22	P23	P24	P31	P32	P33	P34
First main frequency (Hz)	5.25	5.25	5.25	5.25	5.25	5.25	5.25	5.25	1.50	1.50	1.50	1.50
Amplitude (Pa)	3371	3251	2437	1785	2321	2087	1383	1040	754	762	773	781

the water flows into the impeller. Although most circulation generated by the work of impeller is rectified and recovered by the fixed guide vane, there is still certain velocity circulation and reflux in the outlet flow passage, which can also be ascribed to the diffuse type of the outlet flow passage. The streamlines deflect in the outermost section and have friction with the pump casing. In total, the design of the pump flow channel is reasonable, so the stability and safety of operation can be guaranteed.

3.1.2. Analysis of Fluid Pressure Pulsation. Vibration analysis of pressure pulsation enhances both hydraulic and dynamic performance and assures safety and reliability of the pumping station. As shown in Figure 5, four measure points are chosen along the radius direction to conduct vibration response analysis in time and frequency domain, the locations of which are from blade tip to hub, respectively. The measure sections where the measure points are placed are before the impeller, between impeller and the guide vanes, and behind the water-guide cone.

Time history curves and spectrum analysis of pressure pulsation are presented in Figures 6–8 and first main frequency and amplitude are shown in Table 1. Since fluctuation of the nodal pressure remains periodically steady at about $t = 6$ s, the regularity of pressure pulsation is analyzed within the time range of $t = 6$ s to $t = 10$ s. It is clear that the pressure pulsation of the measure points at the same cross section has the similar trend. For the section before impeller, the pressure magnitude varies between 30000 Pa and 44000 Pa and increases with less amplitude from tip to hub with a dominant frequency of 5.25 Hz, shown in Figure 6(b), which equals the product of blades number 3 and rotation frequency 1.75 Hz. Pressure magnitude of the

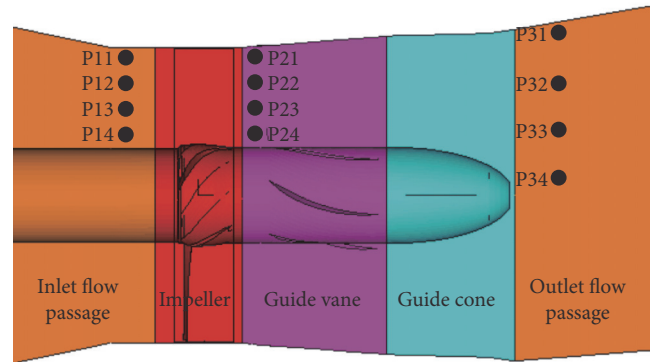


FIGURE 5: Measure point distribution in the flow passage of the pump.

measure points between impeller and guide vanes varies between 40000 Pa and 50000 Pa and has similar vibration features, which illustrates that the pulsation is mainly caused by blades rotation. For the section after water-guide cone, the pressure magnitude varies between 47000 Pa and 51000 Pa and decreases with more amplitude from tip to hub with a dominant low frequency of 1.50 Hz, illustrated in Figure 8(b).

When analyzing these measure points together, we find that the pulsation amplitudes decrease gradually along the flow direction; that is, the pressure pulsation amplitude before the impeller is larger than that between impeller and the guide vanes, and both amplitudes of them are larger than that behind the water-guide cone. Due to the

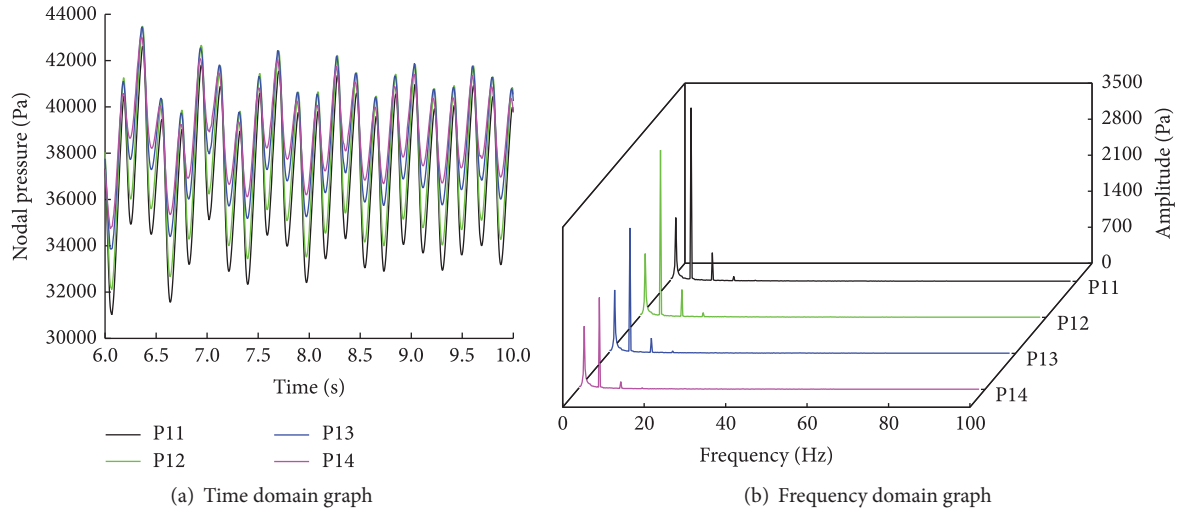


FIGURE 6: Pressure pulsation analysis of measure points before the impeller (P11–P14).

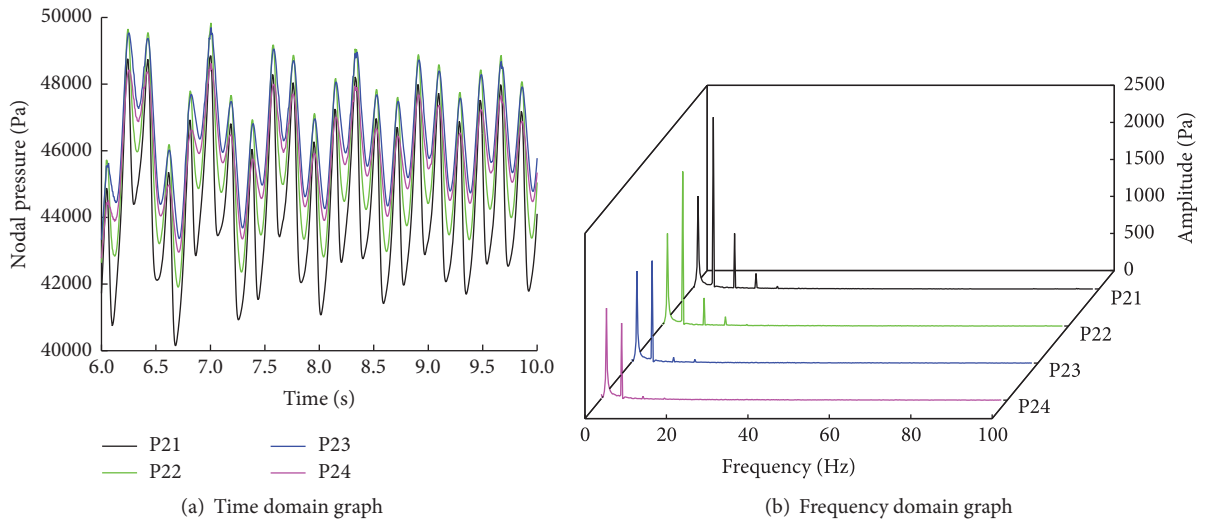


FIGURE 7: Pressure pulsation analysis of measure points between impeller and the guide vanes (P21–P24).

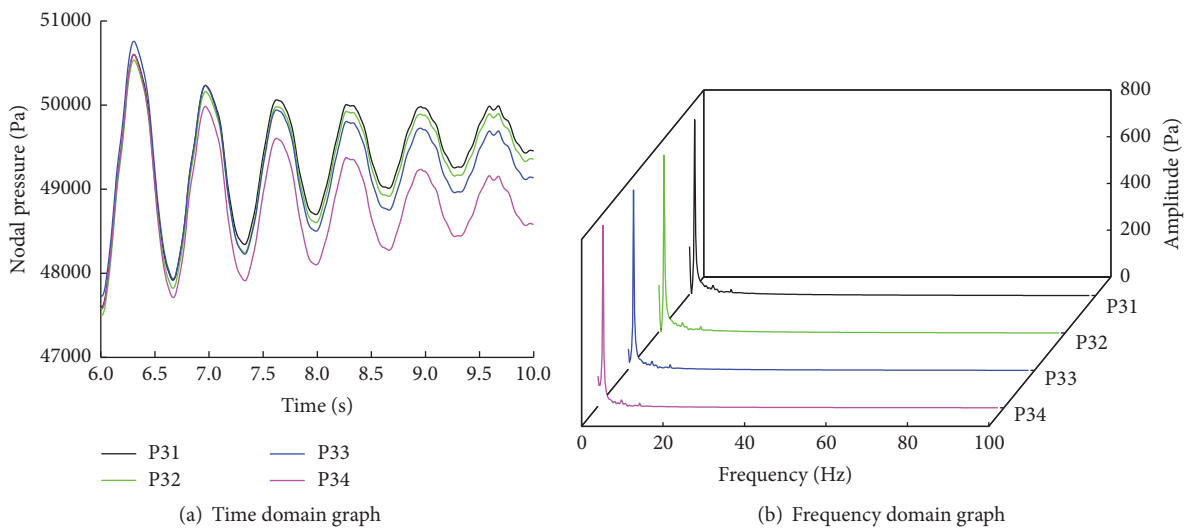


FIGURE 8: Pressure pulsation analysis of measure points behind water-guide cone (P31–P34).

TABLE 2: Main frequency and amplitude of maximum effective stress of the blades.

Frequency (Hz)	0.25	1.75	3.5	7	8.75
Amplitude (MPa)	0.19	0.43	0.25	0.17	0.12
Multiple of the rotating frequency 1.75 Hz	Low frequency	1	2	4	5

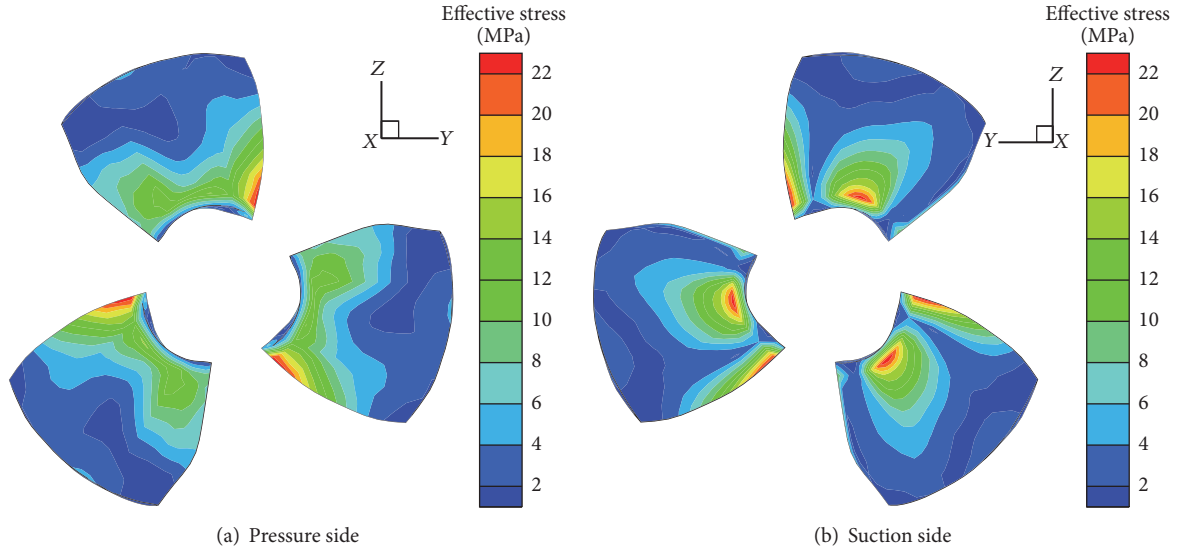


FIGURE 9: Effective stress distribution of the blades.

constraint function of the guide vanes, the pressure tends to be stable and the pulsation amplitude is greatly reduced. Great attention should be paid to the inlet of the impeller chamber in future hydraulic design as the disturbance of the blades has already existed before the water flowed into the impeller.

3.2. Structural Vibration Analysis

3.2.1. Effective Stress and Strain Analysis of the Blades. For pump design, the major mission is to analyze the structural response to the flow induced excitation and diagnose the faults early. Figure 9 shows the effective stress distribution of the blades in both pressure and suction side at $t = 10$ s in dynamic design operation. The maximum effective stress of blades is 23.59 MPa, appearing at the blade root near the leading edge. Because of the huge flow impact generated in the leading edge of the blades, the stress concentration is formed and it is prone to crack and fracture. The effective stress distribution basically declines from the joint of the blade root to the trailing edge and the tip, where the stress is much lower. Figure 10 is the corresponding strain at $t = 10$ s. The distribution of the strain is coincident with that of the stress.

3.2.2. Deformation Analysis of the Blades. Figure 11 is the deformation distribution of the blades at $t = 10$ s in dynamic design operation. The deformation magnitude augments with the increase of the radius in both pressure and suction side. On account of the larger centrifugal force, thinner thickness, and insufficient rigidity of the tip, the maximum deformation

appears at the blade tip, which is consistent with the result of the maximum effective stress distribution.

3.2.3. Velocity Analysis of the Blades. Velocity distribution of the blades at $t = 10$ s in dynamic design operation is shown in Figure 12. We can see that velocity increases gradually with the increase of radius. The maximum velocity magnitude appears at the blade tip, which is coincident with the manual calculation result; that is, $v = \omega \cdot r = 10.99 \times 1.625 = 17.86$ m/s.

3.2.4. Dynamic Stress Analysis of the Blades. Figure 13 is the time history curve and Fourier frequency analysis of maximum effective stress of the blades and Table 2 is corresponding magnitude of the main frequency and amplitude. It is clear that the maximum effective stress changes periodically as time changes, with magnitude varying between 22 and 25 MPa. Frequency analysis illustrated in Figure 13(b) and Table 2 shows that the first main frequency of the maximum effective stress is 1.75 Hz, and the corresponding amplitude is 0.43 MPa, which illustrates the periodically varying stress is mainly influenced by the rotational frequency of impeller. The static stress can not make the blades damaged because the value of maximum effective stress is much less than the limit stress of material. However, practice shows that the alternating stress could cause abrupt fracture of the structure with no significant plastic deformation before occurrence of fracture, even if the stress magnitude is much lower than the yield limit. Therefore, prevention measures of the fatigue of impeller should be taken due to the period variation of the effective stress.

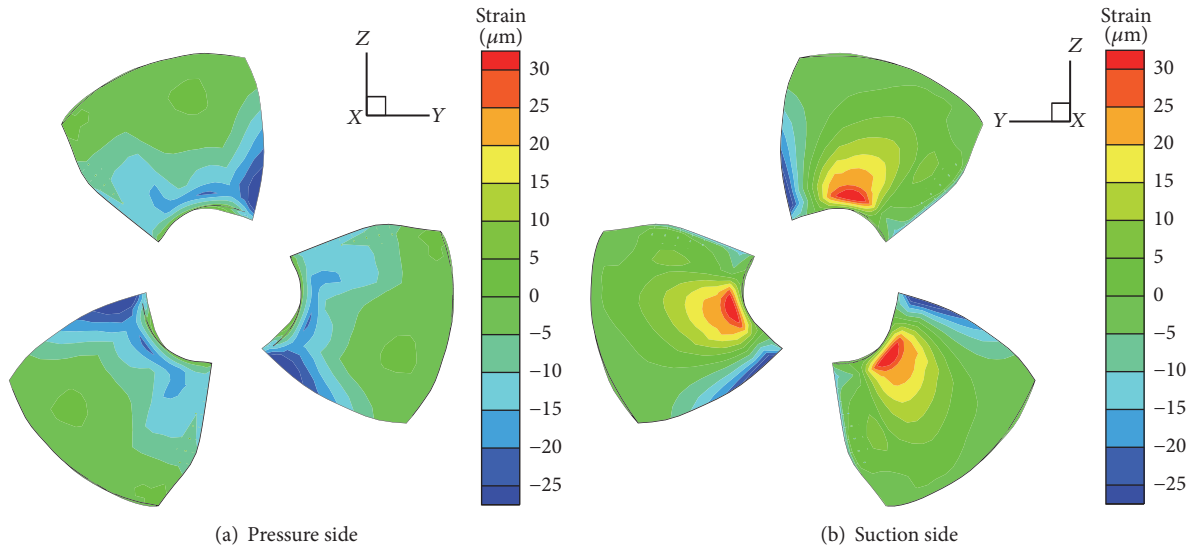


FIGURE 10: Strain distribution of the blades.

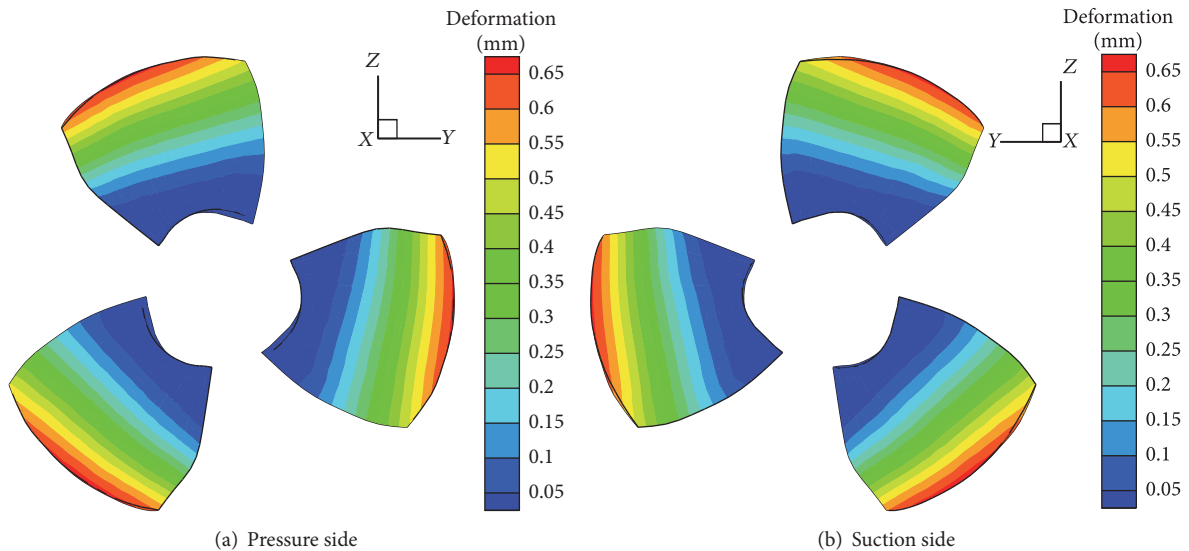


FIGURE 11: Deformation distribution of the blades.

4. Conclusion

In present investigation, numerical simulation of flow condition in a shaft tubular pump was performed and the vibration characteristics of the blades in design condition were analyzed. The numerical method was based on the SST $k-\omega$ turbulence model and the two-way coupled FSI approach under transient state. The following conclusions can be made by analysis of the results:

(1) The flow pattern is steady in the inlet flow passage in design condition. Due to the incomplete recovery of the flow circulation by the fixed guide vane and the diffusion shape of the outlet flow passage, vortex occurs in the center and the streamlines deflect in the outer section of the outlet flow passage, which illustrates that the flow in outlet flow passage is a combination of the axial flow and circumferential

rotation motion. In total, the design of the pump flow channel is rational and the stability and safety of operation can be guaranteed.

(2) Time and frequency domain analysis shows that the fluid pressure magnitude increases with less amplitude from blade tip to hub before impeller and between impeller and guide vanes with a dominant frequency of 5.25 Hz. The fluid pressure magnitude decreased with more amplitude from tip to hub after water-guide cone, and its dominant frequency is 1.50 Hz. Larger pulsation amplitudes appear in the tip of the blades, which indicates that optimizing the airfoil shape and structural parameters of the blade tip is an important way to improve the pressure pulsation condition in pump operation. The dominant frequency shows the main vibration source in fluid flow is the pressure pulsation induced by blade rotation. The pulsation amplitude decreases along the flow direction

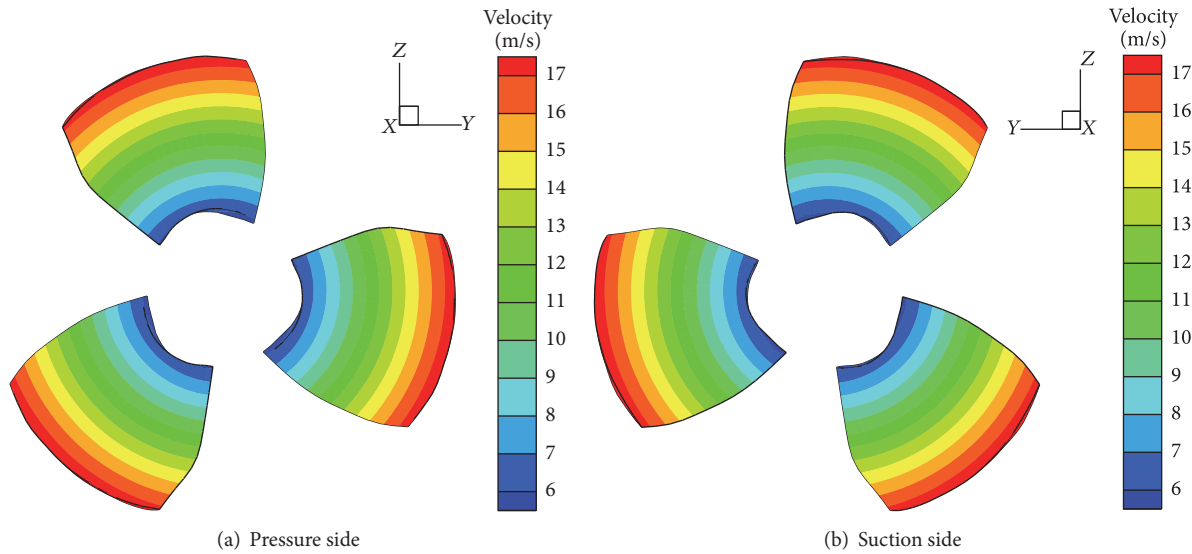


FIGURE 12: Velocity distribution of the blades.

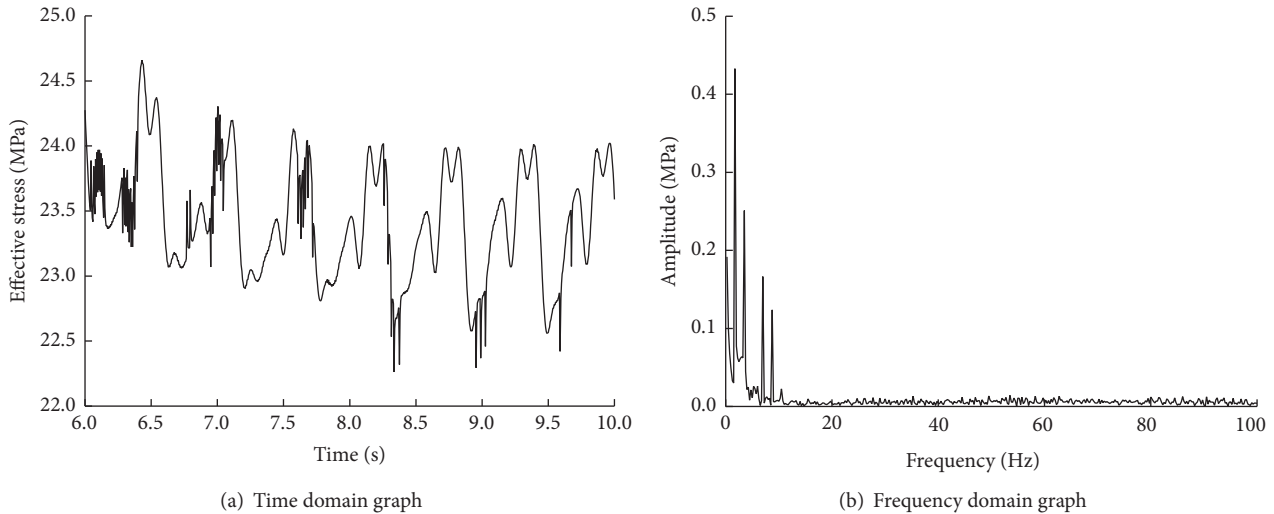


FIGURE 13: Time and frequency domain graph of maximum effective stress of the blades.

with the maximum before the impeller, which illustrates that the fixed guide vane has a function of restricting pressure pulsation and greatly improving the flow pattern in the pump.

(3) Analysis of the stress, strain, deformation, and velocity distribution of the blades is performed based on FSI. The result demonstrates that the maximum effective stress occurs between blade and hub near the leading edge, which requires the designers to attach importance to the strength check of the root. The stress at trailing edge and the tip is comparatively smaller, which is coincident with the result of strain. The tip has maximum deformation, which is prone to friction damage of the blade tip and pump casing because of the tiny clearance between them. Maximum velocity occurs at the tip, which is coincident with the manual calculation results. Although the value of maximum effective stress is much less than the yield limit, prevention measures of the fatigue of

impeller should be taken due to the period variation of the effective stress.

Conflicts of Interest

The authors declare that they have no conflicts of interest.

Acknowledgments

This work was supported by the Priority Academic Program Development of Jiangsu Higher Education Institutions.

References

- [1] S. R. Shah, S. V. Jain, R. N. Patel, and V. J. Lakhera, "CFD for centrifugal pumps: A review of the state-of-the-art," in *Proceedings of the 3rd Nirma University International Conference*

- on *Engineering*, *NUiCONE 2012*, pp. 715–720, ind, December 2012.
- [2] L. Deyou, W. Hongjie, X. Gaoming, G. Ruzhi, W. Xianzhu, and L. Zhansheng, “Unsteady simulation and analysis for hump characteristics of a pump turbine model,” *Renewable Energy*, vol. 77, pp. 32–42, 2015.
- [3] B. Jafarzadeh, A. Hajari, M. M. Alishahi, and M. H. Akbari, “The flow simulation of a low-specific-speed high-speed centrifugal pump,” *Applied Mathematical Modelling*, vol. 35, no. 1, pp. 242–249, 2011.
- [4] H.-J. Choi, M. A. Zullah, H.-W. Roh, P.-S. Ha, S.-Y. Oh, and Y.-H. Lee, “CFD validation of performance improvement of a 500 kW Francis turbine,” *Renewable Energy*, vol. 54, pp. 111–123, 2013.
- [5] M. H. Shojaeefard, M. Tahani, M. B. Ehghaghi, M. A. Fallahian, and M. Beglari, “Numerical study of the effects of some geometric characteristics of a centrifugal pump impeller that pumps a viscous fluid,” *Computers and Fluids*, vol. 60, pp. 61–70, 2012.
- [6] B. Zhu, X. Wang, L. Tan, D. Zhou, Y. Zhao, and S. Cao, “Optimization design of a reversible pump-turbine runner with high efficiency and stability,” *Renewable Energy*, vol. 81, pp. 366–376, 2015.
- [7] F. F. Hu, T. Chen, D. Z. Wu, and L. Q. Wang, “Computation of stress distribution in a mixed flow pump based on fluid-structure interaction analysis,” in *Proceedings of the 6th International Conference on Pumps and Fans with Compressors and Wind Turbines, ICPF 2013*, chn, September 2013.
- [8] J. Pei, S. Yuan, and J. Yuan, “Dynamic stress analysis of sewage centrifugal pump impeller based on two-way coupling method,” *Chinese Journal of Mechanical Engineering (English Edition)*, vol. 27, no. 2, pp. 369–375, 2014.
- [9] W. Shi and G. Wang, “Finite element computation for impeller of axial-flow pump based on fluid-structure interaction,” in *Proceedings of the 2nd Annual Conference on Electrical and Control Engineering, ICECE 2011*, pp. 3935–3938, chn, September 2011.
- [10] X. Tang, Y. Jia, F. Wang et al., “Turbulent flows in tubular pump and fluid-structure interaction characteristics of impeller,” *Paiguan Jixie Gongcheng Xuebao/Journal of Drainage and Irrigation Machinery Engineering*, vol. 31, no. 5, pp. 379–383, 2013.
- [11] X. Zhang, Y. Zheng, X. Mao, W. U. Zaiqiang, K. Kan, and T. Mou, *Strength Analysis of Axial Flow Pump Impeller Based on Fluid Solid Coupling*, Water Resources Power, 2014.
- [12] C. Trivedi and M. J. Cervantes, “Fluid-structure interactions in Francis turbines: A perspective review,” *Renewable and Sustainable Energy Reviews*, vol. 68, pp. 87–101, 2017.
- [13] F. R. Menter, “Two-equation eddy-viscosity turbulence models for engineering applications,” *AIAA journal*, vol. 32, no. 8, pp. 1598–1605, 1994.
- [14] J. Li, C. Zhong, D. Pan, and C. Zhuo, “A gas-kinetic scheme coupled with SST model for turbulent flows,” *Computers and Mathematics with Applications*, 2016.
- [15] S. J. Kim, J.-S. Jung, and S. Kang, “Fully three-dimensional Reynolds-averaged Navier–Stokes modeling for solving free surface flows around coastal drainage gates,” *Journal of Hydro-Environment Research*, vol. 13, pp. 121–133, 2016.
- [16] J. Gao, Q. Zheng, X. Niu, and G. Yue, “Aerothermal characteristics of a transonic tip flow in a turbine cascade with tip clearance variations,” *Applied Thermal Engineering*, vol. 107, pp. 271–283, 2016.
- [17] F. Menter, “Zonal Two Equation k-w Turbulence Models For Aerodynamic Flows,” in *Proceedings of the 23rd Fluid Dynamics, Plasmadynamics, and Lasers Conference*, Orlando, FL, U.S.A..
- [18] F. R. Menter, M. Kuntz, and R. Langtry, Ten years of industrial experience with the SST turbulence model, Turbulence..
- [19] F. R. Menter, *Review of the shear-stress transport turbulence model experience from an industrial perspective*, Taylor Francis, Inc, 2009.
- [20] S.-h. Wei and L.-j. Zhang, “Vibration analysis of hydropower house based on fluid-structure coupling numerical method,” *Water Science and Engineering*, vol. 3, pp. 75–84, 2010.